FINAL TECHNICAL REPORT

PRECISION POINTING CONTROL SYSTEM

13900-6012-R0-01

1 JULY 1972

PPCS SYSTEM DESIGN AND ANALYSIS

Contract No. NAS5-21111

Prepared for

NATIONAL AERONAUTICS AND SPACE ADMINISTRATION
GODDARD SPACE FLIGHT CENTER
Greenbelt, Maryland 20771

TRW
SYSTEMS GROUP

ONE SPACE PARK • REDONDO BEACH, CALIFORNIA 90278

REPORT 13900-6012-R0-01

FINAL TECHNICAL REPORT
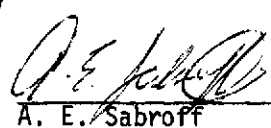
PPCS SYSTEM DESIGN AND ANALYSIS

1 JULY 1972

Prepared by: A. M. Frew
D. F. Eisenhut
R. L. Farrenkopf
R. F. Gates
R. P. Iwens
D. K. Kirby
R. J. Mann
D. J. Spencer
H. S. Tsou
J. G. Zaremba

Approved by: _____
D. K. Kirby
Project Manager

Approved by: _____
A. E. Sabroff
Manager
Control & Sensor Systems Laboratory

iii

PRECISION POINTING CONTROL SYSTEM
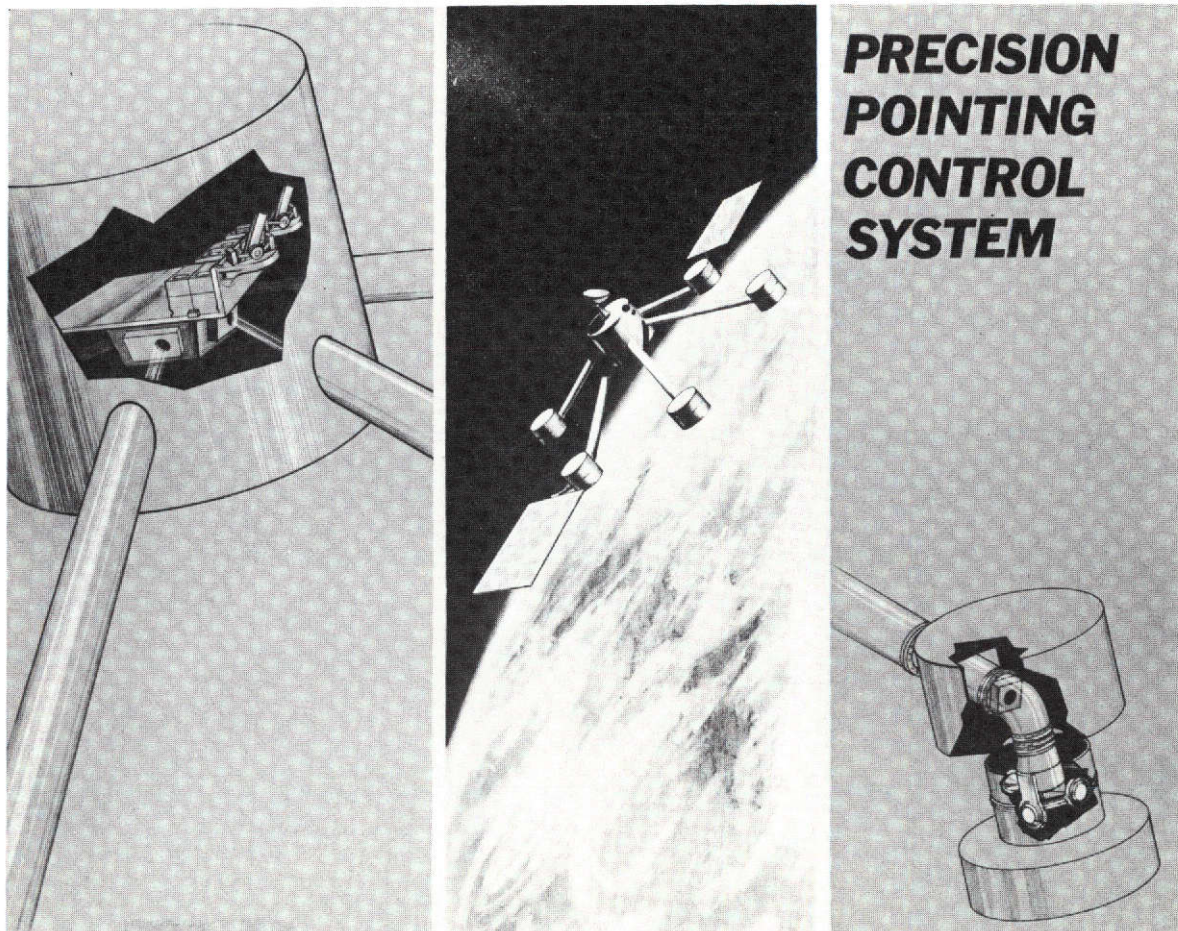
Frontispiece: Artist's Concept of PPCS

TABLE OF CONTENTS.

TABLE OF CONTENTS (Cont'd)

TABLE OF CONTENTS (Cont'd)

LIST OF FIGURES

LIST OF FIGURES (Cont'd)

LIST OF FIGURES (Cont'd)

LIST OF FIGURES (Cont'd)

LIST OF FIGURES (Cont'd)

LIST OF TABLES

LIST OF TABLES (Cont'd)

1.0 INTRODUCTION

The past decade has seen a steady increase in the degree of orientation pre-
cision required by space missions. This growth in precision will continue during
the Seventies, leading to a significant number of spacecraft payloads requiring
attitude determination and control accuracies in the one-to-ten arcsecond region.
In response to this projected requirement, TRW Systems and NASA/Goddard Space Flight
Center have pursued development of the requisite technology through the Precision
Pointing Control System (PPCS) program under Contract NAS5-21111.

The Precision Pointing Control System (PPCS) is an integrated system for
precision attitude determination and orientation of gimbaled experiment platforms.
The PPCS concept developed within NASA [1] configures the system to perform
orientation of up to six independent gimbaled experiment platforms to design goal
accuracy of 0.001 degrees (1σ, per axis). This system operates in conjunction with
a three-axis stabilized earth-oriented spacecraft in orbits ranging from low altitude
(200-2500 n.m., sun synchronous) to 24 hour geosynchronous, with a design goal life
of 3 to 5 years.

Characteristic of such a system are two complementary functions, namely:

- <u>Attitude Determination</u> - the attitude of a defined set of body-fixed
  reference axes is determined relative to a known set of reference
  axes (generally) fixed in inertial space.

- <u>Pointing Control</u> - gimbal orientation is controlled open-loop
  (without use of payload error/feedback) with respect to a defined
  set of body-fixed reference axes to produce pointing to a desired
  target.

This functional dichotomy is noted, in that the pointing function may be quite
mission dependent while development of a precision attitude determination approach
will have more universal applicability.

The requirements for PPCS are designed primarily to support the scientific/
experimenter user community. Action was thus taken during the study to have a ques-
tionnaire broadly distributed to this user community describing the precision atti-
tude determination and pointing control concept being studied and seeking responses
designed to identify potential users. Distribution was made in October 1970 to 168
members of the scientific and engineering community and over 50 replies have been
received. The prepared package and a summary of the replies are given in Appendix A.

The main points observed include:

- Most applications call for three-axis stabilization.

- Orbits range from low altitude to highly eccentric to geosynchronous
  to interplanetary.

- A variety of projected applications require arcsec performance levels.

- Most applications specify both pointing control and attitude determination.

Typical of the projected applications are the following mission-related examples:

- On-board precision attitude determination and control is required for successful operation of a spacecraft payload. An example is the use of PPCS to command point a precision gimbaled payload (e.g., a very high resolution camera) in the absence of a payload-developed error signal (i.e., no autotracking capability).

- On-board precision attitude data is required to augment the operational utility of the spacecraft payload equipment. For instance, PPCS data can be used to point a tracking payload (e.g., a large space telescope)to within the acquisition field of its internal boresight tracker, thus eliminating acquisition/search requirements.

- Off-line precision attitude data is required to support operational payload data evaluation and utilization. An obvious example is the use of PPCS data to simplify evaluation of data from a line scanning device (e.g., a wide angle high-resolution radiometer with a long exposure time); the alternative, reconstruction using landmark data and sophisticated software, may represent a significant cost and operational disadvantage.

As noted, the application of precision attitude determination and control will vary from mission to mission; nonetheless, a single system can be designed such that essential elements meet virtually all requirements without compromise. By recognizing the varied requirements, PPCS has been configured modularly to make best advantage of the ultimate usage. Further, the system design approach has been made applicable to an even broader range of missions, orbits, and spacecraft configurations than had originally been considered.

This report documents the PPCS design and development program. This program is directed toward developing system concepts, hardware and software designs capable of the required performance, and verification of performance through simulation and, in some cases, through test. Development activities are outlined as follows:

- A complete system design capable of meeting all PPCS objectives was defined. Analyses sufficient to demonstrate feasibility of the design were performed.

- Each hardware element (except gyros and computer) was defined to the point where further development requires engineering model fabrication.

- Software associated with attitude determination and experiment pointing was developed. Other software elements were defined conceptually.

- The system, and related hardware and software, was studied through simulation of attitude determination and pointing control and by error analysis.

- The star tracker was built and tested.

This report is the final design report and, as appropriate, incorporates work documented earlier [2-5]. Initially presented is a summary of the overall PPCS system and the key design considerations. Detailed system design is described through the functional and operational characteristics of the system, design definition and requirements allocation for system hardware, and definition of system interfaces. The system analysis details the overall development of the system equations, error analysis, reliability analysis, and observability analysis. Design and performance analysis documents the analysis and simulation efforts which are keyed to more specific performance and design considerations. The work and results discussed make extensive use of the comprehensive attitude determination and pointing simulations developed for PPCS [6-11]. This is followed by an extensive development of each of the hardware assemblies and software, keyed toward the appropriate functional designs. Detailed PPCS engineering model hardware design is documented elsewhere [12].

2.0 SUMMARY

The preliminary design of a Precision Pointing Control System (PPCS) has been developed. This design provides the capability to achieve precision on-board attitude determination and pointing control of multiple gimbaled platforms independently mounted on a carrier spacecraft. The system performs four basic functions, namely:

- Attitude Determination - establish celestial/inertial orientation
- Alignment Reference - measure non-integral reference alignment
- Experiment Pointing - command point (open-loop) gimbal mounted experiments
- Antenna Pointing - command point (or autotrack) antenna gimbal.

2.1 SYSTEM DESIGN

PPCS hardware and software elements are shown in Figure 2-1. For attitude determination, gyros are utilized to maintain inertial attitude and a gimbaled star tracker provides the source of periodic attitude updates. Alignment reference is provided by three-axis autocollimator measurements. A stable mechanical reference is provided for integral mounting of the star tracker(s), gyros, and autocollimators. Experiment pointing is achieved with a precision three-axis gimbal system; antenna pointing with an accurate two-axis gimbal system. The software required for implementing these functions in PPCS is summarized, where the processing is accomplished using an on-board computer whose interface to the sensors and actuators is through a data bus.

The system has the capability of providing one-sigma gimbal pointing accuracies in each axis of better than 0.001 degree (3.6 $\widehat{sec}$) and three-axis attitude determination errors of less than 4 $\widehat{sec}$ (1σ). Error growth between star tracker attitude updates is characteristic due to errors in propagating attitude using the gyros. The use of the gimbaled star tracker provides capability to minimize the effects of this error by selection of the period between updates. Important systematic errors are observable and are compensated for within the system, providing performance limited only by the dynamic (random) error sources. The PPCS system error budget is shown in Figure 2-2. The accuracies achievable with the developed hardware and software designs meet or exceed these budget requirements in all cases.

PPCS hardware assemblies are configured in modular form to take advantage of a partitioned standby redundancy approach using lower failure rate sub-elements to achieve 3 to 5 year life. Thus a flexible configuration results with elements which can, in most cases, be completely cross-strapped with multiple redundancy. With this in mind, PPCS assembly power, weight, and size are shown in Table 2-1. The assemblies as shown, except for the computer and data interface, represent non-redundant ("Simplex") units. For such a "simplex" system, the attitude determination

REFERENCE BLOCK ASSEMBLY

STAR TRACKER ASSEMBLY

PPCS FLIGHT SOFTWARE

EXECUTIVE	1700
ATTITUDE REFERENCE	2120
POINTING CONTROL	775
SUBROUTINES	375
DATA BASE	650

EXPERIMENT GIMBAL ASSEMBLY

DIGITAL COMPUTER ASSEMBLY

EXPERIMENT ELECTRONICS ASSEMBLY

SENSOR ELECTRONICS ASSEMBLY

DATA INTERFACE ASSEMBLY

ANTENNA ELECTRONICS ASSEMBLY

GYRO REFERENCE ASSEMBLY

ALIGNMENT SENSOR ASSEMBLY

ANTENNA GIMBAL ASSEMBLY

Figure 2-1, PPCS System Block Diagram
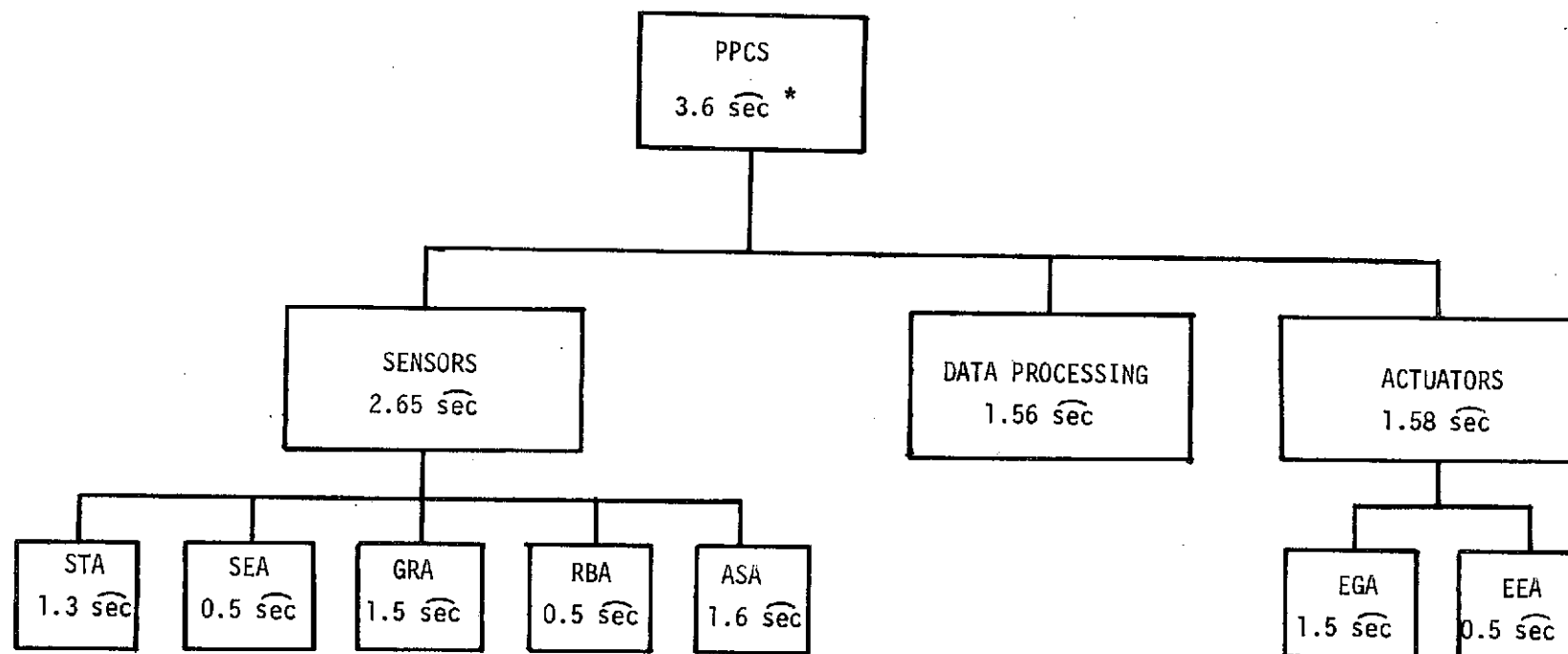
* ALL ERRORS ARE SINGLE-AXIS, 1σ

3.6 sec = 0.001 deg

Figure 2-2. PPCS System Error Budget

Table 2-1. Summary of PPCS Hardware Characteristics

Assembly	Weight (ea)	Size (ea)	Power (ea)
Star Tracker	39	22x16x17	17
Sensor Electronics	6	8x11x6	15
Gyro Reference (TRIAD)	9	6x6x5	15(Unheated)
Alignment Sensor	28	(2) 5x5x10	7.5
Reference Block	Spacecraft/Configuration Dependent (30-120 lbs)		--
Experiment Gimbal	75	33x27x28	30
Experiment Electronics	11	8x16x6	20
Antenna Gimbal	15	12x5x7	2
Antenna Electronics	2	3x8x6	6
Digital Computer*	32	8x17x6	28
Data Interface *	8	6x6x5	10

* Internally redundant.

function (excluding computer and reference block) requires 54 pounds and 47 watts. Each experiment utilized (simplex, including alignment sensor) requires an additional 114 pounds and 58 watts. Additional redundancy is added as appropriate (using modular sub-elements) to achieve particular reliability goals.

2.2 DESIGN DEVELOPMENT HIGHLIGHTS

This section highlights the important design considerations and tradeoffs with respect to system configuration, hardware implementation, and software/algorithm design. The key decision made in configuring the system is, of course, the selection of a gimbaled star tracker. This choice follows directly from basic system objectives namely: development of a system design which will accommodate the full range of orbit from low altitude sun synchronous to geosynchronous, and beyond. Selection of the gimbaled tracker offers an additional advantage - a system which can operate aboard fully stabilized spececraft whose attitude reference is either earth-oriented, sun-oriented, or inertial. Although PPCS is only required to operate on a three-axis stabilized earth pointing vehicle, the additional capability is of importance because of the potential varied missions to which PPCS may have application. It is noted that a system using star mappers on a low altitude earth-oriented spacecraft has been developed [13,14]. However, restrictions are placed upon the inertial motion (and hence altitude in earth-stabilized applications) of the carrier spacecraft.

Detailed design tradeoffs associated with specific elements of the system are described in the following sections. However, it is worth commenting briefly on the overall approach to mission versatility (modularity) and redundancy management to obtain mission lifetimes on the order of 3 to 5 years. PPCS is characterized by stringent performance goals and multiple functions which are necessarily complex. Traditional redundancy approaches have been to duplicate hardware at the assembly level, using the first unit until failure and then switching to the second. With complex assemblies, sometimes a third or fourth unit must be added to achieve the required reliability. This approach is not efficient in that reliability increase per pound (or dollar) of added hardware is low. The PPCS approach implements re-dundancy within assemblies at a functional level, achieving simple interfaces between redundant units and high reliability growth per pound (or dollar) of added hardware.

The functional redundancy approach has the added advantage of permitting great flexibility in tailoring a basic design to a particular reliability requirement. This is particularly important in electronic assemblies whose reliability requirements vary with mission and application. Similarly, mission versatility is achieved through modularity of hardware and software elements, thus providing considerable configuration freedom.

2.2.1 Star Tracker and Electronics

A gimbaled star tracker was developed which provides measurement to accuracies

2-5

on the order of 1 sec. The tracker consists of a telescope/sensor mounted within a two-degree-of-freedom gimbal set of unique design. The choice of detector was a basic decision having considerable impact on the ultimate tracker configuration and performance. Available choices considered include image dissector tubes, photomultiplier tubes (smaller version of dissector), and solid state detectors. Early studies showed that each could provide the required sensitivity with similar signal to noise ratios. However, solid state detectors did not have a history of space flight to demonstrate their performance. On the other hand, considerable successful flight history exists for image dissector type detectors (notably OAO). On this basis, a tube detector was selected.

To achieve ultimate accuracy, it seemed obvious that null operation of the detector was best. Early studies (later confirmed by tracker tests) indicated that servo control of the gimbals to a few arc seconds was reasonably straightforward, so null operation appeared feasible. The photomultiplier tube was, therefore, selected since it is smaller than the image dissector and is designed for null sensing, while the dissector is designed for off null operation.

Selection of an optical design involves choosing a focal length/mechanical package combination which can achieve sub-arc-second stability. Material mechanical stability, as well as thermal considerations, arise. The effect of detector motion can be minimized by selection of longer focal lengths - electronics errors also are minimized by this process. However, thermal bending of the longer telescope becomes more of a problem, and the size and weight penalties are apparent.

The goal was to choose a focal length which allows for sufficient thermal/mechanical motion while not unduly affecting size and weight. A 100 inch focal length was selected which allows less than 500 μinch lateral motion at the detector per arc sec of error. Test and thermal analysis results on this design show that it is, in fact, overly conservative. Based on these results, it appears that a shorter focal length design would satisfy PPCS requirements, with a possible attendant weight reduction. This latter design has, in fact, been pursued subsequently [15].

Two concepts for gimbal bearings were examined - conventional high precision ball bearings and a unique single-ball bearing where a single ball at each end of the shaft suspends the load. The single ball concept uses a sliding contact between the stationary ball and the rotating retainer - as a result, friction is higher than for the normal ball bearing. However, greater precision can be achieved, since bearing noise caused by ball-to-ball irregularities is eliminated also. The single ball concept is simpler, since the only precision components are the ball and the retainer. Servo and torque motor problems caused by the high friction proved relatively easy to solve, so the single ball approach was selected.

2-6

Another major decision was selection of the gimbal angle encoder. The choice here narrowed to Inductosyns or optical encoders. Inductosyns are functionally similar to multispeed resolvers, having an excitation winding and a sine-cosine pair of output windings. The windings are printed conductors imbedded on the faces of two discs which are arranged to rotate coaxially with their faces in close proximity. Multispeed winding patterns up to 360 speed and disc sizes from 3-12 inches in diameter are available. Repeatability to fractional arc seconds can be achieved with the six inch size - better repeatability can be achieved with larger sizes. Comparable accuracy does not appear achievable with optical encoders of comparable diameter, so the 6 inch inductosyn was selected for the encoder. An initial drawback to the approach appeared to be the electronics required to process the outputs to obtain the required resolution. Approaches to this problem were developed, however, which provide relatively simple encoding electronics with fractional arc second resolution.

2.2.2 Gyro Reference

An assembly of single-degree-of-freedom, gas bearing rate integrating gyros are used to measure short-term vehicle dynamic motion.

The fundamental gyro reference decisions related to configuration development for redundancy/performance and choice of the gyro rebalance loop. The choice of rebalance loop is whether to use a pulse technique or an analog rebalance with A/D conversion. From a performance viewpoint, pulse torquing is favored when high input rates are expected, since (in theory at least) only certain specific operating points on the torquer response characteristic are used, and torquer nonlinearity effects are minimized. A further consideration of high rates is torquer power sensitivity - a pulse rebalance technique permits constant torquer power, while analog does not. However, PPCS rates are reasonably small and the error terms above are, therefore, not significant. High frequency (>1 Hz) errors caused by electronics would initially appear harder to control in a pulse system - however, the analog loop uses demodulators, etc., and cannot be entirely free from unwanted noise. A strong case for which approach is best to minimize high frequency noise hasn't been established. These considerations indicate that from a performance point of view, either approach can satisfy PPCS requirements.

Gyro interchangeability appears easier with an analog approach. The gyro torquer is somewhat nonlinear and does have some nonlinear response to the harmonic content of a pulse rebalance train. This effect can (and is) minimized by careful control of torquer parameters and sometimes by optimizing the electronics/gyro interface. These considerations indicate that to assure interchangeability of gyros the analog approach is best. Primarily on this basis, the analog approach was selected for PPCS. Note, however, that either mechanization, if properly done, will satisfy PPCS performance requirements.

2-7

A gas bearing gyro was selected to avoid life limitations of ball bearings. A number of minature gas bearing gyros with PPCS level performance exist - the Nortronics GI-K7G was selected. This unit has a ceramic hydrodynamic gas spin bearing operating in a beryllium float. A taut wire suspension system is used.

The packaging configuration for the Gyro Reference Assembly is primarily a function of the mission life requirements. For a non-redundant configuration, three gyros mounted orthogonally in one package minimizes size and weight. For redundant configurations, a two gyro package used as a building block seems to be a reasonable compromise in size and weight. The gyros can be arranged in either orthogonal or non-orthogonal configurations, depending on the redundancy operating policy. Independent electronics are provided for each gyro. The PPCS baseline configuration uses a dodecahedron arrangement, with four of the six gyros operating.

2.2.3 Alignment Sensor

The alignment sensor was designed for PPCS by Barnes Engineering under sub-contract to TRW [16]. Three-axis information is provided by nulling the measured reflection of a collimated beam using rotating optical wedges and measuring the wedge rotation relative to the alignment sensor reference frame.

In order to measure the respective angles with an accuracy of 1 or 2 sec over a range of 0.5 degree, a null measuring system is a necessity, since no off-null measuring method is known in which the problems of light source intensity stability, detector uniformity and stability, and dozens of other potential problems can be controlled to that accuracy, especially in the presence of even moderate temperature excursions. The key design tradeoff thus rested upon the null tracking approach, since the error signal may be used in one of several ways to cause the collimated beam to sweep in the proper direction until it is normal to the reflector.

The selected method, which is theoretically perfect in its ability to sweep the beam in a predictable manner, is a pair of contra-rotating wedges. This approach employs an identical pair of glass wedges in optical series in the collimated beam immediately in front of the autocollimator objective lens. When the reflector is in the undeviated position, the two wedges are aligned in opposition; i.e., the deviation of one is cancelled by the other, and the two deviations are both parallel to the measuring axis. A reflector rotation causes the wedges to be rotated in opposite directions about the optical axis of the autocollimator. Deviation in the desired direction is accomplished, and deviation in an orthogonal direction is zero due to the cancellation effects of using dual wedges. If the wedges are coupled to a simple resolver, which has an output which is a sine

2-8

function of rotation, the resolver output voltage becomes direct measure of the wedge deviation, hence of the reflector rotation. To achieve the nulling, the orthogonal error signals are converted into polar coordinates. The amplitude of the vector sum is used to rotate the two wedges as a unit to the correct azimuth to null the vector sum. The output of two associated resolvers could then be reconverted to appropriate output components.

The dual-axis contra-rotating wedge pair instrument is used, one each, for both transverse axis rotation and for twist rotation. The second axis of the twist instrument is used to account for cross-coupling. Thus the two instruments become nearly identical in configuration.

2.2.4 Reference Block

Although it is desirable to develop a design which is modular to the extent of being capable to accommodate any of the PPCS equipment configurations while maintaining near-optimum weight and performance, the design of spacecraft structure is basically incompatible with this approach. As a result, a single non-modular design which incorporates the maximum number of assemblies was designed. The extent of design was limited to establishing feasibility of meeting performance requirements with a given geometry, structural concept, and thermal control system.

2.2.5 Computer and Data Interface

A relatively complete study of the design tradeoffs associated with data processing and handling was conducted within TRW [17]. The key design consideration was achieving the reliability objectives. The digital computer is organized in modular form consisting of central processor, main memories, and memory busses. Data interfacing between the computer and other elements is handled by a serial data bus and I/O controller.

Key results of the design tradeoffs indicated that reliability can be approached only by use of switching redundancy techniques, thus leading to the modular organization. The particular organization was straightforward except in the area of I/O, where two basic configurations were considered- namely: integral I/O and non-integral I/O. In the non-integral I/O approach, the organization is such as to separate the processor and I/O functions. The integrated input/output approach is designed such that the input/output processing is integrated with the central processor. This latter approach has the advantage of sharing the memory bus interface, some internal control logic, and buffer registers. However, it is not as flexible as the non-integral approach, and the non-integral approach allows "cross-strapping" of central processors and I/O. From a reliability standpoint, the non-integral input/output approach is superior and was selected.

The data processing requirements are not very stringent for today's state-of-the-art, e.g., >24 bit accuracy, 8K memory, and computational speed typified by a 4 µsec Add time. The requirements are met using MOS/LSI and plated wire technology in the computer.

The data bus concept, wherein the various assemblies of a large system communicate via a minimum of interconnecting cables (ideally one single wire), provides an attractive approach to PPCS data handling. The chosen configuration allows high communication efficiency, ease of reconfiguration, equipment common-ality and a flexible system design approach. A fundamental configuration choice for the data bus is how data traffic will be managed. Choices range from central control by the computer to remote autonomous operation where remote terminals directly control the computer I/O. Central control simplifies remote terminal hardware - at the expense of software complexity and communication efficiency. Remote control (with computational capability at the remote terminal) permits faster response and more efficient bus utilization at the cost of hardware complexity.

A review of PPCS communication requirements showed that a very high percentage of data goes to/from the central computer with relatively little assembly-to-assembly traffic. Control systems as a class are low data rate systems - PPCS, even with its high performance and relative complexity, still has reasonably low traffic. A pre-liminary estimate indicated about 30 KHz data flow for a 6 experiment configuration. Since frequencies of 250 to 500 KHz are easily mechanized on a data bus, communica-tion efficiency isn't likely to be a problem for PPCS. Further, PPCS traffic is likely to be stereotyped in format, with relatively few operating modes - thus simplifying mechanization in a central control concept. On these bases, a baseline concept employing central control was selected using an independent I/O processor with shared memory.

2.2.6 Experiment Gimbal and Electronics

The primary design consideration for the experiment gimbal was developing a configuration suitable to meet coverage requirements of both space pointing (two-axis) and earth pointing (three-axis). This was achieved using a configuration where the inner and outer gimbals are capable of full 360° rotation, and the middle gimbal provides a limited rotation capability to satisfy earth pointing requirements. For space pointing, the middle gimbal axis is deleted (which both simplifies and lightens the unit). Otherwise, the gimbal design is relatively con-ventional with particular care taken to achieve mechanical and thermal symmetry. The electronics design is analogous to that for the star tracker electronics.

2.2.7 Antenna Gimbal and Electronics

The antenna gimbal used for PPCS makes use of an already developed and flight

proven TRW two-axis geared stepper motor drive. Each drive unit contains a stepper motor with integrally attached gearhead, a harmonic drive, dual speed resolver, and supporting bearings. The electronics provides for motor drive and encoding of the multi-speed resolver signals.

2.2.8   Software

The software design is, in general, characterized by achieving desired system performance with the minimum of equation complexity. Throughout the equation development, for example, models derived to compensate for systematic errors in the on-board system are simplified to the level consistent with desired performance. In most cases, for example, this resulted in only first-order terms being retained.

The software is designed to perform executive functions (program control, TLM/CMD, self-test, system test, etc.), attitude determination, and pointing control. The attitude determination software derives inertial attitude by integration of the gyro outputs, and employs a Kalman filter for periodic updates to bound the errors. Development of the attitude determination equations required a variety of tradeoffs to determine the appropriate algorithms and design approach. On the other hand, development of equations for transformations, target selection, and gimbal pointing is straightforward, although algebraically complex. As a result, the primary design effort was directed toward the former.

Choice was available for selection of the kinematic variables used to propagate attitude through the required numerical integration. Euler Symmetric Parameters were selected, as opposed to direction cosines, based upon the use of a four, rather than nine, parameter system of equations; also, the periodic renormalization that must be performed to combat computer roundoff error is much simpler. A closed form solution is utilized, under the constraint that the vehicle rate can be assumed constant over each integration interval. The closed form solution tends to inhibit the truncation error that would normally exist in the power series representation. Design analysis was also conducted to establish the integration step size and the effect of computer (roundoff and truncation) errors.

Because of availability of the star tracker, some inherent flexibility is available in the selection of stars and the storage of a star catalog. The required total catalog is small, generally less than 50 stars for a complete mission. Options for catalog storage include storing only partial catalogs which are periodically updated if on-board storage is a premium. Although it is well known that two independent star sightings are required to determine vehicle attitude, the method of selecting stars is not so straightforward. Four possible approaches to star selection were considered. The baseline technique selected for PPCS is to use stars which have the greatest angular separation from the star used just previously. An additional constraint can be applied that conditionally forces the

use of other stars if a particular star is repeatedly selected, e.g., to gain some additional independent star measurements.

The Kalman filter state vector was limited to six elements (three attitude variables and three gyro biases) to minimize the problem dimensionality while achieving desired performance. Additional states (such as alignment/scale factor parameters in gyros and trackers) were found not to be justified based upon inherent accuracy/stability and/or relative sensitivity. The extended Kalman filter formulation is utilized where linearization takes place about the previous attitude estimate.

The Kalman filter requires apriori definition of the initial state error covariance matrix, the measurement noise covariance matrix, and the state noise covariance matrix. The initial error covariance matrix reflects the initial uncertainty of the state estimates, and the elements are selected apriori based upon the expected initial attitude uncertainty. There appeared to be little influence of the initial estimate for error covariance, but good design practice indicated selection of values larger than the actual expected initial attitude errors.

State noise arises principally from the gyro random drift, and the elements of the state noise covariance matrix are derived apriori based upon the estimated (measured) gyro noise statistics. The influence of state noise on performance was evaluated by evaluating the relative error as a function of state noise parameters. A value of the elements of the state noise covariance matrix can be determined which corresponds analytically to the value of gyro noise assuming a white noise gyro model. The tradeoffs indicate that a good design procedure is to utilize the analytically derived values for the state noise covariance matrix which correspond to a conservative estimate of gyro noise.

The elements of the measurement noise covariance matrix are based upon apriori estimates (measurements) of tracker noise. Tradeoffs were made for selection of elements of the measurement noise covariance matrix utilizing a parameter variation study employing various values of tracker noise and measurement noise covariance values. This tradeoff led to the indication that performance can be best achieved through selection of elements of the measurement noise covariance matrix which are, in fact, optimistic.

The PPCS software is configured in a modular structure which will permit operational flexibility, capability for growth, and ease of modification. The software makes use of state-of-the-art techniques so far as possible, consistent with the capability of present generation spaceborne computer technology. The software is segmented into modules to be executed under control of the PPCS Executive according to a preassigned interactive cycle. Individual program module

interfaces have been allocated based upon cycle requirements of the main computation loops.

3.0 SYSTEM DESIGN

PPCS is designed as an integral system to perform precision attitude determination and gimbal pointing control. This section presents the system-level design definition. A functional description of PPCS is discussed initially, presented within the context of a typical orbital configuration and a detailed system functional block diagram. This is followed by a description of the operational characteristics of the system including pre-launch, initialization, initial convergence and operation, calibration and boresighting, and operating modes.

Definition and allocation of design requirements to the hardware/software elements is dealt with next. These allocations are developed on the basis of meeting overall PPCS requirements, which are summarized, as well as design trade-offs and analyses which are detailed within this section and elsewhere in this report. The section closes with definition and discussion of the system interfaces, both internal (e.g., signal interface) and external.

3.1 FUNCTIONAL DESCRIPTION

The functions characteristic of the PPCS system design are summarized as:

- Development of precise on-board attitude defined relative to the Earth-Centered-Inertial (ECI) coordinate frame, using strapdown gyros and a gimbaled star tracker as primary sensors.

- Development of a precise spacecraft attitude reference relative to a local vertical, orbit normal coordinate frame through on-board ephemeris.*

- Development of a precise alignment reference for from one to six non-integral (e.g., boom mounted) experiment gimbals using optical alignment sensors.

- Pointing from one to six independent gimbaled experiment platforms.

- Pointing an antenna at one of three data relay satellites, either open loop (command steer), or using (optional) autotrack signals.

3.1.1 Configuration

A typical configuration of the PPCS functional elements is shown in Figure 3- These functional elements are of modular design to provide versatility for satisfaction of a wide range of design requirements, and can be employed in various configurations to satisfy particular redundancy and/or performance requirements.

The star tracker functions to provide a direct measure of attitude. The gimbal mounted star sensor electronically tracks the brightest star within the field of view, and the sensor error signal is used to null track via the gimbal servos.

---

*Development of on-board ephemeris not a part of PPCS
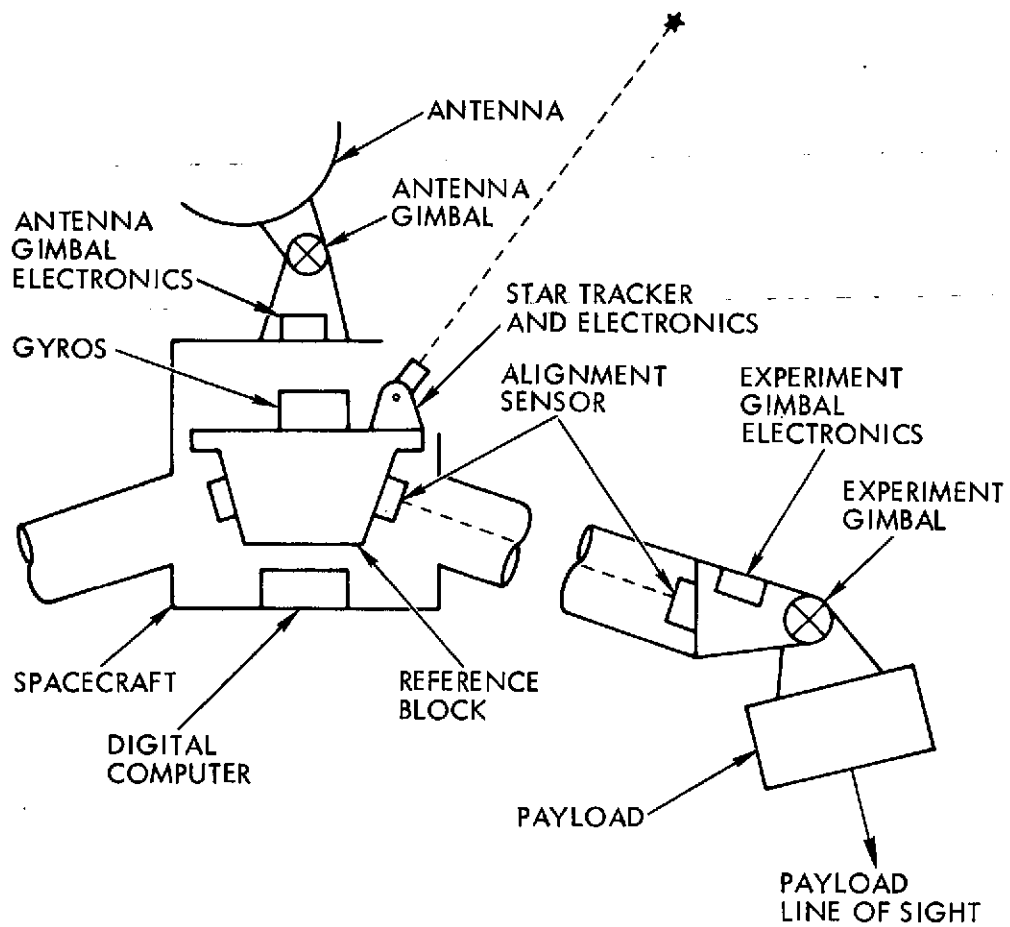
Figure 3-1. Typical PPCS Configuration

Tracker servo control/gimbal drive functions and gimbal readout processing are provided in separate electronics. Both the tracker gimbal angles and sensor error are provided to the computer.

The strapdown gyros provide a short-term measure of incremental attitude. The outputs of each of the N_G rate integrating gyros is a series of pulses, each of which represents a fixed angular rotation of the gyro input axis in inertial space. These pulses are accumulated in a register over the period of an integration step. The register content, $\Delta\theta$, is readout as a data word into the computer each period and reset to zero in a fashion such that no pulses are missed.

The alignment sensor tracks the small-angle rotations of the gimbal base reference (e.g., reflector) relative to the alignment sensor. Alignment information is provided by nulling the measured reflection of an autocollimated beam relative to the known sensor (autocollimator) reference frame. The alignment sensor outputs to the computer include both the measured alignment as well as the sensor error signal.

The Reference Block Assembly is an element whose design, strongly influenced by the spacecraft, provides a stable mounting platform for the critical sensor assemblies. Hard-mounted to the reference block are the star tracker(s), gyros, and autocollimator elements which are required to maintain a stable relative mechanical alignment.

The experiment gimbal functions to provide a precision actuator for the gimbal mounted experiment payload. The gimbal electronics are utilized to develop the gimbal servo drive and provide gimbal readout processing which is output to the computer. Gimbal commands are received from the computer. Analogously, the antenna gimbal and electronics provide the actuation function for antenna pointing.

The on-board digital computer and I/O interface controller are used to implement the system data handling and data processing functions.

3.1.2 Functional Block Diagram

The PPCS system functional block diagram is shown in Figure 3-2. Discussion begins with the inertial attitude determination functions. The N_G gyro output data words are used to construct a vector which represents the total (small-angle) rotation during the integration period. The estimate of rate measured by each gyro is derived by the differentiation of a second-order fit to the measured attitude data. This rate vector is then multiplied by a $3 \times N_G$ "geometry" matrix which account for gyro input axis alignment and scale factor. The result is an estimate of rate about the desired orthogonal reference axes.

Gyro drift bias estimates, computed periodically by the Kalman filter, are used to correct (compensate) the rate estimates. The estimated rates are then
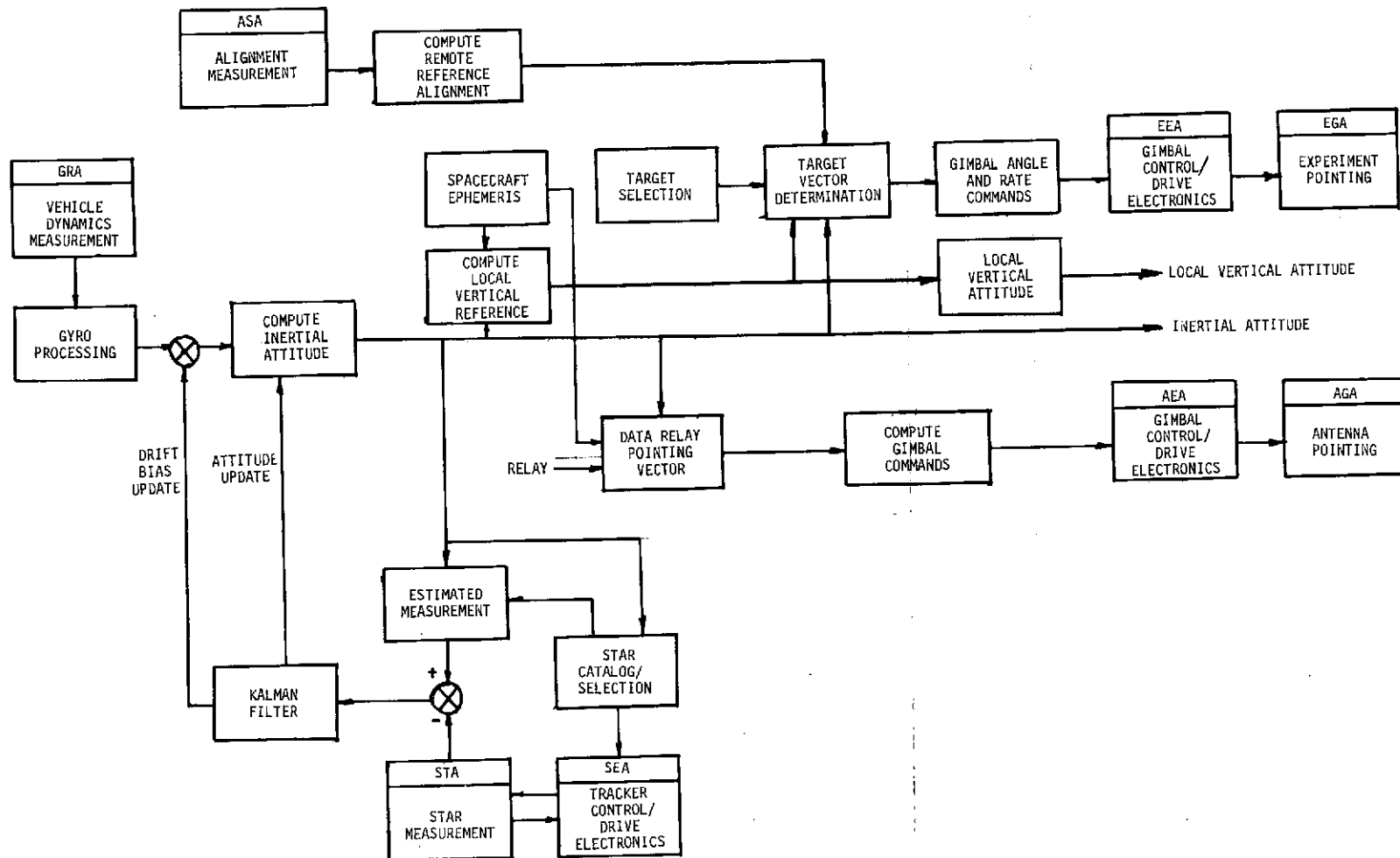
Figure 3-2. PPCS Functional Block Diagram

integrated to provide a continuous, three-axis estimate of attitude relative to an inertial reference frame. Euler parameters are utilized as the kinematic variables, and a relatively simple closed form solution is utilized to compute attitude. The computed attitude is used to generate a direction cosine matrix relating the vehicle to the inertial frame.

Periodically, an update of the kinematic variables and gyro drift estimates is initiated . An on-board star catalog is utilized in a star selection algorithm to define a particular target star. Based upon the current attitude estimates, tracker gimbal angles are commanded such that the star tracker is slewed to point to the target star. The slew "servo control" is provided within the supporting tracker electronics, with gimbal angle/rate commands provided by the computer. Once the tracker has acquired the star, the computer commands the tracker servo to use the sensor error signals, and the tracker then continuously tracks the star at null.

A Kalman filter is used to develop optimum estimates for a six-element state vector, incorporating three attitude variables and three gyro drift bias terms. The error between the measured and estimated gimbal angles, after compensation for known biases and misalignments, is used to generate the measurement residual vector. This vector is multiplied by the Kalman filter gain matrix to develop an incremental correction to the state vector and the estimates of attitude and gyro drift bias updated.

To develop the attitude relative to the local vertical reference (e.g., conventional roll, pitch, and yaw), the inertial attitude is combined with on-board ephemeris data. The ephemeris is used to create a direction cosine matrix relating the local vertical frame to the inertial frame. It is then a simple matter to carry out the appropriate matrix operations. (It is noted that development of an on-board ephemeris is a function which was not within the scope of the PPCS study.)

To determine the attitude of a reference frame other than the primary attitude determination reference, it is necessary to know the relative orientation. If the reference frames are physically close-mounted (integral) and stable, apriori alignment knowledge is sufficient. For systems with non-integral payloads, the three-axis alignment of the remote reference (e.g., gimbal base) is measured to determine the relative orientation. The relative attitude of the gimbal base is established using the measured (and compensated) alignment sensor outputs. The alignment sensor reference is stable and known relative to the attitude determination reference through close mounting on a stable mechanical reference. It is then a simple matter to determine the gimbal base reference relative to any desired coordinate frame, e.g., inertial, local vertical.

3-5

For pointing control of the platforms, target data (periodically stored on-board using data from the ground) is used to generate appropriate target vectors. These target vectors, when transformed relative to the appropriate gimbal base reference, become the basis for generation of steering commands (gimbal angle and rate) for open loop pointing control of the gimbals. Target data is provided relative to one of three coordinate frames, namely - inertial, earth-fixed, or local vertical. In each case, the target vector coordinates are transformed initially to the inertial frame. The target coordinates are then transformed into the experiment gimbal base reference frame using the previously determined gimbal base orientation. Experiment gimbal angle and rate commands are computed by solving for the gimbal angles that would align a set of axes on the gimbaled platform with the appropriate target vectors, accounting for known alignments and biases within the gimbal set. Commands are provided from the computer with servo control implemented within the supporting gimbal electronics.

For pointing the antenna, the target vector (LOS) is computed in inertial coordinates based upon stored data relay satellite ephemeris, and gimbal commands computed in a fashion similar to that for the experiment platforms. The gimbal commands are again output from the computer to the servo-controlled gimbal to implement the pointing commands.

3.1.3   Operational Description

This section describes the overall system operation encompassing prelaunch, launch and deployment, initial operation, and calibration. Prior to launch, the key operations are those of alignment, system calibration, and initialization. Parameter values to be determined and entered into the computer are those which define gyro "geometry", tracker alignment/biases, gyro drift bias, autocollimator alignment/biases, platform gimbal alignment/biases, and Kalman filter parameters (initial state vector estimate, measurement noise covariance, state noise covariance, state error covariance). The values of the parameters established prior to launch are used until appropriate on-orbit calibration is performed (if desired) to generate updated values. Through the periods of launch and orbital injection, the elements of PPCS are disabled or in a quiescent standby mode. During launch, the mechanical elements are protected against the launch environment through caging or other suitable means.

The post launch operational sequence is shown in Figure 3-3. PPCS remains in the quiescent mode during spacecraft deployment, acquisition of the orbit plane/local vertical reference, and initial operation. When desired, the acquisition of the PPCS celestial/inertial attitude reference is initiated by command. Initial attitude uncertainty may be as much as $\pm$ 3 degrees per axis. Thus, it is required to perform a search for the initial target stars. Operationally, this is accomplished
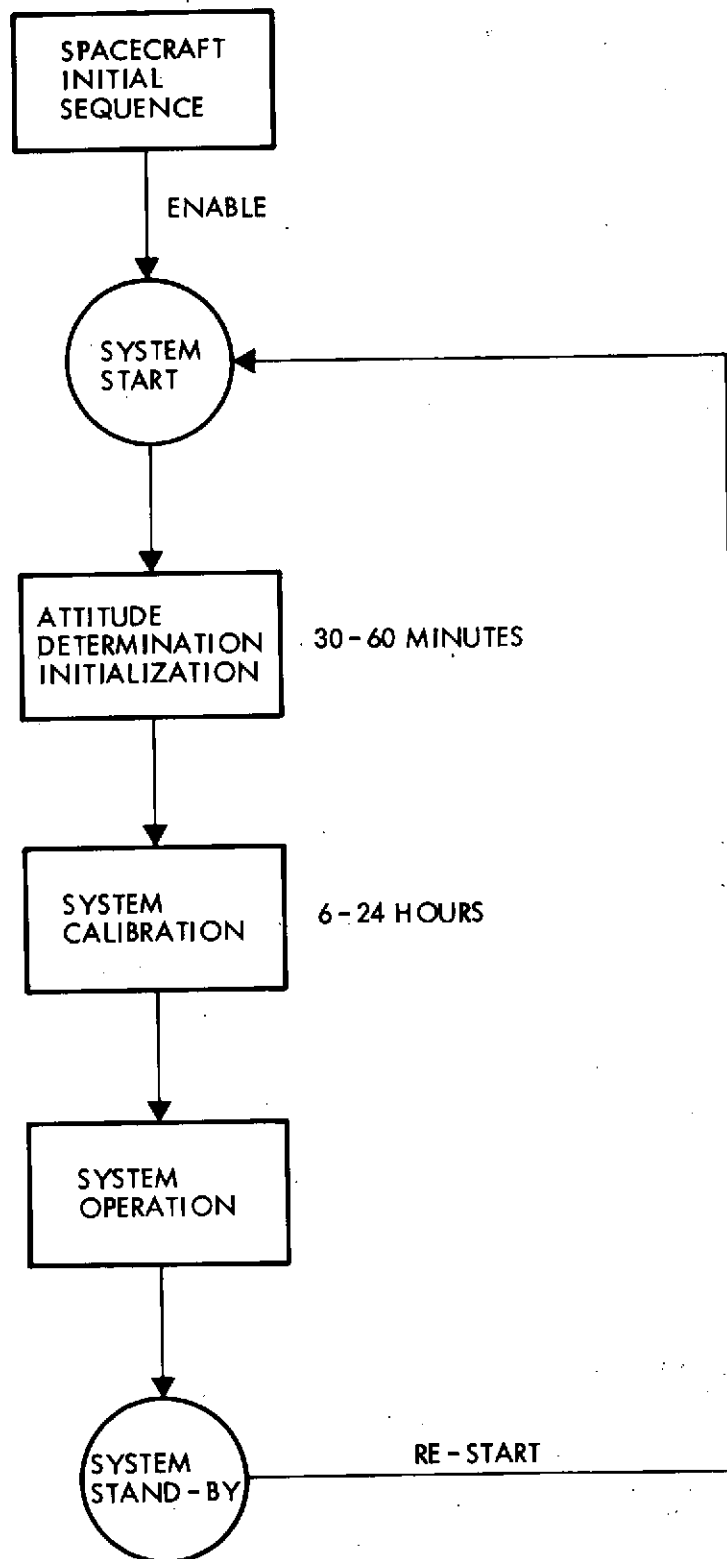
Figure 3-3. PPCS Operational Sequence

by maintaining the attitude reference with the gyros (utilizing the initialized state vector estimates) while the star tracker executes a programmed search to acquire the selected initial star. The uncertainty region of 6°x6° may require up to approximately 11 minutes for complete (worst case) search for the tracker optical FOV of 10x10 m̂in and star recognition time of 0.5 sêc.

After tracking the initial star long enough to extract the required data for the Kalman filter, a second star will be sought. Due to data from the first star, the uncertainty region of the second star will be much smaller (e.g., 6°x1°), requiring a much briefer search. After assimilating data from the first two stars, all subsequent stars can be located without searching. (It has been observed that, in many cases, search is not required after the first star.) A nominal update period of 5 minutes has been established. Thus the star tracker will be slewed to track and measure independent stars prior to each computed update, i.e., every five minutes. It is noted that the system has been designed such that independent star data may be obtained as often as every 30 seconds, if desired. Continuous tracking of a known star is performed at all times except for the time taken to slew between successive stars. Steady-state attitude reference accuracy is established consistent with prelaunch system alignment and bias uncertainties. Typically, 30 to 60 minutes will be required for convergence, during which time thermal equilibrium is reached. The alignment sensors, platform gimbals, and antenna gimbals will be enabled upon command following attitude reference convergence. The alignment sensors may be stepped or slewed in either direction (by command) to achieve initial acquisition of the reflected beam. Once acquired, the autocollimators track automatically.

Gimbal control for each of the experiment platforms is based upon commanded targets transmitted from the ground to the on-board computer. These targets may be stored via the uplink as often as once each orbit. Each of the platforms is controlled separately, generally with different targets. The target commands are time tagged and take one of three forms, namely:

- Angles relative to the local vertical coordinate frame are specified as roll, pitch, and yaw. If the angles are given as zero, the platform is pointed such to align the line-of-sight axis along the local vertical (toward the subsatellite point) and the orthogonal out-of-plane axis normal to the orbit plane. If only pitch and/or roll is specified, the gimbal angle about the line of sight is constrained to zero.

- Latitude, longitude, and radius from the geocenter is specified. The platform is controlled to point the line-of-sight axis toward the particular geographic point on or near the earth surface.

- Right ascension and declination are specified relative to the ECI coordinate frame. The platform is controlled to point to the particular point on the celestial sphere.

The antenna pointing operation is similar to experiment platform operation In the low altitude orbits, the antenna target will be one of three geosynchronous data relay satellites. Orbital geometry will require relatively frequent re-targeting via a slew mode. In geosynchronous application, the antenna is continuously oriented toward a ground station. Ephemeris of the data relay satellites (or alternatively the relay satellite subpoint) will be utilized to generate target vectors on-board.

Prior to operational use, a variety of in-flight calibration and boresighting procedures may be utilized, including end-to-end system calibration using experiment data and attitude reference internal checks (e.g., consistency checks using redundant star tracker and gyro data). These procedures can be periodically conducted throughout the mission, if desired, and can be key to achieving the system performance goal of 0.001 degree pointing accuracy. The initial alignment uncertainties through the launch environment and initial orbital transients, although anticipated to reflect these accuracy goals, are of such a nature as to require capability for on-orbit observation/updating. The predicted on-orbit performance is based upon small contributions of error sources which are not calibrated and long-term stability of those which are.

Attitude determination calibration and pointing control boresighting is accomplished by ground-based support software which processes telemetered data from on-board measurements. This procedure may be conducted "off-line" in the sense that real-time processing is not required. The parameters thus derived are inserted, via ground command, in the on-board software to obtain ultimate system accuracy. The time required for interfacing with PPCS will depend upon the extent of calibration/boresighting required (and should be considerably shorter after the first operational cycle).

The calibration process associated with inertial attitude determination is effective in removing alignment errors of the star tracker and gyros relative to a set of reference axes on the star tracker gimbal base. Boresighting of experiment pointing will require end-to-end data; that is, attitude determination data in conjunction with data from a boresight sensor on the remote experiment serviced by the collimators and experiment gimbal (e.g., landmark data from an imaging payload, gimbal angle data from a tracking payload).

The calibration technique employed for attitude determination calibration is discussed briefly. In general terms, this approach amounts to evaluating the consistency of a series of star sightings and the intervening gyro-developed attitude increment data. The presence of systematic errors will result in measurement inconsistencies yielding information from which the (modelled) error source magnitudes can be identified and subsequently calibrated. On the other hand, if the

system is perfectly calibrated, or if the residual errors have no noticeable effect upon system performance, measurements will be consistent to the degree permitted by system noise.

The calibration is implemented using a Kalman filter which, as in the on-board software, utilizes gyro data and periodic star tracker measurements. However, rather than a six-state filter (as in the on-board system), the calibration software deals with an enlarged state vector including the calibration parameters, e.g., misalignments, biases, etc.

Figure 3-4 displays this attitude determination calibration problem graphically, indicating the various parameters to be calibrated and the associated topology. Gyro calibration parameters include terms defining input axis alignment, drift bias, and scale factor. Star tracker calibration parameters include detector bias/misalignment and gimbal alignment.

Boresighting of the experiment platform assumes availability of a boresight sensor. The boresight sensor data is transmitted to ground via telemetry so that by correlating the gimbal readout data and the boresight sensor data one can determine the measured gimbal angles at the time the known target is within the FOV. The aim is to calibrate the system with several of these measurements by either using several preselected, known targets or by using the same target repeatedly in conjunction with preprogrammed, large angle spacecraft attitude changes. It is clear from physical considerations that the calibration measurements do not only reflect the various misalignments of the pointing system but also reflect the attitude determination errors. Furthermore, using landmarks for calibration of pointing misalignments makes the system sensitive to ephemeris errors.

For the boresighting problem, it is assumed that the attitude determination system has been calibrated separately and that no further improvement in attitude determination through additional calibration measurements is required. The influence of the remaining attitude determination errors must then be discounted as "noise" on the pointing calibration measurements. If the attitude determination errors are consistently biased in the same direction, this is a bad assumption. However, if the attitude determination errors averaged over the calibration measurements yield approximately zero (in the first order terms), then this is a good assumption.

If the attitude determination errors are considered uncorrelated noise on the calibration measurements, then the task of calibrating the misalignments in the pointing system becomes one of estimating constant parameters. Here we are interested in computing the misalignments given the target and the observed gimbal angles. Since the gimbal angle measurements are contaminated by noise, one really cannot "compute" the misalignments but merely obtain a "best" estimate. In this case, the task of estimating the misalignments for sufficiently many observations leads to a
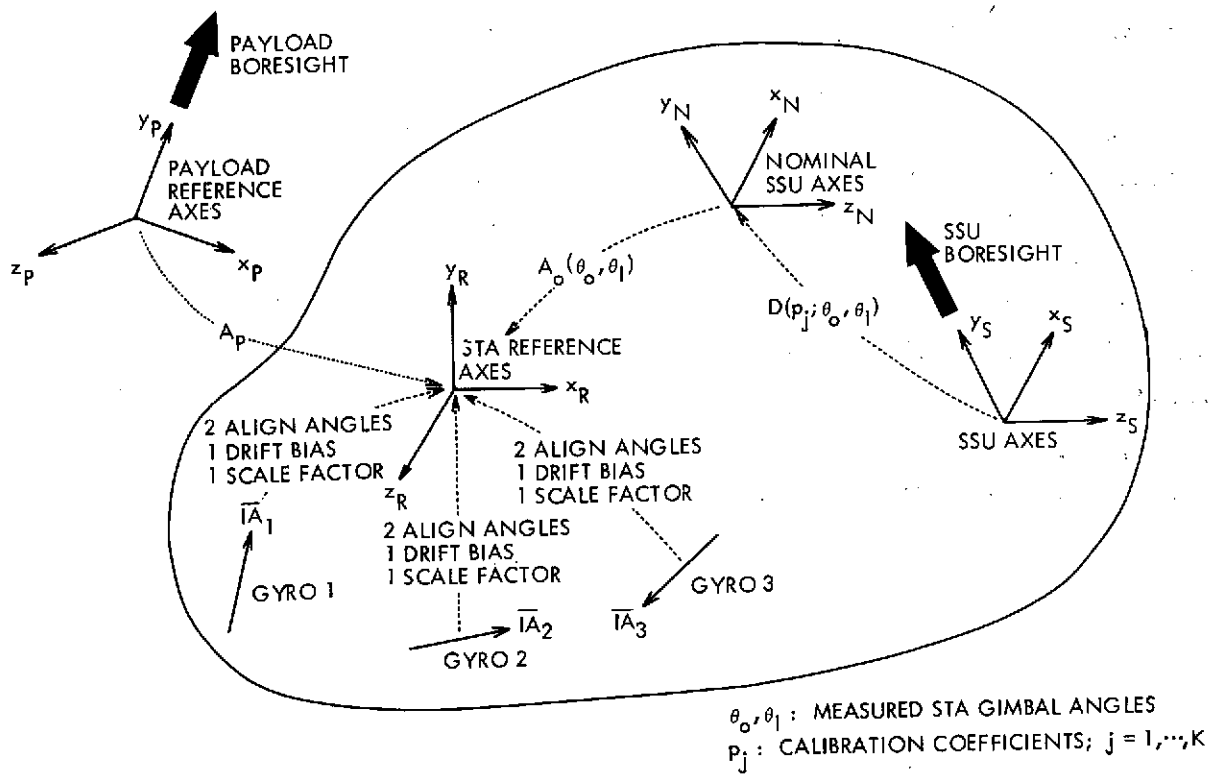
Figure 3-4. Attitude Determination Calibration Topology

one-shot, least squares estimate. It is noted that a state vector could be formed of the attitude variables and pointing calibration parameters, and sequential estimation performed using a Kalman filter. However, it is not anticipated that the additional complexity of such an approach would be required.

In the event of system failures, backup modes of operation are incorporated into the system design. These modes will provide the capability for PPCS to function (in a potentially degraded fashion) in the event of failure or degradation of a component or subsystem. The guideline, operationally, regarding failures is that hard failures will be detected and corrected for on-board, whereas soft failures will be detected and corrected for using ground-based means. The PPCS computer becomes the central element for on-board failure detection. The computer will periodically evaluate the status of the system to detect early failure symptoms.

For attitude determination, the redundant operating gyro, together with the star tracker, provides a means of failure detection for any of the five operating elements without losing attitude reference. If a gyro is detected to be drifting out of tolerance, it will be shut down and one of the standby gyros will be brought to an operating status. The three remaining gyros will maintain the short-term inertial reference during this transition state. A star tracker failure will result in the unit being shutdown and the standby unit brought up to operational status. The four operating gyros will maintain reference during this transition.

Failure in the experiment gimbals or pointing commands will result in the gimbal system being driven to null, if possible.

3.2 REQUIREMENTS DEFINITION/ALLOCATION

PPCS system requirements have been achieved with a design which meets or exceed all performance goals and whose elements are of state-of-the-art design and attractive for flight application. Design requirements for individual hardware assemblies were defined as appropriate to establish the system performance capability. These requirements included such considerations as configuration, accuracy, and reliability and were, in many cases, allocated from the PPCS system requirements. The PPCS system requirements and detailing of the basis for design requirements allocation are summarized in the sections which follow, with the design requirements for each assembly individually considered.

3.2.1 System Requirements Summary

The basic functional requirements may be succinctly stated as:

- Precisely point and maintain the orientation of from one to six independent platforms at earth targets (with three degrees of freedom) or at space targets (with two degrees of freedom).

- Accurately point and maintain the orientation of one antenna with two degrees of freedom.

PPCS system requirements, reflecting the contract Statement of Work, are summarized in Tables 3-1 and 3-2 for performance requirements and component specification, respectively. Several of these requirements are worth comment. For the PPCS design, the accuracy goal was established as the (internal) TRW requirement. It was also considered appropriate to establish an acquisition goal considerably less than the one day requirement, on the order of an hour or less. Finally, life requirement of 3 to 5 years was translated into requirements of numerical reliability to give a quantitative basis for design. A design goal of 0.9 for one year (0.72 for 3 years) was established for PPCS (attitude determination alignment, processing, single experiment, and antenna). A separate goal of 0.98 for one year (0.94 for 3 years) was defined on the attitude determination and data processing functions, respectively, due to their central nature to the overall system.

3.2.2 Star Tracker Assembly

Requirements were developed for the star tracker by consideration of a variety of interacting influences including acquisition period, overall system accuracy, and update frequency. These result in design requirements on the tracker for sensor accuracy, noise, star sensitivity, gimbal freedom, alignment accuracy, and readout uncertainty. The design requirements are summarized in Table 3-3.

The PPCS requirement for acquisition is to accomplish this in less than one day (Table 3-1). As noted earlier, however, it is desirable to be able to

Table 3-1   PPCS Performance Requirements

Description	Requirement
Accuracy (each axis): includes attitude determination, alignment transfer, and experiment pointing control exclusive of ephemeris errors.	Platforms (to local vertical and offset): 0.001 deg (1σ) RMS goal (3.6 sec) 0.003 deg (1σ) acceptable Antenna (to relay satellite) 0.03 deg
Platform coverage	Earth targets, local vertical and offset: ± 45° from local vertical ± 10° about local vertical Space targets, 2 platform complement: 4_π steradian
Antenna coverage	105 degree from upward vertical in any direction
Acquisition time	Not to exceed one day
Orbit	Geosynchronous Low altitude (200 to 2500 nm) sun synch.
Life	3 to 5 years, continuous operation
Environment	Thermal: 10-40°C Vibration: Titan III
Spacecraft Attitude Control	Nominal: ± 1.0 deg, ± 0.02 deg/sec Worst Case: ± 3.0 deg, ± 0.06 deg/sec
Ground Control	Ephemeris/calibration updates: not to exceed once per orbit Latitude, longitude, and radius commands for pointing

Table 3-2   Specification of System Components

● Inertial Reference

  Strap-down gyro system

  State-of-the-art gyros

● Computer

● Six platform drives whose load characteristics (including gimbal)$_2$ are assumed as having mass of 20 slugs and inertia of 100 slug-ft^2.

● Six 3-axis autocollimators to measure up to 0.5 degree over distance of 1 to 10 ft with lateral displacement as large as 0.5 in. at longer distances. (Measurement is to be optical).

● One 2-axis antenna drive. Assume maximum antenna misalignment one min (correction not required) and limit all other errors to one min per axis. Assume antenna to be 4 ft cube, weighing 25 lb, having the gimbal attached to the center of one face.

● Star Tracker whose design is to be compatible with overall system accuracy.

Table 3-3   Summary of STA Design Requirements

Functional

- Provide for acquisition and tracking of stars within sensor optical field of view.

- Provide for acquisition and tracking of stars within mechanical field of view through gimbal motion in 2-axes in response to motor drive signals.

- Provide outputs of the detector error signals and gimbal angular position data.

- Provide a capability for preflight test and calibration in one-g environment.

- Provide for suitable mechanical alignment with respect to other system elements mounted on the Reference Block Assembly.

Performance

- Mechanical field of view shall be not less than +45 degrees about the outer gimbal axis and +15 degrees about the inner gimbal axis.

- The peak gimbal rate capability shall be greater than 3 deg/sec.

- The system must have, as a minimum, sensitivity to and ability to track stars of +3.5 (S-20 Magnitude).

- The sensor optical field of view shall be not less than 10 min x 10 min, and the system must acquire and track stars which enter the field at rates up to 0.25 deg/sec. Acquisition shall occur with 0.5 second after a star of sufficient brightness enters the FOV.

- The STA shall be capable of tracking, to design accuracies, to within 15 degrees of the center of any bright object other than the earth or sun, to within 15 degrees of the limb of the earth, and within 45 degrees of the center of the sun.

- The sensor noise equivalent angle in a 5Hz bandwidth shall be less than 0.5 sec (1σ, per axis).

- Uncertainties in measurement of the star LOS due to the STA shall be less than 1.0 sec (1σ, per axis)

establish acquisition or reacquisition much more rapidly. As a result, the sensor characteristics (e.g., optical field of view, star lock/track, etc.) in conjunction with the gimbal characteristics (e.g., angular freedom, search rate, etc.) must be sufficient to scan the initial attitude uncertainty within a relatively short period of time.

With this in mind, a period of 15 minutes was allocated for search and acquisition of the initial reference star. This reflects itself on the STA as a requirement to be able to search and acquire a star within a 6°x6° celestial field (worst case vehicle motions) in less than a 15 minute period. To assess the realism of this requirement, assume 0.5 sec to lock onto a star within the sensor FOV and determine the required FOV. The resultant tracker optical FOV is approximately 140 $\widehat{min}^2$, e.g., 11.8 $\widehat{min}$ x 11.8 $\widehat{min}$. For a FOV of 10 $\widehat{min}$ x 10 $\widehat{min}$, the search period would require 648 seconds (approximately 11 minutes). In this latter case, as much as 43 degrees of orbital motion would correspond to the star search period in the lowest altitude orbit (200 n.m.). For a star in the orbit plane, this implies a worst case mechanical FOV of greater than $\pm$ 22 degrees. The result for the singular case of the star along the orbit normal is also noted, where relative motion of the star line with respect to the vehicle can be zero. Clearly, the actual cases of interest will be somewhere between. If the gimbal null axis of the tracker lies in the plane of the orbit normal and local vertical and less than 45 degrees above the local horizontal, then a mechanical FOV of $\pm$ 15 degrees is adequate for initial search.

Although gimbal freedom is clearly influenced by the acquisition requirement, star selectivity (including bright object avoidance) and sensitivity play the major roles. The most ideal situation to obtain three axis information with a two-degree-of-freedom tracker is to be able to observe stars whose lines of sight are orthogonal. Therefore, it is desirable to have approximately 90 degrees of gimbal freedom in at least one axis. Gimbal freedom in an orthogonal axis can be limited to the extent of providing sufficient stars. Tracker sensitivity and gimbal freedom can be traded based upon desired star separation, a desire to minimize the star catalog, or desire for multiple stars within the FOV. The star availability studies discussed in detail in Section 5.2 yielded requirements for a threshold magnitude of + 3.5 (S-20) and gimbal freedom of $\pm$ 45 degrees for the outer gimbal and $\pm$ 15 degrees for the inner gimbal based upon considering both low altitude and geosynchronous orbits. Modest gimbal rates, on the order of 3 deg/sec, are required to meet the maximum update frequency capability, i.e., 90 degrees in 30 seconds. The accuracy requirements are based upon the results of the system error analysis.

3.2.3 Sensor Electronics Assembly

The design requirements for the Sensor Electronics Assembly (SEA) include
providing servo control logic/frequency compensation and the drive circuitry for the
STA servos and provision of gimbal readout processing yielding both a measure of
gimbal angle and rate. The design requirements are summarized in Table 3-4. .

Bandwidth and frequency compensation requirements are defined by the star
tracker gimbal servo analysis (Appendix G). In the track mode, angle measure-
ment must be consistent with the error analysis budget allocations. In the slew
regime, degraded accuracy can be accepted to a level consistent with open-loop
pointing to a star well within the 10 min sensor optical FOV.

3.2.4 Gyro Reference Assembly

Requirements on the gyro assembly were developed primarily from considerations
of reliability and accuracy. A detailed specification is provided in Appendix J, ,
with a summary of key requirements shown in Table 3-5. The maximum rate to be
measured is based upon potential spacecraft slew and/or reacquisition motions, and
represents a generous allowance over the worst case specified limit cycle rates of
0.06 deg/sec in all axes, combined with the worst case orbit rate of 0.065 deg/sec
at 200 n.m. The accuracy requirements have been developed on the basis of the error
analysis/allocation of Section 4-2. The gyro bandwidth is selected so as to be
a negligible factor for vehicle motions of the nominal class of carrier spacecraft.

3.2.5 Alignment Sensor Assembly

Assembly design requirements are summarized in Table 3-6. The performance
requirements are influenced by the characteristics of the boom structure mounting
the remote gimbal-base reference to the spacecraft, alignment of the interface
structure, and thermal deformations. Boom structural characteristics have been
assumed using a representative boom design [18]. Brief analysis yields a boom
natural frequency of approximately 1.5 Hz and a total angular deflection of less
than 20 sec.

3.2.6 Reference Block Assembly

The preliminary design requirements on the Reference Block Assembly (RBA) are
straightforward, but critical to a satisfactory system. The RBA must provide
mechanical support for the multiply-redundant Gyro Reference Assembly, the two Star
Tracker Assemblies, and from one to six Alignment Sensor Assemblies. The RBA must
assure stable and observable alignment of the sensor assemblies relative to one
another to within 0.5 sec (1σ, per axis).

Table 3-4   Summary of SEA Design Requirements

Functional

- Provide Inductosyn readout processing for gimbal angle and rate.

- Provide servo and motor drive electronics for tracker gimbal control.

- Condition all STA and SEA telemetry and commands.

Performance

- Inductosyn processing will provide gimbal position and rate signals over the entire range of gimbal travel and all gimbal rates. Operation can be considered in two regimes, slew and track. In the track regime, gimbal angle measurement accuracy must be better than 0.5 sec (1σ). During slew, gimbal angle measurement accuracy may be relaxed by an order of magnitude or two.

- Motor drive circuit design should provide for minimum dependence of drive torque upon position (e.g., by quadrature drive signals, if appropriate).

- Motor drive circuitry bandwidth shall exceed 300 Hz.

- Control electronics will use a computer generated gimbal angle error signal or command during slew which, with appropriate frequency compensation, is combined with an inner loop utilizing rate signal from the inductosyn. During track, the error signal is derived from the sensor output and processed in a similar fashion wholly within the SEA.

Table 3-5   Summary of GRA Design Requirements

Functional

- Provide multiple redundant measure of spacecraft angular rate, using six torque-rebalance rate integrating gyros.

- Provide suitable provision for mechanical alignment with other system elements mounted on the Reference Block Assembly.

Performance

- The maximum input rate about any axis during operation will be 5 deg/sec. The maximum rate about any axis which must be measured is 1.5 deg/sec.

- Quantization shall be less than 0.2 sec.

- The gyro fixed bias shall be less than 5 deg/hr. The random drift shall not exceed 0.005 deg/hr (1σ) during any 30 minute period. As a goal, the random drift rate uncertainty should remain less than 0.002 deg/hr during any 30 minute period.

- Input axis alignment shall be stable to 10 sec over a five year period. In addition, the input axis should remain stable to 3 sec over any 30 day period.

- Torquer scale factor uncertainty shall not exceed 100 ppm, including nonlinearity and random vibration.

- Effective gyro bandwidth shall exceed 5Hz.

3-20

Table 3-6   Summary of ASA Design Requirements

Functional

- Measure the small angle motions in three axes of a remote reference frame.

- Provide suitable provision for mechanical alignment to the RBA.

Performance

- The accuracy goal is 0.5 sec (1σ) for transverse axes and 2.6 sec (1σ) for twist.

- In-spec operation must be provided for distances of up to 10 feet.

- Measurement range must be consistent with +0.5 degree rotation (each of three axes) and +0.5 inch lateral deflection at 10 ft.

- Bandwidth should be sufficient to meet accuracy requirements with the following characteristic sinusoidal motion:

$$10 \text{ sec at } 10 \text{ Hz}$$
$$100 \text{ sec at } 1 \text{ Hz}$$
$$1000 \text{ sec at } 0.1 \text{ Hz}$$
$$1800 \text{ sec at } 0.06 \text{ Hz}$$

  Step inputs should be nulled at 640 sec/sec or faster

3.2.7 Experiment Gimbal Assembly

The design requirements for the EGA are summarized in Table 3-7. The requirements are based primarily on the required operating modes, coverage, and error budget/analysis.

The following operational modes are envisioned for earth experiment control:

(i)   Local vertical and local vertical offset pointing

(ii)   Geographic (landmark) pointing

(iii)   Slew

Mode (i) is a relatively benign regime, in which the experiment gimbal is counteracting spacecraft attitude excursions in order to maintain a fixed experiment orientation relative to the rotating geocentric reference. Mode (ii) requires the gimbal accelerations and relatively high rates associated with tracking a geocentric target. The tracking acceleration and rate requirements are based upon the worst case resulting from the low altitude requirement (200 min).

Mode (iii) includes all transient operations, such as re-targeting, transfer from one steady-state mode to another, etc. This mode determines peak acceleration and rate requirements, these parameters being a function of the speed with which these maneuvers are to be accomplished. The point-to-point slew rate capability was established as a value which would not place severe constraints on the system design while still giving reasonably short periods between tracking targets of interest.

The following operational modes are envisioned for space experiment control:

(i)   Autotrack

(ii)   Space pointing

(iii)   Slew

In the first two modes the experiment LOS is aligned to some quasi-inertial point (e.g., the moon or a star), with the controller maintaining the alignment in the face of spacecraft motions. Gimbal rates will be modest, except when the inner gimbal angle approaches 90 degrees (resulting in outer gimbal rates which can approach several degrees per second). Slew rates depend upon the time allowed for retargeting the experiments and the command strategy employed in reorientation.

3.2.8 Experiment Electronics Assembly

The design requirements for the EEA include providing servo control and drive electronics for the EGA and gimbal readout processing. These requirements are summarized in Table 3-8. Accuracy required is derived from the system error

Table 3-7   Summary of EGA Design Requirements

Functional

● Point precisely in each axis in response to motor drive voltages frcm the Experiment Electronic Assembly (EEA).

● Provide a suitable mechanical interface with the spacecraft structure, e.g., at the end of a deployable boom.

● Provide a suitable mechanical interface with the reflector elements of the alignment sensor at the gimbal base with provisions for precise alignment.

● Provide a suitable mechanical interface for the gimballed experiments (i.e., a mounting "platform") with provisions for precision alignment.

● Provide gimbal angular position data.

● Provide signal and power transmission paths for the experiments.

● Provide mechanical protection during pre-launch, launch and other spacecraft operations prior to PPCS activation.

● Provide a capability for pre-flight test and calibration in a one-g environment.

● Accommodate a wide variety of payloads, either by a single general-purpose design or via multiple designs.

● Include provision for caging at zero gimbal deflection (mechanical or electrical) in the event of a failure affecting experiment control.

Performance and Design

● EGA electro-mechanical design characteristics must be consistent with tracking rates of 1.2 deg/sec, peak slew rates of 3.0 deg/sec, peak accelerations to slew of 0.1 deg/sec^2, and peak accelerations to track of 0.012 deg/sec^2.

● The two-axis gimbal design (for space pointing experiments) shall have gimbal freedom of at least +120 degrees for the outer gimbal and +80 degrees for the inner gimbal.

● The three-axis gimbal design (for earth pointing experiments) will have gimbal freedom of +15 degrees about the line-of-sight axis (i.e., yaw) and +50 degrees in the two transverse axes (i.e., pitch and roll).

Table 3-7   Summary of EGA Design Requirement (Cont'd.)

- The mechanical design must be compatible with achieving a pointing loop bandwidth of 1.0 Hz.

- The total mechanical error associated with the EGA (i.e., misalignments, gimbal non-orthogonality, bearing runout, position encoder, etc.) shall be less than 1.5 sec (1σ).

- Reliability shall be consistent with a 3 to 5 year lifetime.

- Nominal load characteristics are:

Mass:	20 slugs (gimbal plus payload)
Inertia:	100 slug-ft
Mass Unbalance (1g):	0.2 ft-1b (maximum)

  Mass unbalance must be maintained by suitable provision for balanced experiment mounting.

- Thermal design shall be consistent with an ambient range of +10°C to +40°C.

- Structural frequencies should be maximized to the greatest extent consistent with the size and weight constraints.

- Bearing friction and data link torques shall be minimized to the greatest extent consistent with other requirements.

Table 3-8   Summary of EEA Design Requirements

Functional

- Provide motor drive circuitry for experiment gimbal drive motors.

- Provide experiment gimbal control servo electronics.

- Provide Inductosyn excitation and readout processing circuitry.

- Condition all experiment gimbal and control telemetry and commands.

Performance and Design

- The EEA design should duplicate, to the greatest possible extent, the circuits developed for the star tracker electronics.

- Motor drive circuit design should provide for minimum dependence of drive torque upon position.

- Motor drive circuitry bandwidth shall exceed 50 Hz.

- Inductosyn processing will provide gimbal position and rate signals over entire range of gimbal travel and all gimbal rates. Precision data is required for rates up to 2 deg/sec to accuracy of 0.5 sec (1σ), per axis.

- Inductosyn data bandwidth (including processing) shall exceed 100 Hz.

- Electronics will provide for electronically servoing the gimbal angles to zero without computer intervention.

- Design must be consistent with a 3 to 5 year operational life (100% duty cycle).

budget/analysis, and bandwidth and frequency compensation requirements are defined by the experiment gimbal servo analysis (Appendix H).

3.2.9 Antenna Gimbal and Electronics Assemblies

The antenna gimbals are assumed inactive during all operations prior to PPCS turn-on. Activation of the antenna gimbal need not occur until acquisition of the precision attitude reference. For the PPCS operation in low altitude, sun-synchronous orbits, the antenna will be pointed (either command steer or autotrack) at one of three data-relay satellites in a geo-synchronous orbit. Utilization of any particular relay satellite during any time period will be a function of the visibility constraints, with a period of 4 minutes alloted to the retargeting be-tween data transmission to a new data relay satellite. For PPCS operation in geo-synchronous orbit, the antenna will be pointed continuously at a dedicated ground station. The design requirements are summarized in Table 3-9.

3.2.10 Data Interface Assembly

The data transfer requirement is defined by compiling all the signals between each and every assembly. This is mechanized by use of a data list which summarizes the signal characteristics, destinations and originations, resolution of the signal, sampling rate, etc. The signals in the data list include both in-line signals for sensor input and control output, and monitoring signals for checkout and status determination. Virtually all PPCS operational signals identified go to or from the DCA. There is thus no need for other than DCA to user traffic and the bus control format is also greatly simplified. Memory reload, command and telemetry, in any configuration, do not present a significant impact. The data traffic requirement is summarized in Table 3-10.

It is to be noted that data traffic analysis is only one aspect of the data transfer requirement analysis. Another major consideration is the timeliness of the data. The gyro rates, for example, consist of a message which could take several hundred μsec to transmit (at a 500 KBPS data rate). Since the gyro data required by the software assumes simultaneous sampling of all gyros, storage registers must exist in the gyro assembly I/O interface (or GRA). Note also that a minimal inter-pulse interval of 37 μsec occurs from the gyro for a slew rate of 1.5 $^\circ$/sec and a 0.2 $\widehat{\sec}$ pulse magnitude threshold. This timing also demands a storage regis-ter.

Similar considerations apply to experiment and star sensor gimbal drive commands and angle monitors. Initial analysis indicates that mechanical time constants do not demand special timing techniques, such as distinct load and execute commands.

Table 3-9   Summary of AGA and AEA Design Requirements

Functional

- The Antenna Gimbal Assembly shall accurately point in two axes in response to motor drive signals from the Antenna Electronics Assembly.

- Provide gimbal angular position data.

- The AGA design shall provide for an appropriate mechanical interface with both the spacecraft structure and the antenna/communication platform with provision for alignment.

Performance and Design

- The gimbals shall be designed to provide $\pm$ 105 degree angular range about an upward vertical axis.

- Electro-mechanical design characteristics must be consistent with tracking rates of 0.12 deg/sec, peak slew rates of 1.0 deg/sec, and peak accelerations of 0.1 deg/sec^2.

- The total pointing error associated with the AGA and AEA shall be less than 1 min (1σ), per axis. Such a requirement assumes maximum antenna misalignment of one min (for which correction is not required).

- Reliability shall be consistent with a 3 to 5 year life.

- Thermal design shall be consistent with ambient range of +10°C to +40°C.

- The antenna configuration can be characterized as within the envelope of an equivalent 4 ft cube gimbaled at the center of one of the faces and gimbal axis normal to the "sides".

- The mass properties of the antenna are such that the weight is less than 25 pounds, and inertia at the gimbal cg is less than 5 slug -ft^2 about both axes.

- RF cabling across the gimbal will have an equivalent spring constant of less than 5 in-oz/rad.

Table 3-10. PPCS Data Transfer Requirements

System Elements	Minor Cycle (5 per sec)	Monitor Bits (1 per sec)	Major Cycle (1 per sec)	Total BPS
Sensor Electronics (SEA)	189	63	225	1233
Alignment Sensor(s) (ASA)	756	72	153	4005
Experiment Electronics (EEA)	1134	324	1566	7540
Antenna Electronics (AEA)	144	54	108	882
Gyro Reference (GRA)	153	54	108	927
Telemetry*			10000	10000
Spacecraft Interface*		234	348	582
Command*			2000	2000
Total	2565			27169

NOTES:

● Estimates based on a 200 ms minor cycle, 1 sec major cycle.

● Based on six experiments to be controlled, plus the antenna.

● Overhead based on data transfer format is included.

● All transfer is to or from DCA; no other assembly-to-assembly traffic.

---

* Preliminary worst-case estimates

3.2.11 Digital Computer Assembly

The digital computer design requirements are derived primarily from computational characteristics and storage required by the software. These computer design requirements are developed in detail for a laboratory model test computer (Appendix K). A summary of these requirements for the DCA are given in Table 3-11.

The development of the software requirements are based upon the software preliminary design discussed in Section 7.0. The basic computer software for executive supervision and monitoring includes an executive, data bus control, telemetry and command processing, on-board diagnosis, and memory load and reload. The PPCS application software modules perform attitude determination and pointing control.

The computational and storage requirement of these software modules is defined in order to provide the overall computational speed and storage requirements for the DCA. Table 3-12 summarizes the total storage requirements. Storage requirement for the data base (e.g., the star tables, target tables, and ephemeris tables) are also estimated. Table 3-13 summarizes the computational time requirements of key application software modules during the time critical path in terms of number of equivalent add instructions, multiply instructions, and divide instructions required for each module during a one second period.

By assigning a duty cycle and a set of execution time ratios of the multiply and divide instructions to the equivalent add instructions, the execution time requirements for the equivalent add instruction, the multiply and the divide instructions can be derived. The duty cycle is defined as the percent of time the computer is busy in carrying out the computations. Table 3-14 shows the instruction execution time requirements for different duty cycles.

It is to be noted that the estimates on computational time are dependent upon the instruction repertoire of the computer and the data word length. A sophisticated set of instructions will minimize the number of instructions to be executed for a given function. Analysis of the PPCS application program modules indicated that the computer should have an efficient set of arithmetic instructions. Further, the computational time is dependent on the data word. The attitude algorithm design analysis (Section 5.1) indicated that the gyro software modules have to be performed with an accuracy of 24-bit or better; therefore, double precision arithmetic instructions must be provided to ensure adequate accuracy. Use of double precision will also increase the number of instructions executed for a given calculation.

Table 3-11   Summary of DCA Design Requirements

Functional

Provide PPCS computational, data processing, and storage capabilities and provide appropriate interface to the Data Interface Assembly.

Performance

- General-purpose parallel computer employing fractional two's complement arithmetic.

- Data word length of 24 bits required, 32 bits desired.

- Instruction word of sufficient length to decode all instructions and provide adequate address field for direct addressability up to at least 4K, and means to address complete memory without time penalty.

- The instruction repertoire shall include sufficient basic instructions for program control, arithmetic operations, logic instructions, input/output instructions, and data transfer.

- The execution time of the fixed point ADD instruction with index modification of the address shall be four microseconds or less.

- The execution time of the fixed point MULTIPLY instruction with index modification of the address shall be 32 microseconds or less.

- The execution time of the fixed point DIVIDE instruction for double precision dividend with index modification of the address shall be 72 microseconds or less.

- The computer shall have at least one hardware index register which does not require additional time for carrying out the indexing operation.

- The memory shall be a minimum of 8K, of modular design, and expandible to 32K.

Table 3-12. PPCS Storage Requirement Estimates

Element	Program (Words)	Data (Words)
Executive	1400	300
Application Modules:		
Attitude Determination	1339	295
Alignment Reference	118	42
Heading Reference	265	63
Pointing Control	652	123
	2374	523
Subroutines	375	
Data Base		650
Total	4149	1473

NOTE: Assumes single-precision throughout, 24 bit data
word minimum

Table 3-13. Key Application Software Timing Requirements

Elements	Iteration/Sec	Equiv. Add	Equiv. Mult.	Equiv. Div.
Attitude Determination	5	5405	670	90
Alignment Reference	30	25440	3540	180
Heading Reference	5	3005	410	50
Pointing Control	30	35850	4080	720
Total		69700	8700	1040

Table 3-14. Instruction Execution Speed Effect on Duty Cycle

Instruction ╲ Duty Cycle	80%	60%	40%
Add (μsec)	5	3.75	2.5
Multiply (μsec)	40	30	20
Divide (μsec)	90	67.5	45
Ratio: M = 8A, D = 18A			

3.3 SYSTEM INTERFACES

The PPCS system interfaces, both internal and external, are briefly summar-
ized in this section. The internal interfaces considered are primarily electrical
(e.g., assembly-to-assembly signal interfaces) and the external interfaces are pri-
marily spacecraft mechanical interfaces (e.g., alignment/mounting and structural
characteristics).

3.3.1 PPCS Electrical Signal Interface

The PPCS assembly-to-assembly signals are shown in Figure 3-5 at the inter-
face to the Data Interface Assembly (DIA). For ease of visualization, only one
star tracker (1 of 2), two gyro channels (2 of 6), one alignment sensor (1 of 6),
one experiment gimbal and electronics (1 of 6), and the antenna are shown. Elements
not shown are assumed identical in all ways to the representative element shown.
Scale factor and resolution of the signals is shown as extracted from design
requirements.

3.3.2 PPCS/Spacecraft Mechanical Interfaces

Key to the overall PPCS performance is the consideration of mechanical align-
ment, fields-of-view (mounting), and structural characteristics of the PPCS/space-
craft interface. Except for the alignment sensor reflectors, primary elements for
determining attitude reference are integrally mounted on the RBA. In general,
absolute alignment of these elements to the order of a few tens of arcseconds is
not critical. What is critical is knowledge of that alignment through arc-sec
level measurement of the appropriate sensitive axes.

For the alignment sensor reflectors (mounted at the experiment gimbal) align-
ment is relatively critical. For the transverse axis measurements, the plane mirror
must be aligned to an accuracy of 12 sec for limiting the cross-coupling error con-
tribution to 0.1 sec. Similarly, for the twist measuring system, the prism hard
mounted to the support plate is aligned to 15 sec or better. These alignments
across a (potentially) deployed interface are clearly of concern.

Mounting of equipment for appropriate fields-of-view is a considerably less
demanding problem. Of interest are the star tracker, alignment sensor, and experi-
ment and antenna gimbals. The star tracker is mounted within the spacecraft such
that the FOV is optimized with respect to the particular orbit/mission characteris-
tics and spacecraft and environmental constraints. For low altitude PPCS applica-
tions (200-2500 nm, sun synchronous), several possibilities have been evaluated.
These are summarized in Figure 3- 6 . In one typical configuration, the outer gimbal
axis is aligned along the spacecraft roll axis, and the mechanical FOV centered
along a line 45° above the local horizontal in the plane normal to the orbit plane

Figure 3-5, PPCS Signal Interface Block Diagram
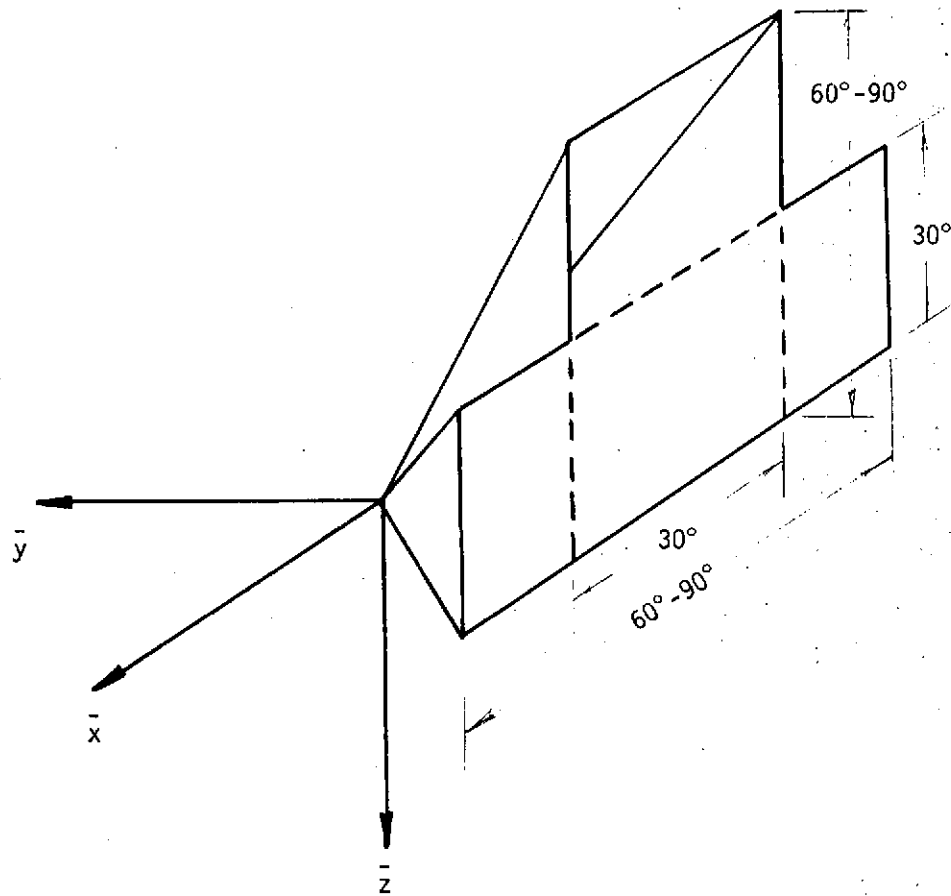
Figure 3-6. Star Tracker Field-of-View Interface

on the side of the spacecraft away from the sun. In another typical configuration, the outer gimbal axis is aligned along the local vertical axis and the mechanical FOV centered along a line 15 degrees above the local horizontal in the plane normal to the orbit plane away from the sun. In both cases, an edge of the FOV lies in the local horizontal plane. In the latter case, a total FOV of $\pm 15°$ x $\pm 30°$ is adequate, and some further reduction in total FOV requirements may be anticipated for some low altitude missions.

For geosynchronous application, a typical arrangement has the outer gimbal axis aligned along the local vertical axis and the mechanical FOV centered along the orbit normal directed toward the north pole. Some deviation from this configuration can be tolerated with relative ease, but in general a full $\pm 15°$ x $\pm 45°$ FOV in the nominal orientation is a good configuration.

The autocollimator elements are mounted with a clear line-of-sight field-of-view to the reflector mounted at the desired reference, i.e., platform gimbal base. Platform gimbals for earth-viewing experiment pointing are typically oriented such that the inner gimbal axis corresponds to rotation about the orbit normal and the boresight is nominally aligned along local vertical. The inner axis (spacecraft attach point) and outer axis (payload attach point) provide ± 45 degrees of gimbal rotation; the middle axis provides ± 10 degrees freedom. The antenna is mounted to observe one of a system of synchronous data relay satellites when operating in low altitude orbits, and mounted for direct earth transmission when operating at geosynchronous altitudes.

Structural considerations relating to PPCS performance are essentially limited to proper stable support of the reference block assembly and support of the non-integrally mounted payload. In the latter case, the structure must be hollow, light-proof, and of sufficient diameter to provide an optical path for alignment sensing using the Alignment Sensor Assembly. The interface structure is to be less than 10 feet in length, have tip deflections of less than 0.5 inch, and natural frequencies less than 1.0 Hz.

A final mechanical interface is with the experiment payload. The payload to be pointed by PPCS must have a mass (including gimbal structure) of less than 20 slugs and an inertia between 10 and 1000 slug-ft^2. Inertias will be known within 5 percent to a set of axes parallel to the payload gimbal reference axes but centered at the gimbal center of mass. Uncompensated momentum associated with platform experiments will be less than 0.1 ft-lbs-sec.

4.0 SYSTEM ANALYSIS

This section presents the system analysis of key areas whose consideration influences the total system. These areas include development of the system equations, the system error analysis, observability analysis, and reliability analysis. The system equations are the basis for simulation and software design. The system error analysis provides support for budget allocation, identification of sensitivity to key error sources, and verification for observed simulation performance. The observability analysis provides a means by which key systematic errors throughout the system can be assured of potential calibration. Finally, the reliability analysis is the means for budget allocation to various hardware elements, for configuration/design tradeoffs, and to lend confidence to achieving three to five year life.

4.1 SYSTEM EQUATIONS

The major portion of the equation development effort revolved about the development of the PPCS simulation programs [6-7]. Those portions of the software considered critical for the flight system were represented by computer models of more or less complexity, depending upon the associated error contributions and performance potential. This section presents the equations summarized in a readily understandable form and as generally appropriate for the flight application. A detailed derivation of these equations, developed in a more general form for simulation, is found in Appendix B.

The approach used in establishing the PPCS system equations was to utilize the minimal equation configuration from the derived computer models, adding complexity only where necessary to obtain significant performance improvements. In general, the only complexity added has been additional terms to compensate for systematic (non-random) errors, i.e., biases and alignments. The equations are presented which perform the following functions:

Gyro Reference
    Rate Derivation
    Attitude Integration
    ECI to Body Transformation

Tracker Reference
    Star Selection
    Aberration Correction
    Tracker Measurement Processing

Kalman Filter

Local Vertical Reference

Alignment Reference

Targeting

Gimbal Steering

4.1.1 Coordinate Systems

The primary orbital and body reference frames are illustrated in Figures 4-1 and 4-2.

4.1.1.1 Earth Centered Inertial Coordinates, {z} (ECI)

The earth centered coordinate system in the coordinate system of the mean equinox and equator of epoch. The axes are:

z_1 in the direction of the vernal equinox

z_2 forms a right-handed orthogonal set with z_1 and z_3

z_3 in the direction of the earth angular velocity

4.1.1.2 Earth Centered Rotating Coordinates, {y^G}

The earth centered rotating coordinate system has as its axes:

y_1^G in the plane of the equator through the meridian of Greenwich

y_2^G forms a right-handed orthogonal set with y_1^G and y_3^G

y_3^G in the direction of the earth angular velocity

4.1.1.3 Local Vertical Orbit Coordinates, {y}

This topocentric, horizontal reference coordinate system has as its axes:

y_1 forms a right-handed orthogonal set with y_2 and y_3

y_2 directed opposite to the direction of the vehicle orbital angular velocity vector

y_3 along the radius vector from the vehicle toward the earth center

4.1.1.4 Body Reference Coordinates, {x}

This reference frame has origin at the spacecraft c.g. and axes:

x_1 roll, directed forward

x_2 pitch, directed rightward to form a right-handed orthogonal set with x_1 and x_3

x_3 yaw, directed downward

4.1.1.5 Tracker Reference Axes, {x^j}

The tracker reference axes define the _nominal_ axes for the tracker when the gimbal angles are zero. The axes form a right-handed orthogonal set such that:

x_1^j along the nominal outer gimbal axis

x_2^j along the nominal optical axis

x_3^j along the nominal inner gimbal axis
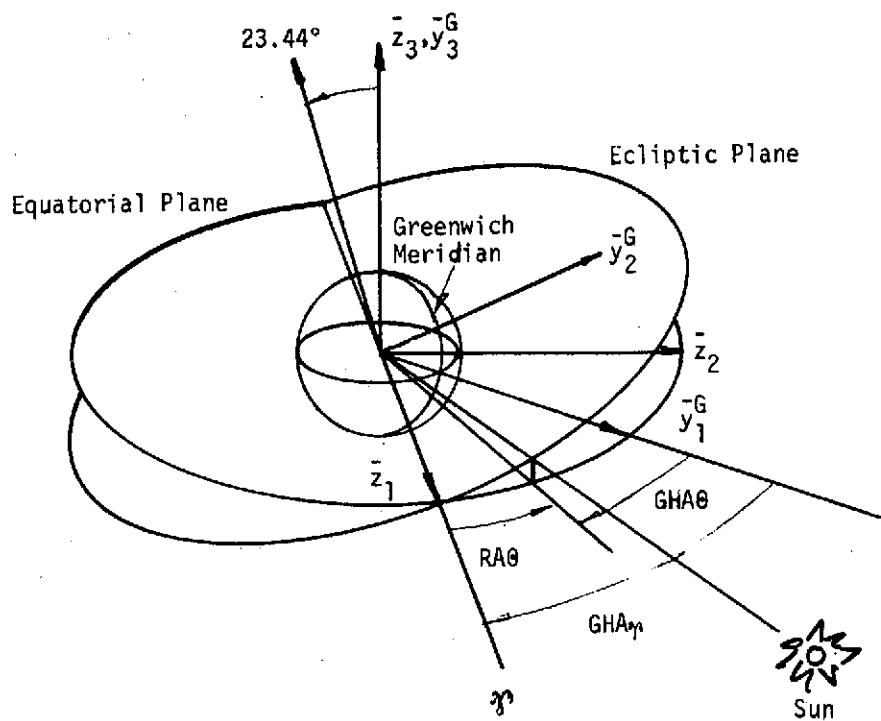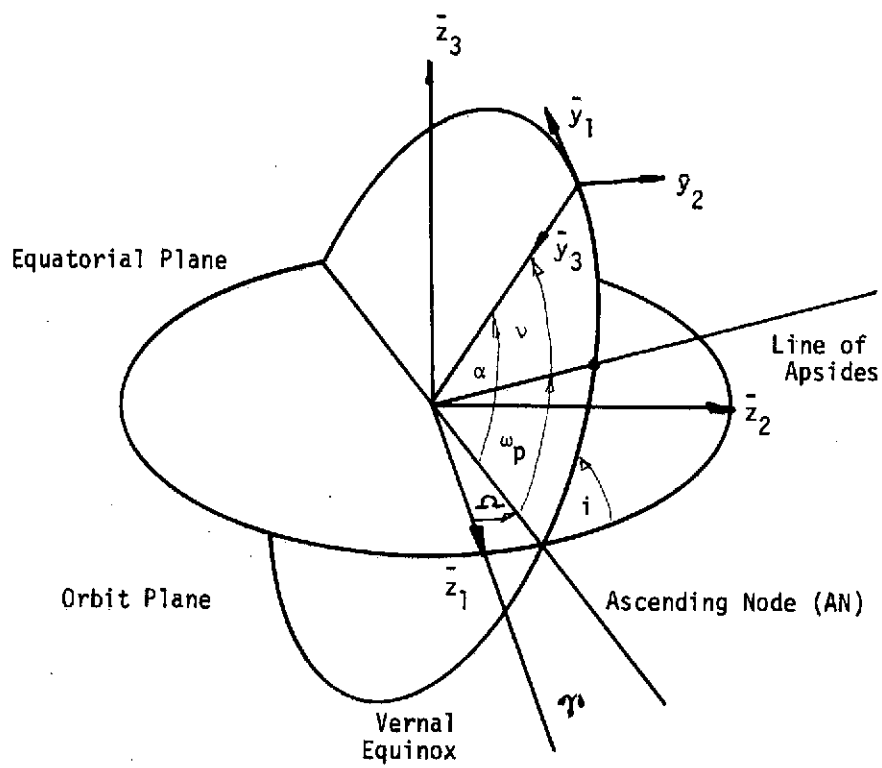
Figure 4-1. Orbital Reference Frames
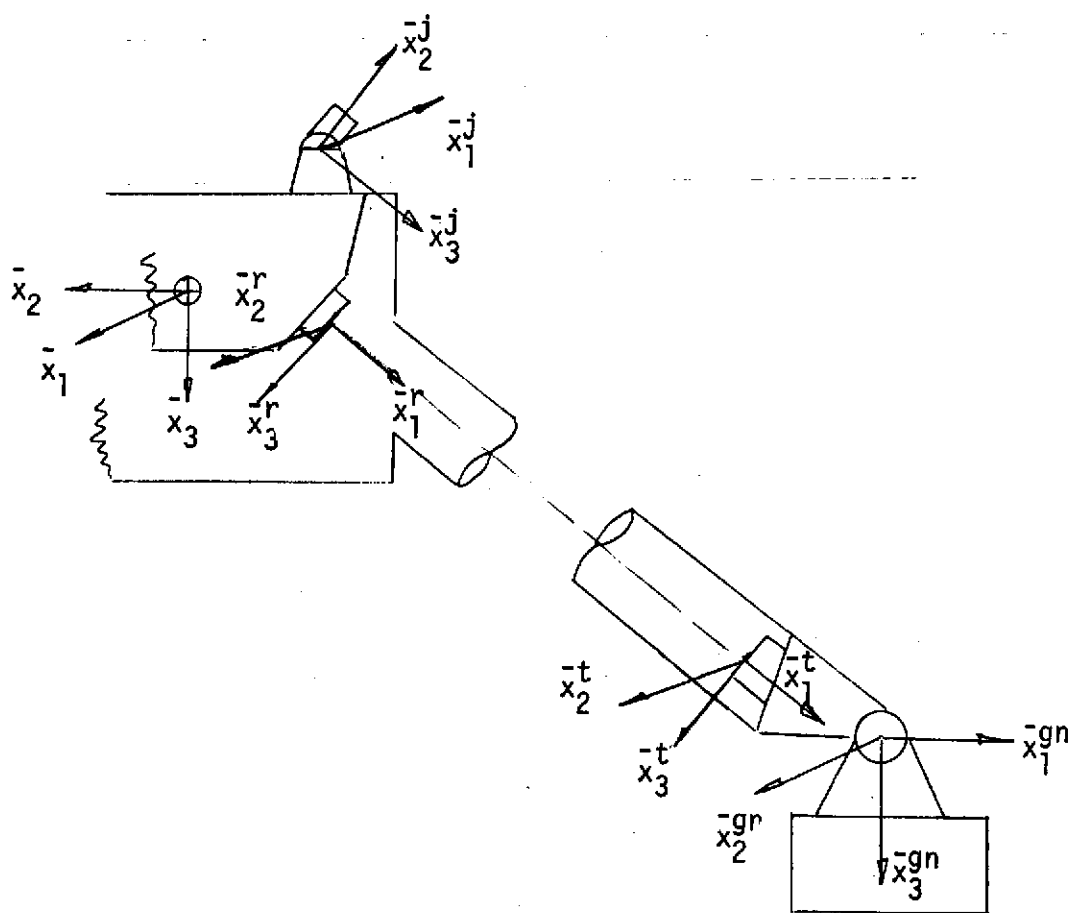
Figure 4-2. Body Reference Frames

4.1.1.6 Autocollimator Reference Axes, $\{x^r\}$

This reference frame is fixed in the autocollimator such that:

x_1^r is along the autocollimator beam LOS

x_2^r in a plane normal to x_1^r (directed as convenient)

x_3^r forms a right-handed orthogonal set with x_1^r and x_2^r

4.1.1.7 Reflector Reference Axes, $\{x^t\}$

This reference frame is fixed in the alignment reflector such that:

x_1^t is normal to the reflector surface

x_2^t is nominally aligned with x_2^r

x_3^t is nominally aligned with x_3^r

4.1.1.8 Gimbal Reference Axes, $\{x^{gn}\}$

The gimbal reference axes define the _nominal_ axes for the gimbal when the gimbal angles are zero. The axes are defined such that:

x_1^{gn} along the nominal outer gimbal axis

x_2^{gn} along the nominal middle gimbal axis

x_3^{gn} along the nominal inner gimbal axis

4.1.1.9 Target Reference Axes, $\{x^p\}$

These axes define the target vector such that:

x_1^p defines the constraint about the LOS to the target

x_2^p forms an orthogonal right-handed frame with x_1^p and x_3^p

x_3^p is along the line-of-sight to the target from the spacecraft

4.1.2 Coordinate Transformations

4.1.2.1 Earth Centered Inertial to Local Vertical

The real-world transformation from ECI to local vertical is determined from the orbital elements as shown in Figure 4-1 . Define

Ω = longitude of the ascending node

i = orbit inclination

α = orbit angle = $\omega_p + \nu$

ω_p = argument of perigee

ν = true anomaly

It follows that

$$\bar{y} = A_{yz} \bar{z} \qquad (4-1)$$

where

$$A_{yz} = \begin{bmatrix} 0 & 1 & 0 \\ 0 & 0 & 1 \\ 1 & 0 & 0 \end{bmatrix} \begin{bmatrix} \cos\alpha & \sin\alpha & 0 \\ -\sin\alpha & \cos\alpha & 0 \\ 0 & 0 & 1 \end{bmatrix} \begin{bmatrix} 1 & 0 & 0 \\ 0 & \cos i & \sin i \\ 0 & -\sin i & \cos i \end{bmatrix} \begin{bmatrix} \cos\Omega & \sin\Omega & 0 \\ -\sin\Omega & \cos\Omega & 0 \\ 0 & 0 & 1 \end{bmatrix}$$

The computer transformation from ECI to local vertical is determined from the on-board ephemeris. (Section 4.1.6)

4.1.2.2 Earth Centered Inertial to Body Axes

The transformation from ECI to body axes is the output of the attitude determination computations, A_{xz} (Section 4.1.3).

4.1.2.3 Earth Centered Inertial to Earth Centered Rotating

Universal time (Greenwich Mean Time, GMT) is defined as

$$GMT = 12^h + GHA\theta \qquad (4-2)$$

where $GHA\theta$ is the Greenwich Hour Angle of the mean sun. It can be found from

$$GHA\theta = GHA\gamma - RA\theta \qquad (4-3)$$

where $GHA\gamma$ is the Greenwich Hour Angle of the mean equinox (Aries) and $RA\theta$ is the right ascension of the mean sun of epoch, where the latter is based upon date and time of epoch [19]. From this,

$$GHA\gamma = GMT - 12^h + RA\theta \qquad (4-4)$$

Converted into radians, $GHA\gamma$ represents the initial value of the angle between the ECI and ECR frames, Δ_0. Subsequently, the product of earth rate and time elapsed since epoch is added to obtain the current value of angle, $\Delta = \Delta_0 + \omega_e(t - t_0)$. The transformation matrix is then

$$A_y G_z = \begin{bmatrix} \cos\Delta & \sin\Delta & 0 \\ -\sin\Delta & \cos\Delta & 0 \\ 0 & 0 & 1 \end{bmatrix} \qquad (4-5)$$

4.1.2.4 Tracker Reference to Sensor Boresight

The transformation from tracker reference to boresight is determined by the gimbal angles and three sets of misalignment angles:

$$
A_{sx}^{j} = \begin{bmatrix} 1 & \alpha_3 & 0 \\ -\alpha_3 & 1 & \alpha_1 \\ 0 & -\alpha_1 & 1 \end{bmatrix} \begin{bmatrix} \cos\theta_I & \sin\theta_I & 0 \\ -\sin\theta_I & \cos\theta_I & 0 \\ 0 & 0 & 1 \end{bmatrix} \begin{bmatrix} 1 & 0 & -\alpha_2^{I} \\ 0 & 1 & \alpha_1^{I} \\ \alpha_2^{I} & -\alpha_1^{I} & 1 \end{bmatrix}
$$

$$
\begin{bmatrix} 1 & 0 & 0 \\ 0 & \cos\theta_o & \sin\theta_o \\ 0 & -\sin\theta_o & \cos\theta_o \end{bmatrix} \begin{bmatrix} 1 & \alpha_3^{o} & -\alpha_2^{o} \\ -\alpha_3^{o} & 1 & 0 \\ \alpha_2^{o} & 0 & 1 \end{bmatrix} \tag{4-6}
$$

4.1.2.5 Alignment Reference to Reflector

The transformation from the alignment reference (instrument axes) to reflector is determined by three Euler angles, with order of rotation such that the final rotation is taken about the boresight axis.

$$
A_{tr} = \begin{bmatrix} 1 & 0 & 0 \\ 0 & \cos\phi & \sin\phi \\ 0 & -\sin\phi & \cos\phi \end{bmatrix} \begin{bmatrix} \cos\theta & 0 & -\sin\theta \\ 0 & 1 & 0 \\ \sin\theta & 0 & \cos\theta \end{bmatrix} \begin{bmatrix} \cos\psi & \sin\psi & 0 \\ -\sin\psi & \cos\psi & 0 \\ 0 & 0 & 1 \end{bmatrix} \tag{4-7}
$$

4.1.2.6 Gimbal Reference to Experiment Platform

The transformation from gimbal base reference to experiment platform is determined by the three gimbal angles and three sets of misalignment angles. Because of the "inside-out" gimbal design, the initial rotation is taken about the inner gimbal such that $A_{ex}{}^{gn}$ =

$$
\begin{bmatrix} 1 & 0 & 0 \\ 0 & \cos\phi & \sin\phi \\ 0 & -\sin\phi & \cos\phi \end{bmatrix} \begin{bmatrix} 1 & \alpha_{\ell 3} & -\alpha_{\ell 2} \\ -\alpha_{\ell 3} & 1 & 0 \\ \alpha_{\ell 2} & 0 & 1 \end{bmatrix} \begin{bmatrix} \cos\theta & 0 & -\sin\theta \\ 0 & 1 & 0 \\ \sin\theta & 0 & \cos\theta \end{bmatrix} \tag{4-8}
$$

$$
\begin{bmatrix} 1 & \alpha_{m3} & 0 \\ -\alpha_{m3} & 1 & \alpha_{m1} \\ 0 & -\alpha_{m1} & 1 \end{bmatrix} \begin{bmatrix} \cos\psi & \sin\psi & 0 \\ -\sin\psi & \cos\psi & 0 \\ 0 & 0 & 1 \end{bmatrix} \begin{bmatrix} 1 & 0 & -\alpha f_2 \\ 0 & 1 & \alpha f_1 \\ \alpha f_2 & -\alpha f_1 & 1 \end{bmatrix}
$$

4.1.3 Gyro Reference Equations

The gyro reference equations include processing of the gyro outputs to derive rate estimates, propagation of attitude using the derived rate, and computation of the direction cosine matrix relating body axes to ECI.

4.1.3.1 Rate Derivation

Each of the N_g operating outputs, $\Delta\tilde{\theta}_i$, is processed to derive the gyro "measured" rate, $\tilde{\omega}_i$. A second order fit is made to the discrete gyro output and differentiated to obtain rate. In this case, the rate measured by each gyro is given by

$$\tilde{\omega}_i = \frac{\Delta\tilde{\theta}_i}{\Delta T} \tag{4-9}$$

where ΔT is the period between gyro counter reset. The computed estimate of rate about the attitude reference axes is determined as a linear combination of the N_g rates derived from the measured gyro outputs. The gyro drift bias is compensated by the addition of a constant term whose value is periodically updated,

$$\hat{\omega} = \hat{G}\tilde{\omega} - \hat{b} \tag{4-10}$$

The matrix, G, is a $3 \times N_g$ "geometry" matrix that relates the gyro input axes to the reference axes and accounts for the gyro scale factors. This matrix is defined as

$$G \triangleq A_\gamma^{-1} \tau \tag{4-11}$$

where the $3 \times N_g$ matrix τ is obtained by a least squares fit to the measured nominal scale factor and alignment and the 3×3 matrix, A_γ, represents a small perturbation between the measured and true scale factor/alignment. The matrix τ is established by preflight measurement. The matrix, A_γ, is determined through preflight and/or flight calibration procedures to establish $\hat{G}$.

4.1.3.2 Attitude Integration

The estimated rate is used in a numerical integration scheme to obtain attitude, where Euler Symmetric Parameters are employed as the kinematic variables. One may establish that

$$\dot{\bar{\rho}} = \frac{1}{2}\Omega\bar{\rho} \tag{4-12}$$

where

$$
\rho = \begin{bmatrix} \xi \\ \eta \\ \zeta \\ \chi \end{bmatrix}, \qquad \Omega = \begin{bmatrix} 0 & \omega_3 & -\omega_2 & \omega_1 \\ -\omega_3 & 0 & \omega_1 & \omega_2 \\ \omega_2 & -\omega_1 & 0 & \omega_3 \\ -\omega_1 & -\omega_2 & -\omega_3 & 0 \end{bmatrix}
$$

If the integration period is selected sufficiently small such that Ω can be taken as constant over the step interval, then the solution can be determined as

$$
\rho_{k+1} = \exp(\Omega_k \, \Delta T/2) \, \rho_k \tag{4-13}
$$

where

$$
\Delta T = t_{k+1} - t_k
$$
$$
\rho_k = \rho(t_k)
$$

and Ω_k represents the constant matrix assumed on the interval $[t_k, t_{k+1}]$. A simple closed form expression for $\exp(\Omega_k \, \Delta T/2)$ is obtained which tends to inhibit the truncation error that would normally exist in the power series representation of the exponential. This closed form representation is given as:

$$
\exp(\Omega_k \, \Delta T/2) = (\cos b\Delta T) \, I + \frac{\sin b\Delta T}{2b} \, [\Omega]
$$

$$\tag{4-14}$$

where

$$
b = \frac{1}{2} \left[\hat{\omega}_1{}^2 + \hat{\omega}_2{}^2 + \hat{\omega}_3{}^2 \right]^{1/2}
$$

4.1.3.3 ECI to Body Transformation

The computed Euler parameters, $\hat{\rho}$, are used to generate a direction cosine matrix which relates the attitude reference axes, $\bar{x}$, the the Earth-Centered Inertial (ECI) reference axes, $\bar{z}$. This is established from the following matrix equality.

$$
\Gamma^2 = \left[\begin{array}{c|c} A_{xz} & 0 \\ \hline 0 & 1 \end{array} \right] \tag{4-15}
$$

where

$$
\Gamma = \begin{bmatrix} \rho_4 & \rho_3 & -\rho_2 & \rho_1 \\ -\rho_3 & \rho_4 & \rho_1 & \rho_2 \\ \rho_2 & -\rho_1 & \rho_4 & \rho_3 \\ \rho_1 & \rho_2 & \rho_3 & -\rho_4 \end{bmatrix}
\tag{4-16}
$$

4.1.4 Star Tracker Reference

The primary purpose of the star tracker reference is to provide a direct measure of attitude which, when compared to the estimated measure, provides a measurement residual (error signal) for the Kalman filter. There are two basic functions performed by the star tracker equations; the first is control of the star tracker including catalog sorting, star selection, and acquisition of appropriate target stars; the second is processing the appropriate sensor measurements.

4.1.4.1 Star Selection

One of the significant benefits obtained from using a star tracker for attitude reference is the inherent flexibility in star selection, both in terms of which stars are selected and the frequency between star measurements. Since the star catalog required is small, data can be stored to include the total of stars available through the whole mission. On the other hand, if storage is a premium, only a segment of the celestial sphere need be stored which is periodically updated.

If a relatively fixed catalog is to be used, as in a geosynchronous orbit or where only a segment is stored, the catalog may be presorted for the particular application using ground-based processing and stored in terms of direction cosines relative to ECI and orbit angle viewing limits. To make the system relatively more autonomous, the on-board catalog (unsorted) can be stored, e.g., right ascension and declination in ECI to minimize memory. In this approach, on-board computation is performed to provide a presorting of stars in terms of orbit angle as defined by viewing constraints. The frequency of such presorting is, of course, dependent on the orbit nodal regression rate and characteristics of vehicle motion. At each star update, the on-board catalog is searched (e.g., on the basis of orbit angle) to determine stars which satisfy present viewing constraints. These stars then form the "mini"-catalog from which target stars may be selected.

Following catalog sorting to define available stars, there remains the question of star selection. Various criteria for star selection are discussed elsewhere (Section 5.3), but the baseline approach is to select that star within the tracker FOV which has the greatest separation from the previous star. This

is done by computing the dot product of each available candidate star vector with the previous star vector, i.e.,

$$c_i = \bar{a}^0 \cdot \bar{a}_i$$

$$\phi_i = \tan^{-1}\left((1 - c_i^2)^{1/2}/c_i\right) \qquad (4\text{-}17)$$

$$\bar{a}^0 \leftarrow \bar{a}_i \text{ for } \phi_{i(max)}$$

4.1.4.2 Aberration Correction

The coordinates of the selected star must initially be corrected for aberration of the apparent star direction since the spacecraft velocity relative to the stars cannot be considered negligible relative to the speed of light. If a_i ($i = 1, 2, 3$) represents the catalog star coordinates in the ECI coordinate set, then the apparent star coordinates corrected and transformed to the attitude reference are given by

$$\begin{bmatrix} u_1 \\ u_2 \\ u_3 \end{bmatrix} = \left(1 - \frac{\beta^a}{c}\right) A_{xz} \begin{bmatrix} a_1 \\ a_2 \\ a_3 \end{bmatrix} + \frac{1}{c} A_{xz} \begin{bmatrix} V_1^a \\ V_2^a \\ V_3^a \end{bmatrix} \qquad (4\text{-}18)$$

where $\bar{v}^a$ is the spacecraft velocity, $V_i^a = \bar{v}^a \cdot \bar{z}_i$, $i = 1, 2, 3$, c is the velocity of light, and β^a is the inner product of $\bar{v}^a$ and the actual star unit vector. The velocity, $\bar{v}^a$, is computed from knowledge of the earth velocity about the sun and the spacecraft velocity about the earth.

4.1.4.3 Tracker Measurement Processing

The objective of the star tracker measurement processing is to develop a measured residual resulting from the difference between measured and estimated tracker outputs. The estimated measurement vector, $\hat{y}$, is differenced with the observed measurement vector, $\bar{y}$, to form the measurement residual, $\delta\hat{y}$, which is used in the Kalman filter for state vector update. The measurement quantity selected is the sine of the inner and outer gimbal angles. Thus, one must develop expressions for the estimated measurement, $\hat{y}$, based upon the star catalog, the estimated attitude, and known misalignments/imperfections in the star tracker. The measurement, $\bar{y}$, is based upon the gimbal readout and detector output.

The corrected star coordinates, u_i, are related to the reference axes through the gimbal angles, detector outputs, and gimbal alignments. The estimated

4-11

measurement vector, $\hat{y}$, is determined as

$$
\hat{y} = \begin{bmatrix} \widehat{\sin\theta_I} \\ \widehat{\sin\theta_0} \end{bmatrix} = \begin{bmatrix} 0 & 0 & -(1 - u_1{}^2)^{1/2} \\ \dfrac{-u_2}{1 - u_1{}^2} & \dfrac{u_1 u_2}{1 - u_1{}^2} & 0 \end{bmatrix} \begin{bmatrix} \hat{\alpha}_1 \\ \hat{\alpha}_2 \\ \hat{\alpha}_3 \end{bmatrix} + \begin{bmatrix} -u_1 \\ \dfrac{u_3}{(1 - u_1{}^2)^{1/2}} \end{bmatrix}
$$

$$(4\text{-}19)$$

where $\hat{\alpha}_1$ and $\hat{\alpha}_3$ are the estimated values of sensor bias relative to the nominal geometric boresight, and $\hat{\alpha}_2$ is the estimated value of non-perpendicularity of the inner gimbal relative to the outer gimbal. The values of $\hat{\alpha}_i$ are established through preflight alignment and calibration and, in addition, the angles are observable in the tracker measurements so that flight calibration can be implemented if desired. The observed measurement vector, $\tilde{y}$, has the form

$$
\tilde{y} = \begin{bmatrix} \sin\tilde{\theta}_I + (1 - u_1{}^2)^{1/2}\ \tilde{\delta}_3 \\ \sin\tilde{\theta}_0 + \dfrac{u_2}{1 - u_1{}^2}\ \tilde{\delta}_1 \end{bmatrix}
$$

$$(4\text{-}20)$$

where $\tilde{\delta}_1$, $\tilde{\delta}_3$ are the measured star coordinates relative to the tracker boresight (detector outputs) and $\tilde{\theta}_I$, $\tilde{\theta}_0$ are the measured Inductosyn angles.

4.1.5 Kalman Filter

The Kalman filter accepts the difference between the measured and computed star tracker variables (measurement residual) and multiplies this difference vector by a gain matrix to obtain updates to the state vector. The Kalman filter for PPCS attitude determination has a state vector consisting of three attitude variables and three gyro biases:

$$
\left.\begin{array}{l} x_1 \\ x_2 \\ x_3 \end{array}\right\} \hat{\rho}^0,\ \text{attitude parameters}
$$

$$
\left.\begin{array}{l} x_4 \\ x_5 \\ x_6 \end{array}\right\} \hat{b},\ \text{gyro bias parameters}
$$

In using the Euler parameters, it is noted that one of the parameters is redundant, being constrained by a simple algebraic relation, i.e., $\rho_1{}^2 + \rho_2{}^2 + \rho_3{}^2 + \rho_4{}^2 = 1$. This makes it possible to unambiguously represent variations in ρ_4 (for $\rho_4 \neq 0$) in terms of variations in ρ_1, ρ_2, and ρ_3. It follows that the Kalman filter need estimate only the latter three variables, and thus its state vector contains only three attitude terms. It is noted that the filter employed for ground-based calibration may have an expanded state vector to incorporate the variables for calibration, e.g., tracker misalignments, $\hat{\alpha}_i$, or gyro "geometry" parameters, $\hat{\gamma}_{ij}$.

The linearization of the equations as required by the filter formulations are taken about the past filter estimate, resulting in the extended Kalman filter. Summarizing the equations for the extended Kalman filter,

$$P = \Phi P \Phi^T + Q \tag{4-21}$$

propagates the error covariance matrix, P, using the state transition matrix, Φ, and the state noise covariance matrix, Q. The optimum gain matrix, K, is computed from

$$K = PH^T [HPH^T + R]^{-1} \tag{4-22}$$

where H is the measurement matrix and R is the measurement noise covariance matrix. The gain matrix is then used to establish a state correction, $\delta\hat{x}$, to the state vector computed as

$$\delta\hat{x} = K\delta\hat{y} \tag{4-23}$$

The error covariance matrix is corrected through use of the gain matrix as

$$P = P - KHP \tag{4-24}$$

and this value of P is then propagated forward at the next update period.

The state transition matrix is the Jacobian of x_{k+N} with respect to x_k. This matrix is propagated between updates based upon the computed gyro reference attitude. The measurement matrix, H, is the Jacobian of y at t_{k+N} with respect to the state, x, at t_{k+N}. Derivation of this matrix follows from a relation demonstrating how variations in the attitude variables influence variations in the star direction cosines, u_i, and the equations relating the u_i to $\bar{y}$ derived earlier.

State noise arises principally from random noise in the output of the gyros, although the matrix, Q, is also used to account for unknown state noise, e.g., model uncertainties, etc. The state noise covariance matrix, Q, is 6 x 6, where the upper left 3 by 3 in Q is a time varying matrix which can be computed a priori. The rest of Q is zero, with the exception of its diagonal elements, which contain terms for the purpose of combating computer roundoff error. In the present case, the upper left 3 x 3 is simplified by including only the diagonal elements as fixed terms which are derived a priori based upon the measured gyro random drift.

The measurement noise covariance matrix, R, is 2 x 2 and the elements are constants whose value is selected based upon the expected (or measured) random noise in the measurements obtained by the detector and inductosyns. Only the diagonal elements are made non-zero.

4.1.6 Local Vertical Reference

The on-board ephemeris, $(\bar{r}, \bar{v})$, is used to establish the relationship of the local vertical reference frame relative to the ECI frame. This is given by

$$\bar{y} = \begin{bmatrix} 0 & 1 & 0 \\ 0 & 0 & -1 \\ -1 & 0 & 0 \end{bmatrix} \begin{bmatrix} \dfrac{\bar{r}}{|\bar{r}|} & \dfrac{(\bar{r} \times \bar{v}) \times \bar{r}}{|\bar{r} \times \bar{v}||\bar{r}|} & \dfrac{\bar{r} \times \bar{v}}{|\bar{r} \times \bar{v}|} \end{bmatrix}^T \bar{z} \qquad (4\text{-}25)$$

It is then a simple matter to derive the direction cosine matrix, A_{xy}, of the body frame (and thus the desired error) from the transformation relationship

$$A_{xy} = A_{xz} A_{yz}^T \qquad (4\text{-}26)$$

where

A_{xz} - is the direction cosine matrix derived from the inertial attitude

A_{yz} - is the matrix derived above from ephemeris

4.1.7 Alignment Reference Equations

The purpose of the alignment reference equations is to determine the relative attitude of a set of reference axes not integrally located and/or aligned with the attitude determination reference axes, e.g., a set of coordinate axes referenced to a reflector mounted to the experiment platform gimbal base. The equations utilize knowledge of the alignment reference relative to the vehicle reference and a measure of the alignment of the remote (reflector) reference relative to the alignment reference. This is a straightforward procedure of forming the appropriate direction cosine matrix using the autocollimator outputs, and performing the appropriate transformations. It follows that

$$
\begin{bmatrix} x_1{}^t \\ x_2{}^t \\ x_3{}^t \end{bmatrix} = A_{tr}\, A_{rx} \begin{bmatrix} x_1 \\ x_2 \\ x_3 \end{bmatrix} \tag{4-27}
$$

where

A_{tr} — is the direction cosine matrix whose elements represent deviation of gimbal base axes from nominal orientation as measured by the alignment sensor. Corrections are introduced into elements of this matrix to account for estimates of alignment sensor readout bias errors.

A_{rx} — is the direction cosine matrix relating the alignment sensor reference axes relative to the attitude reference axes

4.1.8 Targeting Equations

The targeting equations are used to determine the unit target vectors, $\bar{x}_3{}^p$ and $\bar{x}_1{}^p$, relative to gimbal base coordinates. The LOS vector pointing from the spacecraft to the target, $\bar{x}_3{}^p$, is computed initially; then computations are made to account for existing constraints about the LOS, $\bar{x}_1{}^p$. The target vectors are computed initially in the ECI frame, and transformed to the gimbal base coordinate:

The general target geometry is shown in Figure 4-3. The LOS pointing vecto $\bar{p}$, is given by

$$
\bar{p} = \bar{t} - \bar{r} \tag{4-28}
$$

where $\bar{t}$ is the target position vector and $\bar{r}$ the spacecraft position vector. By computing each of these vectors in ECI coordinates,

$$
\bar{p} = \begin{bmatrix} p_1 \\ p_2 \\ p_3 \end{bmatrix}_{ECI} = \begin{bmatrix} t_1 - r_1 \\ t_2 - r_2 \\ t_3 - r_3 \end{bmatrix} \tag{4-29}
$$

and the normalized pointing vector $\bar{x}_3{}^p$ in ECI coordinates is therefore

$$
\bar{x}_3{}^p = \begin{bmatrix} x_{31}{}^p \\ x_{32}{}^p \\ x_{33}{}^p \end{bmatrix}_{ECI} = \frac{1}{\sqrt{p_1{}^2 + p_2{}^2 + p_3{}^2}} \begin{bmatrix} p_1 \\ p_2 \\ p_3 \end{bmatrix} \tag{4-30}
$$

The vector $\bar{x}_1{}^p$ is determined by computation of appropriate vector constraint equat

4-15
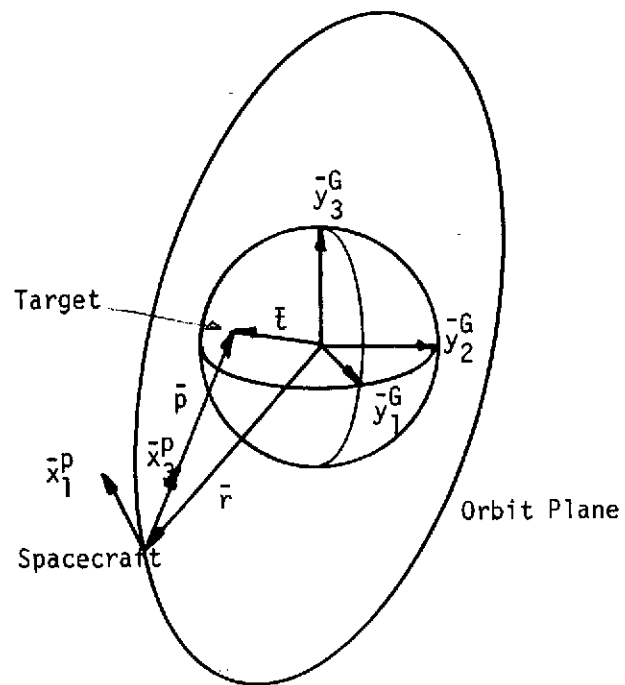
Figure 4-3. Spacecraft-Target Geometry

Targets for experiment gimbal pointing are defined in one of three ways, namely: relative to earth fixed coordinates, i.e., latitude, longitude, and radius; relative to inertial space, i.e., right ascension and declination; or relative to local vertical coordinates, i.e., roll, pitch, and yaw. Each target is stored with a time tag for proper sequencing, this time tag being given in Greenwich Mean Time (GMT). It is assumed that at the initialization of the spacecraft real-time clock, the initial time t_0 is given

$$t_0: \quad (GMT_0 \quad GHA_0{}^{\gamma}) \qquad (4\text{-}31)$$

where GMT_0 is the initial Greenwich Mean Time in decimal hours and $GHA_0{}^{\gamma}$ is the Greenwich Hour Angle of Aries at $t = t_0$ (Section 4.1.2.3). Once t_0 has been established, the spacecraft will maintain both elapsed time T,

$$T = t - t_0 \qquad (4\text{-}32)$$

in seconds and Greenwich Mean Time, GMT, in decimal hours.

For coordinates defined with respect to the local vertical reference frame, {y}, the spacecraft ephemeris is utilized to determine the target vectors with respect to the ECI frame. Thus,

$$\bar{x}^p_{\{z\}} = A_{yz}^T [f: \quad (\phi, \theta, \psi)]^T \bar{x}^p_{\{y\}} \qquad (4\text{-}33)$$

Coordinates for pointing at a geographic target, $\bar{t}$, are defined in spherical Earth-Centered-Rotating coordinates in terms of geographic longitude, latitude and distance from the center of the earth, i.e.,

$$\bar{t}: \quad (\lambda, \phi, r) \qquad (4\text{-}34)$$

These target coordinates are first transformed to spherical ECI coordinates and then to the desired cartesian ECI coordinates from which the target vectors are computed. For targets specified with respect to inertial space, the coordinates provided are right ascension and declination. This is already in a form for direct computation of the target vector in the desired ECI coordinates.

The target vector coordinates relative to ECI, $\bar{x}^p_{\{z\}}$, are in turn transformed relative to the gimbal base reference frame, $\bar{x}^{gn}$,

$$\bar{x}^p_{\{x^{gn}\}} = A_{x^{gn}x^t} \; A_{x^t x} \; A_{xz} \; \bar{x}^p_{\{z\}} \qquad (4\text{-}35)$$

where

A_{xz} — is the inertial attitude direction cosine matrix

$A_{x}t_{x}$ — is the alignment reference direction cosine matrix

$A_{x}gn_{x}t$ — is the alignment (known) of the gimbal base reference relative to the alignment reflector reference

4.1.9 Steering Equations

The steering equations utilize the target vector coordinates defined in the gimbal base reference frame to generate gimbal angle commands, ϕ_{gc}, θ_{gc}, and ψ_{gc}, such that the appropriate experiment axes are precisely aligned with the target axes. The ultimate aim is to determine the gimbal angle commands with compensation terms accounting for known misalignments in the gimbal and readout. The detailed equations for accomplishing this are algebraically complex and are left for detailed development elsewhere (Appendix B). However, since all the misalignments can be considered first order effects, the nominal values of gimbal angles differ only very little from the actual values. Therefore, there is some advantage at this point in computing the "nominal" values of the angles, assuming all misalignments are zero. This provides insight into the approach and is useful in maintaining the correct quadrants in the more complex equations. Note that only those terms of significance for compensating misalignments are included in the on-board implementation.

In order to point at the selected target, the reference axes fixed in the experiment must coincide with the target axes. It follows from the targeting equations that

$$\begin{bmatrix} \bar{x}_1^p \\ \bar{x}_2^p \\ \bar{x}_3^p \end{bmatrix} = C_n \begin{bmatrix} \bar{x}_1^{gn} \\ \bar{x}_2^{gn} \\ \bar{x}_3^{gn} \end{bmatrix} \tag{4-36}$$

where

$$C_n = \begin{bmatrix} \bar{x}^p \\ \{x^{gn}\} \end{bmatrix}$$

Thus,

$$\bar{x}_1^p = c_{11}^n \bar{x}_1^{gn} + c_{12}^n \bar{x}_2^{gn} + c_{13}^n \bar{x}_3^{gn} \tag{4-37}$$

and

$$\bar{x}_3^p = c_{31}^n \bar{x}_1^{gn} + c_{32}^n \bar{x}_2^{gn} + c_{33}^n \bar{x}_3^{gn} \tag{4-38}$$

The matrix, C_n, also can be defined in terms of the gimbal angles such that

$$C_n \triangleq (c_{ij}^n) \triangleq \hat{\phi}_n \hat{\theta}_n \hat{\psi}_n \qquad (4-39)$$

where

$$c_{11}^n = \cos\theta_n \cos\psi_n$$

$$c_{12}^n = \cos\theta_n \sin\psi_n$$

$$c_{13}^n = -\sin\theta_n$$

$$c_{31}^n = \cos\psi_n \sin\theta_n \cos\phi_n + \sin\psi_n \sin\phi_n$$

$$c_{32}^n = \sin\psi_n \sin\theta_n \cos\phi_n - \cos\psi_n \sin\phi_n$$

$$c_{33}^n = \cos\theta_n \cos\phi_n$$

If follows directly from determining the elements c_{ij}^n that

$$\psi_n = \tan^{-1}\left(\frac{c_{12}^n}{c_{11}^n}\right) \qquad (4-40)$$

$$\theta_n = \tan^{-1}\left(\frac{-c_{13}^n}{(c_{11}^n/\cos\psi_n)}\right) \qquad (4-41)$$

$$\phi_n = \tan^{-1}\left(\frac{c_{31}^n \sin\psi_n - c_{32}^n \cos\psi_n}{(c_{33}^n/\cos\theta_n)}\right) \qquad (4-42)$$

For LOS pointing only, the vector $\bar{x}_3^p$ is given in nominal gimbal base coordinates and only two gimbal rotations are required to align the desired pointing axis with $\bar{x}_3^p$. The yaw gimbal angle is therefore set equal to zero, i.e., $\psi_n = 0$. From the previous equations, one obtains

$$c_{31}^n = \sin\theta_n \cos\phi_n$$

$$c_{32}^n = -\sin\phi_n \qquad (4-43)$$

$$c_{33}^n = \cos\theta_n \cos\phi_n$$

so that

$$\theta_n = \tan^{-1}\left(\frac{c_{31}^n}{c_{33}^n}\right) \qquad (4\text{-}44)$$

and

$$\phi_n = \tan^{-1}\left(\frac{-c_{32}^n}{(c_{33}^n/\cos\theta_n)}\right) \qquad (4\text{-}45)$$

4.2   ERROR ANALYSIS

This section presents the PPCS system error analysis. The objective is to perform an authoritative error analysis without resorting to Monte Carlo simulation of the system. Since the PPCS system is complex, a major task in this respect was to select a suitable approach. Direct addition of the variances of the errors without regard to the details of how these errors propagate through the system can be utilized for gross estimates of performance. These results are presented in an initial summary of the system errors. However, it was felt that a weighting of the individual errors according to how they directly affect the attitude determination and experiment gimbal pointing appeared essential in development of a detailed system error analysis.

This has resulted in the development of a comprehensive sensitivity and covariance error analysis from which a flexible digital computer program has been developed (Appendix E) which computes single-axis pointing errors and attitude determination errors using as inputs the uncertainties of the individual system error sources. This analysis is summarized in detail, from discussion of the approach to presentation of results. The detailed definition of hardware error sources and the algebraic details of developing sensitivity matrices are found elsewhere (Appendices C and D, respectively).

4.2.1   Error Summary

This section presents a summary of hardware and system errors which are combined by the simple addition of variances to establish a working estimate of system errors. The total system errors are presented in Table 4-1, which shows both the allocated budget and the achieved performance. For all cases, the budget is met and overall performance is 20% below budget. The hardware and software errors summarized there are expanded in Tables 4-2 through 4-6 to show the details of this error analysis. The values shown for the error sources are discussed and derived in the design analysis and hardware design sections of this report and elsewhere [12].

The pointing errors considered for PPCS are exclusive of those contributed by ephemeris error. Even though not a part of the PPCS error budget, the ephemeris errors must be considered as to the effect on system performance. It is interesting to note that ephemeris errors influence the pointing accuracy differently, depending upon which pointing mode is considered. For example, space pointing of experiments to targets defined on the celestial sphere is independent of ephemeris. Furthermore, the accuracy of pointing relative to local vertical is much less sensitive to ephemeris errors (by the ratio of altitude to orbital radius) than pointing at landmark targets (i.e., latitude, longitude, radius). This latter point becomes

Table 4-1   PPCS Error Analysis Summary

Error Source	Budget Allocation		Design Capability	
	Magnitude (1σ) (sec)	Variance (sec²)	Magnitude (1σ) (sec)	Variance (sec²)
Star Tracker	1.40	1.96	1.14	1.30
Sensor Electronics	0.50	0.25	0.22	0.05
Gyro Reference	1.60	2.56	1.35	1.83
Alignment Sensor	1.60	2.56	1.34	1.80
Reference Block	0.50	0.25	0.50	0.25
Experiment Gimbal	1.50	2.25	0.98	0.96
Experiment Electronics	0.50	0.25	0.22	0.05
Data Processing	1.70	2.89	1.51	2.26
	———		———	
TOTAL (RSS)	3.6		2.92	
	(=0.001 deg)		(=0.00081 deg)	

Table 4-2   Star Tracker and Electronics Error Analysis

Error	Source	Contribution	
		σ (sec)	σ^2 (sec^2)
STA			
SSU Bias/Stability			
Thermo-mechanical Stability	0.18 sec (1σ)	0.18	0.033
Electronic Bias	0.4 sec (1σ)	0.4	0.16
SSU Noise Equivalent Angle	0.35 sec (1σ)	0.07	0.005
SGU Alignment Uncertainty			
Runout	0.5 sec (1σ)	0.5	0.25
Perpendicularity	0.5 sec (1σ)	0.5	0.25
SGU Thermo-mechanical Stability			
Stress Relaxation	0.17 sec (1σ)	0.17	0.029
Thermal Shifts	0.2 sec (1σ)	0.2	0.04
Inductosyn (Mechanical)	0.73 sec (1σ)	0.73	0.53
TOTAL (RSS)		1.14	
SEA			
Inductosyn Processing			
Bias Stability	0.07 sec (1σ)	0.07	0.0049
360 θ	0.04 sec (1σ)	0.04	0.0016
720 θ	0.2 sec (1σ)	0.2	0.04
Resolution	0.23 sec (1σ)	0.065	0.0042
TOTAL (RSS)		0.224	

Table 4-3   Gyro Reference Error Analysis

Error	Source (1σ)	Contribution[1]	
		σ ($\widehat{\text{sec}}$)	σ^2 ($\widehat{\text{sec}}^2$)
GRA			
Drift Bias Compensation[2]	0.002°/hr	0.6	0.36
Random Drift (5 min integration)	0.003°/hr	0.9	0.81
Scale Factor Stability	100 ppm	0.72	0.52
IA Alignment Stability	10 $\widehat{\text{sec}}$	0.36	0.13
Gyro Pulse Weight	0.1 $\widehat{\text{sec}}$	0.1	0.01
TOTAL (RSS)		1.35	

(1)   5 minute update period, bounding value
      Nominal limit cycle, 0.02 deg/sec

(2)   Error in Kalman filter estimate

Table 4-4   Alignment Sensor Error Analysis

Error	Source	Contribution[1]	
	$(\widehat{sec}, 1\sigma)$	$\sigma(\widehat{sec})$	$\sigma^2(\widehat{sec}^2)$
ASA			
Systematic Mech/Elec Errors (Uncompensated)			
Transverse Axes	0.246	0.246	0.061
Twist Axis	0.877	0.51	0.26
Random Mech/Elec Errors			
Transverse Axes	0.1	0.1	0.01
Twist Axis	2.06	1.2	1.44
Stability			
Transverse Axes	0.081	0.081	0.007
Twist Axis	0.256	0.148	0.022
		———	
TOTAL (RSS)		1.34	

(1) Twist Axis Error Distributed over 3 axes
      (Twist Axis only Errors = 2.25 $\widehat{sec}$ (1σ))

Table 4-5   Experiment Gimbal and Electronics Error Analysis

Error	Source	Contribution	
	$(\widehat{sec}, 1\sigma)$	$\sigma(\widehat{sec})$	$\sigma^2(\widehat{sec}^2)$
EGA			
Systematic Errors (Uncompensated)			
Alignment	0.25	0.25	0.062
Runout	0.3	0.3	0.09
Random Errors			
Runout	0.17	0.17	0.029
Thermal Stability	0.5	0.5	0.25
Inductosyn (Mechanical)	0.73	0.73	0.53
		___	
TOTAL (RSS)		0.98	
EEA			
Inductosyn Processing			
Bias Stability	0.07	0.07	0.0049
360θ	0.04	0.04	0.0016
720θ	0.2	0.2	0.04
Resolution	0.23	0.065	0.0042
		___	
TOTAL (RSS)		0.224	

Table 4-6. Data Processing Error Analysis

Error	Source	Contribution	
		$\sigma(\widehat{sec})$	$\sigma^2(\widehat{sec}^2)$
Star Catalog/Aberration Correction	0.1 $\widehat{sec}$	0.1	0.01
Finite Word Length	24 bits (min)	1.0	1.00
Integration Drift (Finite Sample Period)	0.1 $\frac{\widehat{sec}}{min}$ (bound)	0.5	0.25
Pointing Command	1 $\widehat{sec}$	1.0	1.00
	TOTAL (RSS)	1.51	

Note: Filter related performance accounted for in allocated hardware budgets, e.g., Tracker noise accounted for in STA error analysis, gyro bias compensation and random drift in GRA error analysis.

apparent from the geometry shown in Figure 4-4, where this somewhat simplified case considers only in-track ephemeris errors, Δx. To demonstrate the effects which ephemeris errors contribute, relative to PPCS errors, it is most meaningful to consider angular resolution. This is summarized for low altitude orbits in Figure 4-5. Note that ephemeris accuracy on the order of 0.1 n.m. is consistent with PPCS accuracy goals for local vertical pointing and errors up to 0.25 n.m. (≈ 0.5 km) are not inconsistent with PPCS requirements. On the other hand, ephemeris errors must be on the order of 100-200 ft to be consistent with PPCS accuracy requirement/goals for pointing at a given latitude, longitude for low orbital altitude. From a somewhat different perspective, this also says that PPCS accuracy is consistent with ground resolution of 100-200 feet. Developing an on-board ephemeris approach was specifically not part of the scope of PPCS, but it is clear that the question is an important one as regards overall operation and performance and must be carefully addressed.

4.2.2 Covariance Analysis

4.2.2.1 Approach

Development of the system error covariance is based on establishing the sensitivity of the attitude determination and pointing angle commands to the individual system error sources. In general, any system variable, x, can be expressed as

$$x = \hat{x} + \delta x \tag{4-46}$$

where x is the true value of the variable, $\hat{x}$ the estimated value, and δx the error in the estimate. Let now

$$\gamma^g = (\phi_g, \theta_g, \psi_g)^T \tag{4-47}$$

be the three gimbal angle pointing commands and let

$$e = (e_1, e_2, \ldots, e_n)^T \tag{4-48}$$

represent the individual error sources in the system, e.g., misalignments, biases, scale factors, etc. Performing an error sensitivity analysis one may express the
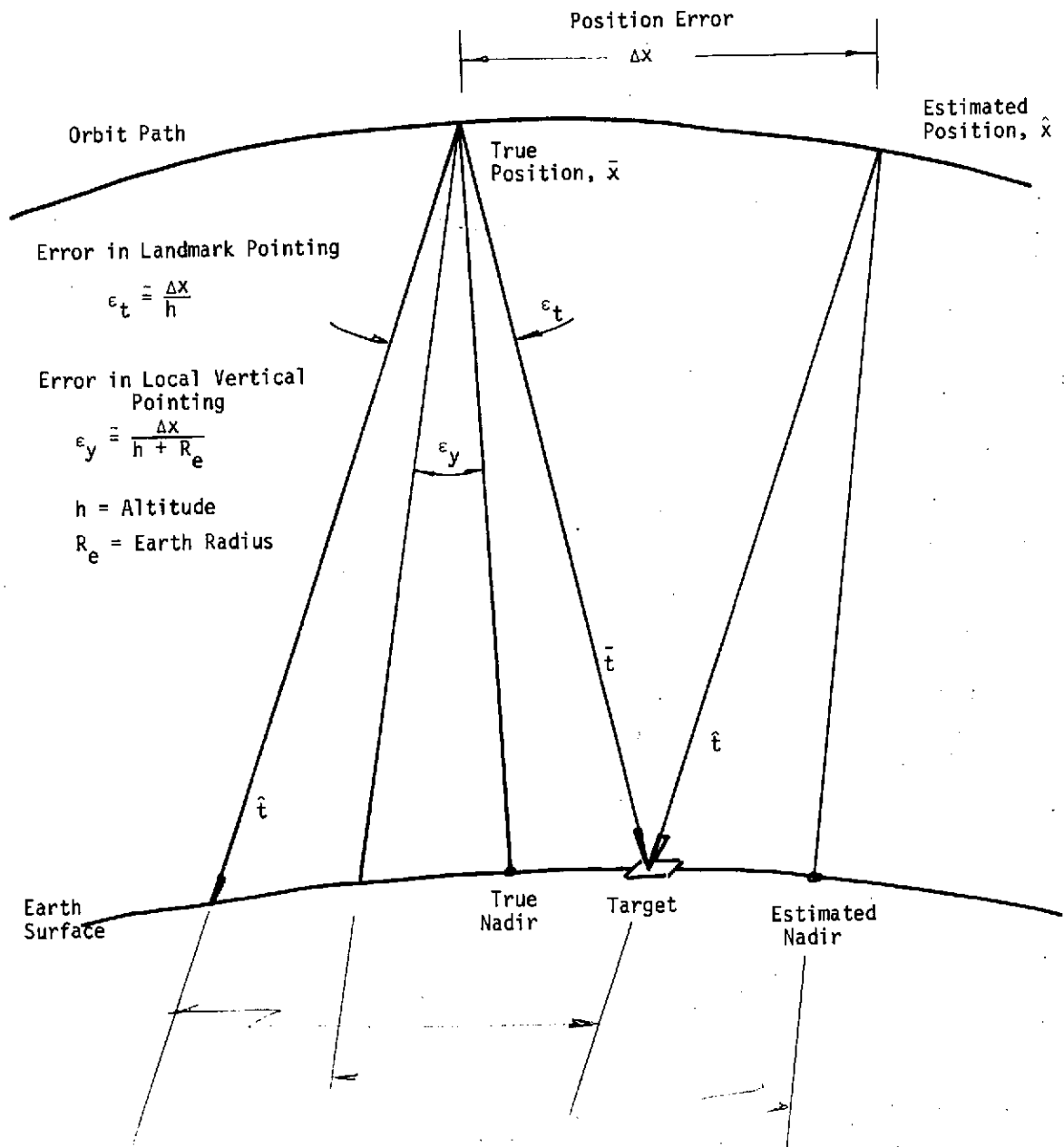
Figure 4-4. Ephemeris Error Geometry
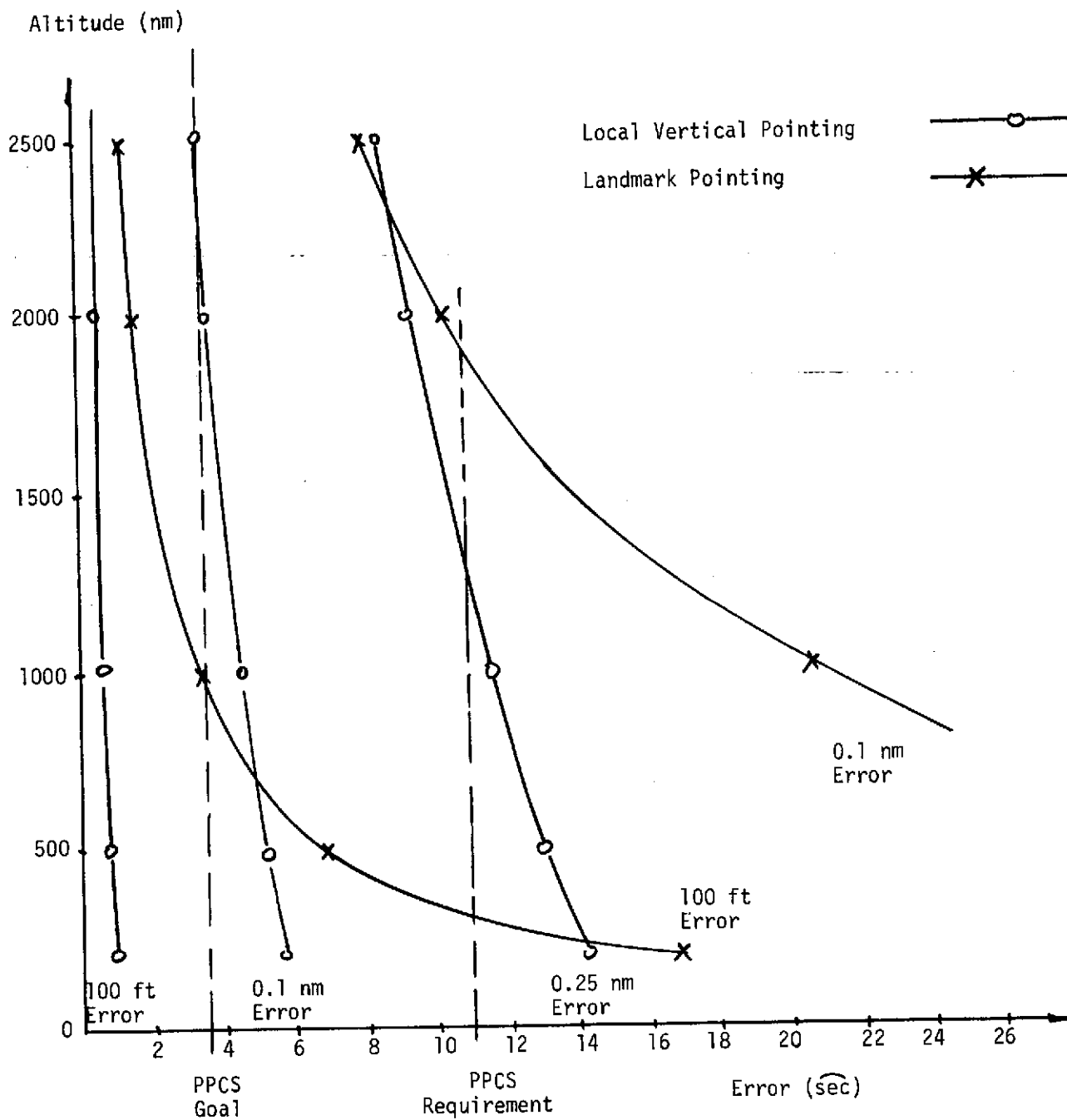
Figure 4-5. Effect of Ephemeris Errors

errors in system pointing by

$$\delta \gamma^g = S \delta e \qquad (4-49)$$

Let the covariance matrix of the pointing error, $\delta \gamma^g$, be

$$P_g(k) = E\left[\delta\gamma_k^g \ (\delta\gamma_k^g)^T\right] \qquad (4-50)$$

and the covariance matrix of the system errors, δe, be

$$R(k) = E\left[\delta e_k \ (\delta e_k)^T\right] \qquad (4-51)$$

where E denotes the expectation operator and where the subscript k denotes "at time t_k." Then clearly

$$P_g(k) = S_k \ R(k) \ S_k^T \qquad (4-52)$$

and given S and R one can determine the gimbal angle pointing error covariance matrix, P_g. The diagonal elements of $P_g(k)$ are the variances of the three single axis pointing errors. It is assumed that all the components of δe_k are Gaussian distributed random variables. Thus, $\delta\gamma_k^g$ is also Gaussian, and the probability that the pointing error will not exceed its standard deviation (1σ) is 0.6826. This assumption seems to be quite justified for almost all error quantities involved and, in general, little error from this interpretation of the variances is expected.

The particular approach taken here is to partition the S matrix into four submatrices as follows:

$$\delta\gamma^g = \left[S_2 \ \middle| \ S_1 \ \middle| \ S_0 \ \middle| \ S_{LOS}\right] \delta e \qquad (4-53)$$

where S_2 indicates the sensitivity of the pointing error to errors in the pointing control system, S_1 the sensitivity to alignment sensing errors, S_0 the sensitivity to attitude determination errors, and S_{LOS} the sensitivity to the target LOS vector in ECI coordinates. Note that S_{LOS} reflects the sensitivity of the overall pointing system to ephemeris errors and errors in geophysical constants.

Since the gimbal angles are, in general, not linearly related to these error sources the matrices S_i consist of partial derivatives evaluated at nominal or a priori estimated values of the current state of the system. The term "state" is to be interpreted in the wider sense, comprised not only of the body rates and the vehicle attitude, but also including the star vector of the currently tracked star, the nominal pointing gimbal angles, and the nominal target LOS vector.

4-31

Hence, $S = [S_2 | S_1 | S_0 | S_{LOS}]$ varies with time according to the time evolution of the system state. Mathematically speaking, the matrix S should also depend on the expected values of the system errors, e. But virtually all error quantities are so small that they may be considered first-order engineering effects and thus they contribute only second-order terms in the gimbal angle errors. Therefore, they can be deleted (set equal to zero) in almost all cases leaving the error sensitivity matrices independent of the <u>a priori</u> estimated values (calibrated values) of the system errors.

The covariance matrix, R, can then be expressed as

$$
R = \begin{bmatrix} P_2 & & & \\ & P_1 & & 0 \\ & & P_0 & \\ 0 & & & P_{LOS} \end{bmatrix}
\tag{4-54}
$$

where P_2 is the error covariance matrix of the pointing control errors, P_1 is the error covariance matrix of the alignment sensing errors, P_0 is the error covariance of the attitude determination, and P_{LOS} is the error covariance of the targeting. The entries of P_2 and P_1 are the 1σ uncertainties of the pointing control and alignment reference, respectively; the entries of P_0 depend on the accuracy of the attitude determination system; and P_{LOS} on the accuracy of the target vectors (including the effects of ephemeris).

4.2.2.2 System Sensitivity

This section presents a summary of the system error sensitivity. Detailed development of the sensitivity matrices is found in Appendix D. The single-axis pointing errors,

$$
\begin{aligned}
\delta\phi_g &\triangleq \phi_g - \hat{\phi}_g \\
\delta\theta_g &\triangleq \theta_g - \hat{\theta}_g \\
\delta\psi_g &\triangleq \psi_g - \hat{\psi}_g
\end{aligned}
\tag{4-55}
$$

are related to the uncertainties in the system errors through the expanded sensitivity relationship shown below.

4-32

$$
\begin{bmatrix} \delta\phi_g \\ \delta\theta_g \\ \delta\psi_g \end{bmatrix}
=
\left[\underbrace{S_s^3 \mid S_\ell^2 \mid S_m^2 \mid S_f^2 \mid S_t^3 \mid S_{tr}^3}_{S_2} \mid \underbrace{S_r^3 \mid S_0^3 \mid S_{LOS}^3}_{S_1} \right]
\begin{bmatrix} \delta\alpha_s \\ \delta\alpha_\ell \\ \delta\alpha_m \\ \delta\alpha_f \\ \delta\alpha_t \\ \delta\theta_{tr} \\ \delta\alpha_r \\ \delta\rho^0 \\ \delta x_3^p \end{bmatrix}
\qquad (4\text{-}56)
$$

where

$$\alpha_s = (\alpha_{s1}, \alpha_{s2}, \alpha_{s3})^T = \text{gimbal "servo" error (dynamic, static, DAC, Inductosyn)}$$

$$\alpha_\ell = (\alpha_{\ell 2}, \alpha_{\ell 3})^T = \text{last gimbal rotation misalignment}$$

$$\alpha_m = (\alpha_{m1}, \alpha_{m3})^T = \text{middle gimbal rotation misalignment}$$

$$\alpha_f = (\alpha_{f1}, \alpha_{f2})^T = \text{first gimbal rotation misalignment}$$

$$\alpha_t = (\alpha_{t1}, \alpha_{t2}, \alpha_{t3})^T = \text{reflector misalignments}$$

$$\theta_{tr} = (\phi_e, \theta_e, \psi_e)^T = \text{alignment sensor angle measurement}$$

$$\alpha_r = (\alpha_{r1}, \alpha_{r2}, \alpha_{r3})^T = \text{alignment sensor misalignment}$$

$$\rho^0 = (\xi, \eta, \zeta)^T = \text{spacecraft attitude}$$

$$x_3^p = (x_{31}^p, x_{32}^p, x_{33}^p)^T = \text{normalized LOS target vector (ECI)}$$

It is noted, however, that although the sensitivity of pointing error to attitude determination error is shown, the sensitivity of attitude determination error to star tracker and gyro error sources has not been explicitly developed. This is done separately for several reasons, including clarity. First, it is useful to develop a separate sensitivity/covariance analysis of attitude determination to particularly understand those errors and to complement the simulation capability. Secondly, since the attitude is periodically updated using the star tracker and propagated between star updates using only gyros, it is necessary to develop separate sensitivity matrices for each condition. Finally, the updates are obtained using a Kalman filter which plays the key role in attitude determination. This, of course, makes an error analysis for attitude determination a different task.

To perform a Kalman filter covariance analysis with six states (drift bias and attitude) seemed undesirable since: (i) this is available through use of the attitude determination simulation; (ii) there are several more error sources besides gyro drift rates and tracker observation noise which have to be accounted for, and the error covariance matrix obtained from the filter would not reflect these errors.

To perform a covariance analysis when all existing error quantities are to be estimated by the filter (if they are observable) again would duplicate the simulation and would also be unrealistic in the sense that the on-board filter possesses only six states. Thus, the best way to handle the filter in the error analysis was to account implicitly for its existence. This is done by attenuating the uncertainties in the gyro drift rate bias and the tracker observation noise according to the filter performance as observed through simulation, i.e., to modify the variances of these errors by the ratio of the a posteriori to the a priori variances of the filter.

The form and characteristics of the attitude determination sensitivity relation are developed. Between star tracker updates, the error sensitivity in the attitude at $t = t_{k+N}$ can be expressed as

$$\delta \rho_{k+N}^{0} = S_{AI}(k + N, k) \begin{bmatrix} \delta \rho_k^{0} \\ ----- \\ \delta p_k(N) \end{bmatrix} \tag{4-57}$$

where N is any positive integer and where

$$\delta \rho_k^{0} = \text{the attitude error at } t_k$$

and

$$\delta p_k(N) = \begin{bmatrix} \delta b_g^{0} \\ \delta \gamma \\ n_G^{0}(k + N - 1) \end{bmatrix} \tag{4-58}$$

where

δb_g^{0} = uncertainties in equivalent gyro drift rate

$\delta \gamma$ = uncertainties in gyro input axis alignments/scale factor

n_G^{0} = equivalent gyro noise

The gyro uncertainty, δp_k, is a function of the step size, N, since it includes the gyro random noise which acts as an independent external input and must be summed over the N integration steps. The remainder of δp contains the uncertainties in the gyro drift rate biases, gyro misalignments, and gyro scale factor

instabilities. Since b_g^O is part of the on-board filter state vector, once the filter has converged the _a priori_ variance of b_g^O will have been reduced substantially. To account for this in the present error analysis, the uncertainty in gyro bias is modified to

$$\delta b_g^O = \mu_b \ \delta b_g^O \tag{4-59}$$

where μ_b is a scalar multiplier reflecting the attenuation of the bias error due to Kalman filtering. By making μ_b a scalar it is assumed that the variance of each component of δb_g^O is equally attenuated, a quite reasonable assumption. In this case μ_b^2 is the ratio of the _a posteriori_ variance of δb_g^O (when the filter has converged) to the _a priori_ variance of δb_g^O (when the filter was initiated).

The errors in the star tracker consist mainly of misalignments and readout errors in the sensor and the inductosyns, where the latter errors include observation noise. One can proceed similarly as before and derive an error sensitivity matrix, S_{AU}, which relates the errors in the star tracker to the attitude determination error at attitude update time. The error incurred at attitude update is not completely independent of the gyro errors, however. This is because one star tracker observation does not yield enough information to determine the vehicle attitude. At least two observations are required and they must be connected in time through the gyro derived attitude. Since, for reasons stated earlier, the Kalman filter is not treated explicitly, it is assumed that whenever a star tracker reading is taken an attitude update is obtained by processing the present star tracker reading with the most recent previous star tracker reading. A fundamental assumption made is that the two readings yield linearly independent star vectors. This processing of the STA data resembles the Kalman filter used in the actual system. It may be regarded as an "extremely finite memory filter" since it combines only the last preceding star tracker reading with the present reading, while the Kalman filter makes use of all the past information thus refining its estimates.

The sensitivity of attitude determination to GRA and STA errors when taking star tracker readings at update periods is given by

$$\delta \rho_{k+N}^O = S_{AU} \begin{bmatrix} \delta q_{k+N} \\ \delta q_k \\ \delta p_k(N) \end{bmatrix} \tag{4-60}$$

Define the tracker error as

$$\delta q = \delta(\alpha_1, \ \alpha_3, \ \alpha_1^I, \ \alpha_2^I, \ \alpha_2^O, \ \alpha_3^O, \ \epsilon_I^O, \ \epsilon_I^I)^T \tag{4-61}$$

where

$\left.\begin{array}{c}\alpha_1 \\ \\ \alpha_3\end{array}\right\}$ SSU errors and SSU misalignments

$\left.\begin{array}{c}\alpha_1^I \\ \\ \alpha_2^I\end{array}\right\}$ Inner gimbal misalignments including bearing run-out

$\left.\begin{array}{c}\alpha_2^O \\ \\ \alpha_3^O\end{array}\right\}$ Outer gimbal misalignments including bearing run-out

ε_I^O Outer gimbal Inductosyn read-out errors

ε_I^I Inner gimbal Inductosyn read-out errors

The tracker error vector, q, has a number of components which contain an additive observation noise term. Again, in the flight software, the Kalman filter will substantially reduce the effects of this observation noise by essentially making a least square fit to the observed measurements. Thus, let in general

$$\delta q_k = \delta q_k^O + \mu_q n_{qk} \tag{4-62}$$

where n_{qk} is the high frequency noise vector associated with the star tracker observations and μ_q reflects the attenuation of the noise by the filter. The cross-correlation between p and q is zero at all times.

4.2.2.3 Covariance Matrix Development

Development of the covariance matrices for pointing errors, although tedious, is straightforward. Development of the covariance matrices for attitude determination is much less so. Consider first the period between updates, where error is a function only of the gyro related errors and attitude determination history. The associated error covariance matrix is given by

$$P_G(k;N) = \left\{ \begin{bmatrix} \delta \rho_k^O \\ \hline \delta p_k(N) \end{bmatrix} \begin{bmatrix} \delta \rho_k^{OT} & | & \delta p_k^T(N) \end{bmatrix} \right\} \tag{4-63}$$

which implies that

$$P_G(k;N) = \begin{bmatrix} P_{\rho\rho}(k) & | & P_{\rho^O p}(k) \\ \hline P_{\rho^O p}^T(k) & | & P_p(k;N) \end{bmatrix} \tag{4-64}$$

4-36

Using the sensitivity matrix,

$$P_{\rho}0(k+N) \;=\; S_{AI}(k+N,\;k)\;P_G(k;N)\;S_{AI}^T(k+N,\;k) \tag{4-65}$$

whenever t_{k+N} does not correspond to an attitude update at which a star tracker reading is taken. These last two equations constitute a recursion relationship by which, given $P_{\rho}0(0)$ and the other submatrices of P_G at t_k, the covariance matrix $P_{\rho}0(k)$ can be computed for all $k > 0$. It then follows that

$$P_p(k;N) \;=\; \begin{bmatrix} P_{bg}0 & 0 & 0 \\ \hline 0 & P_\gamma & 0 \\ \hline 0 & 0 & P_{N_G^0}(k;N) \end{bmatrix} \tag{4-66}$$

where for drift bias uncertainty, $\delta b_g{}^0$, alignment and scale factor, δ_γ, and random drift (noise) $N_G{}^0$,

$$P_{bg}{}^0 \;=\; E\left[\mu_b\;\delta b_g{}^0\;\mu_b(\delta b_g{}^0)^T\right] \tag{4-67}$$

$$P_\gamma \;=\; E\left[\delta\gamma(\delta\gamma)^T\right] \tag{4-68}$$

and

$$P_{N_G^0}(k;N) \;=\; E\left[N_G{}^0(k+N-1)\;N_G{}^0(k+N-1)^T\right] \tag{4-69}$$

Next the submatrix, $P_{\rho}0_p(k)$, will be evaluated. It is established that

$$P_{\rho}0_p(k+N) \;=\; \hat\phi_1{}^0(k+N,\;k)\;P_{\rho}0_p(k) \;+\; \hat\psi_2{}^0(k+N,\;k)\;P_p{}^0(k) \tag{4-70}$$

where

$$P_{\rho}0_p(k) \;=\; 3\left[\overset{3}{P_{\rho}0_{bg}0}(k) \;\Big|\; \overset{9}{P_{\rho}0_\gamma}(k) \;\Big|\; \overset{3}{0}\right] \tag{4-71}$$

and

$$P_p{}^0(k) \;=\; \left\{P_p(k;N)\;\text{with}\;P_{N_G^0}(k+N-1) \;=\; 0\right\} \tag{4-72}$$

which constitutes a recursion relationship by which $P_{\rho 0_\rho}(k)$ can be computed for any $k > 0$. Without loss of generality it may be assumed that

$$P_{\rho} 0(0) = 0 \qquad (4\text{-}73)$$

These expressions are thus used to propagate the error covariance between tracker updates.

It remains to establish the covariance matrix of ρ^0 at the time of a star tracker reading/filter update, i.e., $P_{\rho 0}(k+N)$. The covariance matrix of the associated gyro and star tracker errors is given by

$$P_{ST}(k+N) = E\left\{\begin{bmatrix} \delta q_{k+N} \\ \delta q_k \\ \delta p_k(N) \end{bmatrix} \begin{bmatrix} \delta q^T_{k+N} & \delta q_k^T & \delta p_k^T(N) \end{bmatrix}\right\} \qquad (4\text{-}74)$$

From this, it follows that

$$P_{\rho} 0(k+N) = S_{AU} P_{ST}(k+N) S_{AU}^T \qquad (4\text{-}75)$$

which yields the error covariance matrix of ρ^0 at t_{k+N} when the attitude is updated with a star tracker observation.

4.2.2.4 Covariance Analysis Results

Error sensitivity matrices and standard deviation of the attitude determination and pointing errors were developed using the covariance error analysis computer program. The error sources which correspond to the results are those developed in Section 4.2.1. The results are plotted in Figures 4-6 and 4-7 for attitude determination and pointing, respectively, with data taken over a 30 minute period. Excellent performance is achieved, corroborating the numerical results of both the rough analysis and simulation.

It can be observed that the attitude determination errors are quite uniform in the three vehicle axes. The reason for the uniformity is the particular star configuration used for the attitude updates which does not favor any one particular axis. The vehicle limit cycle and orbit rate also have an observable impact on the system performance due to gyro errors. This state dependence is clearly visible on the graphs through the alternating slope of the error increase during

4-38
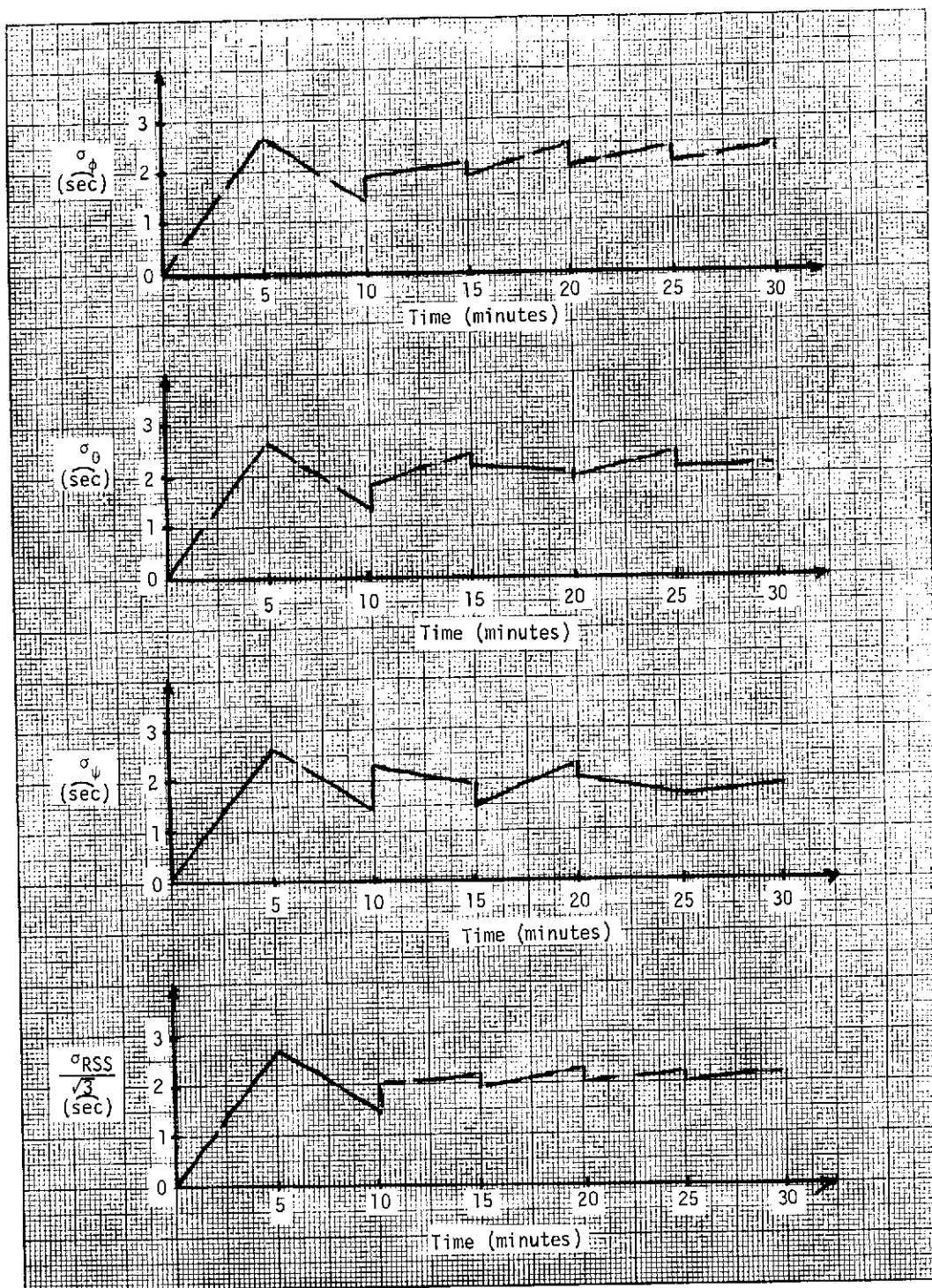
Figure 4-6. Attitude Determination Error Time History
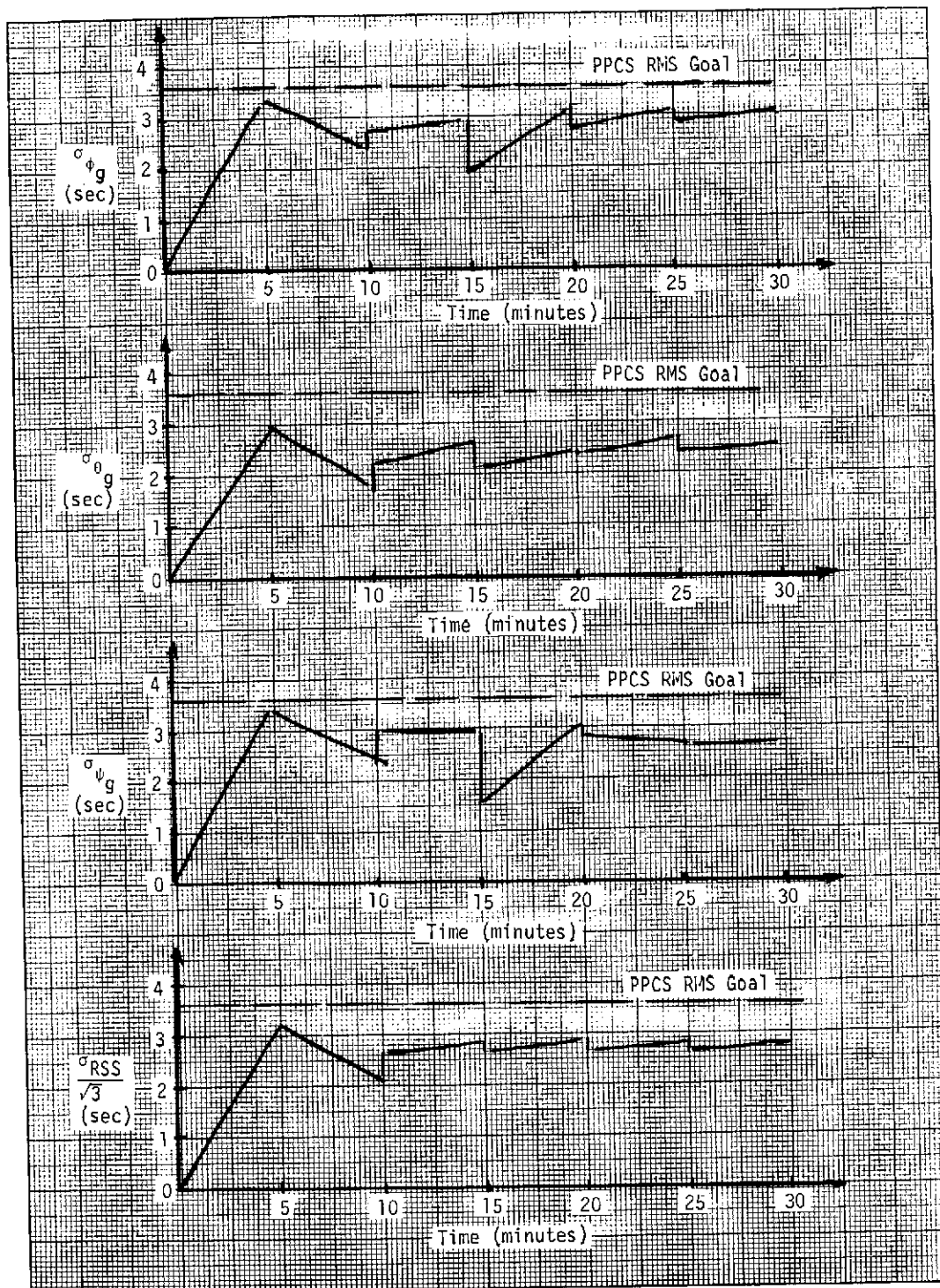
Figure 4-7. Pointing Error Time History

the intervals between updates. The vehicle limit cycle reverses, in this case, in phase with the star tracker updates (every 5 minutes) and therefore adds and subtracts alternately from the orbit rate.

The error sensitivity matrices for several update periods are provided in Tables 4-7, 4-8, and 4-9. In general, the following observations were made on the sensitivity matrices, being careful not to confuse sensitivity with error.

- Attitude determination errors between updating are most sensitive to gyro drift rate bias and gyro noise, in that order. The sensitivity to gyro misalignments and scale factor instability appears to be low. However, this is solely caused by the fact that the body rates are rather small (observe the state dependence of the error).

- Attitude determination errors at update time are again most sensitive to gyro biases and noise since the gyros must be used to interrelate the star tracker measurements taken at different times. The effect of the remaining error sources seems to be very heavily dependent on the location of the tracked stars, particularly on how much new information can really be gained from looking at the second star. When the angle between successive star vectors was very large, the sensitivities to individual SSU and gimbal misalignments and Inductosyn errors varied between 0.2 and 0.6. System improvement by the improvement of one particular misalignment over another was not indicated. The STA errors seem to act in concert, some of them affecting one vehicle axis more than another.

- The sensitivity of the pointing angles to servo errors and to experiment gimbal and alignment sensor misalignments varied between zero and unity and, as expected, most misalignments acted differently on the three different gimbal angles. The sensitivities are dependent on the nominal pointing angles and some of them increase noticeably as the gimbal angles grow in magnitude. It is interesting to note that the sensitivities to mounting misalignments and errors associated with the alignment sensor are always close to unity (examine the sum of the squares per category).

- The sensitivity of the pointing gimbal angles to attitude determination errors was observed at about unity per axis, when the attitude determination error was expressed in Euler angles. (The sensitivities are around 2.0 for Euler symmetric parameters.) It is noted that cross-coupling does definitely exist.

- As expected, the sensitivities of the pointing angles to variations in the line of sight vector are also around unity, depending on the relative target location.

Table 4-7

Sensitivity Matrices, T = 300 sec.

LMU SENSITIVITY MATRIX
T=   300.000
SAI=

```
 9.7530E-01   5.2067E-02   2.0827E-01  -1.4882E+02   3.7911E+00   1.5164E+01
-5.2119E-02   5.2058E-02  -5.2119E-02   1.3276E-03  -1.3261E-03   1.3276E-03
 5.3106E-03  -5.3044E-03   5.3106E-03  -5.0000E+00   0.           0.
```

```
-5.2067E-02   9.7530E-01   5.2067E-02  -3.7911E+00  -1.4882E+02   3.7911E+00
-1.3276E-03   1.3261E-03  -1.3276E-03  -5.2119E-02   5.2058E-02  -5.2119E-02
 1.3276E-03  -1.3261E-03   1.3276E-03   0.          -5.0000E+00   0.
```

```
-2.0827E-01  -5.2067E-02   9.7530E-01  -1.5164E+01  -3.7911E+00  -1.4882E+02
-5.3106E-03   5.3044E-03  -5.3106E-03  -1.3276E-03   1.3261E-03  -1.3276E-03
-5.2119E-02   5.2058E-02  -5.2119E-02   0.           0.          -5.0000E+00
```

STA SENSITIVITY MATRIX
T=   300.000
SAU=

```
 9.6036E-01  -2.3442E-01   9.0050E-01  -3.3374E-01  -1.3034E-01  -3.8638E-01
 9.0050E-01  -2.3442E-01  -1.7678E-01  -8.7500E-01  -1.7678E-01   0.
 6.1872E-01  -6.1872E-01  -1.7678E-01  -8.7500E-01  -4.0045E+00  -1.7126E+02
 2.0913E+02  -1.4024E-03   1.4008E-03  -1.4024E-03  -5.9977E-02   5.9907E-02
-5.9977E-02   7.3238E-02  -7.3153E-02   7.3238E-02  -6.7658E-01  -5.9445E+00
 6.8057E+00
```

```
 1.3767E+00  -1.4065E+00   1.2909E+00  -4.7844E-01   4.4640E-01  -1.4167E+00
 1.2909E+00  -1.4065E+00  -2.1213E+00  -1.0000E+00  -2.1213E+00   0.
 7.0711E-01  -7.0711E-01  -2.1213E+00  -1.0000E+00  -5.5044E+02  -1.4241E+02
 4.1241E+02  -1.9277E-01   1.9254E-01  -1.9277E-01  -4.9872E-02   4.9814E-02
-4.9872E-02   1.4443E-01  -1.4426E-01   1.4443E-01  -1.9545E+01  -5.5809E+00
 1.1722E+01
```

```
 1.6789E+00  -1.8753E+00   1.5743E+00  -5.8347E-01   6.3909E-01  -1.8568E+00
 1.5743E+00  -1.8753E+00  -1.5026E+00  -5.0000E-01  -1.5026E+00   0.
 3.5355E-01  -3.5355E-01  -1.5026E+00  -5.0000E-01  -4.0091E+02  -5.8927E+01
 2.4613E+02  -1.4040E-01   1.4024E-01  -1.4040E-01  -2.0636E-02   2.0612E-02
-2.0636E-02   8.6197E-02  -8.6096E-02   8.6197E-02  -1.4095E+01  -2.5112E+00
 6.7691E+00
```

4-42

Table 4-7. (Cont'd)

POINTING SENSITIVITY MATRICES
T=   300.000

S2=
```
 1.0000E+00  .0.          0.          -1.0000E+00  1.2431E-02
-9.9571E-02   0.          -1.0034E-01  -1.0050E+00   0.
-1.0007E+00  9.3371E-02  .7.0758E-01  -9.3371E-02  -7.0758E-01

 0.          1.0000E+00   0.           0.          -9.9230E-01
-1.2387E-01 -1.0000E+00   0.           0.           0.
-9.2903E-02 -9.9568E-01  6.5692E-02   9.9568E-01  -6.5692E-02

 0.          0.          1.0000E+00   0.           1.2451E-01
-9.9728E-01  0.          -1.0050E+00  -1.0034E-01  -1.0000E+00
-9.9908E-02  9.3381E-03  7.7775E-01  -9.3381E-03   6.3646E-01
```

S1=
```
-7.0758E-01 -9.3371E-02 -7.0753E-01 -7.0758E-01  9.3371E-02  7.0758E-01
-6.5692E-02  9.9568E-01 -6.5692E-02 -6.5692E-02 -9.9568E-01  6.5692E-02
 6.3646E-01 -9.3381E-03 -7.7775E-01 -7.7775E-01  9.3381E-03 -6.3646E-01
```

S0=
```
-1.9693E+00  1.0848E-01 -4.1473E-01
-5.5908E-02 -2.0383E+00 -1.2076E-01
 2.1436E-01  1.3723E-01 -1.9976E+00
```

SLOS=
```
 2.6243E-02 -1.0000E+00 -1.1869E-01
 9.9230E-01   0.          0.
-1.2451E-01   0.          0.
```

Table 4-8

Sensitivity Matrices, T = 600 sec.

IMU SENSITIVITY MATRIX
T=   600.000
SAI=

```
 9.9454E-01  -6.3536E-02   1.0751E-01  -1.4472E+02   2.8948E+00   3.8573E+01
 5.0683E-02  -5.0624E-02   5.0683E-02  -1.0138E-03   1.0126E-03  -1.0138E-03
-1.3508E-02   1.3493E-02  -1.3508E-02  -5.0000E+00   0.           0.


 5.7945E-02   9.6938E-01  -4.6765E-02  -2.8948E+00  -1.4472E+02   5.2698E+00
 1.0138E-03  -1.0126E-03   1.0138E-03   5.0683E-02  -5.0624E-02   5.0683E-02
-1.8455E-03   1.8434E-03  -1.8455E-03   0.          -5.0000E+00   0.


-1.0192E-01   4.1175E-02   9.9454E-01  -3.8573E+01  -5.2698E+00  -1.4472E+02
 1.3508E-02  -1.3493E-02   1.3508E-02   1.8455E-03  -1.8434E-03   1.8455E-03
 5.0683E-02  -5.0624E-02   5.0683E-02   0.           0.          -5.0000E+00
```

STA SENSITIVITY MATRIX
T=   600.000
SAU=

```
-2.0301E-01  -2.5617E-02  -2.0077E-01  -3.0121E-02  -3.9061E-02   6.1500E-03
-2.0077E-01  -2.5617E-02  -3.1308E-01   3.2900E-02  -2.9357E-01   1.0880E-01
 6.8237E-02   9.0583E-02  -2.9357E-01   3.2900E-02  -8.4180E+01   1.3226E+01
 3.9899E+01   2.9480E-02  -2.9446E-02   2.9480E-02  -4.6316E-03   4.6263E-03
-4.6316E-03  -1.3973E-02   1.3957E-02  -1.3973E-02  -3.0688E+00   3.7463E-01
 5.7417E-01


-5.9569E-02  -3.4617E-01  -5.8910E-02  -8.8382E-03  -2.6832E-01  -2.1892E-01
-5.8910E-02  -3.4617E-01  -5.1190E-03   3.1491E-01  -4.7999E-03   1.7769E-03
-1.8486E-01   2.5488E-01  -4.7999E-03   3.1491E-01   1.4078E+01  -6.1649E+01
 7.0304E+01  -4.9301E-03   4.9243E-03  -4.9301E-03   2.1590E-02  -2.1565E-02
 2.1590E-02  -2.4621E-02   2.4592E-02  -2.4621E-02  -8.8852E-02  -2.2163E+00
 2.3245E+00


-7.2097E-02  -3.2781E-01  -7.1299E-02  -1.0697E-02  -2.5561E-01  -2.0554E-01
-7.1299E-02  -3.2781E-01   2.3234E-03  -3.7540E-01   2.1786E-03  -8.0743E-04
 2.2142E-01  -3.0307E-01   2.1786E-03  -3.7540E-01  -1.7817E+01   7.3729E+01
-8.3415E+01   6.2397E-03  -6.2325E-03   6.2397E-03  -2.5820E-02   2.5790E-02
-2.5820E-02   2.9212E-02  -2.9178E-02   2.9212E-02   6.8928E-02   2.6494E+00
-2.7670E+00
```

Table 4-8 (Cont'd)

POINTING SENSITIVITY MATRICES
T=   600.000

S2=
```
  1.0000E+00   0.          0.          -1.0000E+00  -3.9941E-05
  1.7770E-03   0.          1.7775E-03  -1.0000E+00   0.
 -9.9918E-01  -4.0514E-02   7.0653E-01   4.0514E-02  -7.0653E-01

  0.          1.0000E+00   0.          0.          -9.9975E-01
 -2.2457E-02  -1.0000E+00   0.          0.           0.
  4.0514E-02  -9.9918E-01  -2.8648E-02   9.9918E-01   2.8648E-02

  0.          0.          1.0000E+00   0.           2.2471E-02
 -9.9975E-01   0.         -1.0000E+00   1.7775E-03  -1.0000E+00
  1.7754E-03   8.6523E-05   7.0585E-01  -8.6523E-05   7.0536E-01
```

S1=
```
 -7.0653E-01   4.0514E-02  -7.0653E-01  -7.0653E-01  -4.0514E-02   7.0653E-01
  2.8648E-02   9.9918E-01   2.8648E-02   2.8648E-02  -9.9918E-01  -2.8648E-02
  7.0836E-01  -8.6523E-05  -7.0585E-01  -7.0585E-01   8.6523E-05  -7.0836E-01
```

S0=
```
 -1.9017E+00  -4.2649E-02  -6.1806E-01
  5.6520E-02  -2.1022E+00  -1.9083E-02
  6.2129E-01   2.3723E-02  -1.9012E+00
```

SLOS=
```
  1.3273E-02  -1.0000E+00  -1.8150E-02
  9.9975E-01   0.           0.
 -2.2471E-02   0.           0.
```

Table 4-9

Sensitivity Matrices, T = 900 sec.

IMU SENSITIVITY MATRIX
T=   900.000
SAI=

```
 9.7437E-01   6.8969E-02   2.0913E-01  -1.3683E+02   2.1697E+00   6.0481E+01
-4.7918E-02   4.7862E-02  -4.7918E-02   7.5985E-04  -7.5897E-04   7.5985E-04
 2.1181E-02  -2.1156E-02   2.1181E-02  -5.0000E+00   0.           0.
```



```
-4.8359E-02   9.0769E-01   4.8611E-02  -2.1697E+00  -1.3683E+02   4.7151E+00
-7.5985E-04   7.5897E-04  -7.5985E-04  -4.7918E-02   4.7862E-02  -4.7918E-02
 1.6512E-03  -1.6493E-03   1.6512E-03   0.          -5.0000E+00   0.
```



```
-2.0919E-01  -3.5165E-02   9.7616E-01  -6.0481E+01  -4.7151E+00  -1.3683E+02
-2.1181E-02   2.1156E-02  -2.1181E-02  -1.6512E-03   1.6493E-03  -1.6512E-03
-4.7918E-02   4.7862E-02  -4.7918E-02   0.           0.          -5.0000E+00
```


STA SENSITIVITY MATRIX
T=   900.000
SAU=

```
-2.9069E-01   1.9031E-01  -2.2382E-01   1.8550E-01   1.1051E-01   2.4162E-01
-2.2382E-01   1.9031E-01  -1.9253E-01  -1.2786E-01  -1.9040E-01  -2.8566E-02
-1.1559E-01  -6.1666E-02  -1.9040E-01  -1.2786E-01  -6.1724E+01  -3.2134E+01
 3.0402E+00  -2.1616E-02   2.1591E-02  -2.1616E-02  -1.1253E-02   1.1240E-02
-1.1253E-02   1.0647E-03  -1.0635E-03   1.0647E-03  -1.8973E+00  -1.1778E+00
-7.6813E-01
```



```
 1.9893E-01   1.7098E-01   1.5317E-01  -1.2694E-01  -1.7708E-01   1.1819E-01
 1.5317E-01   1.7098E-01  -8.5592E-02  -3.1273E-01  -8.4645E-02  -1.2699E-02
-2.4547E-01  -1.9419E-01  -8.4645E-02  -3.1273E-01  -4.5801E+01  -7.8480E+01
-4.0080E+01  -1.6040E-02   1.6021E-02  -1.6040E-02  -2.7434E-02   2.7452E-02
-2.7484E-02  -1.4036E-02   1.4020E-02  -1.4036E-02  -7.8532E-01  -2.8145E+00
-1.9087E+00
```



```
-2.1291E-01  -3.0359E-01  -1.6393E-01   1.3586E-01   2.3014E-01  -2.4001E-01
-1.6393E-01  -3.0359E-01   2.3124E-02  -3.2340E-01   2.2868E-02   3.4308E-03
-2.4305E-01  -2.1338E-01   2.2868E-02  -3.2340E-01  -1.6894E+01  -8.1126E+01
-5.5215E+01  -5.9163E-03   5.9094E-03  -5.9163E-03  -2.8411E-02   2.8378E-02
-2.8411E-02  -1.9337E-02   1.9314E-02  -1.9337E-02   3.0484E-01  -2.8913E+00
-1.9826E+00
```

Table 4-9 (Cont'd)

PØINTING SENSITIVITY MATRICES
T=   900.000

S2=
```
 1.0000E+00   0.           0.          -1.0000E+00   1.3296E-02
-1.0304E-01   0.          -1.0389E-01  -1.0054E+00   0.
-1.0043E+00   4.7665E-02   7.1011E-01  -4.7665E-02  -7.1011E-01

 0.          1.0000E+00   0.           0.          -9.9178E-01
-1.2797E-01  -1.0000E+00   0.           0.           0.
-4.7408E-02  -9.9888E-01   3.3522E-02   9.9888E-01  -3.3522E-02

 0.           0.           1.0000E+00   0.           1.2867E-01
-9.9712E-01   0.          -1.0054E+00  -1.0389E-01  -1.0000E+00
-1.0377E-01   4.9411E-03   7.8049E-01  -4.9411E-03   6.3373E-01
```

S1=
```
-7.1011E-01  -4.7665E-02  -7.1011E-01  -7.1011E-01   4.7665E-02   7.1011E-01
-3.3522E-02   9.9888E-01  -3.3522E-02  -3.3522E-02  -9.9888E-01   3.3522E-02
 6.3373E-01  -4.9411E-03  -7.8049E-01  -7.8049E-01   4.9411E-03  -6.3373E-01
```

S0=
```
-1.7455E+00   7.0634E-02  -1.0090E+00
 6.5247E-02  -2.3065E+00  -8.6852E-02
 8.1616E-01   1.5432E-01  -1.8354E+00
```

SLØS=
```
 9.1283E-02  -1.0000E+00  -7.5579E-02
 9.9178E-01   0.           0.
-1.2867E-01   0.           0.
```

4.3 OBSERVABILITY ANALYSIS

An observability analysis is performed as a means to determine if, in fact, the significant systematic error sources can be observed (for calibration) in the available measurements. Since the measurements are contaminated by noise and other uncertainties, one cannot really "compute" the misalignments, but merely obtain a "best" estimate. In the task of doing this, the equations can be represented as

$$\overline{\delta Y} = M \overline{\delta \alpha} + \overline{\eta} \tag{4-76}$$

where $\overline{\delta Y}$ is the variation of the measurements, M is the measurement matrix, $\overline{\delta \alpha}$ is the variation of the (misalignment) errors, and η models random uncertainties as additive observation noise. In general, assume there are p parameters to be estimated, that m measurements can be obtained at each calibration point, and that there are n calibration points.

$$\delta Y = \begin{bmatrix} \delta Y(1) \\ \hline \delta Y(2) \\ \hline \delta Y(3) \\ \hline \cdot \\ \cdot \\ \cdot \\ \hline \delta Y(n) \end{bmatrix}_{\{mn \ \times \ 1\}} \tag{4-77}$$

$$H = \begin{bmatrix} M(1) \\ \hline M(2) \\ \hline \cdot \\ \cdot \\ \cdot \\ \hline M(n) \end{bmatrix}_{\{mn \ \times \ p\}} \tag{4-78}$$

and

$$\eta = (\eta(1), \eta(2), \cdots, \eta(n)) \tag{4-79}$$

One then obtains

$$\delta Y = H\delta \alpha + \eta \tag{4-80}$$

The best estimate (in a least square sense) for $\delta\alpha$ is given by

$$\delta\alpha = (H^T H)^{-1} H^T \delta Y \qquad (4-81)$$

The matrix $H^T H$ is sometimes called the information matrix and, no matter how many measurements have been taken, $H^T H$ is always p x p. If $H^T H$ possesses an inverse, i.e., it is non-singular, then all parameters in $\delta\alpha$ are observable and estimates for them can be obtained. (Note that a similar argument holds for sequential estimation.) It is easy to show that if the number of total measurements obtained is less than the number of parameters to be estimated, then $H^T H$ will always be singular. Thus, one must impose that

$$mn \geq p \qquad (4-82)$$

When mn = p (the minimum number of observations), then H is a square matrix and it follows that in this case $\delta\alpha = H^{-1} \delta Y$. If H^{-1} exists, then all parameters are observable. The use of more observations will, of course, improve the estimate, but to establish observability it is sufficient to use only the minimum number of observations. On the other hand, since the measurement matrices M(k) depend on nominal values and thus vary with time, failure to detect observability when the minimum number of required measurements are used does not necessarily mean that the parameter vector is unobservable. A later measurement may yield new, independent information. In certain cases it is immediately obvious that not all parameters are observable, namely: when the matrix M(k) always contains the same linear dependency among its columns, for all k. This happens, for instance, when two parameters always appear in pairs and clearly the parameters are not separately observable. When inobservability of some individual parameters has been established, combining certain of these parameters to one lumped parameter can frequently restore joint-observability.

In the paragraphs which follow, observability of key systematic errors is demonstrated for both attitude determination and experiment pointing. Simulation of the attitude determination calibration, discussed in Section 5.4, verifies the results demonstrated here analytically.

4.3.1 Observability of Attitude Determination Errors

It is readily evident that accurate calibration of the alignment uncertainties of the star trackers and gyros is key to establishing attitude determination estimation accuracies in the 1-3 sec region. The primary attitude determination error sources are:

Star Tracker Assembly
Gimbal alignment uncertainties (including runout)
Inductosyn readout errors
Detector alignment uncertainties, readout error, and noise

Gyro Reference Assembly
Gyro random drift uncertainty
Gyro input axis alignment uncertainty
Gyro scale factor errors

Of these error sources, only the gyro drift rates are included as elements of the state vector in the on-board attitude determination Kalman filter, and need not be considered separately. Of the remaining sources, the detector readout error and noise, gimbal bearing runout, and Inductosyn readout errors can be regarded as contributions which are secondary in nature, perhaps not requiring calibration beyond that determined prior to flight. It is anticipated, then, that the rest of the error sources (i.e., gimbal alignment, detector alignment, gyro alignment, and gyro scale factor) may necessitate a fairly sophisticated flight calibration procedure based upon using these parameters as elements of the state vector to be estimated through use of a ground-based Kalman filter. It is important to establish whether these primary errors can uniquely be isolated from the spacecraft attitude given the measured tracker and gyro outputs.

To obtain an early understanding of the problem, a brief observability analysis was undertaken, assuming a least squares estimate. Considered as elements of the state vector were the following:

$\delta\phi, \delta\theta, \delta\psi$: Attitude variables, 3-vector

α_1, α_3: Detector misalignments, 2-vector

α_1^I, α_2^I: Inner gimbal axis misalignments, 2-vector

α_2^0, α_3^0: Outer gimbal axis misalignments, 2-vector

p_I, p_0: Inductosyn misalignments, 2-vector

The appropriate measurement matrix was developed, and it was determined that four elements are only observable jointly, namely: $\alpha_3 + p_I$, $\alpha_1^I + p_0$; and further, that both outer gimbal misalignments and one of the inner gimbal misalignments could not be separated from the attitude itself except under certain conditions. These conditions amounted to assuming that the gyros are "ideal", an assumption which is not valid in the real world. This leads to consideration of defining a set of

reference axes to which the errors are, in fact, observable under realistic conditions. As the star tracker is the primary attitude reference sensor, it seems reasonable to focus upon the attitude motion of a star tracker related reference as opposed to the motion of some other reference in the spacecraft. No disadvantage results concerning the attitude determination of any vehicle payload provided its orientation is established relative to the star tracker. This is the boresighting problem discussed for payload pointing in Section 4.3.2. .

The axes (x_1', x_2', x_3') are established as follows: The inner and outer gimbals of the star tracker are assumed rotated until both inductosyn electrical read-outs are null and, under this condition, x_1' is chosen to be colinear with the outer gimbal axis; x_3' is taken to lie in the plane of the two gimbal axes and normal to x_1'; and x_2' is defined as completing the right-handed, orthogonal, set. If the tracker thermal deformation and inductosyn read-out instability is insignificant, as expected, this coordinate set will remain stable relative to a stable reference at the tracker gimbal base. Only three tracker misalignments remain under the coordinate definition, namely:

α_2^I - degree to which the inner and outer gimbals are not perpendicular when the inductosyns are nulled.

α_1, α_3 - degree to which the detector optical boresight is not perpendicular to the $x_1' - x_3'$ plane when the inductosyns are nulled.

Relative to (x_1', x_2', x_3') there remains now 15 primary error sources; the three tracker misalignments defined above, nine gyro misalignment and scale factor errors defined by A_γ, and three gyro drift bias errors, $\hat{b}_g^{~o}$.

4.3.1.1 Observability of Tracker Misalignments and Gyro Biases

The tracker misalignments and gyro drift bias error is explored initially for observability. The measurement equation is given as

$$
\begin{bmatrix} y_I \\ \\ y_0 \end{bmatrix} = \begin{bmatrix} -u_1 \\ \\ \dfrac{u_3}{u_5} \end{bmatrix} + \begin{bmatrix} 0 & -u_5 & 0 \\ \\ -\dfrac{u_2}{u_4} & 0 & \dfrac{u_1 u_2}{u_4} \end{bmatrix} \begin{bmatrix} \alpha_1 \\ \\ \alpha_3 \\ \\ \alpha_2^I \end{bmatrix} \qquad (4\text{-}83)
$$

where

$$u_4 = (1 - u_1^2)$$

$$u_5 = (1 - u_1^2)^{1/2}$$

4-51

as the other parameters vanish. Noting that the α's are first order terms, it is straightforward to demonstrate that for any particular star

$$u = \tilde{y} + Y \alpha \tag{4-84}$$

where

$$u = \begin{bmatrix} u_1 \\ u_3 \end{bmatrix} \tag{4-85}$$

$$\tilde{y} = \begin{bmatrix} -y_I \\ c \, y_0 \end{bmatrix} \tag{4-86}$$

$$Y = \begin{bmatrix} 0 & -c & 0 \\ \frac{b}{c} & -y_I \, y_0 & \frac{b}{c} \, y_I \end{bmatrix} \tag{4-87}$$

where

$$c = \sqrt{1 - y_I^2} \tag{4-88}$$

$$b = \sqrt{1 - y_I^2 - a^2 \, y_0^2} \tag{4-89}$$

Suppose now that at time zero the estimated STA reference axes are defined by (v_1, v_2, v_3). These will differ from the actual axes by three first order rotations, so that at time $t_1 = 0$

$$\begin{bmatrix} x_1' \\ x_2' \\ x_3' \end{bmatrix} = \begin{bmatrix} 1 & \theta_3^1 & -\theta_2^1 \\ -\theta_3^1 & 1 & \theta_1^1 \\ \theta_2^1 & -\theta_1^1 & 1 \end{bmatrix} \begin{bmatrix} v_1 \\ v_2 \\ v_3 \end{bmatrix} \tag{4-90}$$

Now take $\theta^i = (\theta_1^i, \theta_2^i, \theta_3^i)$ and $\bar{u}_s^i$ to be, respectively, the attitude and star unit vector at time t_i. Then

$$\bar{u}^{si} = \sum_{j=1}^{3} u_j^i \bar{x}_j = \sum_{j=1}^{3} a_j^i \bar{v}_j \qquad (4-91)$$

where the a_j^i are known since the set (v_1, v_2, v_3) has been established. It follows that

$$U^i \theta^i = a^i - u^i \qquad (4-92)$$

where

$$U^i = \begin{bmatrix} 0 & u_3^i & -u_2^i \\ u_2^i & -u_1^i & 0 \end{bmatrix} \qquad (4-93)$$

$$a^i = \begin{bmatrix} a_1^i \\ a_3^i \end{bmatrix} \qquad (4-94)$$

Taking ω^i to be a constant, first order, spacecraft angular rate on $[t_i, t_{i+1}]$ it follows that

$$\theta^{i+1} = \theta^i + \omega^i (t_{i+1} - t_i) \qquad (4-95)$$

Recalling,

$$\omega^i A_\gamma^{-1} [\omega^{Mi} - b_g^o] \approx \omega^{Mi} - b_g^o \qquad (4-96)$$

since ω^{Mi} can be assumed first order because of ω^i. Summarizing these ideas, it follows that

$$\theta^{i+1} = L^i \begin{bmatrix} b_{g0} \\ \theta^1 \end{bmatrix} + \beta^i \qquad (4-97)$$

where

$$L^i = \begin{bmatrix} -t_i & 0 & 0 & 1 & 0 & 0 \\ 0 & -t_i & 0 & 0 & 1 & 0 \\ 0 & 0 & -t_i & 0 & 0 & 1 \end{bmatrix} \qquad (4-98)$$

$$\beta^i = \sum_{j=1}^{i} \omega^{Mj} (t_{j+1} - t_j) \qquad (4\text{-}99)$$

Combining Equations (4-84), (4-42), and (4-97), it can be shown that

$$Z^{i+1} \begin{bmatrix} b_g^o \\ \theta^1 \\ \alpha \end{bmatrix} = p^{i+1} \qquad (4\text{-}100)$$

where

$$\alpha = \begin{bmatrix} \alpha_1 \\ \alpha_3 \\ \alpha_2^I \end{bmatrix} \qquad (4\text{-}101)$$

$$Z^{i+1} = [U^{i+1} \ L^i \ Y^{i+1}] \qquad (4\text{-}102)$$

$$p^{i+1} = a^{i+1} - \tilde{y}^{i+1} - U^{i+1} \beta^i \qquad (4\text{-}103)$$

Take star sensor measurements at t_1, t_2, $\cdots$, t_5, it follows that the 9 parameters contained in b_g^o, θ^1, and α can be determined, in general, by

$$\begin{bmatrix} b_g^o \\ \theta^1 \\ \alpha \end{bmatrix} = (Z^T Z)^{-1} Z^T p \qquad (4\text{-}104)$$

where

$$Z = \begin{bmatrix} Z^2 \\ \cdot \\ \cdot \\ \cdot \\ Z^6 \end{bmatrix} \qquad (4\text{-}105$$

$$p = \begin{bmatrix} p^2 \\ \cdot \\ \cdot \\ \cdot \\ p^6 \end{bmatrix} \qquad (4\text{-}106)$$

4-54

These parameters are observable provided $Z^T Z$ is non-singular. Since $Z^T Z$ is 10 by 10, analytic establishment of non-singularity conditions is difficult. Approaching this problem numerically via a digital computer, sets of five stars were chosen arbitrarily and $(Z^T Z)^{-1}$ shown to exist in each case. Thus, except for highly improbable star location arrangements, it can be assumed that b_g^o and α are observable.

Finally, it is developed that

$$
\begin{bmatrix} \delta y_I \\ \delta y_0 \end{bmatrix} = \begin{bmatrix} 0 & u_3 & -u_2 & 0 & -u_5 & 0 \\ \dfrac{-u_2}{\sqrt{1-u_1^2}} & \dfrac{u_1 u_2^2}{u_5^3} & \dfrac{u_1 u_2 u_3}{u_5^3} & \dfrac{-u_2}{1-u_1^2} & 0 & \dfrac{u_1 u_2}{u_5^2} \end{bmatrix} \begin{bmatrix} \delta\theta_1 \\ \delta\theta_2 \\ \delta\theta_3 \\ \delta\alpha_1 \\ \delta\alpha_3 \\ \delta\alpha_2^I \end{bmatrix} \quad (4\text{-}107)
$$

The ability to separate tracker biases from the attitude variables depends upon the degree to which the columns of the above coefficient matrix are not dependent for each star selection made. Clearly none of these columns can be expressed as a linear sum of the remaining columns, i.e., α is observable. However, since the inner gimbal travel is limited to 15 deg in the present application (which implies $|u_1| \leq 0.259$), the coefficients of $\delta\theta_1$ and $\delta\alpha_1$ are never very different. Thus some difficulty can be anticipated in calibrating α_1.

4.3.1.2 Observability of the Gyro Scale Factor/Misalignments of A_γ

By previous results, it has been shown that it is possible to calibrate the 3 gyro biases and 3 star tracker misalignments, and to additionally establish the attitude at the initial time (and thus all succeeding times) provided the angular rates are small. It is thus possible to determine the nine A_γ elements, then re-orient the spacecraft through large angles and determine these nine elements again, linearizing about the expected orientation. In fact, only θ^1 requires re-evaluation since α and b_g^o will not change. This can be done repetitively, the attitude after each such reorientation being evaluated.

Let A_i be the direction cosine matrix after the i-th such maneuver and

evaluation. Then

$$A_i = e^{P_i \tau_i} A_{i-1} \qquad (4\text{-}108)$$

where

$$P_i = \begin{bmatrix} 0 & \omega_3^i & -\omega_2^i \\ -\omega_3^i & 0 & \omega_1^i \\ \omega_2^i & -\omega_1^i & 0 \end{bmatrix} \qquad (4\text{-}109)$$

and τ_i is the time duration of application by ω^i.

Recalling the definition of

$$\omega^i = A_\gamma^{-1} [\omega^{Mi} - b_g^0] = A_\gamma^{-1} \tilde{\omega}^{Mi} = \tilde{\omega}^{Mi} - \gamma \tilde{\omega}^{Mi} \qquad (4\text{-}110)$$

where $\omega^{\tilde{M}i}$ is known due to the previous calibration of b_g^0. It follows that

$$R_i = \begin{bmatrix} 0 & \bar{\gamma}_3 \cdot \tilde{\omega}^{Mi} & -\bar{\gamma}_2 \cdot \tilde{\omega}^{Mi} \\ -\bar{\gamma}_3 \cdot \tilde{\omega}^{Mi} & 0 & \bar{\gamma}_1 \cdot \tilde{\omega}^{Mi} \\ \bar{\gamma}_2 \cdot \tilde{\omega}^{Mi} & -\bar{\gamma}_1 \cdot \tilde{\omega}^{Mi} & 0 \end{bmatrix} \qquad (4\text{-}111)$$

where $\gamma_i = (\gamma_{i1}, \gamma_{i2}, \gamma_{i3}), i = 1, 2, 3$. Noting Equation (4-108),

$$R_i = P_i^{\tilde{M}} - \frac{1}{\tau_i} \log (A_i A_{i-1}^{-1}) \qquad (4\text{-}112)$$

Starting with an attitude described by A_0, three of the γ_{ij} can be established by slewing the spacecraft such that $\omega_1^{\tilde{M}}$ is finite and $\omega_2^{\tilde{M}} = \omega_3^{\tilde{M}} \approx 0$ up to first order effects. In this case Equation (4-112) becomes

$$\omega_1^{\tilde{M}} = \begin{bmatrix} 0 & -\gamma_{31} & \gamma_{21} \\ \gamma_{31} & 0 & -\gamma_{11} \\ -\gamma_{21} & \gamma_{11} & 0 \end{bmatrix} = P_1^{\tilde{M}} - \frac{1}{\tau_1} \log (A_1 A_0^{-1}) \quad (4\text{-}113)$$

which establishes γ_{11}, γ_{21}, and γ_{31}. In a similar fashion γ_{12}, γ_{22}, and γ_{32} are determined by reversing the roles of $\omega_1^{\tilde{M}}$ and $\omega_2^{\tilde{M}}$. The same comments apply

to γ_{13}, γ_{23}, and γ_{33} which concludes the determination of the 9 GRA "geometry errors" and proves their observability.

4.3.2 Observability of Experiment Pointing Errors

This section deals with the observability of system errors other than those of attitude determination, namely: alignment sensing and experiment gimbal pointing. The primary error sources are:

<u>Alignment Sensor Assembly</u>
Misalignments
Readout Uncertainties

<u>Experiment Gimbal Assembly</u>
Alignment Uncertainties
Inductosyn Readout Errors

In order for calibration to be successful, the misalignments must be observable in the experiment gimbal angle measurements. As it is unlikely that all misalignments are separately observable, "lumped estimates" are obtained for combinations of some of the misalignments. Although the experiment gimbal is a three degree of freedom gimbal, the calibration targets are assumed to yield a LOS vector, so that only two gimbal angle observations are obtained from each target observation. It is assumed that the third gimbal angle, ψ_g, is commanded to some constant during calibration, although this constant may differ from target to target as long as it is known. Thus, the measurement equation at t_k becomes

$$\delta\gamma^g(k) = \begin{bmatrix} \delta\phi_{gm}(k) \\ \delta\theta_{gm}(k) \end{bmatrix} = M(k)\ \delta\alpha + n(k) \qquad (4\text{-}114)$$

where one would like the misalignment error vector $\delta\alpha$ to contain:

$\delta\epsilon_I$ = Inductosyn error (experiment gimbals), 3-vector

$\delta\alpha_e$ = Boresight sensor misalignments, 3-vector

$\delta\alpha_\ell$ = Last gimbal axis misalignments, 2-vector

$\delta\alpha_m$ = Middle gimbal axis misalignments, 2-vector

$\delta\alpha_f$ = First gimbal axis misalignments 2-vector

$\delta\alpha_t$ = Gimbal base misalignments, 3-vector

$\delta\alpha_r$ = Alignment sensor misalignments, 3-vector

4-57

The measurement matrix, M, is derived for the yaw gimbal angle, ψ_g, commanded at an arbitrary (known) angle, ψ_g^0. From the detailed system equations for gimbal commands one has

$$\phi_g = \phi - \alpha_{e1} \tag{4-115}$$

$$\theta_g = \theta - \alpha_{\ell2} \tag{4-116}$$

$$\psi_g = \psi_g^0 \tag{4-117}$$

If the closed-loop gimbal servo control was perfect, then these angles would also be the gimbal angle servo commands. Since this is not the case (Inductosyn errors, etc.), corrections accounting for the servo errors are made. The gimbal angle commands are then given by

$$\phi_{gc} = \phi_g + \alpha_{s1} \tag{4-118}$$

$$\theta_{gc} = \theta_g + \alpha_{s2} \tag{4-119}$$

$$\psi_{gc} = \psi_g^0 + \alpha_{s3} \tag{4-120}$$

The existing servo error in the ψ_g-gimbal drive, which causes ψ_g to be slightly off null, acts like an additional misalignment of the middle gimbal axis and is accounted for in this manner. The servo errors, α_{si}, are defined by

$$\begin{bmatrix} \alpha_{s1} \\ \alpha_{s2} \\ \alpha_{s3} \end{bmatrix} = \begin{bmatrix} \varepsilon_{I1} + \varepsilon_{e1} \\ \varepsilon_{I2} + \varepsilon_{e2} \\ \varepsilon_{I3} + \varepsilon_{e3} \end{bmatrix} \tag{4-121}$$

where the ε_{Ii} are inductosyn errors and the ε_{ei} are steady-state servo loop errors.

The interest centers on the measured gimbal angles, $\tilde{\phi}_g$ and $\tilde{\theta}_g$, at the instant when a calibration measurement is obtained. It follows that

$$\tilde{\phi}_g = \phi_g + \varepsilon_{I1} \tag{4-122}$$

$$\tilde{\theta}_g = \theta_g + \varepsilon_{I2} \tag{4-123}$$

$$\tilde{\psi}_g = \psi_g + \varepsilon_{I3} \tag{4-124}$$

and, therefore,

$$\tilde{\phi}_g = \phi - \alpha_{e1} + \epsilon_{I1} \qquad (4\text{-}125)$$

$$\tilde{\theta}_g = \theta - \alpha_{\ell 2} + \epsilon_{I2} \qquad (4\text{-}126)$$

One must now relate the variations in the measurements to variations in the pointing misalignment error vector.

The angles, ϕ and θ, are defined by

$$\sin\phi = -u_2 \qquad (4\text{-}127)$$

$$\tan\theta = \frac{u_1 - u_3 u_4}{u_3 + u_1 u_4} \qquad (4\text{-}128)$$

where

$$\begin{bmatrix} u_1 \\ u_2 \\ u_3 \end{bmatrix} = \widehat{\alpha}_m \widehat{\psi}_g \widehat{\alpha}_f \begin{bmatrix} u_1^n \\ u_2^n \\ u_3^n \end{bmatrix} \qquad (4\text{-}129)$$

$$u_4 = \frac{-\alpha_{\ell 3} u_2 + \alpha_{e2}}{\sqrt{1 - u_2^2}} \qquad (4\text{-}130)$$

The column vector, $\bar{u}^n$, is the normalized target LOS vector in nominal gimbal base coordinates. It becomes clear now why the generalization was introduced to allow an arbitrary known value, ψ_g^0, for the third gimbal angle command. Without this freedom, it is evident that the misalignment, $\widehat{\alpha}_f$ and $\widehat{\alpha}_m$, would not be separately observable. The gimbal angle, ψ_g, is the response to the command $\psi_{gc} = \psi_g^0$. The measured value, $\tilde{\psi}_g$, differs from ψ_g by the inductosyn error, ϵ_{I3}, so that in expanded form

4-59

$$\begin{bmatrix} u_1 \\ u_2 \\ u_3 \end{bmatrix} = \begin{bmatrix} 1 & (\alpha_{m3} - \epsilon_{I3}) & 0 \\ -(\alpha_{m3} - \epsilon_{I3}) & 1 & \alpha_{m1} \\ 0 & -\alpha_{m1} & 1 \end{bmatrix} \begin{bmatrix} \cos\psi_{gm} & \sin\psi_{gm} & 0 \\ -\sin\psi_{gm} & \cos\psi_{gm} & 0 \\ 0 & 0 & 1 \end{bmatrix}$$

$$\begin{bmatrix} 1 & 0 & -\alpha_{f2} \\ 0 & 1 & \alpha_{f1} \\ \alpha_{f2} & -\alpha_{f1} & 1 \end{bmatrix} \begin{bmatrix} u_1^n \\ u_2^n \\ u_3^n \end{bmatrix} \qquad (4\text{-}131)$$

At this point it is noted that the static servo equilibrium error, ϵ_e, will not enter the calibration procedure at all since the measured gimbal angles are used as the observables. It is also evident that none of the three inductosyn errors is separately observable, but that they all merge with other misalignments. For simplicity then, just one of the errors is carried and, by convention, let the inductosyn errors be included with the misalignments, i.e.,

$$\alpha_{e1} - \epsilon_{I1} \rightarrow \alpha_{e1} \qquad (4\text{-}132)$$

$$\alpha_{\ell2} - \epsilon_{I2} \rightarrow \alpha_{\ell2} \qquad (4\text{-}133)$$

$$\alpha_{m3} - \epsilon_{I3} \rightarrow \alpha_{m3} \qquad (4\text{-}134)$$

Taking the variations and applying the above convention, it follows that

$$\delta\tilde{\phi}_g = \delta\phi - \delta\alpha_{e1} \qquad (4\text{-}135)$$

$$\delta\tilde{\theta}_g = \delta\theta - \delta\alpha_{\ell2} \qquad (4\text{-}136)$$

Next, the variations $\delta\phi$ and $\delta\theta$ are evaluated. After partial differentiation of Equation (4-127) and (4-128) and some algebraic manipulations, one obtains that

$$\begin{bmatrix} \delta\phi \\ \delta\theta \end{bmatrix} = G \begin{bmatrix} \delta u \\ \hline \delta\alpha_{\ell3} \\ \hline \delta\alpha_{e2} \end{bmatrix} \qquad (4\text{-}137)$$

where G is a 2 x 5 matrix whose entries are given by

$$g_{11} = 0 \tag{4-138}$$

$$g_{12} = \frac{-1}{\cos\phi} \tag{4-139}$$

$$g_{13} = g_{14} = g_{15} = 0 \tag{4-140}$$

$$g_{21} = \cos^2\theta \; \frac{u_3(1 + u_4^2)}{(u_3 + u_1 u_4)^2} \tag{4-141}$$

$$g_{22} = \cos^2\theta \; \frac{-(u_3^2 + u_1^2)(\alpha_{e2}u_2 - \alpha_{\ell 3})}{(u_3 + u_1 u_4)^2 (1 - u_2^2)^{3/2}} \tag{4-142}$$

$$g_{23} = \cos^2\theta \; \frac{-u_1(1 + u_4^2)}{(u_3 + u_1 u_4)^2} \tag{4-143}$$

$$g_{24} = \cos^2\theta \; \frac{(u_3^2 + u_1^2) \, u_2}{(u_3 + u_1 u_4)^2 \sqrt{1 - u_2^2}} \tag{4-144}$$

$$g_{25} = \cos^2\theta \; \frac{-(u_3^2 + u_1^2)}{(u_3 + u_1 u_4)^2 \sqrt{1 - u_2^2}} \tag{4-145}$$

Substituting into the previous equations yields

$$\begin{bmatrix} \delta\phi_{gm} \\ \delta\theta_{gm} \end{bmatrix} = G_u \begin{bmatrix} \delta u_1 \\ \delta u_2 \\ \delta u_3 \end{bmatrix} + \begin{bmatrix} -1 & \vdots & \\ & \vdots & G_{e2} \\ 0 & \vdots & \end{bmatrix} \begin{bmatrix} \delta\alpha_{e1} \\ \delta\alpha_{e2} \end{bmatrix} + \begin{bmatrix} 0 & \vdots & \\ & \vdots & G_{\ell 3} \\ -1 & \vdots & \end{bmatrix} \begin{bmatrix} \delta\alpha_{\ell 2} \\ \delta\alpha_{\ell 3} \end{bmatrix} \tag{4-146}$$

where

$$G_u = \left\{ \text{first 3 columns of G} \right\}$$

$$G_{\ell 3} = \left\{ 4^{th} \text{ column of G} \right\}$$

$$G_{e2} = \left\{ 5^{th} \text{ column of G} \right\}$$

The next task is to determine δu. Using Equation (4-131) one obtains, after some algebraic manipulations,

$$\delta u = \widehat{\psi}_{gm}\delta u^n + U^n \begin{bmatrix} \delta\alpha_{m1} \\ \delta\alpha_{m3} \\ \delta\alpha_{f1} \\ \delta\alpha_{f2} \end{bmatrix} \qquad (4\text{-}147)$$

where

$$U^n = \begin{bmatrix} 0 & -s_3 u_1^n + c_3 u_2^n & s_3 u_3^n & -c_3 u_3^n \\ u_3^n & -c_3 u_1^n - s_3 u_2^n & c_3 u_3^n & s_3 u_3^n \\ s_3 u_1^n - c_3 u_2^n & 0 & -u_2^n & u_1^n \end{bmatrix} \qquad (4\text{-}148)$$

and where

$$s_3 \triangleq \sin\psi_{gm} \quad \text{and} \quad c_3 \triangleq \cos\psi_{gm} \qquad (4\text{-}149)$$

From the system equations, one obtains that

$$u^n = A_{gt} \widehat{\alpha}_t^T A_{tr} \widetilde{\alpha}_r A_{rx} A_{xz} x_3^p \qquad (4\text{-}150)$$

where x_3^p is the normalized target LOS vector in ECI coordinates. Let

$$
\begin{aligned}
z_5 &= A_{xz} x_3^p & \delta z_5 &= \delta A_{xz} x_3^p \\
z_4 &= A_{rx} z_5 & \delta z_4 &= A_{rx} \delta z_5 \\
z_3 &= \alpha_r z_4 & \delta z_3 &= \delta\widehat{\alpha}_r z_4 + \widehat{\alpha}_r \delta z_4 \qquad (4\text{-}151)\\
z_2 &= A_{tr} z_3 & \delta z_2 &= A_{tr} \delta z_3 \\
z_1 &= \widehat{\alpha}_t^T z_2 & \delta z_1 &= \delta\widehat{\alpha}_t^T z_2 + \widehat{\alpha}_t^T \delta z_2 \\
u^n &= A_{gt} z_1 & \delta u^n &= A_{gt} \delta z_1
\end{aligned}
$$

Making use of previously obtained result (Appendix D) for the expansion of δA_{xz},

one obtains that

$$\delta u^n = A_{gt} \left[Z_2 \;\vdots\; A_{tr} Z_4 \;\vdots\; 2A_{tr} A_{rx} r^o X_3{}^p C \right] \begin{bmatrix} \delta\alpha_t \\ \hline \delta\alpha_r \\ \hline \delta_\rho{}^o \end{bmatrix} \qquad (4\text{-}152)$$

where

$$Z_2 = \begin{bmatrix} 0 & z_{23} & -z_{22} \\ -z_{23} & 0 & z_{21} \\ z_{22} & -z_{21} & 0 \end{bmatrix} \qquad (4\text{-}153)$$

and

$$Z_4 = \begin{bmatrix} 0 & -z_{43} & z_{42} \\ z_{43} & 0 & -z_{41} \\ -z_{42} & z_{41} & 0 \end{bmatrix} \qquad (4\text{-}154)$$

Substituting for δu and δu^n, one finally obtains

$$\begin{bmatrix} \delta\phi_{gm} \\ \delta\theta_{gm} \end{bmatrix} = \begin{bmatrix} -1 & \vdots & G_{e2} \\ 0 & \vdots & \end{bmatrix} \begin{bmatrix} \delta\alpha_{e1} \\ \delta\alpha_{e2} \end{bmatrix} + \begin{bmatrix} 0 & \vdots & G_{\ell 3} \\ -1 & \vdots & \end{bmatrix} \begin{bmatrix} \delta\alpha_{\ell 2} \\ \delta\alpha_{\ell 3} \end{bmatrix} + G_u u^n \begin{bmatrix} \delta\alpha_{m1} \\ \delta\alpha_{m3} \\ \delta\alpha_{f1} \\ \delta\alpha_{f2} \end{bmatrix}$$

$$(4\text{-}155)$$

$$+ G_u \widehat{\psi}_{gm} A_{gt} \left[Z_2 \;\vdots\; A_{tr} Z_4 \;\vdots\; 2A_{tr} A_{rx} r^o X_3{}^p C \right] \begin{bmatrix} \delta\alpha_t \\ \hline \delta\alpha_r \\ \hline \delta_\rho{}^o \end{bmatrix}$$

which may be rewritten as

$$\begin{bmatrix} \delta\phi_{gm} \\ \delta\theta_{gm} \end{bmatrix} = \left[\overset{2}{M_e} \;\vdots\; \overset{2}{M_\ell} \;\vdots\; \overset{2}{M_m} \;\vdots\; \overset{2}{M_f} \;\vdots\; \overset{3}{M_t} \;\vdots\; \overset{3}{M_r} \;\vdots\; \overset{3}{M_{\underline{e}}} \right] \begin{bmatrix} \delta\alpha_e \\ \delta\alpha_\ell \\ \delta\alpha_m \\ \delta\alpha_f \\ \delta\alpha_t \\ \delta\alpha_r \\ \delta_\rho{}^o \end{bmatrix} \qquad (4\text{-}156)$$

4-63

The matrices M_i must now be evaluated at nominal quantities. Since all the misalignments are very small quantities, their nominal values are without loss of generality taken as zero. The nominal measured autocollimator angles are also assumed zero. Denoting nominal quantities by a carat, one obtains that

$$\hat{\alpha} = 0 \quad \text{(all misalignments vector)} \tag{4-157}$$

$$\hat{A}_{tr} = I \tag{4-158}$$

$$\hat{z}_4 = A_{rx}\, \hat{A}_{xz}\, x_3{}^p \tag{4-159}$$

$$\hat{z}_2 = \hat{z}_4 \tag{4-160}$$

$$\hat{u}^n = A_{gt}\, A_{rx}\, \hat{A}_{xz}\, x_3{}^p \tag{4-161}$$

$$\hat{u} = \widehat{\psi}_{gm}\, \hat{u}^n \tag{4-162}$$

$$\cos\hat{\phi} = \sqrt{1 - \hat{u}_2{}^2} \tag{4-163}$$

$$\cos^2\hat{\theta} = \frac{\hat{u}_3{}^2}{\hat{u}_3{}^2 + \hat{u}_1{}^2} \tag{4-164}$$

where the nominal spacecraft attitude $\hat{A}_{xz}$ is obtained from the attitude determination system.

Using these nominal values, one obtains

$$\left[\hat{M}_e \; \vdots \; \hat{M}_\ell\right] = \begin{bmatrix} -1 & 0 & \vdots & 0 & 0 \\ 0 & -(1 - \hat{u}_2{}^2)^{1/2} & \vdots & -1 & \hat{u}_2(1 - \hat{u}_2{}^2)^{1/2} \end{bmatrix} \tag{4-165}$$

$$\hat{M}_m = \begin{array}{|c|c|} \hline -\hat{u}_3(1 - \hat{u}_2{}^2)^{1/2} & \hat{u}_1(1 - \hat{u}_2{}^2)^{1/2} \\ \hline \dfrac{\hat{u}_1 \hat{u}_2}{\hat{u}_1{}^2 + \hat{u}_3{}^2} & \dfrac{\hat{u}_2 \hat{u}_3}{\hat{u}_1{}^2 + \hat{u}_3{}^2} \\ \hline \end{array} \tag{4-166}$$

$$\hat{M}_f = \begin{bmatrix} -c_3\hat{u}_3(1 - \hat{u}_2{}^2)^{1/2} & -s_3\hat{u}_3(1 - \hat{u}_2{}^2)^{1/2} \\[2mm] s_3 + \dfrac{c_3\hat{u}_1\hat{u}_2}{\hat{u}_1{}^2 + \hat{u}_3{}^2} & -c_3 + \dfrac{s_3\hat{u}_1\hat{u}_2}{\hat{u}_1{}^2 + \hat{u}_3{}^2} \end{bmatrix} \qquad (4\text{-}167)$$

$$\left[\hat{M}_t \mid \hat{M}_r\right] = \begin{bmatrix} 0 & -(1 - \hat{u}_2{}^2)^{1/2} & 0 \\[2mm] \dfrac{\hat{u}_3}{\hat{u}_1{}^2 + \hat{u}_3{}^2} & 0 & \dfrac{-\hat{u}_1}{\hat{u}_1{}^2 + \hat{u}_3{}^2} \end{bmatrix} \begin{bmatrix} \cos\psi_{gm} & \sin\psi_{gm} & 0 \\ -\sin\psi_{gm} & \cos\psi_{gm} & 0 \\ 0 & 0 & 1 \end{bmatrix}$$

$$\cdot\; A_{gt}\left[\hat{\underline{Z}}_2 \mid -\underline{Z}_2\right] \qquad (4\text{-}168)$$

and $\hat{M}_0$ need not be evaluated for the one-shot estimate.

It is evident from this that, for all time, the matrices $\hat{M}_t$ and $\hat{M}_r$ satisfy

$$\hat{M}_r = -\hat{M}_t \qquad (4\text{-}169)$$

and that, therefore, the reflector and autocollimator misalignments will not be separately observable. The reflector misalignments are lumped with the autocollimator misalignments to yield

$$\delta\alpha_{tr} \triangleq \delta\alpha_t - \delta\alpha_r \qquad (4\text{-}170)$$

and

$$\hat{M}_{tr} \triangleq \hat{M}_t = -\hat{M}_r \qquad (4\text{-}171)$$

The measurement matrix would then be given by

$$M = \left[\overset{2}{\hat{M}_e} \mid \overset{2}{\hat{M}_\ell} \mid \overset{2}{\hat{M}_m} \mid \overset{2}{\hat{M}_f} \mid \overset{3}{\hat{M}_{tr}}\right] \qquad (4\text{-}172)$$

4-65

and the parameter vector by

$$\delta\alpha \;=\; \begin{bmatrix} \delta\alpha_e \\ \hline \delta\alpha_\ell \\ \hline \delta\alpha_m \\ \hline \delta\alpha_f \\ \hline \delta\alpha_{tr} \end{bmatrix} \tag{4-173}$$

From physical considerations it also appears doubtful if the alignment sensor misalignments, α_{tr}, can be separately observed from the gimbal mounting misalignments, α_f. The only large angle orthogonal rotation that separates the misalignments is A_{gt}, which is fixed; it merely indicates the nominal gimbal base orientation relative to the reflector. Combining Equations (4-131) - (4-134) with (4-150), one obtains

$$u \;=\; \hat{\alpha}_m \, \widehat{\psi}_{gm} \, \hat{\alpha}_f \, A_{gt} \, \hat{\alpha}_t^{\,T} \, A_{tr} \, \hat{\alpha}_r \, A_{rx} \, A_{xz} \, x_3^{\,p} \tag{4-174}$$

Because $\widehat{\psi}_{gm}$ represents a single rotation about axis 3, it follows that this above equation may be rewitten as

$$u \;=\; \hat{\alpha}_{m1} \, \widehat{\psi}_{gm} \, \hat{\alpha}_{fm} \, A_{gt} \, \hat{\alpha}_t^{\,T} \, A_{tr} \, \hat{\alpha}_r \, A_{rx} \, A_{xz} \, x_3^{\,p} \tag{4-175}$$

where

$$\hat{\alpha}_{fm} \;=\; \begin{bmatrix} 1 & \alpha_{m3} & -\alpha_{f2} \\ -\alpha_{m3} & 1 & \alpha_{f1} \\ \alpha_{f2} & -\alpha_{f1} & 1 \end{bmatrix} \tag{4-176}$$

Consider

$$v \;=\; \hat{\alpha}_{fm} \, A_{gt} \, \hat{\alpha}_t^{\,T} y \tag{4-177}$$

where v and y represent 3-dim vectors. Taking the variation and evaluating at nominal values yields

$$\delta v \;=\; \delta\hat{\alpha}_{fm} \, A_{gt} y \,-\, A_{gt} \, \delta\hat{\alpha}_t y \tag{4-178}$$

where we have used $\delta(\hat{\alpha}_t^{\,T}) = -\delta\hat{\alpha}_t$. Note that, in general, for small angle orthogonal

rotations one has that

$$\widehat{\delta\alpha_t}y = (y) \times (\delta\alpha_t) \qquad (4\text{-}179)$$

where x signifies the vector cross product. Applying this to the above equation,

$$\delta v = (A_{gt}y) \times \delta\alpha_{fm} - A_{gt}[y \times \delta\alpha_t] \qquad (4\text{-}180)$$

$$\delta v = -A_{gt}[y \times (\delta\alpha_t - A_{gt}^T \delta\alpha_{fm})] \qquad (4\text{-}181)$$

$$\delta v = -A_{gt} Y (\delta\alpha_t - A_{gt}^T \delta\alpha_{fm}) \qquad (4\text{-}182)$$

where analogously to Equation (4-175) and previous notation

$$\delta\alpha_{fm} = (\delta\alpha_{f1}, \delta\alpha_{f2}, \delta\alpha_{m3})^T \qquad (4\text{-}183)$$

and clearly

$$Y = \begin{bmatrix} 0 & -y_3 & y_2 \\ y_3 & 0 & -y_1 \\ -y_2 & y_1 & 0 \end{bmatrix} \qquad (4\text{-}184)$$

Noting that one may write

$$G_u \delta u = \hat{M}_{ml}\delta\alpha_{ml} + \hat{M}_{fm}\delta\alpha_{fm} + \hat{M}_t\delta\alpha_t + \hat{M}_r\delta\alpha_r \qquad (4\text{-}185)$$

it is apparent from the previous development that

$$\hat{M}_{fm} = -\hat{M}_t A_{gt}^T \qquad (4\text{-}186)$$

Furthermore, since

$$\hat{M}_t = -\hat{M}_r \triangleq \hat{M}_{tr} \qquad (4\text{-}187)$$

then

$$G_u \delta u = \hat{M}_{ml}\delta\alpha_{ml} - \hat{M}_{tr}A_{gt}^T\delta\alpha_{fm} + \hat{M}_{tr}\delta\alpha_{tr} \qquad (4\text{-}188)$$

which clearly indicates a constant linear dependency among the columns of M represented by the matrices $\hat{M}_{fm}$ and $\hat{M}_{tr}$. It also follows that one may merge the

4-67

dependent quantities by the replacement

$$\delta\alpha_{tr} \leftarrow \delta\alpha_{tr} - A_{gt}^T \, \delta\alpha_{fm} \qquad (4\text{-}189)$$

which is, in fact, a redefinition of $\delta\alpha_{tr}$ as

$$\delta\alpha_{tr} \stackrel{\Delta}{=} \delta\alpha_t - \delta\alpha_r - A_{gt}^T \, \delta\alpha_{fm} \quad \cdot \qquad (4\text{-}190)$$

Thus the misalignments $\delta\alpha_t$, $\delta\alpha_r$, and $\delta\alpha_{fm} = (\delta\alpha_{f1}, \; \delta\alpha_{f2}, \; \delta\alpha_{m3})^T$ are not separately observable, as was suspected. The observable and unobservable parameters are summarized as

o Separately Observables:

$$\alpha_{e2}, \; \alpha_{\ell3}, \; \alpha_{m1}$$

o Jointly Observables:

$$\alpha_{e1} \leftarrow \alpha_{e1} - \alpha_{I1}$$

$$\alpha_{\ell2} \leftarrow \alpha_{\ell2} - \alpha_{I2} \qquad (4\text{-}191)$$

$$\alpha_{m3} \leftarrow \alpha_{m3} - \alpha_{I3}$$

$$\alpha_{tr} \stackrel{\Delta}{=} \alpha_t - \alpha_r - A_{gt}^T \begin{bmatrix} \alpha_{f1} \\ \alpha_{f2} \\ \alpha_{f3} \end{bmatrix}$$

o Unobservables

$$\alpha_{e3}$$

The parameter vector $\delta\alpha$ is now constituted as

$$\delta\alpha = \left[\delta\alpha_{e1}, \; \delta\alpha_{e2} \;\middle|\; \delta\alpha_{\ell2}, \; \delta\alpha_{\ell3} \;\middle|\; \delta\alpha_{m1} \;\middle|\; \delta\gamma_{tr1}, \; \delta\alpha_{tr2}, \; \delta\alpha_{tr3} \right]^T \qquad (4\text{-}192)$$

The new 3-vector, α_{tr}, is a lumped parameter, consisting of misalignments of the alignment sensing system, gimbal mounting misalignments, and the misalignment α_{m3} of the middle gimbal. None of these misalignments is separately observable. The experiment misalignment α_{e3}, representing a small rotation of the experiment about the LOS has disappeared completely, since it is unobservable. Furthermore, the Inductosyn errors have disappeared from the parameter vector. They are now lumped with other misalignments, since they are not separately observable.

The measurement matrix is given by

$$M(k) = \left[\hat{M}_e(k) \mid \hat{M}_\ell(k) \mid \hat{M}_{m1}(k) \mid \hat{M}_{tr}(k) \right] \qquad (4\text{-}193)$$

with the submatrices defined as

$$\hat{M}_e(k) = \begin{bmatrix} -1 & 0 \\ 0 & -(1 - \hat{u}_2^2)^{1/2} \end{bmatrix} \qquad (4\text{-}194)$$

$$\hat{M}_\ell(k) = \begin{bmatrix} 0 & 0 \\ -1 & \hat{u}_2(1 - \hat{u}_2^2)^{1/2} \end{bmatrix} \qquad (4\text{-}195)$$

$$\hat{M}_{m1}(k) = \begin{bmatrix} -\hat{u}_3(1 - \hat{u}_2^2)^{1/2} \\ \dfrac{\hat{u}_1 \hat{u}_2}{\hat{u}_1^2 + \hat{u}_3^2} \end{bmatrix} \qquad (4\text{-}196)$$

$$\hat{M}_{tr}(k) = \begin{bmatrix} 0 & -(1 - \hat{u}_2^2)^{1/2} & 0 \\ \dfrac{\hat{u}_3}{\hat{u}_1^2 + \hat{u}_3^2} & 0 & \dfrac{-\hat{u}_1}{\hat{u}_1^2 + \hat{u}_3^2} \end{bmatrix} \widehat{\psi_{gm}}A_{gt} \begin{bmatrix} 0 & z_3 & -z_2 \\ -z_3 & 0 & z_1 \\ z_2 & -z_1 & 0 \end{bmatrix}$$

$$(4\text{-}197)$$

where

$$\{u\} = \widehat{\psi}_{gm} A_{gt} A_{rx} A_{xz} \{x_3^p\} \qquad (4\text{-}198)$$

$$\{z\} = A_{tr} \widehat{\alpha}_r A_{rx} A_{xz} \{x_3^p\} \qquad (4\text{-}199)$$

It follows that there are eight parameters which are candidates for estimation and, since two measurements are obtained from each target, at least 4 targets are required for calibrating the system. More targets should be used, however. From the analytic representation of the measurement matrix M it appears that no further time-consistent dependencies exist among the columns of M and, if one would take eight appropriate gimbal angle measurements (four independent targets), the resulting 8 x 8 square matrix H should be invertible. This has been checked by a

digital program and confirmed. Thus, the information matrix H^TH is nonsingular in general and the parameters appearing in $\delta\alpha$ are observable and can be estimated and calibrated.

4.4 RELIABILITY ANALYSIS

This section presents the final PPCS reliability analysis. System reliability goals and redundancy concepts were developed early [5], and the present discussion extends these concepts and updates the reliability analysis using the completed hardware designs.

PPCS is designed for a 3-5 year operating life. No specific numerical reliability requirement has been specified, which is appropriate for the present development status of PPCS where a significant task of the development effort is to identil appropriate reliability goals for equipment of this type. PPCS reliability activit' have, therefore, been directed toward insuring that proven, conservative designs are used and establishing configuration flexibility so that appropriate redundancy choices can be made when numerical reliability requirements are specified for a particular mission. While a tentative system configuration selection is made on the basis of a numerical reliability prediction for that configuration, caution should be used in drawing conclusions from that data. Individual mission requirements could result in significantly different configuration recommendations and therefore radically differing reliability. Further, design evolutionary changes, such as introduction of LSI into the electronics, will substantially affect numerical reliability and probably configuration selection as well.

4.4.1 PPCS Reliability Policy

Reliability requirements vary not only in system lifetimes, but in the maintenance policy to be employed. Manned missions tend toward high reliability extrem for relatively short periods between maintenance (the Saturn guidance computer). Also, there is a man directly involved in system operation and in the maintenance. Thus, these systems, the space shuttle is an example, employ standby redundancy with automatic reconfiguration only during infrequent time-critical periods. The emphasis is on the availability of spares when failures occur. A very different situation exists on long lifetime interplanetary probes where man is only involved via command and telemetry. The possibilities of catastrophic failure before recognition or effective action by man can lead to a requirement for complex failure detection and reconfiguration or massive redundancy in the form of majority logic.

The PPCS system has few, if any, recognizable modes where redundancy must be employed within a very short time. Catastrophic system failure is not envisioned if significant delays exist before detection and correction of fault. A long, unmaintained lifetime (high 3 year survival probability) is desired, however. Alsc for PPCS, there is a man "in the loop" (and ground data processing), but there can be long delays between his periods of visibility. In addition, these periods may be short-lived leaving little time for complex diagnosis.

Accordingly, employment of redundancy will be performed strictly by the ground upon recognition of failures. It is desirable to perform "hard" failure detection on-board, however, to increase the probability of effective action via ground commands with minimum on-board hardware/software impact. Monitored values which exceed thresholds, such as voltages or gyro spin motor rates, serve as hard failure cues. More sophisticated recognition techniques may be required to detect, for example, a frozen gimbal or "soft" failures, such as a degraded component or an intermittent fault. As a result, soft failure detection will be done on the ground. Overall, no on-board automatic reconfiguration will be employed.

The techniques of protective redundancy may be divided into two major categories: massive (also called masking) redundancy and selective redundancy. Through permanently connected, concurrently operating replicas, the effect of a faulty component is masked in massive redundancy. Examples include "quadded" components, majority voting (e.g., TMR) between multiple units, and adaptive logic elements including threshold logic. Selective redundancy encompasses those schemes which first diagnose a failure, then apply corrective action. Diagnosis may be performed concurrently without interruption of system operation or on a "time-out" basis where system operation is periodically halted for diagnostic testing.

Figure 4-8 shows the effects on reliability in employing some typical redundancy techniques. It is clear that longer lifetimes are attained for the same weight (i.e., number of redundant units) with selective redundancy. Power also is much less since TMR, for example, requires 3 times the power of a simplex system. A prime with two passive backups requires only slightly more power than the simplex system. Selective redundancy techniques are therefore favored for PPCS.

The selective redundancy approach is taken one step further, to the level of functional redundancy within assemblies. The approach and the advantage of the approach is illustrated by the example of Figure 4-9. Consider an assembly having a failure rate of $10,000 \times 10^{-9}$ failures per hour. Reliability for 5 years would be 0.645, generally unacceptably low. Duplicating the assembly doubles the weight (and cost), and raises the reliability to 0.922, a significant increase, but not typically high enough for a single assembly. Functional redundancy, assuming in this case that identical complexity functions capable of being cross-strapped can be identified, raises the reliability to 0.980. Note that the weight is the same (approximately) as the dual redundant case, assuming that functions selected are simple to cross strap (a necessary criteria for their selection). A task, then, of the PPCS reliability considerations has been careful identification of functional elements to be made redundant with minimum interface problems. This also supports the design approach to accommodate in-flight maintenance/recovery capability.
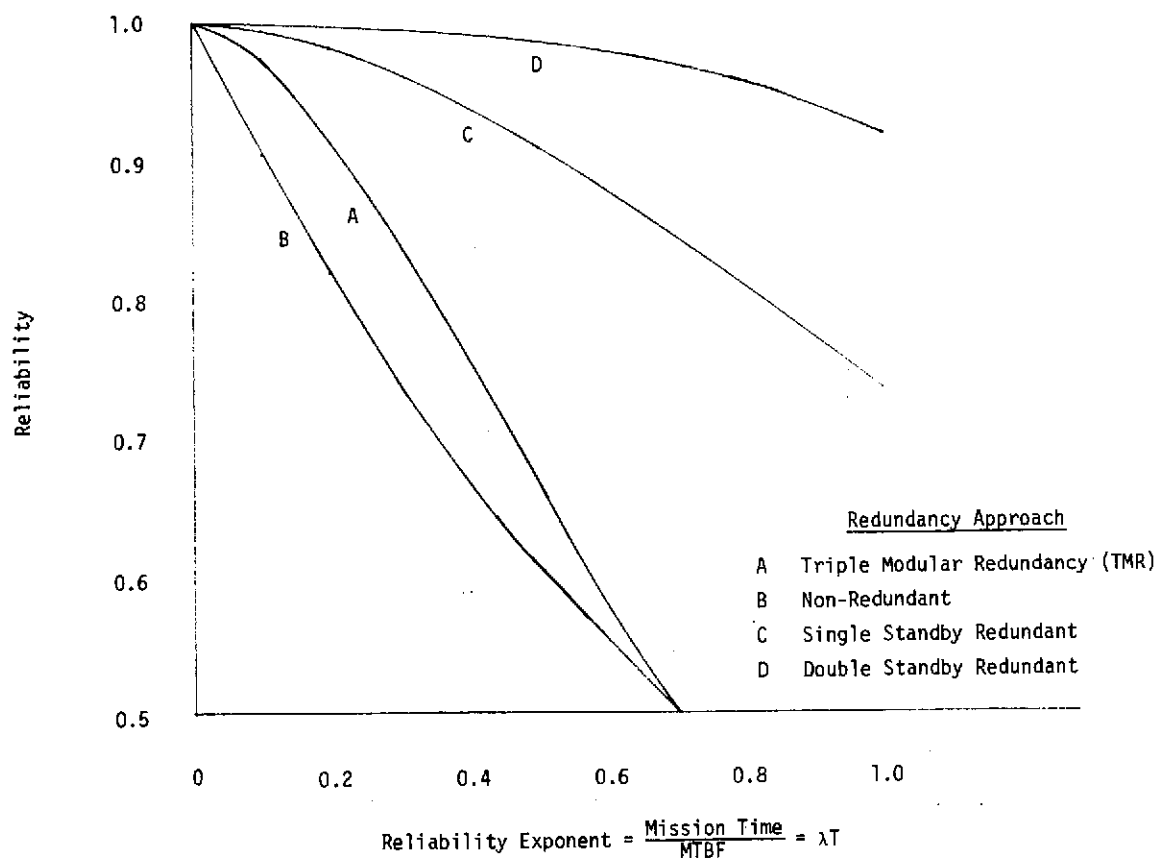
Figure 4-8.   Comparison of Redundancy Approaches

$$\lambda = 10,000 \times 10^{-9}$$
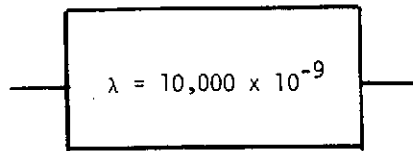
$$R = \epsilon^{-\lambda t} = .645 \quad \text{(Five Years)}$$

a) Non Redundant Assembly

$$\lambda_{on} = 10,000$$

$$\lambda_{off} = 1,000$$
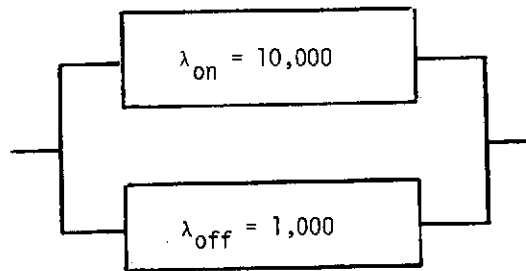
$$R = \epsilon^{-\lambda \, on \, t} [1 + \frac{\lambda_{on}}{\lambda_{off}} (1 - \epsilon^{-\lambda \, off \, t})]$$

$$R = .922 \text{ (Five Years)}$$

b) Dual Redundant Assembly

$$\lambda_{on} = 2000 \quad \lambda_{on} = 2000 \quad \lambda_{on} = 2000 \quad \lambda_{on} = 2000 \quad \lambda_{on} = 2000$$

$$\lambda_{off} = 200 \quad \lambda_{off} = 200 \quad \lambda_{off} = 200 \quad \lambda_{off} = 200 \quad \lambda_{off} = 200$$
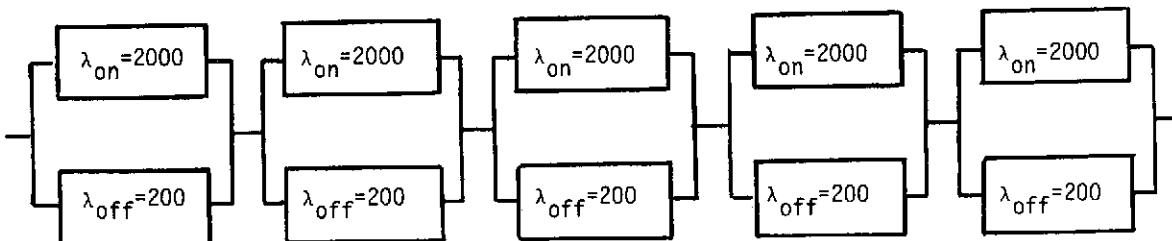
$$R = \left(\epsilon^{-\lambda \, on \, t} [1 + \frac{\lambda_{on}}{\lambda_{off}} (1 - \epsilon^{-\lambda \, off \, t})] \right)^{5}$$

$$R = .980 \quad \text{(Five Years)}$$

c) Functionally Redundant Assembly

Figure 4-9. Example of Functional Redundancy

4.4.2 PPCS Reliability Summary

The PPCS reliability block diagram is shown in Figure 4-10. The redundancy configuration shown achieves a three year probability of success for attitude determination of 0.94 and for data processing of 0.963 (against a goal of 0.94 for each). End-to-end (including antenna) single experiment success probability is 0.751 (against a goal of 0.72). These predicted reliabilities are quite promising and indicate 3-5 year performance can be achieved by PPCS class systems. The required redundancy is moderate, with a single standby functional element often being sufficient. Other life extending considerations, such as experiment duty-cycling, backup operating modes and possible design simplifications resulting from introducing large scale integration of selected electronics are, of course, not reflected in the present analysis.

Dual star trackers are used, each with internal functional redundancy involving the motors/motor electronics and the inductosyn/encoding electronics. Note that the sensor electronics is incorporated within the star tracker reliability block. The star trackers are normally operated with one unit off, although both can be operated simultaneously.

The gyro reference consists of six gyros in a non-orthogonal configuration. Each gyro has independent electronics and can be operated independently of all others. Normally four are on, which gives failure detection capability.

Functional elements for data processing include the control processor, the memory, and the input/output processor, which incorporates a dual-redundant data bus structure. One element of each type is required for operation. Any combination of elements is satisfactory with element selection made by power switching. Four memory units were required to achieve the necessary reliability-functional subdivision within the memory leads to difficult interfaces and increased electronic complexity.

The alignment sensor incorporates functional redundancy in the electronics and the angle encoder function. Three angle encoder channels are required for operation--the standby unit can replace any of the operating units.

Experiment gimbal control uses functional redundancy in a manner similar to the star tracker--dual motors/motor electronics and dual inductosyns/encoding electronics are used on each gimbal axis. Normally, both channels are operated on to allow thermal equalization on the gimbal. In the event of a failure, the failed channel would be turned off, resulting in a slight thermal imbalance and some degree of potential performance degradation.
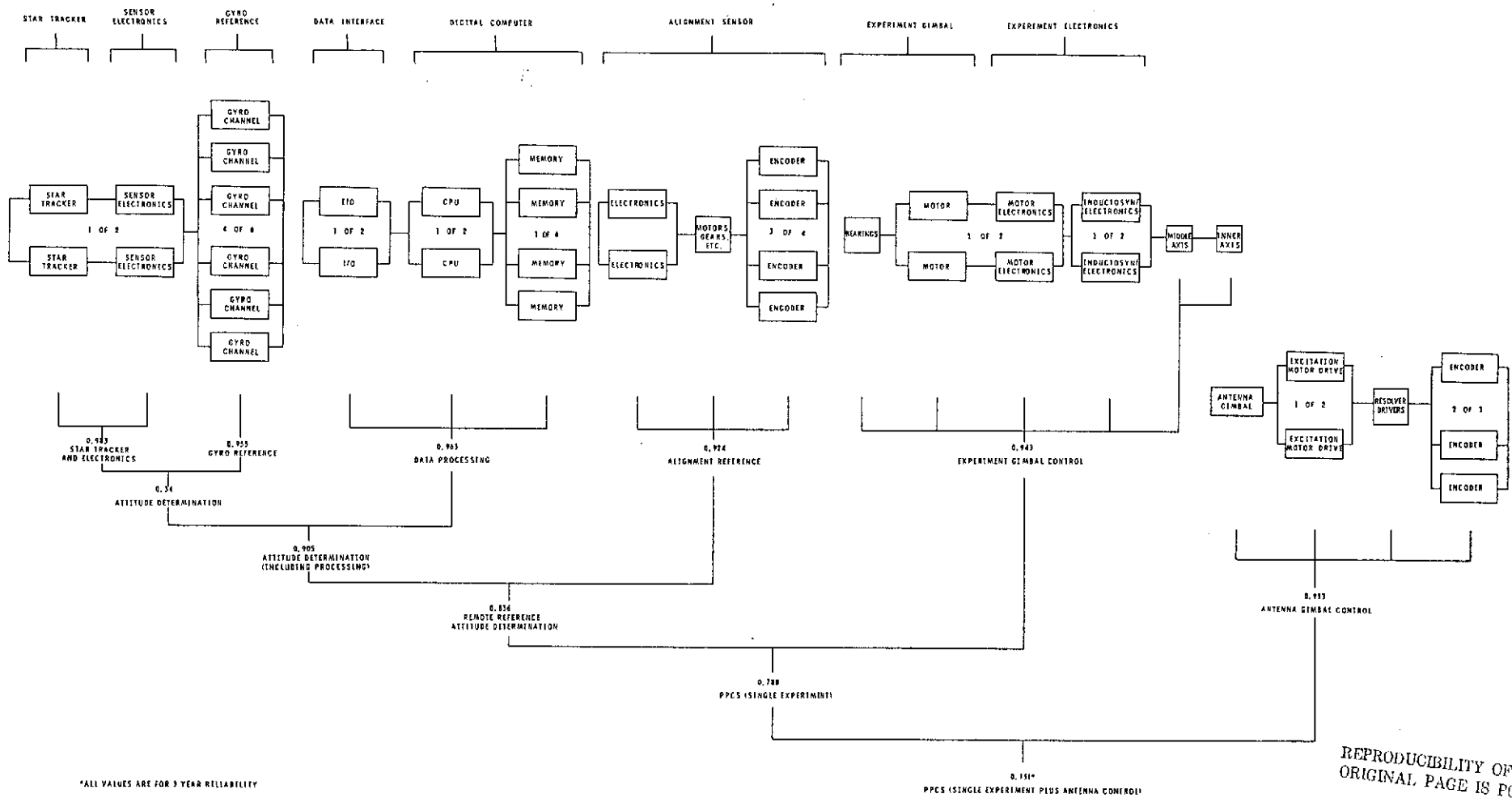
Figure 4-10. PPCS Reliability Block Diagram

Antenna control uses a similar approach, except that the motor and the resolver are not duplicated. Configurations having dual motor windings and dual resolvers exist. However, their use doesn't seem warranted here, since high reliability is achieved without them.

4.4.3 Detailed Reliability Analysis

The following sections provide the detailed PPCS reliability analysis. Configuration tradeoffs are developed and reliability calculations are made for each configuration.

4.4.3.1 Gyro Reference Assembly

Reliability of the Gyro Reference is a function of gyro MTBF and the selected redundancy configuration. For PPCS, it is assumed that the basic building block consists of a gyro with associated electronics. For tradeoff purposes, the assumption was made that any 3 gyro channels were sufficient for PPCS operation. For the six-pack configuration ultimately selected (four operating gyros), a separate Monte Carlo reliability analysis was run.

To study the effect of gyro MTBF, the PPCS gyro electronics were combined with several (assumed) gyro MTBF's and the resulting 3-year reliability was computed for several redundancy configurations. Gyro MTBF's ranging from 25,000 hours to 500,000 hours were used. Redundancy configurations included: A 6-pack, a 5-pack, and a 4-pack (any three gyros operable assumed acceptable in each case); two 3-packs (dual redundant); and a non-redundant 3-pack. It was assumed spare gyros were turned off until needed. The results are shown in Figure 4-11. The 6-pack reliability hits 0.9 at a gyro MTBF of about 65,000 hours and passes 0.99 at about 350,000 hours gyro MTBF. The gyro used in PPCS is the Northrop GI-K7G, an air bearing unit with an extensive field operating history--about 500 K7G gyros have been delivered to the C5A program. Field operating data, analyzed by a procedure developed by Duane and Codier, supports a 30,000 hour MTBF for gyros being produced in early 1970. Early K7G units used ceramic bearings, while current designs are Ferrotic bearings--eliminating a failure mode caused by spalling of the ceramic bearings. If these early units are removed from field failure history, early 1970 gyros would have an MTBF of 50,000 hours. Northrop has analyzed the cause-of-failure data and determined that two-thirds of the failures are associated with system incompatibilities (i.e., induced failures by an agency outside the gyro). Exclusion of this failure type would raise the predicted MTBF to 150,000 hours. Finally, the field data is based on aircraft use, with one-g operation, multiple starts, and non-benign environment. For a space mission, Northrop considers an MTBF of 250,000 hours for the GI-K7G to be conservative. This value has been used in the present analysis.

4-77
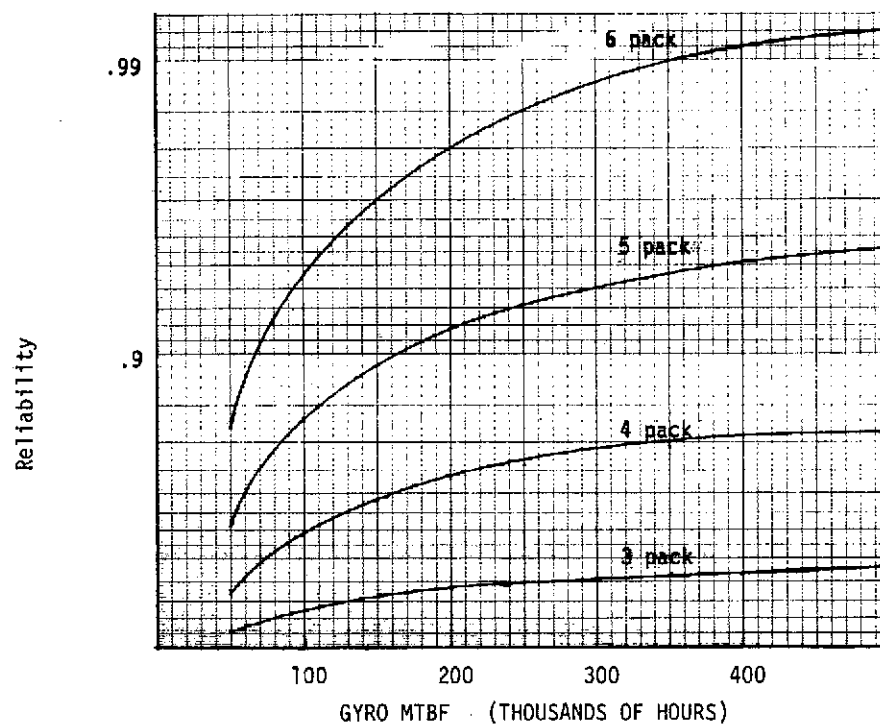
Figure 4-11. Gyro Reference Reliability as a Function of Gyro MTBF

The 5-pack and 4-pack configurations offer interesting possibilities, especially for shorter missions or where lower cost/weight constraints are premium. The 5-pack achieves 0.996 one year reliability for a gyro of 250,000 hours MTBF, while the 4-pack achieves 0.961 one year reliability.

A further evaluation of gyro reference reliability as a function of configuration was made, assuming a fixed 250,000 hour gyro MTBF. Reliability as a function of time out to five years is plotted in Figure 4-12 for several gyro configurations. The PPCS baseline design has assumed six gyro channels would be required--this choice still appears justified, particularly for longer time periods, since it is the only configuration remaining above 0.9 for five years. Again, the other configurations may be of interest for shorter missions or where weight/power constraints are severe.

The selected configuration is the 6-pack operated with redundant gyros turned off until needed. This policy was adopted after considering K7G gyro failure mechanisms. The prominent failure mode is bearing contamination caused by particles deposited in the bearing due to gas migration through the bearings. This gas migration is minimized by reducing gyro temperature--which is achieved by turning standby units off. Non-start failures have not been observed by Northrop below at least 1000 start-stops, a figure which PPCS would not exceed.

A more detailed analysis of the 6-pack configuration was made to account for the PPCS operating policy. Four gyros are normally operated on to provide a capability for failure detection. After failures have occurred, this policy can be modified to allow operation with only three gyros on. However, because of geometric considerations (discussed in 6.3), only 10 of the possible 20 three gyro configurations give performance equal to the four gyro case. A Monte Carlo analysis technique was used to compute the reliability of the 6-pack under this operating policy, giving the results below:

Years	R(t)
1	0.9973
2	0.9803
3	0.955

4.4.3.2 Star Tracker and Sensor Electronics

The star tracker and sensor electronics are analyzed as a unit because of the extensive number of interfaces between them. The star tracker consists of a two axis gimbal with a star sensor which has integral electronics. The tracker incorporates two gimbal drive motors and two inductosyns (resolver-like angle encoders) per axis to achieve thermal and mechanical stability. They can also be used to provide redundancy, since each motor is sized to drive the gimbal by itself and
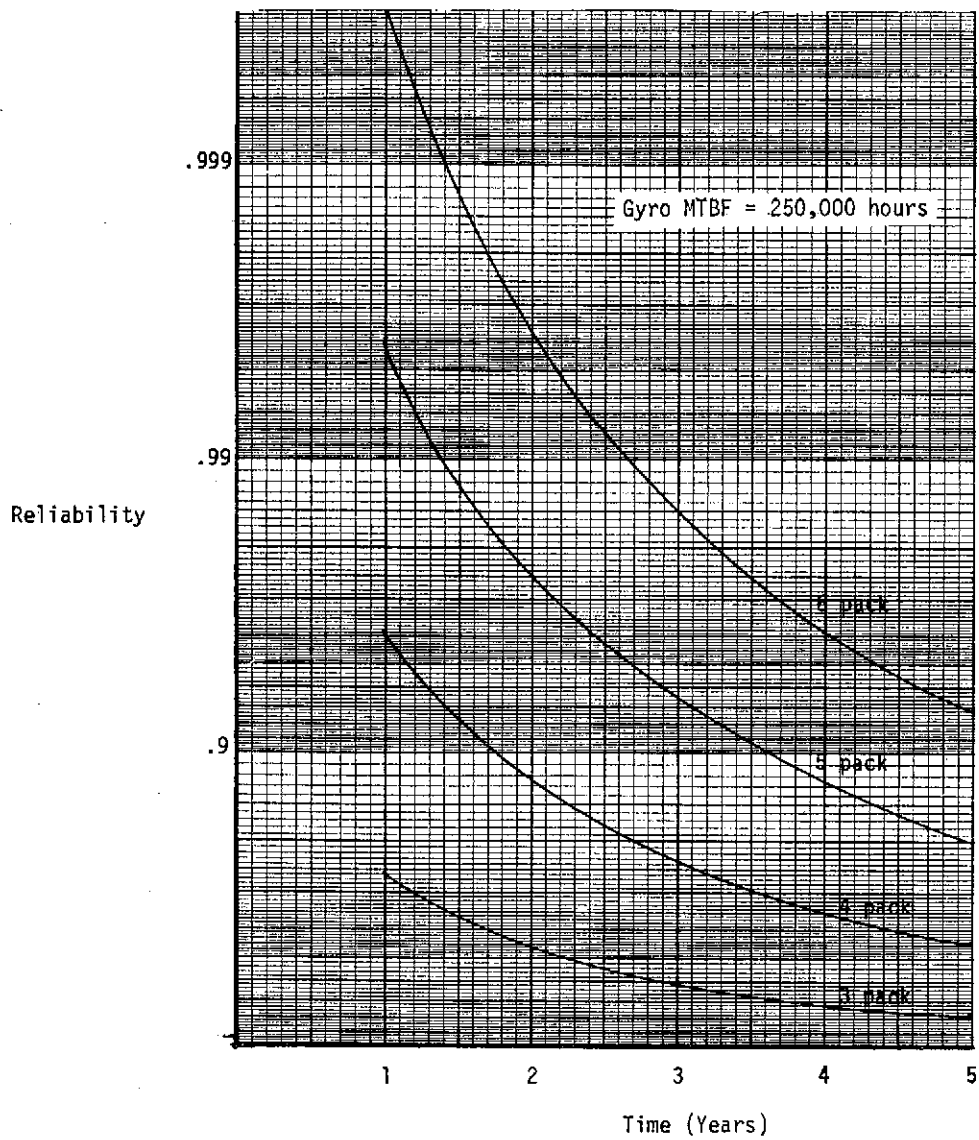
Figure 4-12. Gyro Reference Reliability

either inductosyn can provide gimbal angle readout. Each inductosyn has an asso-
ciated pre-amplifier on the gimbal to raise the output level for transmission to
the sensor electronics.

The sensor electronics is separate from the tracker and provides control of
the gimbal motors and provides excitation to the inductosyns and encodes the result-
ing outputs into a gimbal angle readout which is provided to the digital computer.

The possible redundancy configurations for the star tracker/sensor electronics
is limited by the difficulty of the interfaces involved. Cross strapping of the
encoding electronics (the most complex part of the sensor electronics) would require
relays at the input, due to the very sensitive signals from the inductosyn. Relays
at the output would also be required to cross-strap the motor electronics, due to
the high power levels involved. For many reasons, this approach is not attractive.
Other possibilities for redundancy have been identified which avoid these problems--
they make use of the "extra" motors and inductosyns already present for thermal-
mechanical stability reasons. Figure 4-13a and b shows non-redundant and dual-re-
dundant (non-cross strapped) star tracker configurations. Figure 4-13c shows the
functionally redundant configuration achieved (without cross strapping) providing
separate electronics for each of the dual motors and inductosyns on each gimbal
axis. Figure 4-13d extends this approach to two star trackers.

The reliability versus time for each configuration is plotted in Figure 4-14..
The two tracker functionally redundant configuration (4-13d) is required for rea-
sonable 3-5 year reliability and is, therefore, the PPCS baseline configuration.
The single-tracker functionally redundant configuration (4-13c) is of particular
interest for 1-2 year missions, in that only a single star tracker is required.

4.4.3.3 Alignment Sensor

The alignment sensing function is implemented by stepper motor driven optical
wedges which are used to detect angular deviations of an internally generated light
beam. Wedge rotation is detected by a resolver. Electronics are required to gen-
erate the light beam and to control and readout the wedge rotation. The resolver
readout is identical to that used in the antenna electronics.

The mechanical and optical elements are grouped as a functional element--they
are, of course, difficult to make redundant. The electronics can easily be made
redundant, since relatively simple interfaces exist. The electronics are considered
as two functional elements, one associated with the wedge angle encoding and the
other associated with wedge motor drive and control. Figure 4-15a shows a non-
redundant configuration. An extra electronics functional element is added in
Figure 4-15b. Reliability for each configuration is tabulated below:

| INDUCTOSYN EXCITATION | INNER AXIS ANGLE ENCODER | OUTER AXIS ANGLE ENCODER | INNER AXIS MOTOR ELECTRONICS | OUTER AXIS MOTOR ELECTRONICS | STAR TRACKER |

a) NON-REDUNDANT CONFIGURATION

| INDUCTOSYN EXCITATION | INNER AXIS ANGLE ENCODER | OUTER AXIS ANGLE ENCODER | INNER AXIS MOTOR ELECTRONICS | OUTER AXIS MOTOR ELECTRONICS | STAR TRACKER |

| INDUCTOSYN EXCITATION | INNER AXIS ANGLE ENCODER | OUTER AXIS ANGLE ENCODER | INNER AXIS MOTOR ELECTRONICS | OUTER AXIS MOTOR ELECTRONICS | STAR TRACKER |

b) DUAL REDUNDANT CONFIGURATION

GIMBAL BEARINGS — INDUCTOSYN — EXCITATION — PREAMP — ENCODER — MOTOR — MOTOR ELECTRONICS — STAR SENSOR UNIT

INDUCTOSYN — EXCITATION — PREAMP — ENCODER — MOTOR — MOTOR ELECTRONICS

(A) OUTER AXIS   (B) OUTER AXIS   (A) INNER AXIS   (B) INNER AXIS

GIMBAL BEARINGS — INDUCTOSYN — EXCITATION — PREAMP — ENCODER — MOTOR — MOTOR ELECTRONICS — STAR SENSOR UNIT

INDUCTOSYN — EXCITATION — PREAMP — ENCODER — MOTOR — MOTOR ELECTRONICS

(A) OUTER AXIS   (B) OUTER AXIS   (A) INNER AXIS   (B) INNER AXIS

c) FUNCTIONALLY REDUNDANT CONFIGURATION (SINGLE STAR TRACKER)

GIMBAL BEARINGS — INDUCTOSYN — EXCITATION — PREAMP — ENCODER — MOTOR — MOTOR ELECTRONICS — STAR SENSOR UNIT

INDUCTOSYN — EXCITATION — PREAMP — ENCODER — MOTOR — MOTOR ELECTRONICS

(A) OUTER AXIS   (B) OUTER AXIS   (A) INNER AXIS   (B) INNER AXIS

d) FUNCTIONALLY REDUNDANT (DUAL STAR TRACKER)

Figure 4-13, Star Tracker/Sensor Electronics Redundancy Configuration
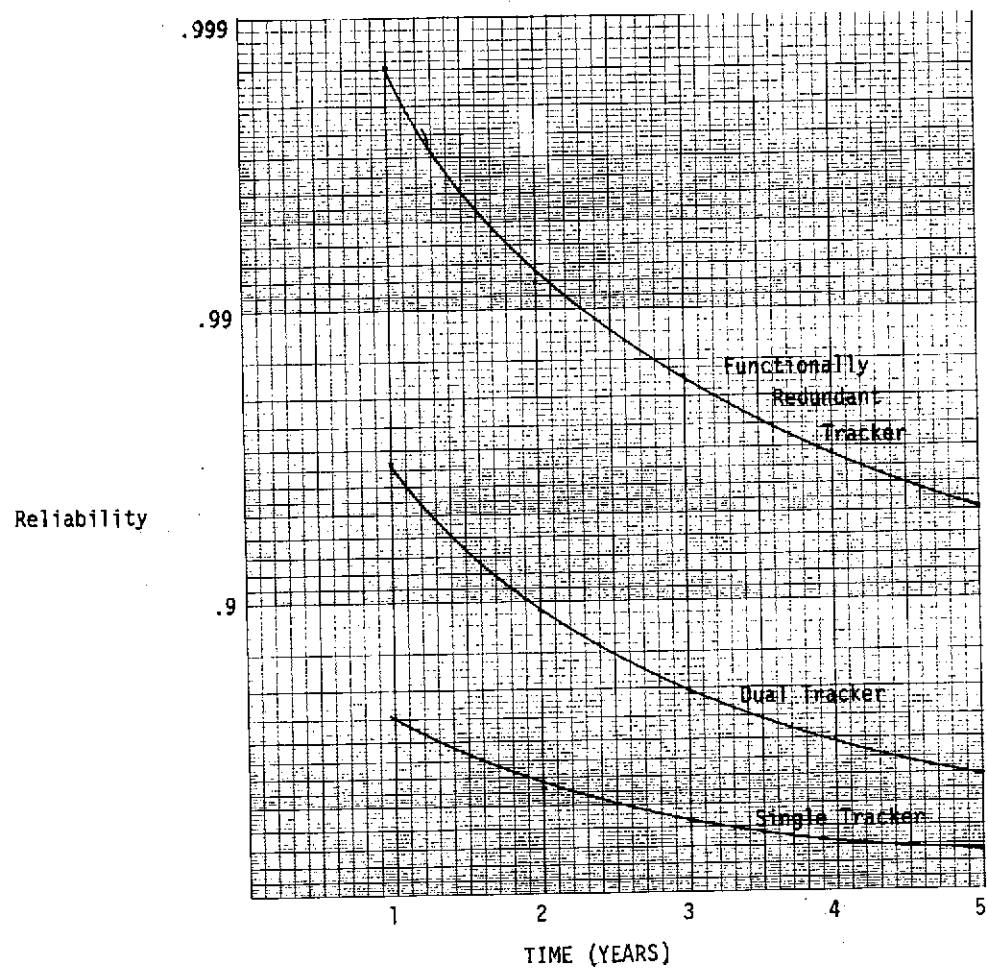
Figure 4-14. Star Tracker/Sensor Electronics Reliability
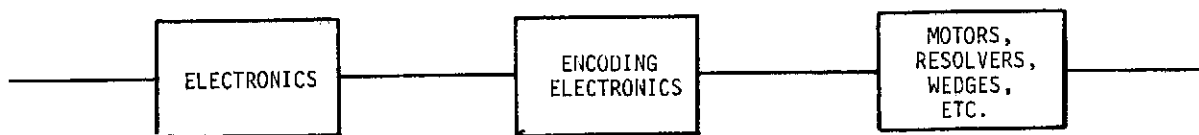
a) ALIGNMENT SENSOR (NON-REDUNDANT)
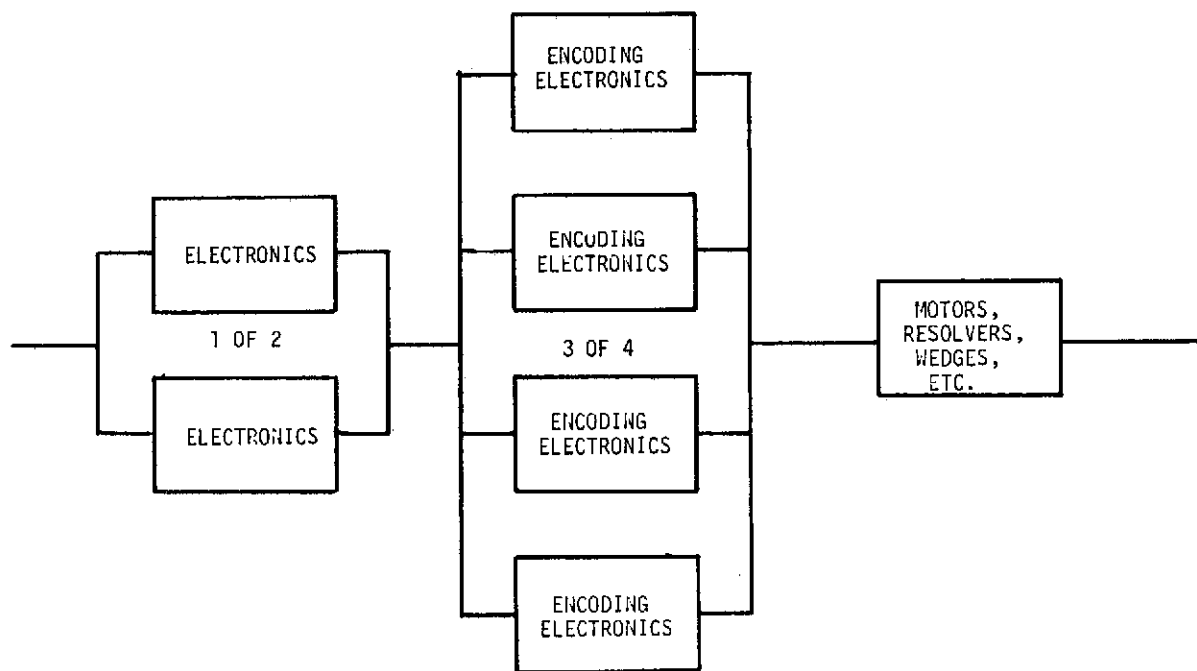
b) ALIGNMENT SENSOR (FUNCTIONALLY REDUNDANT)

Figure 4-15. Alignment Sensor Redundancy Configurations

Time (years)	R(t) (Non-Redundant)	R(t) (Functionally Redundant)
1	0.853	0.983
2	0.728	0.957
3	0.621	0.924
4	0.529	0.885
5	0.452	0.842

The functionally redundant configuration was selected for the single experiment spacecraft configuration. Note that for a multiple-experiment spacecraft configuration, the electronics functions should be grouped in a central assembly with redundancy incorporated only as necessary to achieve the overall desired reliability. There may be cases where all experiments are not operated simultaneously, which will allow less electronics channels.

4.4.3.4 Digital Computer and Data Interface

The digital computer organization was strongly influenced by reliability considerations. It was immediately apparent that no existing non-redundant computer could provide 3-5 year life with acceptable reliability. Two computers in dual redundancy improves that situation, but is not an efficient redundancy approach. Accordingly, an early identification of possible functional elements capable of being cross-strapped was made. It immediately became apparent that the memory was the major difficulty. For relatively small memories (8K) as required for PPCS, the memory electronics dominate the failure rate. Circuit complexity is not a smooth function of the number of memory cells. Figure 4-16a and 4-16b show typical plots of circuit complexity versus memory size for a 3-D core memory. Word drivers can handle a certain load, if designed reliably, so that no additional electronic complexity is incurred until an entire new set is required, whereupon, a jump in complexity occurs. This maximum is set by parameters such as array delay or waveform distortion. Similarly for the bit-sense circuits, complexity is constant up to some maximum number of cells, and then the bit and sense lines are segmented and additional hardware is required. Hence, for small memory arrays, the circuit complexity dominates and varies with the number of circuits, while for very large memory arrays, the circuit complexity is very nearly proportional to the number of memory cells. These curves are for core memories, but the same general trend exists for other technologies with different break points. Plated wire generally requires more complex circuitry than core memories.

Based on the above arguments, a minimum size memory functional element of 8K words was selected, for which a projected failure rate of 17,200 x 10^{-9} failures per hour is typical using 1975 technology plated wire. Compared to other functional elements such as the CPU, I/O, etc., the memory has inherently a much larger failure rate which leads to greater replication of the memory in the computer redundancy configuration.

4-85
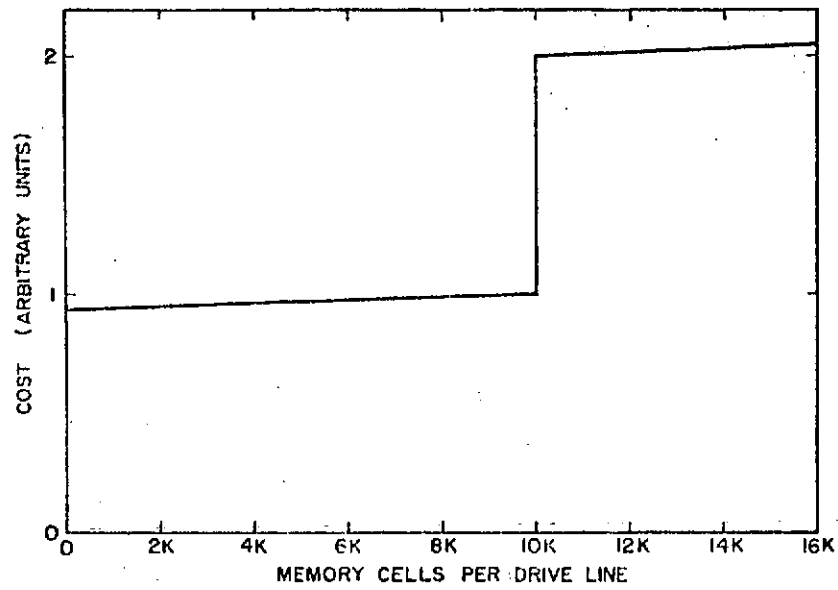
a) Word-Drive-Circuit Cost vs Loading
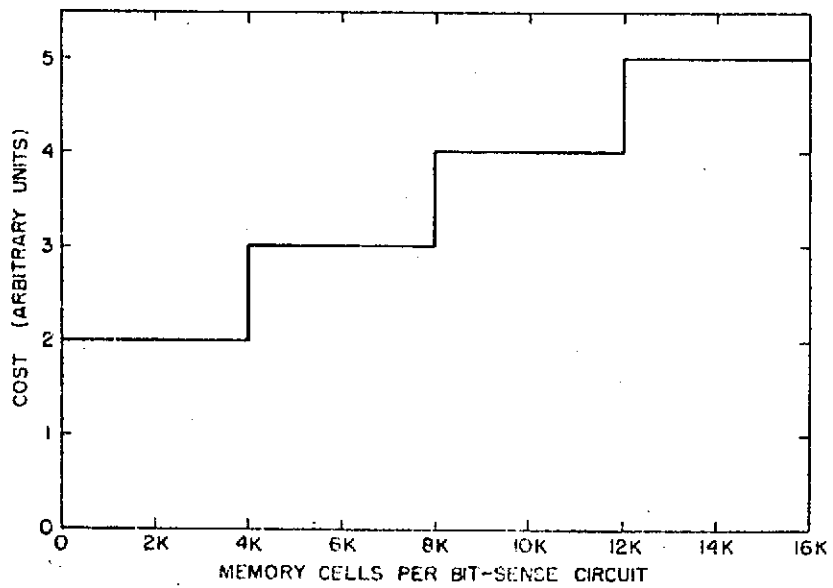
b) Bit-Sense-Circuit Cost vs Loading

Figure 4-16. Memory Reliability Trades

The other functional elements defined are the Central Processing Unit (CPU), Interface Control Unit (ICU), and the Memory Bus. The CPU and ICU functions can be combined into one element or separated. Four computer configurations were evaluated, each having four memory modules. Two configurations combine the CPU and ICU, while two separate these functions. Dual and triple redundancy of the CPU/ICU were studied. Figure 4-17a and b show the four configurations.

The three year reliability is tabulated below:

Configuration	Memory (4)	Bus (2)	CPU (2 or 3)	CPU-ICU (2 or 3)	ICU (2 or 3)	Total
I	0.9973	0.9986	0.9840		0.9826	0.9629
II	0.9973	0.9986	0.9990		0.9985	0.9935
III	0.9973	0.9986		0.9604		0.9565
IV	0.9973	0.9986		0.9960		0.9919

Configuration I was selected, since it achieves reliability comparable to other PPCS critical functions and requires less hardware than other configurations.

4.4.3.5 Experiment Gimbal and Electronics

The experiment control function is implemented with a three (or two) axis gimbal and associated electronics. This analysis assumes a three-axis gimbal. Configuration flexibility exists in the electronics but not the gimbal for readily apparent reasons. The gimbal does include two motors and inductosyns per axis, and is therefore, partially redundant. A non-redundant block diagram is shown in Figure 4-18a. Note that the electronics are similar to the star tracker sensor electronics, except that three encoders and motor electronics channels must be functioning at once. Here, as in the star tracker/sensor electronics, possible redundancy configurations are limited by the difficulty of the interfaces included. Further, duplication of the gimbal (as done with the star tracker) is not reasonable, since it implies dual gimbal payloads. The redundancy approach selected is similar to that selected for an individual star tracker, where use is made of the dual motors and inductosyns available on each gimbal axis. Figure 4-18b shows the resulting redundancy configuration.

Reliability for each configuration is tabulated below:

Time (years)	R(t) (Non-Redundant)	R(t) (Functionally Redundant)
1	0.812	0.993
2	0.660	0.973
3	0.536	0.943
4	0.436	0.905
5	0.354	0.861
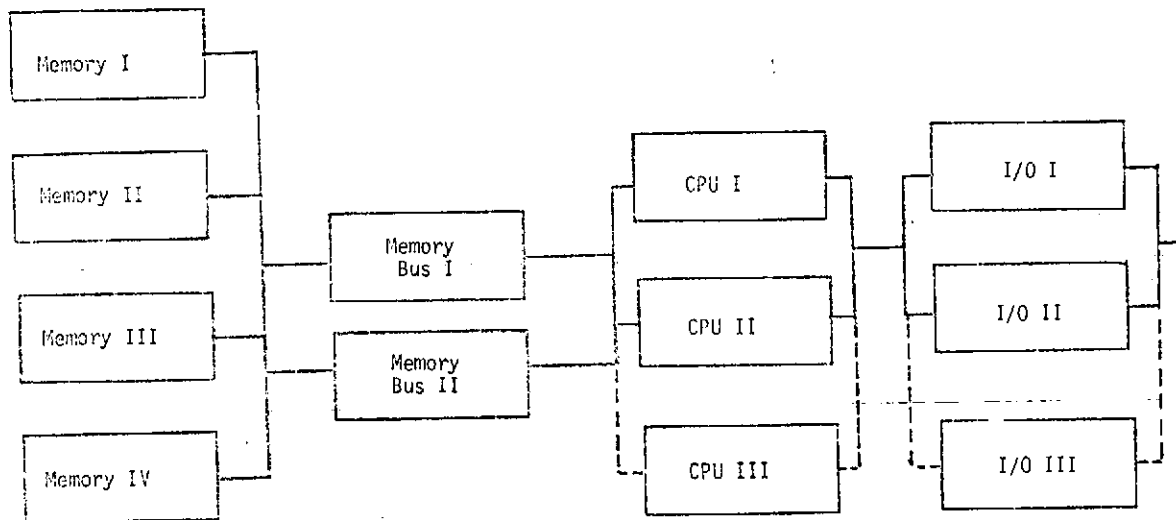
a) Modular Approach
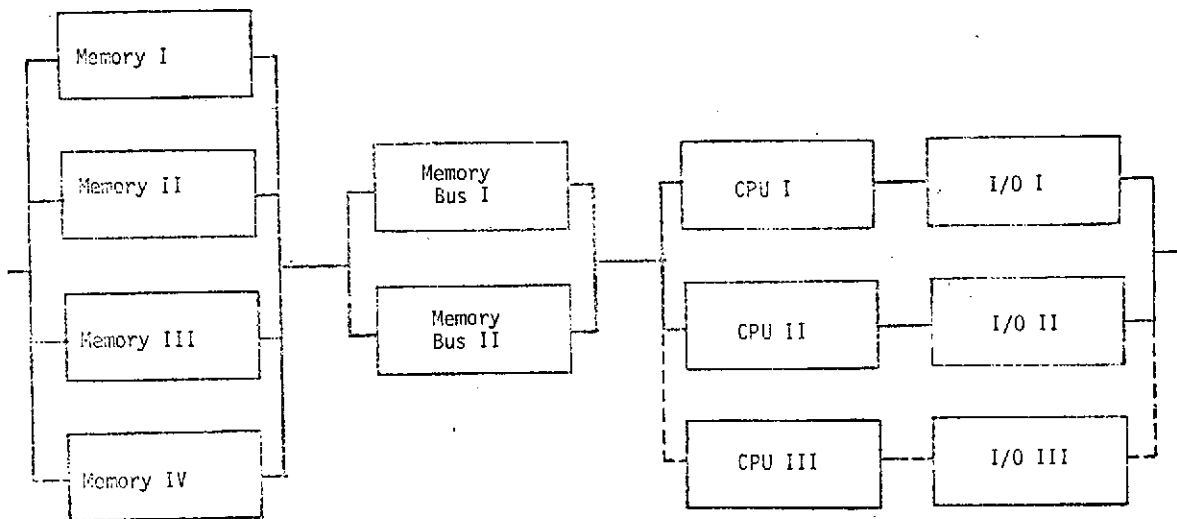
b) Integrated I/O Approach

Figure 4-17. Computer-I/O Configuration Trades

```
┌──────────┐     ┌──────────┐     ┌──────────┐   ┌──────────┐   ┌──────────┐
│EXPERIMENT│     │INDUCTOSYN│     │  INNER   │   │  MIDDLE  │   │  OUTER   │
│  GIMBAL  │─────│EXCITATION│─────│  AXIS    │───│   AXIS   │───│   AXIS   │
│          │     │          │     │ ENCODER  │   │ ENCODER  │   │ ENCODER  │
└──────────┘     └──────────┘     │ & MOTOR  │   │ & MOTOR  │   │ & MOTOR  │
                                  │ELECTRONICS│  │ELECTRONICS│  │ELECTRONICS│
                                  └──────────┘   └──────────┘   └──────────┘
```

a) EXPERIMENT CONTROL CONFIGURATION (NON-REDUNDANT)

INNER AXIS   MIDDLE AXIS OUTER AXIS
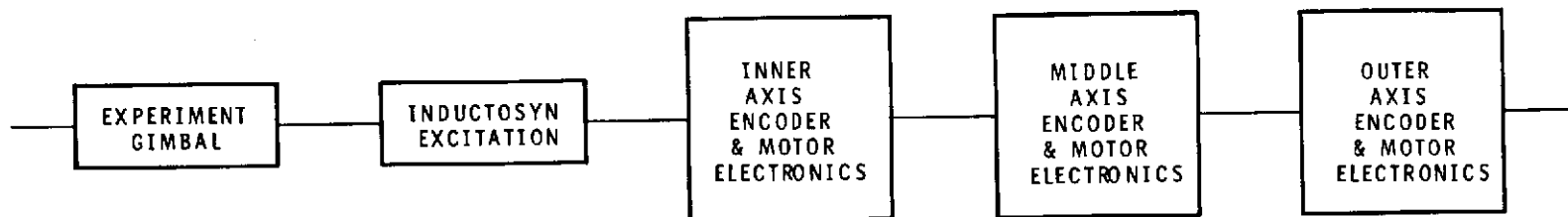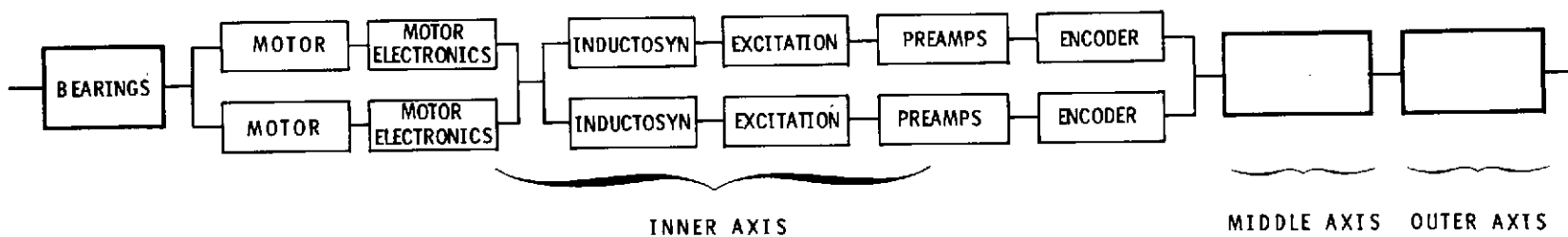
b) EXPERIMENT CONTROL CONFIGURATION (FUNCTIONALLY REDUNDANT)

Figure 4-18, Experiment Gimbal/Electronics Redundancy Configurations

4.4.3.6 Antenna Control

The antenna control function is implemented by a two-axis gimbal and associated control electronics. Figure 4-19a shows a non-redundant configuration. Redundancy is relatively easy to implement in the antenna electronics, since the angle encoding function has much less stringent performance requirements compared to the star tracker. Further, the antenna gimbal motor is a stepper motor which is driven by a logic-type driver which can more easily be cross-strapped than, say, an analog power amplifier. Figure 4-19b shows a redundant configuration where an additional functional element of each type has been added to the electronics (except for the resolver drive amp, which is hard to cross-strap).

The reliability for each configuration is tabulated below:

Time (years)	R(t) (Non-Redundant)	R(t) (Functionally Redundant)
1	0.923	0.989
2	0.852	0.975
3	0.787	0.958
4	0.727	0.940
5	0.671	0.920

The functionally redundant configuration was selected as a baseline since it provides adequate reliability for this function. Additional redundancy could easily be added if this function is particularly critical for a given mission.

4.4.4 Design Life/Wearout

Some aspects of equipment reliability do not readily lend themselves to a "random failure rate" reliability analysis. Bearings and gears exhibit a definite wearout failure mechanism; electronics must be designed to account for component drifts with time, temperature, and natural environments; and mechanical assemblies, where high precision is required, must be designed to conservative stress limits to preserve required performance capability. This section treats these aspects of PPCS design.

4.4.4.1 Star Tracker Assembly

Design life/wearout considerations for the star tracker include the gimbal bearing, the data link (a wire wrap-up using rolamite principles), the ITT F4004 detector tube, and precision mechanical assemblies (from a stress relaxation and launch survivability viewpoint). The gimbal suspension bearing is a unique design, using two balls per axis held in conical retainers. Rotary movement of the gimbal is achieved by sliding contact between the ball and one of the retainers. No
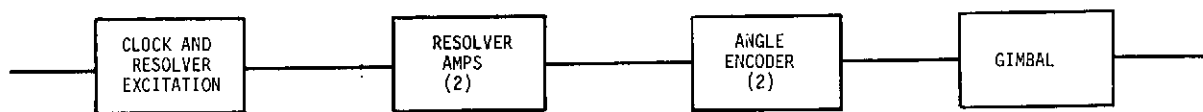
a) Antenna Gimbal/Electronics Configuration (Non-Redundant)
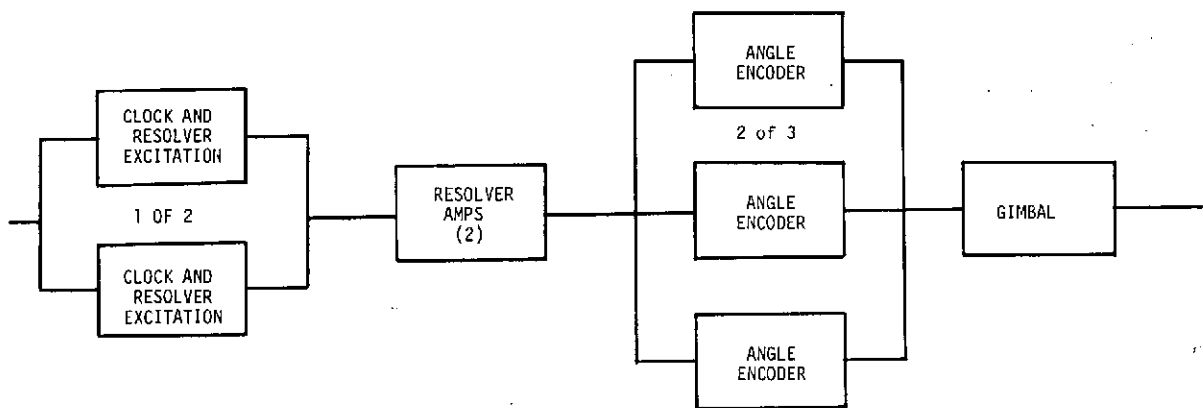
b) Antenna Gimbal/Electronics Configuration (Functionally Redundant)

Figure 4-19. Antenna Gimbal/Electronics Redundancy Configurations

existing rationale for computing wear for this configuration is known. A life test which simulated five (5) years of PPCS operation was conducted on the star tracker gimbal bearing and data link. No discernible wear was discovered, nor were there any lubrication problems [20].

The data link consists of several electrical conductors arranged in a flat strip and surrounded by a common shield. This strip is placed in a rolamite configuration between the rotating parts of the gimbal. Gimbal rotation causes the bend in the strip to "roll", causing a bending force in the conductors. The smallest bend radius is 0.3 inches. The maximum bending stress is 25,000 psi--this value assumes only the conductor carries the load, which is conservative. The engineering model uses copper conductors, for which the allowable bending stress is 36,000 psi. The flight design will specify 3/4 H beryllium copper which will allow 150,000 psi. Either design provides adequate stress margin.

The gimbal and the star sensor must survive launch induced loads without precision alignment shifts. All design has been constrained to stress levels below the precision elastic limit for the material used. Further, to avoid stress cycle hysteresis effects, materials will be stress cycled during assembly. This has been demonstrated to lower hysteresis effect. Extensive space experience (OAO, Mariner, Luner Orbiter) of tubes similar to the star sensor detector (ITT--F4004) has shown no wearout mechanisms. The only degradation item has been photocathode damage caused by excess light from sun/moon inadvertently striking the tube while operating. PPCS avoids this by actuating a shutter and by also turning off the voltage to the tube when a bright source is in the FOV.

4.4.4.2 Alignment Sensor Assembly

The alignment sensor uses stepper motor and gearhead to drive optical wedges to achieve error signal nulling. The required rotational life has been estimated at 160 million steps of the stepper motor or 40 million rotations. These values are considerably less stringent than the Antenna Gimbal, which uses a similar actuator, so that similar care in design/assembly will assure adequate life. The wedges are supported by ball bearings--here again the required rotations are low compared to other PPCS applications and no life problem is anticipated.

4.4.4.3 Experiment Gimbal Assembly

The EGA uses ball bearing gimbal suspensions and has a data link of identical design to that used in the star tracker. An estimate of the required operating life for the bearings was made, assuming continuous operation at 0.7 degree per second for five years. A total of 613,000 rotations result. Using normal bearing life calculations, a life of 1.52×10^9 rotations and a reliability of greater than 0.9999 for the 613,000 rotations is predicted.

4.4.4.4 Antenna Gimbal Assembly

The AGA uses a stepper motor drive which acts through a gearhead and a harmonic drive to effect output motion. Areas of interest from a design life/wearout viewpoint include the harmonic drive bearing rotational life, gearhead rotational life, gearhead stress, gear surface durability, and motor bearing life. A rough estimate of AGA duty cycle can be made, assuming that the antenna must slew slightly more than 360° per orbit, tracking first one data relay satellite, slewing to a second, tracking for part of an orbit, slewing to another (or the first), etc. For five years in a 100 minute orbit, one obtains 30,000 equivalent full rotations of the output shaft. The gear reduction gives 540 million rotations of the input pinion.

The harmonic drive required rotational life is 30,000 revolutions. The vendor (USM Corporation) has conducted an extensive three year life test program which showed that the life was limited by the wave generator ball bearing. This bearing follows the classical ball bearing load-life-speed relationships. Operating at full rated load and speed, the life is 1.75 million revolutions, which is well in excess of the requirement.

The gearhead input shaft turns 540 million revolutions. Several gear manufacturers rate life of their units at 1000 hours under full load and at 5600 to 10,000 rpm. This gives a life of from 3.4×10^8 to 6×10^8 revolutions, which again is considerably in excess of the requirement. The operating stress on the gearhead is complicated by the stepping action of the drive motor. The dynamic gear tooth load capability has been computed at 5.62 pounds. A maximum possible dynamic load is 3.21 pounds, so the gear is adequately designed for stress.

The gear wear mechanism of interest is surface pitting. To prevent pitting, the compression endurance limit of the material must not be exceeded. The maximum dynamic load was used with the wear load limit design equations to specify the required gear hardness to meet the wear requirement. A hardness of 400 Bhn or Rc43 is required. Typical hardness for BuOrd gearheads is about Rc38, so a special hardness requirement will be specified. The stepper motor bearing also must turn 540 million revolutions. The rated life of the bearing has been computed as 7.75×10^9 revolutions, which provides good assurance of adequate life.

4.4.4.5 Electronics

Reliable long-term operation of electronics is dependent on conservative design practices. On PPCS, all electronic components are characterized for the full range of environments to be encountered and for changes with time. Circuit design assures that operation within specification occurs for the worst case combination of component parameters. Further, manufacturers ratings for components are derated for all applications at TRW.

5.0 SYSTEM DESIGN AND PERFORMANCE ANALYSIS

This section discusses analytical and simulation work performed to support
the design and verification of particular key elements of the system and software
functional design. Included are attitude algorithm design analysis, star avail-
ability studies and star catalog definition, star selection approaches, and
attitude determination performance analysis using the detailed PPCS simulations
designed for software design/verification [11].

5.1 ATTITUDE ALGORITHM DESIGN ANALYSIS

There are two basic types of computational effects associated with strap-
down inertial reference systems, namely: errors incurred in the digital
algorithm used for processing (integration) of the gyro outputs and computer
roundoff. The first error is often broken down further into ortho-normalization,
truncation, and commutation error. The difference in the latter two is often
blurred and the division seems somewhat artificial since both errors are inti-
mately connected with the digital integration method used. By commutation
error, one generally means the absence of information concerning the sequence
of the spacecraft rotations which commute only for infinitesimally small angles;
truncation error refers to errors in the digital integration algorithm caused
by the truncation of those higher order terms in a Taylor series expansion
which are independent of the commutation effect. To clarify this point further,
consider the case where the vehicle rate is constant (not necessarily along a
principal axis of the body). In this case, no matter what the gyro sampling
rate, the order of rotations is unambiguously contained in the samples of the
three components of $\bar{\omega}$. Thus no commutation error exists when $\bar{\omega}$ = constant.
A clear-cut definition of the two errors is then the following: In a Taylor
series expansion of the integral (which represents the vehicle attitude des-
cribed by some kinematic variables), all those terms neglected in the inte-
gration algorithm which contain derivatives of $\bar{\omega}$ constitute the commutation
error and all the others terms neglected which do not contain derivatives of
$\bar{\omega}$ constitute the truncation error.

5.1.1 <u>Gyro Processing</u>

In the evaluation of these computational effects, the outputs of the gyros
are assumed to be free of drift, scale factor, and alignment errors. These
errors are disjoint from the computational errors discussed in this section
and their effect on the overall system performance is treated separately. The
system uses rate integrating gyros whose outputs consist of small angular

quantities $\Delta\theta_k$ defined by

$$\Delta\theta_k^i = \int_{t_{k-1}}^{t_k} \omega^i (t) \, dt \tag{5-1}$$

so that the average rate measured by the ith gyro over the interval $[t_k, t_{k+1}]$ is given by

$$\overline{\omega_k^i} = \frac{\Delta\theta_{k+1}^i}{T} \tag{5-2}$$

where $T = t_{k+1} - t_k$ is the sampling period for the gyros.

The Euler symmetric parameters used to describe the kinematics of the spacecraft have the advantage that the direction cosine matrix can be kept orthonormal by merely enforcing a single equation. Renormalization of the Euler parameters accordingly after each integration step prevents ortho-normalization errors from occurring, and this type of error can therefore be dismissed. The kinematic equations of the spacecraft are given by the linear vector differential equation

$$\dot{\rho} = \frac{1}{2} \Omega \rho \tag{5-3}$$

In practice, the vehicle attitude is computed by

$$\hat{\rho}_{k+1} = e^{\frac{1}{2} \bar{\Omega}_k T} \hat{\rho}_k \tag{5-4}$$

where $\bar{\Omega}_k$ denotes evaluation of the matrix Ω at the average body rate, $\hat{\omega}$. If the body rate is constant over a sampling period, then neither a truncation error nor a commutation error is incurred since this equation gives the exact solution to the kinematic equations.

In order to assess the actual computational error incurred, the attitude vector $\rho(t_k + T)$ is first expanded into a Taylor series about t_k.

$$\rho(t_k + T) = \rho(t_k) + \dot{\rho}(t_k) T + \frac{1}{2} \ddot{\rho}(t_k) T^2 + \cdots \tag{5-5}$$

Making repeated use of Equation (5-3) and regrouping terms, one obtains

$$\rho(t_k + T) = \left[I + \frac{1}{2} T \Omega_k + \frac{\left(\frac{1}{4}\right) T^2 \Omega_k^2}{2} + \frac{\left(\frac{1}{8}\right) T^3 \Omega_k^3}{3!} + \cdots \right] \rho(t_k) \quad + \tag{5-6}$$

$$+ \frac{1}{4} T^2 \dot{\Omega}_k \rho(t_k) + [\frac{1}{12} \dot{\Omega}_k \Omega_k + \frac{1}{24} \Omega_k \dot{\Omega}_k] T^3 \rho(t_k)$$

$$+ \frac{1}{12} T^3 \ddot{\Omega}_k \rho(t_k) + \cdots$$

The first square bracketed term on the RHS of equation (5-6) consists of all terms which do not contain derivatives of Ω_k. A closed form expression of the term is clearly $e^{(1/2)\Omega_k T}$ and use of this exponential would, therefore, eliminate all truncation errors. The remaining terms, if neglected would constitute the commutation error with the second and third order terms in T being predominant and with 4th and higher order terms in T adding only very insignificantly to the error, provided, of course, that the derivatives of $\bar{\omega}$ are bounded and T is small.

Consider now a Taylor series expansion of $\bar{\omega}(t)$ about t_k which yields

$$\bar{\omega}(t) \approx \bar{\omega}(t_k) + \dot{\bar{\omega}}(t_k) [t - t_k] + \frac{1}{2} \ddot{\bar{\omega}}(t_k) [t - t_k]^2$$

$$(5-7)$$

$$t_{k-1} \leq t \leq t_{k+1}$$

where third and higher order terms have been neglected. The justification for this is the interval restriction on t and the fact that these terms will contribute only 4th and higher order terms in T in the evaluation of the commutation error and these terms may be assumed negligible. Now the average body rate over $[t_k, t_{k+1}]$ is given by

$$\bar{\omega}_k = \frac{1}{T} \int_{t_k}^{t_{k+1}} \bar{\omega}(t) \, dt \qquad (5-8)$$

which, when the series expansion is substituted, yields

$$\bar{\omega}_k = \bar{\omega}(t_k) + \frac{1}{2} T \dot{\bar{\omega}}(t_k) + \frac{1}{6} T^2 \ddot{\bar{\omega}}(t_k) \qquad (5-9)$$

from which it follows that

$$\Omega_k = \bar{\Omega}_k - \frac{1}{2} T \dot{\Omega}_k - \frac{1}{6} T^2 \ddot{\Omega}_k \qquad (5-10)$$

Substitution of Equation (5-10) into Equation (5-6) yields after regrouping terms

$$\rho(t_k + T) = \left[I + \frac{1}{2} T \bar{\Omega}_k + \frac{\left(\frac{1}{4}\right) T^2 \bar{\Omega}_k^2}{2} + \frac{\left(\frac{1}{8}\right) T^3 \bar{\Omega}_k^3}{3!} + \cdots \right] \rho(t_k) \quad (5\text{-}11)$$
$$+ \frac{T^3}{48} [\dot{\Omega}_k \Omega_k - \Omega_k \dot{\Omega}_k] \rho(t_k) + O(T^4)$$

where $O(T^4)$ denotes all fourth and higher order terms in T and where again all terms involving no derivatives of Ω_k are contained in the first bracketed term on the RHS. It is important to note here that all second order terms contributing to commutation error have cancelled as well as all those third order terms which contained $\ddot{\Omega}_k$. Recognizing the exponential in the bracketed term, this equation may be rewritten as

$$\rho(t_k + T) = e^{\left(\frac{1}{2}\right) T \bar{\Omega}_k} \rho(t_k)$$
$$+ \frac{T^3}{48} [\dot{\Omega}_k \Omega_k - \Omega_k \dot{\Omega}_k] \rho(t_k) + O(T^4) \quad (5\text{-}12)$$

It is now evident that the use of Equation (5-4) for computing the vehicle attitude eliminates truncation error and that the third order term in Equation (5-12) represents the commutation error, assuming fourth and higher order terms in T as negligible.

5.1.2 <u>Integration Drift Error Due to Commutation Error</u>

We will now relate the integration drift error to the length of the sampling period T. For any continuous vehicle rate $\bar{\omega}(t)$, $t_k \leq t \leq t_{k+1}$, there exists a state transition matrix $\Phi(k + 1, k)$ which yields the exact solution to the kinematic equation and therefore

$$\rho_{k+1} = \Phi(k + 1, k) \rho_k \quad (5\text{-}13)$$

Defining the error in the computed attitude by

$$\delta\rho \triangleq \rho - \hat{\rho} \quad (5\text{-}14)$$

and making use of (5-4) and (5-12) results in

$$\delta\rho_{k+1} = \left[e^{\left(\frac{1}{2}\right) T \bar{\Omega}_k} \right] \delta\rho_k + \frac{T^3}{48} [\dot{\Omega}_k \Omega_k - \Omega_k \dot{\Omega}_k] \hat{\rho}_k \quad (5\text{-}15)$$

Neglecting again fourth and higher order terms in T one obtains that after N attitude computation steps

$$\| \delta \rho_{k+N} \| \leq \left\| \left(\prod_{j=0}^{N-1} e^{(\frac{1}{2}) T \bar{\Omega}_k + j} \right) \delta \rho_k \right\| + N T^3 \| E \| \tag{5-16}$$

where the double bars denote the Euclidean norm, where the fact that $\| \hat{\rho}_k \| =$ has been used, and where

$$\| E \| = \left(\max_{k \leq j \leq k+N-1} \right) \frac{1}{48} \| \dot{\Omega}_j \Omega_j - \Omega_j \dot{\Omega}_j \| \tag{5-17}$$

Let t_k and t_{k+N} correspond to the times where attitude updates are obtained. Since we are at the moment only interested in the computational errors incurre in the integration of the gyro rates between the updates, one may assume $\delta \rho_k = 0$. Thus the total integration error (consisting only of commutation error) accumulated between attitude updates satisfies

$$\| \delta \rho_{k+N} \| \leq N T^3 \| E \| \tag{5-18}$$

Let $\theta = (\theta_1, \theta_2, \theta_3)^T$ be Euler rotation angles which describe the attitude of the spacecraft relative to the same inertial reference frame as ρ. Then it can be shown that

$$\| \delta \rho \| = \frac{1}{2} \| \delta \theta \| \tag{5-19}$$

and noting that the time between updates is $\Delta T_{up} = NT$, one obtains

$$\| \delta \theta_{k+N} \| \leq 2 \Delta T_{up} T^2 \| E \| < \| \delta \theta \|_{max} \tag{5-20}$$

where $\| \delta \theta \|_{max}$ represents the maximum permissible three-axis (RSS) integration error between updates. It follows that the sampling period T must satisfy

$$T \leq \sqrt{\frac{\beta}{2 \| E \|}} \tag{5-21}$$

where β denotes the maximum permissible integration drift rate error defined by

$$\beta = \frac{\| \delta \theta \|_{max}}{\Delta T_{up}} \tag{5-22}$$

The Euclidean norm of a square matrix is the positive square root of the largest eigenvalue of the product of the matrix and its adjoint. Hence

$$||\Omega|| = ||\bar{\omega}|| \qquad \text{and} \qquad ||\dot{\Omega}|| = ||\dot{\omega}|| \qquad (5-23)$$

and

$$||E|| < \frac{1}{24} ||\bar{\omega}||_{max} ||\dot{\bar{\omega}}||_{max} \qquad (5-24)$$

so that we impose the stronger requirement on T,

$$T \leq 2 \sqrt{\frac{3\beta}{||\bar{\omega}||_{max} ||\dot{\bar{\omega}}||_{max}}} \quad \text{(units: rad, sec)} \qquad (5-25)$$

Figure 5-1 shows plots of β versus T for equality in the above equation for various values of $||\bar{\omega}||_{max}$ and $||\dot{\bar{\omega}}||_{max}$. Typical values are assumed as follows:

$$||\bar{\omega}|| \leq 1.05 \cdot 10^{-3} \text{ rad/sec} = 0.06 \text{ deg/sec}$$

$$||\dot{\omega}|| \leq 2 \cdot 10^{-3} \text{ rad/sec}^2 = 0.114 \text{ deg/sec}^2$$

so that for a maximum permissible integration drift error of $\beta = 0.1$ sec/minute one obtains that $T \leq 0.21$ sec. The value chosen for the system is 200 ms. The described gyro processing scheme permits then a rather large sampling period without producing large integration drift errors. In fact, when $\bar{\omega}$ remains constant over several sampling intervals no errors due to gyro output processing are incurred whatsoever.

In the derivation of the commutation error it has been assumed that the derivatives of $\bar{\omega}$ are bounded which justified the deletion of fourth and higher order terms in the Taylor series expansion. Since an infinite number of higher order terms have been neglected a more precise bound on the derivatives is in order. It is given by

$$||\bar{\omega}^{(n)}|| \leq (n + 1)!, \; n \geq 3 \qquad (5-26)$$

which assures the insignificance of the fourth and higher order terms for sufficiently small T.[*] For smooth vehicle limit cycles these conditions are

---

[*]A small number of the $\bar{\omega}^{(n)}$ may satisfy the weaker inequality

$$||\bar{\omega}^{(n)}|| \leq \frac{(n + 1)!}{T^{n - 3}}, \quad n \geq 3$$
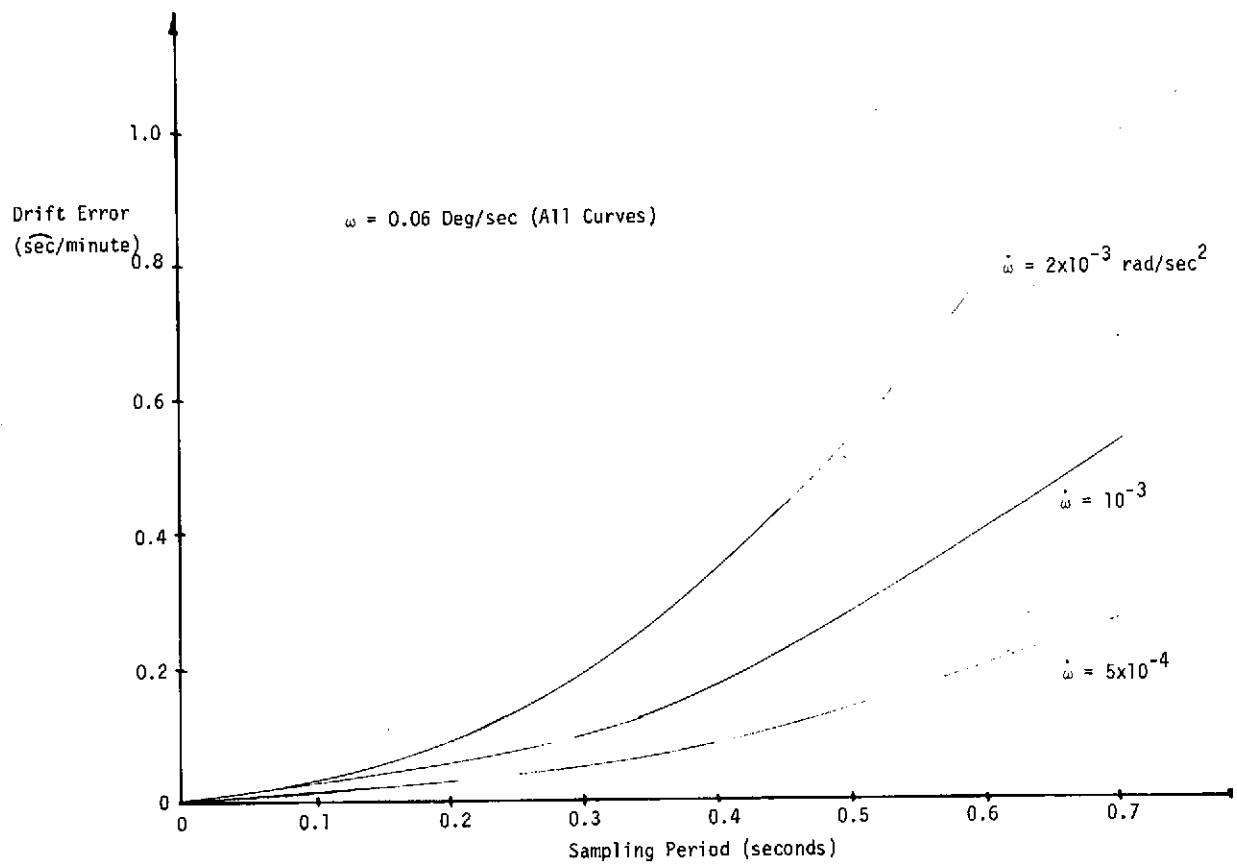
Figure 5-1. Computation Error Effects

almost always satisfied, but for limit cycles controlled by torque impulse attitude control systems they are violated at singular points, namely at the turn-on and turn-off times of the reaction jets. This is a familiar problem in numerical integration. The solution for this is to size the sampling period T according to the imparted acceleration $\bar{\omega}$, even if the higher order derivatives do not satisfy the smoothness assumption. The errors will arise only when integrating across the singular points where the higher order derivatives of $\bar{\omega}$ tend to infinity. The committed error will still be relatively small, and if it occurs only an infrequent number of times between the usual attitude updates, its effect will remain essentially insignificant.

Computational delay must also be considered since the computed attitude must be available in real time. Assuming that the computed attitude is available at times t_k, the gyros are being read at times $t_k - \delta_c$ where δ_c is the computation delay. Thus a gyro output at $t_k - \delta_c$ is now denoted by $\Delta\theta^i(t_k - \delta_c)$.

Using a second order polynomial fit for the integral of gyro rate, it is easy to show that an estimate for $\dot{\omega}^i(t)$ is given by

$$\hat{\dot{\omega}}^i(t) = \frac{\Delta\theta^i(t_{k+1} - \delta_c) - \Delta\theta^i(t_k - \delta_c)}{T^2}, \quad t_{k-1} \leq t \leq t_{k+1} \qquad (5\text{-}27)$$

and that therefore the average rate $\omega_{\overline{k}}^i$ of Equation (5-2) should now be taken as

$$\omega_{\overline{k}}^i = \frac{\Delta\theta^i(t_{k+1} - \delta_c)}{T} + \left[\frac{\Delta\theta^i(t_{k+1} - \delta_c) - \Delta\theta^i(t_k - \delta_c)}{T^2}\right]\delta_c \qquad (5\text{-}28)$$

The error incurred in this linear extrapolation of $\omega_{\overline{k}}^i$ must ultimately be charged to the computation delay δ_c. The effect of δ_c can be further analyzed and it can be shown that its contribution is very small for small δ_c.

It should also be noted at this point that with or without computation delay the presented gyro output processing method could be further refined by employing the estimate $\hat{\dot{\omega}}^i$ to include the terms $(T^3/48)[\hat{\Omega}_k \Omega_k - \Omega_k \hat{\Omega}_k]\rho(t_k)$ of Equation (5-12) in the attitude computations. This would virtually eliminate all errors in the integration of the gyro outputs at the expense of a few more computations.

5.1.3 Computer Roundoff Error

The computer roundoff error incurred in the digital processing of the gyro output signals is treated analytically and expressions relating the mean and variance of the errors to the computer wordlength are presented.

In general the analytical determination of computer roundoff error incurred in a large and complicated computational algorithm is a very tedious task. Therefore only the approach and the obtained results will be discussed here.

The characteristics of the computer arithmetic are assumed to be as follows:

- Fixed point

- 2's complement fractional

- Single precision

- Double precision accumulation of dot products

The computer word length inclusive of the sign bit is denoted by w, and the number of significant bits by $t, (t = w - 1)$.

In fixed point arithmetic, one usually represents a real number x by a binary computer word X where

$$x = 2^Q X \qquad \text{and} \qquad |X| < 1 \tag{5-29}$$

The quantity 2^Q is the scale factor of x where Q may be a positive or negative integer including zero.

In the present system, rounding does not consist of mere truncation. If t is the least significant bit available for a binary number X, then rounding is accomplished by adding $(1/2)(2^{-t})$ to it (adding a 1 in the $t + 1^{st}$ significant bit in the accumulator) and only thereafter is the word truncated to t significant bits. The advantage of this rounding method is that the statistical mean of the roundoff error is zero and no biased drift error results. Note however, that the variance of the error does increase with the number of computations performed and this point will now be pursued.

The exact product of two real numbers x_1 and x_2 is given by

$$y = x_1 x_2 = 2^{(Q_1 + Q_2)} X_1 X_2 \tag{5-30}$$

If X_1 and X_2 are each represented by t significant bits, then a word permitting 2t significant bits would be required to store $Y = X_1 X_2$. When Y is rounded to t significant bits, a roundoff error ϵ is incurred so that the computed value of y is actually given by

$$y_c = x_1 x_2 + \epsilon \tag{5-31}$$

where in terms of the computer word length, w, the roundoff error satisfies

$$|\varepsilon| \leq (2^{Q_1 + Q_2}) \cdot (1/2)2^{-(w-1)}$$

or equivalently

$$|\varepsilon| \leq 2^{Q_1 + Q_2 - w} \tag{5-32}$$

Proceeding similarly as has been done for multiplication, roundoff errors incurred in the encoding of system parameters, in a shift-right operation (for scale factor change to prevent overflow), in division, and in double precision accumulated dot products, are derived. All these rounding errors can be bounded by inequalities of the type

$$|\varepsilon| \leq b \tag{5-33}$$

where the bound b is a function of the Q's of the numbers participating in the particular operation and of the computer word length w.

In statistical terms, the roundoff error ε is uniformly distributed on [-b, b] with mean

$$E(\varepsilon) = 0, \tag{5-34}$$

variance

$$Var(\varepsilon) = \frac{b^2}{3} \tag{5-35}$$

and successive roundoff errors in string computations are assumed to be uncorrelated.

The roundoff error in one iteration of the strapdown attitude algorithm can now be traced by distinguishing in each arithmetic operation between the true value and the computed value. Precise estimates for the Q's of the variables appearing in the computations can be obtained since the orders of magnitude are well known. In evaluation of the roundoff error, account has been taken also for the computations that correct the gyro outputs.

Because of a large difference in the Q's appearing in the individual operations, it turns out that the roundoff error incurred in the computation

$$\hat{\rho}(k+1) = e^{(\frac{1}{2})T\,\bar{\Omega}_k}\,\hat{\rho}(k) \tag{5-36}$$

absorbs all previously committed errors. This occurs when several shift-right operations are performed on the entries of $\rho^{(1/2)T\,\bar{\Omega}_k}$ in order to obtain a $Q = 0$ for the matrix elements. The roundoff error can then be expressed as

$$\hat{\rho}_c(k+1) - \hat{\rho}(k+1) \triangleq \begin{bmatrix} \varepsilon_1 \\ \varepsilon_2 \\ \varepsilon_3 \\ \varepsilon_4 \end{bmatrix} = \begin{bmatrix} \varepsilon_{10} \\ \varepsilon_{20} \\ \varepsilon_{30} \\ \varepsilon_{40} \end{bmatrix} + \begin{bmatrix} \varepsilon_{11} & \varepsilon_{12} & \varepsilon_{13} & \varepsilon_{14} \\ \varepsilon_{21} & \cdots & & \\ \vdots & & & \\ \varepsilon_{41} & \cdots \cdots & \varepsilon_{44} \end{bmatrix} \begin{bmatrix} \hat{\rho}_1(k) \\ \vdots \\ \vdots \\ \hat{\rho}_4(k) \end{bmatrix}$$

(5-37)

where the ε_{i0} are the errors incurred in forming the dot products of the matrix times vector multiplication indicated in Equation (5-36), and where the ε_{ij}, $j \neq 0$, are the roundoff errors in the entries of the matrix $e^{(1/2)T \bar{\Omega}_k}$. All the ε_{ij}, $i = 1, \cdots, 4$, $j = 0, 1, \cdots, 4$, are uncorrelated and uniformly distributed on $[-b_{ij}, b_{ij}]$ and, since $Q = 0$ for all variables involved,

$$b_{ij} = 2^{-W}, \forall_{i, j}$$

(5-38)

It follows that

$$E(\varepsilon_{ij}) = 0$$

(5-39)

and

$$\text{Var}(\varepsilon_{ij}) = \frac{2^{-W}}{3} \triangleq \sigma_0^2$$

(5-40)

From (5-37) one obtains then

$$E(\varepsilon_i) = 0$$

(5-41)

and

$$\text{Var}(\varepsilon_i) = E(\varepsilon_i^2) = 2\sigma_0^2, \quad i = 1, 2, 3, 4$$

(5-42)

Equation (5-42) defines the variance in the roundoff error for one Euler symmetric parameter for one iteration. For easier interpretation of this result we convert again to Euler angles. Denoting the roundoff error in an Euler angle by $\delta\theta_i$ one obtains

$$E(\delta\theta_1^2 + \delta\theta_2^2 + \delta\theta_3^2) = 32\sigma_0^2$$

(5-43)

or equivalently

$$\sigma_{||\theta||} = (0.672) \cdot 10^6 \cdot 2^{-W} \widehat{\text{sec}}$$

(5-44)

The attitude computation

$$\hat{\rho}(k+1) = e^{(\frac{1}{2})T \bar{\Omega}_k} \hat{\rho}(k)$$

(5-45)

is performed many times before an attitude update is obtained. Each time a new $\hat{\rho}$ is computed a new roundoff error vector, ε, with the above derived statistics, is incurred. However, the previous $\hat{\rho}$ was already in error. Thus one has for the computed value of $\hat{\rho}(k + 1)$ that

$$\hat{\rho}_c(k + 1) = [e^{(\frac{1}{2}) T \bar{\Omega}_k} + \bar{\bar{\varepsilon}}] \, [\hat{\rho}(k) + \varepsilon(k)] + \varepsilon_0 \qquad (5\text{-}46)$$

where $\varepsilon(k)$ is the error in the previously computed $\hat{\rho}_c(k)$, and the matrix $\bar{\bar{\varepsilon}}$ and the vector ε_0 identify directly with the corresponding quantities in Equation (5-37). Recalling that the entries of $(1/2)T \, \bar{\Omega}_k$ are small and retaining only the first order terms, the above reduces to

$$\hat{\rho}_c(k + 1) = [e^{(\frac{1}{2}) T \bar{\Omega}_k} + \bar{\bar{\varepsilon}}] \, \hat{\rho}(k) + \varepsilon_0 + \varepsilon(k) \qquad (5\text{-}47)$$

and by Equation (5-37)

$$\hat{\rho}_c(k + 1) = \hat{\rho}(k + 1) + \varepsilon(k + 1) + \varepsilon(k) \qquad (5\text{-}48)$$

and consequently,

$$\hat{\rho}_c(k + N) = \hat{\rho}(k + N) + \varepsilon(k + N) + \varepsilon(k + N - 1) + \cdots + \varepsilon(k + 1) + \varepsilon(k) \qquad (5\text{-}49)$$

If an attitude update has been obtained at $t = t_k$, then $\hat{\rho}(k)$ may be considered free of roundoff errors associated with the repetitive computations and $\varepsilon(k) = 0$. Furthermore, since the $\varepsilon(k + j)$, $j = 1, N$, are independently and identically distributed, the total roundoff error, for N iterations, denoted by the vector

$$e = \sum_{j=1}^{N} \varepsilon(k + j), \qquad (5\text{-}50)$$

satisfies

$$E(e_i) = 0$$

and

$$E(e_i^2) = N \, E(\varepsilon_i^2) = 2N\sigma_0^2, \quad i = 1, 2, 3, 4 \qquad (5\text{-}51)$$

Converting to Euler angles, as before, one has

$$\sigma \, (||\theta||, N) = (0.672) \cdot 10^6 \cdot 2^{-W} \sqrt{N} \; \widehat{\sec} \qquad (5\text{-}52)$$

which represents the one sigma, three-axis (RSS) roundoff error after N attitude computations. Because of the special rounding procedure used, the mean of the error is zero, eliminating a biased drift error. The one-sigma error represents the uncertainty in the roundoff error which grows as the square root of the number of attitude computations. Figure 5-2 shows a plot of $\sigma(||\theta||, N)/ \sqrt{N}$ obtained from Equation (5-52).

The present design will use a gyro sampling period of 200 msec (as determined in the previous discussion) and the nominal period between attitude updates from star sightings is 5 minutes. Thus N = 1500 and $\sqrt{N} \approx 39$. If the criteria is imposed that the three-axis one-sigma uncertainty in the roundoff error should be less than 1.5 $\widehat{sec}$ (<0.9 $\widehat{sec}$/axis) after 5 minutes, the computer word length must satisfy

$$w \geq 24 \text{ bits}$$

Because of the Central Limit Theorem, the probability of the occurrence of errors may be interpreted in the Gaussian sense after a number of iterations.

5.2   STAR AVAILABILITY/CATALOG DEFINITION

A star availability study was conducted for the purpose of assuring sufficient stars within the tracker field-of-view to maintain desired performance. Two basic orbits were considered for varying times of the year -- a 500 n.m., noon, sun-synchronous circular orbit; and a 24 hr circular, equatorial orbit. The number of stars visible to the star tracker at any given point in orbit is clearly dependent upon the nominal mounting of the star tracker, the inner and outer gimbal angle limits, the sensitivity of the detector, and region over which the tracker motion is precluded in order to avoid damage by the incident radiance of bright objects, i.e., sun, earth, moon, etc. A general digital computer program was developed to determine star availability, i.e., which stars are observable within the tracker FOV (Appendix F). The program input includes specification of the gimbal FOV, star tracker mounting geometry, sensitivity threshold, orbit, and bright object angular constraints. Stars up to 4th magnitude of the Yale University Observatory Catalog were used for the studies. Tracker FOV and mounting geometry are defined in Figure 5-3 .

The general approach was to determine the number of stars available at discrete orbit angles (e.g., every 15 degrees) for various times of the year. Typical results are illustrated for one case at low altitude in Figure 5-4 Of interest is the observation that star availability is a relatively strong function of both orbit angle and time of year. Using data generated in this
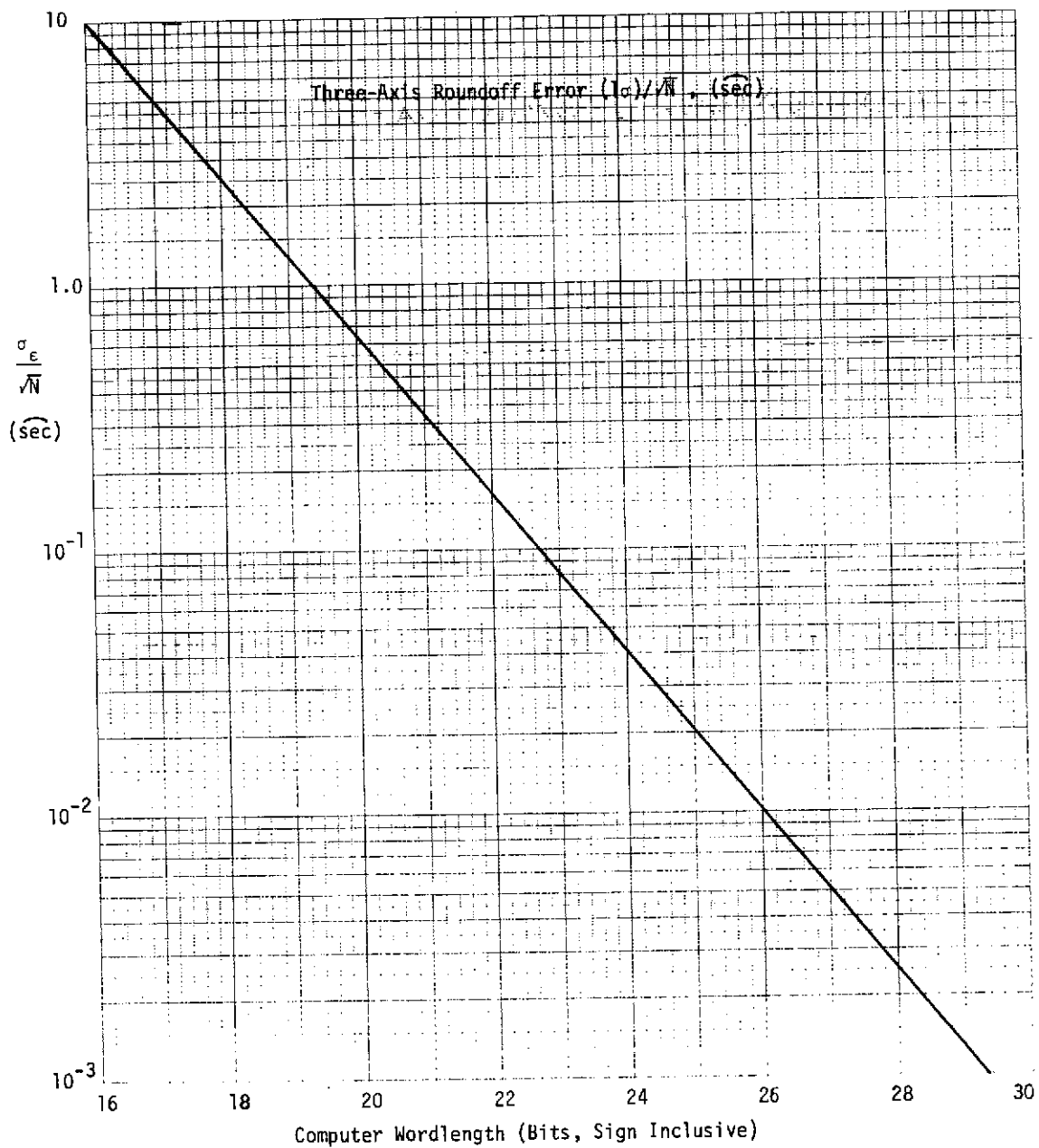
Figure 5-2. Roundoff Error Effects

FOV: $\pm \beta \times \pm \gamma$

$\bar{x}_1$, Roll

$\bar{x}_2$, Pitch

$\bar{x}_3$, Yaw

α : Elevation of nominal boresight ($\theta_0 = \theta_I = 0$)

β : FOV Half-Angle ("Azimuth")

γ : FOV Half-Angle ("Elevation")
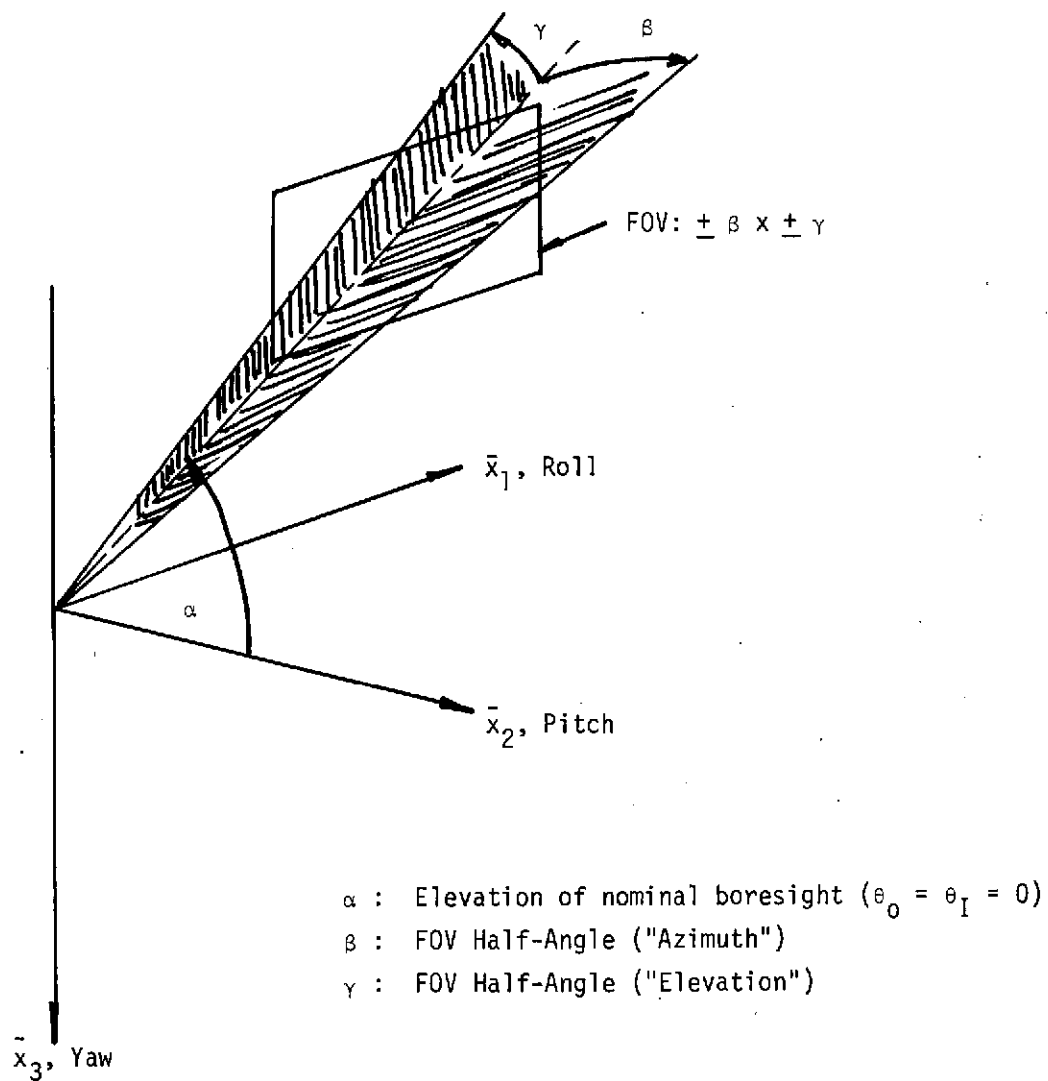
Figure 5-3. Star Tracker FOV and Mounting Geometry
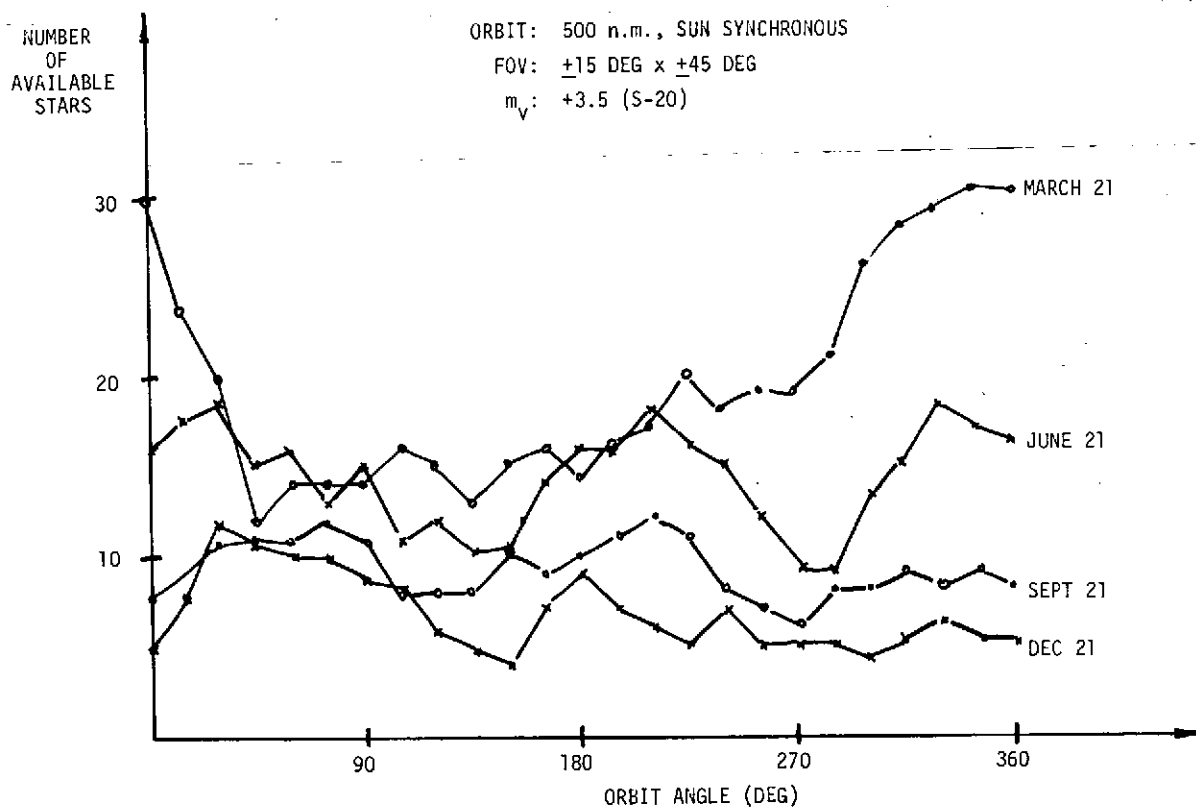
Figure 5-4. Summary of Star Availability

fashion, tradeoffs could be conducted with regard to required FOV, sensitivity, and tracker mounting. Several cases are discussed in the following paragraphs which illustrate the tradeoffs conducted and present the key results used as a basis for system design.

The tradeoff of tracker sensitivity is illustrated in Figure 5-5, where all other parameters have been maintained unchanged. These results are based upon data taken for 12 times during the year, i.e., monthly intervals. For the case of sensitivity to stars to 3.5 magnitude, at least one star is available at all times and there is 95% probability that three or more stars are available. For the case where sensitivity is reduced to include only stars to 2.7 magnitude, there results only 95% probability of any stars and probability for three or more stars has been reduced to 70%. Furthermore, the probability for five or more stars is less than half for $m_v = 2.7$ than $m_v = 3.5$. Thus, the impact of sensitivity is fairly severe if one establishes criteria for 100% availability and/or high probability of multiple stars.

The influence of tracker FOV and mounting orientation is illustrated in Figure 5-6, where the star sensitivity is selected at $m_v = 3.5$. The best results occur for $\beta = 45°$, $\gamma = \alpha = 15°$, i.e., the long side of the FOV on the local horizon. In this case, at least 4 stars are available at all times, and there is 90% probability of there being six stars available. With the same nominal FOV orientation and the outer gimbal freedom reduced to ± 30 degrees, the results remain reasonably good. Two stars are always available and there is greater than 90% probability of there being 4 stars. The availability drops off rapidly above seven stars, but that region of the curve is relatively less significant. The third curve again uses the larger FOV rotated to have the shorter side along the local horizontal, i.e., $\gamma = \alpha = 45°$, $\beta = 15°$. In this case (also shown in the previous figure), only one star is available at all times, but there is a 95% probability that three or more stars will be available. The reduced availability here is primarily a result of maintaining the sensor boresight more than 45° away from the sun. Based on the studies, as illustrated above, a conservative selection was made to require sensitivity to + 3.5 (S-20) magnitude, and have outer gimbal freedom of ± 45° and inner gimbal freedom of ± 15°.

Star availability was studied in a similar fashion for geosynchronous orbits. The result for the selected system parameters is illustrated in Figure 5-7, where the sensor nominal boresight is aligned along the pitch axis directed North. As a result, the data is limited to the stars in the Northern Hemisphere. In this case, three stars are always available and there is greater
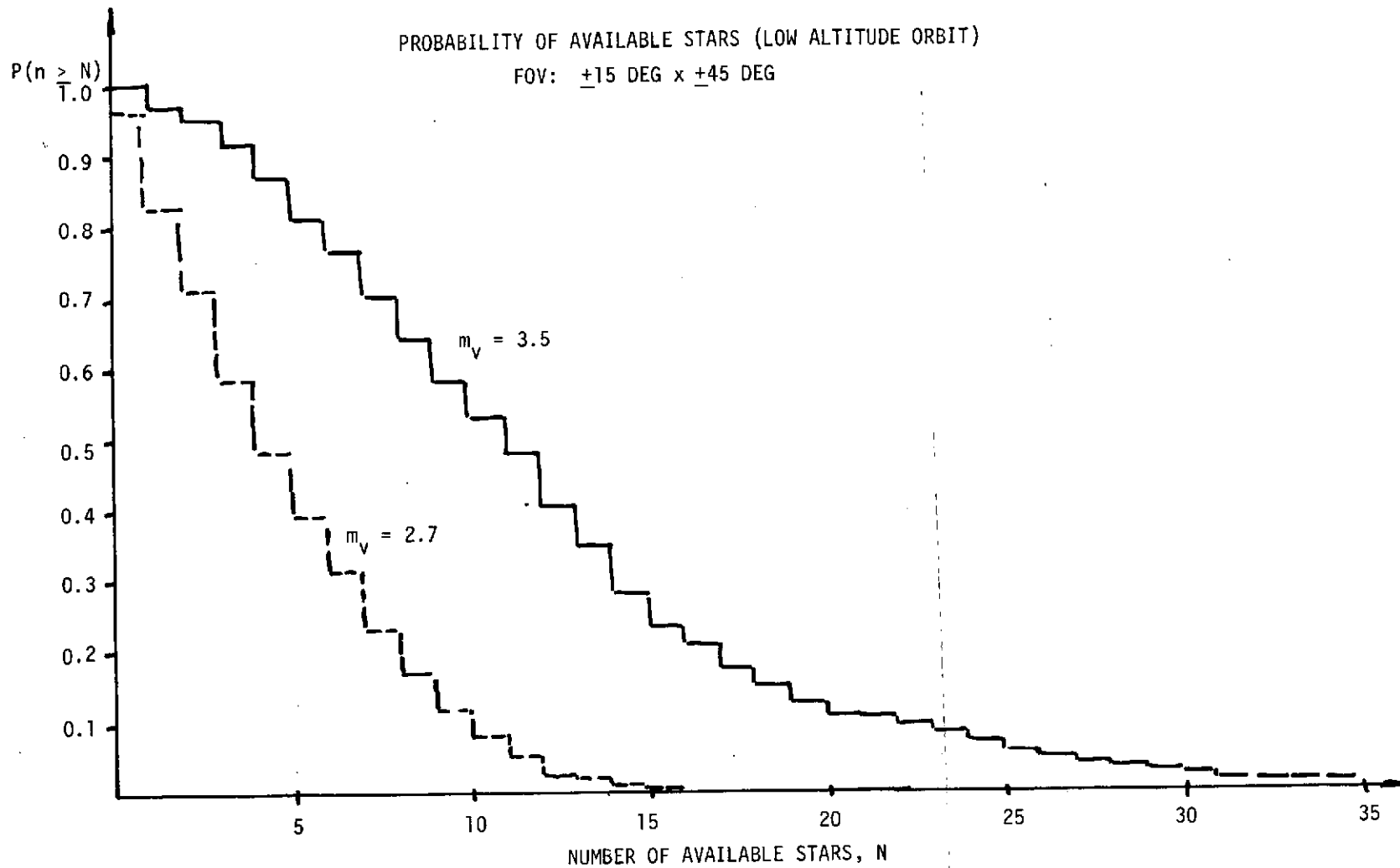
Figure 5.5. Star Sensitivity Tradeoffs

PROBABILITY OF AVAILABLE STARS (LOW ALTITUDE ORBIT)

$m_V = +3.5$ (S-20)

$\alpha = 15°$, $\beta = 45°$, $\gamma = 15°$

$\alpha = 45°$, $\beta = 15°$, $\gamma = 45°$

$\alpha = 15°$, $\beta = 30°$, $\gamma = 15°$

$P(n \geq N)$

NUMBER OF AVAILABLE STARS, N
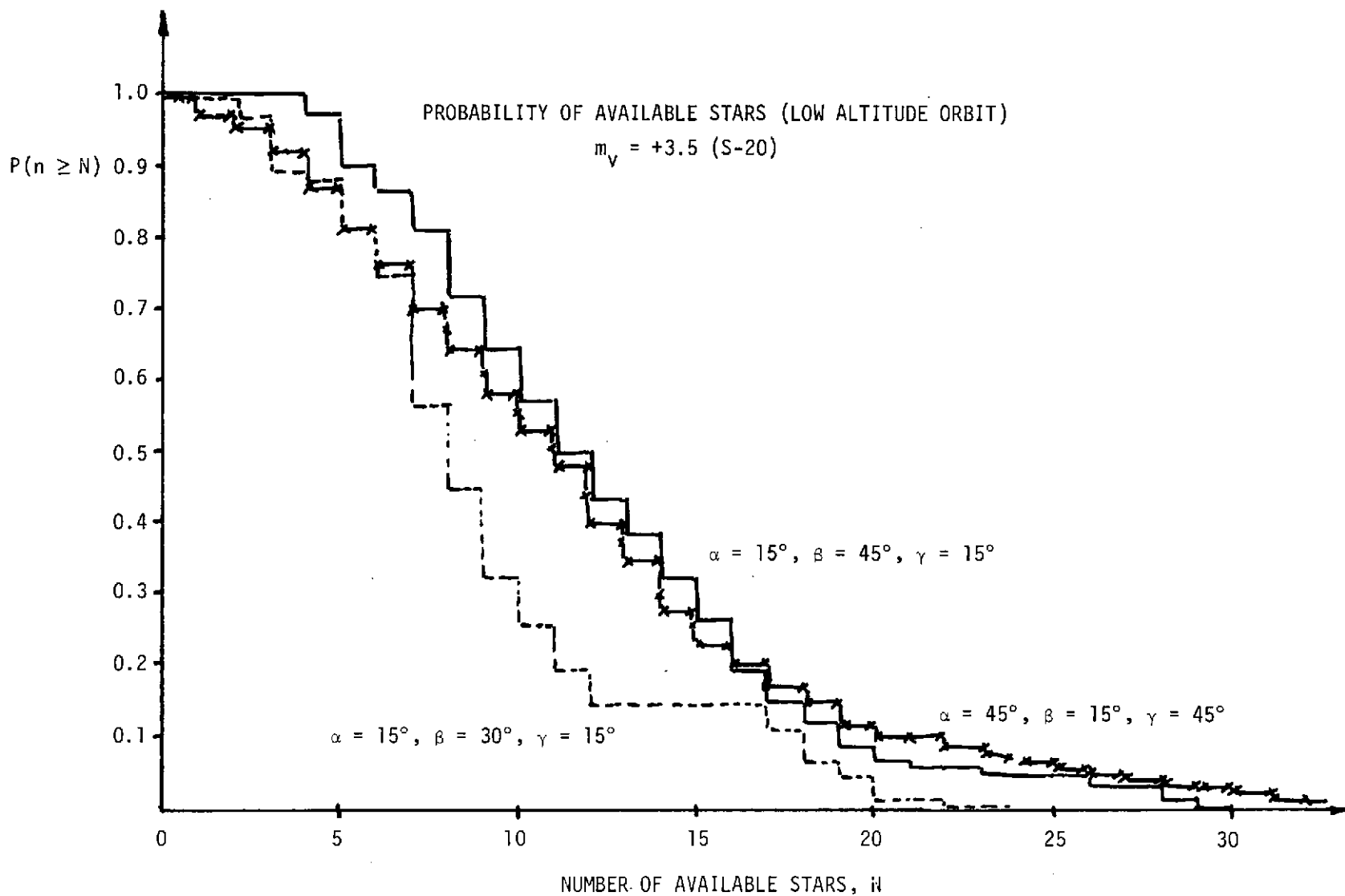
Figure 5-6. Star Availability Trades As A Function of Mounting and Tracker FOV
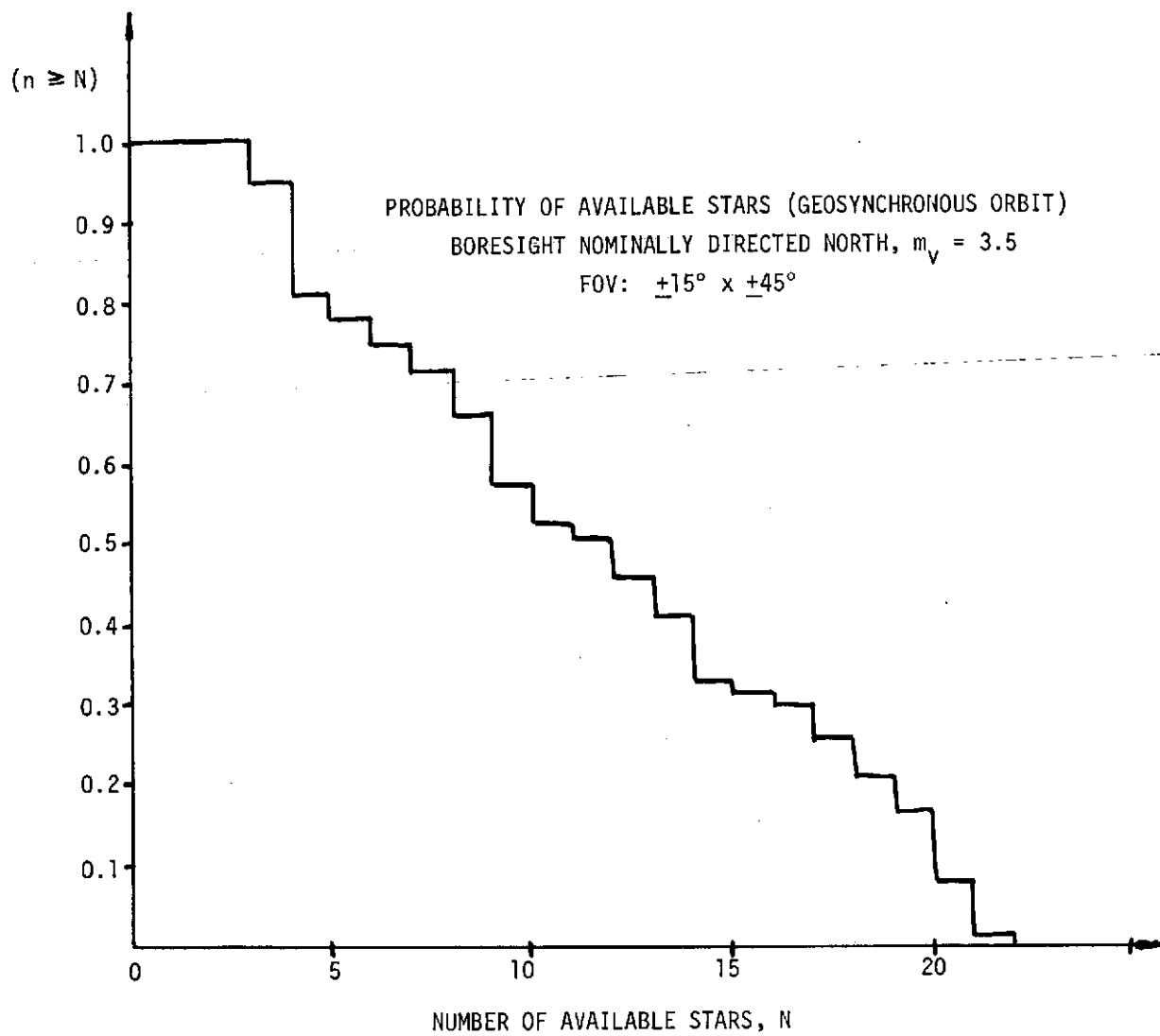
Figure 5-7. Star Availability in Geosynchronous Orbit

than 80% probability of there being five stars within the FOV. These results were also used to support the field-of-view and sensitivity requirements on the tracker.

Based upon the selected tracker requirements, definitive star catalogs may be developed for both the low altitude sun-synchronous and geosynchronous orbits. The criteria employed in generating the catalogs included:

- Independence from time of year or orbit position, i.e., catalog adequate for all time

- Maintain approximate 15 degree separation of all stars in catalog with other stars in catalog

- Provide a minimum of 3 stars always in the FOV

- Maintain greater than 5 degree separation of all stars in catalog with all other known stars with magnitude greater than +4

The resultant master catalog for the low altitude orbit (i.e., good for all time) consists of 42 stars, all brighter than m_v = 3.3. It is noted that only 8 to 12 of the stars would be required to satisfy the criteria during any single orbit, the number being a function of the time of year. This star catalog is summarized in Table 5-1.

The catalog for geosynchronous orbit consists of 24 stars and is summarized in Table 5-2. With so few stars, this catalog has not been fully optimized.

5.3 STAR SELECTION

While the Kalman Filter provides the best linear estimate of attitude, it does so under the constraint of a given star selection sequence. Thus, it becomes important to establish an effective selection method. As a result, several approaches for star selection, each with intuitive appeal, have been considered.

In order to gain some insight into the significance of star location, it is instructive to consider the attitude estimation accuracy resulting from just two star measurements. It is well known that at least two independent star readings are required to determine spacecraft attitude, even if the star sensors take ideal uncorrupted measurements. This results, of course, from no information regarding rotation about the line-of-sight for a single sighting. Consideration will focus upon the attitude estimate of an inertially oriented vehicle whose star tracker gimbal readings are corrupted by zero mean, white noise of standard deviation σ_r. Suppose that (z_1, z_2, z_3) represents a

5-21

Table 5-1. Star Catalog for Low Altitude (All Times of Year)

Yale Catalog No.	Right Ascension	Declination	Magnitude
2491	100.91355	-16.67130	-1.46
7001	278.94600	38.74930	.04
1713	78.22530	- 8.23967	.0487
1708	78.54330	45.96600	.658
2943	114.38010	5.31833	.688
5056	200.84850	-10.97430	.7019
5340	213.52800	19.35900	.7217
3982	151.63950	12.13100	1.242
8728	343.94400	-29.79800	1.249
1790	80.82720	6.32167	1.382
1791	81.03390	28.57170	1.509
6134	246.83250	-26.35970	1.638
2990	115.80930	28.10170	1.78
6879	275.47800	-34.40030	1.809
15	1.65666	28.89630	1.913
2421	98.93760	16.42830	1.93
936	46.49190	40.81970	2.087
5953	239.58000	-22.52030	2.202
5793	233.31150	26.83000	2.209
6556	263.34000	12.58930	2.225
4534	176.83350	14.75930	2.229
2827	110.68515	-29.23200	2.326
3781	345.76800	15.01870	2.437
4554	178.00800	53.88700	2.44
6378	257.10900	-15.67700	2.49
5685	228.79200	- 9.25867	2.492
2095	89.34975	37.20000	2.545
39	2.87058	14.99630	2.572
6175	248.82000	-10.49870	2.58
4057	154.52700	20.02000	2.635
3748	141.47790	- 8.51933	2.647
617	31.31280	23.29130	2.655
188	10.46942	-18.17030	2.674
4357	168.07350	20.70370	2.677

Table 5-1. Star Catalog for Low Altitude (All Times of Year)(Continued)

Yale Catalog No.	Right Ascension	Declination	Magnitude
7194	285.11250	-29.91770	2.68
2845	111.32700	8.35133	2.733
603	30.44955	42.16900	2.761
553	28.19220	20.63570	2.777
1910	83.90385	21.12730	2.849
5531	222.25050	-15.90830	2.895
7235	285.96300	13.81570	2.99
8322	326.28900	-16.28630	3.046
4825	189.98550	- 1.26300	3.049
8308	325.62750	9.72467	3.053
7949	311.20950	33.84200	3.087
911	45.12600	3.96400	3.133
5235	208.26600	18.57000	3.153
1702	77.85090	-16.23970	3.162
8775	345.53400	27.89630	3.168
7710	302.38650	- .91867	3.177
8634	339.93900	10.65770	3.283
8709	343.21200	-15.99800	3.34

Table 5-2. Star Catalog for Geosynchronous Orbit

Yale Catalog No.	Right Ascension	Declination	Magnitude
1708	78.54330	45.96600	.658
7924	310.06800	45.14770	1.349
2088	89.26005	44.94430	1.931
1017	50.47560	49.73100	2.192
264	13.66217	60.53530	2.404
4301	165.40950	61.93130	2.432
424	31.96755	89.08570	2.508
21	1.83834	58.96300	2.561
8162	319.44300	62.44170	2.626
5563	222.79650	74.29170	2.72
403	20.89740	60.05770	2.807
1122	55.12425	47.67570	2.838
7528	295.97700	45.04830	2.849
6705	268.95300	51.48900	2.861
8238	322.05300	70.40270	2.897
168	9.64608	56.34630	2.898
6396	257.17500	65.75630	3.052
5735	230.24550	71.95230	3.1
542	27.98805	63.51330	3.216
3569	134.22195	48.16930	3.312
6132	245.88150	61.57930	3.346
153	8.76851	53.71300	3.388
6536	262.41600	52.33930	3.41
915	45.58380	53.36970	3.439

right-handed, orthogonal coordinate set defined such that the first star sighted lies on the z_2 axis and the second lies in the z_2-z_3 plane. Suppose further that the star tracker axes are related by a first order rotation to these defined axes, i.e.,

$$
\begin{bmatrix} x_1' \\ x_2' \\ x_3' \end{bmatrix} = \begin{bmatrix} 1 & \theta_3 & -\theta_2 \\ -\theta_3 & 1 & \theta_1 \\ \theta_2 & -\theta_1 & 1 \end{bmatrix} \begin{bmatrix} z_1 \\ z_2 \\ z_3 \end{bmatrix}
\tag{5-53}
$$

and that initially

$$
E(\theta_i) = 0
\tag{5-54}
$$

$$
i, j = 1, 2, 3
$$

$$
E(\theta_i \, \theta_j) = \sigma^2 \, \delta_{ij}
\tag{5-55}
$$

where δ_{ij} is the Kronecker delta. Then the initial error covariance matrix, P_0, satisfies for $\theta = (\theta_1, \theta_2, \theta_3)^T$,

$$
P_0 = E(\theta \, \theta^T) = \sigma^2 \, I
\tag{5-56}
$$

After the i-th star has been considered, the error covariance matrix for this inertially oriented vehicle, P_i, is given by the standard equation

$$
P_i = P_{i-1} - P_{i-1} H_i^T [H_i P_{i-1} H_i^T + R]^{-1} H_i P_{i-1}
\tag{5-57}
$$

where R is the measurement noise covariance matrix ($\sigma_r^2 \, I$) and H_i is the measurement matrix associated with the i-th star, i.e.,

$$
H_i = \frac{\partial (y_I^i \, y_0^i)}{\partial (\theta_1, \, \theta_2, \, \theta_3)}
\tag{5-58}
$$

Noting that the first star lies on the z_2 axis, it follows that after one measurement

$$
P_1 = \sigma^2 \begin{bmatrix} \dfrac{\sigma_r^2}{\sigma^2 + \sigma_r^2} & 0 & 0 \\ 0 & 1 & 0 \\ 0 & 0 & \dfrac{\sigma_r^2}{\sigma^2 + \sigma_r^2} \end{bmatrix}
\tag{5-59}
$$

which illustrates the fact that no improvement of the estimate in θ_2 results whereas estimates in θ_1 and θ_3 improve considerably if σ_r/σ is small. Adopting the trace ratio

$$n_i = \frac{\text{trace } P_i}{\text{trace } P_0} \tag{5-60}$$

as a measure of the improvement, it follows that

$$n_1 = \frac{1}{3} \left[1 + \frac{2\,\sigma_r^2}{\sigma^2 + \sigma_r^2} \right] \tag{5-61}$$

which illustrates the condition that even under noiseless conditions, one-third of the initial error remains since only two axis information is provided by each star.

Taking a second star reading and defining a_2 to be its projection on $\bar{z}_2$, it follows after considerable algebra that

$$n_2 = \frac{(\beta - 1)\,(3\beta^2 + 2a_2^2\,\beta - a_2^2)}{3\,(\beta + a_2^2)\,(\beta^2 - a_2^2)} \tag{5-62}$$

where

$$\beta = \frac{\sigma^2 + \sigma_r^2}{\sigma^2} \tag{5-63}$$

This result is plotted in Figure 5-8 as a function of the sine of the angle separating the two stars. This figure is quite revealing. It demonstrates the desirability of separating the two stars as far as possible, but shows that this condition has much greater impact when the measurement noise is small compared to the attitude uncertainty (i.e., γ is small). Applying this consideration to the Kalman Filter with a large initial uncertainty, quick convergence is anticipated even using stars which are not widely separated. Once reasonably good accuracy has been achieved, γ rises in value and further improvement becomes more difficult. Figure 5-8 also demonstrates that if the two stars are colinear (or if one star is measured twice), improvement results only if the measurements are comparatively noisy compared to the attitude uncertainty. This again agrees with intuition.

The other side of the spectrum is to consider a means for optimum star selection. The optimum sequence of star selection is a problem in dynamic programming. To illustrate, suppose zero mean white noise is the only
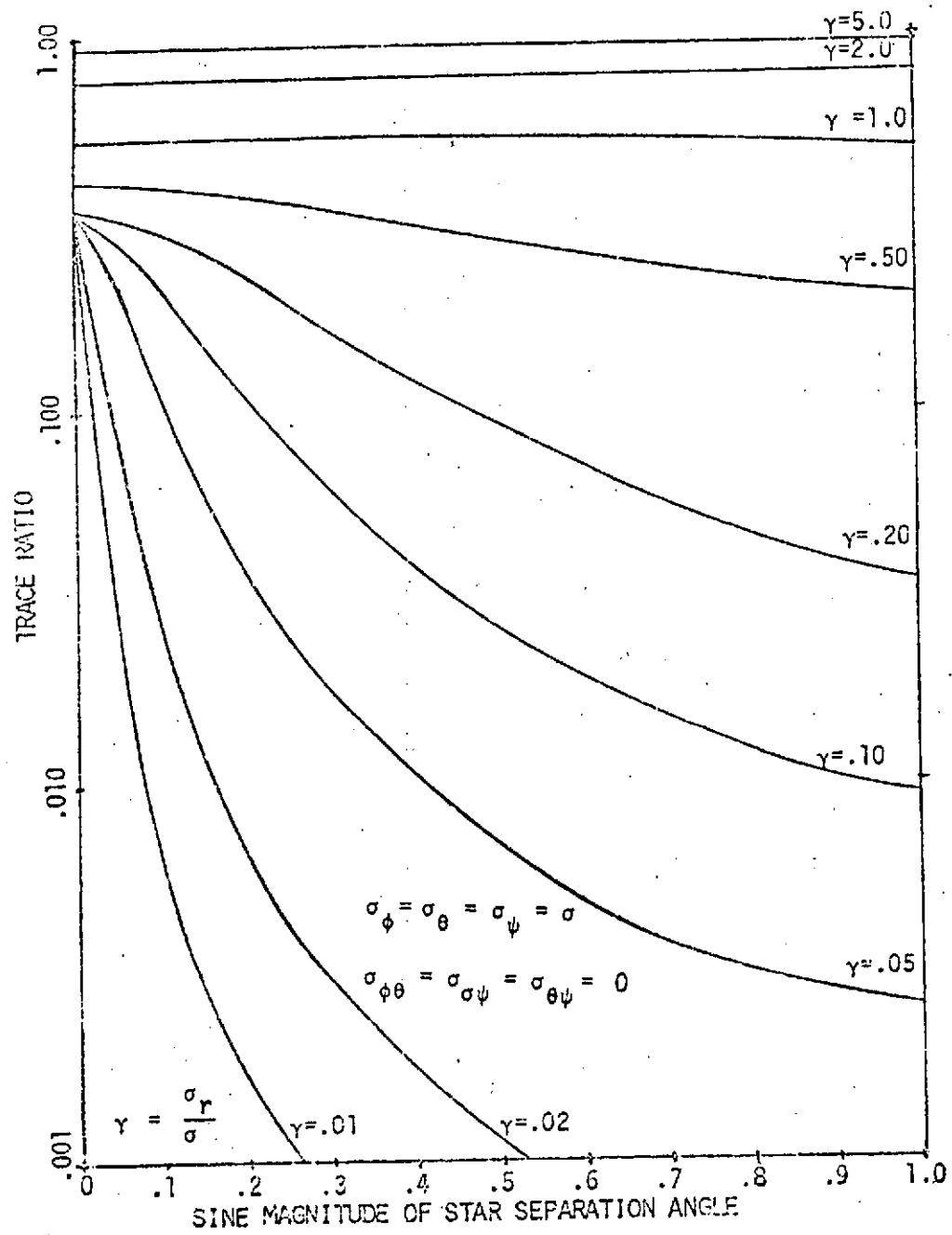
Figure 5-8. Star Selection Considerations (Two Star Case)

corrupting system influence. The recursive filter equations are then given by

$$\hat{P}_i = \Phi_i \ \hat{P}_{i-1} \ \Phi_i^T + Q_{i-1} \tag{5-64}$$

$$\hat{P}_i = \hat{P}_i - \hat{P}_i \ H_i^T \ [H_i \ \hat{P}_i \ H_i^T + R_i]^{-1} \ H_i \ \hat{P}_i \tag{5-65}$$

where Q and R represent the state and measurement noise covariance matrices, respectively; Φ_i is the state transition matrix and

$$P_i = \{p_{jk}^i\} = E \ [\theta(t_i) \ \theta^T \ (t_i)] \tag{5-66}$$

Defining

$$P_i = [p_{11}^i \ p_{22}^i \ p_{33}^i \ p_{12}^i \ p_{13}^i \ p_{23}^i]^T \tag{5-67}$$

P_i propagates according to some function

$$P_i = f \ (p_{i-1}, \ \alpha) \tag{5-68}$$

where α is an index identified in a one-to-one fashion with the visible stars at time t_i. Note that p contains the six unique elements of the symmetric matrix P. Regarding P as the error ellipsoid, a somewhat more revealing set of six states involves the three major axes and three (Euler) rotations describing the orientation of these axes relative to some pre-defined inertial set.

The optimization problem is now stated as:

> Given an initial error covariance matrix, P_0, and
> given N star readings separated in time from each
> other by some fixed amount, determine that star
> selection sequence which minimizes the final trace
> of P.

Noting that P_0 implies p_0, define $J_i(p_0)$ to be the minimum possible final trace of P permitted i star readings. Applying the Principle of Optimality, the optimum sequence can, in principle, be determined by imbedding its solution within a family of such solutions for increasing i. The optimal selection must satisfy

$$J_i(p_0) = \underset{\alpha}{Min} \ J_{i-1} \ (f(p_0, \ \alpha)) \qquad i = 1, \ 2, \ \cdots, \ N \tag{5-69}$$

$$J_0(p_0) = \text{trace of } P_0 \tag{5-70}$$

5-28

No attempt has been made to solve this problem numerically as p is six dimensional. The purpose here was merely to illustrate the concept involved in such a selection, and to lend insight and motivation regarding this problem.

Four approaches (methods) have been considered for on-board star selection. The methods considered include the following:

● Widest Star Separation Method

This method, motivated by the two star results, selects that available star which is furtherest separated from the previous selection. This method appears to work well.

● Least Used Star Method

This approach operates by choosing that available star which has been least used for measurement in the past. This method tends to promote stars just entering the tracker field-of-view.

● Minimum Trace Method

This is a local optimization method based upon the optimal selection approach discussed above for $N = 1$. Each time a measurement is to be taken, the visible stars are scanned and the selection based upon that candidate which best minimizes the trace of P_1.

This approach is summarized, such that given

$$P_0 = \begin{bmatrix} \sigma_\phi^2 & \sigma_{\phi\theta}^2 & \sigma_{\phi\psi}^2 \\ \sigma_{\phi\theta}^2 & \sigma_\theta^2 & \sigma_{\theta\psi}^2 \\ \sigma_{\phi\psi}^2 & \sigma_{\theta\psi}^2 & \sigma_\psi^2 \end{bmatrix} \tag{5-71}$$

one must determine $B = [b_{ij}]$ such that

$$BP_0B^T = \begin{bmatrix} d_1 & 0 & 0 \\ 0 & d_2 & 0 \\ 0 & 0 & d_3 \end{bmatrix} \quad d_2 \leq d_1, d_3 \tag{5-72}$$

The trace of P_1 (tr P_1 = $[\sigma_\phi^2 + \sigma_\theta^2 + \sigma_\phi^2]$) is then minimized by selection of the star whose coordinates are $\{b_{21}, b_{22}, b_{23}\}$.

Selection of the star closest to the optimal selection is the best choice, as the results degrade symmetrically about the optimum. In actuality, this approach appeared to show virtually the same results as the widest separation method.

● Maximum Projection Method

This is a method motivated by questions of observability (see Section 4.3) and is particularly applicable to the periods of star tracker flight calibration. This method selects that visible star whose absolute value of u_1 (corresponding to the sine of the inner gimbal angle) is maximized, and thus best tends to separate the bias, α_1, from the roll attitude.

5.4   ATTITUDE DETERMINATION PERFORMANCE ANALYSIS

This section discusses in detail the results of simulation studies of the inertial attitude determination estimation process. The tasks required in order to establish the effect of the many interacting influences of the system on overall performance is one of large proportion. As a result, some selected areas were pursued in greater detail than others, although a relatively comprehensive portrayal of attitude determination performance was achieved. There resulted two classes of runs, namely: 1) those runs which simulate the on-board system utilizing a six-element state vector and 2) those runs which simulated the use of an expanded state vector to represent, primarily, the ground-based calibration of the on-board system.

The objectives in simulating extensively the on-board system was to evaluate PPCS performance under a variety of conditions that are considered realistic in practice, establish the system sensitivity, and establish design criteria as appropriate. The purpose of the calibration runs is to support development and evaluation of an inflight calibration approach that will accurately evaluate observable system parameters and biases which contribute to estimation errors and, therefore, lead to ultimate system performance.

5.4.1 Baseline System Performance

Presented initially is the attitude determination convergence and steady-state performance representing the final system design baseline. The system parameters are summarized in Table 5-3. The first two runs shown demonstrate the convergence characteristics of the system. These runs differ only in the period between updates. In one case (Figure 5-9) the period is one minute while in the second case (Figure 5-10) it is five minutes. Different update periods were considered to determine the correlation, if any, between update frequency and convergence period. It is noted that in each case, sighting of the first star reduces the estimation error to the range of 20-30 sec, although the error covariance is not reduced to this level until the second star sighting. In general, the error will also require two sightings to be reduced to this error level. With one minute updates, the second star brings the estimation error below 10 sec after which the system exhibits a damped oscillatory behavior in both the estimation error and the error covariance. Two distinct frequencies appear to exist, one associated with update frequency, the other a low frequency behavior which appears to be a characteristic of the filter. This is particularly noted in correlation of the error covariance of the two runs shown in Figure 5-11.

The run with a five minute update has a performance envelope which exhibits very similar characteristics to the general behavior of the previous run. In this case, convergence to the 10 sec region does not occur until after the third update

Table 5-3 . PPCS Baseline Design Parameters

Star Tracker Parameters

Misalignment of Boresight Axes   0.44 $\widehat{sec}$ (outer), 0.44 $\widehat{sec}$ (inner)

Inner Axis/Outer Axis Perpendicularity   0.5 $\widehat{sec}$

Runout: First power coefficients: 0.35 $\widehat{sec}$
         Second power coefficients: 0
         Third power coefficients: 0

Inductosyn Readout: θ   0.5 $\widehat{sec}$
                      360θ   0.37 $\widehat{sec}$
                      720θ   0.58 $\widehat{sec}$

Star Sensor Noise: 0.35 $\widehat{sec}$ (each axis)
Inductosyn Noise: 0.06 $\widehat{sec}$ (quantization, each axis)

Gyro Parameters

Drift Bias (equivalent 3-axis): 1.8 deg/hr (each axis)

Input Axis Misalignment: typical 3-6 $\widehat{sec}$

Scale Factor Uncertainty: typical 25 ppm

Gyro Noise: 0.1 deg/hr (1 second smoothing)

Filter Parameters

Initial Error Covariance $P(I, I)$, $I = 1, 2, 3$; 4×10^{-10} rad^2

                                  $P(I, I)$, $I = 4, 5, 6$; 4×10^{-14} $(rad/sec)^2$

State Noise Covariance $Q(I, I)$, $I = 1, 2, 3$; 1×10^{-11} rad^2

                                  $Q(I, I)$, $I = 4, 5, 6$; 1×10^{-18} $(rad/sec)^2$

Measurement Noise Covariance $R(I, I)$, $I = 1, 2$;   0.1 $\widehat{sec}^2$
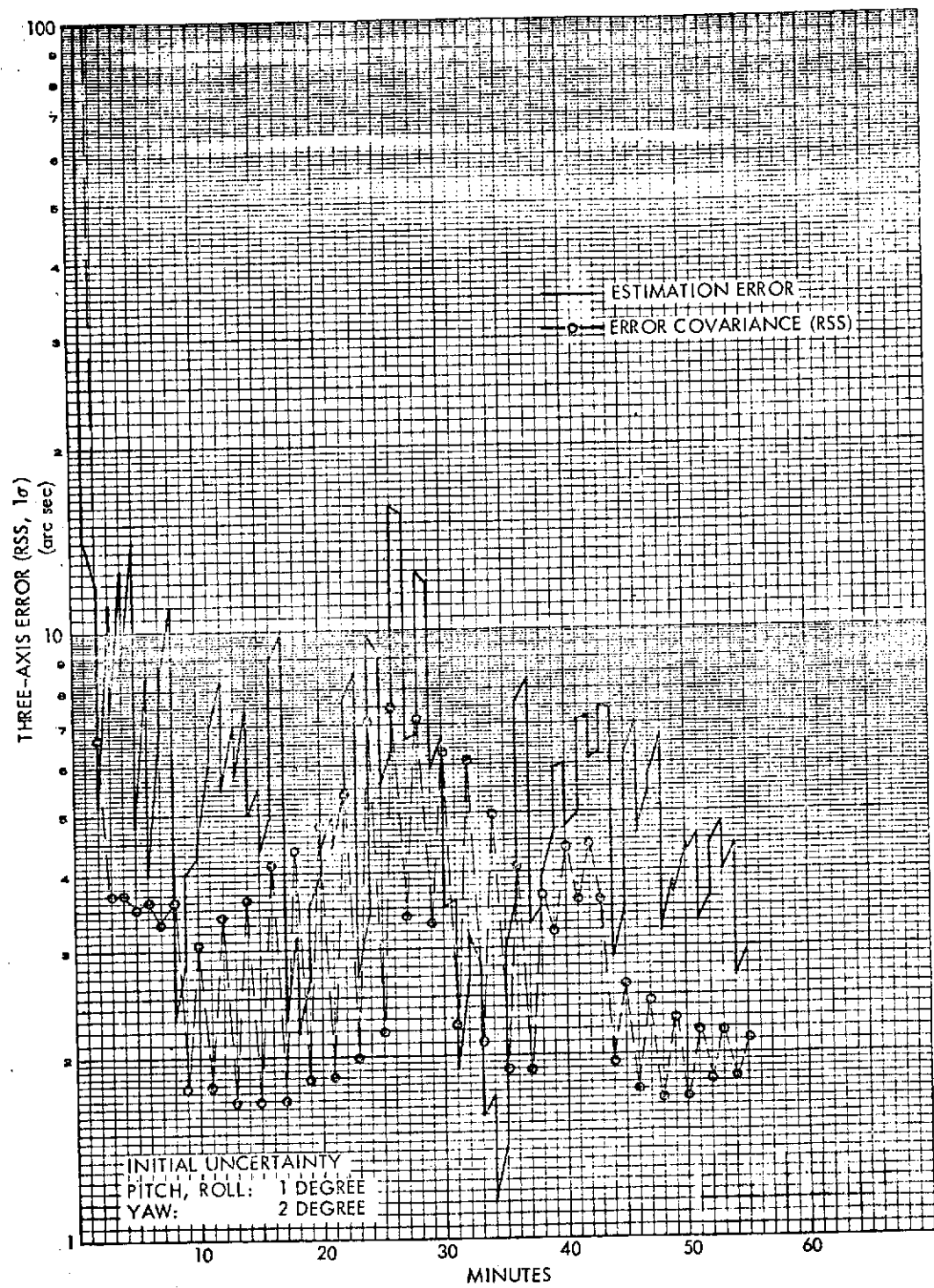
Figure 5-9. Attitude Determination Convergence (1 Minute Updates)
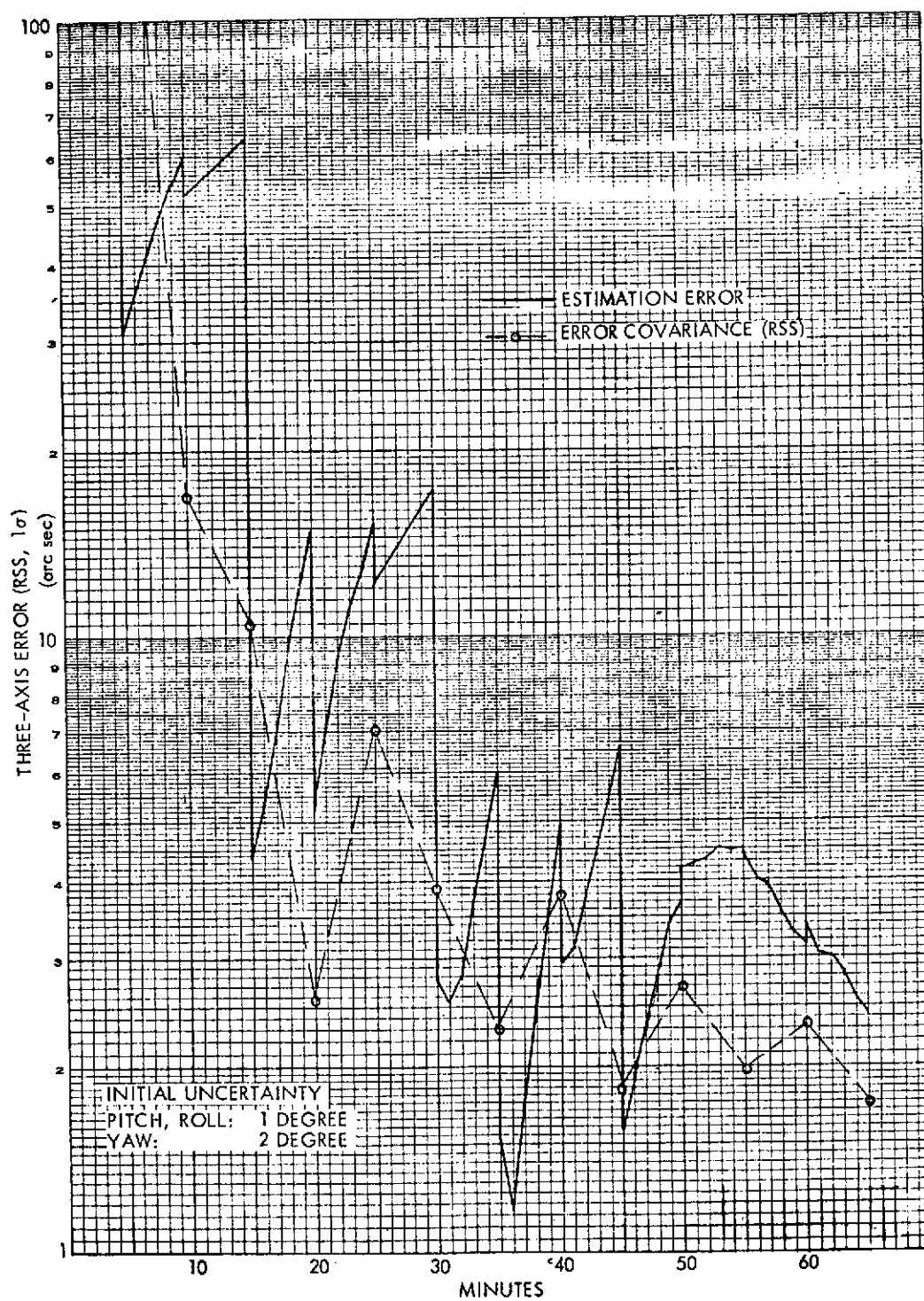
Figure 5-10. Attitude Determination Convergence (5 Minute Updates)
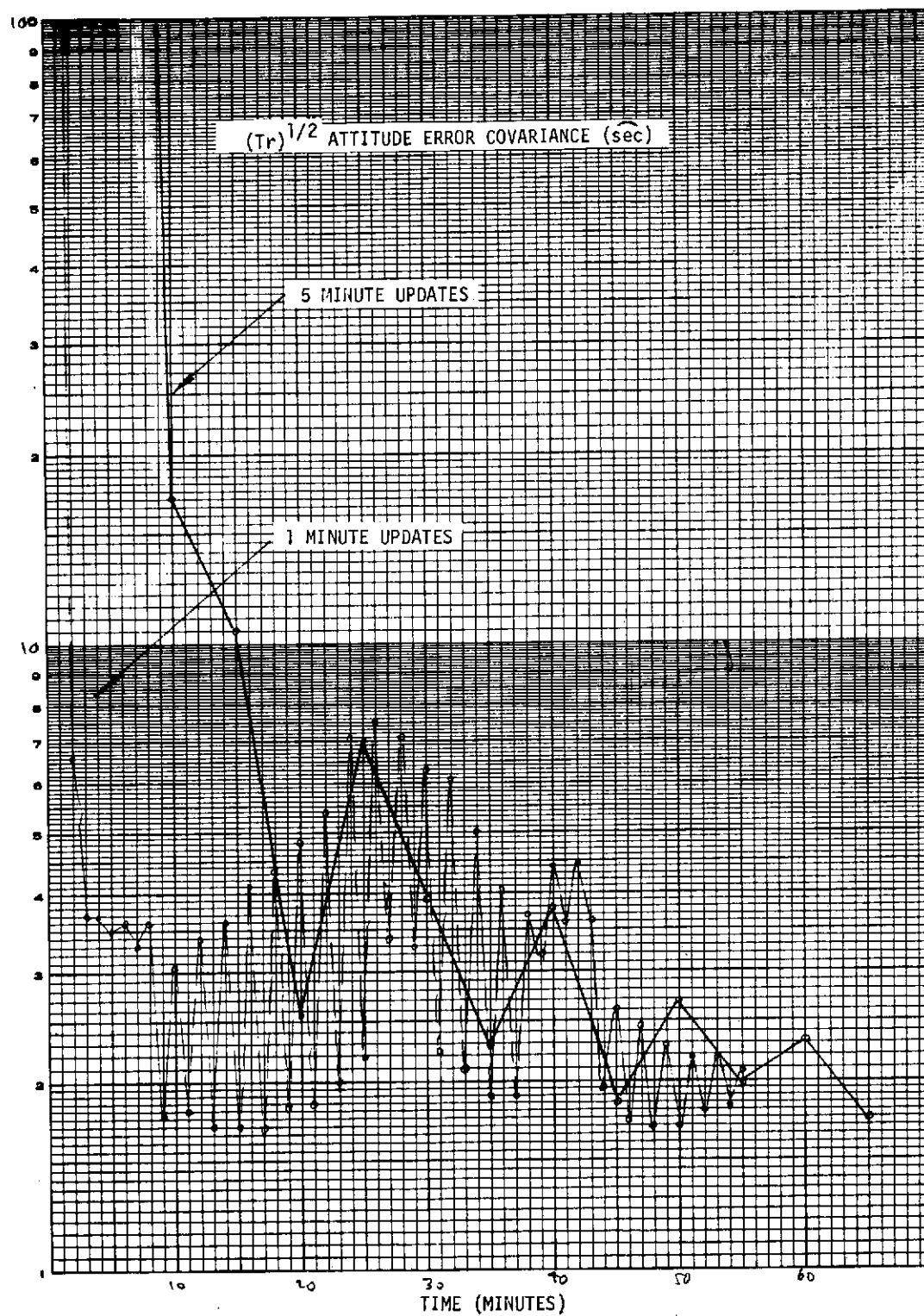
Figure 5-11.   Covariance Behavior During Initial Convergence

(15 minutes), but the behavior indicates that convergence to steady-state, overall, is apparently not greatly affected by the update interval. The interesting observed correlation in time of the error covariance suggests that convergence performance is more strongly tied to basic filter dynamics and orbit geometry than to the actual period between updates.

The baseline system steady-state run was initiated with an attitude estimation error of approximately 10 sec, resulting in an initial transient over the first few updates. The actual error correlates well with the error covariance (the filter estimate of the error), and the performance shown in Figure 5-12 also correlates well with error analysis, reaching a three-axis RSS steady-state value of 2-3 sec. Although not shown explicitly, the filter estimate of gyro bias was initiated as 0.05 deg/hr. The filter reduced this error by an order of magnitude with three filter updates.

5.4.2 Parameter Variation Studies

Parameter variation studies were conducted with the objective of determining the following performance characteristics:

- Evaluation of performance versus filter update interval

- Evaluation of star selection procedures/criteria

- Influence of gyro random drift

- Influence of sensor and readout noise

- Performance as influenced by selection of:
    - initial error covariance matrix
    - state noise covariance matrix
    - measurement noise covariance matrix

- Influence of sensor (hardware) alignment and bias errors

- Influence of initial conditions

Over 40 runs were taken with parameters varied as summarized in Table 5-4.

5.4.2.1 Benchmark System Performance

In conducting parameter variation studies, a benchmark system was defined early in the study from which effects of variations in system errors could be evaluated. The parameters defined for this benchmark case are summarized in Table 5-5. (Note that this represents only a benchmark, and not the final design whose performance was presented earlier.)

The performance which results is summarized in the time histories shown in Figures 5-13 and 5-14. Performance in each axis appears to be similar. Because
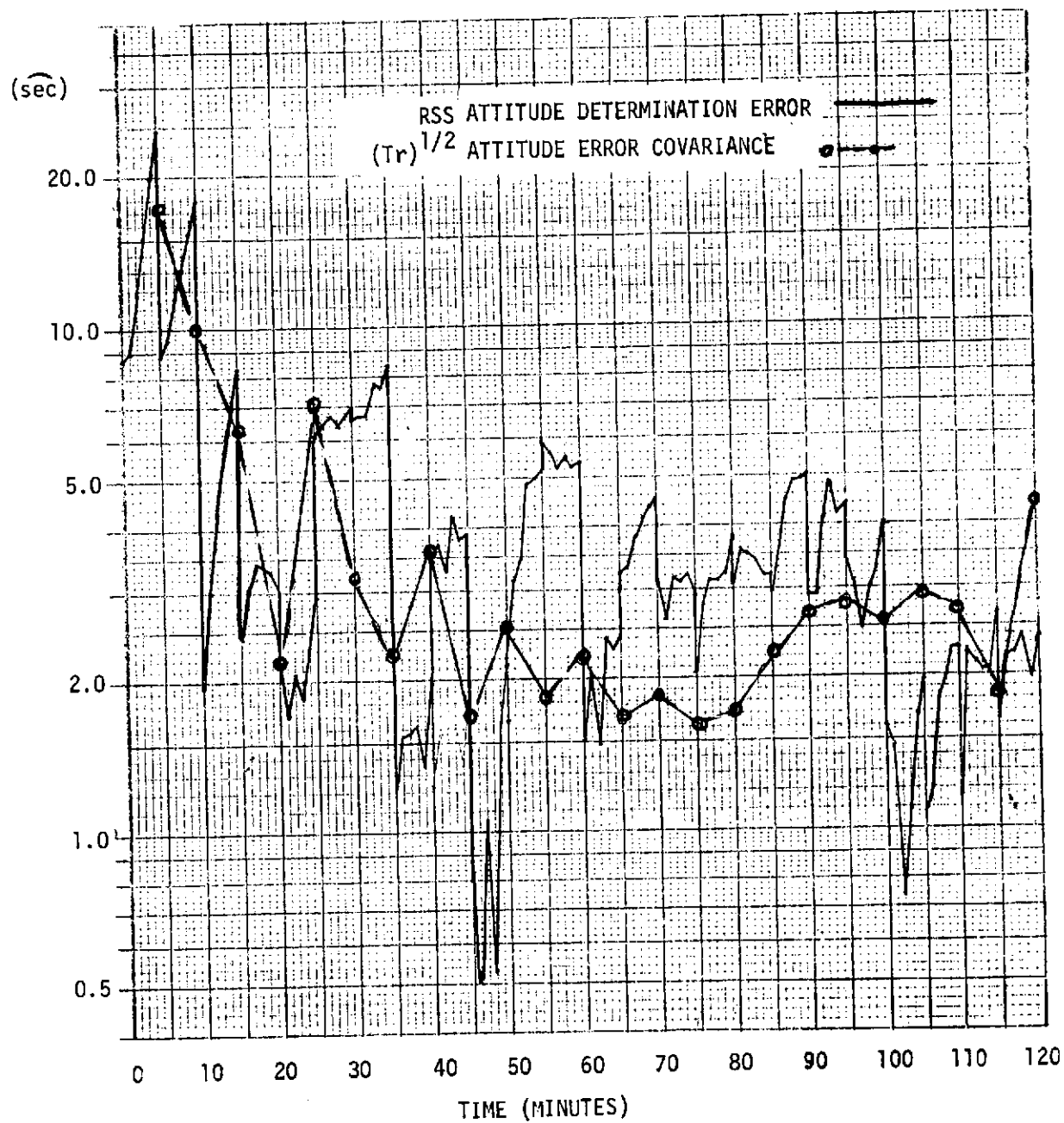
Figure 5-12. PPCS Baseline Performance (Steady-State)

Table 5-4 . Parameters Varied and Range

Initial Error Covariance Matrix

$P(I, I)$, $I = 1, 2, 3$: $4 \times 10^{-8} \ (rad)^2 \rightarrow 4 \times 10^{-12} \ (rad)^2$

$P(I, I)$, $I = 4, 5, 6$: $4 \times 10^{-12} \ (rad/sec)^2 \rightarrow 4 \times 10^{-16} \ (rad/sec)^2$

Sensor Noise

     $0.3 \ \widehat{sec} \rightarrow 1.0 \ \widehat{sec}$

Inductosyn Noise

     $0.5 \ \widehat{sec} \rightarrow 1.5 \ \widehat{sec}$

Gyro Noise

     $0 \rightarrow 2$ deg/hr

Update Period

     1 minute $\rightarrow$ 15 minutes

State Noise Covariance Matrix

     $Q(I,I)$, $I = 1,2,3$: $3 \times 10^{-11} \ (rad)^2 \rightarrow 1 \times 10^{-3} \ (rad)^2$

     $Q(I,I)$, $I = 4,5,6$: $1 \times 10^{-16} \ (rad/sec)^2 \rightarrow 1 \times 10^{-20} \ (rad/sec)^2$

Measurement Noise Covariance Matrix

     $0.1 \ \widehat{sec}^2 \rightarrow 10 \ \widehat{sec}^2$

Table 5-5 . Parameter Variation Benchmark Case

Orbit:

500 nm, high-noon, sun synchronous, 21 March

Altitude at perigee, 500 nm
Eccentricity, 0.001
. Inclination, 99.5 deg
Longitude of Ascending Mode, 0 deg
Argument of Perigee, 0 deg

Star Tracker Parameters:

Nominal Base Orientation: Boresight 45 deg above local horizon in pitch/
yaw plane, outer gimbal along roll

Gimbal Limits: $\pm$45 deg (outer), $\pm$15 deg (inner)

Misalignment of boresight axes: 0.3 $\widehat{sec}$ (outer), 0.2 $\widehat{sec}$ (inner)

Misalignment of gimbal base: Roll: 0.707 $\widehat{sec}$
                                  Pitch: 0.29 $\widehat{sec}$
                                    Yaw: 0.71 $\widehat{sec}$

Inner/outer axis perpendicularity, 0.5 $\widehat{sec}$

Inductosyn readout bias uncertinaty, 1 $\widehat{sec}$ (outer), -0.87 $\widehat{sec}$ (inner)

Runout Coefficients: 0.5 $\widehat{sec}$ (typical)

Inductosyn Readout: θ, 0.5 $\widehat{sec}$ (typical)
                       360θ, 0.1 $\widehat{sec}$ (typical)
                       720θ, 0.2 $\widehat{sec}$ (typical)

Sensor Noise: 0.3 $\widehat{sec}$ (each axis)

Inductosyn readout noise: 0.5 $\widehat{sec}$ (each axis)

Table 5-5 . Parameter Variation Benchmark Case (continued)

<u>Gyro Parameters</u>:

Drift bias (equivalent 3-axis), roll, 0.0052 deg/hr
                                     pitch, 0.029 deg/hr
                                       yaw,   -0.0196 deg/hr

Input axis misalignments, 0 sec

Scale factor uncertainty, 100 ppm (each gyro)

Gyro noise, 0.206 deg/hr

<u>Filter Parameter</u>: Update Period, 5 minutes

Initial Attitude Estimation Error: 7.6 sec (roll), -3.95 sec (pitch),
1.5 sec (yaw)

Initial Gyro Bias Estimation Error: 0.0052 deg/hr (roll), 0.029 deg/hr (pitch),
-0.0196 deg/hr (yaw)

Initial Attitude Error Covariance: $P(I, I)$, $I = 1, 2, 3$; 4×10^{-10}

Initial Gyro Bias Covariance: $P(I, I)$, $I = 4, 5, 6$; 4×10^{-14}

State Noise Covariance: $Q(I, I)$, $I = 1, 2, 3$; 3×10^{-12}

                        $Q(I, I)$, $I = 4, 5, 6$; 1×10^{-18}

Measurement Noise Covariance $R(1, 1) = R(2, 2) = 1.0$ sec

                        $R(1, 2) = R(2, 1) = 0$
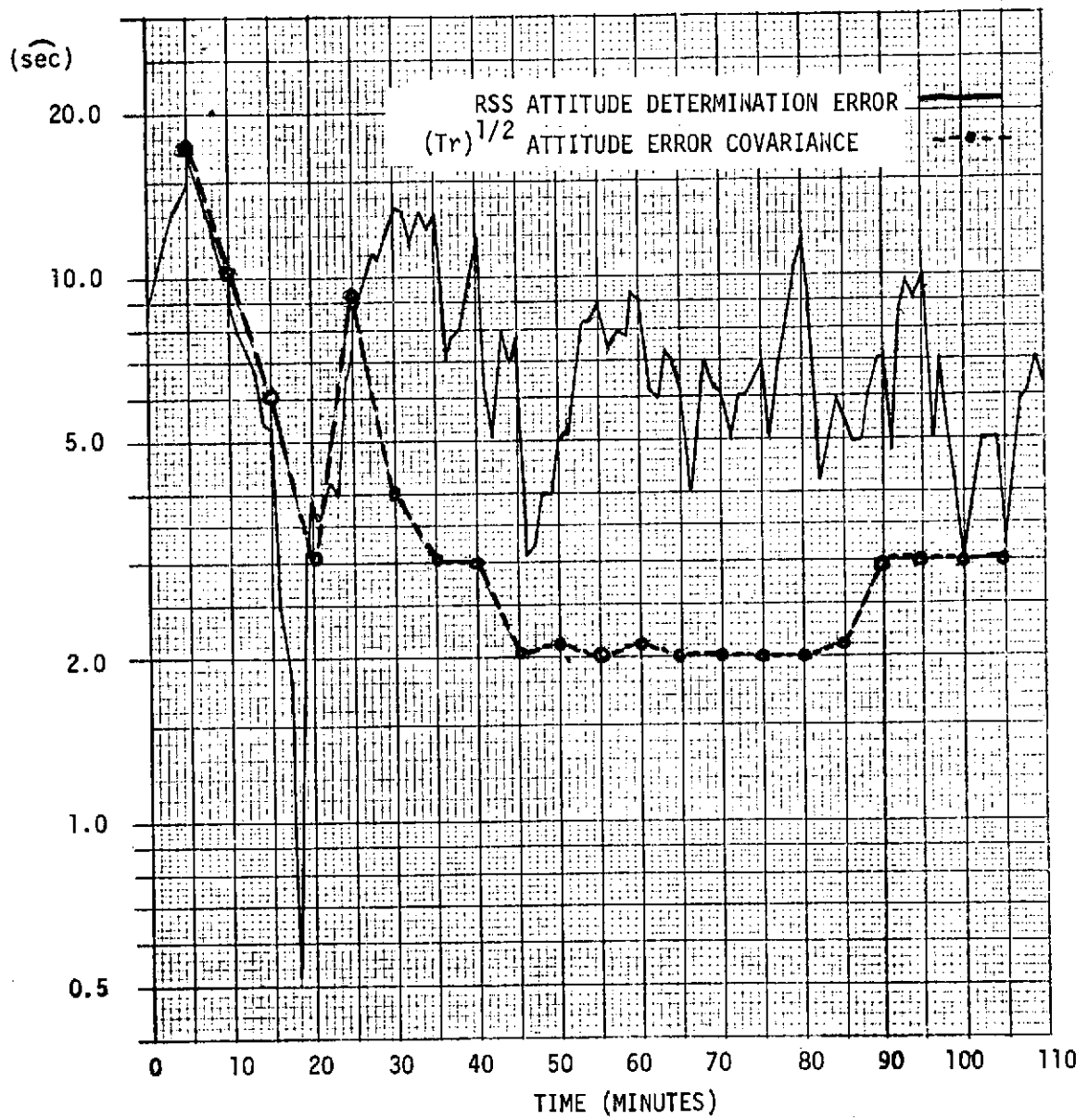
Figure 5-13. Benchmark Performance (Three-Axis RSS)
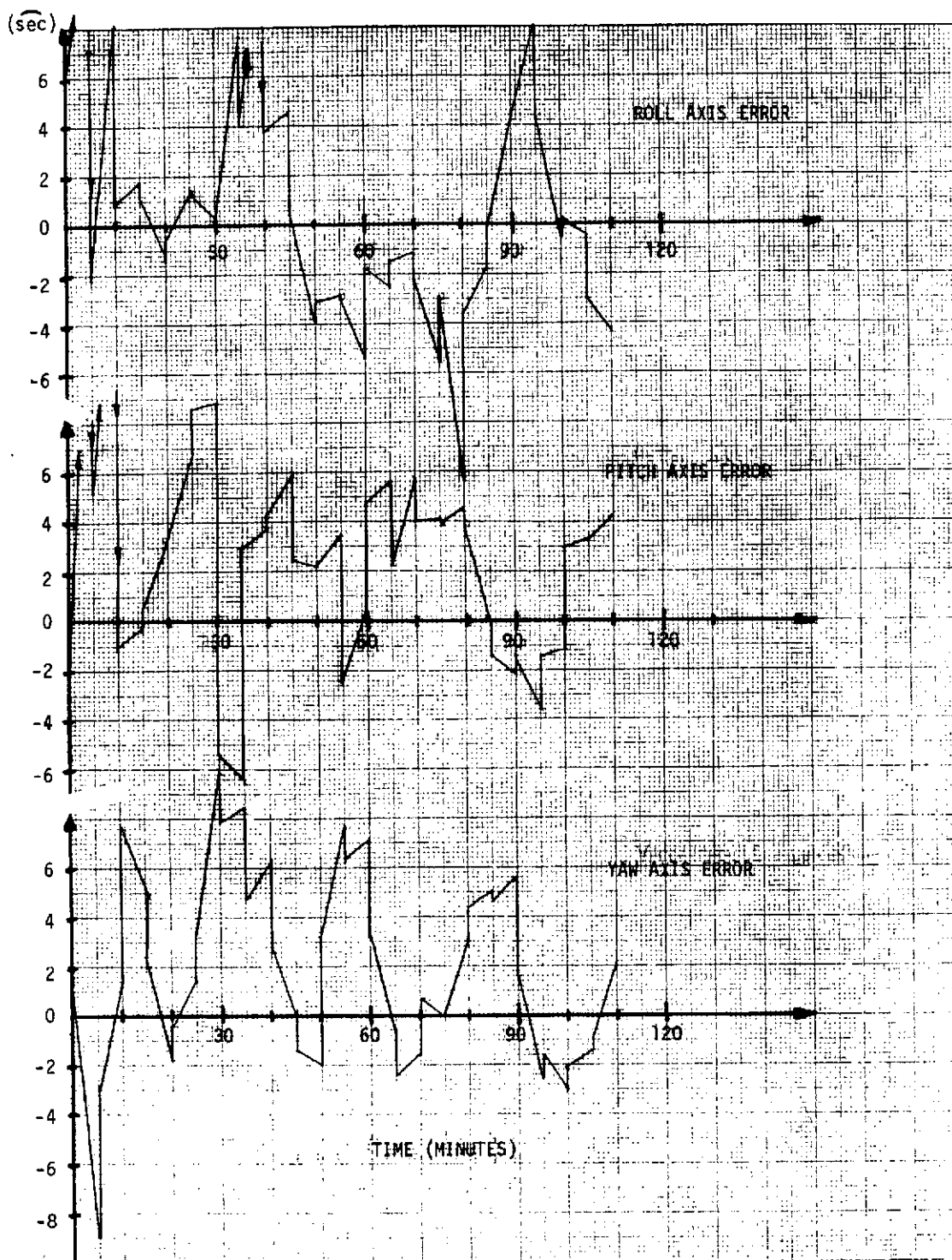
Figure 5-14. Benchmark Performance (Each Axis)

the initial attitude uncertainty was small, there is no dramatic covergence behavior exhibited. A three-axis RSS steady-state estimation error of approximately 6 $\widetilde{sec}$ results. The three-axis error covariance measure oscillates some initially, but the transient damps quickly with a steady-state value on the order of 2-3 $\widehat{sec}$. It is noted, Table 5-6, that this covariance error appears dominated by the term which corresponds to the pitch axis, i.e., the filter is least certain about the pitch estimate. This can be seen by observing the error covariance matrix at the end of the simulated run, P_F, and considering the relative magnitude of the term P_{22} which (for the associated geometry) corresponds closely to the value for pitch. It is also of interest to note that the other values of the final error covariance matrix are of the same order as the elements of the Q-matrix, indicating that the elements of Q are probably contributing significantly to the lower bound of the values of P.

5.4.2.2 Initial Error Covariance Variation Studies

Sensitivity of performance to selection of initial values of the error covariance matrix was studied through a series of simulation runs where initial attitude and gyro bias covariance terms were varied without modification of the initial errors. A summary of the parameter variation matrix is given in Table 5-7. The results from these runs are summarized in Figure 5-15, normalized to the case where selection of the initial covariance corresponds to the actual initial and bias uncertainties.

System performance appears most sensitive to the gyro bias covariance. Since the gyro bias is important during periods between updates, a good estimate is key. The covariance matrix converges very rapidly, as can be seen from the time histories, and the filter solution for the gyro bias proceeds at a somewhat slower rate. Thus it is helpful to raise the initial bias uncertainty to enhance more accurate solution. The larger the initial value of the bias covariance terms, the greater opportunity the filter may have to make meaningful corrections to the gyro bias estimates. Sensitivity to attitude covariance appears small, although a slight trend is evident from the results. The trend indicates that a somewhat optimistic estimation of initial error covariance is warranted where the gyro bias covariance is also optimistic. However, a conservative selection of attitude error covariance seems to desensitize the system somewhat to the gyro bias covariance selection without much impact on performance. This latter point, plus the fact that initial attitude uncertainty was small, leads one to adopt a design practice of conservative selection of elements of the initial error covariance matrix.

Selected runs are shown in Figures 5-16 through 5-19, with little observed difference in performance. The time behavior of the attitude error RSS variance is

Table 5-6. Benchmark Covariance Matrices

Initial Error Covariance Matrix:

$$
P_o = \begin{bmatrix}
4 \times 10^{-10} & & & & & \\
 & 4 \times 10^{-10} & & & & \\
 & & 4 \times 10^{-10} & & & \\
 & & & 4 \times 10^{-14} & & \\
 & & & & 4 \times 10^{-14} & \\
 & & & & & 4 \times 10^{-14}
\end{bmatrix}
$$

"Steady-State" Error Covariance Matrix:

$$
P_F = \begin{bmatrix}
4 \times 10^{-12} & 2 \times 10^{-12} & 4 \times 10^{-13} & & & \\
2 \times 10^{-12} & 2 \times 10^{-11} & -3 \times 10^{-12} & & & 10^{-15} \\
4 \times 10^{-13} & -3 \times 10^{-12} & 4 \times 10^{-12} & & & \\
 & & & 2 \times 10^{-17} & & \\
 & & & & 3 \times 10^{-17} & \\
 & 10^{-15} & & & & 2 \times 10^{-17}
\end{bmatrix}
$$

State Noise Covariance Matrix

$$
Q = \begin{bmatrix}
3 \times 10^{-12} & & & & & \\
 & 3 \times 10^{-12} & & & & \\
 & & 3 \times 10^{-12} & & 0 & \\
 & & & 1 \times 10^{-17} & & \\
 & & & & 1 \times 10^{-17} & \\
 & 0 & & & & 1 \times 10^{-17}
\end{bmatrix}
$$

Table 5-7   Error Covariance Parameter Variation Summary

P(I,I), I = 1,2,3	P(I,I), I = 4, 5, 6
4×10^{-8} (1700 $\widehat{\sec}^2$)	4×10^{-12} ($\cong 0.17$ $(\frac{deg}{hr})^2$)
4×10^{-8}	4×10^{-14} ($\cong 0.0017$ $(\frac{deg}{hr})^2$)
4×10^{-9} (170 $\widehat{\sec}^2$)	4×10^{-13} ($\cong 0.017$ $(\frac{deg}{hr})^2$)
4×10^{-9}	4×10^{-14}
4×10^{-10} (17 $\widehat{\sec}^2$)	4×10^{-12}
4×10^{-10}	4×10^{-13}
4×10^{-10}	4×10^{-14}
4×10^{-10}	4×10^{-15} ($\cong 0.00017$ $(\frac{deg}{hr})^2$)
4×10^{-10}	4×10^{-16} ($\cong 0.000017$ $(\frac{deg}{hr})^2$)
4×10^{-11} (1.7 $\widehat{\sec}^2$)	4×10^{-14}
4×10^{-11}	4×10^{-15}
4×10^{-12} (0.17 $\widehat{\sec}^2$)	4×10^{-14}
4×10^{-12}	4×10^{-16}

(True) initial attitude uncertainty:
    Roll, 7.63 $\widehat{\sec}$; Pitch, -3.95 $\widehat{\sec}$; Yaw, 1.46 $\widehat{\sec}$

(True) initial bias uncertainty:
    Roll, 0.0052 deg/hr; Pitch, 0.029 deg/hr; Yaw, -0.0196 deg/hr

Normalized Steady-State Error
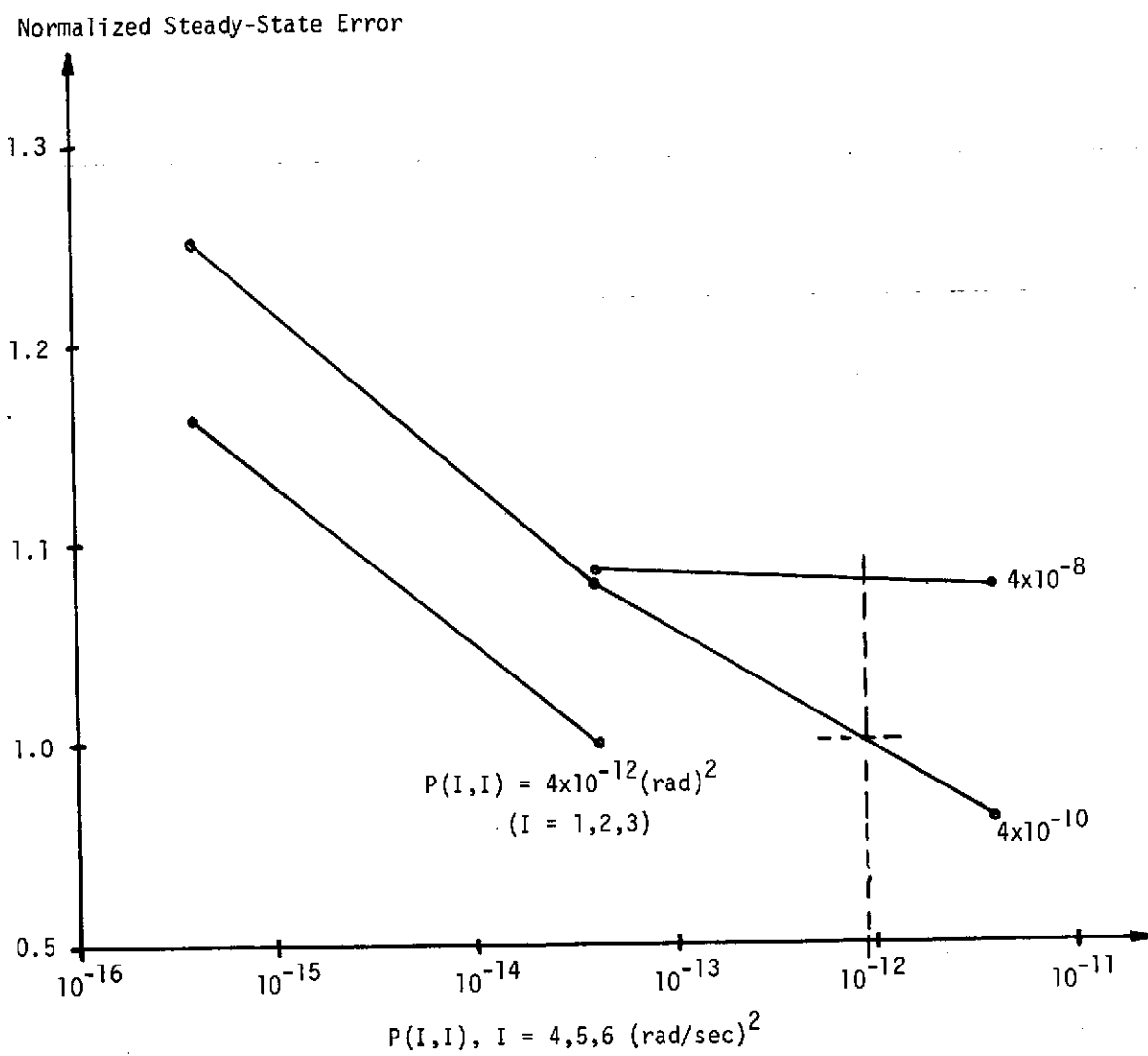
Figure 5-15. Summary of Error Covariance Variations
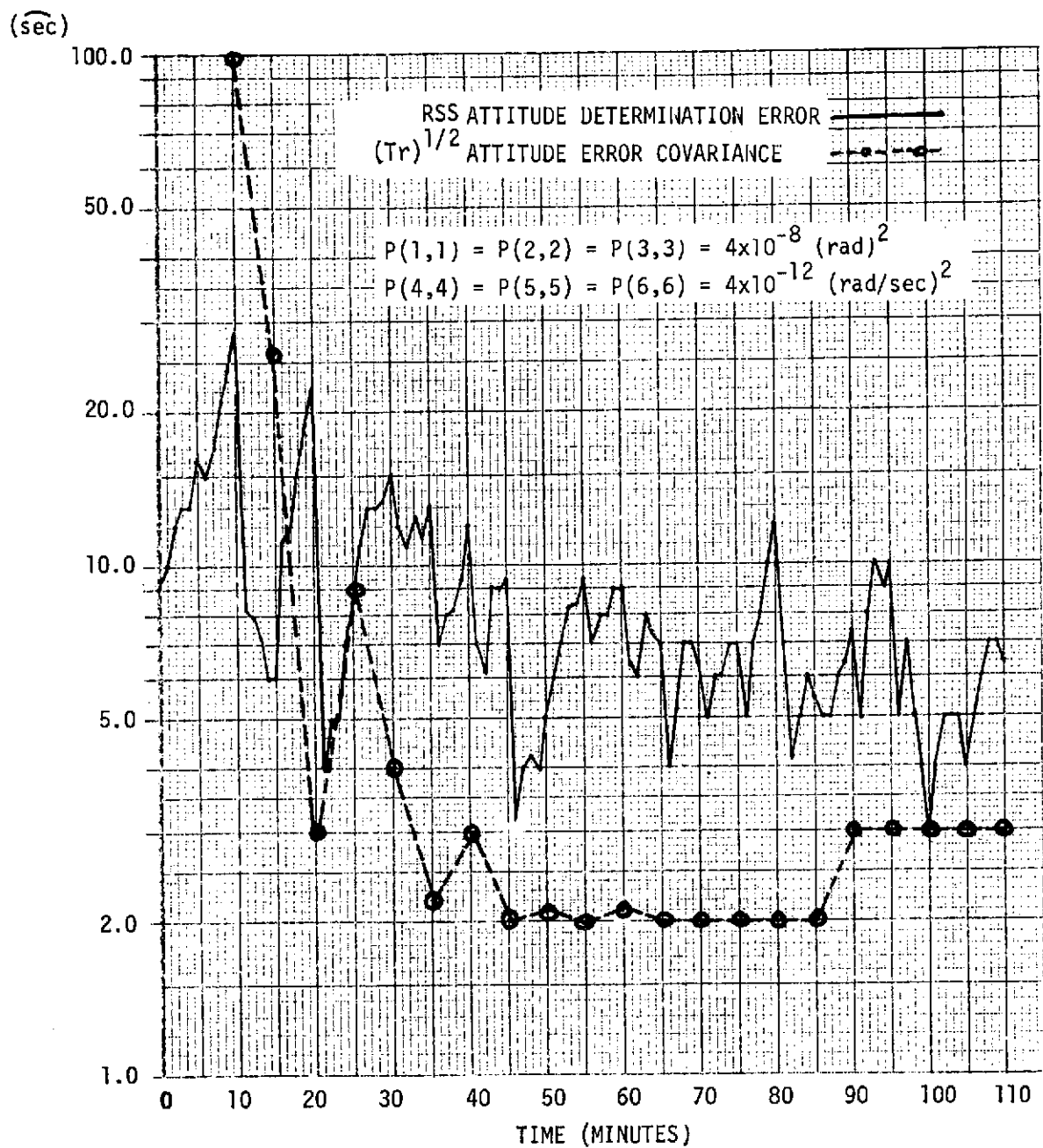
Figure 5-16. Error Covariance Variation Run
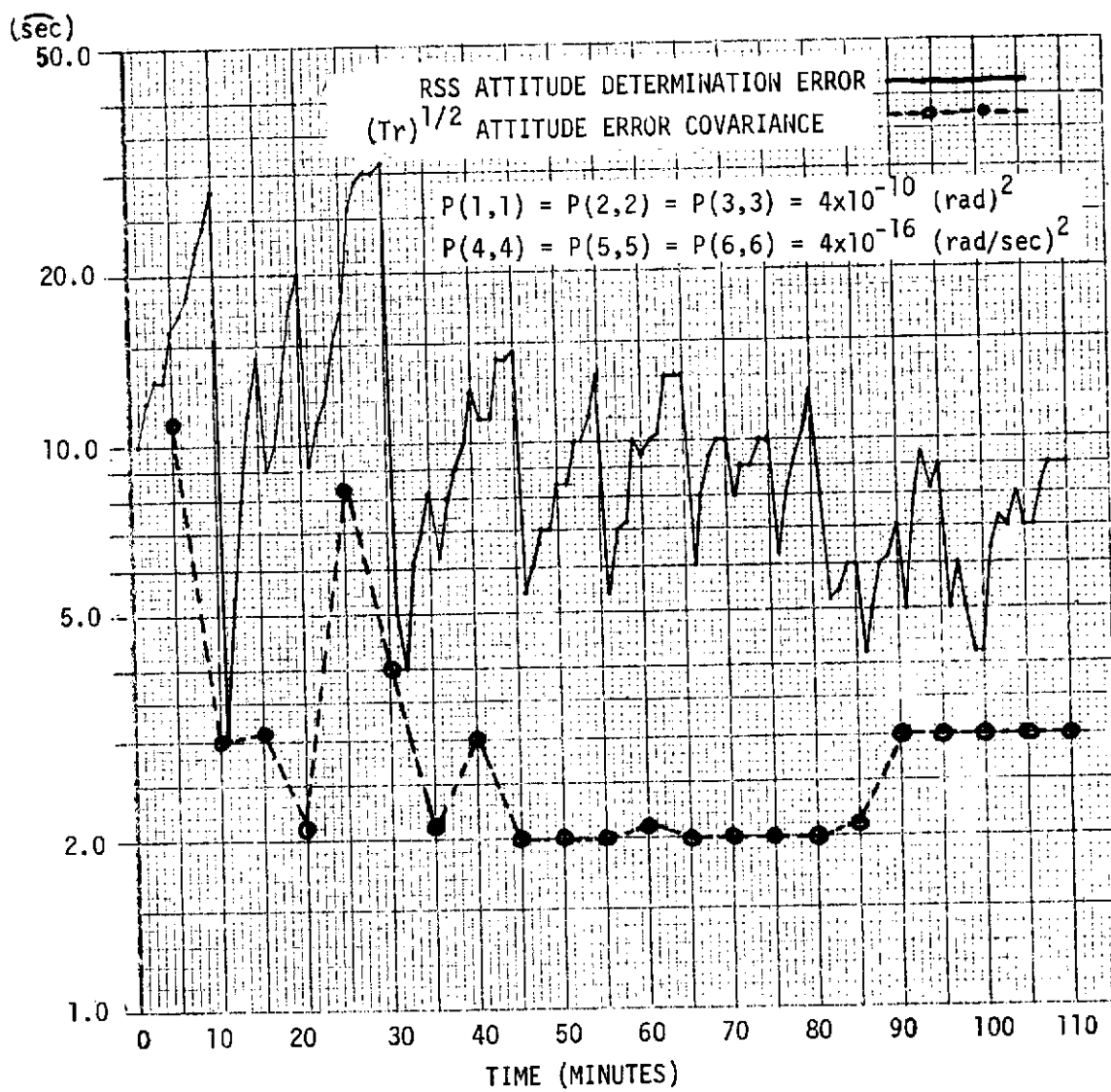
Figure 5-17. Error Covariance Variation Run
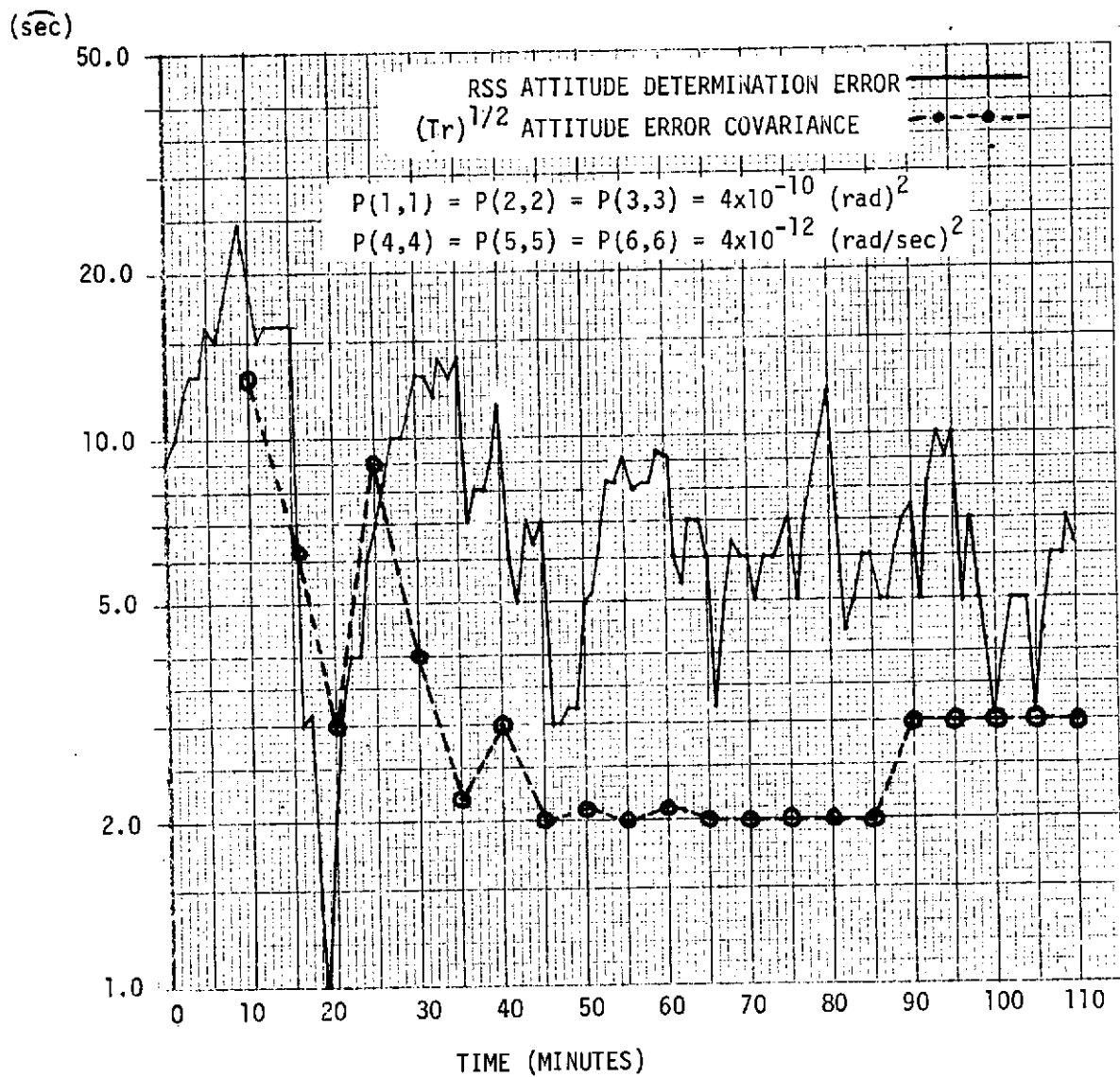
Figure 5-18. Error Covariance Variation Run
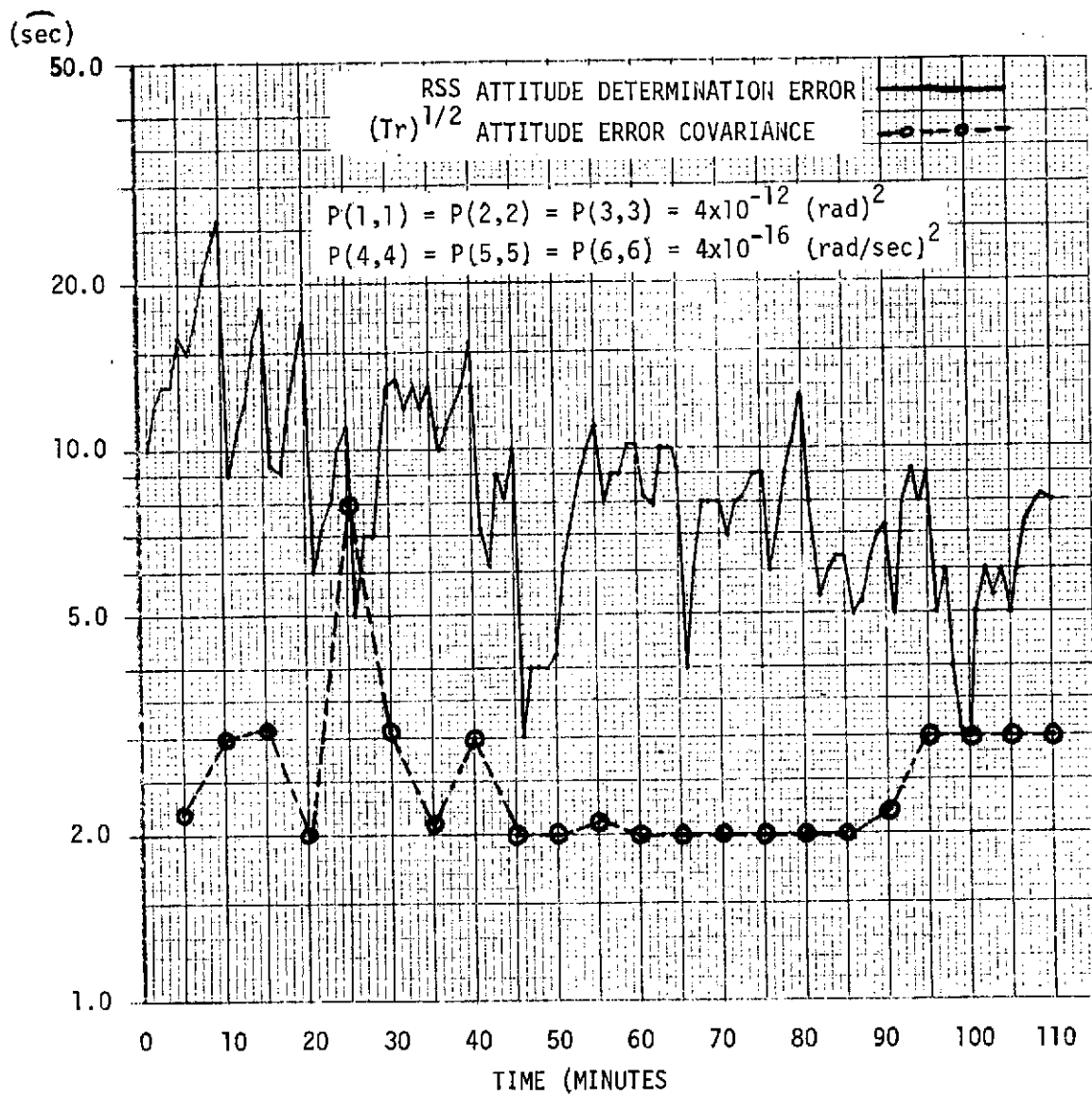
Figure 5-19. Error Covariance Variation Run

is of interest. Note that after the initial transient (on the order of several update periods) the error covariance is virtually identical independent of the initial value. This behavior is keyed strongly to the state noise covariance and measurement noise covariance, as will be seen in later cases.

5.4.2.3 Measurement Noise/Noise Covariance Variation Studies

Sensitivity to sensor noise, Inductosyn readout noise, and selection of the measurement noise covariance matrix was determined through a series of runs (summarized in Table 5-8) which varied all parameters in combinations. The results can be summarized by considering the influence of these parameters on estimation error as shown in Figure 5-20, where the results were normalized to the case where selection of the initial covariance of unity (i.e., 1.0) most closely corresponds to the actual noise (the case of σ_{nRSS} = 1.12 $\widehat{sec}$). The results are quite interesting. It is reflected that, in general, one may find performance slightly improved by selection of an optimistic value for the noise covariance matrix and potentially significant degradation through selection of a conservative value for the measurement noise covariance. Note that the nominal point(i.e., Q≈1) for the three curves where σ_n > 1.0 $\widehat{sec}$ represent quite similar behavior. The fourth curve represents markedly different behavior because the nominal covariance value is considerably changed from the other cases, i.e., Q ≈ 0.3

The measurement noise covariance matrix, somewhat independent of actual sensor measurement noise, appears to play a key role in establishing the performance characteristics. This can be seen by considering the time histories of the attitude error covariance depicted in Figure 5-21. As a result of the error covariance being significantly increased (factor of 3) through a change of two-orders-of magnitude in the measurement noise covariance, the attitude estimates are assumed by the filter to have less certainty and are less influenced by additional measurements that would actually tend to reduce the error. Looking at the actual performance of several runs summarized in Figures 5-22 through 5-25, the time history among the various runs does not differ greatly. It is also of interest to notice that the error covariance does not provide a good observable measure of system performance for these cases, i.e., the error covariance indicates performance a factor of two or three better than that achieved. Thus, a certain amount of caution must be used in applying good judgement to the externally observed performance, i.e., to the filter derived statistics.

5.4.2.4 Gyro Noise/State Noise Covariance Variation Studies

This section presents the performance tradeoffs associated with effects of short-term gyro random drift and selection of elements of the state noise covariance matrix. Three areas are considered, namely: characteristics of gyro drift (noise) model, gyro noise variations, and noise covariance variations.

Table 5-8. Summary of Runs

Measurement Noise Covariance	SSU Noise	Inductosyn Noise
W(1,1) = W(2,2) = 0.1		
	0.3	0.5
	0.3	1.5
	1.0	0.5
	1.0	1.5
W(1,1) = W(2,2) = 1.0		
	0.3	0.5
	0.3	1.5
	1.0	0.5
	1.0	1.5
W(1,1) = W(2,2) = 10.0		
	1.0	0.5
	1.0	1.5
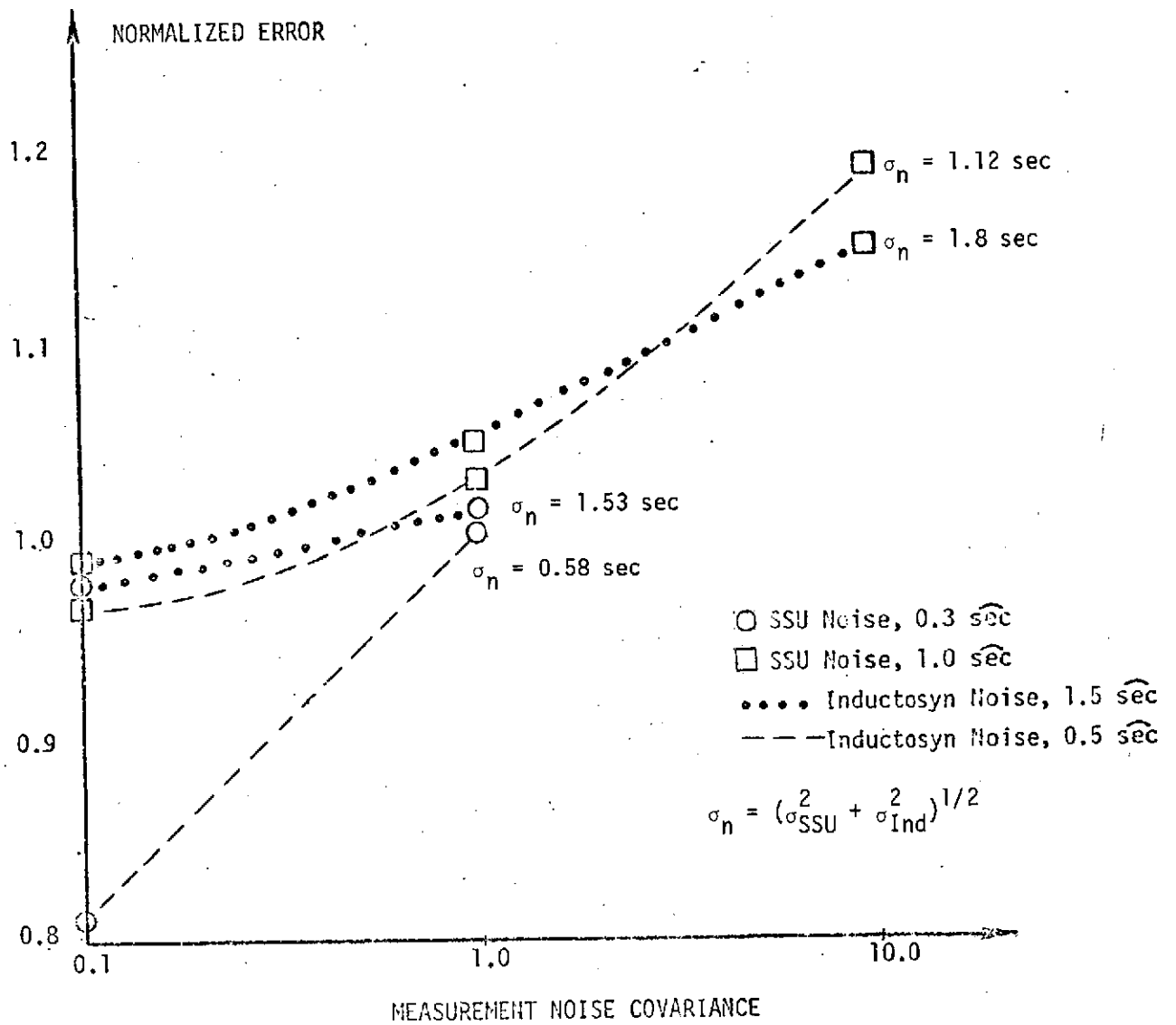
Figure 5-20. Measurement Noise Sensitivity
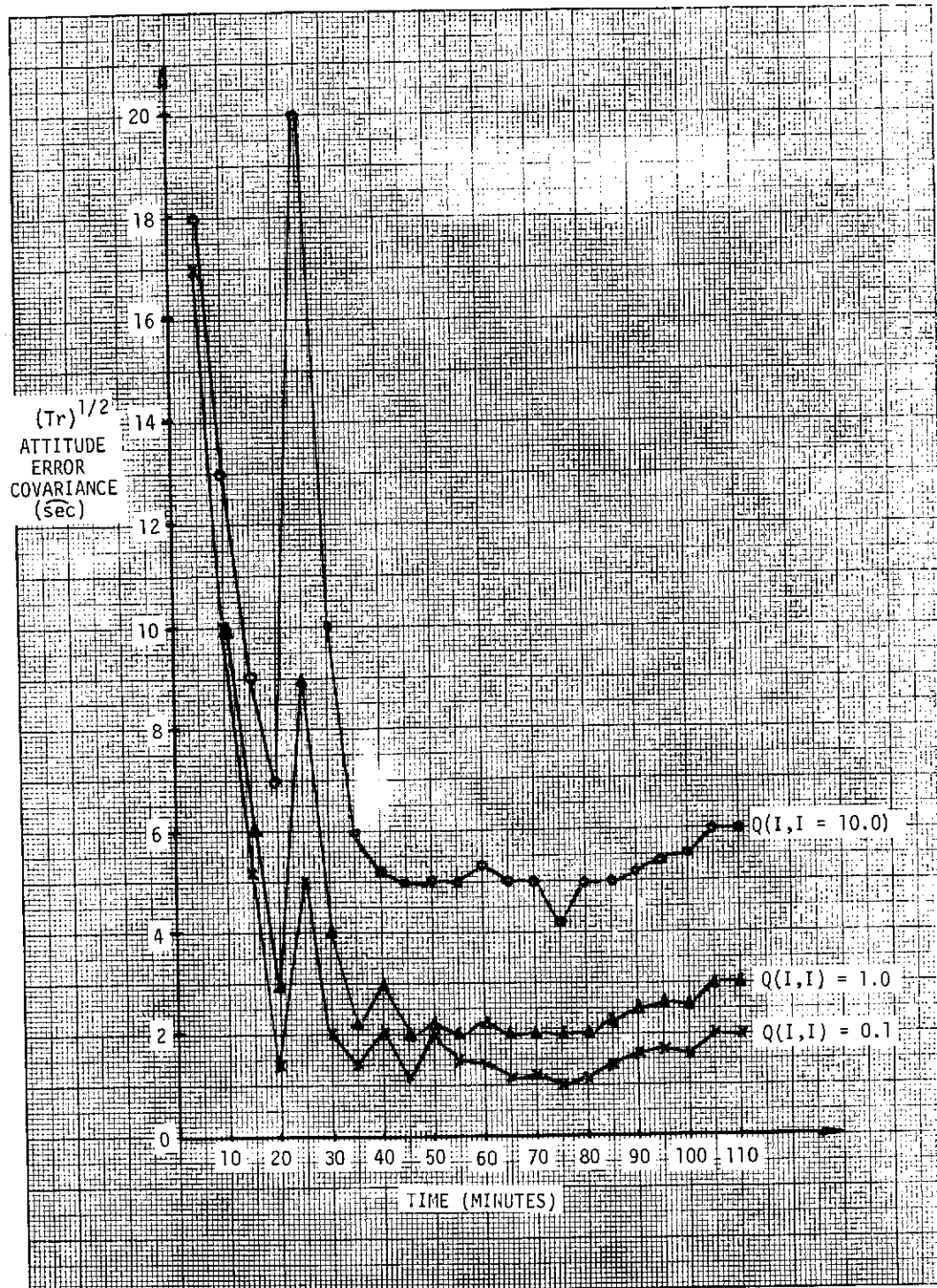
Figure 5-21. Influence of Measurement Noise Covariance on
Attitude Covariance Behavior
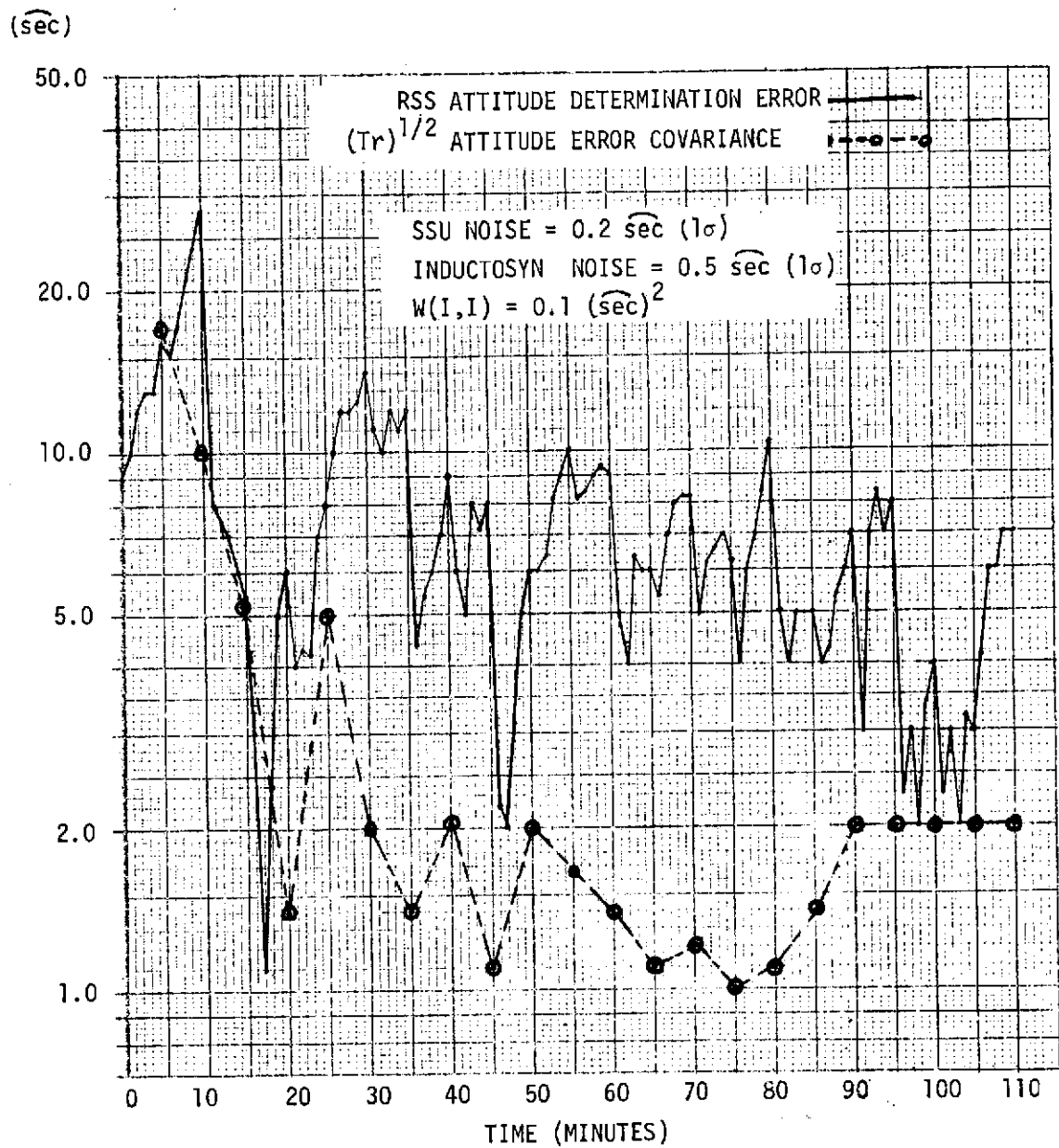
Figure 5-22. Measurement Noise/Noise Covariance Variation Run
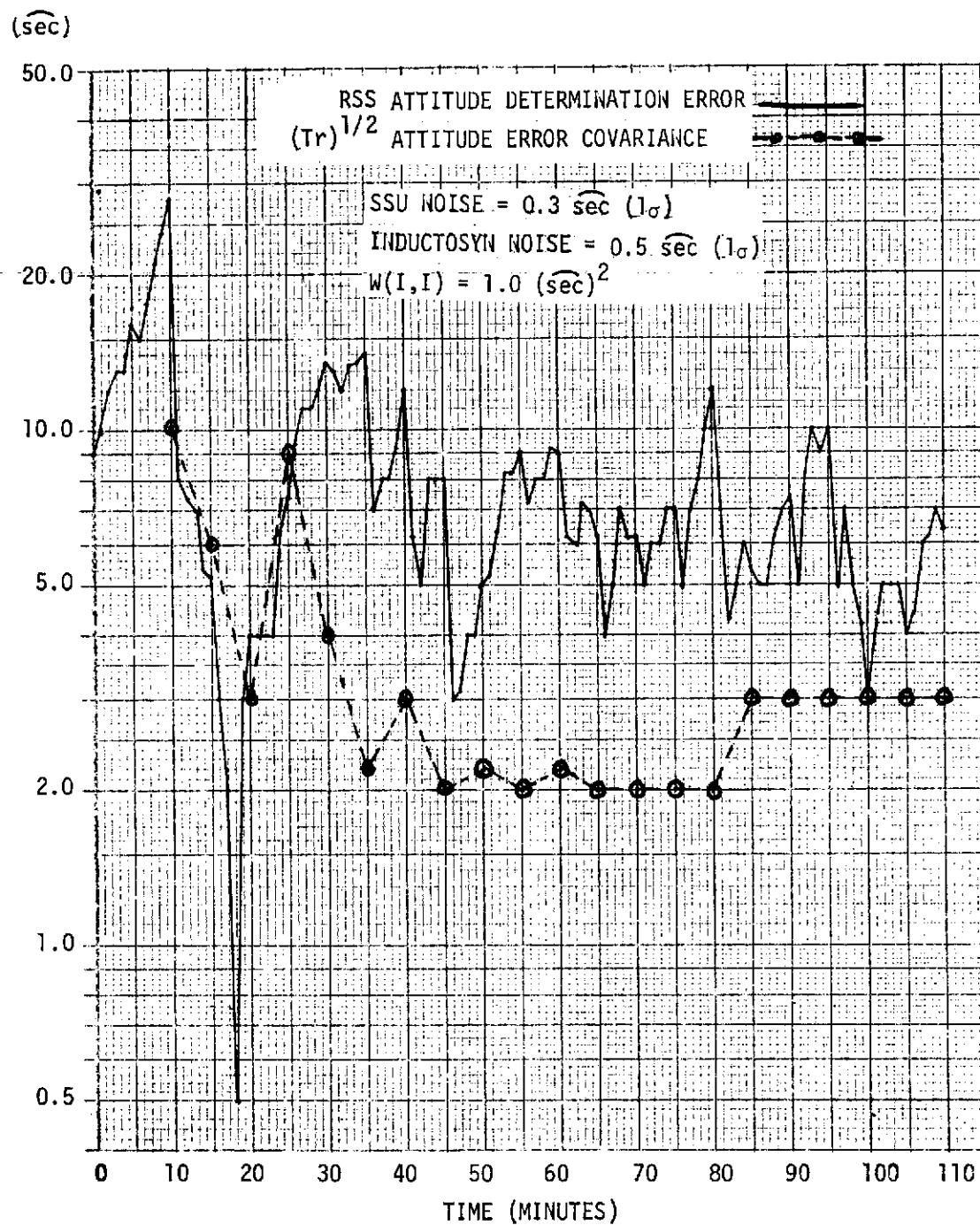
Figure 5-23. Measurement Noise/Noise Covariance Variation Run
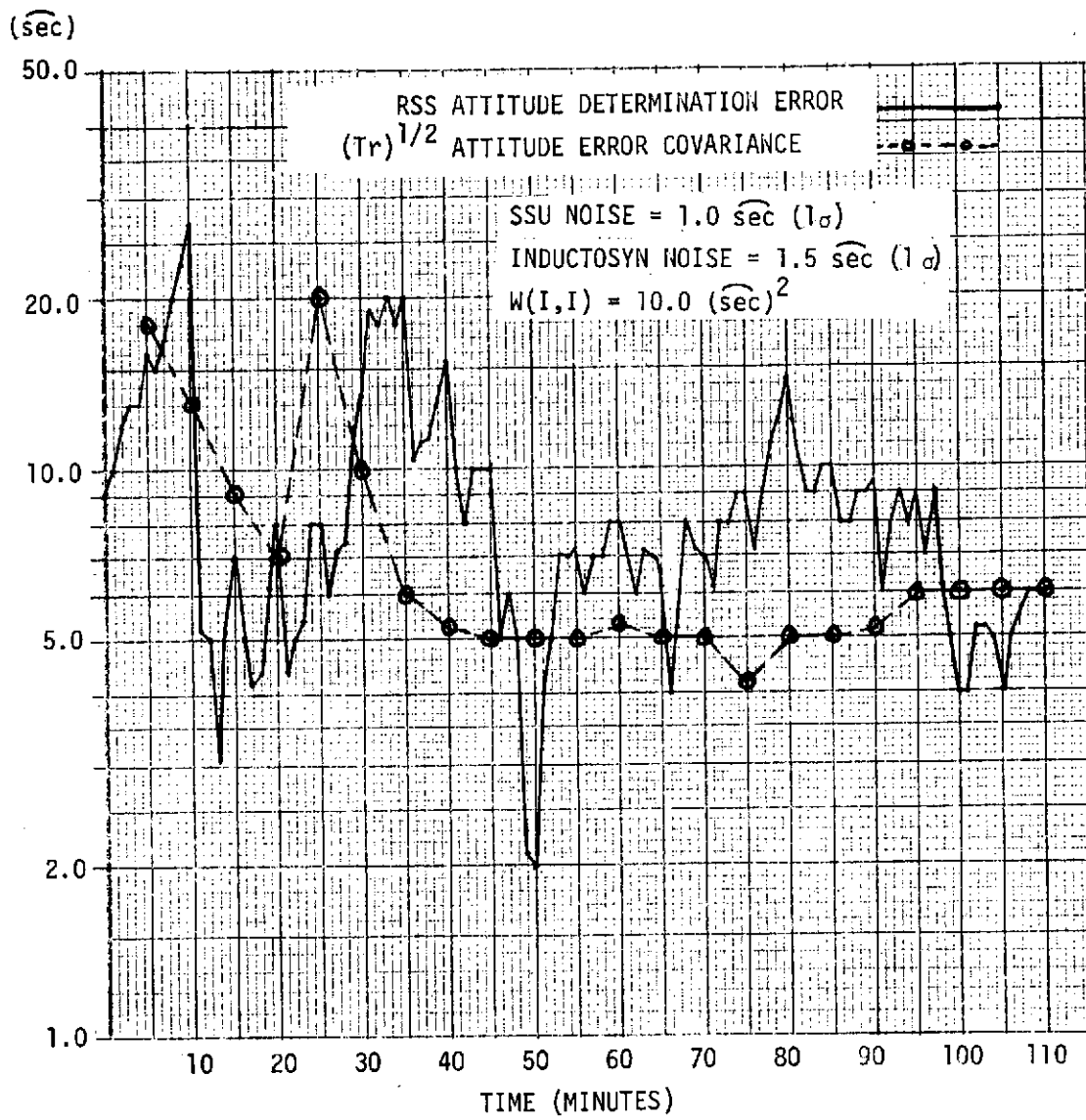
Figure 5-24. Measurement Noise/Noise Covariance Variation Run
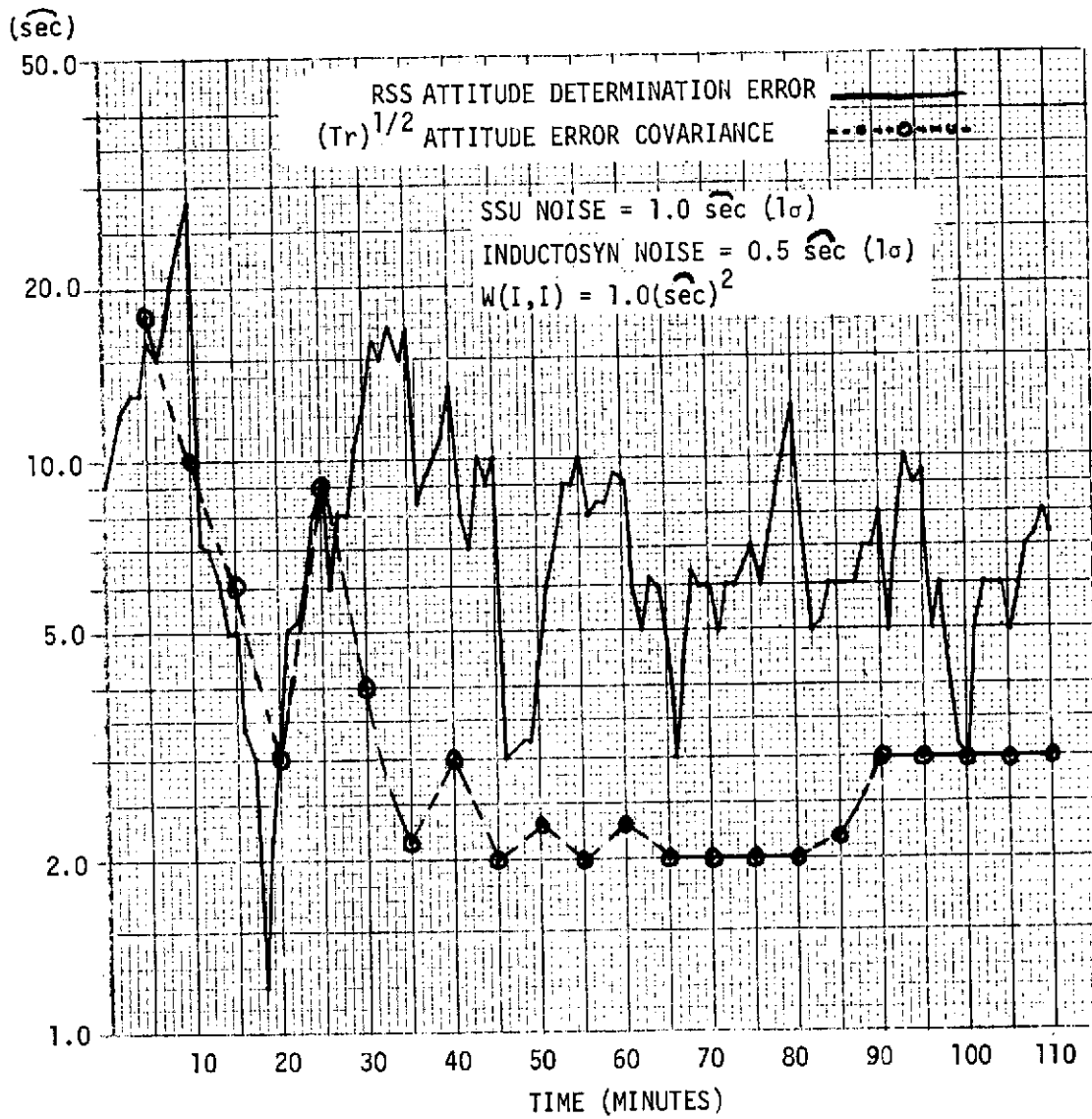
Figure 5-25.   Measurement Noise/Noise Covariance Variation Run

Gyro Noise Model

The short-term gyro random drift has been modelled by equivalent white noise. This noise term can be considered in either of two ways, namely: as the equivalent rate noise that results from deriving rate from a noisy attitude increment, $\Delta\theta$, or as the noise that, when propagated, yields the appropriate attitude variance just prior to update. One might argue that these should, in fact, be the same. However, it is observed from data that different phenomena may govern the noise statistical characteristics as seen over the integration period (200 ms) as opposed to those observed over the update period (nominally 5 minutes). Thus, a variety of gyro noise values have been investigated to understand influence of this key parameter.

It is of interest to consider the results of test data in establishing the values for gyro noise to be used in the simulation. Test data available from both the Nortronics GI-K7G and Honeywell GG-333Agas bearing gyros (see also Section 6.3) presented in Figure 5-26. It is noted that the integration step (used in the simulation only) is 1 second. This was done to conserve computation time/cost. Thus, it is the 1 second smoothing (averaging period) data that is of interest. The data shows values in the range of 0.04 to 0.1 deg/hr. During simulation, values primarily used were in the range of 0.02 to 0.2 deg/hr.

Gyro Noise Variation

Sensitivity of the system to gyro short-term random drift (noise) was evaluated by another series of simulation runs. The standard deviation in the white noise model for short term gyro noise was varied over several orders of magnitude. The effect was very dramatic, accentuated by the fact that the state noise covariance matrix was maintained at a fixed value for all runs. That value was analytically derived based upon six gyros, each with short-term random drift of 0.0033 deg/hr (over a 5 min smoothing time). This corresponds approximately to 0.057 deg/hr over a 1 second smoothing time. The results can be seen in Figure 5-27. As shown, an increase of an order of magnitude in noise causes the estimation accuracy to degrade by a factor of 2, an increase of 2 orders of magnitude degrades accuracy by a factor of more than 16. Again, it is noted that when the proper statistics are not provided to the filter, the attitude error covariance shows very poor correlation with the actual performance of the filter. The simulation time histories are presented in Figures 5-28 through 5-31.

State Noise Covariance Matrix Variations

Sensitivity of the filter to selection of the elements of the state noise covariance matrix was evaluated by a further series of simulation runs. In this
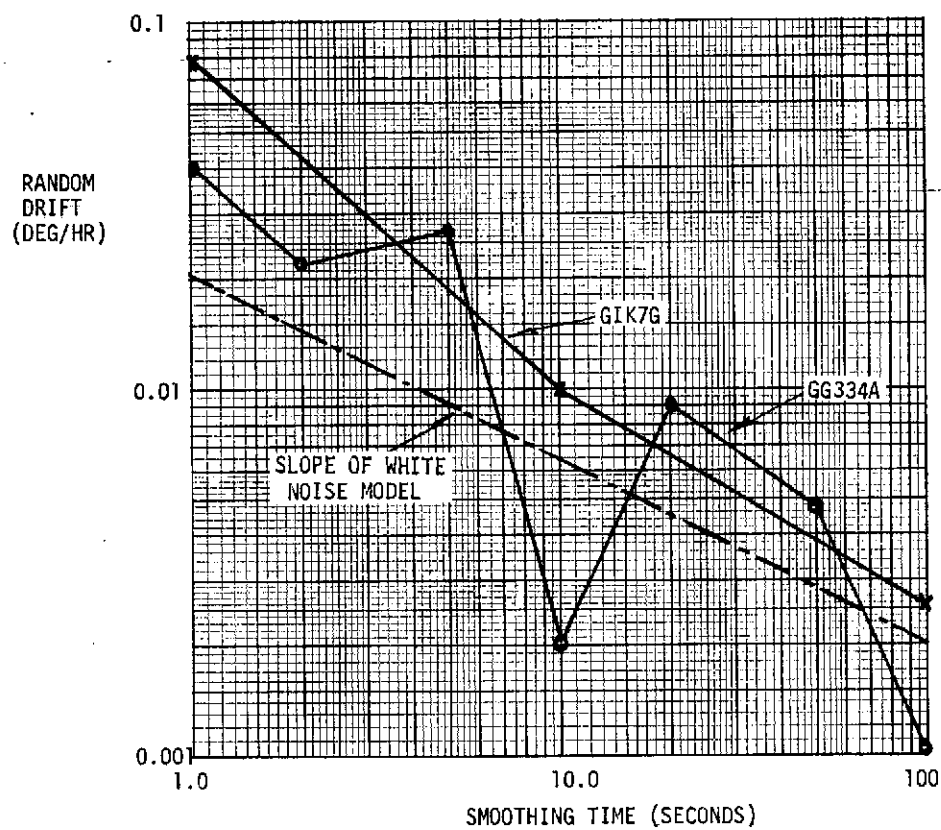
Figure 5-26. Gyro Random Drift Characteristics
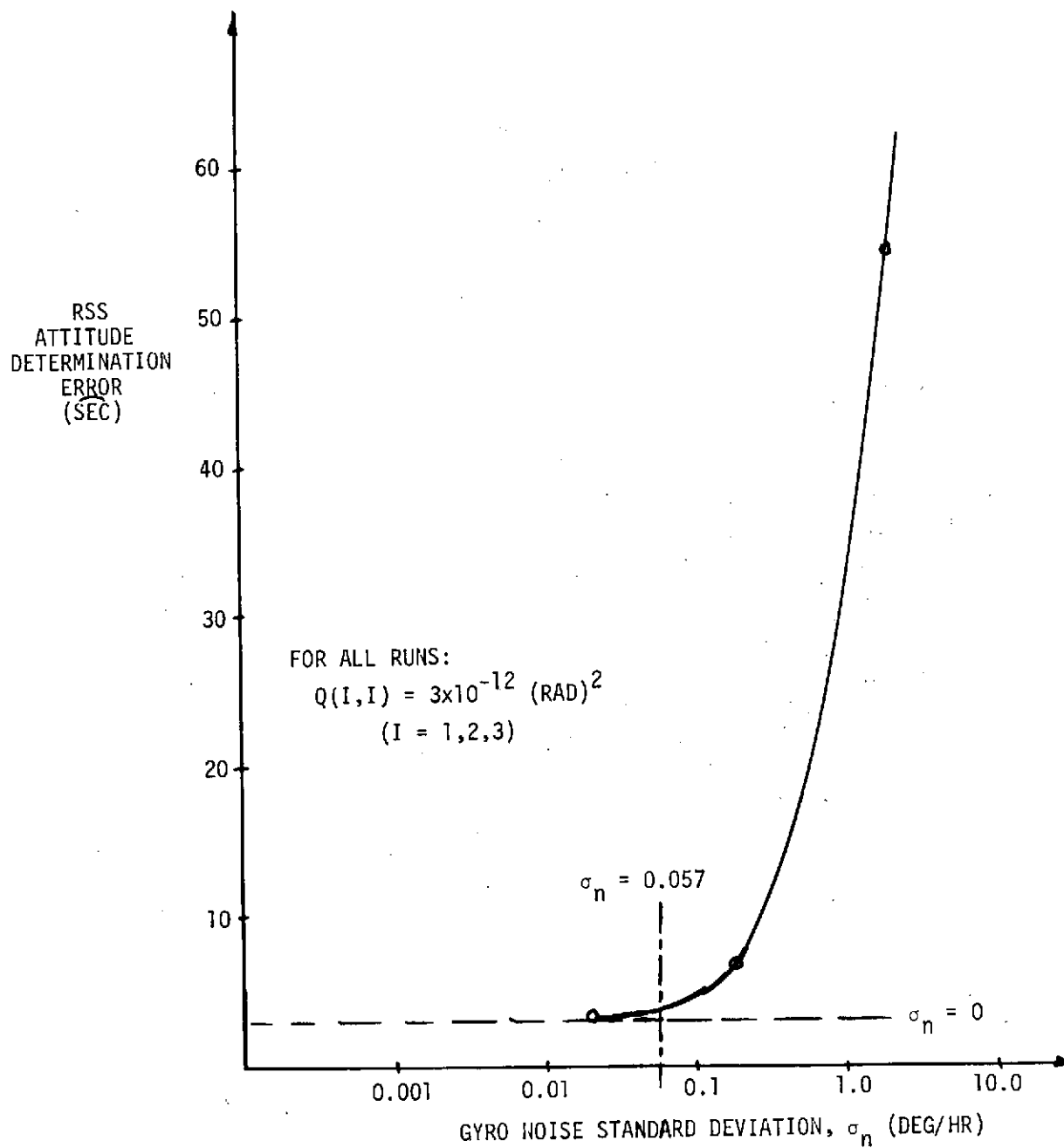
Figure 5-27. Effect of Gyro Noise on Attitude Determination Performance
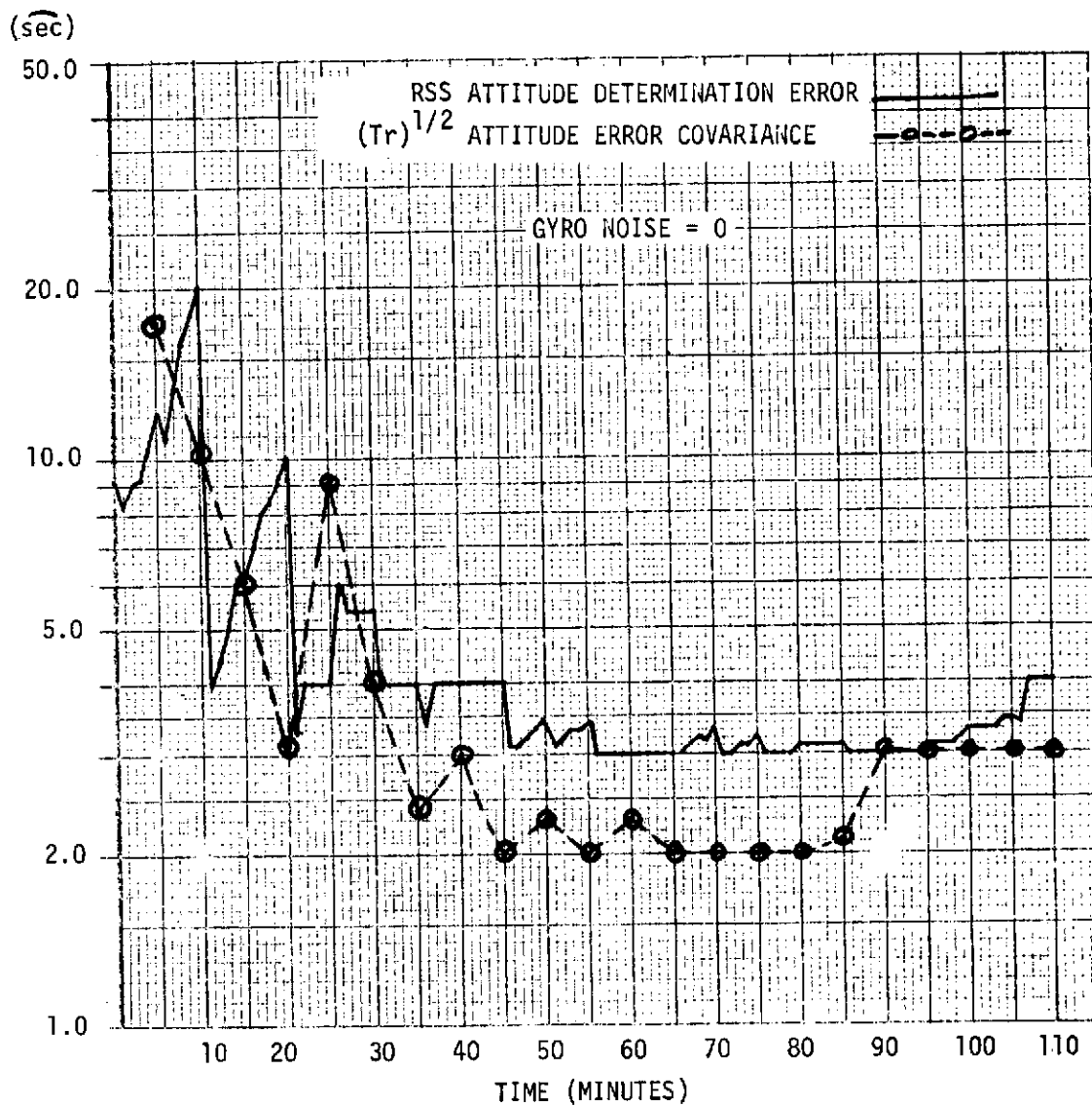
Figure 5-28. Gyro Noise Variation Run, $\sigma_n = 0$
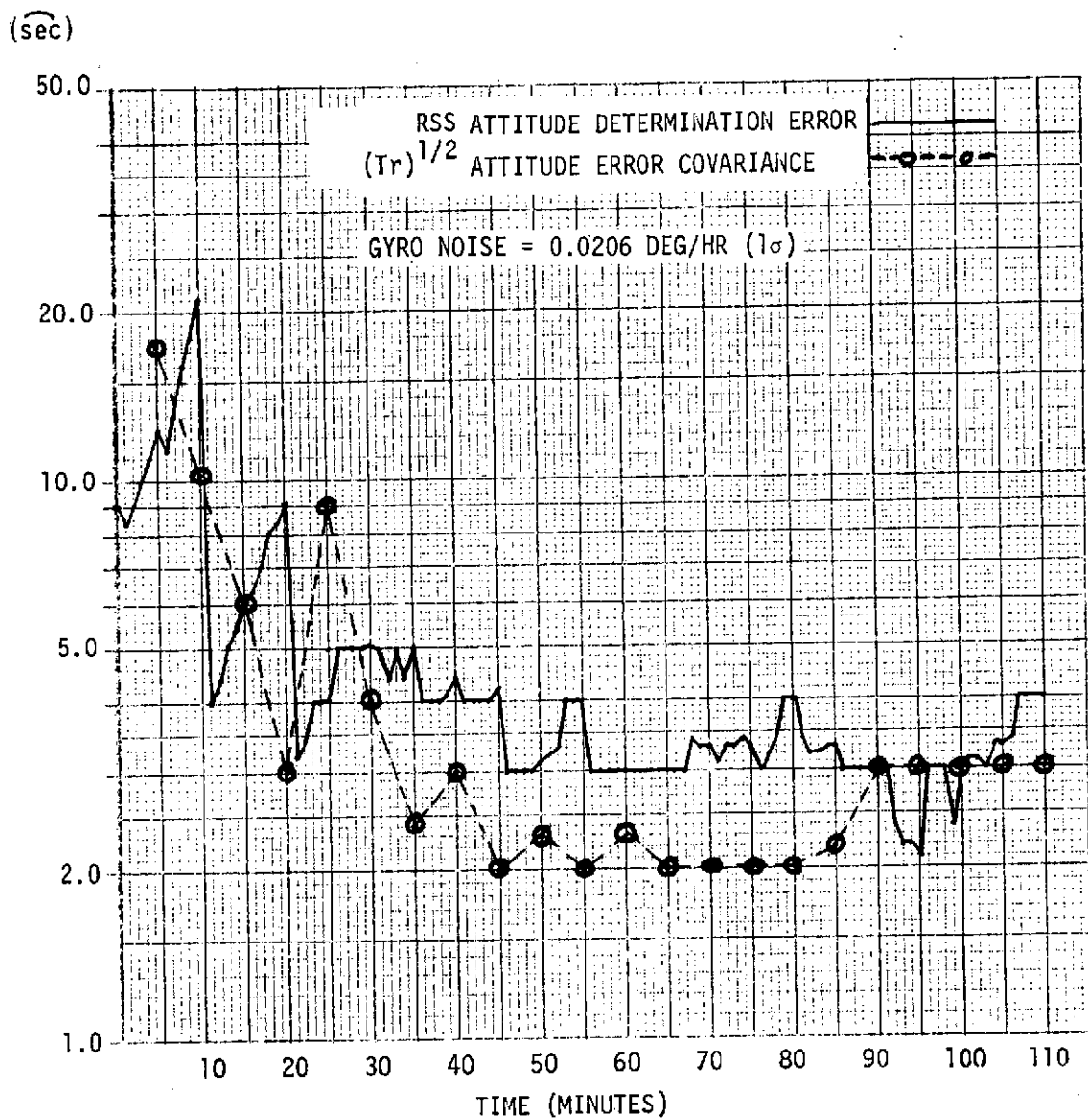
Figure 5-29. Gyro Noise Variation Run, σ_n = 0.0206 Deg/Hr
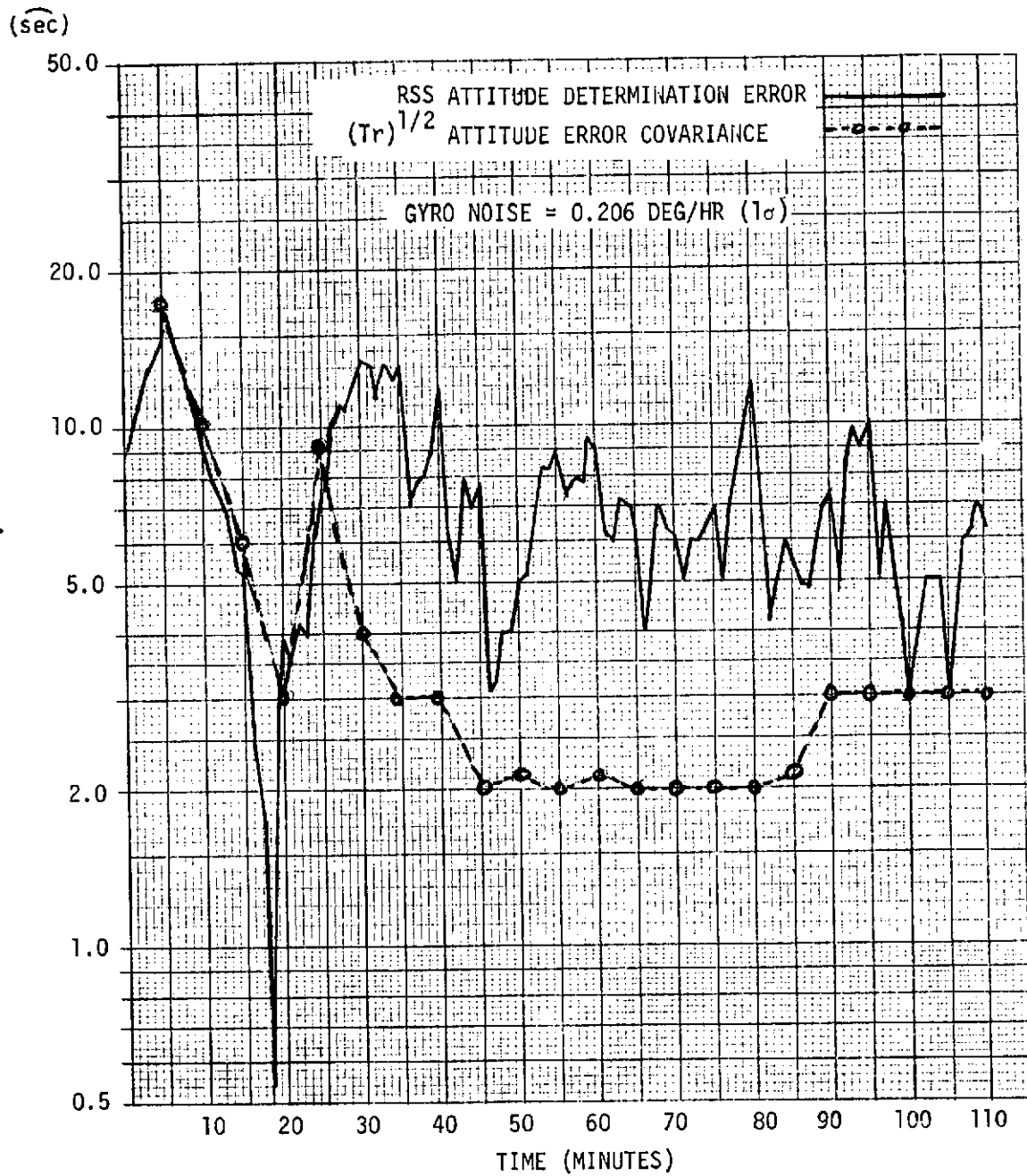
Figure 5-30. Gyro Noise Variation Run, σ_n = 0.206 Deg/Hr

5-64
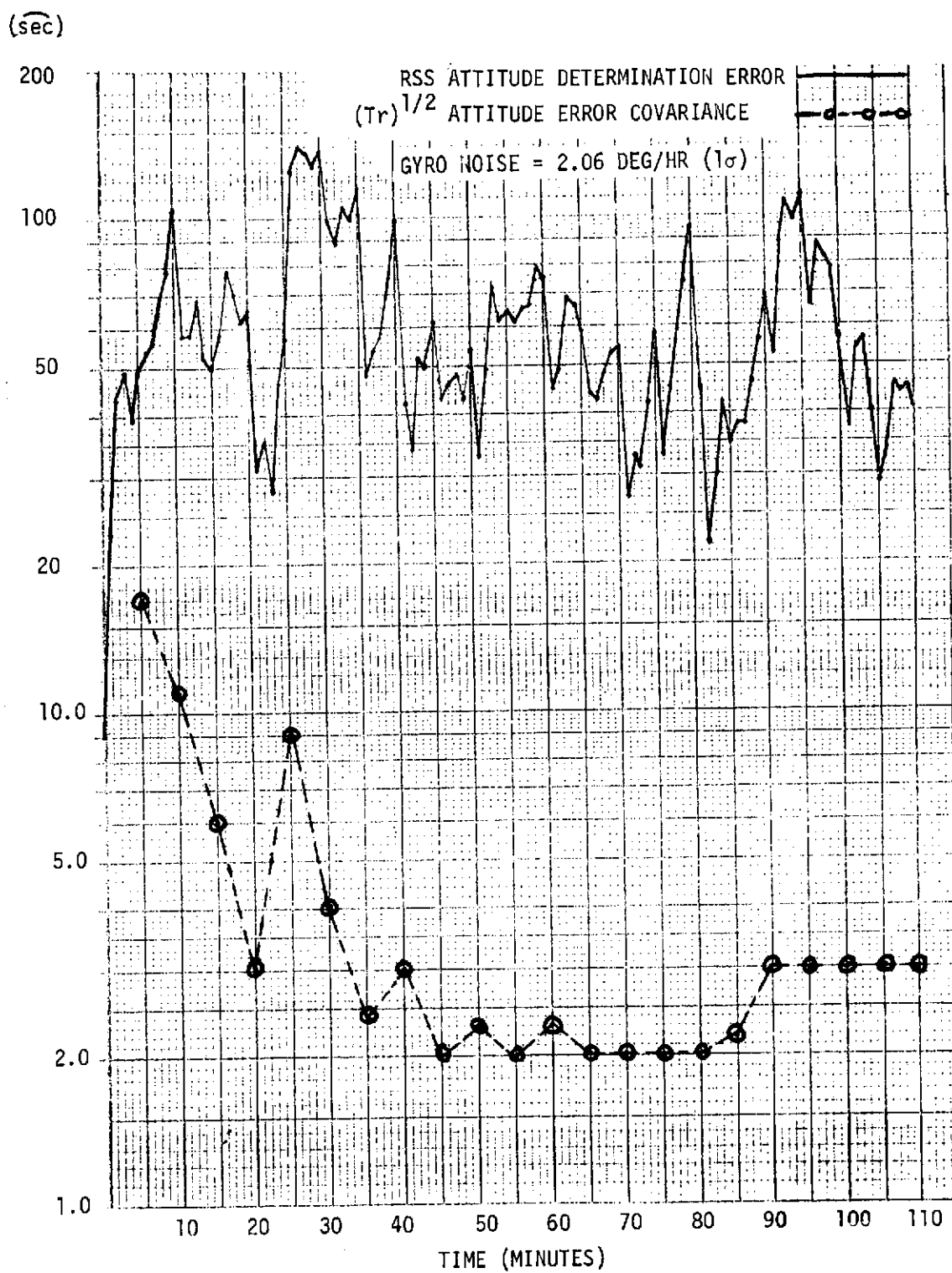
Figure 5-31. Gyro Noise Variation Run, σ_n = 2.06 Deg/Hr

case, the standard deviation in the white noise model for short term gyro noise was fixed, and the elements of the state noise covariance matrix were varied over two orders of magnitude (summarized in Table 5-9). The interesting trends of behavior that result are summarized in Figures 5-32 and 5-33. As the state noise covariance given to the filter is increased from the nominal value (that value which corresponds to the computed variance, based upon the known (simulated) one-sigma gyro noise), the attitude error covariance increases with increasing slope. Comparing this behavior to that of the actual estimation error, the latter exhibits a tendency to decrease indicating an observed improvement in actual behavior for optimistic selection of elements for state noise covariance. However, this behavior trend has been observed to reverse dramatically as the state noise covariance is further in-. creased. Thus, the error covariance was a reasonable indication of the behavior to be expected, although apparently more sensitive to the effects of large parameter variation. A decrease in selected values of the state noise covariance appears to have little influence.

The state noise terms corresponding to the bias states were not examined extensively, but the same trend seems to be evidenced. Optimism in selection of the matrix elements improves the actual estimation performance, but the behavior of the error covariance is degraded. As witnessed from previous results, however, significant deviation from approximately selected values will lead to degraded performance.

The influence of the state noise covariance matrix on the attitude error covariance measure is shown in Figure 5-34. It is interesting to note the influence of the uncertainty introduced into the filter by means of the state noise elements. The smallest value shown for Q corresponds to a relative (three-axis) contribution of 0.38 $\widehat{sec}$ to the error covariance (which has a value in the range of 1.5-2 $\widehat{sec}$). The value of Q one order of magnitude larger has the relative (three-axis) contribution of 1.2 $\widehat{sec}$ to the error covariance (which for this case has increased to the 2-3 $\widehat{sec}$ region). The large value of Q corresponds to 3.8 $\widehat{sec}$ (three-axis) and has a significant influence on the error covariance which raises the range to 4.6 $\widehat{sec}$. Selected simulation cases are shown in Figures 5-35 through 5-38.

5.4.2.5 Update Interval Variation Studies

The effect of update interval on system performance was also evaluated through a series of simulation runs, where update period was varied through the range from one minute to fifteen minutes. The expected behavior is summarized in Figure 5-39, based upon the analytical white noise relationship. The observed effect in the simulation runs was relatively inconclusive, due primarily to the finite time over which filter operation was simulated. For the cases simulated, the only variable was the time between filter updates. The overall system behavior, when normalized,

Table 5-9. State Noise Sensitivity Runs

$Q(I,I)$, $I = 1,2,3$ (rad^2)	$Q(I,I)$, $I = 4,5,6$ $\left(\frac{\text{rad}}{\text{sec}}\right)^2$
3×10^{-11}	1×10^{-18}
1×10^{-11}	1×10^{-18}
3×10^{-12}	1×10^{-16}
3×10^{-12}	1×10^{-17}
3×10^{-12}	1×10^{-18}
3×10^{-12}	1×10^{-19}
3×10^{-12}	1×10^{-20}
1×10^{-12}	1×10^{-18}
3×10^{-13}	1×10^{-18}
1×10^{-13}	1×10^{-18}

σ_n = 0.0206 deg/hr (All Cases)
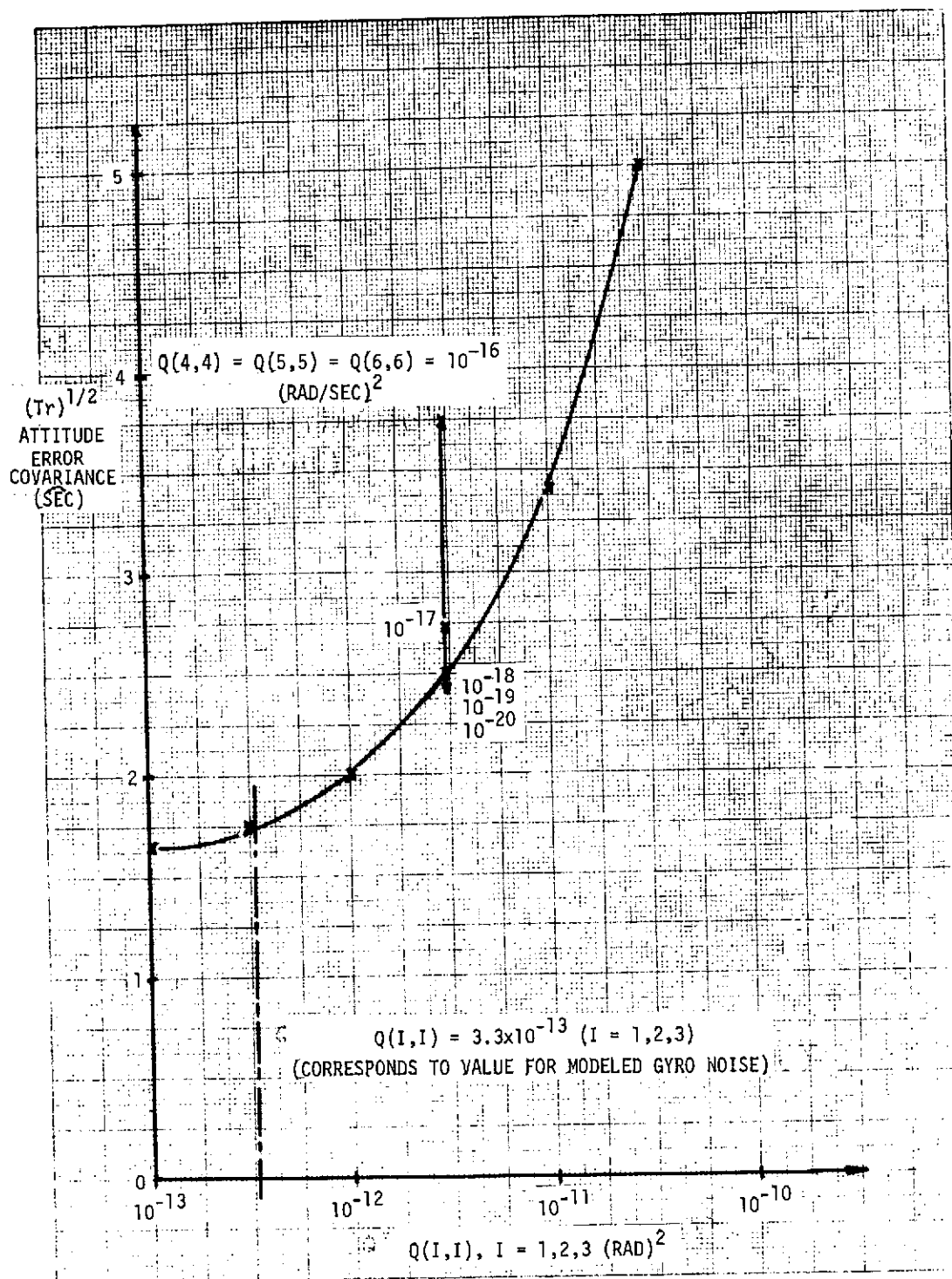
Figure 5-32. Attitude Error Covariance As Influenced
By State Noise Covariance
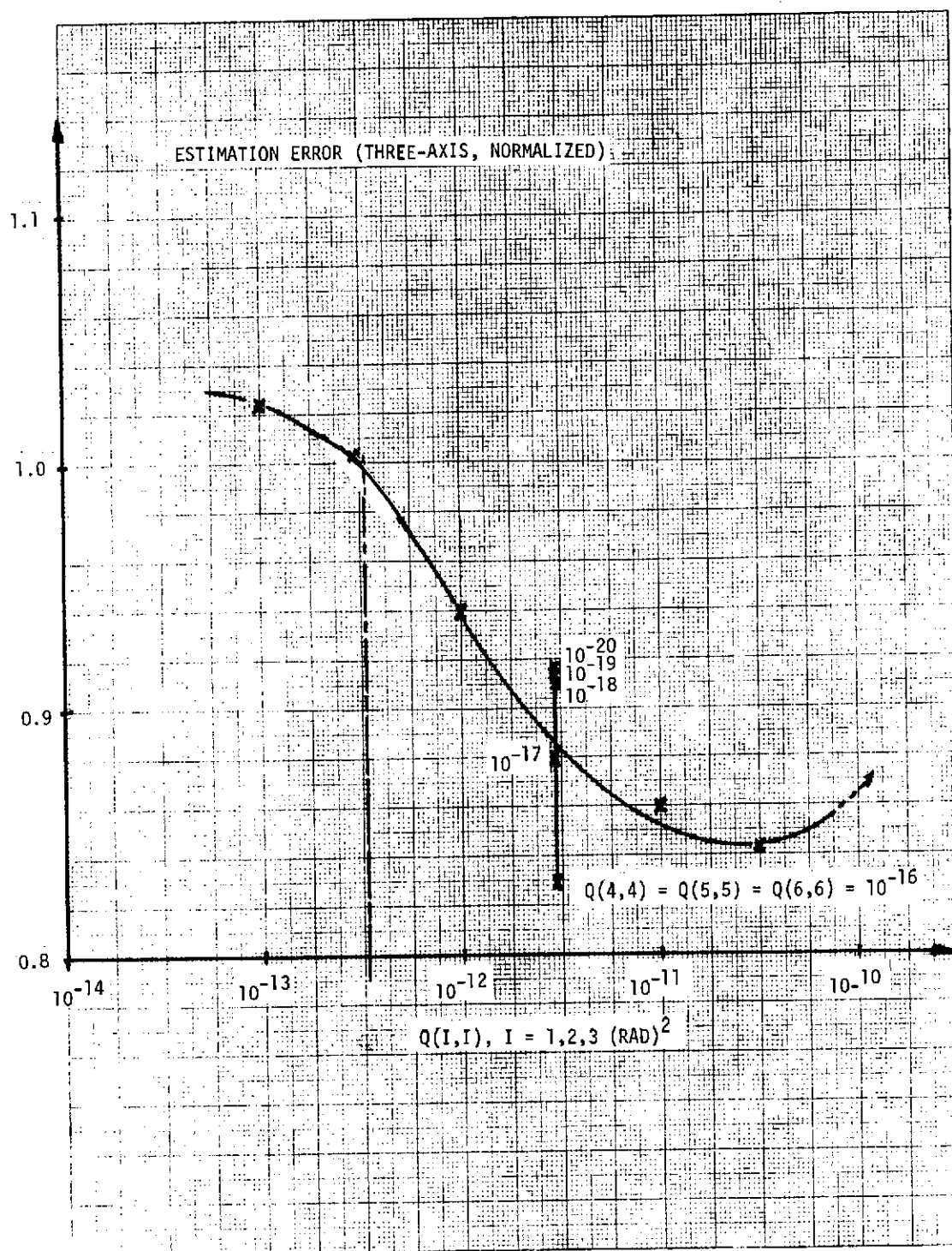
Figure 5-33. Influence of State Noise Covariance Elements
On Attitude Determination Error
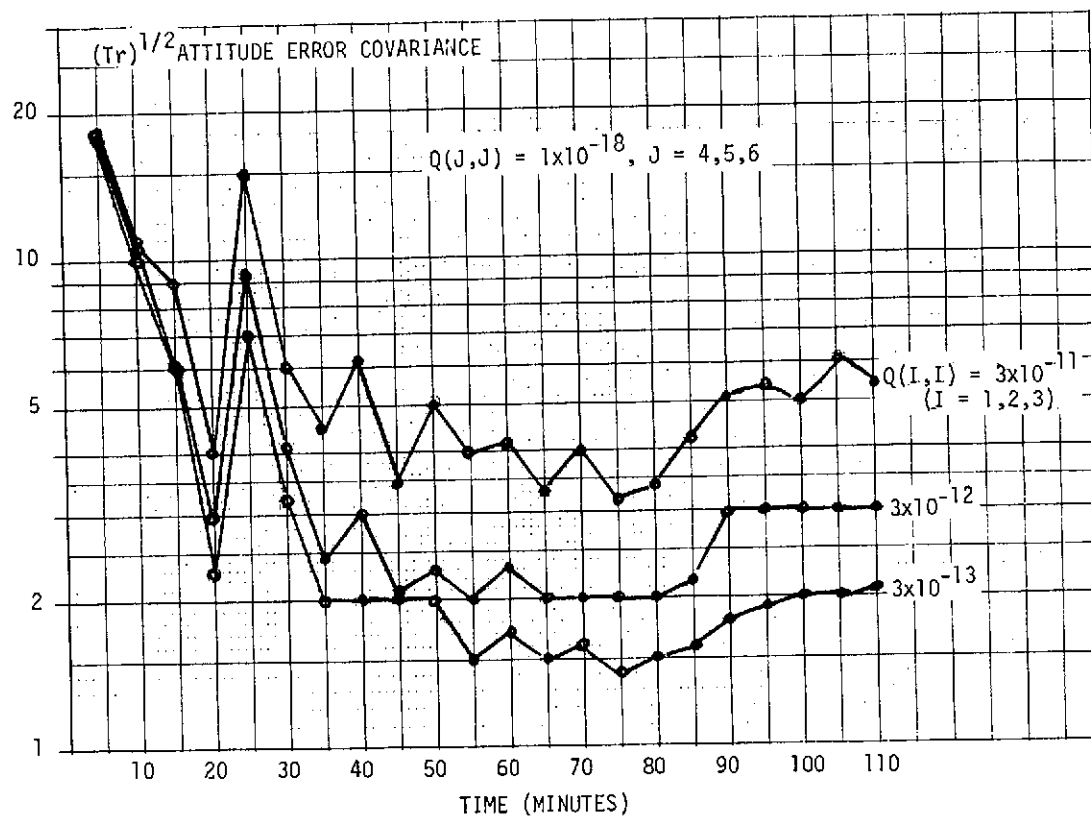
Figure 5-34. Attitude Error Covariance Time Histories As
Influenced By State Noise Covariance
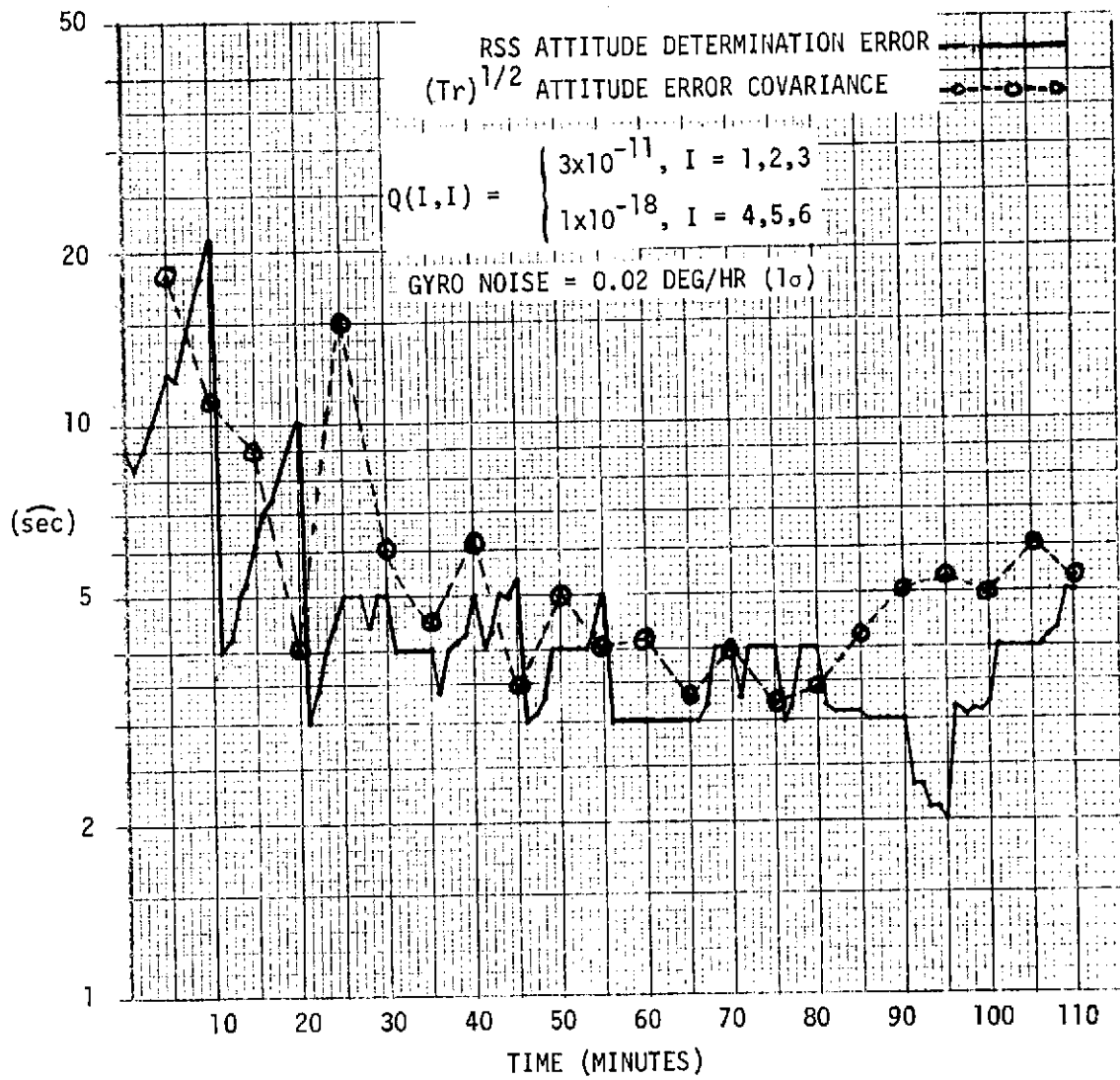
Figure 5-35. State Noise Covariance Variation Run
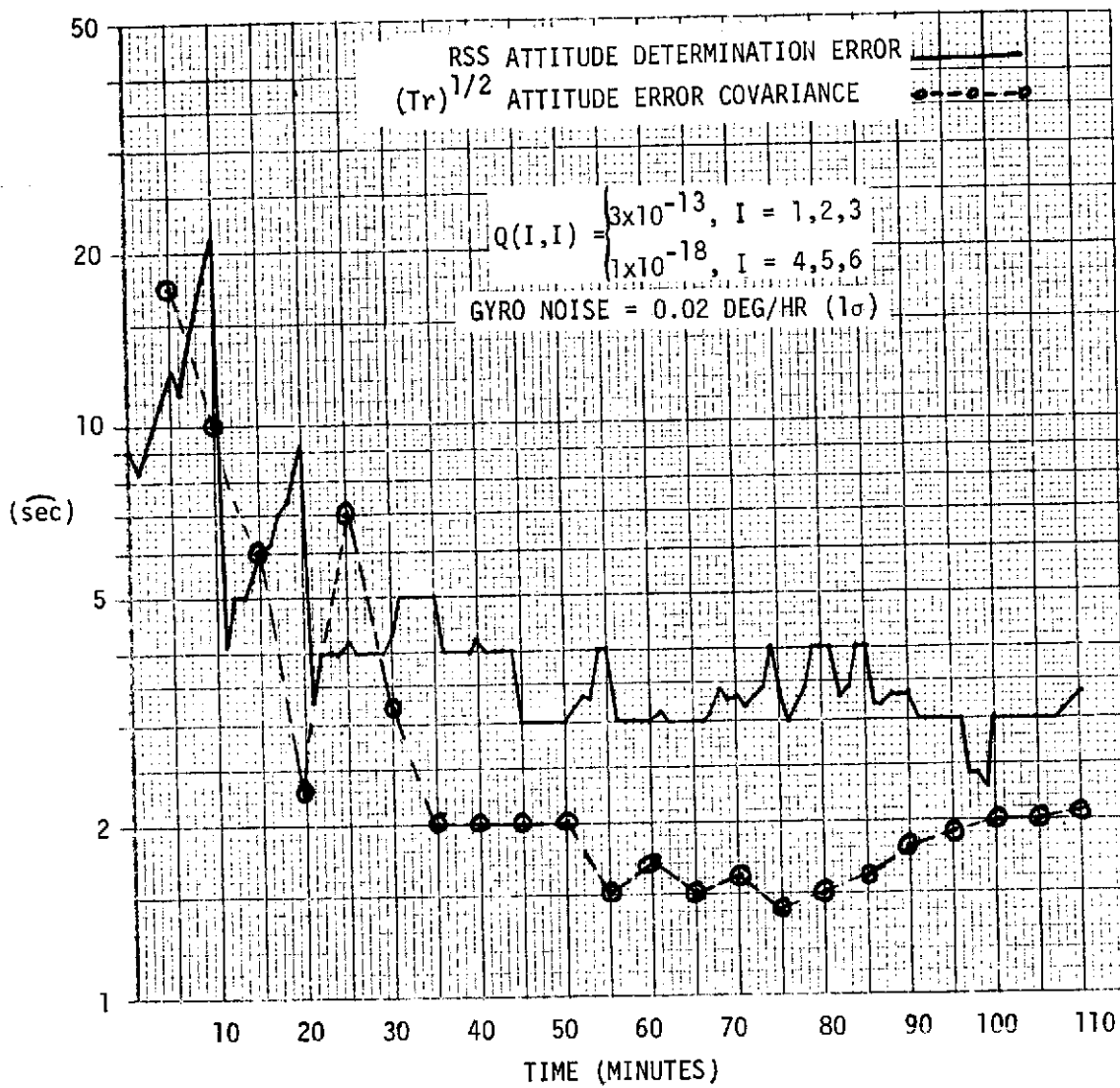
Figure 5-36. State Noise Covariance Variation Run
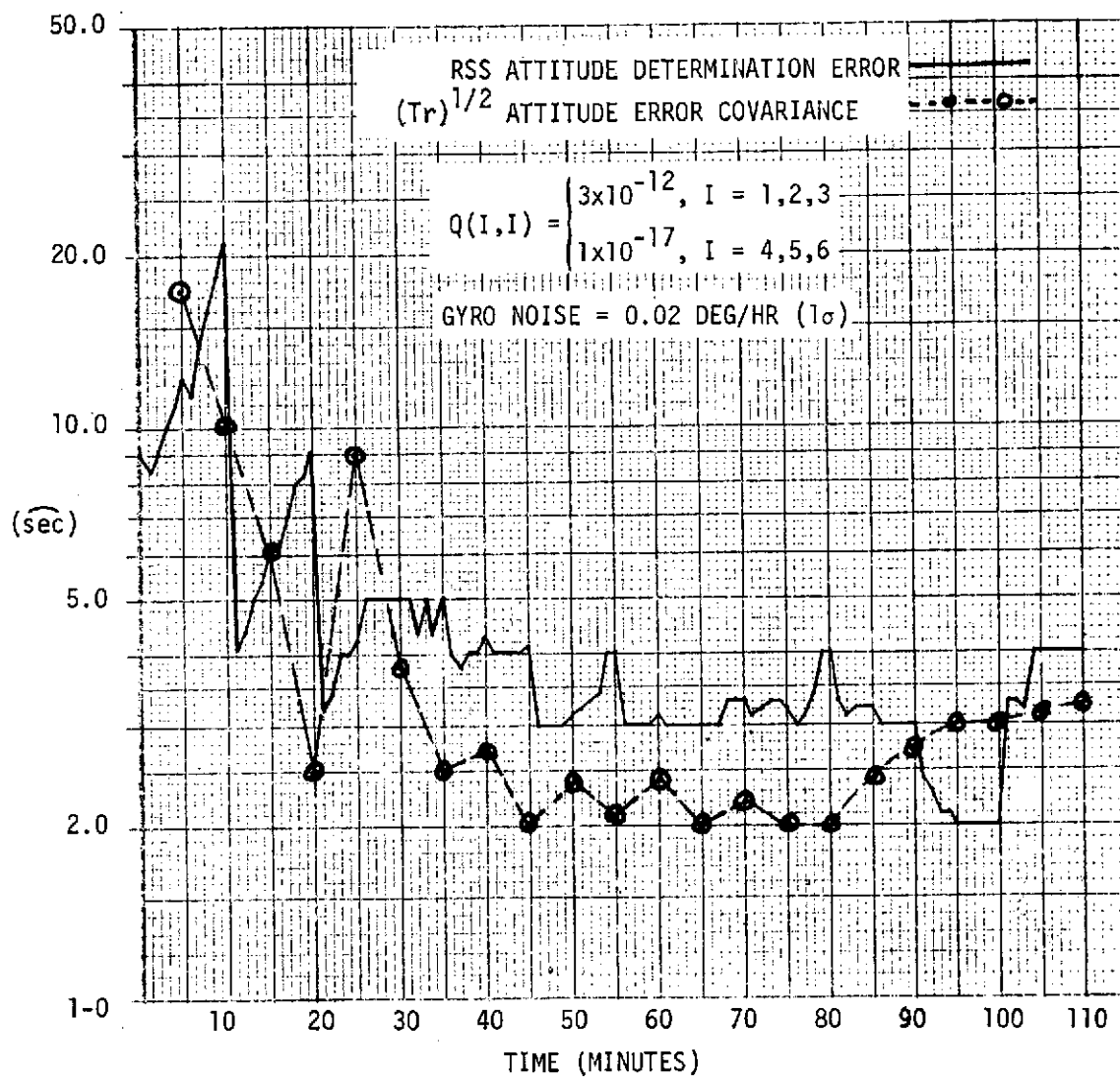
Figure 5-37. State Noise Covariance Variation Run

5-73
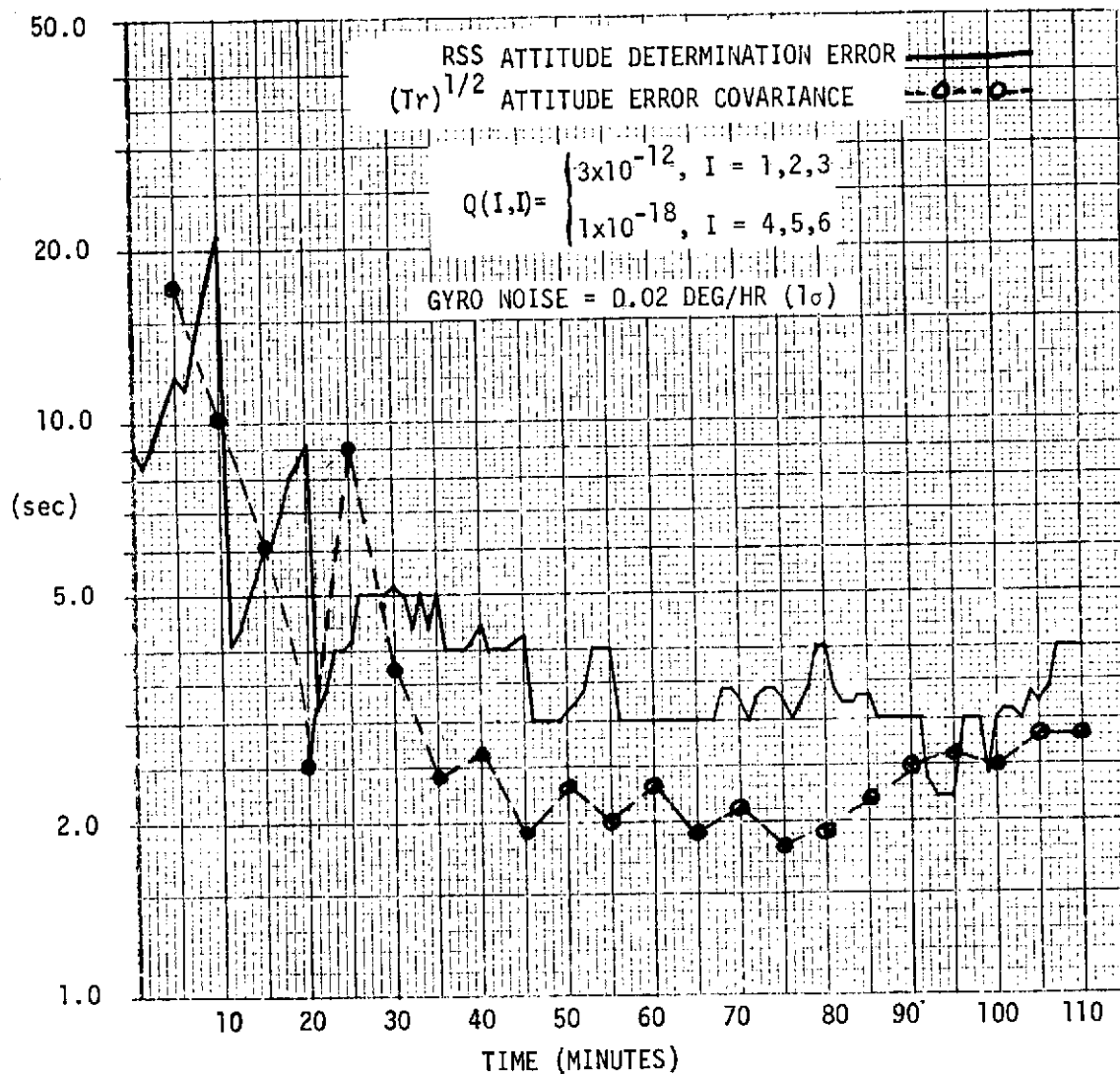
Figure 5-38. State Noise Covariance Variation Run

$$\frac{\sigma_e}{\sigma_{eo}} = \left(\frac{\sigma_b}{\sigma_{bo}}\right)\left(\frac{\Delta T}{\Delta T_o}\right)^{1/2}\left(\frac{t}{t_o}\right)^{1/2}$$

□ MARKS SIMULATED RESULTS (GYRO EFFECT ONLY)

NOTE: x MARKS SIMULATED RESULTS
o MARKS CORRESPONDING ANALYTICAL RESULTS

$\frac{\sigma_b}{\sigma_{bo}} = 1, \frac{\Delta T}{\Delta T_o} = 2$

$\frac{\sigma_b}{\sigma_{bo}} = 1, \frac{\Delta T}{\Delta T_o} = 1$

$\frac{\sigma_b}{\sigma_{bo}} = 0.5, \frac{\Delta T}{\Delta T_o} = 1$

NORMALIZED TIME, t/t_o
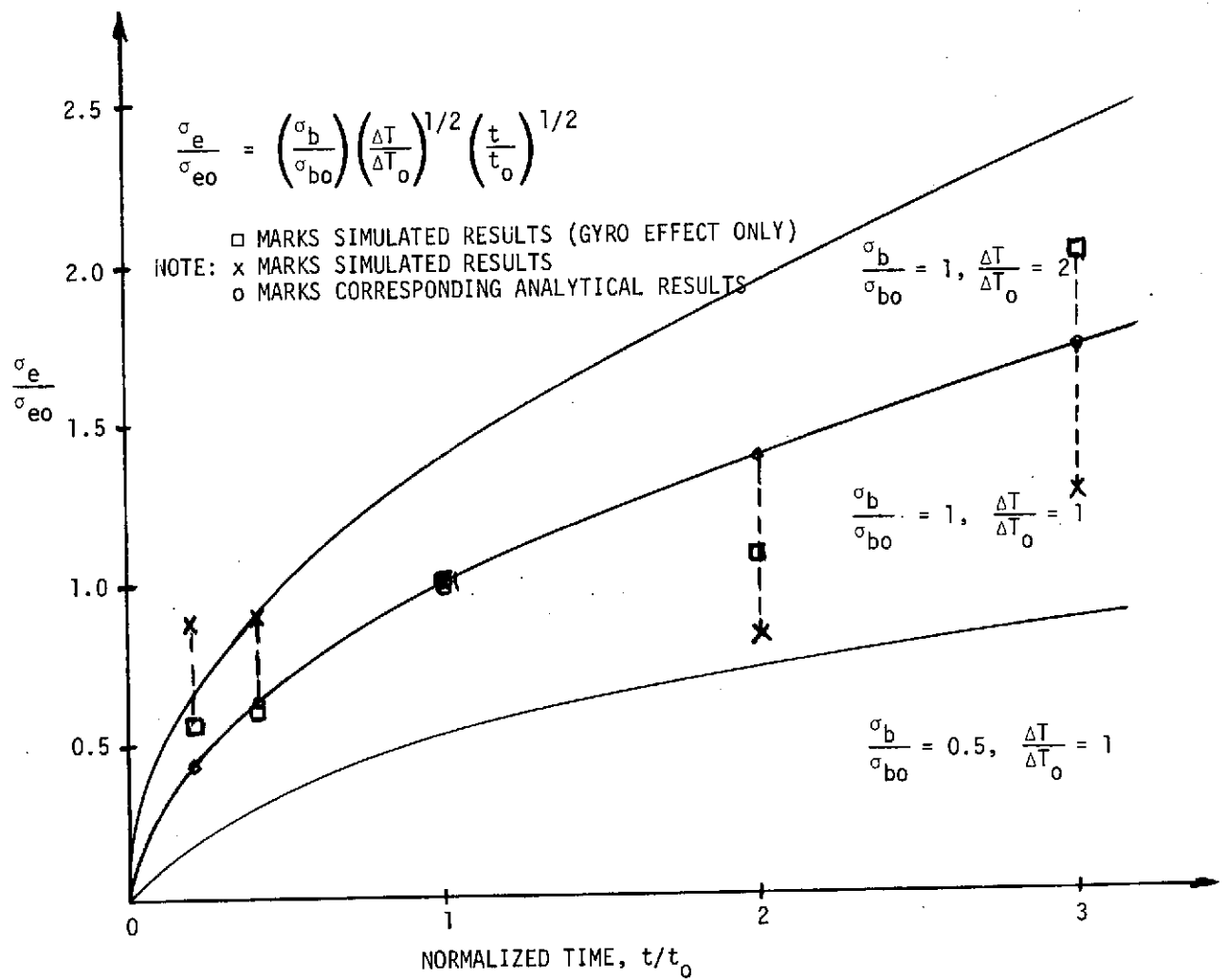
Figure 5-39. Effects of Modeled Short-Term Gyro Random Drift

5-75

appears only slightly effected by the choice of update period. As expected, if only behavior between updates is considered, the analytical prediction (on a normalized basis) well represents the behavior. Several cases are shown in Figures 5-40 through 5-43.

5.4.3 Calibration Performance Evaluation

Simulation runs were conducted to explore the calibration of key sensor parameters. The runs were primarily concerned with verifying the conclusions reached earlier regarding observability. Two of these runs are presented. The first relates to flight calibration of three STA misalignments and three gyro biases. The parameters utilized for this run are summarized in Table 5-10. Because of anticipated problems in calibrating α_1, and Maximum Projection Method was chosen for star selection.

The results of this run are summarized in Table 5-11, which lists gyro drift bias, STA misalignments, and attitude estimation errors both initially and after one orbit. Clearly the drift rates and two of the three STA misalignments have been accurately estimated and with high confidence. As expected, the estimate of α_1 is poorer, with a 2 $\widehat{sec}$ residual estimation error. Note that the filter uncertainty of 3.5 $\widehat{sec}$ is also relatively large. Additional filtering would continue to improve this result, and it is concluded that the STA misalignments and gyro bias can effectively be calibrated.

The purpose of the second run was to support the analytically demonstrated observability of the nine GRA "geometry" parameters, Y_{ij}, related to scale factor and IA alignment uncertainty. An idealized star tracker was employed in this case and, as Table 5-12 shows, each of the nine parameters is accurately estimated with high confidence.
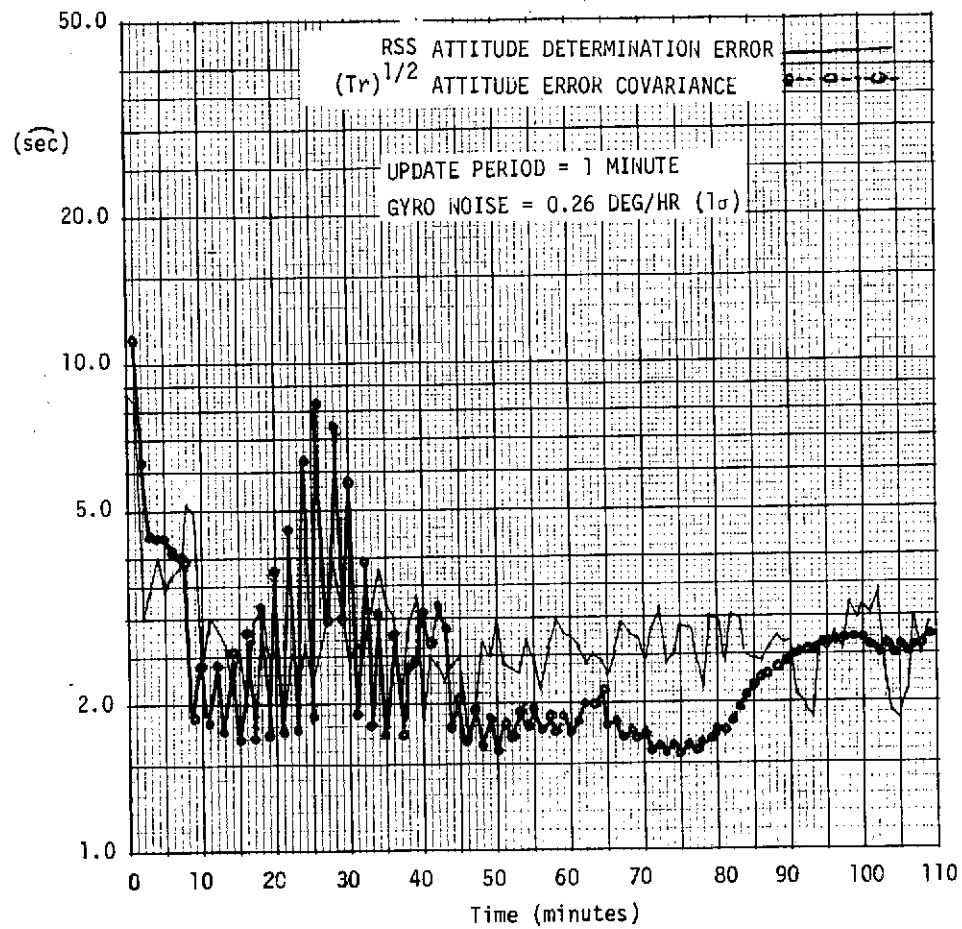
Figure 5-40. Update Period Variation Run (Period = 1 Minute)
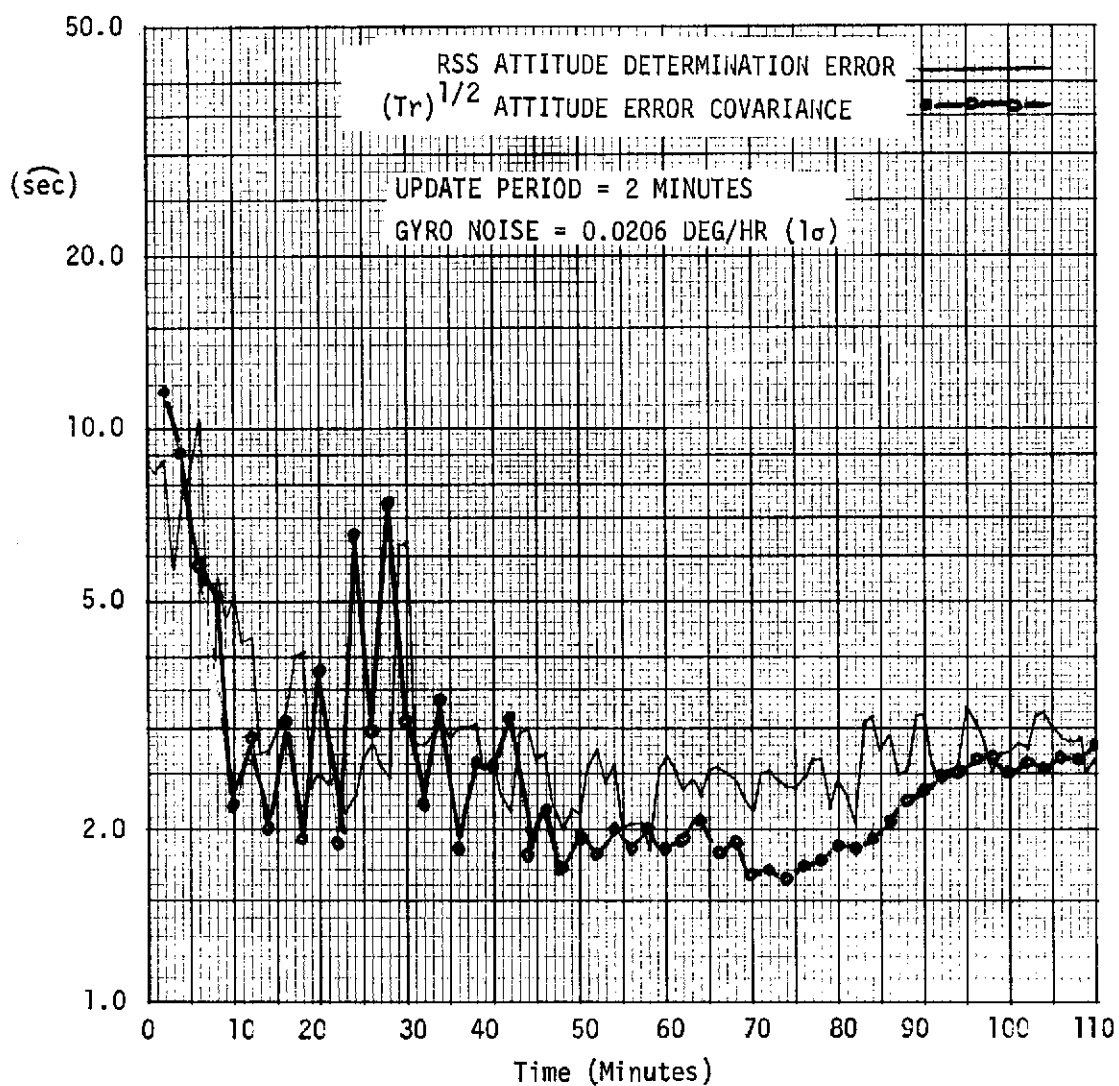
Figure 5-41. Update Period Parameter Variation (Period = 2 Minutes)
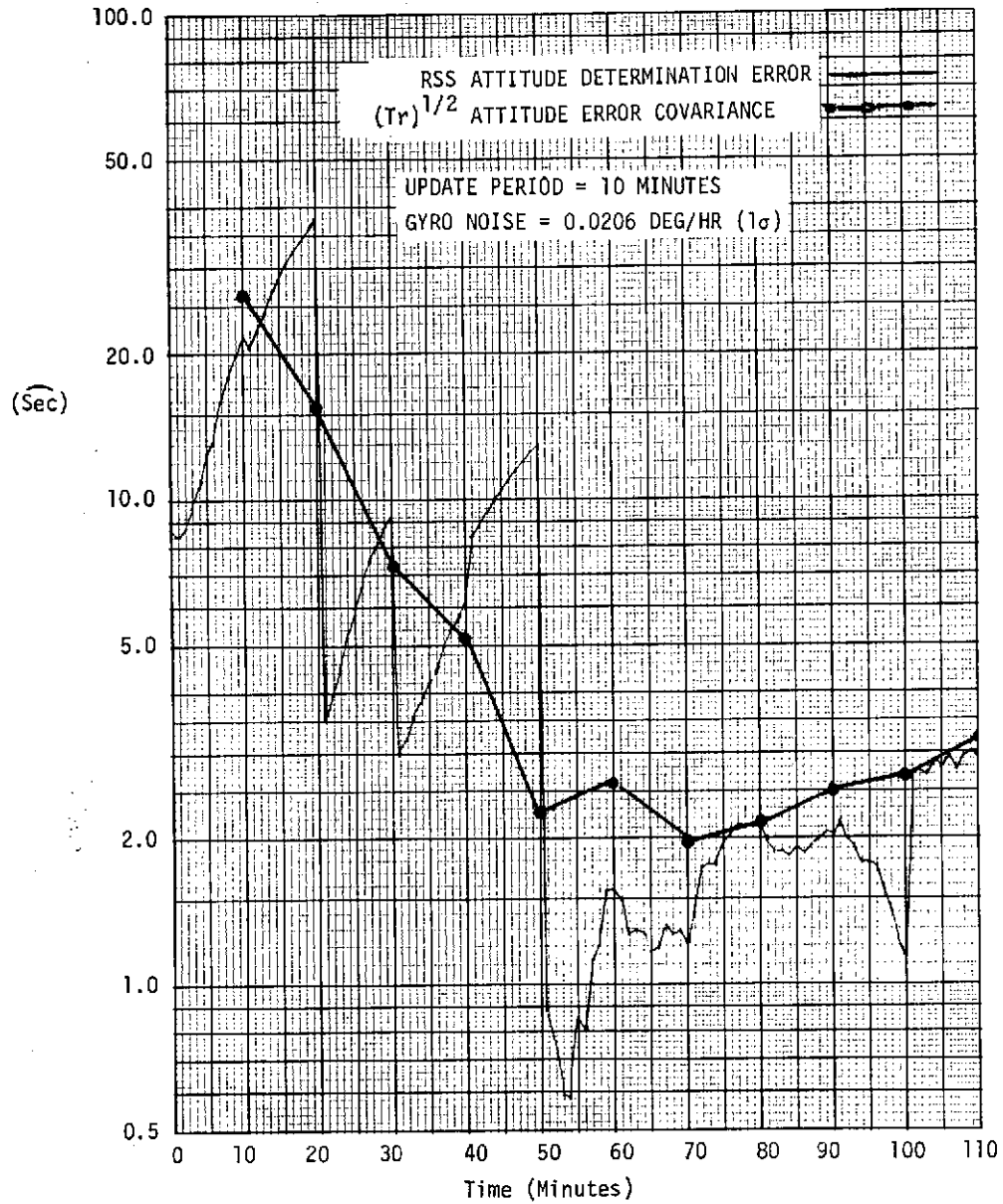
Figure 5-42. Update Period Variation Run (Period = 10 Minutes)
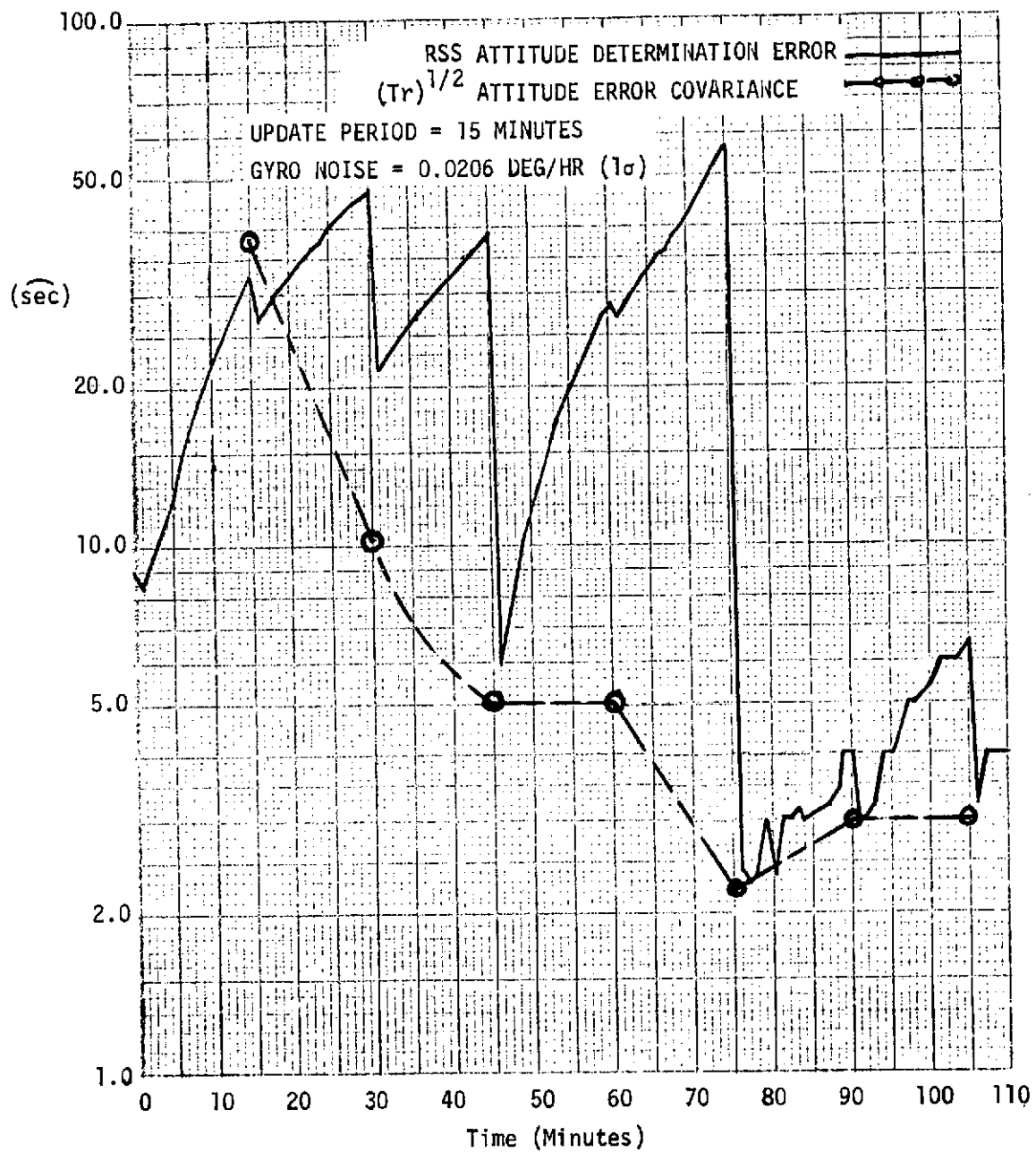
Figure 5-43. Update Period Variation Run (Period = 15 Minutes)

Table 5-10   Parameters for STA, Gyro Bias Calibration Run

Gyro Parameters:

      Drift Bias - 2.062 deg/hr

      Gyro Noise - 0.208 deg/hr (1σ) (200 ms int step).

      Misalignment and Scale Factor Errors - Typically 6 to 25 sec

Star Tracker Parameters:

      Misalignments (3) - 5 sec magnitudes

      Inductosyn and Bearing Run Out Coefficient - Typically 0.25 to 0.50 sec

      Detector Noise (2) - 1.3 sec (1σ)

Orbit:

      Synchronous equatorial

Filter Conditions:

      9 State - 3 attitude variables; 3 gyro drift rates; 3 STA biases

                    Drift bias estimate (3) - 2.0 deg/hr

                    Attitude Estimation Error, 3 axis RSS - 371 sec

                    STA Bias Estimates (3) - 0 sec

      Initial   Error Covariance Matrix - consistent with actual errors

                    Measurement Noise Covariance Matrix - 0.5 sec diagonal terms

                    State Noise - Consistent with gyro noise influence

      Star Selection Method - maximum projection method

Table 5-11. Results of Calibration Simulation Run

	Actual at t=0	Estimate t=0	$\sigma(t_0)$	Actual t=24 hr	Estimate t=24 hr	Std. Dev. t=24 hr
Attitude Determination Error RSS (sec)	371.1	0.	320.0	3.976		5.169
GRA Drift Rates (deg/hr)						
b_{g01}	2.063	2.0	0.06	2.0626	2.0601	0.0043
b_{g02}	2.063	2.0	0.06	2.0626	2.0635	0.0055
b_{g03}	2.063	2.0	0.06	2.0626	2.0574	0.0038
STA Biases (sec)						
α_1	5.	0.	5.1	5.	2.91	3.50
α_2	-5.	0.	5.1	-5.	-5.05	0.37
α_3	5.	0.	5.1	5.	4.77	0.28

Table 5-12   Calibration of Gyro Misalignments

	Actual Value (Constant)	Estimate t=0	$\sigma(t_0)$ t=0	Estimate t=2400	$\sigma(t)$ t=2400
γ_{11} (sec)	4.0	0.	10.3	3.94	0.32
γ_{12}	11.0	0.	10.3	10.91	0.31
γ_{13}	3.0	0.	10.3	2.87	0.39
γ_{21}	- 7.0	0.	10.3	- 7.12	0.85
γ_{22}	- 6.0	0.	10.3	- 6.69	0.68
γ_{23}	8.0	0.	10.3	7.65	1.05
γ_{31}	- 5.0	0.	10.3	- 4.69	0.56
γ_{32}	- 3.0	0.	10.3	- 3.28	0.36
γ_{33}	12.0	0.	10.3	11.91	0.70

6.0 HARDWARE DESIGN

This section presents the functional design and analysis of each of the PPCS hardware assemblies. The presentation for each assembly generally includes a functional design description, detailed design tradeoffs, design analysis, and error analysis. Detailed design (including layouts, schematics, and detailed hardware performance/design characteristics) is presented separately [12]. The hardware development status is summarized below. Except for the gyro reference, computer, and data interface, the design has been detailed to a level consistent with engineering model development/fabrication.

Star Tracker - engineering model developed and tested on company sponsored program. Detailed design documentation available in internal TRW documents and PPCS Star Tracker Data Book.

Sensor Electronics - detailed design completed with development of detailed preliminary schematics. Detailed design documentation available in TRW documents and PPCS Data Book.

Gyro Reference - functional design completed including selection of instrument, packaging concept, circuit functional design, and assembly level specification (Part I).

Alignment Sensor - detailed design completed and documented with development of detailed preliminary drawings/schematics [16].

Reference Block - a representative detailed design for a fully configured PPCS was developed.

Digital Computer - detailed functional design [17] and development of laboratory computer specification (Part I).

Data Interface - detailed functional design of I/O [17] with use of TRW developed data bus design to level of detailed schematics.

Experiment Gimbal and Electronics - design complete to level of detailed mechanical layouts and supporting analysis. Electronics design same as Sensor Electronics.

Antenna Gimbal and Electronics - detailed design completed with development of detailed drawings and schematics.

6.1 STAR TRACKER ASSEMBLY

The Star Tracker Assembly (STA) consists of a Star Sensor Unit (SSU) incorporating the detector, optics, and electronics mounted within a two degree-of-freedom Sensor Gimbal Unit (SGU). The design of the sensor is based upon the use of an image dissector as the basic detector. Advantages of this detector are high resolution, reliable operation over a long period of time, simple and rugged construction, lack of a thermionic cathode, and a linear dynamic range of several orders of magnitude. The image dissector has also been proven in space applications.

The precision gimbal design was based upon the use of a unique single-ball bearing at each end of the shaft that supports the load. This concept makes use of a sliding contact between a stationary ball and a rotating assembly. Great care was taken to achieve thermal and mechanical symmetry to obtain a stable structure. Nearly identical drive housings at the ends of each axis are connected by an I-beam ring, itself mechanically symmetrical.

6.1.1 Star Sensor Unit Design

The star sensor has two functional modes of operation, search and track. In the search mode, the total optical FOV is scanned in steps by a much smaller instantaneous field-of-view (IFOV). Mode control circuits terminate the search scan on the brightest star present in the search FOV. In the track mode, a small cruciform tracking pattern provides spatial modulation of the star signal, and a feedback tracking loop keeps the star image centered in the detector aperture, regardless of sensor motion.

The SSU is comprised of the following major elements:

- Optical System. The function of the optical system is to collect and focus the stellar radiant energy on the detector. A sun shade and sun shutter are provided for protection.

- Detector. The detector incorporated in the SSU is an image dissector. The image dissector converts the stellar optical image into an electron image stream which is modulated by magnetic deflection to obtain star position information.

- Electronics. The electronics provide the voltages and waveforms to operate the image dissector and to process the video signal from the image dissector to develop the two-axis error signals.

Each of these is discussed in greater detail in the following sections. The SSU errors are also summarized in a separate section.

6.1.1.1 Optics Design

The design of the optical system went through several iterations before settling on the final configuration. The final choice was based upon thermal stability more than optical acuity. Since the detection scheme determines the centroid of the optical image, no attempt was made to have a diffraction limited system. The design selected is a folded Gregorian telescope as shown in Figure 6-1.

The synthesis of the basic two-element system is as follows:

$$\text{Let } F = \text{system effective focal length} = 100 \text{ inches}$$

f_1 = focal length of first element

f_2 = focal length of second element

$$D = \frac{1}{F} = .01$$

$$d_1 = \frac{1}{f_1}$$

$$d_2 = \frac{1}{f_2}$$

t = effective air space = 13.5 inches

t^1k = back focal length (effective distance from second element to final focal point) = 8.75 inches

$$\text{Now } D = d_1 + d_2 (1 - td_1)$$

$$\text{and } \frac{t^1k}{F} = (1 - td_1)$$

Solving the second of these equations, one obtains:

$$d_1 = \frac{1.0875}{13.5} = .0805556$$

$$\text{and } f_1 = \frac{1}{d_1} = 12.413786$$

Thus, the radius of curvature of the first element is 24.827572. From this, the equations then yield:

$$d_2 = 1.03492$$

$$f_2 = .966258$$

and the radius of curvature of the second element is 1.932516.

These radii were then used as a starting point in conducting computer ray traces. Slight changes were made as necessary to reduce the blur circle to within acceptable limits. In order to make the results more exact, the faceplate of the

EFFECTIVE FOCAL LENGTH - 100.857187 INCHES

PRIMARY MIRROR - RADIUS OF CURVATURE - 24.827572
ASPHERIZED - 0.0000007

TERTIARY MIRROR
RADIUS - 1.933477

4.500

3.00

2.000

6.750
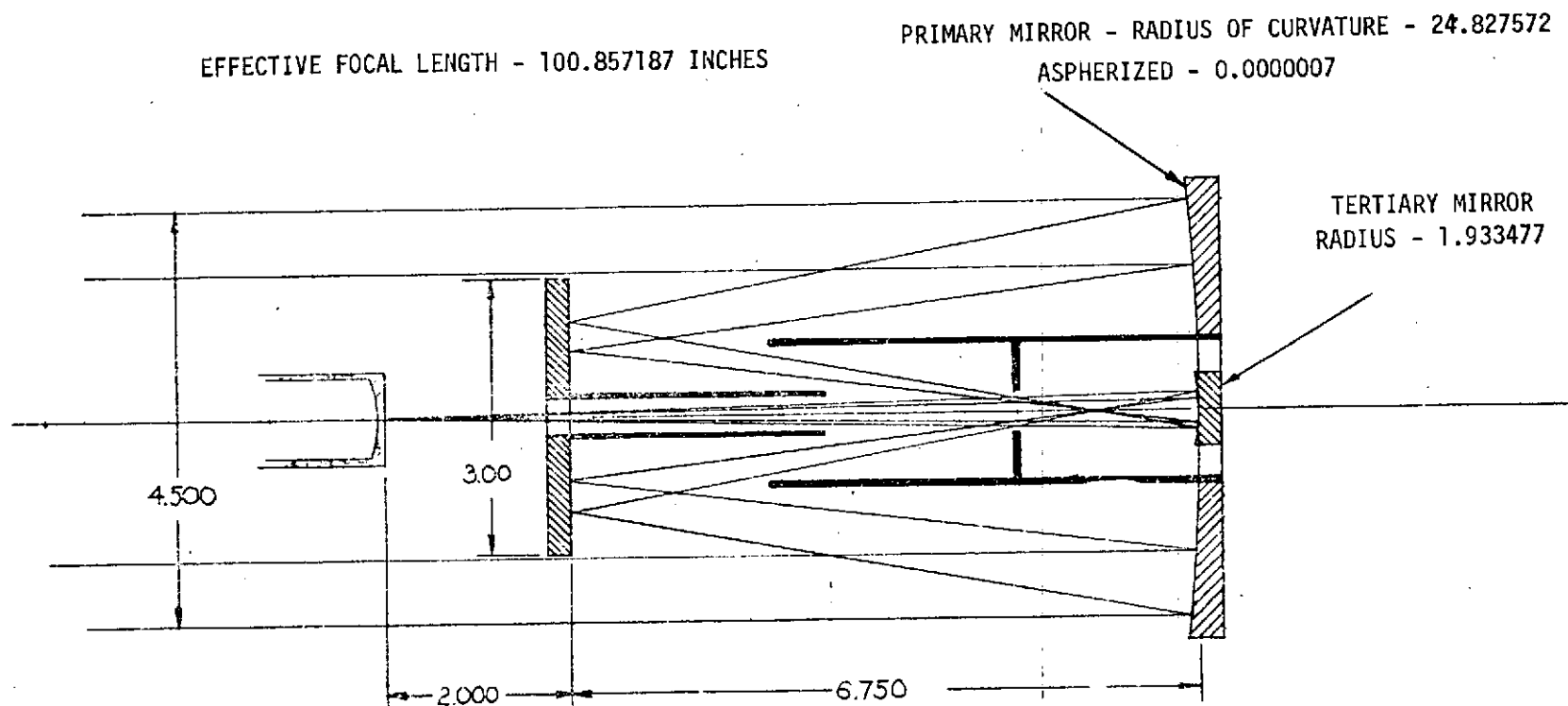
Figure 6-1. Star Sensor Unit Optics Design

image dissector was included. The index of the faceplate glass was taken as 1.523 and the radius of curvature of the photocathode was taken as 1.23 inches. The resultant system gave a blur circle of 0.002 inches diameter for on-axis rays; for the worse case rays (7.07 m̂în), the blur circle is 0.0024 inch.

The Star Sensor optical-mechanical layout is shown in Figure 6-2. The location of the image dissector coaxial to the optical system provides a very large central obscuration. This is no constraint on the design optically and, in fact, provides a sun shade effect which makes a long sun shade unnecessary. This arrangement also provides a location for the bright object sensor, which uses the sensor sun shade as a field stop. A concern of the mechanical design is potential movement due to vibration during the launch environment. The structural and dynamic analysis show that the stress levels in the tube area are small and it is thus anticipated that any deformation of the Delrin spacer will not be permanent and that the tube will return to its original position.

The collecting aperture is obtained by computing the area of collecting optics. It is given by

$$A = \frac{\pi}{4} (D_1^2 - D_2^2)$$

where D_1 is the usable outer diameter of the primary mirror and D_2 is the usable inner diameter of the primary mirror. In this design, D_1 is 4.5 inches and D_2 is 3.1 inches, so that A = 8.35 sq. in. There will be some obscuration from the supporting web, which will amount to 0.59 sq. in. Thus the collecting aperture is 7.76 sq. in. (50 sq. cm).

The transmission efficiency of the optical system is an important factor in scaling the optical system. Therefore, a significant amount of effort was expended in obtaining reasonable data on mirror surface reflectivities. Optical Coating Labs, Inc., was contacted for information concerning their enhanced silver over-coated with dielectric. The losses in this mirror surface increase rapidly at wavelengths less than 4300Å. This surface was temporarily discarded in favor of evaporated aluminum. While the spectral curve is not as high as the other in the visible range, it is flatter across the peak of the S-20 range. However, since this surface must be overcoated with a protective finish, the losses introduced by the coating are taken into consideration. Since there are three reflecting surfaces in the optical system, the losses occur three times. Figure 6-3 shows the resultant optical system spectral transmission, $T(\lambda)$, across the spectral band of interest, where the average transmission is above 60 percent.

SUN SHADE

BRIGHT OBJECT SENSOR   F4004 TUBE   SECONDARY MIRROR

SHUTTER   TERTIARY MIRROR
& FOCUS ADJUST
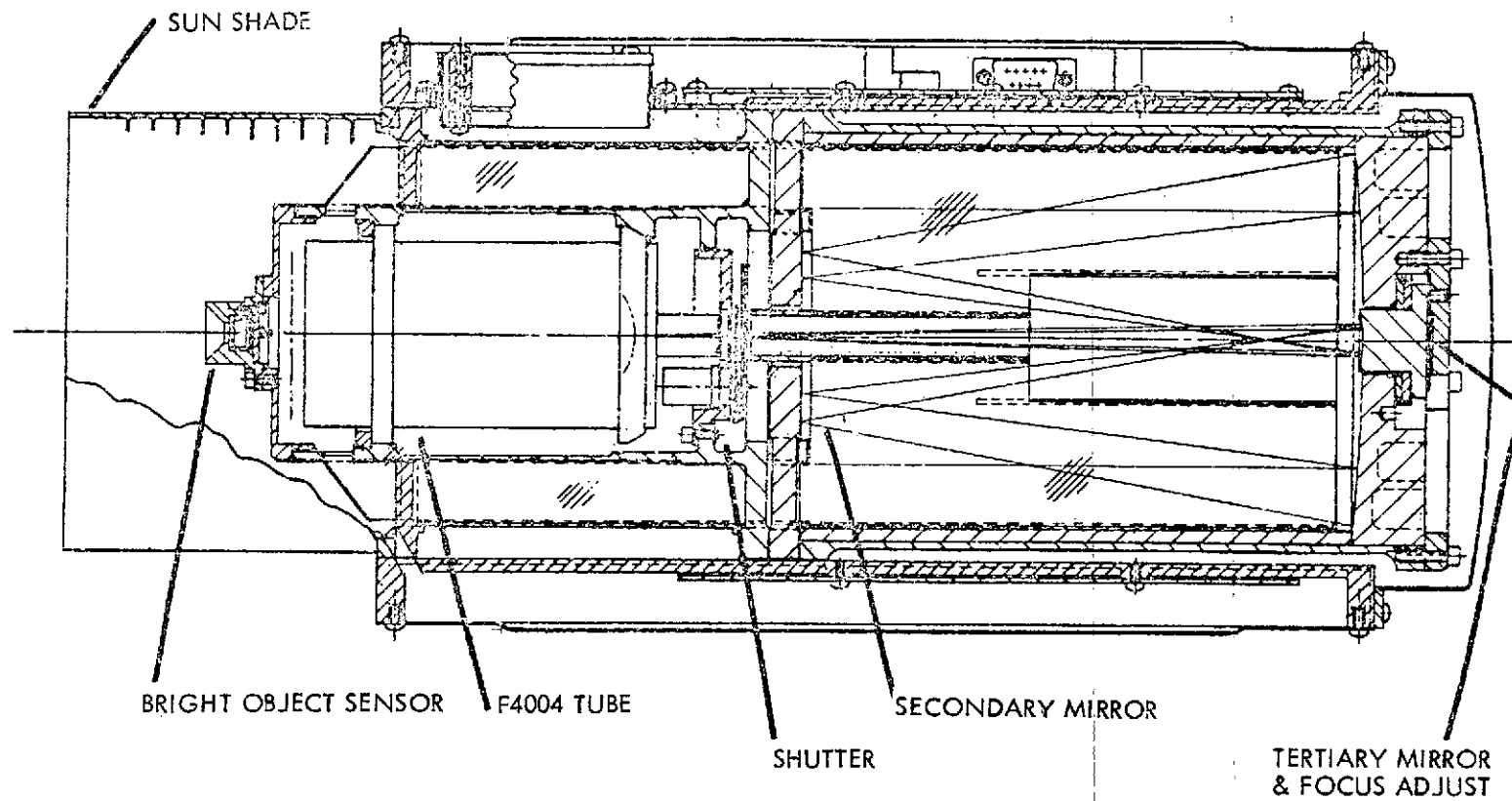
Figure 6-2.   Star Sensor Optical/Mechanical Layout
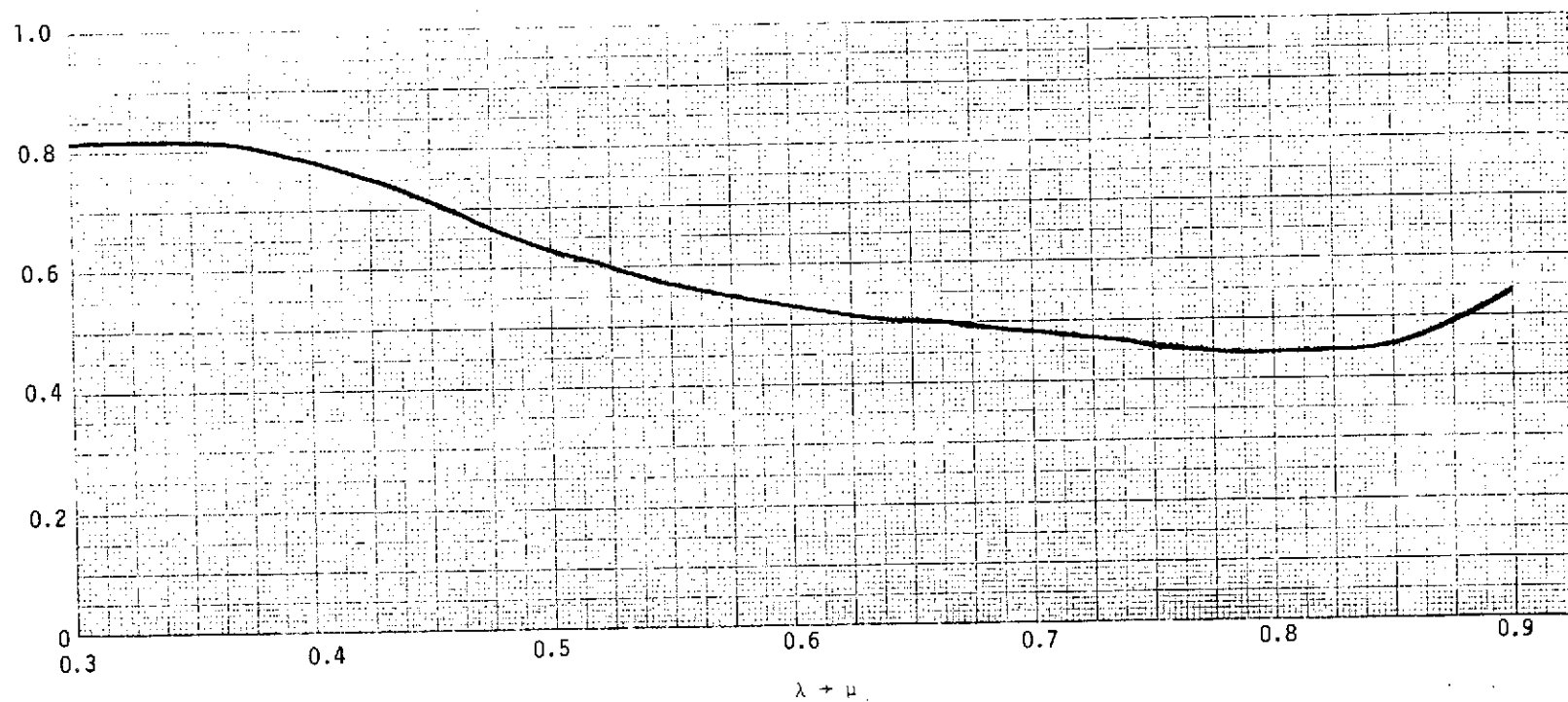
Figure 6-3. Transmittance of Total Optical System (3 Mirrors)

6.1.1.2   Detector

The detector used is an image dissector type F-4004. The photocathode of the image dissector is an S-20 surface. The normalized spectral response is shown in Figure 6-4. The peak response, K , is nominally 0.064 amperes/watt. The F4004 has a 15-stage secondary emission multiplier structure, giving it a nominal gain of 10^6. In most cases, the gain will exceed this by an order of magnitude; as a margin of safety, the nominal value is used. The anode current of the F4004 image dissector is given by

$$I_A = AGK_1K_2 \int_{.3\mu}^{.8\mu} S_{20}(\lambda)T(\lambda)H(\lambda)d\lambda = 267 \text{ nanoamperes}$$

where $S_{20}(\lambda)$ = Normalized spectral response of photocathode

$T(\lambda)$ = Spectral transmission of optical system

$H(\lambda)$ = Relative spectral energy distribution of star light (See Figure 6-5).

K_1 = Peak spectral response of S-20 = .064 amperes/watt

K_2 = Peak spectral energy of +2.5M AOV star = 8.1×10^{-15} watts/cm^2

A = Collecting aperture of optical system = 7.76 sq. in.

G = Secondary emission multiplier gain = 10^6
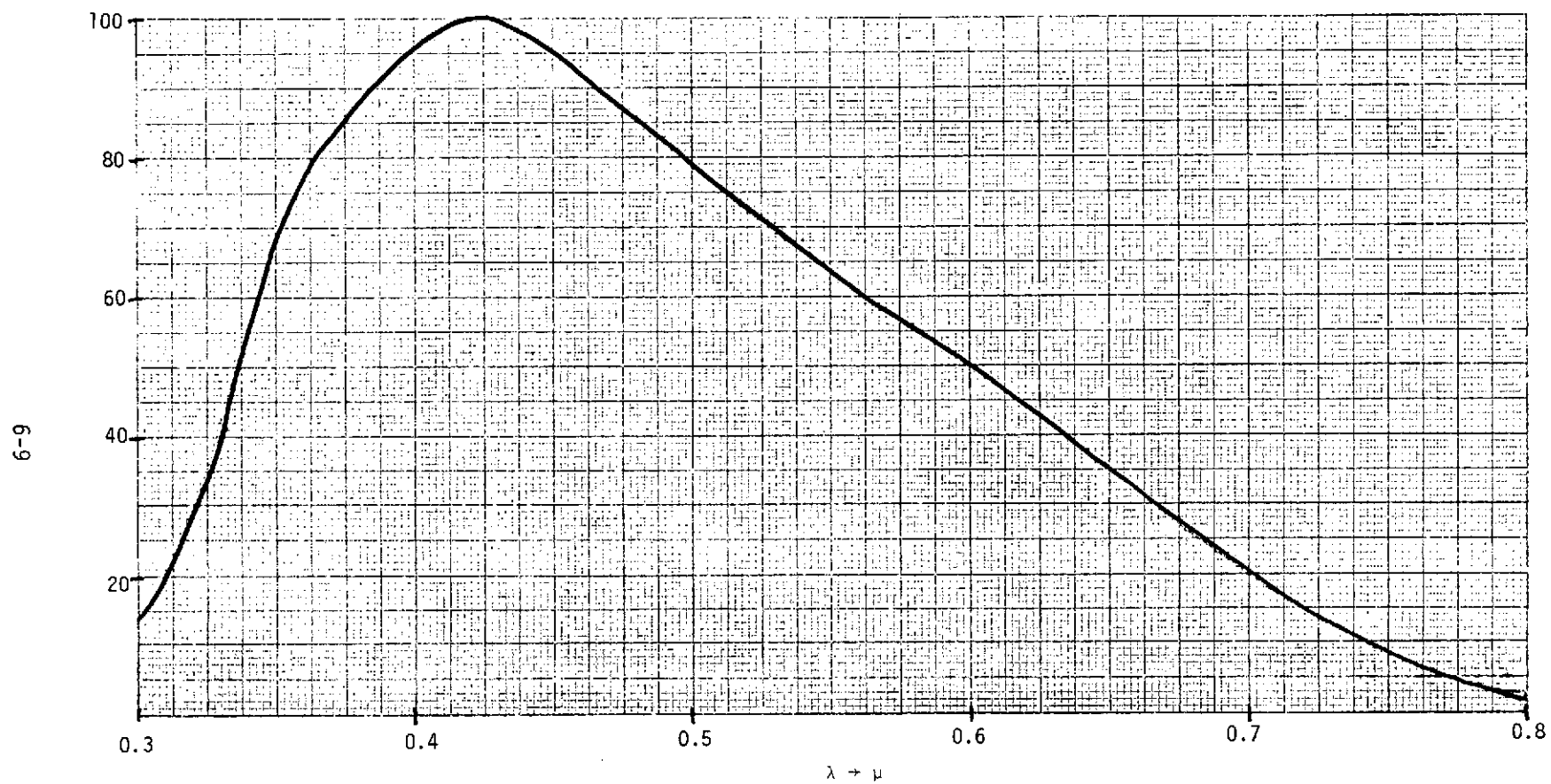
Figure 6-4. Normalized Spectral Response of S-20 Photocathode

6-9
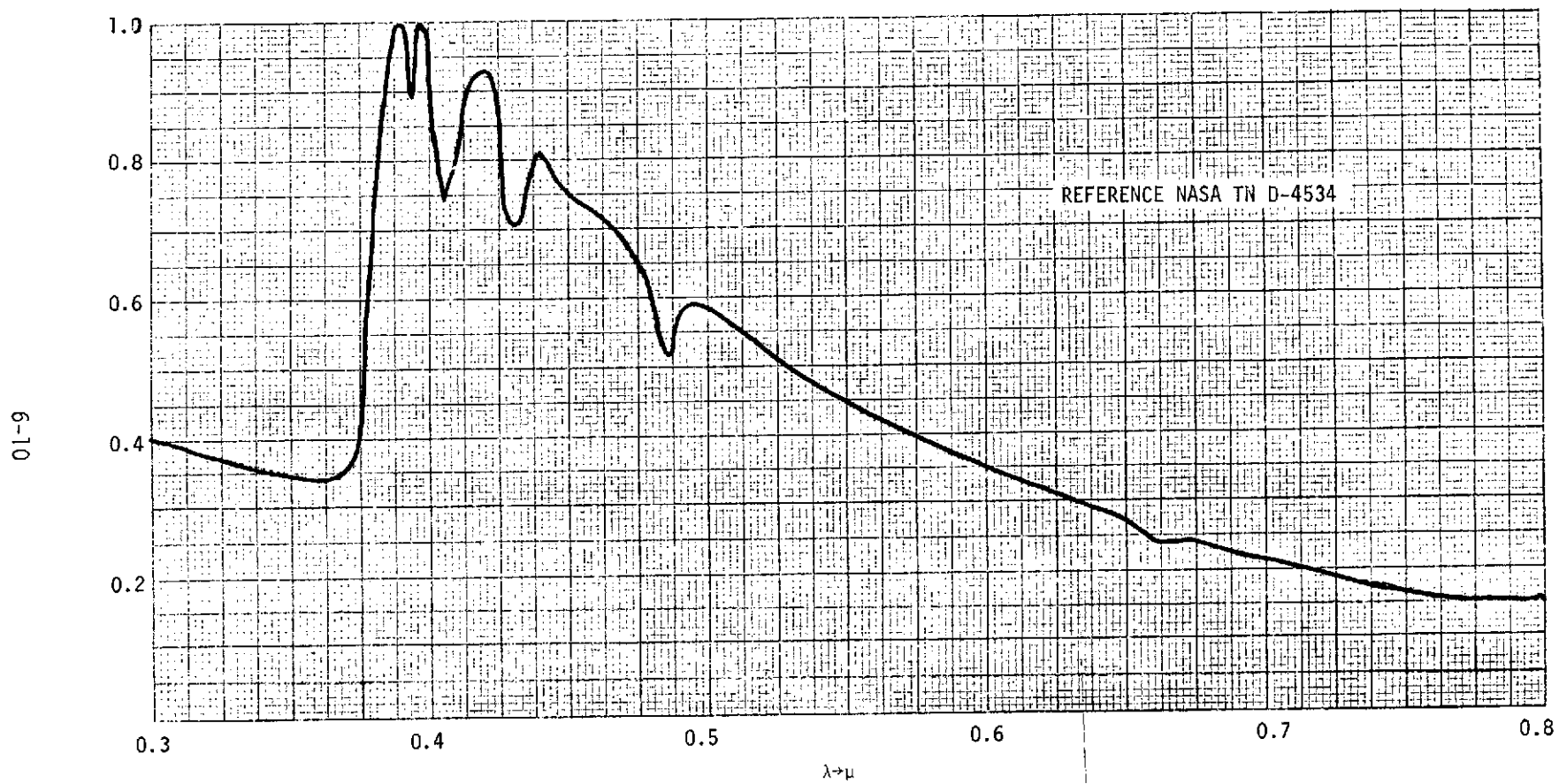
Figure 6-5. Normalized Spectral Distribution for Class AOV Star

6.1.1.3 Electronics

The star sensor electronics is composed of several functional blocks, as illustrated in Figure 6-6, which are summarized:

- **Video Processor.** The video processor performs the following functions. During the search mode, automatic gain and threshold control circuits select only the largest video pulse present and send it to the mode control logic. When in the track mode of operation, the image dissector video is shaped into a digital pulsewidth-modulated signal and is fed to the demodulator. A digital star-presence signal and an analog star-magnitude signal are also developed.

- **Mode Control Logic.** The mode control logic establishes the mode of operation: search or track. The timing of the search cycle, the gating of the tracking loop, and search-scan waves are also controlled by the mode logic.

- **Demodulator.** The demodulator circuits consist of timing gates to process the pulsewidth-modulated video and precision voltage switches which develop the tracking loop correction error voltage at the input to the tracking integrator.

- **Tracking Integrators.** This circuit consists of an integration stage (op-amp) which provides correcting dc voltages to the deflection generator to keep the star image centered in the image-dissector aperture by taking the integral of the error demodulator output.

- **Scan Generator.** The scan generator provides three separate circuit functions. A triangular waveform is generated by a counter-integrator combination and is used as the track mode scan waveform. Two binary counters and D/A converters are used to develop the stairstep-type search mode scan waveforms. The above scan waveforms and the dc-correcting voltage from the tracking integrator are summed in current dividers to provide the deflection coil current required.

- **Error Amplifier.** The dc component of the deflection coil current is determined by a current sampling resistor and the corresponding voltage is then amplified and filtered to give the required output pointing error gradient.
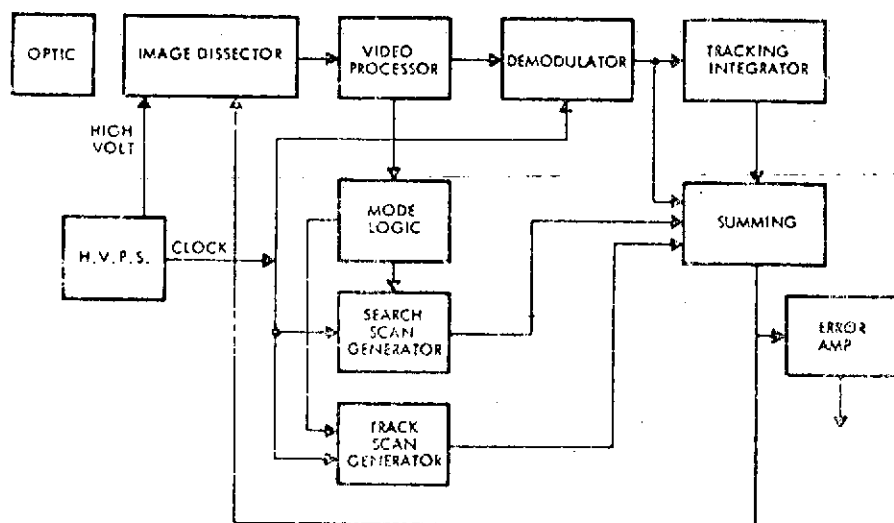
(Only one error channel is shown.)

Figure 6-6. Functional Block Diagram of Star Sensor

6.1.1.4   Star Sensor Unit Errors

This section summarizes the errors attributable to the SSU. The numbers given in Table 6-1 are based primarily upon breadboard test data and analytical error analysis.

Electronic Bias Errors

Three different sources of sensor electronics null shift errors are identified as:

V_{d1} = equivalent input dc level shifts to the track integrator.

This term includes:

(a) Error detector summing point variations.

(b) Integrator op-amp input offsets.

(c) Video waveshape variations.

V_{d2} = Equivalent input dc level variations to the deflection coil driver.

This term includes:

(a) Coil driver input op-amp offsets.

(b) Acquisition sweep input dc level variations.

V_{d3} = Equivalent input dc offsets of the output error amplifiers.

The sensor output voltage in terms of these three error terms and the input angle θ_i has been derived. Using the design parameters, the sensor output variations are then:

$$\Delta Vo = 3.7 \; \Delta V_{d3} + (13 \times 10^{-6}) \; \Delta V_{d2} + .67 \; \Delta V_{d1}$$

The values of ΔV_{d1}, V_{d2}, and V_{d3} have been calculated, and the total RSS overall output voltage variation is then:

$$\Delta Vo = \left\{ [3.7(\pm.942)]^2 + [(\pm120)(13 \times 10^{-6})]^2 + [(\pm1.75)(.67)]^2 \right\}^{1/2}$$

$$= \pm 3.68 \; mv$$

With an output error gradient of 20 millivolts/sec, the ΔVo of ±3.68 millivolts then represents a sensor pointing angle uncertainty of ±0.18 sec.

Table 6-1. Star Sensor Unit Error

	Arc Seconds (1σ)
NOISE	
● Short Term	
Shot Noise	0.11
Dark Current	NEG
Background Variations	NEG
Secondary Emission Noise	NEG
Preamp Noise	NEG
● Long Term	
Thermal (Opto-Mechanical)	.2
Power Supply Drifts	NEG
Stray Magnetic Fields	0.15
RSS NOISE	0.27
BIAS	
● Null	
Opto-Mechanical Alignment	0.2
Offsets-Electronics:	
Error Amplifier Input	0.17
Coil Driver Input	0.002
Track Integrator Input	0.06
Star Intensity Bias	0.02
Cross Coupling Effects	0.05
Thermal (Opto-Mechanical)	0.13
RSS BIAS	0.305
RSS TOTAL	0.41

Thermal Effects

In particular, three effects are considered. The first is the effect of linear thermal expansion on the blur circle and the focal length. The second is the effect of a temperature gradient across the telescope tube on the boresight axis alignment. Third is the effect of a temperature gradient across the image dissector mounting surface on the location of the boresight axis.

The optical system of the SSU has been designed completely of aluminum so that as the temperature changes the radius of curvature of the mirrors change as well as the separation of the mirrors. Thus, in theory at least, the minimum amount of defocussing occurs. However, another effect which occurs is that the effective focal length of the system will change which, in turn, will change the error gradient out of the sensor. Analysis shows that for a $10^o C$ temperature change, the spot size growth due to this defocussing is 4.004×10^{-6} inches. This represents less than .01 sec and can easily be tolerated. The increase in focal length will change the error gradient from 20 mv per sec to 20.0045 mv per sec. It is thus apparent that the thermal sensitivity to defocussing is extremely low and can be considered negligible.

If we consider the secondary mirror as the fixed plane in the optical system, then, when the telescope tube is heated on one side, the primary mirror will tilt with respect to the secondary. In addition, the primary-tertiary system will be displaced laterally. This is because the telescope tube will curve as it is unevenly heated. The radius of the center of curvature of the tube can be found one of two ways. The first is to assume that R will be very much larger than 6.75 inches and use the relationship for one sec of tilt

$$R = \frac{6.75}{4.84 \times 10^{-6}} = 1.394628 \times 10^6 \text{ inches}$$

If the primary-tertiary mirror system is tilted by 1 sec and this ray traced through the system, there is an error introduced of 1.89 sec. Thus, one must maintain thermal gradients well below the level where the telescope assembly will bend by 1 sec. Table 6-2 is a summary of the results of a thermal analysis of the SSU showing, that for most expected thermal variations, the angular distortion between the mirrors is less than 1 sec. The conditions of B and E are extreme, since the total power dissipation is only 2.7 watts. Therefore, the sun load effects are the predominant error cause. Representative star/tracker/sun conditions and thermal conditions were evaluated to establish the error in the Table.

Table 6-2. Summary of Thermal Analysis Results

Condition	Pressure	Average ΔT Across Mirror Spacing Tube (°F)	Angular Distortion Between Mirrors (Arc-Second)	Maximum Diametrical Gradient Across the Mirrors	
				Primary (°F)	Secondary (°F)
A. 10°F Radiant Ambient Variation Across Electronics	Vacuum	.057	.20	.0044	.024
B. 1 Watt Power Dissipation Variation Across Electronics	Vacuum	.031	.11	.0037	.011
C. Sun Load Along Axis of Electronics	Vacuum	.12	.43	.0099	.097
D. 10°F Radiant Ambient Variation Across Gimbal Axis	Vacuum	.13	.46	.0097	.050
E. 1 Watt Power Dissipation Across Gimbal Axis	Vacuum	.22	.77	.014	.080
F. Sun Load Along Axis of Gimbal	Vacuum	.23	.85	.017	.14

The effect of mechanical stability of the detector tube is treated briefly. The relationship between angular movement and linear distance on the photocathode is given by a simple geometric expression as,

$$d = f_\ell \times \tan \theta$$

where f_ℓ is the focal length of the optical system. In the case of the SSU

$$d = 100 \times 4.84 \times 10^{-6} = .000484 \text{ inches/sec}$$

Thus, if the image dissector photocathode should move laterally by .001 inches, error of 2 sec would ensue.

The effect of nonuniform thermal heating of the telescope will be considered by assuming a 1°C per inch gradient across the telescope at the support plane of the image dissector. Thus, the radial distance on one side of the dissector will expand more than the other and the center of the dissector will no longer be half-way between the two sides. Integrating to find the expansion,

$$E_1 = 23.8 \times 10^{-6} \int_0^{2.25} y \, dx = 23.8 \times 10^{-6} \int_0^{2.25} x \, dx$$

$$= 23.8 \times 10^{-6} \left. \frac{x^2}{2} \right|_0^{2.25} = 60.24375 \times 10^{-6} \text{ inches}$$

on one side and

$$E_2 = 23.8 \times 10^{-6} \int_{2.25}^{4.50} y \, dx = 23.8 \times 10^{-6} \int_{2.25}^{4.25} x \, dx$$

$$= 23.8 \times 10^{-6} \left. \frac{x^2}{2} \right|_{2.25}^{4.50} = 180.731 \times 10^{-6} \text{ inches}$$

on the other. The total expansion is 240.975×10^{-6} inches, so that the midpoint is 120.4875 inches from one side. The center of the dissector is displaced from this by 60.2435×10^{-6} inches. This amounts to 0.125 sec. It should be noted that the temperature gradient assumed here is very much higher than that calculated in the

thermal analysis (in fact, almost 7 times larger) so that one would expect more like 0.02 sec displacement.

Electronic Noise

The zero mean, white gaussian noise was predicted to be the same as that observed in test data. For star irradiance in the +1.0 to +2.0 magnitude region, the noise is approximately 0.2 sec (1σ). For a +3.5 magnitude star (25μA anode current), the noise has increased to approximately 0.35 sec (1σ).

6.1.2   Sensor Gimbal Unit Design

The dominant design criteria for the Sensor Gimbal Unit (SGU) was to achieve accuracy on the order of one sec in the space environment and be able to substantiate the performance during ground test. Meeting this requirement demands extreme gimbal rigidity. A compromise between rigidity and weight is to conceive a gimbaling system in which structural moments are nominally zero and which possesses thermal symmetry. The first aspect of this concept is achieved by a gimbaling configuration in which the sensor (SSU) mass is centered between the supporting bearings of the inner gimbal; the mass of all components associated with the outer gimbal is centered between the outer gimbal suspension; and the mass of the entire system is contained in the ground plane. Thermal symmetry is achieved by developing identical power dissipation on each side of the payload and the outer gimbal assemblage. This offers elimination of thermal shifts of the initially established relationships of the gimbal axes. However, achievement of thermal symmetry requires the use of two motor drives and two encoding systems per gimbal, hence some unit weight compromise is inherent.

The SGU consists of the inner gimbal drive assemblies, the gimbal ring, and the outer gimbal drive assemblies. The SSU is directly interfaced (on both sides) with the inner gimbal drive assembly as shown in Figure 6-7 . A structural I-beam ring connects the inner gimbal to the outer. The latter,via its gimbal housing mounting pads, is attached to the reference block. The material choice for the gimbal structure, except when subsequently noted, was aged 6061 aluminum alloy. This selection was based to provide dimensional stability, stiffness, and manufacturing flexibility inasmuch as this gimbal represents an engineering model. For flight models, where weight and larger stiffness are the problems, beryllium alloys would be used.
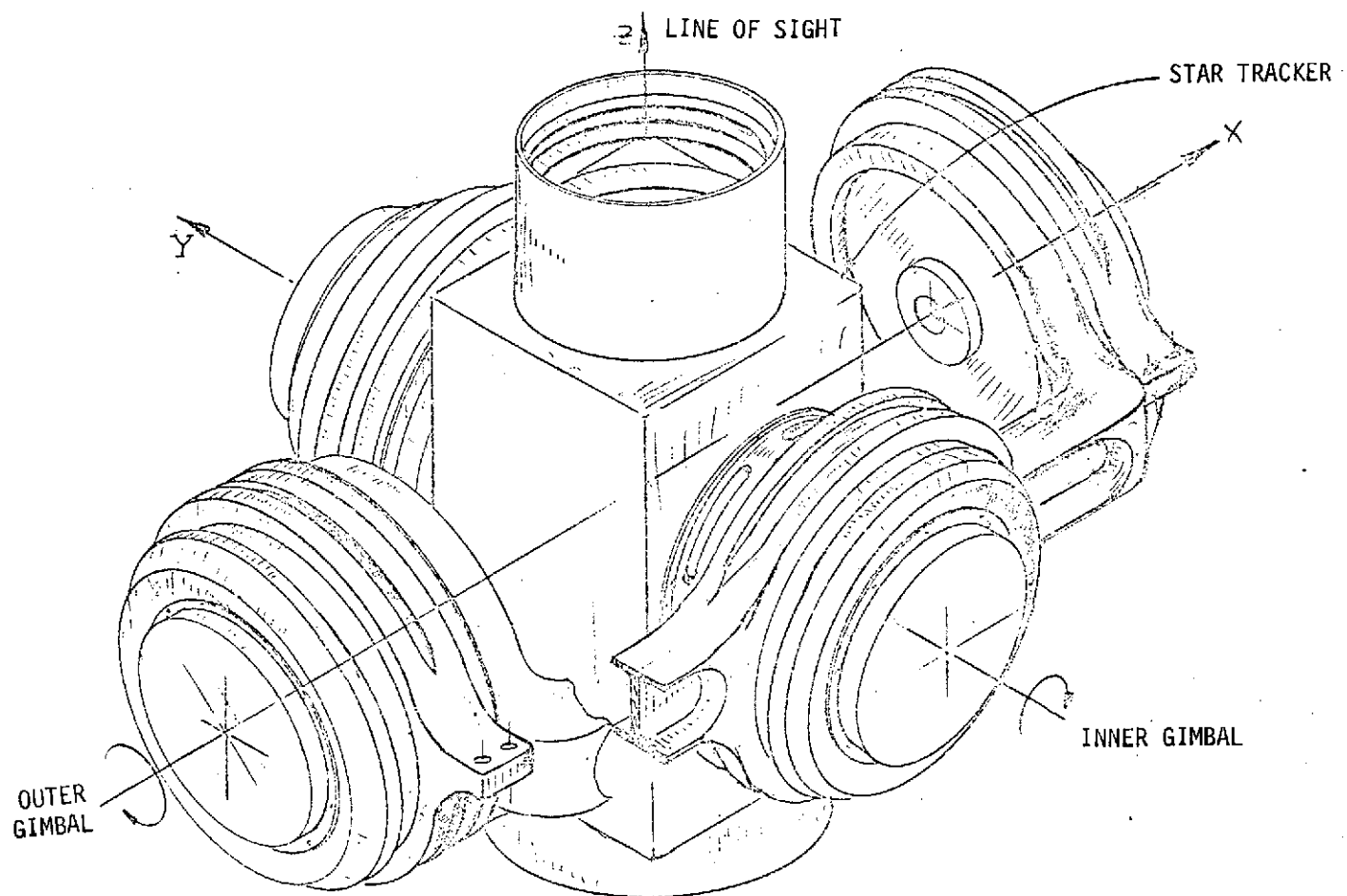
Figure 6-7. Star Tracker Configuration

The most significant components of the SGU are contained within the gimbal drive housings shown schematically in Figure 6-8 and in exploded view in Figure 6-9 . The housings are essentially identical in performance and general configuration. Each housing contains the following subassemblies: the gimbal angle encoder, the gimbal suspension, gimbal caging mechanism, the data link assembly, and the drive motors.

6.1.2.1 Inductosyn Encoder

The selected encoding element for measuring rotation are two resolver units (commercially known as Inductosyns) per axis. One unit is a single speed and the other has a 360 speed capability. Both resolvers are manufactured on a single set of plates. To comply with the thermal symmetry criteria, a disc equipped with a thermal blanket is mounted on the opposite side of the gimbal to achieve similar power dissipation on each side of the payload. The resolver patterns are printed on aluminum discs, one being attached to the payload side, and the other to the housing sleeve within a gap of 5 to 7×10^{-3} inch. To minimize signal noise, the resolver output is preamplified on the gimbal prior to its introduction to an "off-gimbal" signal conditioning circuit. For proper mechanical alignment and initial indexing, the Inductosyn stationary (stator) element is provided with sufficient mounting freedom to afford minimization of eccentric and nonparallel motions.

6.1.2.2 Gimbal Suspension

The gimbal design features a one-ball bearing configuration. The geometry of this scheme provides a self-alignment feature and facilitates the fabrication of the gimbal system by providing inherent reference for the establishment of two mutually perpendicular planes which contain the rotational axes of the gimbals.

The desired axes are established by a line of contact of the balls with the cone surfaces of their retaining cups. The accuracy of the retainment of the established gimbal axes is set by the cups radii of contact and the ball sphericity. Since the ball sphericity can be obtained to two parts per million and the cups radius of contact is established by lapping, and since all other critical surfaces are indexed to the payload balls, the achievement of very accurate alignment is possible.
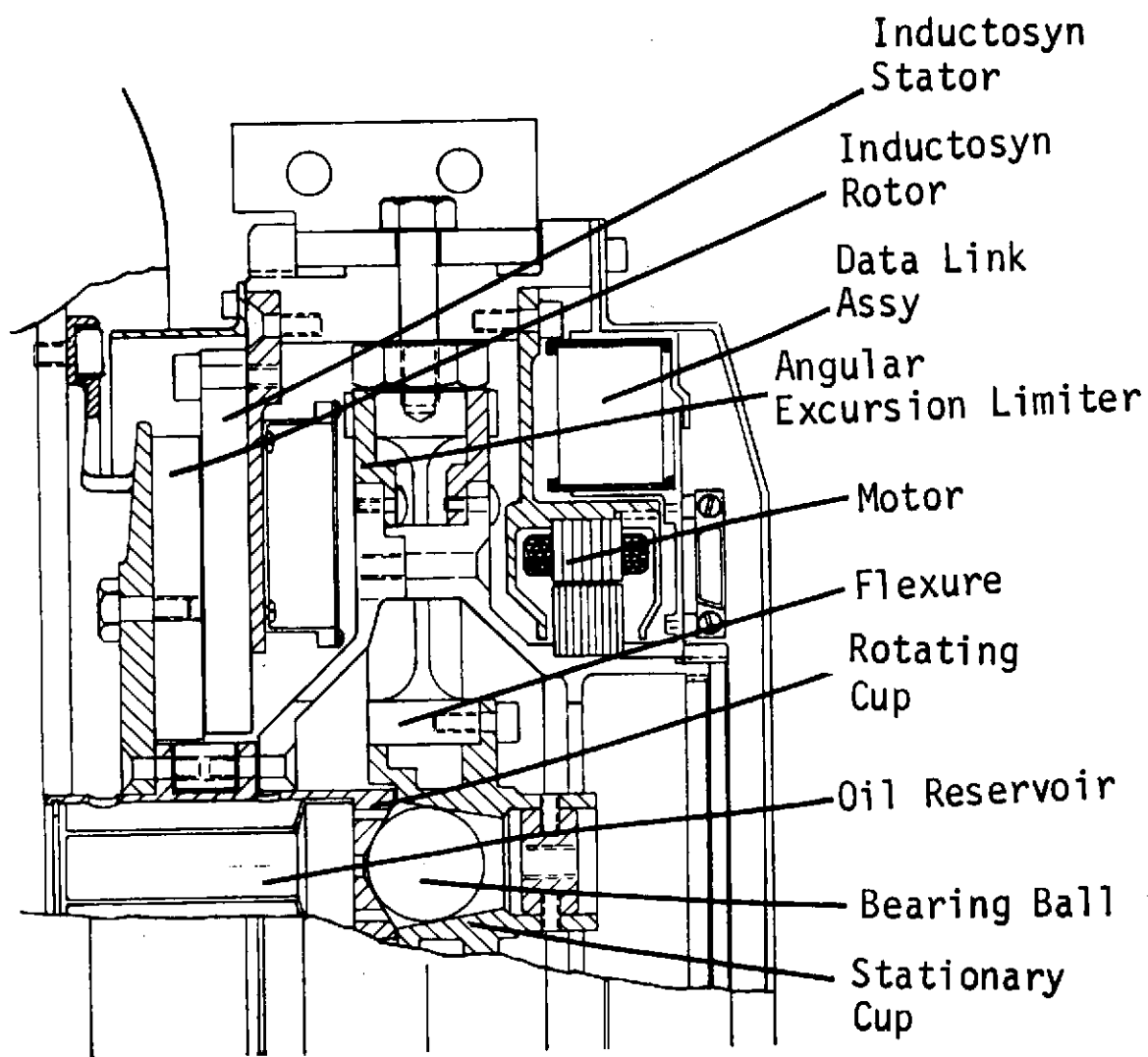
Figure 6-8. SGU Gimbal Drive Housing

INDUCTOSYN ELECTRONICS

STATIONARY BALL RETAINER

GIMBAL HOUSING
DRIVE SLEEVE

BEARING BALL

DATA LINK ASSEMBLY

MOTOR STATOR

MOTOR ROTOR

MOTOR DRIVE HOUSING

CAGING MECHANISM

ROTATING BALL RETAINER

STATOR, INDUCTOSYN
ROTOR,

INDUCTOSYN INTERFACE MOUNT
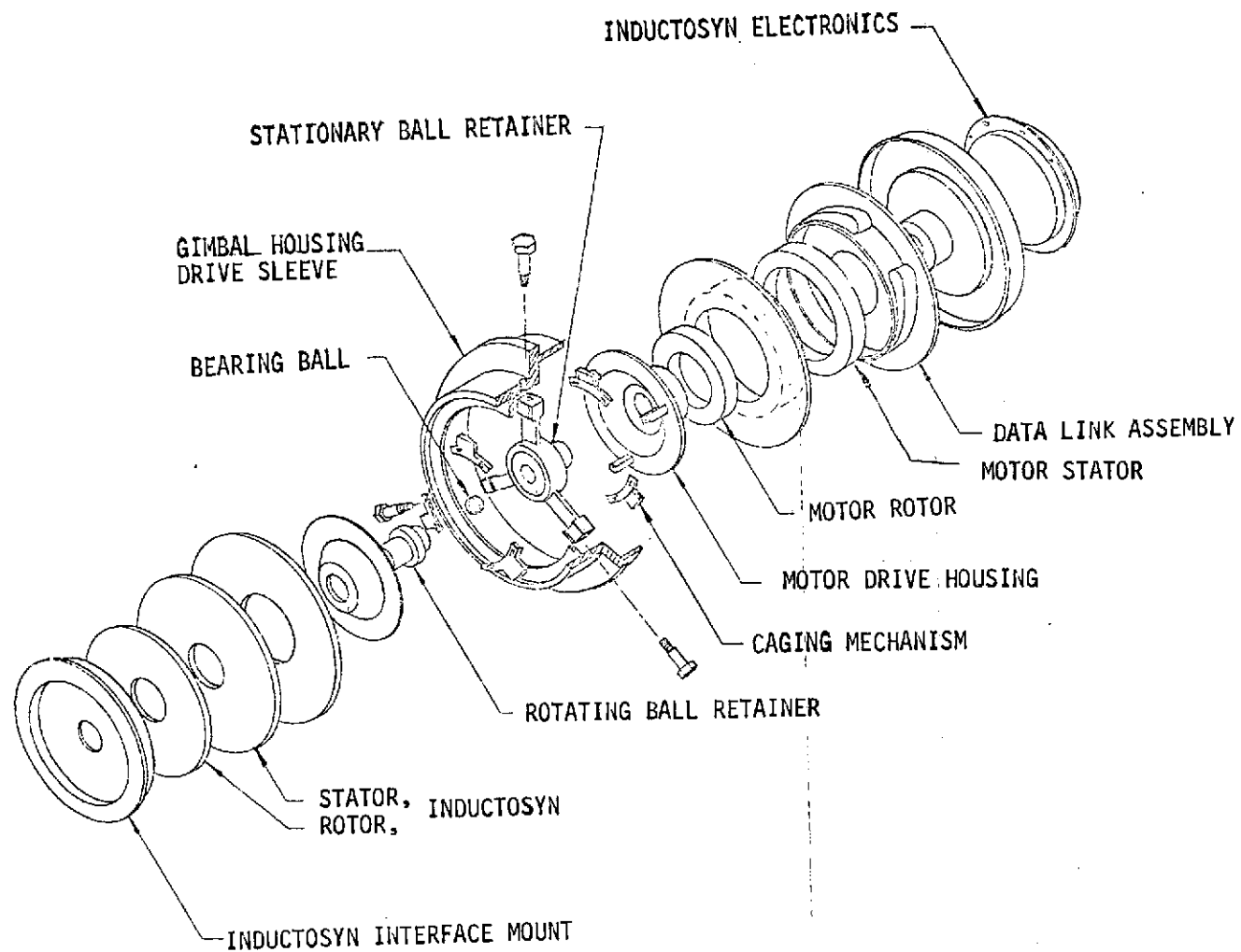
Figure 6-9. Gimbal Drive Components (Exploded View)

As shown in Figure 6-10 , the suspension consists of two single spherical balls supporting each axis. Each ball locates itself via two cone type cups. One cup (rotating retainer) is located on each side of the SSU and the other cup (stationary retainer) is attached through a flexure to the gimbal frame. The included cone angles of the stationary and rotating retainers are 20 and 120 degrees respectively. Furthermore, the rotating retainer is inclined 40 minutes of arc with respect to the centerline passing through the centers of the spherical balls; the stationary cup cone is eccentrically offset with respect to the centerline of the cylindrical shaft containing the cone. The shaft element is housed in the bore of the bearings preload flexure, which is an intermediate element between the retainer and the gimbal frame.

The purposeful inclination and offsets of the rotating and the stationary retainers provides adjustment capabilities to accommodate accumulation of tolerance and the elimination of runout. Specifically, by rotation of the stationary retainers, perpendicularity of the gimbal axes can be established; also the relative motion of the rotating cups with respect the body of the payload can essentially eliminate undesirable shaft runout. By virtue of the inclination of the rotating c , lubrication of all the sliding surfaces is facilitated by a continually changing (nutating) circle of contact. The lubricant is provided to the bearing balls and the rotating retainer contact surfaces by Nylasint reservoirs located inside a shaft comprising the rotating retainer. A configuration of slots in the rotating retainer provides lubricant to the space surrounding the ball below the nominal line of sliding contact, as well as to the space outside the line of sliding contact. The excess holes for the lubricant are also filled with Nylasint material. This affords flow of lubricant directly into the bearing chamber by wicking action, thus eliminating the molecular flow lubrication of the bearing vestibular surfaces.

The retainers are made from stellite and the balls from tungsten carbide. Carbide was chosen for its hardness, known dimensional stability, and relatively good porocity. Stellite Alloy No. 6B was selected mainly to obtain reasonable hardness and the non-magnetic properties desired. The combination of these materials and the particular geometric configuration allows direct application of bearing loads approaching 200 lbs with no visible Brinelling. Larger loads can be accommodated by using different material for fabrication of the retainers.

The friction torques are a function of the preload, the ball diameter and the coefficient of friction. For this design, frictional torques approaching 35 and 60 in-oz for the inner and the outer axes, respectively, were determined.

ROTATING
RETAINER

STATIONARY
RETAINER

BEARING BALL
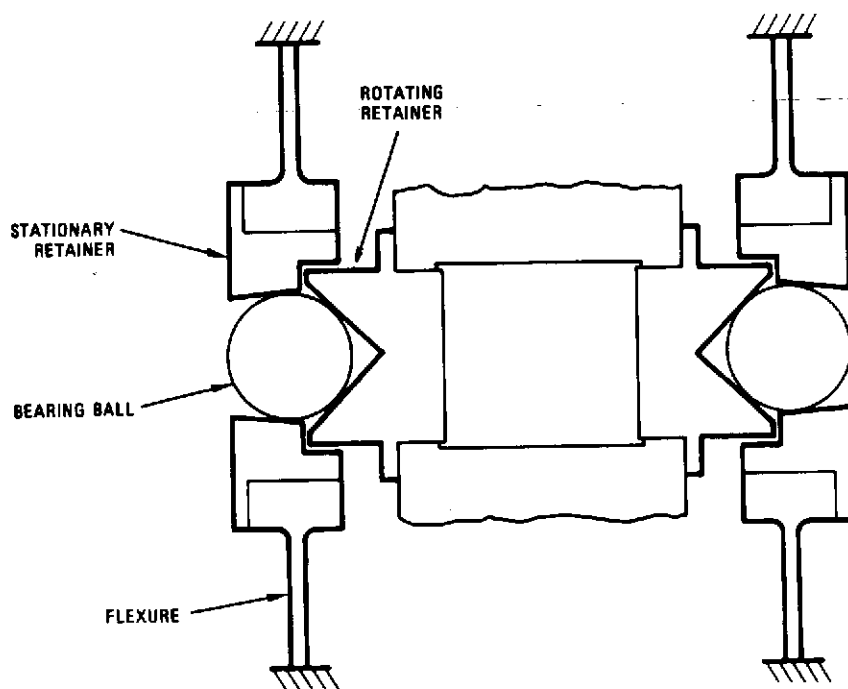
FLEXURE

Figure 6-10. SGU Suspension System Concept

The design success of the single ball bearing suspension concept significantly depends on the performance characteristics of the flexures that support the station-ary retainers of the spherical balls. Functionally, the flexures provide clearance support for the stationary retainers, bearing preload characterized by minimal changes due to temperature variation (and hence minimal gap changes between the stators and rotors of the inductosyn encoders), and continual measurement of the location of the ball centers as well as the changes of preload and friction torques in the direction of rotation.

Structurally, the flexure consists of a hub with a bore which accepts the stationary retainers. The outboard end of the stationary retainers, after appropriate alignment schedules, are clamped to the flexure hub. The hub is supported by three flexure elements located 120 degrees apart. Each element has a cross sectional area of 0.10x0.75 inches with the larger dimension perpendicular to the rotational axes. The outboard end of the flexural elements have a solid section of which four sides are flat and are guided by mating surfaces of the two-section housing sleeve. The outboard section of the flexure terminates with double threaded boss. The internal thread is used to provide radial tension to the flexure members by pre-loading them to the housing sleeve and outer thread is used to lock the preload bolt to the sleeve and at the same time preload the bolt to tensions larger than those applied to the flexure elements. The latter aspect is useful in providing additional torsional rigidity when needed.

6.1.2.3 Gimbal Caging Mechanism

The gimbal suspension is provided with a caging stops system which protects the bearings and the payload from exposure to excessive stresses by introducing mechanical components in parallel with the element of interest during phases of abnormal excitation. The introduced elements are always of higher structural stiffness than the principal elements of interest. To affect caging condition, the drive motors must rotate their payloads an angle greater than 45° and 15° for the outer and inner gimbals, respectively. The motors are required to maintain the caged condition (note that other concepts such as detenting are also feasible for the subject design). At the caged region, six sector elements of the rotating members are allowed to approach their mating components on the stationary portion of the gimbal to within 1.5×10^{-3} inches. Such arrangements during abnormal excitation periods provides three directional restraints and snubbing of the payload after nominal deflection of the preload flexure. For the baseline design, the load dis-tribution between the caging mechanism and the bearing balls is in a ratio of 1/10 such that forces not greater than 40 lbs will be absorbed by the bearings. Because the line of contact between the ball and the retainers nutates as a function of

displacement, for the chosen caging concept (which requires excursions greater than the operational angular displacements), brinelling (should it take place) occurs in the circle of contact regions which are never operationally used.

6.1.2.4   Data Link

The data link provides transmission of electrical signals without excessive restraint torques. The design utilizes an "S" folded conductor strip which is attached at the ends of and slides between a cylindrical stationary member attached to the housing sleeve and a smaller diameter cylindrical component (the rotating member) attached to the motor shaft. The inner and the outer members are lined with nylon rings to provide electrical insulation and mechanical guide for the rolamite action of a 6 conductor strip. There are four such strips providing the capability of $\pm$ 60° motion with restraints not exceeding 1/2 in-oz. Both the stationary and the rotating members of this assembly are made from beryllium Appropriate electrical connectors (miniature) are attached to the periphery of the rotating and stationary component. The data link itself is so designed that it can be removed from the system without disturbing the various electrical interconnections.

6.1.2.5   Drive Motors

Each gimbal motor drive assembly is identical in performance and general configuration. It consists of a two phase permanent magnet motor and appropriate support structure. The motor has 24 poles and 4 skewed slots between pole spaces. The commutation to the motor is provided by the Inductosyn resolver signal which is conditioned to provide the required power in terms of sine and cosine functions with periods satisfying the number of poles (12 speed). Interconnecting of the sine and cosine inputs to the respective motor winding results in a brushless motor exhibiting DC torquer characteristics. Each gimbal drive (two drives for each gimbal) was sized to provide redundancy such that one motor can drive the expected loads. The two motor drive concept not only satisfies the thermal symmetry design criteria, but also can provide almost complete elimination of motor slot ripple by appropriate indexing of the motor set.

6.2   SENSOR ELECTRONICS ASSEMBLY

The Sensor Electronics Assembly controls and drives the motors of the star tracker gimbal and provides the electronics to encode the gimbal angles from the inductosyn signals. Figure 6-11 shows a block diagram of the SEA for one gimbal axis (the excitation and some of the mode control circuitry are common to both axes). The Encoding Electronics has as its function the processing of both a multi-speed and single-speed inductosyn to produce a precision measure of gimbal angle, and to develop a rate signal for local damping of the motor. In slew the motor is driven at a rate specified by the computer. In track mode the star sensor error signal is used.

6.2.1   Encoding Electronics

Angle encoding is accomplished by driving the inductosyn rotor with a low-distortion sinusoidal 10 kHz signal. The inductosyn stator produces a pair of signals at the same frequency whose amplitudes are respectively proportional to the sine and cosine of gimbal angle. For high precision, the particular inductosyn used has a single-speed and a 360-speed section on the same disc pair. Both are encoded to produce digital angle data.

Because of their low level the inductosyn signals are first amplified by a set of d.c. amplifiers located on the gimbal in the immediate vicinity of the inductosyn. The single-speed and the multi-speed encoders convert the incoming sine-cosine amplitude data into a digital position output using a form of double-angle phase technique. Each encoder is mechanized as a pair of trigonometric phaselock loops. An analog rate signal is also developed for local damping of the motor.

6.2.1.1   The Inductosyn

The inductosyn is a pair of discs, in this case 7" in diameter, which are mounted such as to rotate coaxially with respect to one another with facing surfaces in close proximity. The facing surfaces have printed conductors, forming winding circuits which may be flux linked, disc-to-disc. One disc, designated the rotor, has a single winding; the other, the stator, has two windings. The winding geometry is arranged so that the transformation coupling from rotor to stator varies trigonometrically with relative disc rotation. The two stator windings are in mechanical quadrature to one another. Thus the device is electrically identical to a synchro resolver, except for a very low coupling efficiency and for a larger number of poles than are normally found in a conventional resolver.
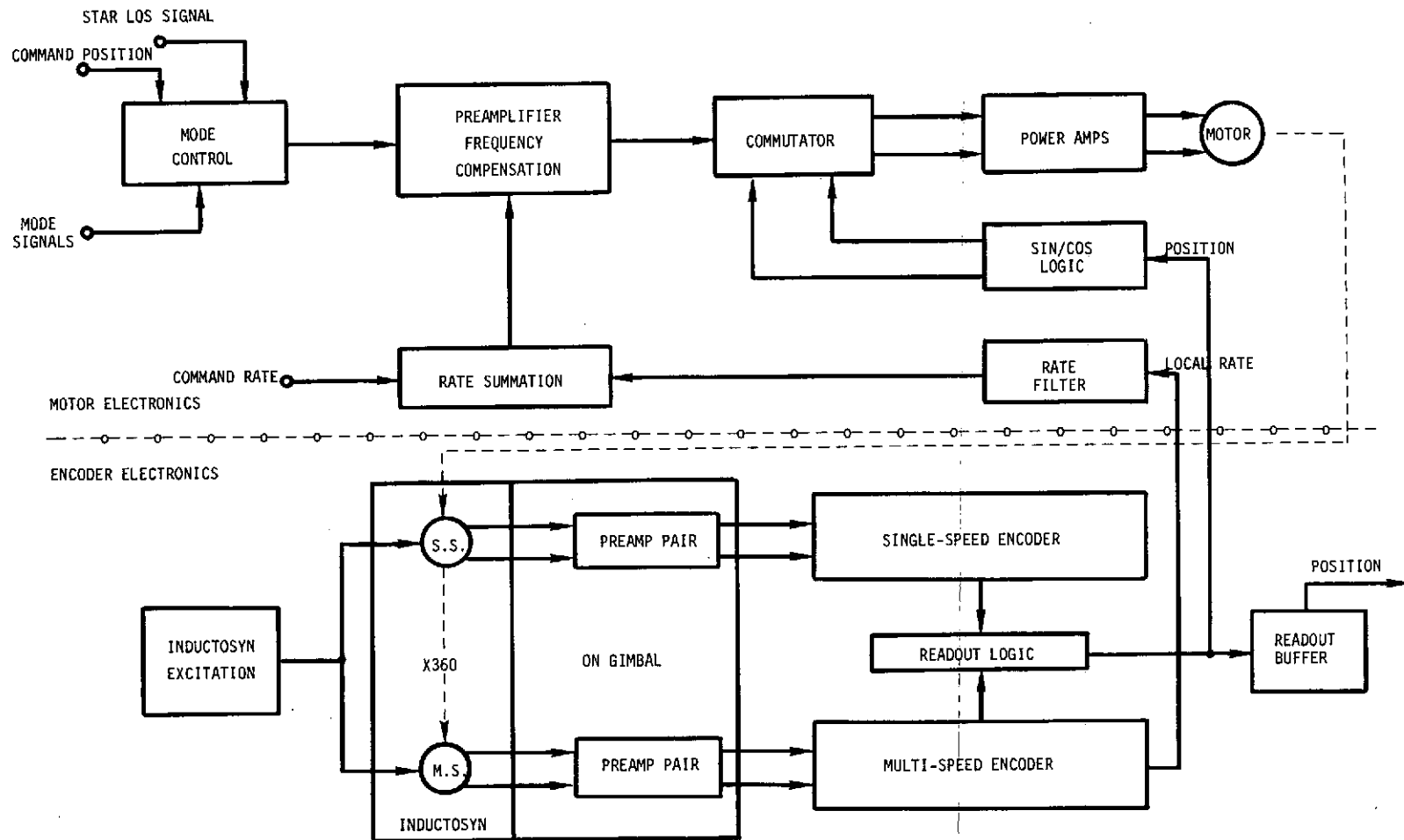
Figure 6-11. Sensor Electronics Assembly (Processing Shown for One Axis)

In the present case, the inductosyn to be used has 720 poles. Hence, one degree of mechanical rotation carries the rotor through 360 electrical degrees. If the two rotor windings are respectively identified as the sine and cosine windings, then their output voltages are

$$V_s = kV_m \sin 360\,\theta \, \sin \omega_e t$$

$$V_c = kV_m \cos 360\,\theta \, \sin \omega_e t$$

where the primary (rotor) voltage is

$$V_e = V_m \sin \omega_e t$$

and where k is the inductosyn transformation ratio (some very small fraction of the order of 1/1000), θ is the relative disc angle, and ω_e is the excitation frequency.

Since such a device can indicate angle unambiguously over only a one-degree range, an additional resolver section is placed on the same discs, this one forming a 2-pole resolver. Encoding a disc angle then consists in encoding two resolver sections separately and combining the results in such a way as to yield a single unambiguous datum.

Table 6-3 lists electrical characteristics for a typical PPCS prototype inductosyn. Of particular concern are the values of voltage attenuation. The inductosyn transformation ratio has the characteristics:

$$k = Ae^{-bs}$$

where s is the disc-to-disc spacing, and A and b are arbitrary constants. From the data in Table 6-3, the respective sections have transformation ratios:

$$k_1 = (2.265 \times 10^{-3})e^{-0.0869s}$$

$$k_{360} = (1.20 \times 10^{-3})e^{-0.877s}$$

where s is in units of thousandths of an inch. The nominal design spacing is 0.007". Hence

$$k_1 = 1.235 \times 10^{-3}$$

$$k_2 = 0.652 \times 10^{-3}$$

Table 6-3. Inductosyn Data, S/N 002

Data taken at 10 kHz.

	Fine 720 Pole	Coarse 2 Pole	
Rotor Impedance	15.5 + j2.6	1.313	
Stator Impedance	5.5 + j1.2	$\frac{S1-S3}{0.499}$	$\frac{S2-S4}{0.457}$
Phase Shift	89°	75°	
Accuracy	±1.6 sec	±18 min.	
Voltage Attenuation:			
Rotor Excited			
0.005" gap	1290	680	
0.010" gap	2000	1050	
Stator Excited			
0.005" gap	420	--	
0.010" gap	800	--	
Coincidence at Sine Z.C.	8 minutes		

Table 6-4 evaluates transformation ratios for spacing from 5 to 10 milli-inches. A spacing of 7 mils has been selected.

6.2.1.2   The Excitation Section

The Excitation Section provides drive to the inductosyn rotors at a frequency of 10.5 kHz and a nominal power level of 2 watts per rotor. Figure 6-12 shows its block diagram. A precisely controlled frequency of 1.26 mHz, generated by a crystal oscillator, is divided down with a modulo of 120, resulting in the desired 10.5 kHz. This is filtered to a high purity sinusoidal function, which is thereafter power amplified to drive the rotors.

The rotors are hooked in a series-parallel arrangement. This tends to equalize the power distribution among the rotors, partially compensating for the impedance difference between the single-speed and the multi-speed windings. In this hookup the multi-speed rotors still receive a greater share of the power.

Table 6-4. Transformation Ratios

Single-Speed $\quad k_1 = (2.265 \times 10^{-3})\ e^{-0.0869s}$

s(mils)	e^{rs}	k_1
5	1.54	1.470×10^{-3}
6	1.68	1.343×10^{-3}
7	1.84	1.235×10^{-3}
8	2.00	1.131×10^{-3}
9	2.19	1.037×10^{-3}
10	2.39	0.952×10^{-3}

Multi-Speed $\quad k_{360} = (1.20 \times 10^{-3})\ e^{-0.0877s}$

s(mils)	e^{rs}	k_{360}
5	1.55	0.775×10^{-3}
6	1.69	0.710×10^{-3}
7	1.85	0.652×10^{-3}
8	2.02	0.597×10^{-3}
9	2.20	0.547×10^{-3}
10	2.40	0.500×10^{-3}

CRYSTAL OSCILLATOR 1.26 MHZ

FREQUENCY DIVIDER ÷ 120

MODULATOR

FILTER

POWER AMP

V_e

R_s 1.3 Ω

R_s 1.3 Ω

ROTORS

R_m 16 Ω

R_m 16 Ω
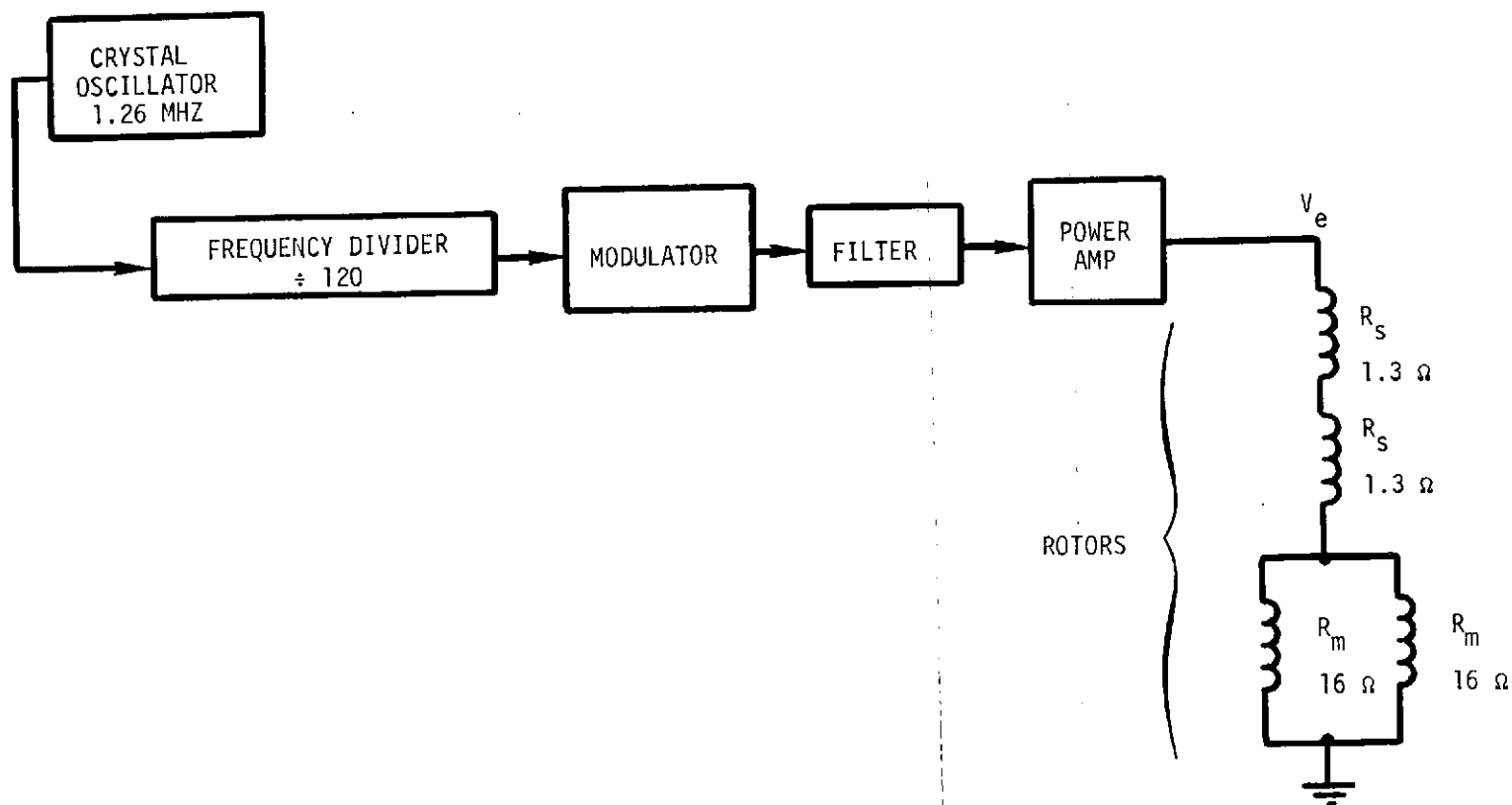
Figure 6-12. Excitation Section Block Diagram

This is acceptable because the single-speed has a lower attenuation than the multi-speed.

If R_s is the impedance of the single-speed rotor and R_m is that of the multi-speed rotor, then the total impedance is

$$R_{tot} = 2 R_s + 1/2 R_m$$

For a given excitation voltage V_e the multi-speed voltage is

$$V_m = \frac{1/2 R_m}{2 R_s + 1/2 R_m} V_e$$

The total current is

$$I_{tot} = \frac{V_e}{2 R_s + 1/2 R_m}$$

of which 1/2 supplies one multi-speed rotor

$$I_m = (1/2) \frac{V_e}{2 R_s + 1/2 R_m}$$

The per unit multi-speed power is then

$$P_m = \frac{1/4 R_m}{(2 R_s + 1/2 R_m)^2} V_e^2$$

For a given power in R_m the excitation voltage must be:

$$V_e = \left(\frac{P_m}{R_m}\right)^{1/2} (4 R_s + R_m)$$

For P_m = 2 watts and the values of Figure 6-12, V_e = 7.50 volts RMS. This leads to the following voltage division for each element:

$$V_s = 0.92 \text{ volts RMS}$$

$$V_m = 5.65 \text{ volts RMS}$$

6.2.1.3 The Preamps

Because the inductosyn output signals are at such low level, adequate signal transmission to the relatively remote SEA requires preamplifiers

located on the gimbal in the immediate vicinity of the inductosyn. There are two pairs per inductosyn. Each preamp has a nominal gain of 100. The dominant requirement is that a Sine/Cosine pair have as nearly identical amplitude gains as possible. In a flight application high precision components would be utilized. A gain match of $\pm$ 0.01% seems entirely feasible.

6.2.1.4 Phaselock Loop

The heart of the inductosyn encoding technique used is the quadrature phaselock loop. To study the action of this type of loop, first consider the simplified, non-quadrature phaselock loop pictured in Figure 6-13. The input sinusoidal function has a frequency of 10 kHz. This is chopped by the phase detector by a switching function, Q_f, which is the most-significant bit of a binary counter. The functioning of the phase detector can be represented as that of a switch (electronic in actuality) which is open for Q_f = 0 and closed for Q_f = 1.

The phase detector output is filtered to recover its DC component and the result is applied to the input of a voltage controlled oscillator. This has a characteristic as shown in Figure 6-13. With a zero volt input it has a nominal output frequency of 5.12 mHz for this illustration. Positive or negative input voltages cause increase or decrease in the frequency up to some saturation limits.
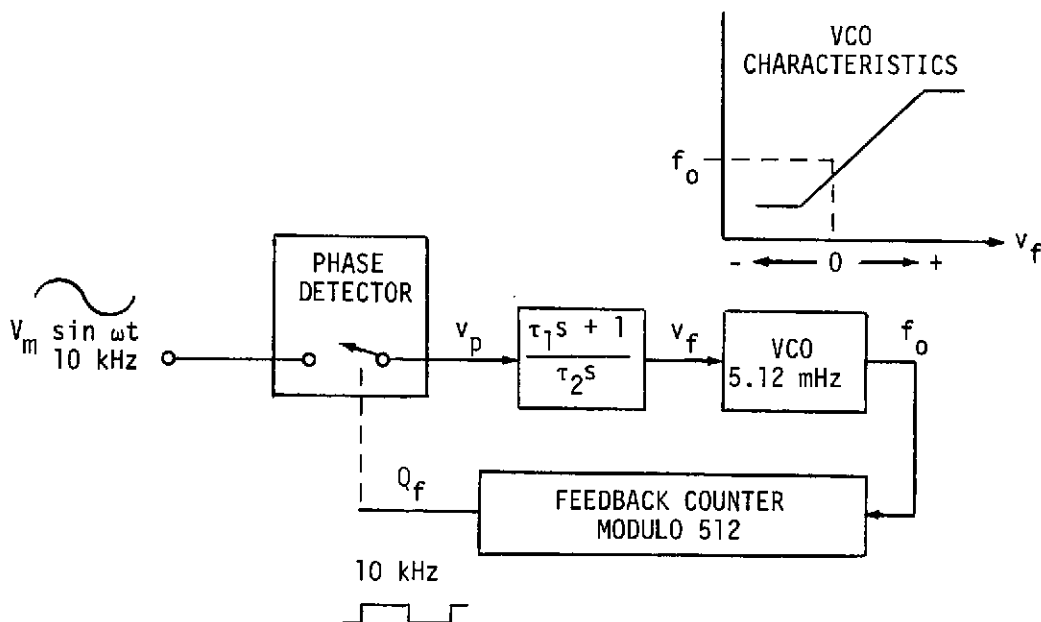
Figure 6-13.   Basic Phaselock Loop

The VCO frequency is divided by a factor of 512 by a 9 stage feedback counter. The nominal frequency of the counter output, Q_f, is therefore 10 kHz. Figure 6-14 shows the phase detector output for three different phase relationships between the loop input signal and the feedback counter. The condition in Figure b is stable. Note that here the phase detector output, v_p, has an average value of zero. In Figure a the counter is displaced in phase by -45°. The resultant v_p has a net negative average value. After filtering, this net DC component causes the VCO to decrease in frequency so that the counter loses in phase until the relationship of B is achieved. Figure c illustrates the opposite case, where the VCO will speed up, gaining in phase to achieve the condition of B.

If the input signal is:

$$v_i = V_m \text{Sin } \omega t$$

and if the relationship of Figure 6-14b defines zero relative phase, then the phase detector for any relative phase ϕ can be described as:

$$v_p = \begin{cases} v_i & \text{for } (\phi + \frac{3\pi}{2}) \leq \omega t \leq (\phi + \frac{\pi}{2}) \\ 0 & \text{for } (\phi + \frac{\pi}{2}) \leq \omega t \leq (\phi + \frac{3\pi}{2}) \end{cases}$$

Then the DC component of v_p is

$$v_p \Big]_{DC} = \frac{1}{2\pi} \int_{\phi + \frac{3\pi}{2}}^{\phi + \frac{\pi}{2}} v_i dt = \frac{1}{2\pi} \int_{\phi + \frac{3\pi}{2}}^{\phi + \frac{\pi}{2}} V_m \text{Sin } \omega t \ d(\omega t)$$

$$= \frac{V_m}{\pi} \text{Sin } \phi$$

This phase detector characteristic is shown graphically in Figure 6-15. It is to be noted that there are nulls for $\phi = 0$ and for $\phi = \pi$. But for the chosen loop sense the one at $\phi = \pi$ is unstable, i.e., a slight perturbation will send the loop one way or the other toward the null at $\phi = 0$ or 2π.

We turn now to the quadrature phaselock loop, illustrated in Figure 6-16. There are now two inputs, assumed to be the outputs of a resolver such that their amplitudes are trigonometrically related to a mechanical shaft angle θ:
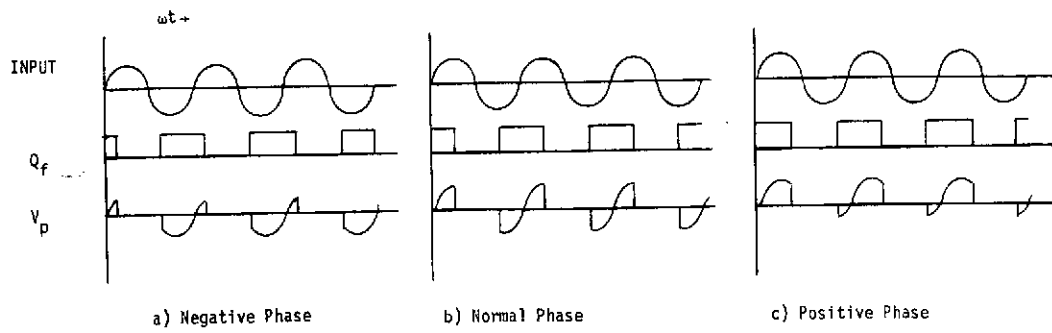
Figure 6-14.   Phase Detector Action
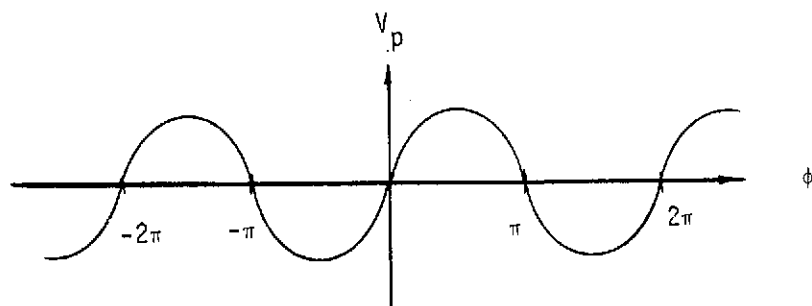
Figure 6-15.   Phase Detector Characteristics

$$v_s = V_m \sin \theta \sin \omega t$$

$$v_c = V_m \cos \theta \sin \omega$$

The feedback counter now has two outputs:

$$Q_f = \begin{cases} 1 \text{ for } (\phi + \frac{3\pi}{2}) < \omega t \leq (\phi + \frac{\pi}{2}) \\ \\ 0 \text{ for } (\phi + \frac{\pi}{2}) \leq \omega t \leq (\phi + \frac{3\pi}{2}) \end{cases}$$

$$R_f = \begin{cases} 1 \text{ for } (\phi + \pi) \leq \omega t \leq (\phi + 2\pi) \\ \\ 0 \text{ for } \quad \phi \quad \leq \omega t \leq (\phi + \pi) \end{cases}$$

i.e., R_f is of the same frequency as Q_f, but is retarded in phase by 90°.

The Q_f switching function is used to drive the cosine section of the phase detector, and the R_f function is used for the sine section. The DC component of the output of the cosine section is

$$v_{pc}\bigg]_{DC} = \frac{1}{2\pi} \int_{\phi + \frac{3\pi}{2}}^{\phi + \frac{\pi}{2}} V_m \cos \theta \sin \omega t \, d(\omega t)$$

$$= \frac{V_m}{\pi} \sin \theta \cos \phi$$

while the corresponding member for the sine section is

$$v_{ps}\bigg]_{DC} = \frac{1}{2\pi} \int_{\phi + \pi}^{\phi + 2\pi} V_m \sin \theta \sin \omega t \, d(\omega t)$$

$$= - \frac{V_m}{\pi} \sin \theta \cos \phi$$

When the two are summed equally into the filter

$$v_p\Big]_{DC} = \frac{V_m}{\pi} [\sin \phi \cos \theta - \cos \phi \sin \theta]$$

$$= \frac{V_m}{\pi} \sin (\phi - \theta)$$

The form of this phase detector characteristic is identical to that of the simple loop, except that instead of tracking the input at zero relative phase, the feedback counter now tracks at a phase dependent on the resolver shaft angle. The loop forces the function Sin (ϕ - θ) to null. Hence, ϕ = θ. As the inductosyn rotates, the feedback counter changes its phase correspondingly.

The phase of the counter is measured simply by sampling its numerical contents each cycle at some reference instant. If the resolver were ideal, this reference instant could be derived as the positive zero crossing of the resolver excitation voltage. But because of slight variations in phase shift across the resolver, it must be derived from the resolver output set. One method would be to detect the positive and negative zero crossing of both outputs, and logically select one of the four based on the relative signs and amplitudes of the signals. This is somewhat clumsy. The alternative is to make two opposite loops, one which tracks with a positive ϕ and one with a negative ϕ. For the loop described above ϕ = θ. By a simple change of switching functions from the feedback counter it is possible to get a phase detector characteristic:

$$v_p'\Big]_{DC} = \frac{V_m}{\pi} \sin (\phi' + \theta)$$

For this loop ϕ' = - θ. The phase difference between the two counters is then 2θ. The readout can be mechanized such that one counter is sampled when the other is at zero phase.

The two-loop system is a so-called "double angle" encoding technique. It has the advantages that many system errors are effectively compensated and that common circuit designs are used for both loops. Its disadvantage, in some applications, is a factor of 2 redundancy where encoding is required over 360 electrical degrees. Figure 6-17 describes the phases of the two counters, ϕ and ϕ', for some arbitrary angle. For zero angle the two vectors are vertical and diverge for positive increasing angle. Encoding in effect consists in
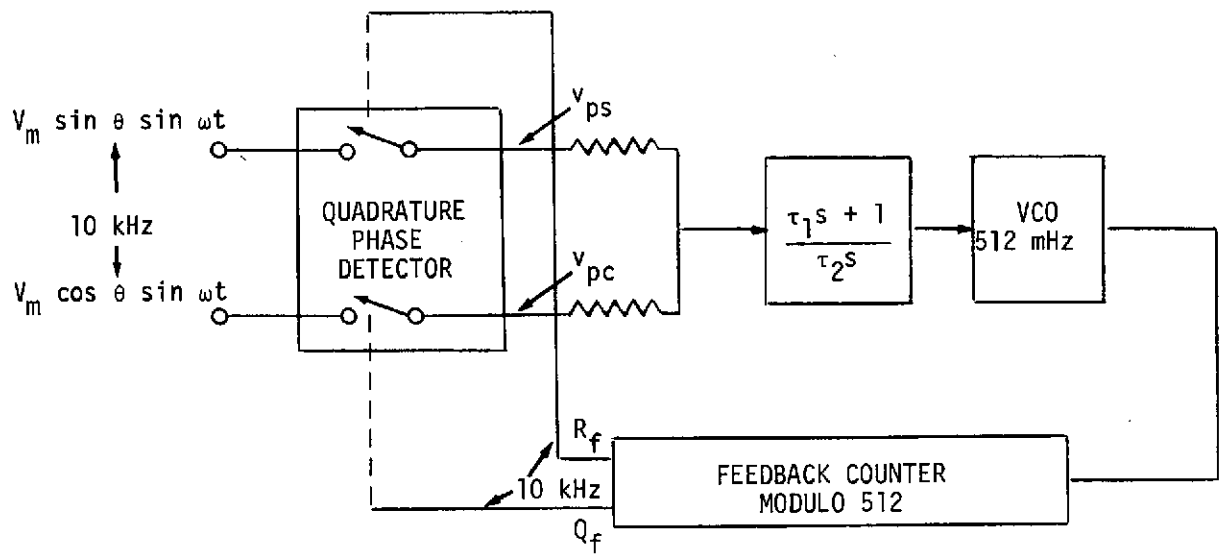
Figure 6-16   Quadrature Loop
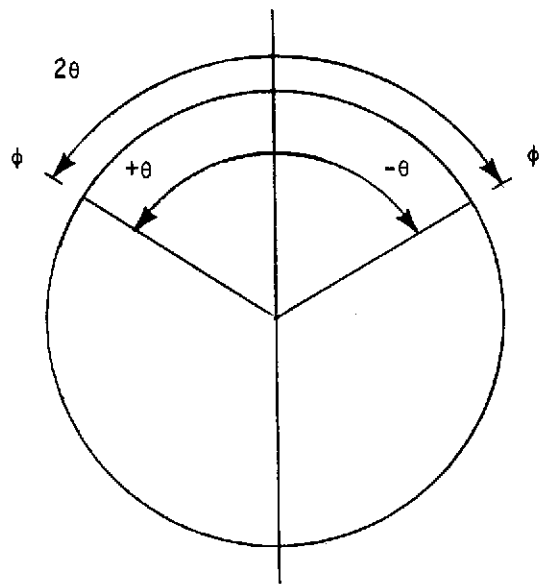
Figure 6-17   Feedback Counter Phases

measuring the phase difference between the two counters, equal to 2θ. But after 180 degrees the phases are again coincident, and the range from 180 degrees to 360 degrees cannot be distinguished from that between zero to 180 degrees without additional mechanization. Fortunately, in this application, the encoding range of the multi-speed section can be over 1/2 degree (180 electrical degrees), with the "splice" in data to the single-speed section at this level. And the range of travel of either gimbal axis is less than 180 mechanical degrees, hence ambiguity resolution is unnecessary in the single speed section.

6.2.1.5   The Multi-Speed Encoder

The multi-speed encoder, containing two opposite phaselock loops, is shown in Figure 6-18. Each loop is of the basic form previously described, with one notable exception. The positive loop operates with its feedback counter having a slightly different modulo (division factor) than that of the negative loop. This permits the vernier logic to extract approximately 5 additional bits of encoding resolution.

It is desired to encode to a resolution equivalent to 1/4 arc second. Taking account of the inductosyn speed ratio and the 1/2 degree double-angle range of the multi-speed section, this amounts to dividing 1/2 degree into some 8,000 parts. Since 1/2 degree is associated with one cycle of the signal 10 kHz, this means that the counting rate would need to be about 80 mHz if the encoder were mechanized by direct conventional means. This frequency is not practical for presently available logic elements suitable for spacecraft application.

Instead, the required resolution is obtained via a vernier technique. The positive feedback counter has a modulo of 8 x 31, while the negative counter has a modulo of 8 x 32. Thus, the resolution including vernier interpolation is 8 x 31 x 32 = 7936. Meantime, the VCO frequencies and the counter rates are kept at a manageable 2.5 mHz.

In essence, angle readout consists in measuring the relative phase of the feedback counters. For the 8 most-significant bits, this is done by extracting the contents of one counter at the instant when the other counter passes zero phase, i.e., when its MSB falls from ONE to ZERO. The vernier provides additional resolution as required. Mechanization involves comparing the relative phases of the two VCO's and noting the contents of the low-order end of the two counters at the instant of coincidence.

6-40
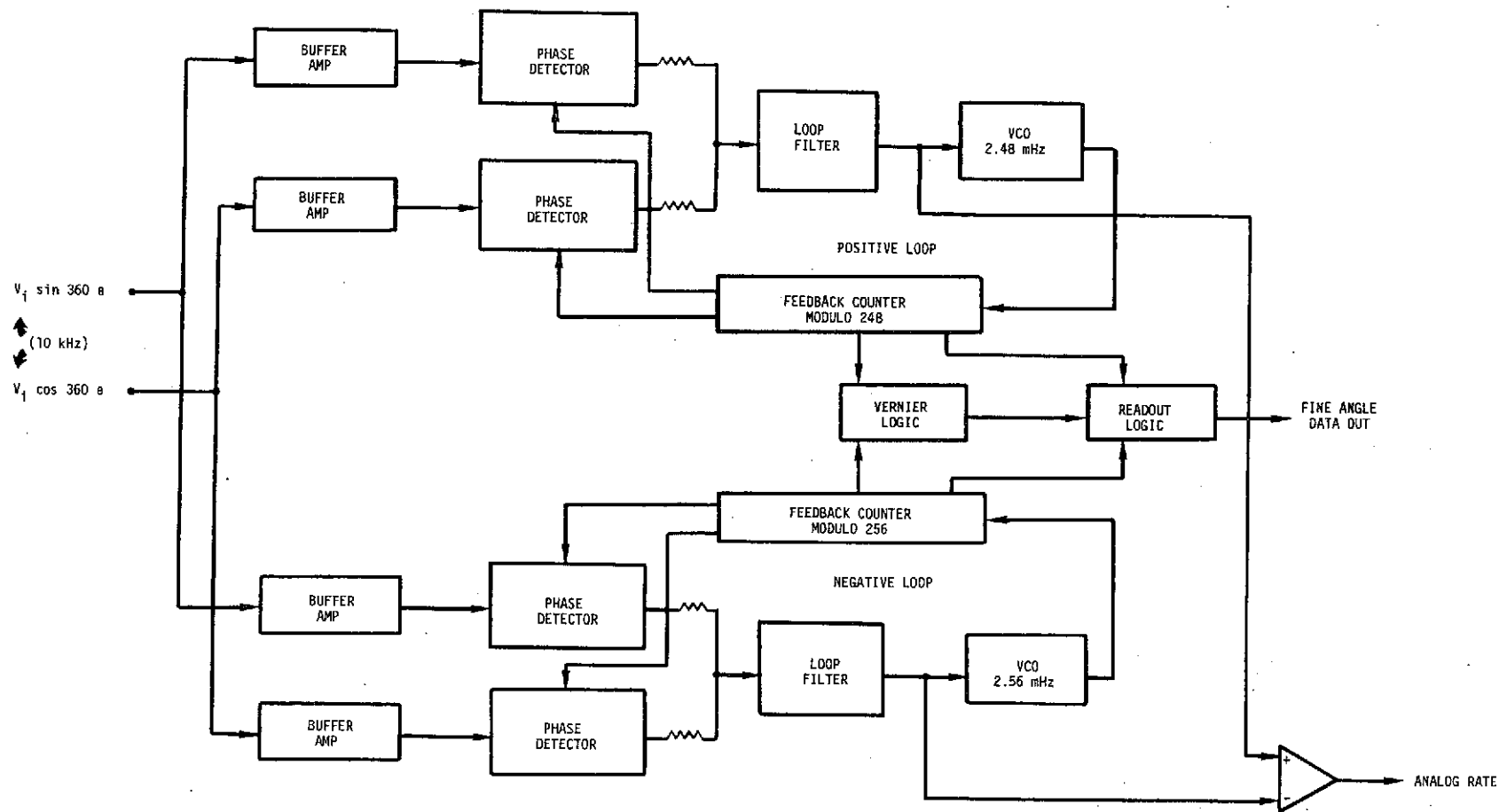
Figure 6-18. Multi-Speed Encoder

Auxiliary to the task of angle encoding, the multi-speed encoder provides a rate signal output. The details of this aspect will be discussed later, as will questions of loop dynamics and accuracy.

6.2.1.6   The Single-Speed Encoder

The single-speed encoder is entirely similar to that for the multi-speed, except that it receives as inputs the single-speed inductosyn signals. It has different feedback counter moduli, and therefore different VCO frequencies, and it has no rate signal development.

Because it also is a double-angle system, the total encoding range is 180°. This range is encoded to a resolution identical in weight to that of the most-significant bit of the multi-speed encoder - 1/2 degree. Thus, there is one redundancy or "overlap" bit in the total data determination. In this way, the classic two-range encoder ambiguity, resulting from slight offsets between the two encoders is resolved. The method involves adding +1, 0, or -1 to the high-order data field, based on a logical comparison of the bits at the data splice.

The feedback moduli are 8 x 9 x 10 = 80 respectively. Thus the VCO frequencies are 720 and 800 kHz. The venier is mechanized against the 9 and 10 submodulo factors, so that the net resolution is 8 x 9 x 10 = 720.

6.2.1.7   Loop Dynamics

Each of the phaselock loops is a phase servo, and as such, has certain dynamic stability considerations involved with the gains of the various elements. These elements are the phase detector, the loop filter, and the VCO.

The earlier derivation leading to phase detector characteristics can be used as a basis to determine the phase detector gain, except that the actual detectors are full-wave and must therefore be adjusted by a factor of 2 (a half-wave detector was used for simplicity of illustration in the basic discussion). The DC component of a full wave detector is therefore

$$V_p \Big]_{DC} = \frac{2V_m}{\pi} \sin(\phi - \theta)$$

where V_m is the equivalent peak value of the compound signal input, θ is the electrical input angle, and ϕ is the relative phase of the feedback counter. Since the loop tracks such as to force this quantity to zero, it is justified to use the approximation:

Sin x ≃ x for x small

Hence, for purposes of dynamic analysis the phase detector gain is:

$$K_d = \frac{2V_m}{\pi} \text{ (volts/radian)}$$

The design of the VCO permits considerable latitude in gain choice since the basic circuit is extremely high-gain, and must incorporate an input voltage attenuator. Since a rate signal is to be developed from the VCO input voltage, it is desirable to choose the gain as low as possible. However, it must be large enough to accommodate for VCO internal frequency drifts due to component variations. If the VCO's center frequency (grounded input) shifts by 10%, the frequency gain must be large enough that the prior stage is able to remain within its unsaturated voltage output range and still force the VCO to the proper frequency. The gain is therefore chosen in the vicinity of 1%/volt. Referred to the input of the phase detector, the VCO gain is therefore

$$\frac{K_o}{s} = \frac{0.01 \, \omega_e}{s} \text{ (radians/volt)}$$

Note that the gain is that of an integration with respect to frequency, since the variable of control is phase.

The loop filter functions to adjust the behavioral properties of the loop as desired. Acquisition (achieving phaselock), errorless response in the presence of shaft velocity, and a usable rate signal require double integration. Adequate phase margin dictates a zero prior to unity overall gain (open loop). Finally, additional poles are required beyond unity gain to reduce the unavoidable second harmonic (20 kHz) component in the output of the phase detector. This component results in a phase modulation of the VCO and hence a departure from encoding linearity to the extent that it is allowed through the loop filter.

Figure 6-19 shows a proposed open-loop dynamic design. There are two origin poles, one due to K_o/s characteristic of the VCO and one in the loop filter. Z_1 is a lead at 25 Hz in the loop filter. P_2 is a simple lag in the loop filter, where P_3, P_4 are a doublet pair at 2 kHz with a damping ratio of 0.7. The loop bandwidth is 200 Hz (unity gain point). The phase margin is 56° and the gain margin is about 14 db. Of special interest is the fact that the 20 kHz attenuation is in excess of 100 db or $1:10^5$, compared with the multi-speed encoder resolution of the order of $1:10^4$. Hence, the second harmonic
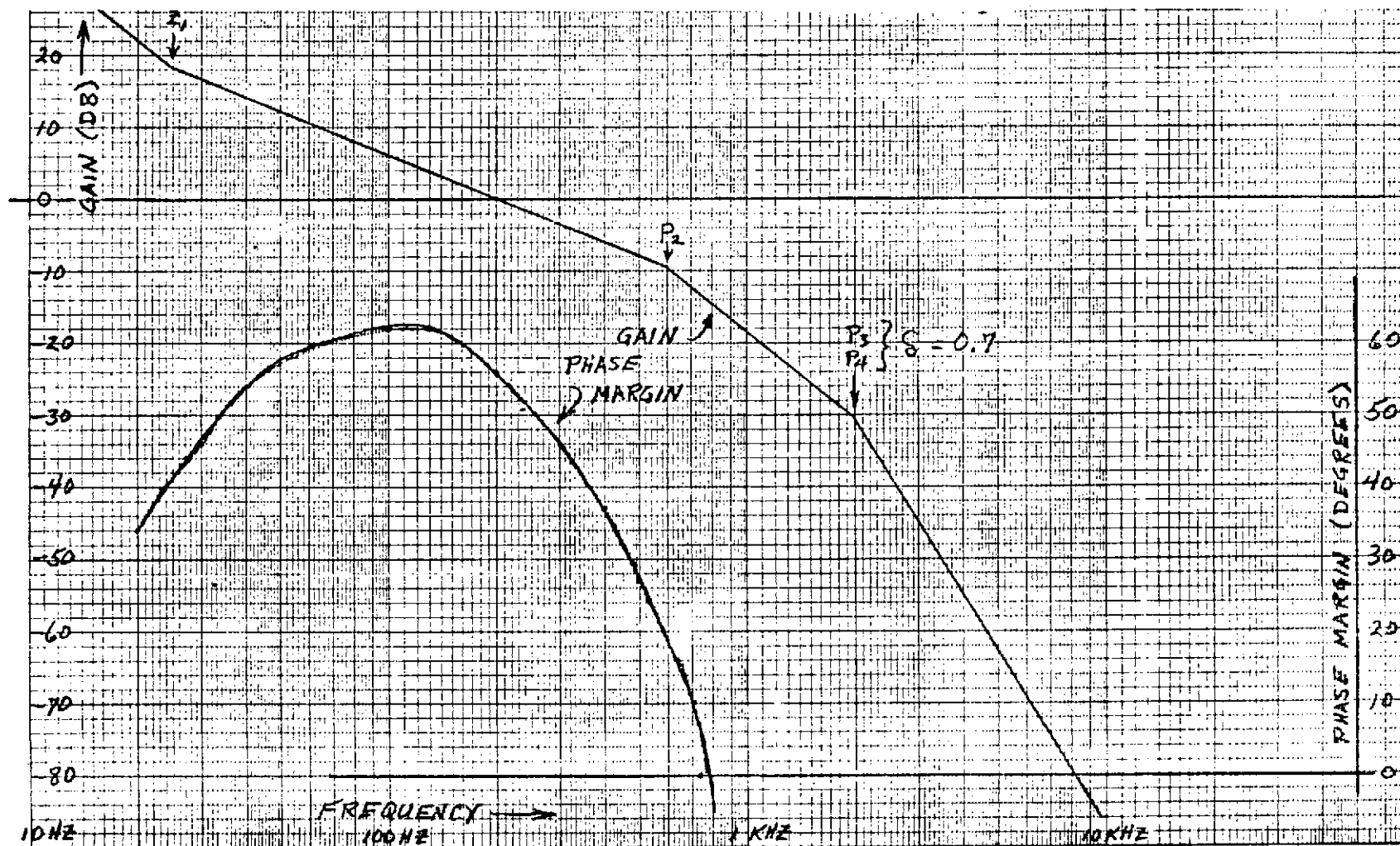
Figure 6-19. Phase Lock Loop Open Loop Frequency Response

error due to the phase detector is reduced to insignificance.

A classic problem associated with phaselock loops is acquisition of phase-lock. A first-order loop cannot acquire if the VCO differs from the input signal by an amount greater than the loop bandwidth. With a second-order loop acquisition is possible with frequency differences many times the loop bandwidth. The pull-in time can be obtained as:

$$T_p = \frac{(\Delta\omega)^2}{2 \zeta\omega_n^3}$$

where $\Delta\omega$ is the frequency difference and ω_n is the loop bandwidth.

Using the design choice as discussed for the VCO, the frequency difference cannot be greater than 10% of 10 kHz. With a 200 Hz bandwidth, this loop will acquire in about 1/100 second.

6.2.1.8 The Rate Signal

A rate signal is derived from the VCO input voltages of the multi-speed loops. If the input signal to the multi-speed encoder is

$$v_s = V_m \text{Sin } 360 \ \theta \ \text{Sin } \omega_e t$$

$$v_c = V_m \text{Cos } 360 \ \theta \ \text{Sin } \omega_e t$$

but if there is some shaft rate ω_s, then

$$\theta(t) = \omega_s t + \theta_0$$

Substituting:

$$v_s = V_m \text{Sin } 360 \ (\omega_s t + \theta_0) \ \text{Sin } \omega_e t$$

$$v_c = V_m \text{Cos } 360 \ (\omega_s t + \theta_0) \ \text{Sin } \omega_e t$$

The ensuing discussion is valid for any θ. It is much simplified by taking $\theta_0 = 0$. Then

$$v_s = V_m \text{Sin } 360 \ \omega_s t \ \text{Sin } \omega_e t = \frac{V_m}{2} [\text{Cos } (\omega_e - 360 \ \omega_s)t$$

$$- \text{Cos } (\omega_e + 360 \ \omega_s)t]$$

6-45

$$v_c = V_m \cos 360 \, \omega_s t \, \sin \omega_e t = \frac{V_m}{2} [\sin (\omega_e - 360 \, \omega_s)t$$

$$- \sin (\omega_e + 360 \, \omega_s)t]$$

In other words, shaft velocity causes a double-sideband modulation of the excitation carrier frequency. With a double-angle system, one loop tracks the upper sideband and one the lower. As a result, one VCO exhibits a positive frequency shift, while the other exhibits a negative shift for a given velocity sense. Because of the speed ratio the magnitude of the shift is $360 \, \omega_s$ in each. If the VCO frequencies shift, their input voltages must have changed some ΔV to cause such shift. The difference in the voltage shifts is

$$V_v = 2 \, \Delta V = 720 \, \frac{\omega_s}{K_o}$$

where K_o is the radian frequency gain of the VCO, taken previously as corresponding to 1%/volt (Note: the strategem of using percentage frequency units permits us to speak of the VCO gain at the input and the output of the feedback counter in the same breath).

$$K_o = 0.01 \, \omega_e = 0.01 \, (2\pi \, f_e)$$

For shaft rates expressed in degrees per second, d:

$$V_v = 720 \, (\frac{2}{360} \, d) \, 1/[0.01 \, (2\pi \, f_e)]$$

$$= 200 \, d/f_e = 2 \times 10^{-2} d \text{ (volts)}$$

In the track mode, rates of the order of 0.1 degree per second are expected, while slew rates will be some 10 times greater. Hence, respective signal amplitudes of 2 and 20 millivolts can be expected.

It was stated previously that one or the other VCO input voltages could change by several volts due to internal oscillator drifts. However, these drifts can be expected to occur very slowly, since they are the result of ageing and thermal effects on components. Since the gimbal servo local (SEA internal) rate feedback is intended only for stabilization in the upper frequency portion of the bandwidth, the rate signal can be filtered with a bandpass extending from about 0.2 Hertz to about 200 Hertz, rates below 0.2 Hertz being covered by the computer. Thus, any spurious DC components due to VCO drifts will be filtered out. In addition, a passband gain of about 100 is required to amplify the rate difference to usable levels.

6.2.1.9 Accuracy

In discussing accuracy for this system, attention will be confined to the multi-speed encoding process. Obviously, the single-speed section needs to be only accurate enough to fill in its portion of the data field unambiguously. Furthermore, only electronic accuracy will be treated here. For convenience, the discussion will at first be in terms of electrical angle, ignoring the speed ratio 360 of the multi-speed inductosyn. Finally, much of the discussion will not be exact. For the most part we will merely attempt to bound the errors, dealing in orders of magnitude.

Table 6-5 identifies the principle potential error sources, their nature, and an assignment of the expected magnitude of each. In some cases, notably $\Delta\phi_e$ and $\Delta\phi_h$, the formulas are merely intuitive bounds, since the exact analyses have not been attempted. By the nature of an error is meant the form that a graph of the error as a function of shaft angle would take. Some are constant with θ and some are cyclic.

Table 6-5. Encoding Errors

Error Type	Form	Nature	Magnitude (Electrical)
Excitation harmonics	$\Delta\phi_e \leq \frac{\Delta V}{V}$	Harmonic	2×10^{-4} rad
Cross coupling	$\Delta\phi_c = 1/2 \frac{\Delta C}{C}$	2nd Harmonic	10^{-3} rad
Trig gain unbalance	$\Delta\phi_g = 1/2 \frac{\Delta k}{k}$	2nd Harmonic	2.5×10^{-4} rad
Phase detector offset	$\Delta\phi_d = \frac{\Delta V}{K_d}$	Offset	2×10^{-4} rad
Phase detector harmonic	$\Delta\phi_h \leq F_o(s)$	2nd Harmonic	10^{-5} rad
Phase servo error	$\Delta\phi_p = \frac{\Delta\omega}{K_v}$	Offset	3×10^{-4} rad
		TOTAL	20×10^{-4} rad
			10^{-1} degree
			6 minutes
		360-Speed Equivalent	1 second

It is known that the phase tracking is sensitive to distortion of the excitation voltage waveshape. For example, square wave excitation will describe a triangular error function. The details of this phenomenon have not been analyzed. It is sufficient to say that the radian error can certainly not be greater than the distortion ratio. Quantitatively, it seems reasonable to expect that the total harmonic content of the excitation can be limited to 0.02%.

In any resolver system, care is taken to provide isolation between the sine and cosine channels. Cross-coupling causes a second harmonic error. The cause is similar to that for gain unbalance, analyzed below. Cross-talk isolations between shielded conductors are typically of the order of -90 db/ft. If a factor of 20 greater than this is allowed for length, connectors, etc., the magnitude of $\Delta\phi_c$ is estimated at 10^{-3} radian.

Prior to phase detection the inductosyn signals are amplified by the preamps and buffered at the input of the main processing electronics. The phase detectors themselves involve active gain processing. Each of these circuits is a potential source of gain unbalance and thence of error. If the inductosyn output signals are:

$$V_s = V \sin \theta, \quad V_c = V \cos \theta$$

then after preamplification the signals are

$$V_s' = k_s V \sin \theta, \quad V_c' = k_c V \cos \theta$$

where k is the net gain of each channel. The problem is to find what is the disturbance of the angular information content of the signals if $k_s \neq k_c$.

Inherently:

$$\theta = \operatorname{Tan}^{-1} \frac{V_s'}{V_c'} = \operatorname{Tan}^{-1} \frac{k_s \sin \theta}{k_c \cos \theta}$$

The sine and cosine can be represented as Cartesian coordinates.

$$y = \sin \theta$$

$$x = \cos \theta$$

This error analysis will utilize the method

$$\Delta\theta = \frac{\partial\theta}{\partial y} \Delta y + \frac{\partial\theta}{\partial x} \Delta x$$

The expression for θ:

$$\theta = \text{Tan}^{-1} \frac{k_s y}{k_c s}$$

is differentiated

$$d\theta = [1 + \frac{k_s y}{k_c s}]^{-1} \ d(\frac{k_s y}{k_c s})$$

$$= \frac{k_c xy \ dk_s - k_s xy \ dk_c}{(k_c s)^2 + (k_s y)^2}$$

But since the nominal k's are equal,

$$\Delta\theta = \frac{xy}{x^2 + y^2} \ \frac{\Delta k_s - \Delta k_c}{k}$$

By substitution:

$$\Delta\theta = \frac{\text{Sin } \theta \ \text{Cos } \theta}{\text{Sin}^2\theta + \text{Cos}^2\theta} \ \frac{\Delta k_s - \Delta k_c}{k}$$

$$= \frac{1}{2} \text{Sin } 2\theta \ \frac{\Delta k_s - \Delta k_c}{k}$$

If the gain variations are represented as:

$$\Delta k_s = k_s - k, \ \Delta k_c = k_c - k$$

Then

$$\Delta\theta = \frac{1}{2} \text{Sin } 2\theta \ \frac{k_s - k_c}{k}$$

The units are radians. We see that the error due to gain unbalance is a "two cycle per cycle" function with absolute value maxima at 45°, 135°, etc. or, for the multi-speed inductosyn channel, at 1/8, 3/8, 5/8, and 7/8 degrees. The amplitude in radians is proportional to the percent gain unbalance:

$$\Delta\theta_{max} = \frac{k_s - k_c}{2k}$$

As discussed in a previous section, a gain balance within 0.01% per amplifier seems feasible. We take the figure 5×10^{-4} to allow for several sources. The net contribution is then 2.5×10^{-4} radians for $\Delta\phi_g$.

Phase detector offset has the effect of introducing a spurious phase error. This is best understood by reference to Figure 6-15. If a small DC is imagined summed with the function, a vertical shift occurs. The magnitude

of the accompanying horizontal phase shift is proportional to the phase detector slope, i.e., its gain K_d, as given in Section 6.2.1.7. The source of this DC is input offset drift in the operational amplifiers used for the phase detector and/or the loop filter. A typical instrumentation operational amplifier exhibits offset voltage drift of the order of 10^{-6} volt per °C and 10^{-10} amp per °C. Allowing a source impedance of 10 k ohms, the net voltage drift is about 2×10^{-6} per °C. Allowing a 50°C temperature range and several sources indicates an error voltage of about 2×10^{-4} radian.

Error due to phase detector second harmonic has been discussed in a previous section. Because of the special loop filtering techniques employed, its contribution is negligible.

Phase servo error is analogous to the classic "gain-slope" error in any servo. In this case it is given by

$$\Delta\theta_p = \frac{\Delta\omega}{K_o K_d F(0)}$$

where $\Delta\omega$ is the VCO frequency drift, K_o the VCO gain constant, K_d the phase detector gain constant, and $F(0)$ is the DC gain of the loop filter. This latter would be infinite if the "origin" pole of the loop filter were a perfect integrator. Practically, this value limits at the open-loop gain of the operational amplifier used to mechanize the filter, about 90 db. Using orders of magnitude

$$\Delta\omega/K_o \approx 10 \text{ volts}$$
$$K_d \approx 1$$
$$F(0) \approx 3 \times 10^4$$

Then

$$\phi_p \approx 3 \times 10^{-4}$$

The simple sum error of all system contributions is about 2×10^{-3} radians or 6 minutes, single-speed equivalent. The 360-speed equivalent thereof is one arc second. The greatest contribution is that due to cable cross-coupling. Unfortunately, this is the most difficult to get a confident analytic handle upon.

It is to be noted that this error discussion has relied on certain engineering assumptions with respect to its primary input data. Elements such as harmonic purity of a signal, shielding isolation, achievable gain

balance, etc. are extremely difficult to estimate. Therefore, the error analysis can be expected to yield merely a gross indication of system accuracy.

6.2.2 Motor Electronics

The signal processing and power management required for driving the gimbal motors is designated the motor electronics. The processing consists of signal selection, based on mode, conditioning of the rate signals for combining with the primary error input; power management consists in forming the torque vector components to be applied to the respective windings, and power amplification of these to a level suitable for the given motor.

The servo error input is selected either from the star sensor signal or from a computer commanded quantity, depending on mode. Selection is made by an analog switch.

Considerations in filtering the SEA local rate, derived from the multi-speed inductosyn encoder, have been discussed in a previous section. The filtered quantity is combined with the computer rate and inserted into the frequency compensating preamplifier for servo damping. The preamplifier mechanizes the required gain-frequency transfer function desired for overall servo dynamic characteristics. The transfer function is essentially that of an integral plus proportional.

The output of the preamplifier can be somewhat identified as signifying a desired motor torque magnitude. If the motor were a simple DC torque type, this signal could be applied directly, assuming a suitable power level. However, considerations of weight and efficiency have dictated the choice of a two-phase multi-speed motor. As a consequence, vectorial processing of the motor torque angle is required.

Consider first the case of a single-speed, two-phase motor. The stator has two windings upon four poles. Current applied to one winding produces an internal flux in, say, the 0° - 180° direction, depending on the current direction. Current in the other winding causes flux along the 90° - 270° axis. Thus, it is possible to produce a flux vector in any direction by varying the direction and magnitude of the currents within the two windings. The rotor has a two-pole permanent magnet which reacts against the electrical field to produce torque. For a given field strength, torque is a maximum when the field direction differs from the PM flux direction by 90°. Thus, to produce continuous rotation with constant torque, the field vector must be rotated so as to always lead the rotor flux direction by 90°, but its magnitude must be

kept constant. This implies that the winding currents must be varied in a trigonometric manner as a function of the shaft angle. Whether accomplished electronically or by carbon brushes and segments, this process is referred to as commutation.

A multi-speed variation on this device merely adds more poles, such that a complete electrical revolution carries the shaft through only a fraction of a shaft revolution. It is functionally equivalent to a single-speed motor with a step-down gearhead. In the present case the speed ratio is 12.

The brushless motor drive requires the formation of the sine and cosine of 12θ, θ being the shaft angle, to control the relative direction of the motor field vector, and the multiplication of these quantities by the servo error variable to control its strength. Figure 6-20 indicates the functional mechanization of the motor drive circuitry. Shaft position in digital form from the inductosyn processing is converted to trigonometric coordinates by the sin/cos logic (Figure 6-11) and applied to the switch inputs of two simple digital-to-analog converters. The servo variable is applied as the converter reference voltage input. Since a D/A converter has a transfer function of the form

$$V_{out} = V_r \left[1 - \sum_{n=0}^{N} D_n \frac{1}{2^n} \right]$$

where V_r is the analog reference input voltage, usually a constant but here a variable, and where the converter has binary digital inputs D_0, D_1 --- D_n --- D_N, then the operation is that of multiplying an analog quantity by a digital quantity.

The multiplying D/A converters are quantized to 0.5 shaft degree, or 6 motor electrical degrees. If the motor commutation rule of 90° leading flux vector is violated, the torque varies as a cosine function of the electrical angular departure from ideal. Hence, some variation is tolerable. Advantage is taken of this to simplify the sin/cos logic. The digital functions are formed as "stairstep trapezoid" approximations to the time trigonometric functions. Figure 6-21 is provided to study this situation. The "sine" and "cosine" functions consist of ramps with linear portions 60 electrical degrees wide and flat tops 30 electrical degrees wide. Amplitudes are 24 steps peak-to-peak, indicating 5 bit D-A converters. The cycle interval is 30 shaft degrees. Also shown is the analogous "Lissajous" pattern into which the combined functions are mapped as the motor field vector versus electrical angle. The ideal
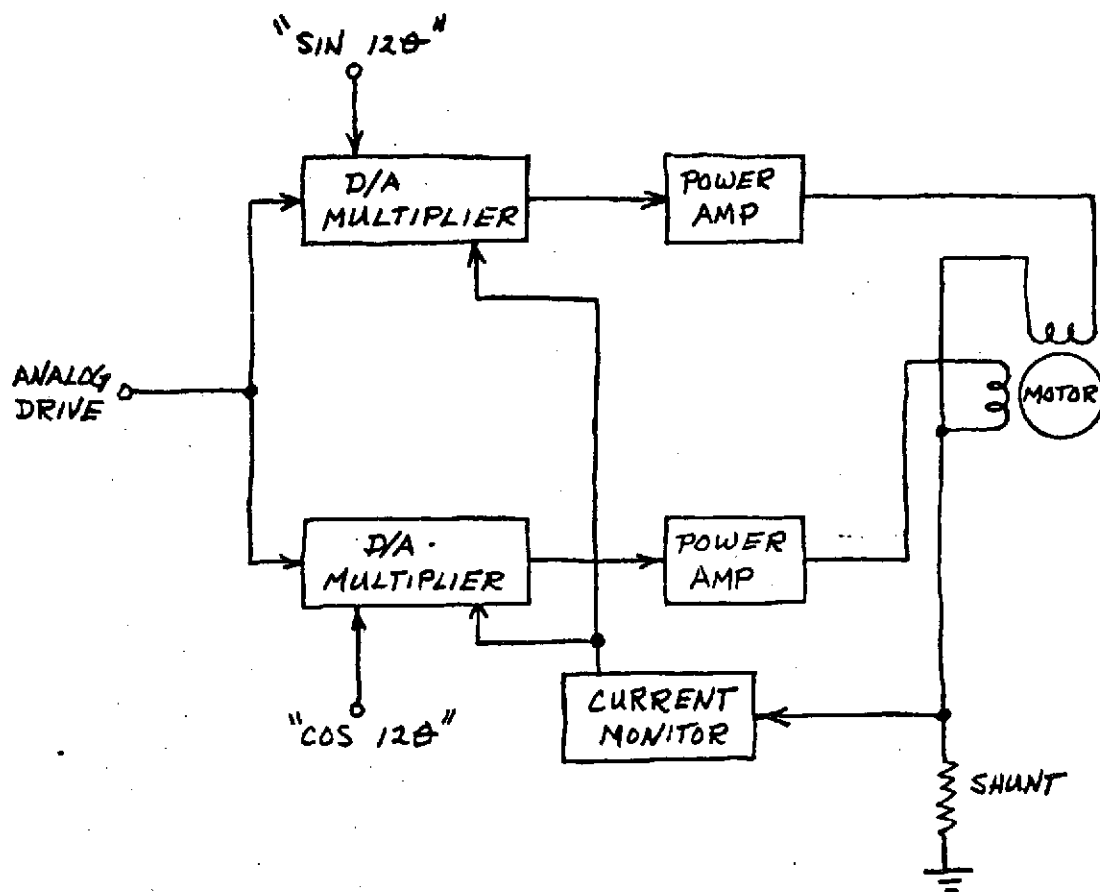
Figure 6-20. Motor Drive Circuit Block Diagram
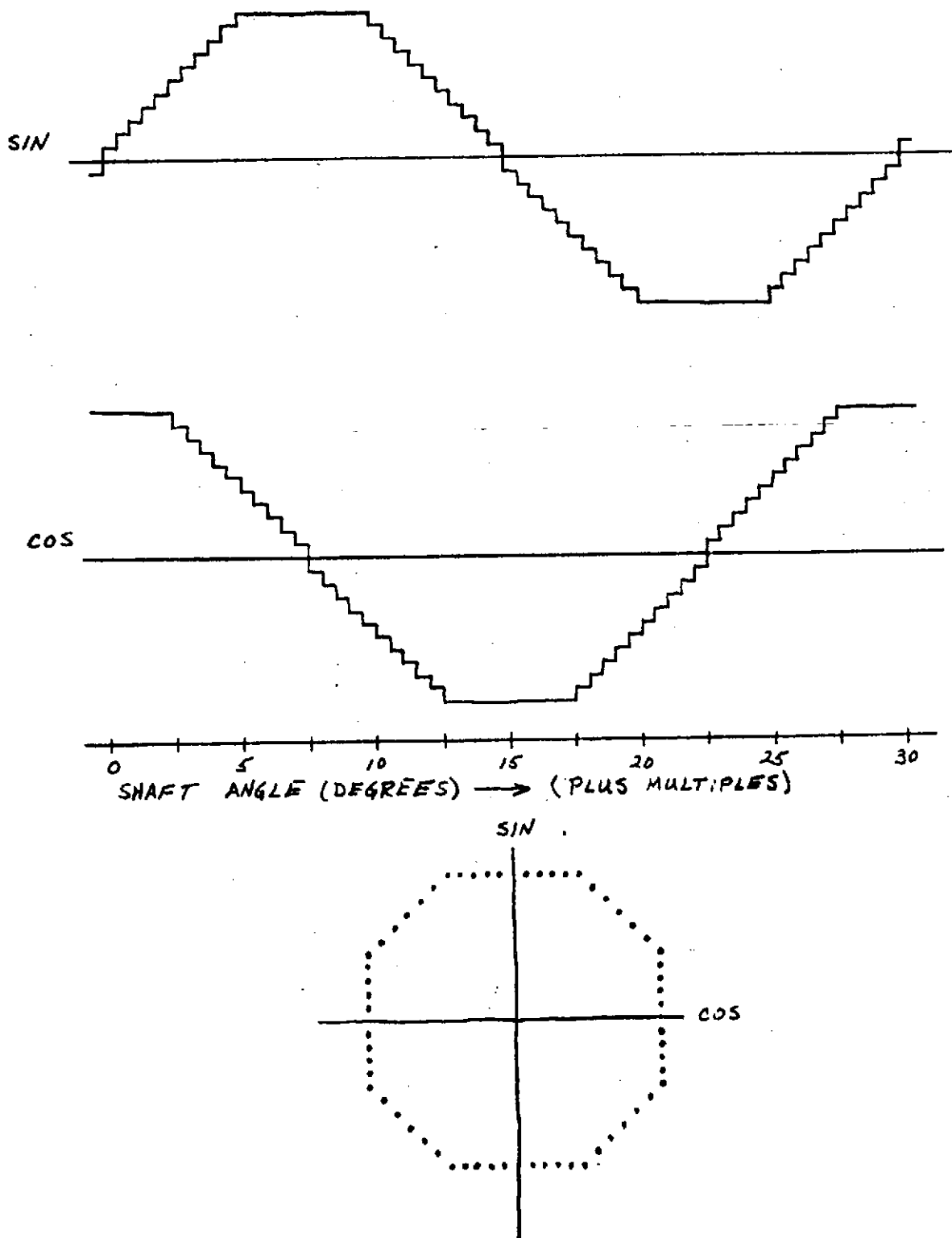
Figure 6-21. Simplified "Sine-Cosine" Function Generation

case, true sine and cosine, would map a perfect circle. With the approximation described, an octagon is traced. (Note that this description is normalized to unit servo error input magnitude.) The departure from a circle whose radius is a mean of the octagon radii is ± 4.3%. This is then equivalent to the torque ripple which will be experienced.

The motor is rated at 18 volts nominal, 6 watts per winding, or 0.8 x 2 x 6 - 9.5 watts for peak excitation at 45 electrical degrees. It has been elected to utilize linear (vs proportional duty-cycle switching) motor power amplifiers. Although the efficiency of this type circuit is poor, operation at high power levels will occur so seldom that recourse to the complexity of higher efficiency circuits does not seem warranted.

6.3 GYRO REFERENCE ASSEMBLY

This section presents the functional design considerations associated with the gyro reference. Three areas were of particular interest, namely: configuration, gyro instrument selection, and loop electronics design. These are treated in the sections which follow.

6.3.1 Configuration

The gyro reference assembly is configured based primarily upon redundancy considerations, as discussed in Section 4.4, and performance considerations which will be discussed here. The configuration selected has each of six gyros positioned with the input axis nominally perpendicular to parallel faces of a regular dodecahedron. This configuration is shown in Figure 6-22. The axes are aligned such that the orthogonal attitude determination reference frame will be parallel to three appropriate orthogonal edges of the dodecahedron. With this constraint, none of the gyro input axes will be parallel to any of the attitude determination reference axes. This arrangement is optimum for six instruments, because it minimizes the effects of errors and failures on performance. In this configuration, no three gyro input axes are coplanar so that the system is capable of operation with any subset of three gyros.

It is apparent from Figure 6-22 that not all combinations of m out of 6 gyros will yield equally good performance. It is of interest to consider the operating configurations (m operating out of the 6) and the effect of this operating configuration on meeting the assembly performance requirements. Some of the possible combinations do not yield a well balanced spatial distribution of the input axes and, as a result, the rate derived may be very susceptible to gyro errors. To determine the relative advantages of certain combinations, it is advantageous to compute the error covariance matrix of the gyro assembly errors and compare the different combinations.

Assume that

$$\tilde{\omega} = A\bar{\omega} + \bar{\epsilon}$$

where A is a 6 x 3 matrix whose rows are defined by the direction cosines of the gyro input axes. Assume that the covariance of the measurement error is given by

$$E\left[\bar{\epsilon}\,\bar{\epsilon}^T\right] = \sigma_g^2 I$$

which identifies the error sources as uncorrelated with equal error statistics. In this case, the least squares, weighted least squares, and minimum variance estimate

$$\sin \alpha = [(5+\sqrt{5})/10]^{\frac{1}{2}}$$

$$\cos \alpha = [(5-\sqrt{5}/10]^{\frac{1}{2}}$$
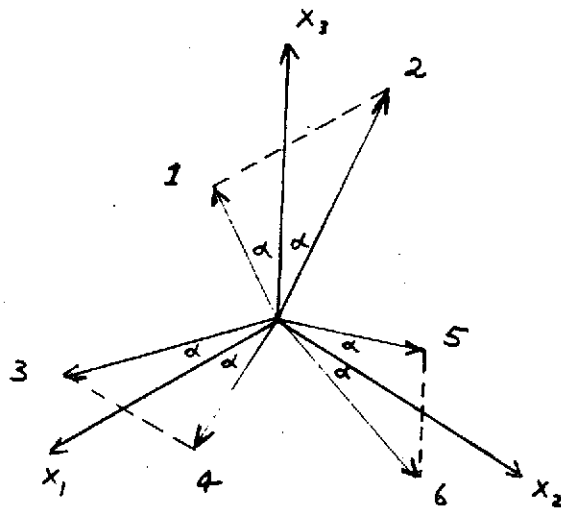
Figure 6-22. Gyro Input Axis Geometry (Dodecahedron Configuration)

for $\bar{\omega}$ coincide and is given by

$$\hat{\omega} = B\bar{\omega}$$

where

$$B = (A^T A)^{-1} A^T$$

The error covariance matrix for the estimate is given as

$$P = \sigma_g^2 (A^T A)^{-1}$$

An analogous result is obtained by considering the results of Appendix C, in this case considering the elements, γ, representative of misalignment and scale factor errors. The same assumptions are made, i.e., gyro misalignments and the scale factor instabilities are statistically independent and the gyro misalignments and scale factor errors are independently and identically distributed. Denote the respective variances by σ_ϵ^2 and $\sigma_{k_r}^2$. Then it follows (from Appendix C) that the covariance matrix of $\delta\gamma$ is given by

$$P_\gamma = E[\delta\gamma\delta\gamma^T] = \sigma_\epsilon^2 CC^T + \sigma_{k_r}^2 DD^T$$

The square root of the diagonal elements of P_γ are, of course, the standard deviations of $\delta\gamma$.

Consider initially the configuration which assumes all six gyros are operating. This yields

$$P_\gamma = \frac{1}{2} \sigma_g^2 I$$

and all the γ_{jk} are uncorrelated and their standard deviations are improved by $1/\sqrt{2} = 0.707$ with respect to the standard deviation of the individual gyro misalignments, with scale factor instability already included. Note also, that even if $\sigma_\epsilon^2 \neq \sigma_{k_r}^2$, as long as these variances have the same order of magnitude, as is always the case, the off-diagonal terms of P_γ will be so small that they can be neglected and the elements of the vector $\delta\gamma$ are uncorrelated with each other.

It is noted that, in a similar fashion,

$$P_{b_g^o} \triangleq E\left[\delta b_g^o (\delta b_g^o)^T\right] = \tau E\left[\delta b_g (\delta b_g)^T\right] \tau^T$$

yields

$$P_{b_g^o} = \frac{1}{2} \sigma_{b_g}^2 I$$

6-58

where the individual gyro biases are assumed to be independently and identically distributed with variance $\sigma_{b_g}^2$. Hence, the potential improvement in accuracy due to the redundancy in the dodecahedron gyro configuration is again 0.707.

Consider now the cases where less than all six gyros are operating. For the case of operating three of the possible six gyros, there result 20 possible combinations. Of the 20 possibilities, 10 combinations are relatively poor, in terms of equivalent statistics, in comparison to the remaining 10. The statistics for the better combinations are summarized as

$$\text{RSS:} \quad (tr\ P)^{1/2} = 2.036\ \sigma_g$$

$$\text{RMS:} \quad (tr\ P)^{1/2}/1.732 = 1.175\ \sigma_g$$

For the remaining combinations,

$$\text{RSS:} \quad (tr\ P)^{1/2} = 3.295\ \sigma_g$$

$$\text{RMS:} \quad (tr\ P)^{1/2}/1.732 = 1.905\ \sigma_g$$

If four out of six gyros are operated, there result only 15 combinations, but the statistics correspond to that of three equivalent orthogonal gyros such that

$$\text{RSS:} \quad (tr\ P)^{1/2} = 1.732$$

$$\text{RMS:} \quad (tr\ P)^{1/2}/1.732 = 1.0$$

With performance being an important consideration along with redundancy, four gyros are utilized for operation. A tabulation of the configurations and associated "geometry" matrices and performance statistics is provided in Appendix I.

6.3.2 Gyro Instrument Selection

Precision gyros of the general type required for PPCS are available or under development for a large number of current and/or future space programs. Of those available, the subminiature inertial grade gas bearing gyros appear most suited to the PPCS application. Table 6-6 lists parameters for subminiature high performance gyros. The GG334 and 25IRIG gyros are included for comparison. Of these, the Nortronics K7G has the largest production base and performance/reliability data background, and is selected for the PPCS application. This unit is a single degree of freedom gyro which has a ceramic hydrodynamic gas spin bearing operating in a beryllium float. The float is constrained along the output axis by means of a taut wire suspension system. The unit has a moving coil pickoff and a permanent magnet torquer.

Table 6-6. Gas Bearing Gyro Characteristics

	Size Inches	Weight	Spin Power Watts	Angular Momentum g-cm^2/sec	Random[1] Drift °/hr
Subminiature					
Honeywell GG134	1.5x2.8	6.4 oz	4.	50,000	.004
Kearfott Alpha III G	1.4x2.5	10.2 oz	3.3	50,000	.002
Northrop K7G	1.6x3.25	10 oz	3.2	120,000	.002
Standard[2]					
Honeywell GG334	2.5x4.7	1 lb 10 oz	3.5	200,000	.002
Bendix 25 IRIG	2.4x3.8	1 lb 8 oz	6.0	500,000	--

[1] From manufacturers data. Test conditions vary but these numbers appear to be derived under comparable conditions.

[2] There are approximately 10 other inertial grade gas bearing gyros available. Most are heavier, some have smaller random drifts than those in the table.

The reliability considerations were detailed earlier in Section 4.4. Comparative performance is dealt with briefly here. There appears to be little difference in performance between any of the subminiature gas bearing gyros in a zero-g, low vibration, temperature controlled environment. All of the gyros listed in Table 6-6 meet the PPCS random drift performance requirement. A composite of drift stability data from different sources is shown in Figure 6-23. Some of the data is from analog torquer tests, some from digital, and the sampling methods vary. Nonetheless, the curves are representative of GG334 and K7G performance, and show considerable similarity between gyros. Figure 6-24 presents the same data in terms of 1σ integrated drift (attitude) data as a function of sample time. In both figures, the mean value of drift has been removed and the values plotted are RMS (one-sigma) randomness. Figure 6-25 is a typical histogram of K7G drift data.

6.3.3 Rebalance Loop Electronics

The primary electronics tradeoff is selection of pulse or analog rebalance loop. Analog was selected after consideration of the factors discussed below; however, it is clear that either approach would satisfy PPCS requirements.

Pulse rebalance offers several advantages in terms of both gyro performance and electronics implementation. A binary rebalance loop with its fixed weight current pulse operates the gyro at fixed torquer power and (theoretically) at one point on the torquer response curve. For high rate torquing, this has obvious gyro performance benefits. For PADS, with its low rates, this factor is less significant. Electronics advantage include the use of saturating torquer drivers, reducing component stress and thermal dissipation. A possible disadvantage of pulse torquing is increased electronic noise; however, the analog approach uses demodulators and cannot be entirely far from unwanted noise.

Analog rebalance provides a simple control loop which is easily analyzed. Analog rate information is provided directly, an occasional advantage. Gyro torquer harmonic nonlinearity effects of pulse torquing are eliminated, minimizing the degree of interface "tweaking" required. This last factor, assuring ease of gyro interchangeability, was of prime consideration in selecting the analog approach.

Since a digital output is required, the voltage-to-frequency converter (VFC) is a key circuit element. Figure 6-26 shows a block diagram of the VFC. A precision integrator of the operational output is impressed upon a pair of level detectors connected in parallel. Their individual outputs are either high or zero depending on their output condition. One level detector is high when the integrator output is greater than a reference threshold of +70 millivolts, otherwise its output is zero. Similarly, the other level detector is high when the integrator output is less than -70 millivolts, and zero otherwise. When either level is
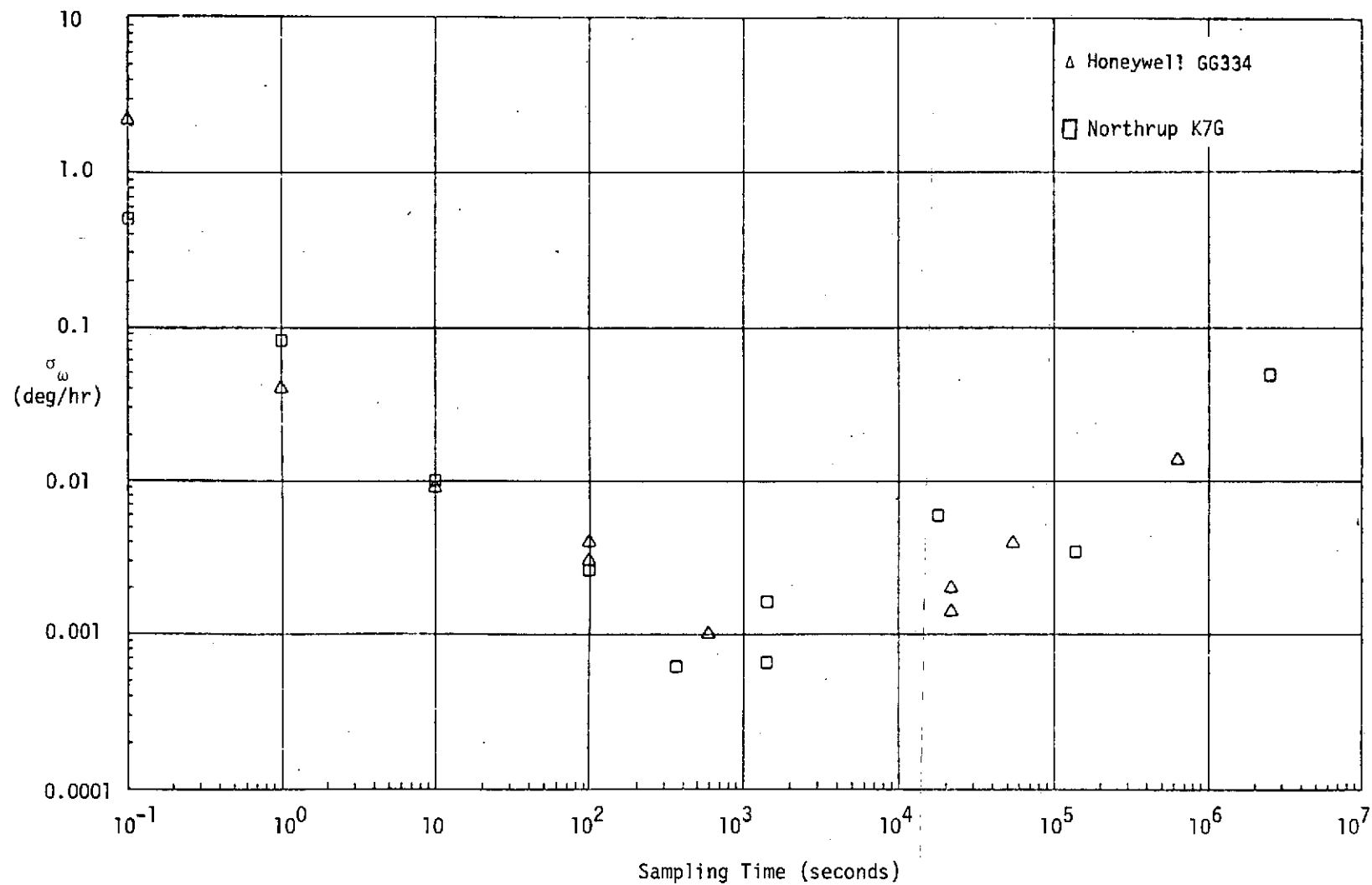
Figure 6-23. Gyro Random Drift As A Function of Sampling Interval
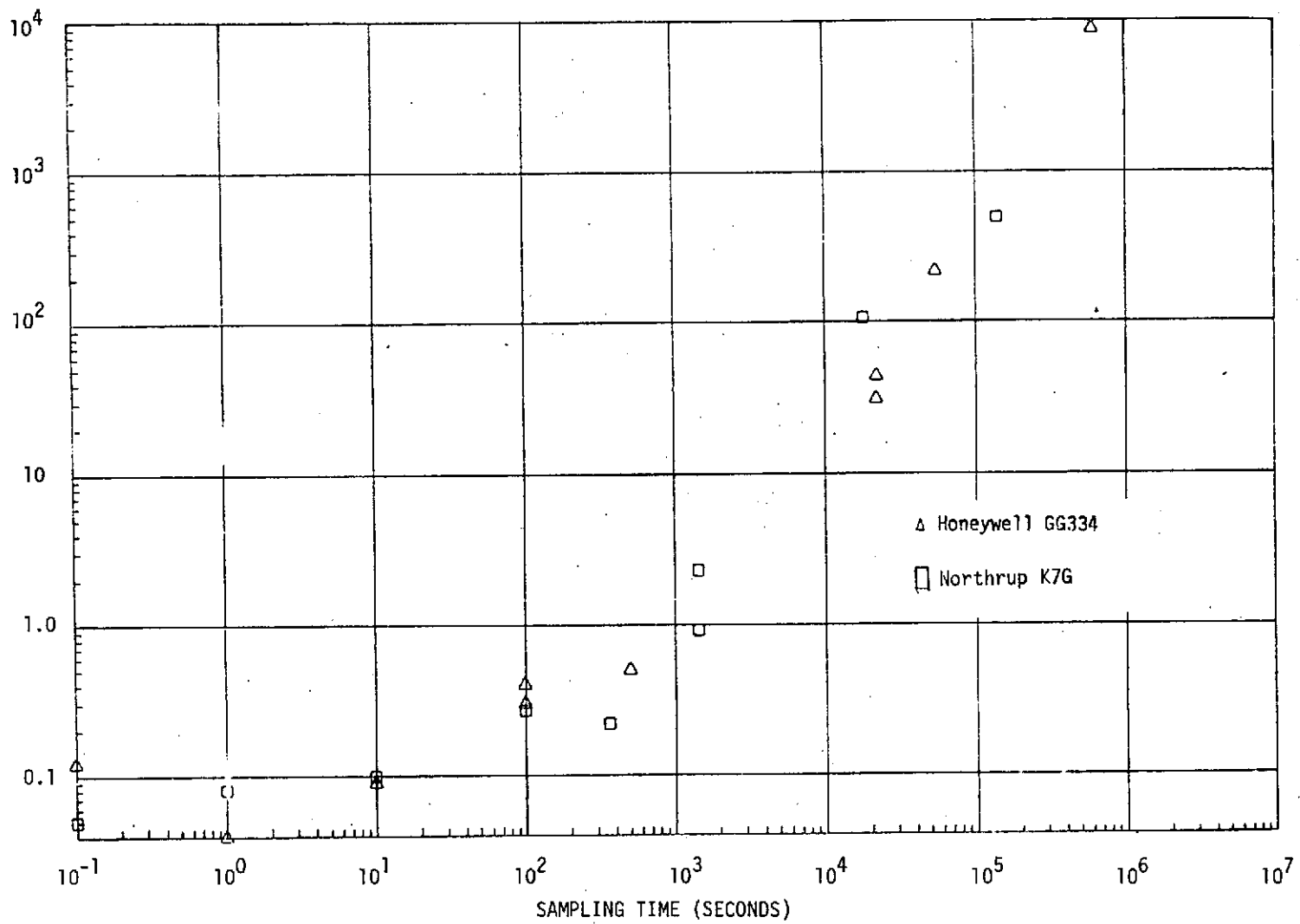
Figure 6-24. Attitude Noise As A Function of Sampling Interval
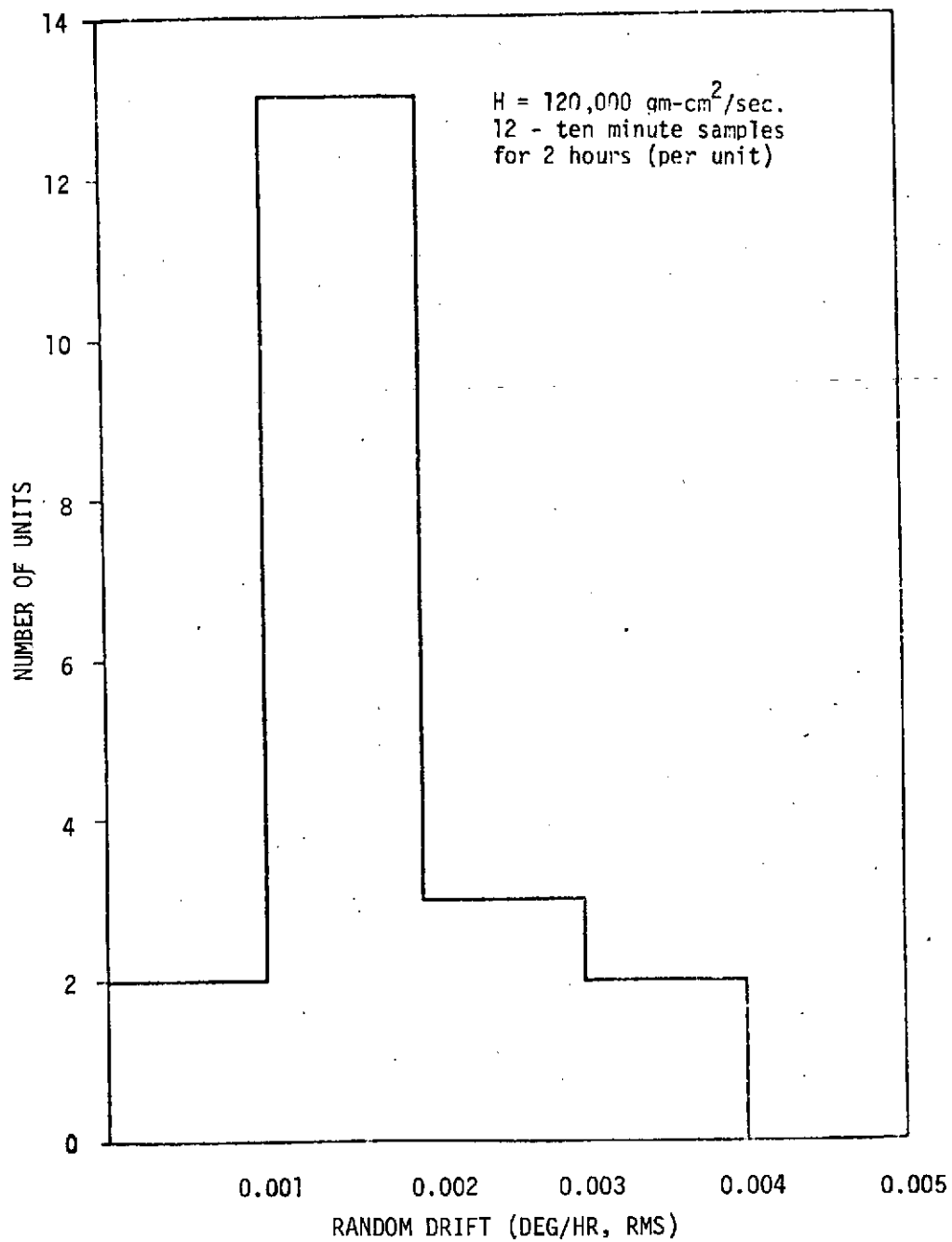
Figure 6-25. Histogram of K7G Drift Data
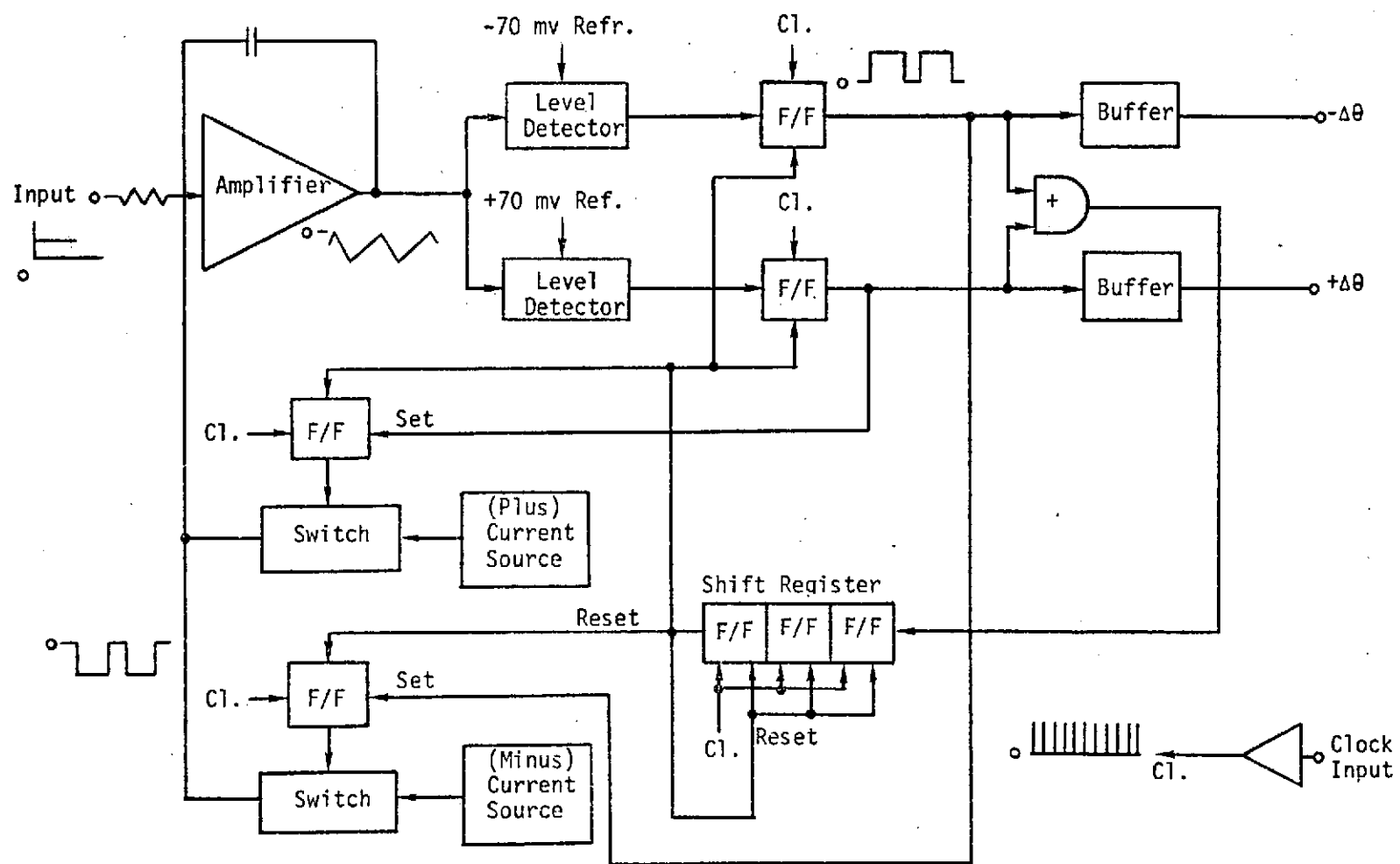
Figure 6-26. Voltage-To-Frequency (VFC) Block Diagram

high, the logic connected to the level detector output commands a precision current source and a current switch to provide a rebalance pulse of current to the input of the integrator. The polarity of the applied pulse is determined by the sign of the threshold that was exceeded, and the pulse start time and length are controlled by the clock signal. The result is a pulse-on-demand feedback loop which provides constant area current pulses of the proper sign, in synchronism with the clock frequency, which tends to hold the integrator output within the threshold values. The VFC output consists of two pulse trains indicating that positive or negative current pulses have occurred. Each output pulse represents a fixed amount of rebalance charge applied to lower the voltage across the integrating capacitor. The result is that the algebraic sum of the two pulse trains is proportional to the VFC input volt-seconds, which in turn is proportional to the gyro input angle rotation. A breadboard of the VFC has been tested for bias and scale factor stability.

Bias stability of the VFC with respect to time is shown in Figure 6-27. This data was obtained over a period of 24 hours at laboratory ambient temperature (73°F).

VFC bias stability with respect to temperature is shown in Figure 6-28. The circuit was placed in an oven and measurements were made at 75°F, 100°F, and 125°F. The circuit was allowed to soak for one hour at each temperature before circuit power was applied. Ten measurements were recorded at each temperature. Maximum, minimum, and average data for each temperature is shown.

VFC scale factor error (pulses per second) versus output pulse rate for three positive and three negative input voltages is shown in Figure 6-29. The temperature sensitivity of the VFC scale factor is shown in Figure 6-30. Both positive and negative input voltages were used during this test; the test temperature range was from 100°F to 125°F.

The sensitivity of the VFC scale factor to changes in line voltage is shown in Table 6-7. This test was conducted with constant input voltage (positive and negative); measurements were made by varying one supply voltage while holding the other supplies constant. Data was also taken while simultaneously decreasing all supplies.
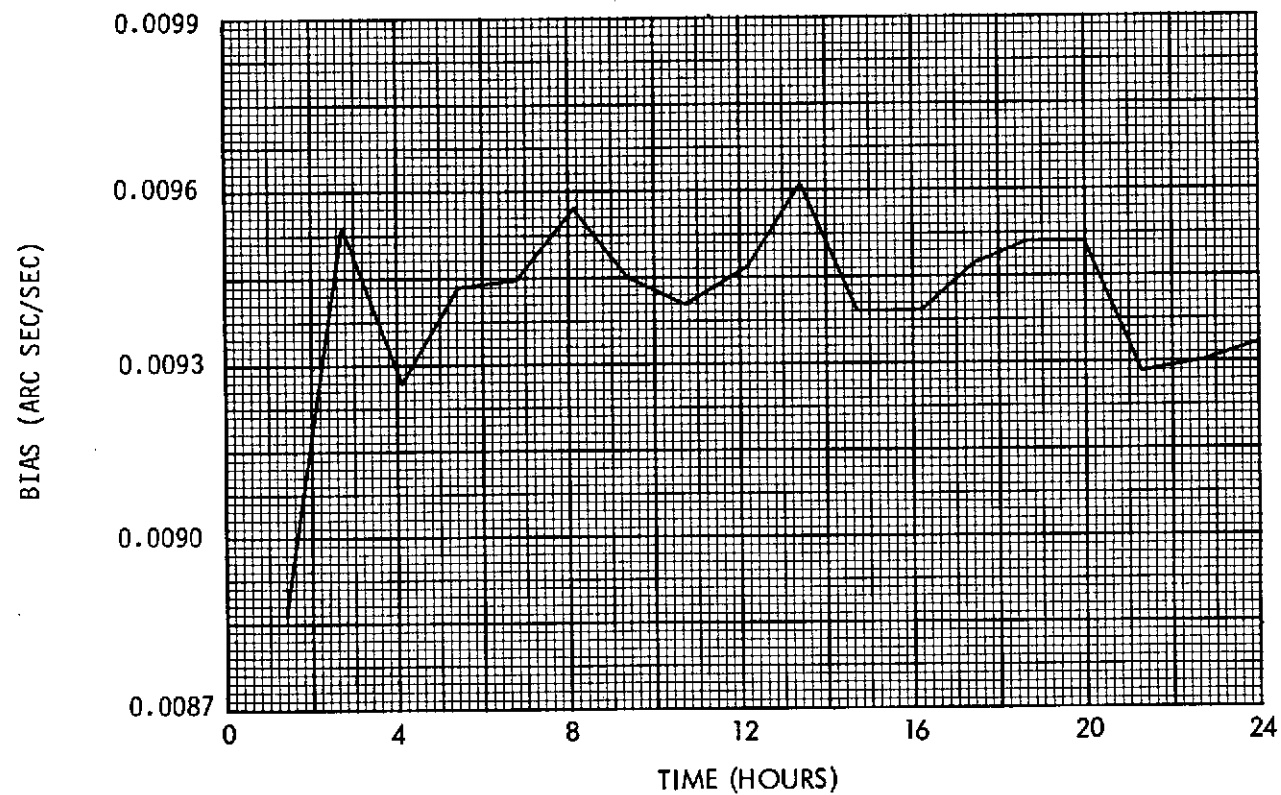
Figure 6-27. VFC Bias Stability Vs. Time
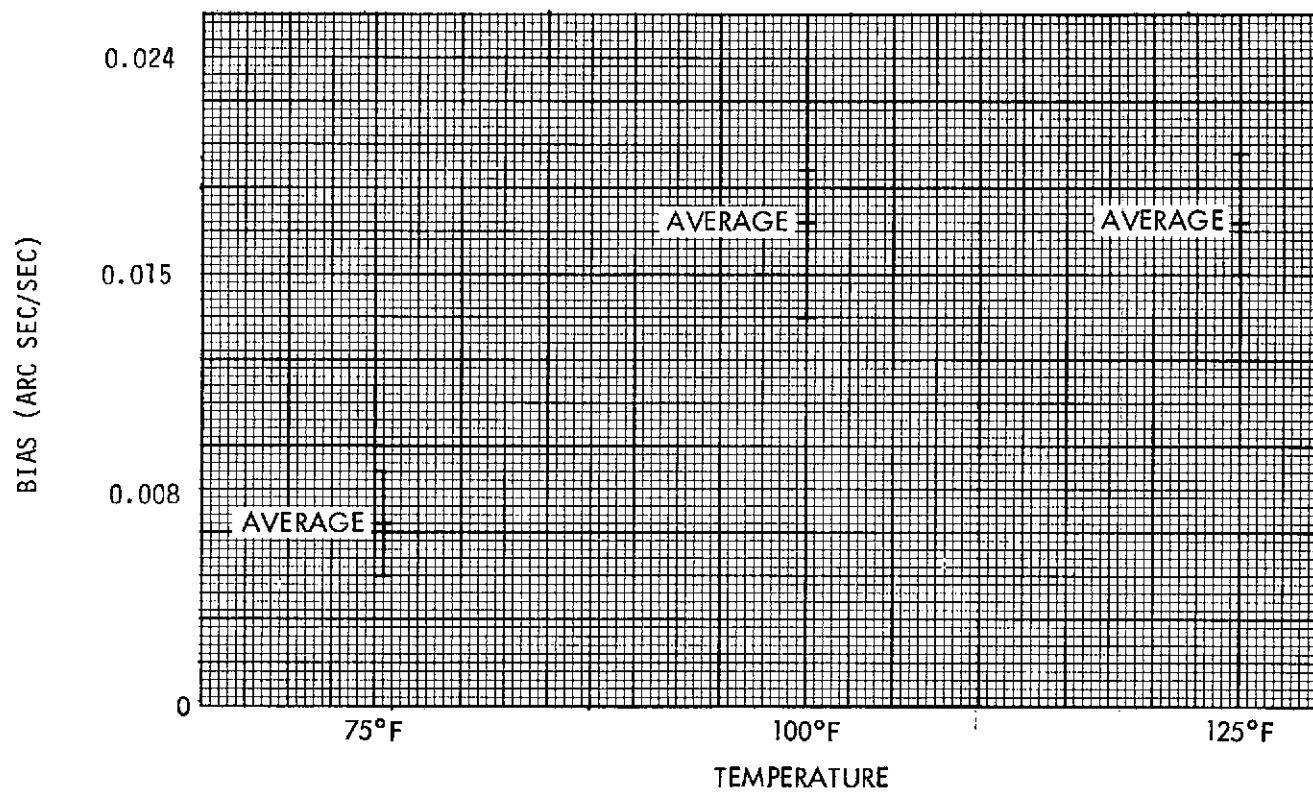
Figure 6-28. VFC Bias Vs. Ambient Temperature
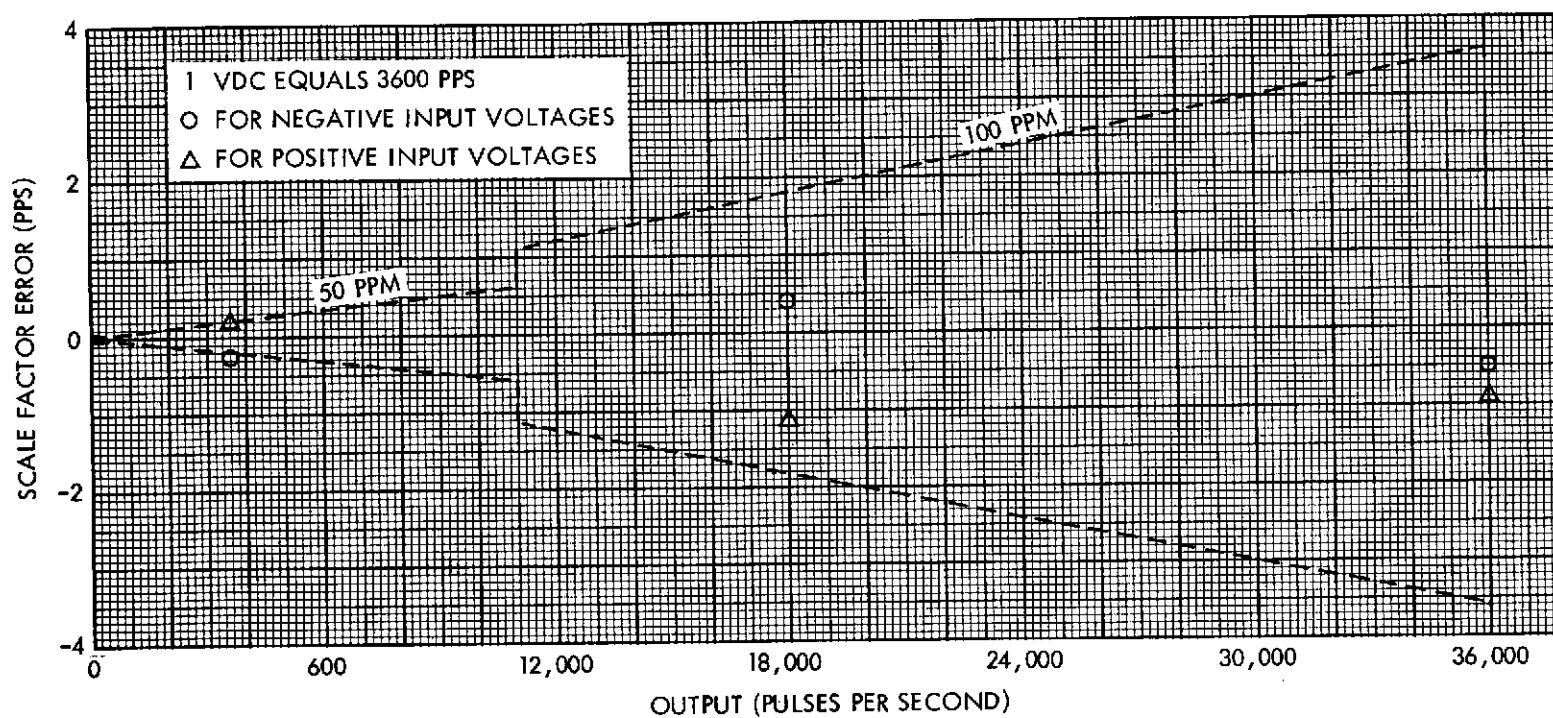
Figure 6-29. VFC Scale Factor Error Vs. Output Pulse Rate
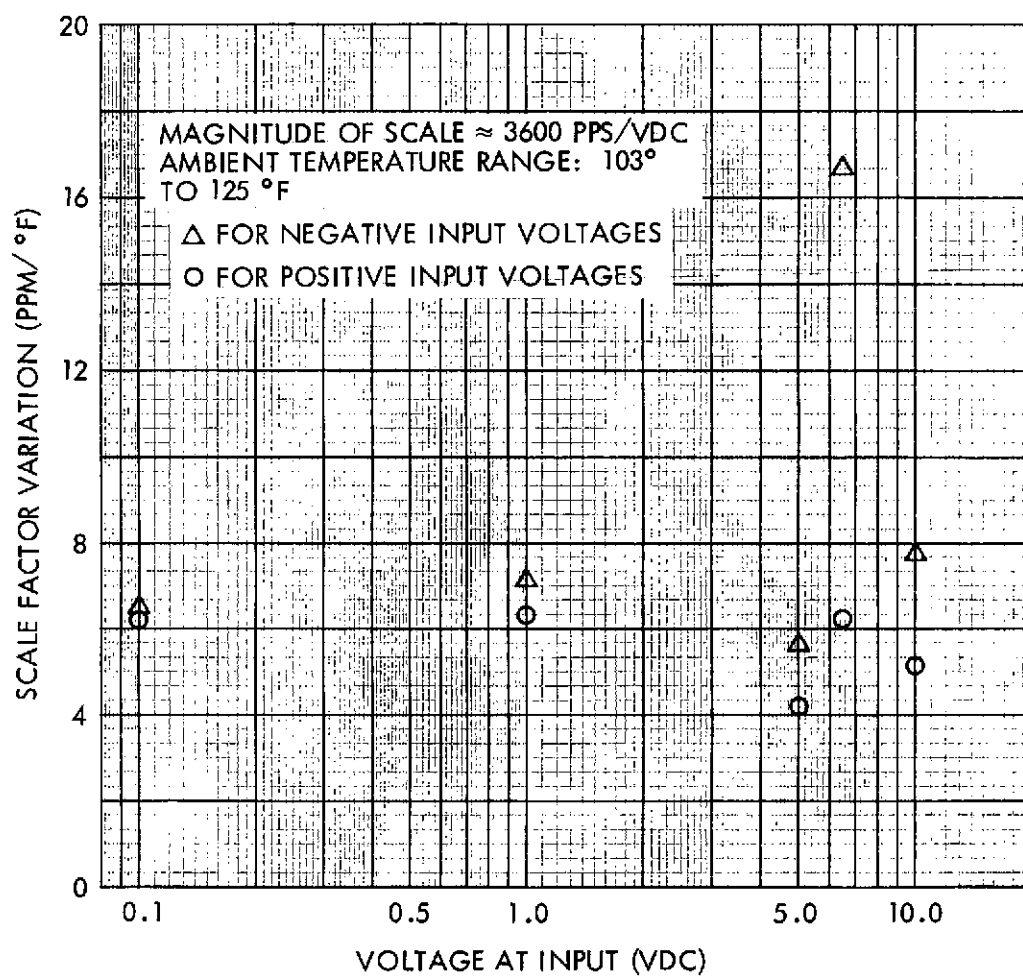
Figure 6-30. VFC Scale Factor Vs. Temperature

Table 6-7. VFC Scale Factor Sensitivity to Line Voltage

LINE VOLTAGE (VDC)	INPUT VOLTAGE (VDC)	SENSITIVITY IN PPM PER % VOLTAGE CHANGE
15	10	0.8
-15	10	0.8
18	10	3.1
15	-10	1.2
-15	-10	0.8
18	-10	1.1
DECREASE THE MAGNITUDE OF THE THREE SUPPLIES	10V	6.6 PPM/%
	-10V	28 PPM/%

6.4   ALIGNMENT SENSOR ASSEMBLY

The Alignment Sensor Assembly for PPCS was designed by Barnes Engineering
[16] under TRW subcontract. This section summarizes the functional design, trade-
offs, and design analysis.

6.4.1   Functional Description

The Alignment Sensor Assembly will consist of a dual-axis measuring auto-
collimator cooperating with a plane mirror for measuring rotation about the two
axes transverse to the line of sight, and a dual-axis instrument used with two
dihedral (Porro) reflectors for measuring the "twist angle" about the line of sight
axis. The second axis of the latter instrument provides for cross-coupling compensation.

This is shown in Figure 6-31, where twist is defined as rotation about the
X-axis and transverse rotations are about the Y and Z axes.

The beam from the twist-rotation instrument is inclined to the axis about
which rotation is measured by as large an angle as the geometry of the mount allows.
Fitting of all necessary components inside the required ten-inch diameter results
in a maximum angular off-set of $1.6°$. The beam used in measuring twist-rotation is
made to traverse the system twice, however, and the resulting sensitivity of this
measuring channel is 1/18 that of the transverse channels. Note that this does not
mean that the combined error budget for X measurement is 18 times as great as that
of the Y and Z channels, however, since some components of error apply with equal
force to each system.

A null measuring tracking autocollimator is used in each case, with optical
wedges which are rotated to deflect the return beams to a measured null. Measure-
ment of the wedge rotation provides the measure of the angular rotation of the
(remote) reference surface. This can be seen in more detail in Figure 6-32.
A source reticle and lens images the source on a collimating lens to produce the
collimated beam. This beam then passes through two pairs of optical wedges (the
twist system also has two pair) each having the function of compensating and
measuring one mode of rotation. Initially the wedges in each pair are opposed and
the deviation of the first is cancelled by the second. The collimated beam proceeds
without deviation and is reflected by the mirror (or Porro for the twist system) and
returns to the autocollimator where it is imaged on separate detector reticles. The
reticles have an opaque area matching the source reticle so that, for no mirror
deviation, the return image is blocked by the opaque area and no error signal is
produced. Mirror rotation causes the image to move off center and produces an
error signal which is detected and used to drive the wedges. They rotate in
opposite directions and thus each pair produces beam deflection in only one axis.
The wedges are driven until the error signal is nulled - the rotation required is a
measure of the mirror angular motion.

Z

−X

Y

4.5 INCH DIA. MIRROR

Y,Z AUTOCOLLIMATOR

120 IN.

a. TRANSVERSE MEASUREMENT

Z

−X

Y

4.5

4.5

PORRO REFLECTOR

Q

b. TWIST MEASUREMENT

X AUTOCOLLIMATOR

PORRO REFLECTOR
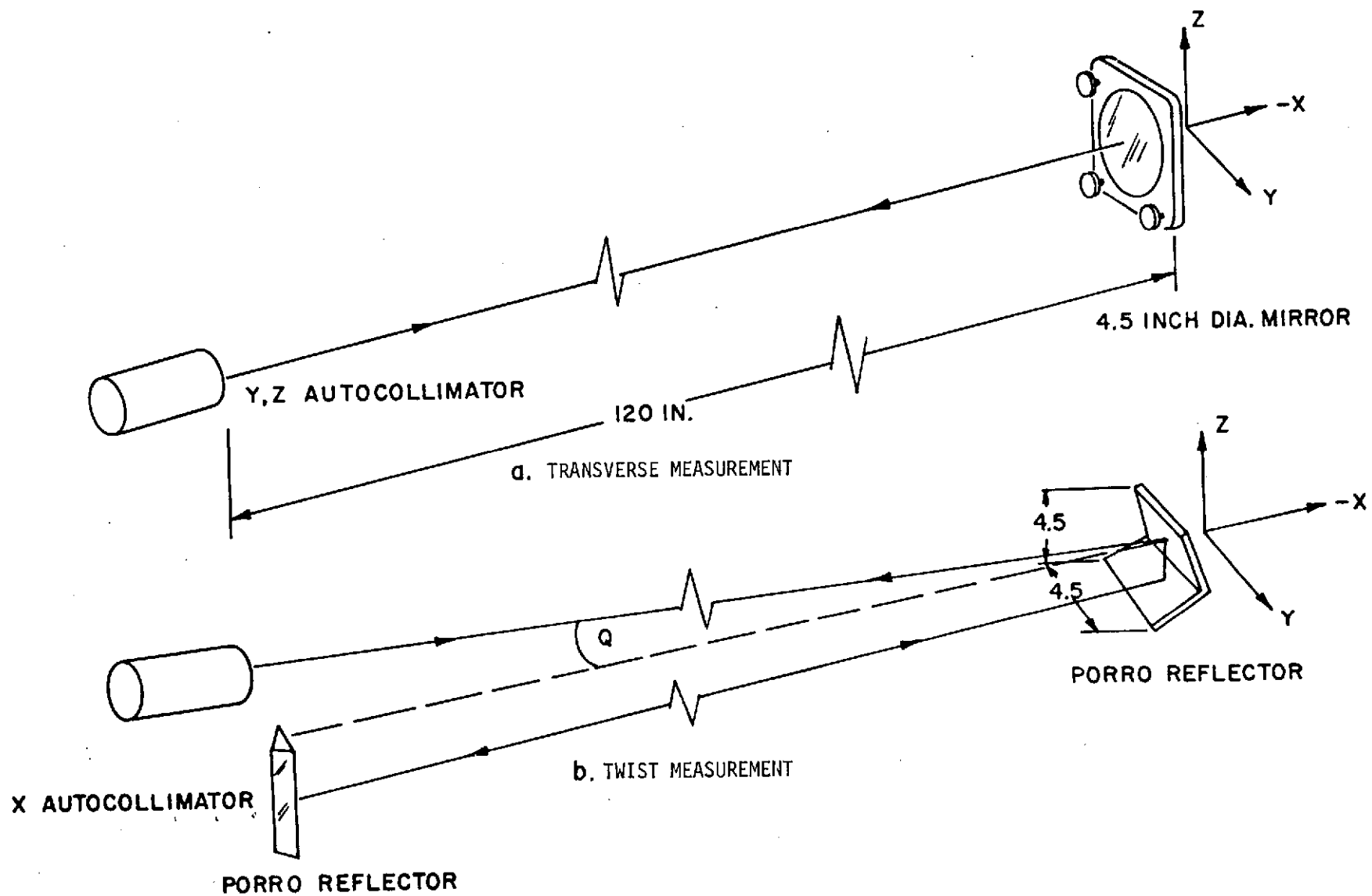
Figure 6-31.   Alignment Sensor Optical System Diagram
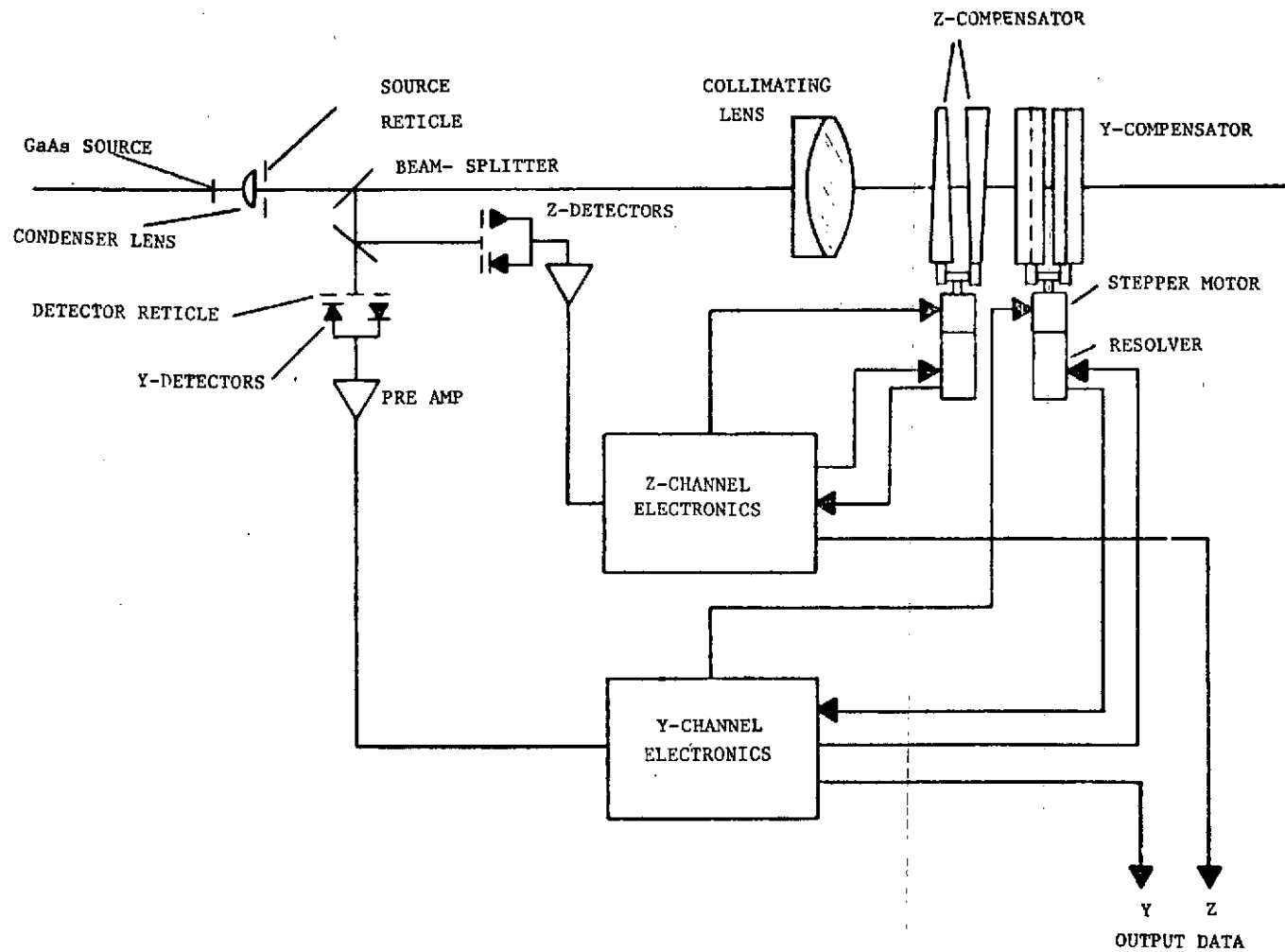
Figure 6-32. Dual Axis Autocollimator Functional Block Diagram

The reference which is to be monitored and which carries the reflectors will be subjected to six degrees of freedom of translation and rotation. It is clearly important to be able to measure each of the three rotations without errors associated with the other five degrees of freedom. If error contributions arise in a predictable manner from the other motions, however, these can be removed from the final output.

The systems described below are essentially free from coupling errors due to translation, although combinations of all three rotations can give rise to predictable errors. When the rotations are large enough for the error contributions to be unacceptable, they can be compensated for by manual or automatic computation means. Small but finite imperfections in the dihedral angle and the surface flatness of the remote Porro reflector, when combined with translation in the Z-direction, do introduce significant errors in the measurement of X-rotation and become the limiting contributions to the error budget.

6.4.2 Transverse Rotation Measurement

The possible approaches for the transverse measurement system are reviewed briefly with comments as to the dominant reasons for rejecting those not used.

- Single-axis instrument with plane mirror. Consider a single-axis autocollimator designed to measure Z-rotation. Since the mirror will also rotate about Y, we must recognize the fact that for a Y-rotation of 0.5 degree at 120 inch distance, the reflected beam motion at the autocollimator is about 2 inches. Therefore, most of the beam would fall outside the autocollimator aperture and the response of the system would be seriously degraded.

- Single-axis autocollimator with Porro reflector. The chief problem in this case is a coupling error introduced by combined X-rotation and translation parallel to the axis of rotation being measured. This has a magnitude equal to t x X/D where t is the translation, X is the rotation, and D the distance. Its maximum value is 7.6 sec. A second problem is that a measured component which should appear in the output, representing the combined effect of rotation about the two axes orthogonal to the one being measured, does not do so when a Porro reflector is used. This term can have a maximum value of 16 sec.

- Dual-axis instrument with Porro reflector. This is a trivial case included for completeness but clearly not usable because of insensitivity to one mode of rotation.

- Dual-axis instrument with plane mirror and single wedges associated with each axis of rotation. This combination has problems with stability, particularly when rotation has taken place about both axes.

The choice has been made by elimination, therefore, and points to the dual-axis autocollimator with two independently operating pairs of contra-rotating wedges and a plane mirror. An important feature of the selected design lies in the provision for an analog error function output to supplement the wedge-resolver output. Thus while the high accuracy of the wedge-resolver combination provides the wide measuring range, a servo lag of several steps limits the obtainable accuracy.

As will be shown later, a lag of as much as 2 $\widehat{sec}$ can be realized in the servo system. Therefore, a ramp function covering that range and representing the "raw" error signal will also be read out and will reduce the uncertainty. By periodic in-flight calibration, this ramp function can reduce the error to less than 1/4 $\widehat{sec}$. Calibration will be obtained by disabling the servo and causing the stepper to advance by a certain number of steps. The change in error signal will be observed and divided by the angular equivalent of the steps to provide the scale factor calibration. The procedure is slightly complicated by the fact that the relationship between steps and angle is not constant, but varies from 0.6 $\widehat{sec}$ per step at zero displacement to 0.3 at 60° wedge position.

The "slit" and detector dimensions naturally have a strong influence on system characteristics. In the transverse measuring system, the source reticle will be 0.005 inches square. This dimension is only 1/10 the maximum image size which vignetting considerations would allow and, consequently, image intensity along the edges is about 90% that at the center, which is favorable from the standpoint of signal-to-noise. It subtends 200 $\widehat{sec}$ at the objective lens and therefore the ramp function of signal vs. deviation has that extent.

Each channel will include a pair of unbiased Silicon detectors which are mounted on a common substrate (glass) and the active areas of which are separated by 0.005 inch. Thus the image has a geometrical size equal to the gap between detectors. This provides maximum stability in the presence of temperature and aging effect.

The image, which is nominally equal in size to the source reticle, actually is slightly increased by aberration and/or diffraction. The energy distribution across the edges has the familiar sigmoid profile, but since there is some energy falling on each detector at null, the ramp function of signal vs. angle has good linearity even for small deviations.

In both the X and the Y-Z autocollimators the image will be held at the same position on the detectors, both in the sensitive and insensitive directions. Thus, inequalities of responsivity or lack of straightness along the edges of the detectors do not contribute spurious null shifts.

The X-rotation autocollimator, however, has a somewhat elongated slit. This extra length provides more signal, which is necessary to give a satisfactory value of signal-to-noise.

The length of each detector is the same in both systems in both the insensitive direction and the sensitive direction. This will provide a small margin at each end of the insensitive direction; the other dimension is designed as the maximum which can be utilized for acquisition. At 120 inches, the reflected beam will completely miss the aperture when the reflector has rotated through 0.0052 rad. The displacement of the image at the focal plane is thus defined as 0.0052 for 0.026 in. The excursion which can be monitored is given by the sum of the image width plus the detector width. Therefore, the detectors will respond when the reflector is near enough to alignment so that the reflected beam is captured.

The detectors will be N on P silicon based on experience reported by Philco-Ford which shows this type to be substantially more resistant to radiation damage in space environment than the more commonly used P on N. They will be selected for responsivity matched to within 5 percent.

6.4.3 Twist Measurement

This measuring system includes the autocollimator and a "vertical" dihedral (Porro) reflector at the base, separated as far as possible to give a large off-axis "look angle" to the "horizontal" Porro reflector mounted at the plate. As an aid in explanation, and with no loss in generality, it will be postulated that the XY plane is "horizontal". The beam from the autocollimator irradiates the remote Porro, which reflects the beam back to the Porro at the base. The beam is reflected to the remote Porro for a second pass, then back to the autocollimator.

X-rotation of the remote plate generates a vertical motion of the reflected beam at the autocollimator equal to 4 x sine θ where θ is the offset or look angle. With the dimensions permitted by the 10-inch diameter constraint, $\theta = 1.6$ degrees. X-translation will be insignificant, and Y-translation will be accommodated by the aperture of the reflector, which is greater than that of the collimated beam.

Z-translation, however, introduces two problems. First is the effect of error in the dihedral angle which is normally 90 degrees. If the reflector is an assembly of mirrors, the reflected beam is split by the roof edge into two segments and they diverge or converge in the vertical plane by 4 times the dihedral angle error. If the reflector is a prism, the divergence is 4 n e, where n is the index of refraction and e the angle error. Since n will be about 1.5, the angle error multiplication is about 6, and after the second traverse of the system, the divergence between the two portions of the beam falling on either side of the roof edge is about 12 e.
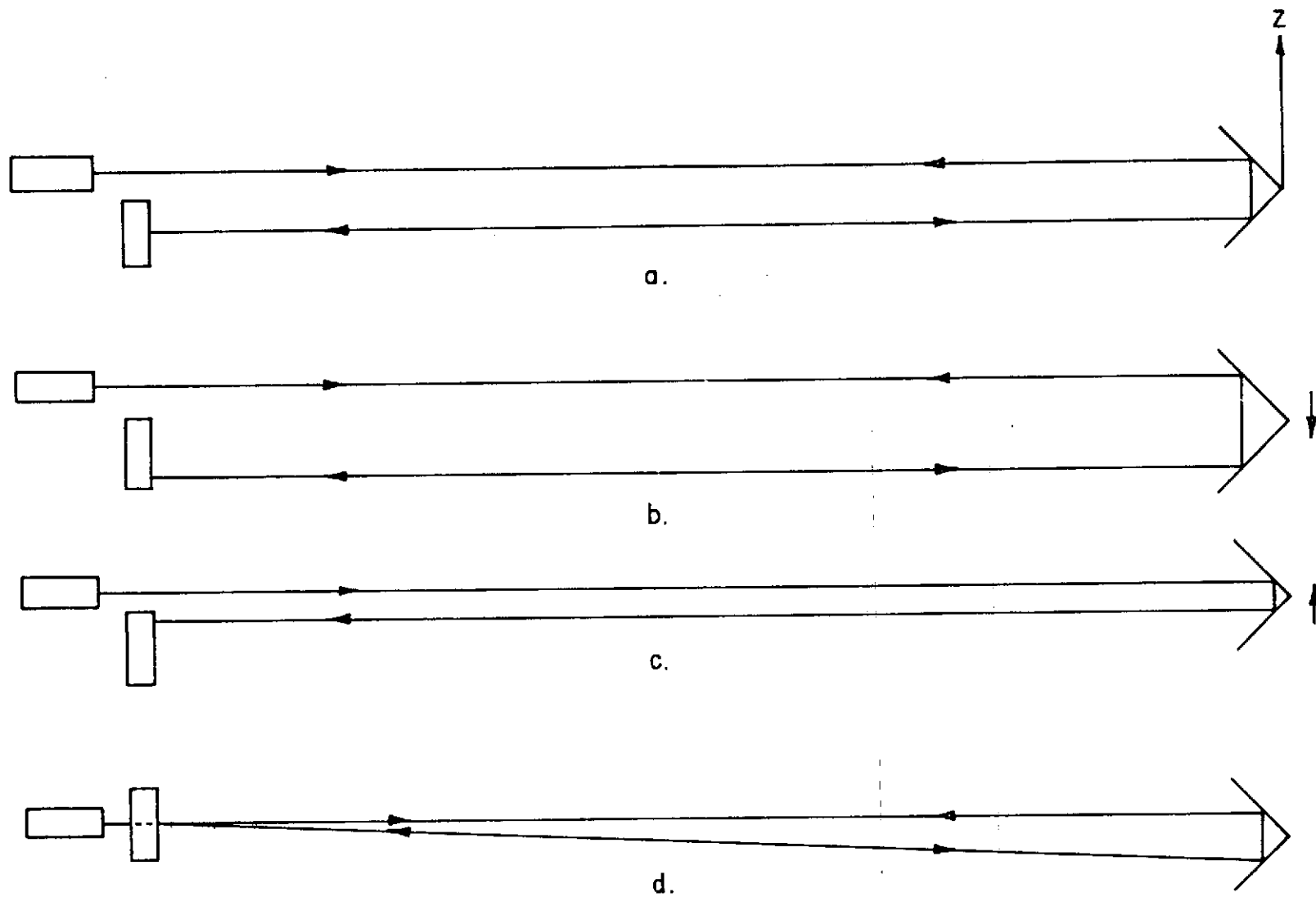
Figure 6-33. Z-Translation In X-Rotation Sensing

The result is that two images will be formed in the plane of the detectors, separated by an amount proportional to this angle. If the original collimated beam is exactly bisected by the roof edge, they will be of equal intensity and this image splitting might be tolerable, since one image would be on each detector. However, the translation 0.5 inch in the Z direction would result in a pronounced change in relative intensity in the two images, resulting in an unbalanced signal indistinguishable from the X-rotation effect being measured.

If the effect of this reflector error is to be limited to 1 sec, for example, the image doubling should be limited to about 1/18 sec, since errors in the sensing direction are multiplied by 18 when quantized to X-rotation. Angle error in the reflector should be limited to 1/12 x 1/18 or 1/216 sec, a requirement which is a full two orders of magnitude beyond the state-of-the-art.

A solution for this has been found as follows. The prism is doubled in "vertical" size, that is, the projected width of each half of the prism is a full 2.25 inches. The collimated beam normally falls in the center of the upper half, not straddling the roof edge. It is then reflected to the lower half and then back to the vertical Porro, which reflects it again to the large Porro and back to the autocollimator.

This effect is illustrated in Figure 6-33a, where the normal position of the remote reflector is depicted. The center of the beam from the autocollimator is incident at the center of the upper half of the reflector, from where it is reflected to the lower face and then to the vertical Porro adjacent to the autocollimator. It then retraces the same path to the autocollimator.

Figures 6-33b and 6-33c illustrate the change in path when the remote reflector is displaced vertically. A reflector displacement of ± 0.5 inch produces a displacement of ± 1.0 inch of the beam reflected to the vertical Porro. Its height must be 2.0 inches plus the collimator aperture diameter, or 3.25 inches, if no intensity loss in the image is permissible.

Note further that the source reticle has finite dimensions, and thus the auto-collimator beam has a divergence equal to h/f, where h is the reticle size and f the focal length. The beam cross section increases with increasing distance, therefore. Nevertheless, if the aperture stop of the system is at the autocollimator objective, as is usually the case, there is no need to increase the size of the reflector beyond the diameter of the autocollimator aperture. The outer part of the beam will not reenter the autocollimator after reflection no matter how large the reflector is made.

Figure 6-33d illustrates a final point about the remote reflector requirement. The dimensional limitations prevent the mounting of the vertical Porro below the autocollimator as shown in 6-33a through c. However, by making the dihedral

angle of the remote reflector 80° 28' instead of 90°, the reflected beam is made to meet the vertical Porro.

Although Porro prisms normally have a dihedral angle of 90° so that the reflected beam is 180° from the incident beam, the essential nature of the reflector is the insensitivity of the reflected beam to rotation of the reflector about its roof edge. This characteristic is preserved, even though the dihedral angle is other than 90°.

A second problem associated with the remote reflector, although introducing an error of much smaller magnitude, is also less easy to correct. This is the effect of residual power in the reflector due to curvature of the reflecting surfaces, and, if a solid prism is used, of the hypotenuse face to a lesser degree. The effect of rotation about Y and Z axes is treated. Since the roof edge is nominally parallel to Y, the system is, to a very close approximation, insensitive to rotation about Y. The extremely small coupling effects of simultaneous X, Y, and Z rotations are treated elsewhere [16].

Rotation about the Z axis produces a "sweeping" of the reflected beam so that the most obvious effect would be that it would no longer illuminate the vertical Porro. If the source reticle or slit is made large enough so that some portion of the beam is always captured by the vertical Porro, this would appear to be an adequate solution.

The dimension of the image actually formed in the focal plane of the auto-collimator is limited, however, by the geometry illustrated in Figure 6-33c. The limiting size of the image is determined by the angular subtense of the autocollimator as "seen" from the vertical Porro.

If the angular spread of the beam is made large enough, therefore, so that the $\pm$ 0.5 degree Z-rotation is always accommodated as described above, the portion of the image actually appearing in the plane of the detectors would vary in response to Z-rotation.

If perfect straightness and uniform sensitivity of the detector edges could be assured, this effect would be allowable. In practice, this cannot be relied upon, and either a special configuration of the detector system must be provided, or a second set of wedges must be provided to compensate for Z-rotation.

The latter procedure has been selected, and will operate as follows. When Z-rotation occurs, this will be measured by the Y-Z autocollimator. By means of a comparison circuit, a pair of wedges in the X-rotation system similar to those in the Y-Z system will be driven by an equal amount. The result is that the beam will always be incident on the remote Porro at the same angle and will be reflected to the vertical Porro and back again. This is illustrated in Figure 6-34a and b.

6-80

a.X- ROTATION SYSTEM

b.X- ROTATION SYSTEM WITH Z-ROTATION

c. VIGNETTING OF X ROTATION SYSTEM
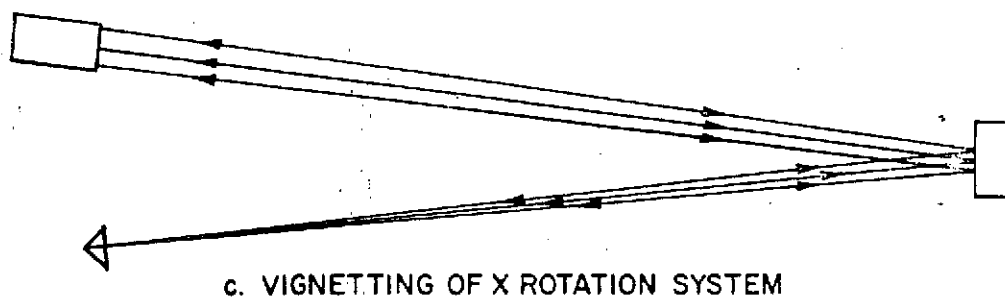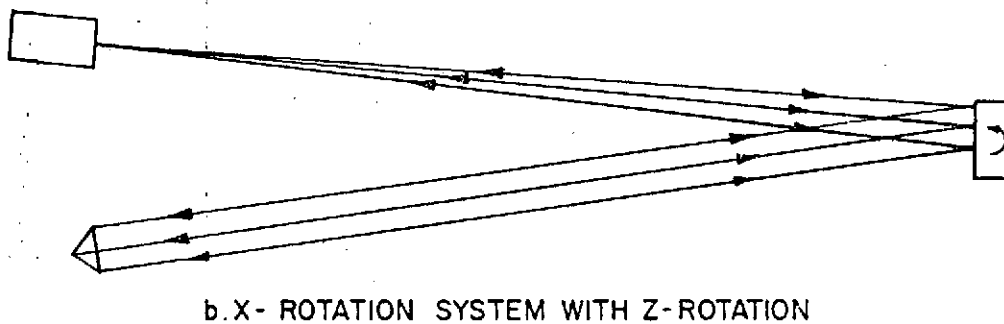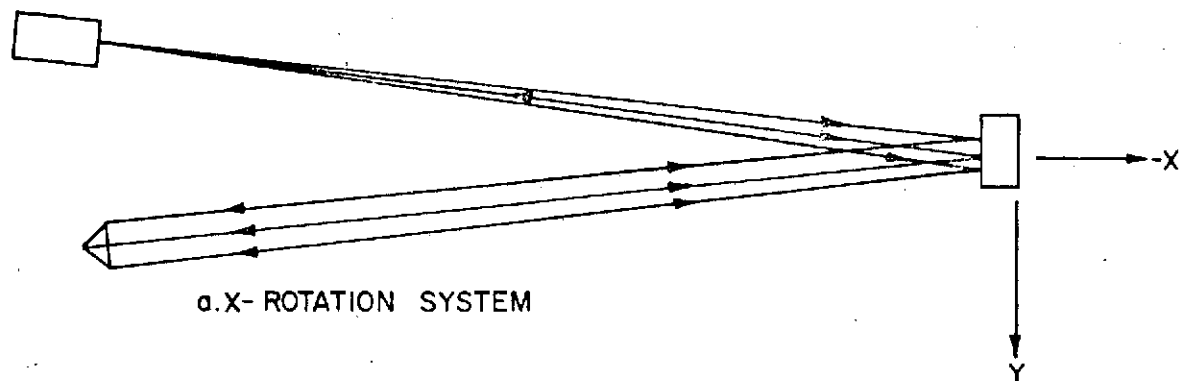
Figure 6-34. Twist Axis Geometry

A long source slit is no longer needed, and most importantly, the image will be held at the same position on the detectors.

The maximum image dimension which can be formed in the focal plane is given by the expression:

$$L\ max = d\ f/D$$

where   d is the aperture diameter of the autocollimator

   f is the focal length of the autocollimator

   D is the total distance from the autocollimator to the vertical Porro.

Using the following dimensions,

   d = 1.25 inches

   f = 5 inches

   D = 240 inches

then   L max = 0.026 inch.

However, since the intensity goes to zero at the extremes of an image of that dimension, the slit length will be made a little less, e.g., 0.020 inch. In the orthogonal, sensitive direction the slit width will be 0.005 inch.

The appearance of the image is shown in Figure 6-35. The length of the image is limited by vignetting. The intensity is maximum at the center of the image and decreases in all directions therefrom. The rate of decrease is governed by the function which describes the common area when one circle is moved laterally over another circle of the same size, and is surprisingly close to a linear decrease from the center.

The reason for a narrow slit in the sensitive direction is obvious, since this provides a higher rate of intensity change on the detector than would be the case if the slit were wide enough to be subject to substantial vignetting in the measuring direction. The calculations of signal level are based on the average intensity along the edges of the image, which for the dimensions chosen is 0.5 times that at the center.

The reason for matching the detector gap to the geometrical width of the slit and its image is that this procedure provides a minimum susceptibility to electrical null shift in the presence of differential change in responsivity of the two detectors due to temperature change or aging.

Diffraction and/or aberration cause the image edges to be blurred beyond the geometrical width shown, which provides assurance against a dead zone. Performance

DETECTOR A

DETECTOR B

↑ SENSITIVE
DIRECTION
OF IMAGE
↓ MOTION

a. NO Z-ROTATION

DETECTOR A

DETECTOR B

b. Z-ROTATION = 0.5°
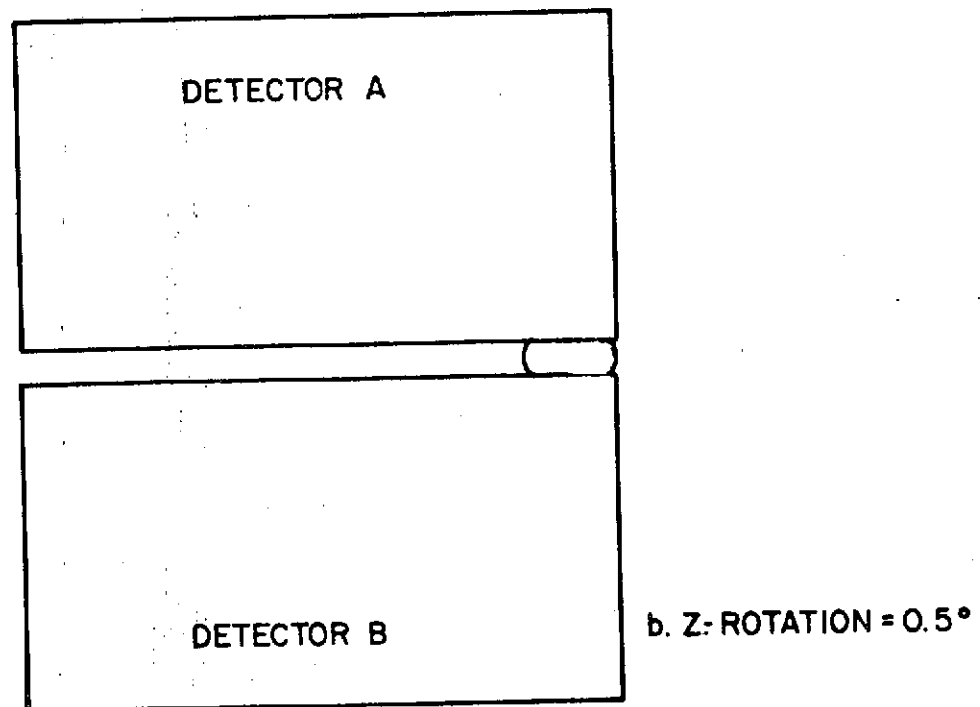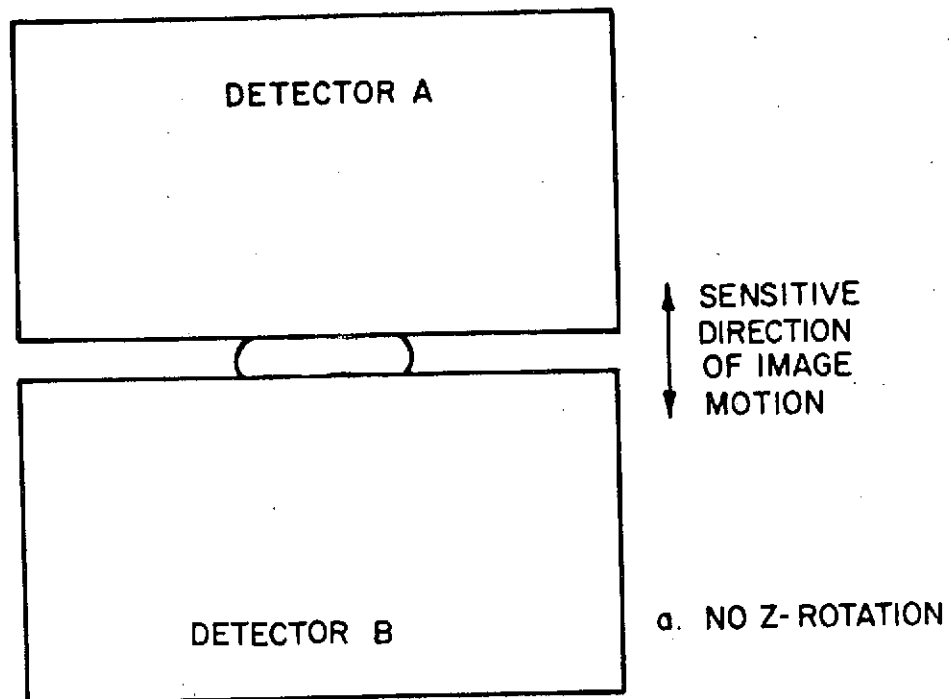
Figure 6-35.   Image Formation at X-Rotation Detectors
(Long Slit, No Compensating Wedges)

is optimized, however, by matching the detector gap to the geometrical or theoretical image width, allowing the blurred edges to spill over onto the detectors.

6.4.4 Dynamic Analysis

The basic blocks that define the dynamics of the wedge rotation servo system are shown in Figure 6-36.. This model excludes the modulated carrier and demodulator system which does not materially affect the dynamics.
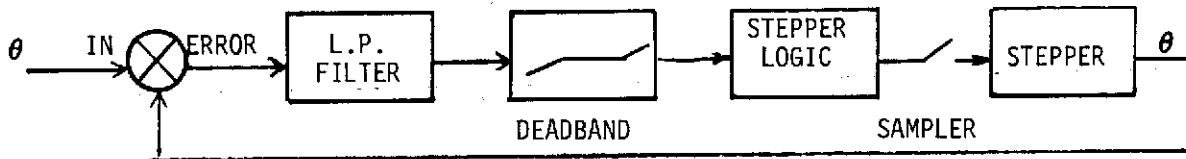
Figure 6-36   Wedge Rotation Servo Block Diagram

The blocks shown, and their functions are:

● Low-Pass filter whose function is to reduce system noise by keeping the bandwidth small while not distorting the error signal sufficiently to cause system error; i.e., it must be chosen to maximize the system S/N.

● Deadband. This block is necessary to prevent the system from "hunting". Its magnitude must exceed one step ($\pm$ one-half step) of stepper motion. System noise and overshoot will determine its minimum value.

● Stepper logic. This block puts out a forward direction signal whenever its input is positive indicating that the "error" is positive and a reverse direction signal for a negative input.

● Stepper. This block contains the non-linear stepper dynamics.

The system is sized based upon the maximum specified rate of the remote reference which has been defined as 0.56°/sec (200 sec/sec), and the wedge design which produces an optical reduction of 120:1. The weight of each step is selected to represent 0.5 sec and thus contribute negligibly to errors. In order to achieve 200 sec/sec, a stepper rate of 400 steps/sec is required. In addition, due to the optical reduction, each step produces a wedge rotation of 1 min. Finally, with each step of the stepper motor itself selected as 45 degrees, a total gear reduction of 2700 is required. Performance analysis was performed using digital simulation, with results to a sinusoidial input shown in Figure 6-37, assuming a system deadband of $\pm$ 1 step. Damping is enhanced by a method of shorting the quadrature coil (0°) just after energizing the 45° coil.

Although performance is important, it is recalled that system error is not a function of the indicated servo error. An analog error signal is also provided

ERROR

RESPONSE

INPUT

DEAD BAND = ± 1 STEP
COULOMB FRICTION = ·05 IN OZ
                      AT STEPPER
2 COIL   SHAFT
DAMPING RATIO ζ ≈ 0·4

1 STEP = 1 MIN AT WEDGE
       = 0·5 SEC TARGET
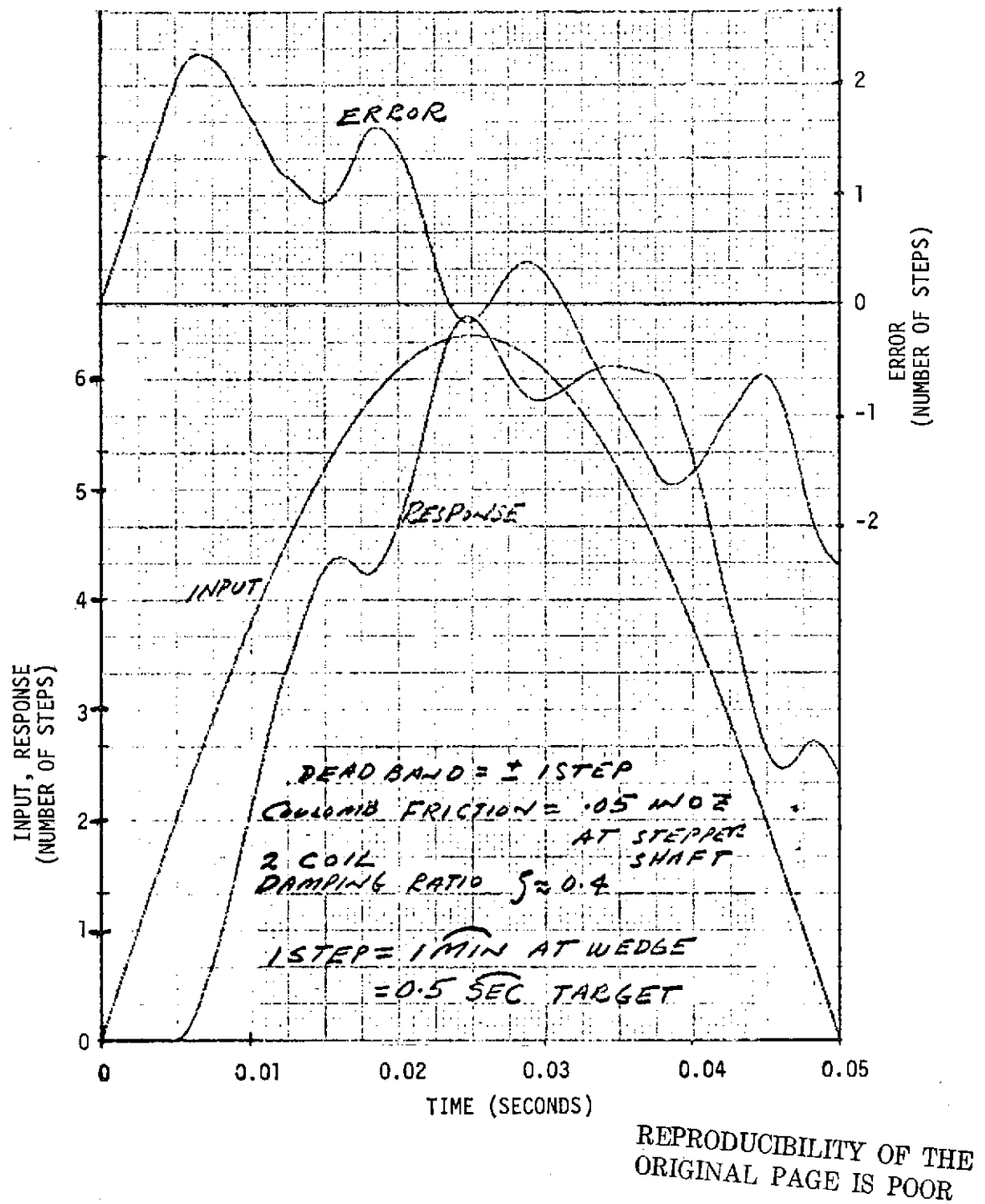
Figure 6-37. Alignment Sensor Servo Dynamic Characteristics

directly from the preamp-postamp stage, and the measured angle is determined by the algebraic sum of the servo-resolver output and the "raw" or residual error signal. A considerably larger deadband than the one step indicated would be tolerable.

6.4.5 Error Analysis

The assembly error budget is summarized in Table 6-8. In many cases, it is necessary to establish the maximum error that could result from certain events or defects, and then to decide how these should be treated statistically in order to derive a fair estimate of error.

With a normal distribution of probabilities, it is customary to divide the maximum by three to obtain the standard deviation. For deviations which are uniformly distributed between maximum and minimum values, however, the standard deviation is derived by dividing the extremes by $\sqrt{3}$. Information is not available to indicate whether the angular deviations and transverse displacements are normally or uniformly distributed. Even if uniformly distributed, however, several of the error contributions are dependent on simultaneous occurrence of two or more events, in which case the maxima should be divided by numbers even greater than three.

The maximum error contribution comes from the residual curvature of two reflecting surfaces of the Porro prism. The maximum error due to this defect, when coupled with maximum translation parallel to Z, is 6 sec. But this is arrived at by a combination of three events. If uniformly distributed, the maximum value should be divided by 3.17; if normally distributed, by about five. Similarly with certain cross-coupling errors. Therefore, the approach which has been adopted is to divide all maxima by three, which is felt to be on the conservative side.

The development of the various contributions to the error budget is summarized in the following sections.

6.4.5.1 Noise Equivalent Angle, Transverse Rotation

Assuming an output of 2.0 MW from the gallium arsenide source and a Lambertian radiating diameter of 0.38 cm, the radiance N is calculated to be 0.56 w/cm^2 ster.

Transmittance T of the entire system is given by the following:

$$T = 0.075 \times 0.995^{30} \times 0.98 = 0.063$$

where   0.075 is the resultant efficiency of three beam-splitter encounters.

               0.995 is the transmittance of each airglass surface

               0.98 is the reflectance of the mirror.

Table 6-8   ASA Error Budget Summary

Source	Y-Z system (1_σ)	X system (1_σ)
Noise equivalent angle	<0.01 $\widehat{sec}$	0.03 $\widehat{sec}$
Detector null shift	0.01	0.08
Thermal bending	0.01	0.23
Analog signal error	0.08	0.08
Orthogonality	0.17	
Alignment to X, Y, Z	0.10	0.07
Alignment of Z follower		0.33
Resolver Alignment to wedges	0.10	0.10
Resolver Linearity	0.04	0.04
Cross-coupling	0.10	0.80
Mirror error	0.10	
Prism error-large		2.0
-small		0.5
TOTAL (RSS)	0.28 $\widehat{sec}$	2.25 $\widehat{sec}$

Then irradiance H_{max} at the center of the image is given by

$$H_{max} = \pi N \ T \ d^2/4f^2$$

$$= 1.76 \times 10^{-3} \ w/cm^2$$

where   d   = diameter of collimator aperture = 3.2 cm

         f   = focal length of collimator = 12.7 cm

The average intensity along the edge of the image is reduced below that at the center by the factor V (for vignetting). For a square image 0.013 cm on each side, with the aperture, focal length and distance indicated, V = 0.77. Then,

$$H_{ave} = 1.35 \times 10^{-3} \ w/cm^2$$

The image area dA falling on the detector due to a 1 sec deviation is given by dA = h dw, where

     h = height of image in insensitive
          direction = 0.013 cm

    dw = image width moved

$$= 2f \times 4.8 \times 10^{-6} = 1.23 \times 10^{-4} \ cm$$

Then,   dA = $1.56 \times 10^{-6} cm^2$ and power on detector, P, is given by

$$P = 2.1 \times 10^{-9} \ w$$

Signal E = 2100 microvolts P-P, where R = responsivity = 10^6 v/w.

Noise includes detector noise and that of the FET input.

Detector NEP = $\sqrt{A \ \Delta F}/D*$ = 3.6×10^{-12} w

where: A   =   0.01 cm^2 (two detectors)

         f   =   320 Hz

        D* = 5×10^{11} at 0.9 micrometers

Noise signal = R x NEP = 3.6 microvolts

         FET voltage noise = 0.18 microvolts

         FET current noise = 0.04

         These are both negligible when compared with detector noise.

Then, RSS noise = 3.6 microvolts rms

= 18 microvolts P-P

Then S/N = 2100/18 = 117

and NEA = N/S = 0.009 $\widehat{sec}$

6.4.5.2   Noise Equivalent Angle, Twist Rotation

$$N = 0.56 \ w/cm^2 \ ster$$

$$T = 0.155 \times 0.995^{30} \times 0.98^6$$

$$= 0.118$$

Then H_{max} = $3.3 \times 10^{-3} \ w/cm^2$

For a slit 0.051 x 0.013 cm,   V = 0.50

Then H_{ave} = $1.65 \times 10^{-3} w/cm^2$

$$h = 0.051 \ cm$$

$$dw = 4f \times sin\theta \times 4.8 \times 10^{-6}$$

or $dA = 3.5 \times 10^{-7} \ cm^2$

Then P = $1.65 \times 3.5 \times 10^{-10} w$

= $5.8 \times 10^{-10} w$

E = 580 microvolts

Noise signal = 3.6 microvolts rms

= 18 microvolts P-P

Then S/N = 580.18 = 32

and NEA = 0.03 $\widehat{sec}$

6.4.5.3 Detector Null Shift

The detectors are separated by a distance equal to the geometrical image size, so that at null the only energy on each detector is that due to diffraction and/or aberration. Although the two detectors (silicon) are made of the same material, it must be presumed that their responsivities will be slightly different.

At a given temperature the image will yield a null signal when it is shifted so as to fall slightly more on the detector of lower responsivity. At a different temperature, although both detectors may be presumed to have an equal temperature coefficient of responsivity, a small null shift will result. This shift can be shown to be equal to

$$S = \frac{S_n \times \delta \times r \times \Delta T}{2 + \delta + 2r \; \Delta T}$$

where   R = Nominal responsivity

      δ = Fractional difference in responsivity

      r = Temp. coefficient of responsivity

      T = Temperature change

      S_n = Angular subtense of image on each detector at null

For detectors of the type to be used

      δ will be not over 5 per cent

      r is approximately .004/°C

      T will be taken as 15°C

      S_n = 10 $\overparen{sec}$

Then ΔS = 0.011 $\overparen{sec}$ in Y or Z

         = 0.25 $\overparen{sec}$ in X

Thus, even over the full temperature change, this effect is small in comparison to the error tolerance.

6.4.5.4   Analog Signal Error

The servo analysis indicates residual lags of slightly more than two steps, or 1.2 sec, when the deadband is set at two steps (+1). However, it may be found desirable to increase the deadband for one of several possible reasons. This can readily be done since the analog error signal is always available as a separate output.

Assuming a possible maximum servo lag of 5 sec, the error in the analog output for the same value must be estimated. The system has been designed such that the analog signal can be calibrated on command by disabling the servo and causing the stepper to take a convenient number of steps such as ten, corresponding to an average value of 5 sec. The resulting error signal change then provides an in-flight calibration of the analog output.

The residual error is then due to changes in output since the last calibration. A high estimate is a five percent residual error in scale factor calibration, which at 5 sec lag produces 0.25 sec maximum error.

6.4.5.5   Orthogonality

Non-orthogonality of the scanning directions of the wedges in the dual-axis autocollimator by 1 min can produce an error of 0.5 sec. A fine adjustment is provided in the design whereby one wedge assembly can be rotated relative to the other by motions as small as 1 min. At assembly, with autocollimator operative and directed at a mirror, one pair will be exercised through its full range while the output of the orthogonal channel is monitored. Adjustment of the wedge assembly will be made until the coupling error of the second channel is reduced to 0.5 sec or less.

6.4.5.6   Alignment

Alignment to X, Y, and Z axes

The procedures for aligning the elements to the defined axes have been developed in detail, with the achievable accuracy in Y and Z of 0.30 sec, and in X of 0.20 sec.

Alignment of Z-follower in X rotation channel

The requirement and procedure for this step are similar to those used to achieve orthogonality in the Y-Z system. However, since other error contributions are larger, the effort to reduce this value to 0.5 sec is not justified, and 1.0 sec will be the maximum allowed.

6.4.5.7 Resolver

Resolver Linearity

The linearity specification of the 16-speed output of the resolver is ±15 sec over the $\pm60°$ excursion, with a design goal of 10 sec. Taking the 15 sec limit and dividing by the angular magnification of the wedges, 120, we find that the maximum residual system error due to this cause is 0.13 sec.

Resolver Alignment to Wedges

The necessity for aligning the resolver zero to the zero-deviation position of the wedges results in an achievable maximum residual error of 0.30 sec due to this cause.

6.4.5.8 Reflector Errors

Mirror Error

The tracking action of the autocollimator in the Y-Z subsystem causes the beam to move across the face of the mirror. In addition, translation causes different areas of the mirror to be used. Residual curvature of the mirror can then cause errors in the direction of the reflected beam. For a reasonably tight specification of 0.05 wavelength maximum departure from flatness, the effect is found to be 0.30 sec maximum error.

Prism Errors (X-rotation Subsystem)

Residual curvature of the reflecting surfaces on the large Porro prism, coupled with allowable "vertical" translation (parallel to Z) produces a shift in the direction of the reflected beam of 0.33 sec. However, when this is quantized in terms of X-rotation, the necessary multiplication by 18 produces a maximum error of 6.0 sec. This is by far the largest error contribution, and therefore deserves considerable attention.

Assuming a flatness specification of 0.025 wavelength, which is the severest practicable tolerance, the cumulative effect of three surfaces (hypotenuse and two reflecting surfaces) and the fact that the beam traverses this prism twice produces potential system errors of more than 10 sec.

By specifying that the hypotenuse be hand-figured by the optician to achieve an overall uniformity of reflected wavefront of 0.125 wavelength, a residual system error of 8.4 sec was calculated. In addition to this is the problem of inhomogeneity in the glass of which the prism is made. The total path length (two passes) is 9 inches, and with even the best available grade of homogeneous fused silica, additional angle errors would be experienced.

Consideration has been given to the use of two first-surface reflectors to form an air prism. The problem to be solved with this approach is to make a supporting frame to hold the reflectors in a very stable angular relationship to each other, particularly in the presence of temperature changes. This problem has been solved satisfactorily, and the advantages of a mirror assembly can be realized. These include the fact that the effect of curvature of the reflecting surfaces in a solid prism is increased by a factor equal to index of refraction of the glass, or about 1.5. Also, there is no hypotenuse face to add its own curvature effects. Finally, the problem of homogeneity of the glass is no longer relevant. By this means, the residual system error can be reduced to 6.0 sec maximum in the presence of a full 0.125 wavelength curvature on each reflector and a maximum Z translation of 0.5 inch.

The sectional view through the reflectors is shown in the sketch in Figure 6-38.
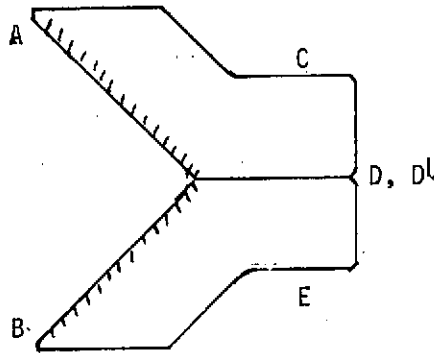
Figure 6-38   Sectional View Through Reflector

Each reflector is cut from one piece of fused silica (commercial grade). In addition to the reflecting faces, however, surfaces D and D^1 are also polished flat to a small fraction of a wavelength and then optically contacted. This is somewhat similar to the practice of wringing gage blocks, and produces a cohesion which is not dependent on air pressure. The bonding strength approaches that of the bulk material, and separation is extremely difficult.

In addition, the two reflectors will be gripped by a frame across surfaces C and E by means of which the assembly will be mounted. A protective frame will also surround the other sides, but kinematic design will be employed to avoid stressing the assembly, and the forces between D and D^1 will be supplemented by the mechanical design.

The small Porro prism will be similarly designed, and its residual system error is one-fourth that of the large reflector.

6.5 REFERENCE BLOCK ASSEMBLY

The function of the RBA is to provide structural mounting surfaces for the Star Tracker Assembly (STA), Gyro Reference Assembly (GRA), and Alignment Sensor Assemblies (ASA). The principal requirement is to maintain a stable geometrical relationship between each of the assemblies, limiting angular changes to 0.5 sec. The following functions are associated with the above requirement:

- The RBA must be capable of withstanding the launch vibration and shock environments while maintaining levels seen at each of the assemblies within compatible limits.

- The temperature gradients within the RBA must be low, to minimize thermal deformation stresses, and stable, to limit cyclic thermal deformations to acceptable levels.

Although it would be desirable to formulate an RBA design which is flexible or modular to the extent of being capable of accommodating any of the configurations while maintaining optimum weight and performance, the design of spacecraft type structures is incompatible with this type approach. In addition, the design of any particular RBA configuration is intimately tied to the basic spacecraft design. For these reasons, a single, non-modular design, which incorporates the maximum number of assemblies mounted in an 8.0 foot diameter spacecraft was investigated. The extent of the design conception and investigation was limited to establishing the feasibility of meeting performance requirements with a given geometry, structural concept and thermal control system.

Figure 6-39 is a layout drawing of the RBA configuration investigated. The overall shape is that of an equilatreal triangle, 10.0 inches deep, with tapered legs tying to the spacecraft supports located at each vertex. The structure is made of 6061 aluminum with caps on each face and webs which form a very stiff, highly conductive unit capable of distributing heat loads to minimize thermal gradients. The selection of three-point mounting was made to minimize bending loads in the principal, most flexible RBA plane. Because the spacecraft thermal control system and structure will undoubtedly allow motion of the RBA supports in all three axes to occur, loads will be imposed on the RBA. With three-point support, bending loads in the principal RBA plane will be limited to those generated by torques, which can be kept low through proper design of the supports. Bending loads in the other two planes are less critical since the RBA stiffness is much higher in these planes and distortion is only of interest to the extent that it couples into the principal plane. The star trackers are overhung from one leg of the triangle to minimize the size of the viewing window required in the
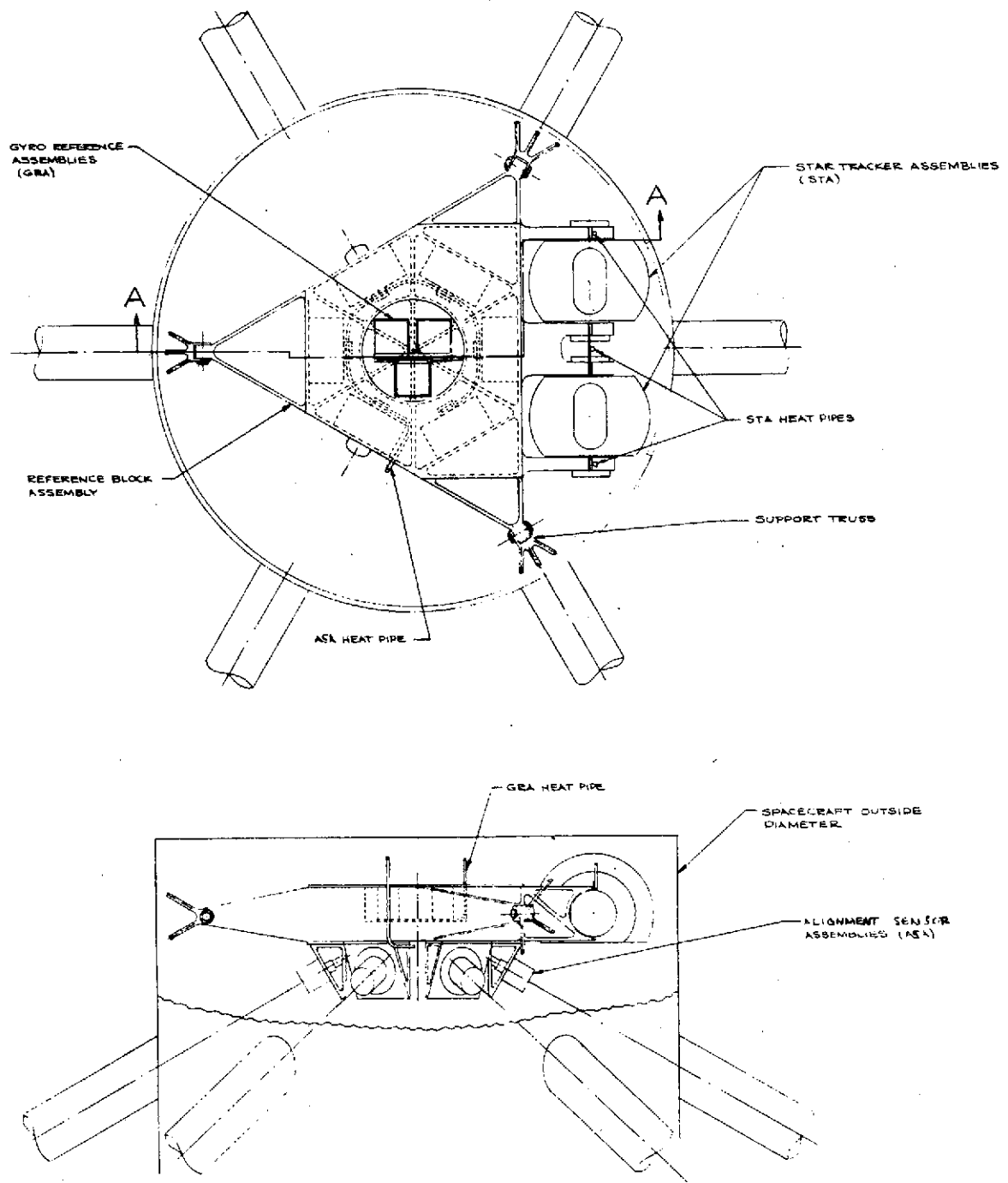
Figure 6-39. Reference Block Assembly Layout

spacecraft. The modular elements of the GRA are mounted at the geometrical center of the triangle and each ASA is mounted on the opposite side of the RBA arranged hexagonally in line with each of the experiment booms.

6.5.1 Structural Design

The following considerations are pertinent to the structural design of the RBA:

- The unit must have the strength to withstand the launch vibration and shock levels.

- The launch loads imposed on the RBA and its transmissibility must be compatible with the load limits for each of the mounted assemblies.

- Thermal gradients and resultant deformation must be limited so that short term changes are maintained below 0.5 sec between any two assemblies.

- Material selection and fabrication processes must be directed towards producing a finished product with low residual stresses since these, over a period of time, will produce analastic and plastic deformations whose magnitude may be difficult ot predict.

The nature of the RBA concept necessitates that either the assemblies themselves be designed to withstand relatively high launch loads, or that vibration isolation be accomplished at the RBA mounts. Isolation cannot be implemented at the RBA-assembly interface. The preliminary design shown in Figure 6-39 is intended to be an extremely stiff structure with natural frequencies sufficiently removed from booster and spacecraft resonances to achieve good isolation. It is expected that the design will be either conductivity or stiffness limited rather than strength limited. It can be shown that with 10.0 g's at each assembly, the maximum bending stress will be less than 500 psi.

6.5.2 Thermal Design

The chosen thermal control system for the reference block assembly may be generally categorized as a heat pipe design. The design consists of the following components (and/or requirements):

- An insulation blanket over the entire RBA to isolate the assembly from the spacecraft environment (particularly from temperature differences across the spacecraft)

- A highly conductive material, such as aluminum or beryllium, for the Reference Block Assembly structure, to avoid local temperature perturbations

- Insulation standoffs (approximately 0.100-inch fiberglass) to thermally isolate heat sources, such as gyro units, from the RBA.

- Aluminum base plates under each electronic box to thermal couple the box to the evaporator end of the heat pipe

- Heat pipes to carry the heat from the various heat sources to an external radiator

- A radiator outside the insulated assembly to distribute the heat dissipated by the electronic assemblies on the RBA.

The principle of the heat pipe design is illustrated in Figure 6-40. The gyro units and the alignment sensor units represent major heat sources, which would cause unacceptable temperature disturbances if these units were coupled to the RBA. However, this design approach isolates these boxes from the RBA with insulation standoffs. Since the entire RBA and attached boxes are insulated, the power dissipation within this insulation cocoon would cause excessively high temperatures unless the heat is removed. The heat pipes are used for that purpose; heat dissipation of each assembly is absorbed by the "evaporator" section of the heat pipe, and is carried away to the external radiator (which is the "condenser" end of the heat pipe). Thus, the net heat dissipation from an electronic package to the RBA is essentially zero.

Only about 1 per cent of the power dissipation is absorbed by the RBA via the insulation standoffs. Conservative temperature gradient calculations show that the RBA will sustain gradients less than 0.5°F if the structure is 0.10 to 0.25-inch thick where the heat dissipating units are located.

The radiator size depends on whether it is mounted inside or outside the spacecraft. If there is some zone on the outside surface that has negligible solar or earth heating, the radiator can be mounted externally and its area will be approximately 5.5 ft^2. If the radiator cannot be mounted outside, a rather large fin (about 20 ft^2 of the surface area) will be needed to distribute the heat to the spacecraft interior.

Several different schemes were evaluated for meeting the requirements of negligible thermal deformation of the RBA, including:

- Using a material with a very low coefficient of expansion, such as Invar, Cer-vit or graphite-composite

- Using thermal control devices to achieve very small temperature gradients.

In considering thermal control methods, three systems were evaluated: a fluid loop system, a heat pipe system with the RBA uninsulated, and that selected using a heat pipe system with the RBA insulated.

Gyro Units
(mounted to top
surface of RBA)

Heat Pipe
(Evaporator End)

Aluminum Base Plate

Radiator

Alignment Sensor Units
(mounted to bottom
surface of RBA)

Aluminum Base Plate
with Integral Heat Pipe

Heat Pipe
(Evaporator End)

NOTE: Two heat pipes in
parallel for redundancy

Radiator (located outside the
insulated RBA)

Heat Pipe
(condensor end)
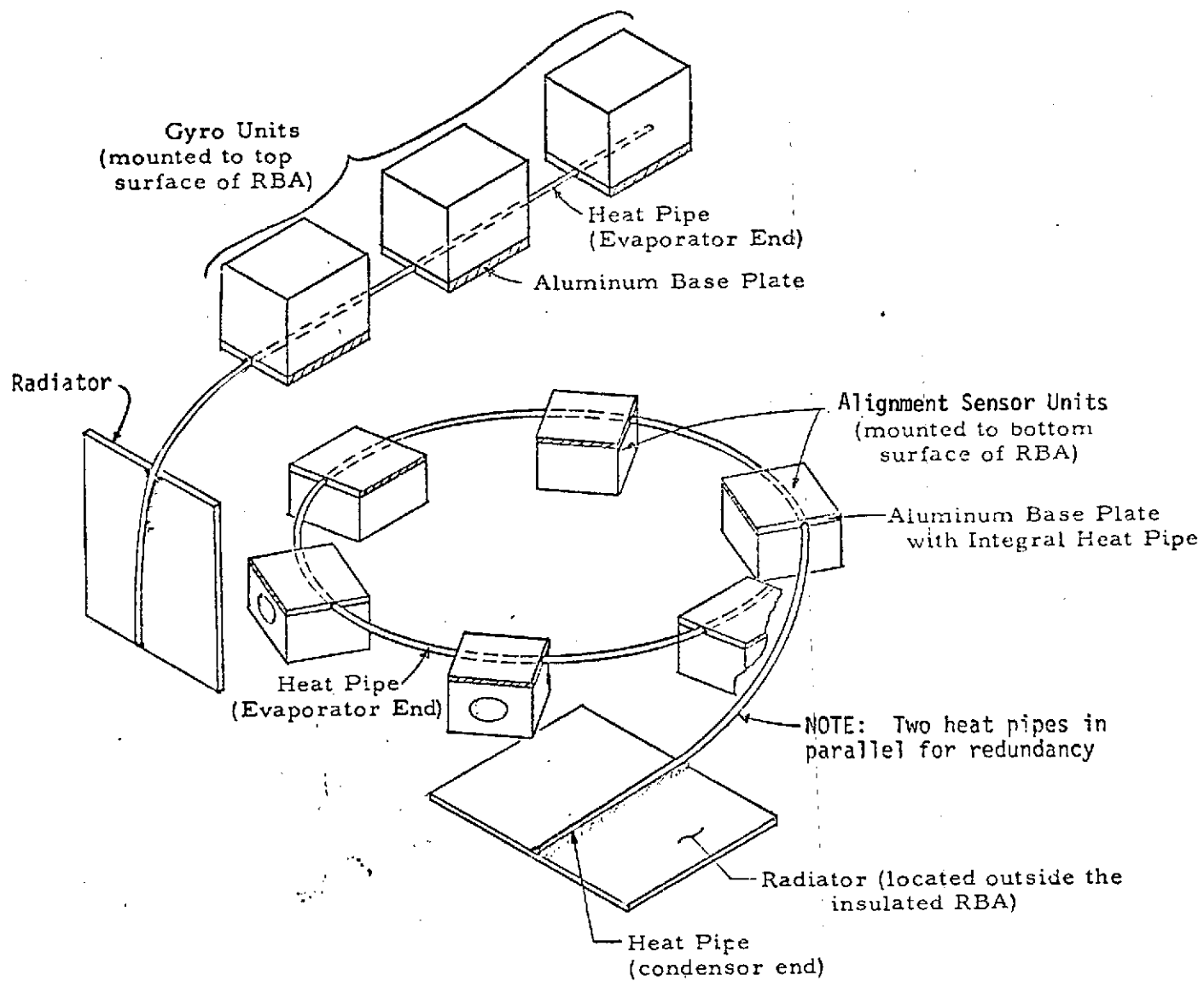
Figure 6-40. Thermal Control Scheme for Reference Block Assembly

The easiest solution, from a thermal viewpoint, would be to construct the RBA from a material with a very low coefficient of thermal expansion (α). Then temperature differences up to 5°F could be tolerated. Some materials in this class are Invar steel, Cer-vit (ceramics) and graphite-composites. The graphite-composites are of interest because of their low weight to strength characteristics; however, this class of materials is relatively new and there is a lack of data concerning its long-time dimension stability. Ceramics were discarded because of their poor mechanical properties (brittleness). Invar is not attractive because of its high density (500 lb/ft^3) and its lack of good dimensional stability.

A fluid loop system was considered but found impractical for two reasons: the life or mean-time-to-failure of pumps is too short for this application without extensive redundancy, and the system is complex and would require of the order of 25 watts of electrical power to drive the pumps.

Another scheme uses heat pipes to distribute heat from local sources uniformly over the whole RBA. In theory, the method appears to be a logical way to solve the problem; in practice, however, the scheme has subtle deficiencies which make it impractical for the very small thermal gradients that are required. The problem is not in the heat pipe, per se, but in transferring heat to and from the pipe. Temperature differences in the RBA up to 5°F may result even though the heat pipe vapor is completely isothermal. And, these gradients will vary (time-wise) due to changing side-to-side temperature gradients inside the spacecraft.

The principle of the selected approach is to isolate the RBA from all heat sources (both electronic equipment and the spacecraft), and to transfer electronics heat dissipation via heat pipes to an external radiator. Thus, in the absence of heat sources, the RBA will not be subjected to temperature gradients. Insulation blankets isolate the RBA from the potentially non-uniform spacecraft environment, and insulation standoffs are used to isolate each electronic assembly. The assemblies are in good thermal contact with the evaporator (warm) end of the heat pipe via the aluminum base plate, so nearly all the heat dissipation is transferred directly to the heat pipe. The distribution of heat from a typical electronics box was considered, from which it was noted that over 95 per cent of the heat dissipation is carried away from the RBA by the heat pipe, and only a minimal amount is absorbed by the RBA.

The heat pipes carry the electrical power dissipation to a radiator, which is a simple flat plate acting as a radiation fin. The radiator temperature can vary (like ±15°F) without affecting the temperature distribution of the RBA. However, temperature variations of the radiator will be reflected by similar temperature variations in the electronic boxes that are coupled to the radiator via heat pipes.

For that reason, the radiator can be mounted on an external surface if there is negligible solar or earth heating. A criterion would be that the absorbed energy be less than 15 Btu/ft^2-hr. This results in an externally mounted radiator which would require about 5.5 ft^2 of surface area. If the orbit characteristics or space-craft configuration do not permit an external location, then the radiator can be mounted internally with some penalty in surface area as noted earlier.

A "gas-controlled" heat pipe can compensate for some changes in the radiator's environment. This second-generation heat pipe can effectively change the length of the radiator by using a non-condensable gas in con-junction with the normal working fluid. TRW recently fabricated a gas-controlled heat pipe for OAO, and has also designed and built a gas-controlled heat pipe to control the temperature of a Lunar Surface Magnetometer to be carried by Apollo.

Thermal analyses were conducted in three parts to demonstrate the feasibility of the design concept: the first step was to determine if the boxes could be both well coupled to a heat pipe and well isolated from the RBA; the second step was to determine thermal gradients in the RBA due to residual heat leaks through the insulation standoffs; and the third step was to size a radiator for the total power dissipation load. This type of approach was used to verify the principle of the approach.

In general, this scheme makes the RBA/spacecraft thermal interfaces very simple. Since the RBA is isolated by insulation blankets from the spacecraft interior, the RBA is not sensitive to side to side gradients, top to bottom gradients, local hot or cold spots, or other local perturbations. The main consideration is providing a constant environment to the radiator. The stability of the environment does not affect the RBA, but it does affect the temperature level of the electronic boxes. Thus, if the boxes can vary $\pm$ 15°F about a mean temperature level, then the radiator temperature level can be allowed to vary by $\pm$15°F due to its surrounding environments. If the radiator is located internally, the electronic boxes will be approximately 40°F warmer than the spacecraft average temperature level. The RBA, however, will operate near the mean temperature of the spacecraft since its thermal coupling to the spacecraft is better than its coupling to the electronic boxes.

Consider a case of the worst thermal gradient across the total RBA being assumed between the largest separation of critical assemblies, i.e., between the STA and the most remote ASA. Because the RBA is completely wrapped in an insulation blanket and will be provided with thermal isolators at the mounting points, it is

well insulated from the spacecreft. Indications are that the transient, or once-per-orbit, changes in gradients will be less than 10 per cent of the steady-state gradients. Therefore,

$$\theta_{trans} < 0.15 \ \widehat{sec}$$

6.6   EXPERIMENT GIMBAL AND ELECTRONICS

The Experiment Gimbal Assembly (EGA) configuration discussed is suitable for baseline requirements for earth and space pointing. Modifications necessary to accommodate alternate payloads will be identified later. Figure 6-41 is a schematic of the earth pointing EGA configuration. The payload is divided into two parts and mounted at the ends of the Y-axis shaft. Dividing the load into two parts is necessary to achieve low mass unbalance forces. The alternative to this division is designing a gimbal to surround the payload which, of course, would be much heavier. The X and Y axes are capable of full 360° rotation which makes this configuration suitable for use in space pointing. The space pointing configuration would be modified to delete the Z axis, which both simplifies and lightens the unit. This configuration was arrived at through studies which considered a number of alternates. In all cases, the selected configuration is both lighter and has a greater potential angular excursion which makes it suitable, with simplifying modifications, for the space-pointing configuration.

Each gimbal axis is supported by angular contact ball bearings which are axially preloaded. The outer races of the bearings are attached to the housing by means of flexures which allow the position of the center of rotation and the axial load to be adjusted. The flexures are relatively flexible so that when a given axial or radial bearing load is reached, sufficient deflection occurs to allow preloaded stops to contact, thereby limiting the loads which the bearings must transmit. The preloaded stops also cause the natural frequency of the shaft and its associated mass to change once contact occurs. Thus, magnification ratios are reduced without depending upon friction damping. The contacting stops are 45° to the axis of rotation which causes them to act in both the radial and axial directions. In order to allow radial shaft motion greater than .005 inches, which is a typical value for the torque motor air gap, stops are provided on the motor to prevent rotor and stator contact and the stator is mounted on three spring preloaded shoes which permit radial motion. The typical gap setting for the inductosyn is also .005 inches.
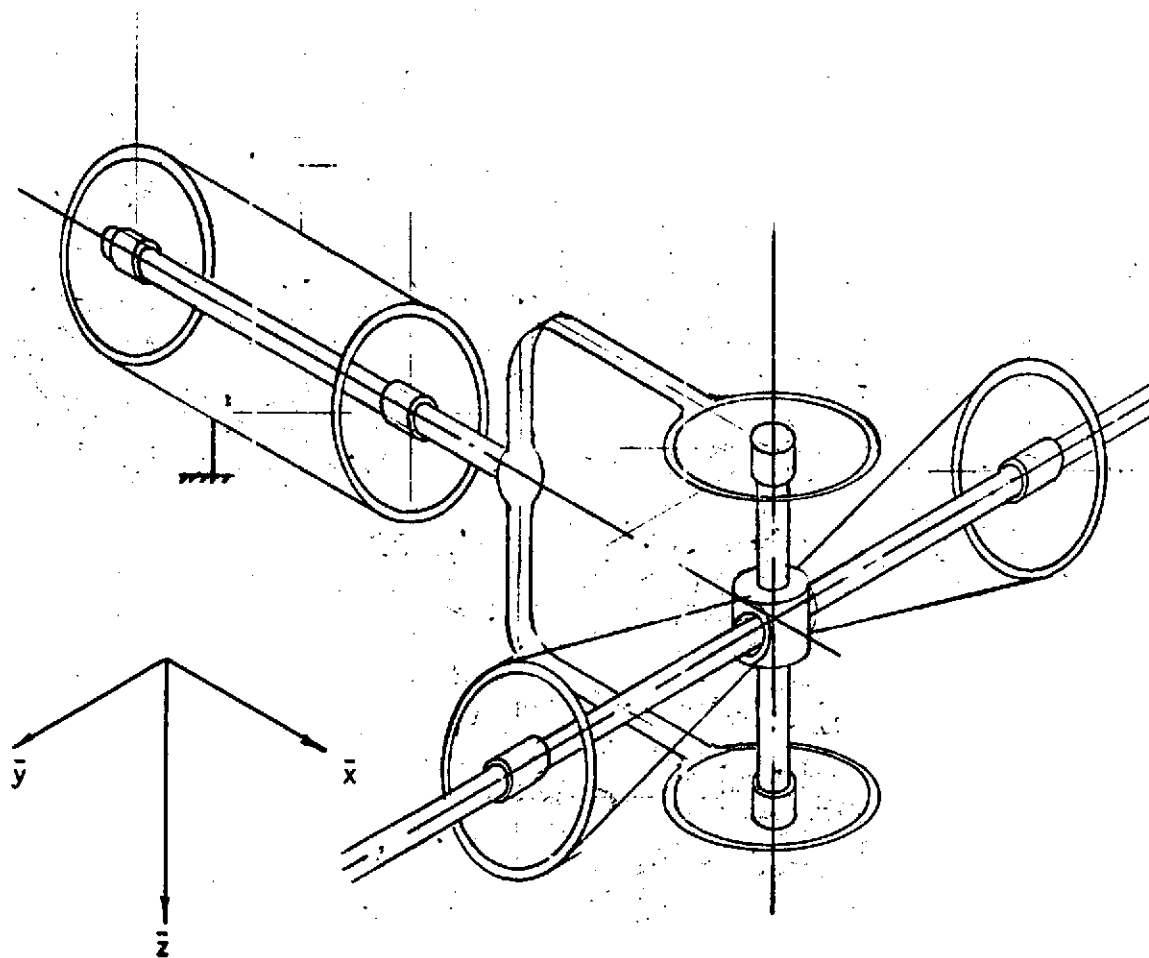
Figure 6-41. Experiment Gimbal Configuration

Greater axial shaft motion is permitted by providing stops which prevent the plates from contracting and mounting the stator on flexures which permit axial, but not radial motion.

In the interests of minimizing friction and rotational spring constants, wire routing between the housing and shafts is accomplished by means of flat cable wraps similar to those used on the star tracker gimbals. Tests on similar units have shown that both friction and spring constants are reduced to negligible levels.

In order to achieve a runout accuracy of 0.5 sec, the inner races of the bearings are pressed onto the shaft prior to grinding the grooves. In this way the grooves for both bearings on the shaft can be ground in a single setup, thus minimizing runout and achieving maximum parallelness between the inner race grooves. In order to implement this feature, the gimbal ring must be split to allow assembly of the Z-axis shaft. This joint, as well as all others in the unit, must be designed to permit a minimum amount of motion during launch vibration.

In order to be able to servo the EGA on the ground with the payload installed, the bearing loads must be relieved to reduce friction. If the full payload were supported by the bearings, the running bearing friction per axis would be between 30.0 and 60.0 oz - in, depending upon the axis. This is far in excess of the servo system capability. Therefore, two hydrostatic gas bearings are provided for each axis to relieve bearing loads on the ground. By means of a special test fixture, one axis at a time can be supported by the gas bearings thus lifting the shaft off the preloaded stops, relieving all radial bearing load and reducing friction torque to that generated by the axial preload and the gas bearings. Using this technique, it is estimated that friction torque can be reduced to 5.0 oz - in. All rotating air bearing pads, with the exception of the inboard pad on the X-axis, can be designed for removal prior to launch. Consideration can be given to aligning the axis under test vertically to minimize shaft deflections and approach the zero gravity configuration more closely. This technique requires the use of a high capacity thrust bearing. Bearing lubrication will be provided by means of oil impregnated in nylasint reservoirs. Excape of the oil is limited by means of labyrinth seals. These supply and containment techniques have been proven on a number of TRW space qualified electromechanical devices.

The torque motors chosen are DC brushless, full rotation types. Note that two motors are used on both the Y and Z axes to produce symmetrical thermal gradients at the gimbal ring and the Y and Z axes. A single motor is used on the X-axis located close to the boom attach flange for thermal isolation. Axial thermal symmetry will not be important on the X-axis. The prime concern will be establishing uniform temperature at each cross section to minimize bending distortions.

The only reasonable alternative to ball bearings, for this application, are large angle rotational flexure pivots. However, no flexure designs for this amount of angular excursion are known to exist. The use of single ball pivots similar to those used on the Star Tracker Assembly gimbal is impractical because of high friction for the payloads considered.

Because of the large payload, significant shaft strength is required for support on the ground. With the bearing size on the layout, approximately 300,000 psi is generated in bending. Information obtained from bearing manufacturers indicates that with the basic EGA design, 0.5 s̃ec repeatable and 0.5 s̃ec non-repeatable runouts are obtainable within the state-of-the-art.

Because of the size of the payload and boom, it is appropriate to investigate the launch vibration in some detail and set up special requirements for the EGA. The following is a summary of the manner in which the vibration requirements were established:

- It is assumed that the payload will be latched to the spacecraft during launch so that the majority of the payload launch load is taken through the spacecraft structure rather than through the precision EGA. The fundamental frequency of the experiment package - latch support must be greater than 25.0 Hz in all directions.

- It is assumed that the booster vehicle is a Titan IIIC producing maximum axial vibration loads of 10.0 g's and lateral loads of 4.0 g's. The primary excitation frequency of the booster is approximately 21.0 Hz. Higher frequency inputs are roughly equivalent to the random cycles specified for Titan-launched equipment to account for aerodynamic induced vibration.

A preliminary linearized X-axis dynamic analysis using the TRW STRU-PAK TM Program was performed to determine loads on the primary EGA members and relative deflections. A four degree of freedom model was used as shown in Figure 6-42. The four natural frequencies are:

$$f_{n1} = 123.8 \text{ cps}$$

$$f_{n2} = 226.0 \text{ cps}$$

$$f_{n3} = 896.9 \text{ cps}$$

$$f_{n4} = 5608. \text{ cps}$$

The maximum displacements occur at the first natural frequency as tabulated below:

Coordinate	X Half Ampl. (Inches)	X/386 (g's)	Phase Angle (Degrees)
1	.0023	3.6	7.00
2	.0137	21.5	89.09
3	.0137	21.5	89.11
4	.0110	17.3	-87.44

The maximum displacement occurs at the Z-axis radial flexures which compress by 0.0247 inches. Including the effect of the preloaded stops could, of course, substantially reduce this deflection.

The relatively low loads and high natural frequencies shown above are encouraging since they indicate that the flexure stiffnesses may be substantially increased, the resultant displacements reduced, and the preloaded stops eliminated. The stiffnesses of the flexures would then be dictated by the force-position characteristics of the air bearing support fixture which, along with the flexure stiffness, will determine the degree of accuracy with which the flexures can be unloaded. In redesigning the flexures, every effort will be made to use a design which is contin- uous about the diameter as opposed to the three-member approach shown both to minimize distortion of the outer bearing race and produce uniform temperatures about the bearing diameter.

PAYLOAD ATTACH POINT
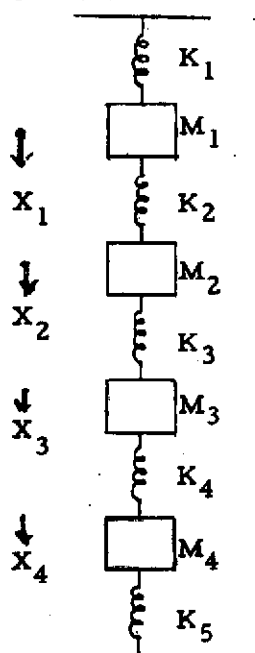
K_1 = Equivalent Y-Axis Shaft Stiffness

M_1 = Y-Axis Mass

K_2 = Y-Axis Radial Flexure Stiffness

M_2 = Y-Axis Housing

K_3 = Equivalent Z-Axis Shaft Stiffness

M_3 = Z-Axis Mass

K_4 = Z-Axis Radial Flexure Stiffness

M_4 = Gimbal Ring and X-Axis Shaft Mass

K_5 = X-Axis Axial Flexure Stiffness

BOOM ATTACH

Figure 6-42. X-Axis EGA Dynamic Model

6-107

A schematic representation of the thermal control scheme is shown in Figure 6-43. All areas of the EGA, with the exception of narrow bands on the housing, are insulated with 20 layers of 0.25 mil aluminized Mylar sheet which forms a 1/4 inch layer. The exposed bands are radiating areas which reject excess heat. Heaters are bonded to the bands and controlled by means of thermistor sensors located in strategic areas. The Y and Z axis bands are painted white; the X axis, which is more significant thermally because of non-symmetry, is covered with secondary surface mirrors to minimize radiant heat input and resultant distortions. Critical sections will be controlled to a nominal temperature of 70°F. Heater power required to maintain this control will be highly dependent upon the orbit. A maximum of 72.0 watts is estimated for the worst case condition.

The experiment gimbal electronics is very similar to the Sensor Electronics, which supports the star tracker. The inductosyn encoding function is implemented in identical circuits. The motor electronics have an additional stage of power amplification to drive the larger motor.
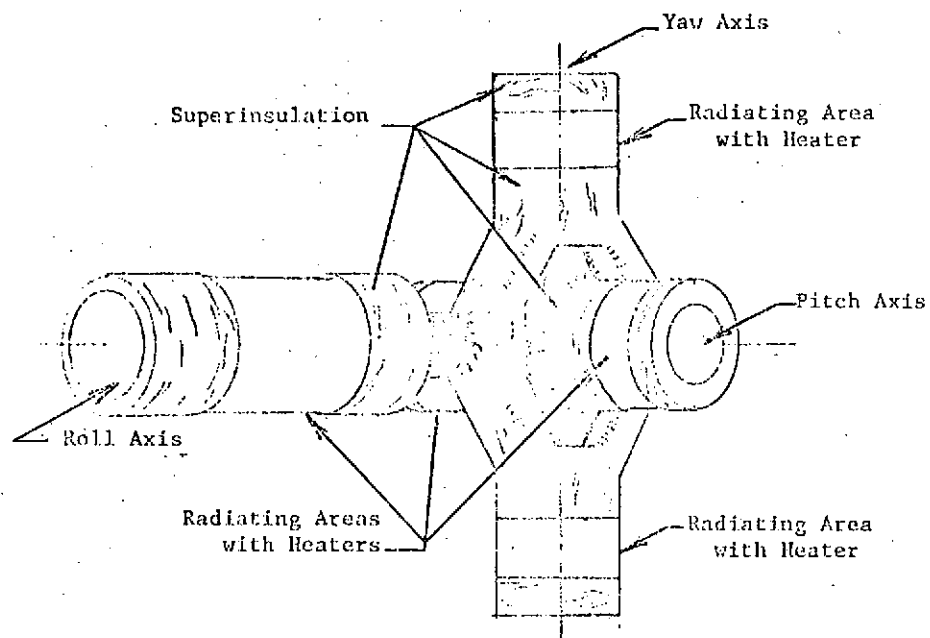
Figure 6-43. EGA Thermal Control

6.7 ANTENNA GIMBAL AND ELECTRONICS

The antenna gimbal is a two axis drive assembly which is controlled to point the antenna. An Az-El configuration was considered initially, but this leads to the requirement for high gimbal rates when tracking an overhead target from a limit cycling spacecraft. Figure 6-44 shows the configuration selected where the inner gimbal (attaches to antenna) has an angular range of +90 degrees and the outer gimbal (attaches to mast on spacecraft roof) has a range of +110 degrees. The gimbal consists of two identical assemblies stacked as shown with the axes perpendicular, but non-intersecting. The outer gimbal axis is parallel to the spacecraft pitch axis and the inner axis is parallel to roll. In the stowed condition, the inner gimbal is constrained from rotating by an electro-explosive pin puller at the drive periphery and the outer gimbal is pinned to the spacecraft mast.

6.7.1 Drive Unit Design

Each drive unit contains a stepper motor with integrally attached gearhead, a harmonic drive, dual speed resolver, and supporting bearings. The drive unit is designed to retarget the antenna over 180° in less than four minutes. A step resolution of 0.005 degree is desired to meet pointing accuracy requirements. This leads to a stepping rate of 160 steps per second for a 90° stepper and an overall gear ratio of 18,000. This ratio is made up of a 120:1 harmonic drive and a 150:1 gearhead. For the size 8 Kearfott motor selected, running torque is about 0.25 in-oz which, reflected through the gearhead, requires a torque capability of 37.5 in-oz. A size 15 integrally attached gearhead is selected.
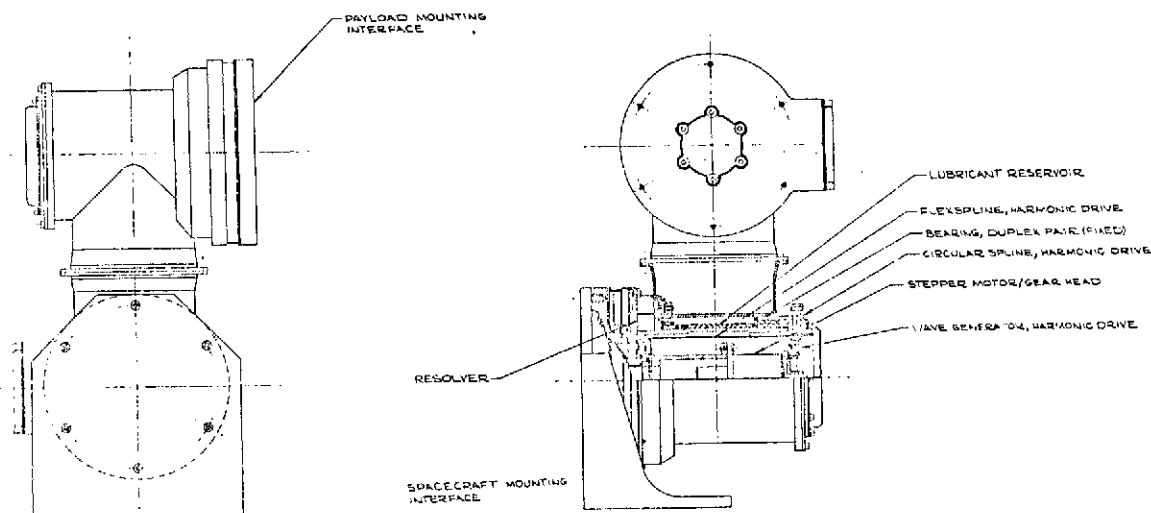
Figure 6-44a. Antenna Gimbal Assembly Layout (Unit)
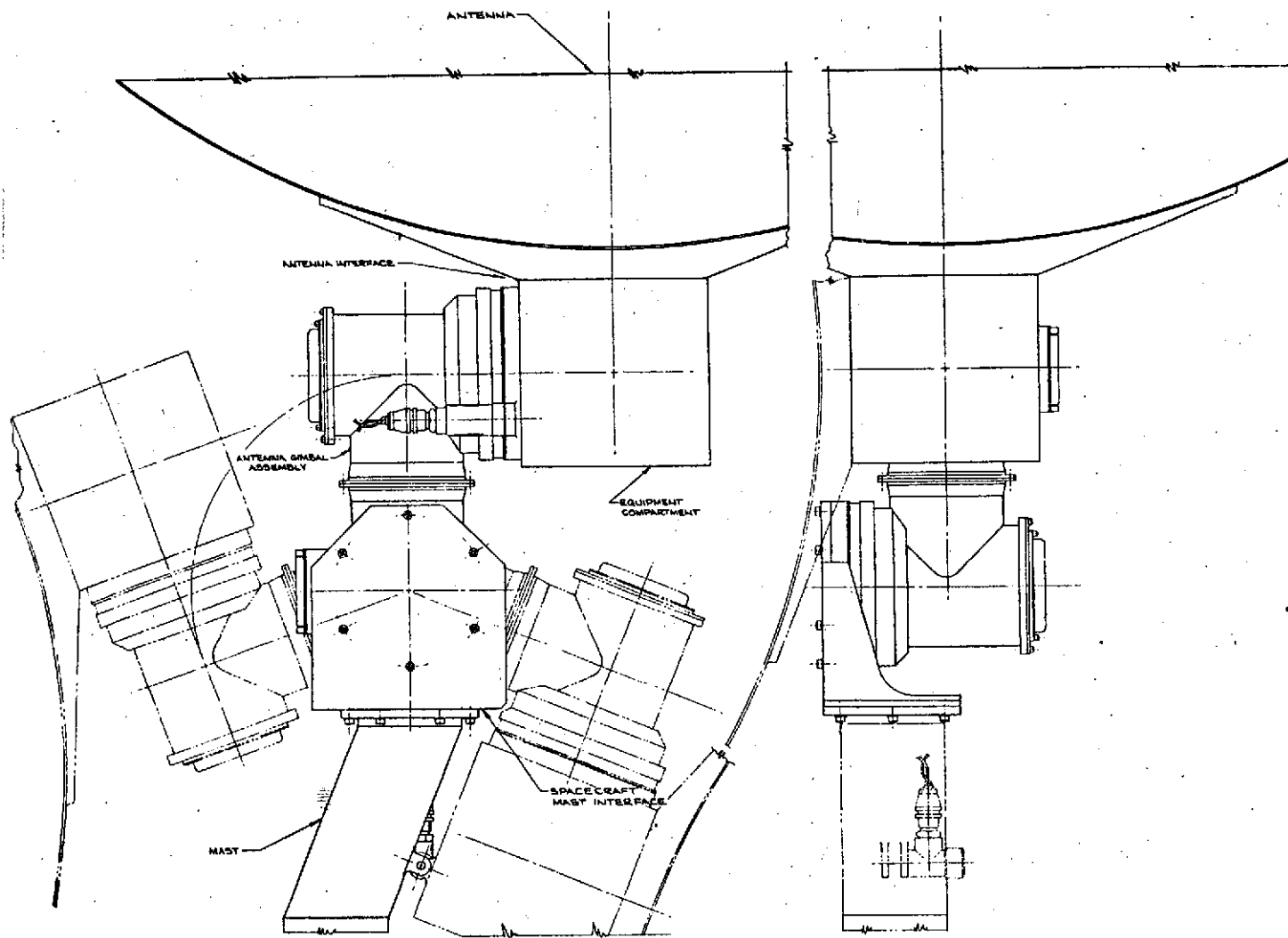
Figure 6-44b. Antenna Gimbal Assembly Configuration (Mounted)

The output motion of the gearhead is reduced further by another stage of gear reduction. The harmonic drive was selected to obtain high reduction ratio and high torque capacity in a small package and to obtain low backlash. The harmonic drive, depicted in Figure 6-45, consists of three elements; the circular spline, the flexspline, and the wave generator. The circular spline is a rigid internal toothed ring. This meshes with the flexspline, a thin flexible ring of slightly smaller diameter with external teeth. The wave generator consist of a ball bearing with thin races which have been deflected into an elliptical shape by the elliptoidal hub upon which the bearing is mounted. When the hub and inner race are rotated, the shape of the outer ring rotates at the same speed. In the basic harmonic drive configuration as a speed reducer, the wave generator is the input element. As the wave generator rotates, it imparts the ellipse-like shape to the non-rigid flex- spline. The shape of the flexspline, but not the flexspline itself, rotates at the input speed of the wave generator. This action forces the flexspline teeth into engagement with the circular spline teeth. Since the flexspline has two less teeth than the circular spline, a relative motion results between the two members as the wave generator advances the position of teeth engagements. Either member, the flexspline or the circular spline, can be held stationary and the other becomes the output member.
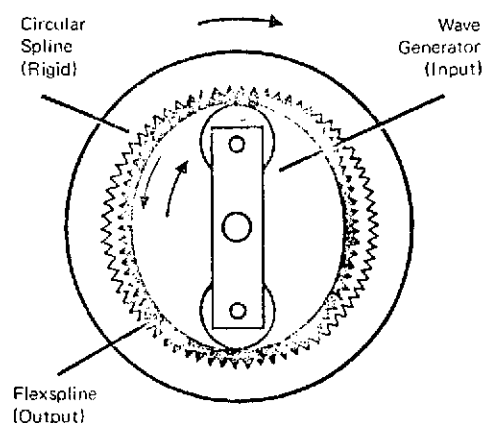
Figure 6-45   Harmonic Drive Configuration

In the AGA the flexspline is fixed and, therefore, the circular spline is the output. A special harmonic drive was configured for this application for packaging of the stepper motor/gearhead within the flexspline shell. The output shaft of the

gearhead is coupled to the wave generator through an oldham coupling which is integral with the wave generator. The coupling eliminates critical alignment requirements between the two stages.

To provide high accuracy readout signal, a dual speed resolver is direct mounted on each axis. The sine and cosine outputs of the resolver are applied to an electronic encoding system which converts the resolver signals to digital angular information. The dual speed resolver consists of 32-speed sine and cosine windings for high accuracy information and single speed sine and cosine windings to resolve the position ambiguity of the multi-speed output.

During launch the antenna/communication platform will be constrained or snubbed to avoid backdriving the AGA. However, this snubbing will not necessarily relieve the launch loads on the AGA bearings. Therefore, ball bearings of the torque tube variety were selected to meet the anticipated high loading and also for packaging convenience. A pair of angular contact duplex bearings and a radial bearing are used in each axis. The duplex pair is fixed to one end of the assembly, and the radial bearing is fixed to the housing at the other end but allowed to float on the shaft to accommodate thermal expansion.

Low vapor pressure fluid lubricant is applied in a thin film on all bearings and gear surfaces, and on the inner walls of the assembly. Sintered nylon reservoirs (Nylasint) impregnated with the fluid are placed near the bearings and gears. The phenolic retainers in the bearings are also impregnated with oil to act as reservoirs. Oil outgassed from the reservoirs reaches equilibrium with the oil coated surfaces or replaces the oil which is lost by effusion through the resolver gaps. Further replenishment of the lubricant is furnished by surface mobility of the fluid.

6.7.2 Electronics Design

The Motor Control Unit provides sequenced drive power to the actuator stepper motor on command. Mode switching is provided to enable either command or autotrack inputs for closed loop control of the gimbal actuator.

Figure 6-46 shows a schematic of the split two-phase stepper motor. Each phase consists of two coils in series with a command power connection. To accomplish rotation in one direction, the coils would be energized in the sequence shown. Rotation in the opposite direction occurs by reversing the sequence, i.e., transposing (2) and (4). A mechanical step occurs at each transition with four steps constituting a complete electrical cycle.
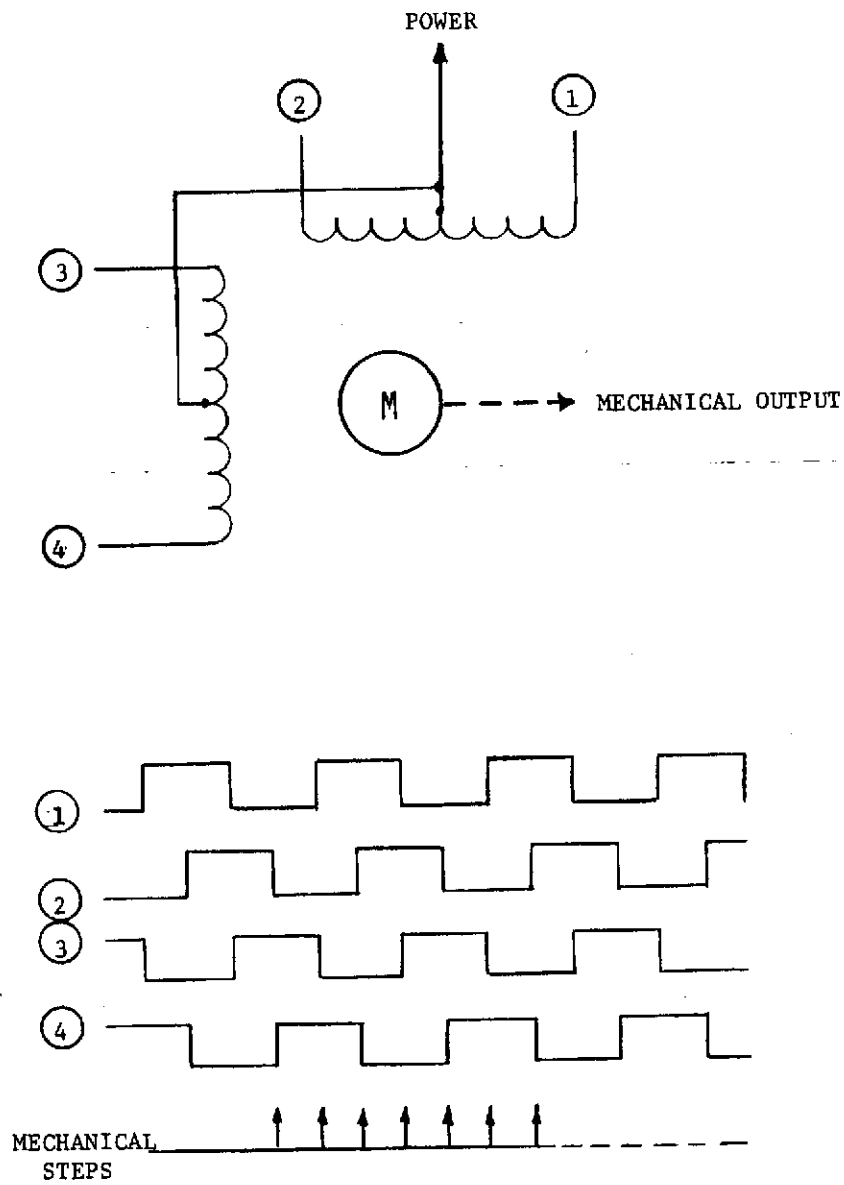
Figure 6-46. Split 2-Phase Stepper Motor and Operating Sequence

Figure 6-47a shows one channel of the Motor Control Unit. Input command signals are conditioned such that error magnitude and sign are converted to sense and step data for the gray code counter. Power is enabled to the coil driver on demand from the conditioning logic to minimize power consumption. The gray counter outputs provide the sequencing consistent with the step motor requirements. Mode switching logic is provided to accept autotrack inputs.

The Position Encoding Unit digitizes the outputs of a 32-speed wire wound resolver to provide 16 bit data representing the antenna gimbal angle over a range of $\pm$ 110 degrees. Figure 6-47b is a block diagram of the position encoding electronics which employs the "double angle" technique for generating highly accurate resolver to digital information. The sinusoidal excitation for the multispeed resolver is derived by dividing the output of a 1.024 MHZ crystal controlled oscillator by 1024 to obtain a 1000 Hz square wave. This is filtered to recover the fundamental and then power amplified for application to the resolver rotor. The resolver stator outputs, which are amplitude modulated as a function of shaft angle, are characterized by (E sin θ sin ωt, E cos θ sin ωt, E sin 32 θ sin ωt, E cos 32 θsin ωt).

The multi-speed outputs are buffered and converted to phase modulated outputs by means of precision phase shifting circuitry. After summation, the outputs are E' sin (ωt - 32θ). The phase relation of the two outputs is compared by detecting the zero crossings of the sinusoids. The detected outputs then gate 1.024 MHZ clock pulses into a 10 bit fine interval counter to obtain a count proportional to 32 times the resolver shaft angle. The "double angle" scheme results in fine counter contents that repeat every 5.625 degrees of resolver shaft rotation and each pulse contained therein is equivalent to .00549 degree of shaft rotation.

In order to provide non-ambiguous shaft angle data over the required dynamic range, the single speed resolver windings are digitized in a similar manner. The output E sin θsin ωt is shifted in time phase by 90 degrees and summed with E cos $\theta$$\omega$t to provide an output of E' sin (ωt + θ). This output is zero detected and the phase difference between it and the reference is measured by integral counting. The count accumulated in the coarse interval counter provides 8 bits of angle data. After the coarse counter is corrected, the six most significant bits are transferred as angle data.

In the output resolver output equations presented above, the phase shift of 25 $\pm$ 8 degrees from rotor to stator was neglected. Since the $\pm$ 8 degree variation is a function of temperature, the excitation voltage is unsuitable as a reference voltage used to compute phase angle. To obtain a suitable reference, the single

Figure 6-47a. Motor Control Unit

Figure 6-47b. Position Encoding Unit

speed ($E \sin \theta \sin \omega t$, $E \cos \theta \sin \omega t$) is squared and summed, yielding a sinusoid at twice the excitation frequency. The zero crossings of this voltage are detected, then divided by two to obtain the reference voltage for the system.

The ambiguity detection circuitry corrects for $\pm$ 0.5° misalignment between the single speed and 32-speed connters, as well as deciding which electrical cycle the 32-speed is measuring. This detection is made every fourth cycle of the carrier frequency after both the coarse and fine angles have been measured. Detection is performed by looking at the most significant bit of the fine counter and the decoded output of the first two bits of the coarse counter, which divides the angle into 1.4 degree increments. After comparing these two signals (providing the magnitude of both the coarse and fine angles) and with the receipt of the strobe signal from the control logic, the coarse counter is either counted up one pulse, counted down one pulse, or remains at its present count. All of this results in a correct 16 bit binary word - 6 bits in the coarse counter and 10 bits in the fine counter, representing the resolver shaft angle with the least significant bit equal to .00549 degree.

Sources of analog error in the encoder have been analyzed. They include:

- Voltage-follower gain mismatch
- Sine/cosine cross-coupling
- A-θ converter error
- Harmonic distortion
- Zero-crossing offset
- Logic Phase Stability

The error equation for each source is listed below:

Gain Mismatch $\qquad \Delta\theta_{max} = \dfrac{\overline{K_s} - K_c}{K_s + \overline{K_c}}$, where K_s, $\underline{K_c}$ are gain of sine

channel and cosine channel respectively, and the bars denote maximum and minimum values.

For a mismatch of 5×10^{-4}, an encoding error of 0.014 degrees (electrical) results. This is reduced by 1/32 by the resolver speed ratio.

Sine/cosine cross-coupling

$\qquad \Delta\theta_{max} = K$, where K is the fraction of signal cross-coupling.

For 66 db isolation, 0.03 degrees electrical is the error.

Amplitude-to-phase Converter

$$\Delta\theta_{max} = 7/6 \ \frac{\Delta R}{R}$$, where R is the gain setting resistor

value in the converter.

For $\pm$ 0.04% resistors, this amounts to 0.027 degrees, electrical.

Harmonic Distortion

$$\Delta\theta_{max} = a$$, where a is the relative amplitude of the harmonic

component in the resolver excitation.

For 0.1% harmonic content, the error is 0.057 degrees, electrical.

Zero-Crossing Offset

$$\Delta\theta = \frac{\Delta V}{V_m}$$, where ΔV is the zero-crossing offset voltage and

V_m is the peak voltage at the zero crossing detector.

For $V = \pm$ 2mv and V_m = 8 volts, the error is 0.014 degrees, electrical.

Logic Phase Stability

$$\Delta\theta_{max} = \frac{\Delta t}{T_e} \ 2\pi$$, where Δt is the differential delay of the

zero crossing detector and counter, and T_e is the excitation

frequency.

For $\Delta t = \pm$ 100 nanoseconds and $T_e = 10^{-3}$ sec, the error is 0.036 degrees,
electrical.

Summary

Gain Mismatch		0.014°
Cross-Coupling		0.030°
A-ϕ Converter		0.027°
Harmonics		0.057°
Z. C. Offset		0.014°
Logic Phase Stability		0.036°
Total,	Sum	0.188° electrical
	RSS	0.081° electrical
÷32-speed,	Sum	0.0056° mechanical
	RSS	0.0025° mechanical

6.8 DIGITAL COMPUTER ASSEMBLY

This section presents the digital computer assembly functional design and certain design tradeoff results. Neither the design considerations nor tradeoffs have been exhaustively investigated. Discussion focuses upon the configuration and detailed design considerations for the central processor, memory, and memory bus [17].

6.8.1 Configuration/Organization

The key consideration relating to design of the PPCS DCA is achieving the required 3-5 year life with high probability. Various approaches have been taken in the past to achieving high reliability in aerospace computers. For example, the IBM Saturn guidance computer was separated into seven modules which then individually employed TMR. Duplex memories with and without parity checks have been widely used. The NASA OAO computer used extensive quadded-logic while others have relied on distributed functions, special number systems, and careful implementation. None have achieved the lifetime required of the PPCS computer.

The basic difficulty in achieving long computer lifetimes is experienced with the memory. Although CPU lifetimes of 100,000 hours MTBF are achievable with LSI, no memory statistics exist for values of 1/3 of this. There is thus a basic incompatibility in these relative lifetimes and a varying need for redundancy across the computer components. Ideally, the design lifetime is obtained at minimum weight and power penalty, thus carefully partitioning the system and applying redundancy in keeping with the reliability of each part. This, of course, leads to the consideration of multiprocess and modular computer designs.

From reviews of the design of some multi-processors and long-life fault tolerant computers, it appears that a good approach for the PPCS computer is to partition the modular computer on the basis of major function and lifetime considerations. This modular computer concept has the capability of greater memory replication than processor (or logic units) replication. This is a desirable factor as the current memory technology cannot meet the low power and high reliability of micro-miniaturized detail logic. Furthermore, memory power tends to be high compared to processors when implemented with higher integrated circuitry.

Techniques for redundant memories have been rare due to the difficulty inherent in memory organization preventing replication at a low enough complexity level. One possibility is the use of redundant electronics, such as sense and drive amplifiers, with non-redundant memory elements. Such an architecture involves critical design consideration to avoid single point failures, yet allows switching or majority employment of redundant segments. These problems have not been satisfactorily solved to date and there exists significant risk in adopting such approaches for PPCS.

6-120

Another aspect of the memory organization is a desire for read-only memory for program storage. Plated wire memories are inherently NDRO and may be used in this mode. However, a strict adherence to this requirement would necessitate memory segments utilizing different techniques for RWM and ROM. Segmentation leads to new redundancy problems due to power and reliability inequities. The present possibilities seem to involve employment of redundant memory modules within the redundant computer or the modular computer concept. These two approaches are shown in Figure 6.48. The several advantages to independent computers include:

- Simple fast computer/memory interface

- Memory faults each to diagnose and switch within a given computer

- Initial checkout and overall concept is simple - desirable for PPCS.

On the other hand, the modular approach has the advantage of higher reliability for the same degree of replication and, hence, a lower power and weight penalty for the same life-time. It also lends itself well to a mixture of memory types if required. Retaining high speed diagnosis of faulty memories and system checkout become more difficult with the modular organization. Reconfiguration, however, may not be too complex if simple power switching is employed. The ultimate decision between these two approaches for PPCS is based upon a reliability versus complexity tradeoff, and leads to selection of the modular redundant approach. The PPCS DCA utilizes dual central processor units (CPU), four modular memory units (MMU), and a dual redundant memory bus structure interfacing the CPU's, MMU's, and Data Interface Assembly.

6.8.2   Central Processor Design

The computational sizing indicates that the majority of the instructions required are related to arithmetic operations. Special emphasis has been given to this class of instruction. Special instructions such as sine, cosine, arctangent, square root are desirable for PPCS but require a significant amount of hardware to implement. The commonly used CORDIC algorithm for implementing these special instructions is suited for machines with matrix shift and multiple general-purpose registers. Since the primary driving factor for the PPCS DCA design is high reliability and minimum power, it is decided that the best choice is to implement a relatively fast multiply instruction instead of these special instructions in hardware.

A set of double precision instructions is provided to facilitate programming for accuracy required above that of the single word. It includes not only the add and subtract instructions, but also load, store, compare, complement, absolute,

6-121
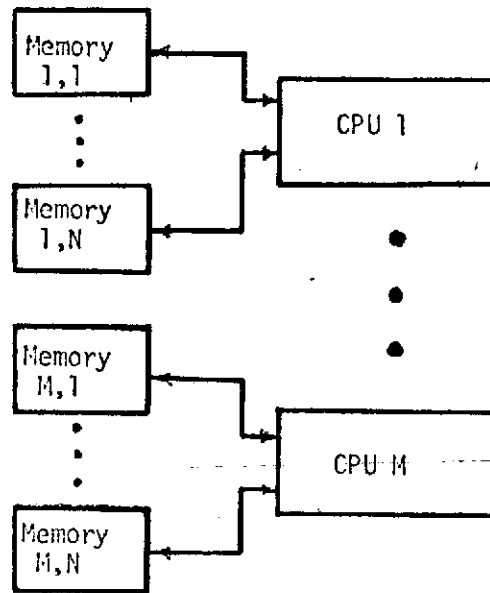
a) Independent Standby Computers
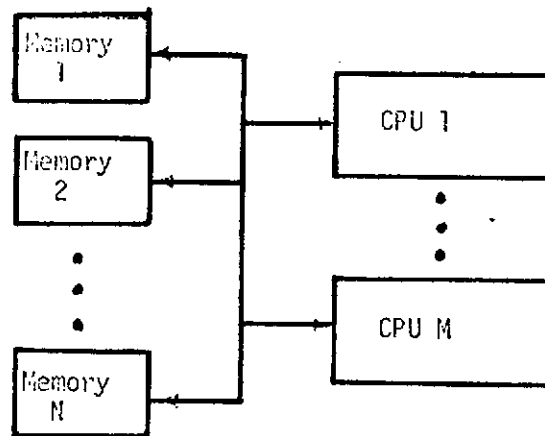
b) Modular Redundant Computer*

* Selected Approach:

    M = 2
    N = 4

Dual Memory Bus Structure

Figure 6-48. Candidate Digital Computer Organizations

shift, justify and skip instructions. Double precision multiply and divide instructions are not included because they take a significant amount of hardware to implement and will not be used often.

To facilitate program control, a complete set of unconditional, arithmetic, and subroutine jump instructions are included. A set of input/output instructions tailored to the data bus operation is also included. Provision is included for four external interrupts.

6.8.2.2 Serial Versus Parallel Arithmetic

The design requirement for PPCS is relatively moderate in terms of processing speed, but very severe in terms of reliability. Therefore, it appears that serial (or serial-parallel) arithmetic may be considered to satisfy the computational speed, and to minimize hardware required.

The speed as represented by the adder time is plotted in Figure 6-49 against the number of bits in parallel to be handled simultaneously. Two sets of curves are shown, one for MOS/LSI (automated design based on Banning cells), and one for bipolar MSI (based on TI-5400). Each set consists of three curves corresponding to the data word lengths of 16, 24 and 32 bits. The PPCS requirements can be implemented by use of bit-slice logic partitioning. Therefore, only one chip design is required. The number of bits in parallel on each chip is dependent on the technology and the function to be performed. A MOS/LSI chip can handle two to four bits on a chip, whereas a bipolar MSI chip can handle about 25 to 50% of the MOS/LSI chip. Therefore, the incremental cost between a serial and a parallel implementation is the cost of additional number of chips required, but not in the cost of additional chip design. The former is small as compared with the latter.

For a computer with the same number of instructions, the control logic is slightly higher for serial implementation than for parallel implementation due to additional control signals required to manipulate bits and to keep count of the bits being handled in serial. A preliminary estimate indicated that the difference may be approximately 20%, which tends to offset some of the hardware savings in the arithmetic unit.

Based on these performance and implementation trades, it is concluded that parallel implementation is preferred.

6.8.2.3 Organization and Block Diagram

The organization of the central processing unit is modular and bus oriented. It is partitioned for LSI implementation. The most cost effective approach at present is MOS/LSI in order to approach the reliability goal and power requirement. The CPU block diagram is shown in Figure 6-50.
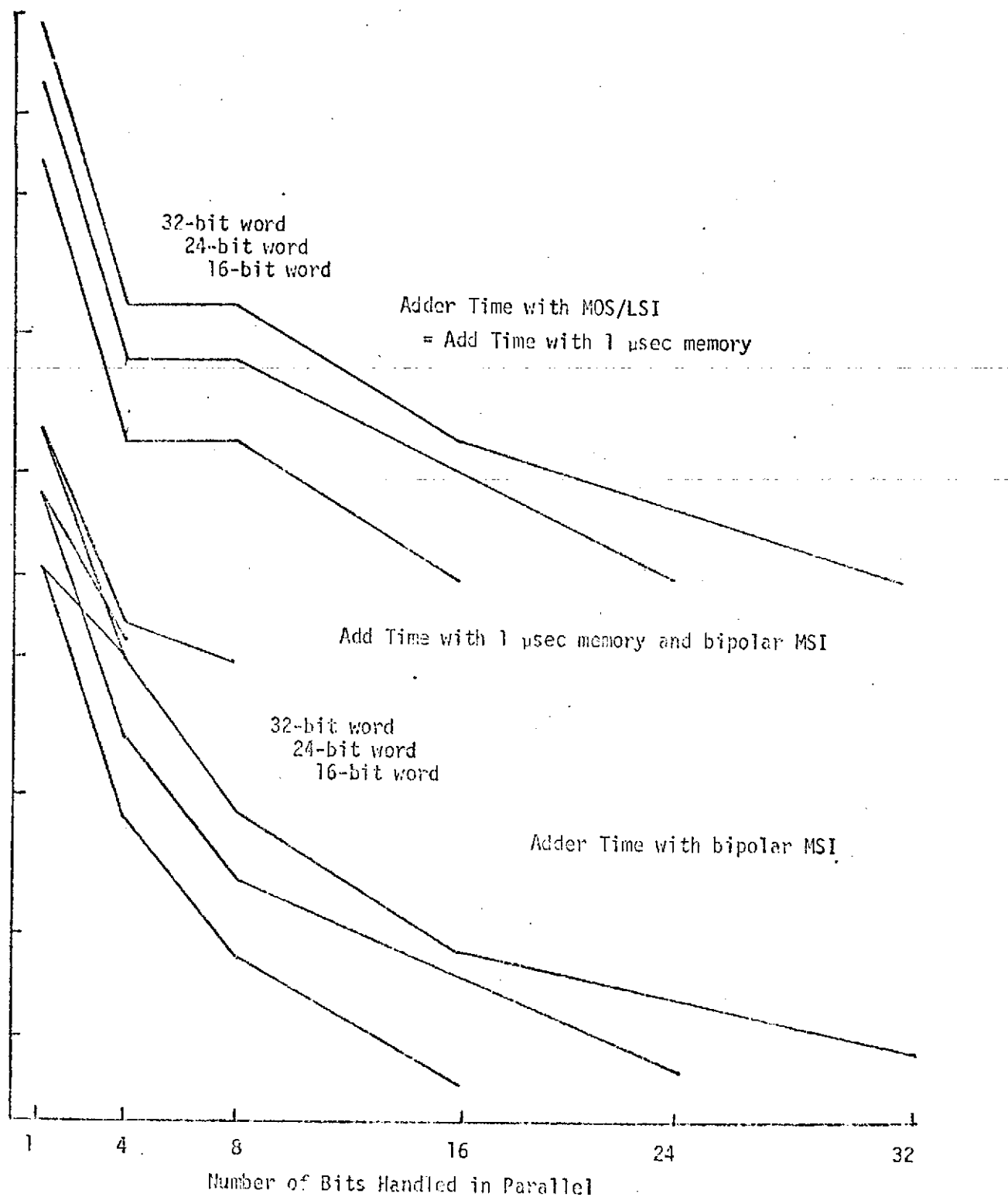
Figure 6-49. Arithmetic Unit Design Trades
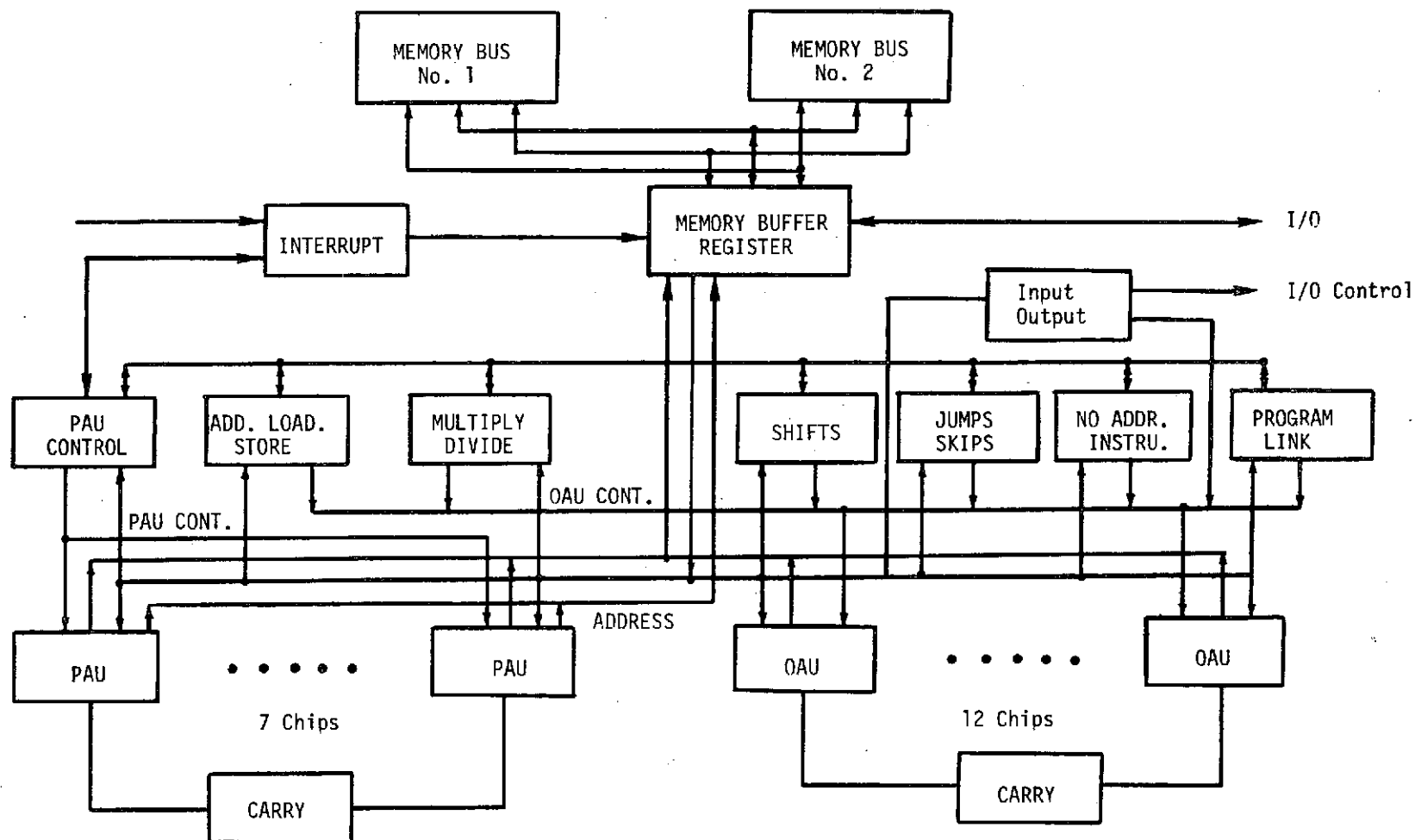
Figure 6-50. CPU Block Diagram

Since the MOS/LSI circuit speeds are slow and maximum performance is required of the processor, the normal computer arithmetic unit is replaced by two arithmetic units. Each unit is preassigned a specific task in executing an instruction and both work in parallel.

The Operand Arithmetic Unit (OAU) performs arithmetic and data handling associated with computer data. The Program Arithmetic Unit (PAU) performs similar functions on program addresses and program control words.

The controlling of these two units in conjunction with the memory system and Input/Output is the responsibility of the control modules or chips. These control modules decode all of the instructions and generate the control signals necessary for the operation of the processor. The control modules are somewhat flexible in that the instruction repertoire can be broken up in many ways so as to meet pin and chip size restraints.

The OAU, besides containing an accumulator and multiplier quotient register, also requires a holding register and a second multiplier register. The latter register is necessary in order to execute multiplication in the specified time.

In general, instruction addresses are formed on the PAU modules and sent to the memory via the memory address lines. The instruction then appears in the memory register and is sent via the memory output bus to the control modules and the PAU. The appropriate control module decides if it is the destination of the operation code. (All control modules look to see if they are being enabled.) The PAU meanwhile is both sending the address of the operand and doing address modification in case the address is to be indexed. The control module now initiates a read memory cycle and the operand appears on the memory output bus. The appropriate control module now directs the OAU to accept and, if necessary, manipulate this operand in the prescribed fashion. Upon completion of the operation, the control module initiates an instruction fetch memory cycle and the sequence continues.

The partitioning of the CPU into modules or LSI chips is directed towards minimizing both the number and number of types of modules or chips. For example, the same carry module is used in both the Operand Arithmetic Unit (OAU) and in the Program Arithmetic Unit (PAU). The OAU itself is made up of two bit arithmetic unit slices, as is the PAU. This method of partition is quite flexible: the computer word length can be modified by changing the number of OAU modules, up to a maximum of 30-bit words. The address field may increase by adding PAU chips up to a maximum of 16-bit address, which would directly address 65K words. The number of index registers may be increased in 4 register increments, by adding a set of PAU modules. Module types required for the functional CPU design (Table 6-9)

Table 6-9. CPU LSI Modules

Module Type	Number Required
Operand Arithmetic Unit	12
Program Arithmetic Unit	7
Carry	4
PAU Control	2
Add Control	1
Multiply Control	1
Shift Control	1
Jump Control	2
Program Link	2
Number Address Control	1
I/O	2
Interrupt	1
Contingency	4
Total	40

include the PAU modules, OAU modules, and carry modules described above as well as modules which control execution and instructions (e.g., Add type, multiply, shift, jump, etc.)

6.8.3   Main Memory Unit Design

This section deals with the functional design of the non-volatile, random access memory units for the PPCS DCA. Memory type, organization, and a selected plated wire design are discussed. Although it is understood that reliability in the order of 5 years MTBF is the prime consideration, other factors which affect memory performance must be interleaved. The factors of power, volume, speed and cost have different weights for various applications, and each must be considered if implementation of a most effective memory design is to be made. The factors which most directly affect reliability are the electrical circuits, the storage element, and the number and quality of interconnections. _ _____ _ __ ___ .

The two prime candidates for use as the storage element are ferrite cores and cylindrical thin films (plated wire). Ferrite cores have been used over a sufficient time span to enable a high confidence level for manufacturing use and in failure rate reporting. The cores' basic construction and use in a wired stack configuration yields failure modes which are basically dependent on wire interconnections and wire quality unless excessive temperature extremes and vibration effects are not properly designed for. Stock figures on reliability which may be expected are in the order of 10^7 MTBF or higher. The limiting factor in core memories is the circuitry used.

Plated wire long term reliability is highly dependent on the thin film aging effects. Although plated wire and, in particular, thin film effects have been theorized for some time, its practical application in space has been relatively new. Most aging failure data has been obtained from accelerated aging tests. These estimates, however reasonable for most applications, must be carefully analyzed for high reliability or extreme environmental conditions (temperature and radiation). As has been evidenced in programs such as Poseidon and Minuteman, all failure aspects must be thoroughly studied.

Most plated wire reports relate life expectancy to be 10^5 hours which is reasonably close to the demands of a 5 year MTBF. Improvements in plated wire are being continually made and corresponding life expectancy must be continually updated. The NDRO characteristics of plated wire are highly desirable since this minimizes the vulnerability of stored information loss due to transients and some power failures.

Circuitry may generally be considered the limiting factor in memory design reliability when comparing semiconductor and monolithic I. C. components failure rates with cores or plated wire failure rates. Typically, 15,000 hours to 30,000 hours as an MTBF may be used as an achievable figure for core or plated wires. Plated wires use more circuitry than core memories for most general applications in the speed ranges of 1 μsec and slower.

Organization of the memory (2D, 2-1/2D, 3D) is basically determined by the storage element used (plated wire or core). The memory word-data bit length is also a factor which may influence circuitry totals, each specification and product being somewhat different and requiring a different optimum configuration.

For core memories, the overall complexity per bit (i.e., per memory element) decreases with memory size, as a result of the higher dimensional organizations. This is indicated in Figure 6-51 which presents a normalized reliability for various memory sizes where x is the reliability per bit for a given type 16K x 32-bit memory. It is to be noted that the power requirements are configuration dependent. An example of power requirement variations in core design is in temperature requirement. Higher temperatures require more lithium in core construction in order to be more stable in output over the higher temperature ranges. This lithium core requires higher drive currents to obtain reliable core turnovers. For the 1 μsec cycle time range, plated wire requires 35 μw/bit to 150 μw/bit and core requires approximately 350 μw/bit to 600 μw/bit. Again, the volume requirements of both plated wire and core memory are also configuration-dependent. Volume as a function of memory capacity and word length is shown in Figure 6-52. For plated wire, one can achieve approximately 1000 bits/cu in, whereas for core, one can determine an average of 800 bits/cu in.

The weight of the wire memory is comparable to that of the core memory. The weight is also configuration-dependent. The weight of a core memory with cycle time between 1.0 to 1.75 μsec as a function of configuration is shown in Figure 6-53. The weight is normalized by the weight of a 16K 36-bit memory.

Plated wire memories seem particularly attractive because they are designed for non-destructive read-out. This feature has two advantages: namely, read requires less power, and memory contents can only be altered by a write operation. For the first point, restoring data in a core memory requires about 12 times the address current, on the average, if a 24-bit memory has half of its bits zero. Although plated wire memories must be able to write also, and therefore must be able to supply such currents, writing new data is a less common operation; in such a simple operation as moving a word from one memory location to another, only one-fourth of the memory accesses involve writing new information.
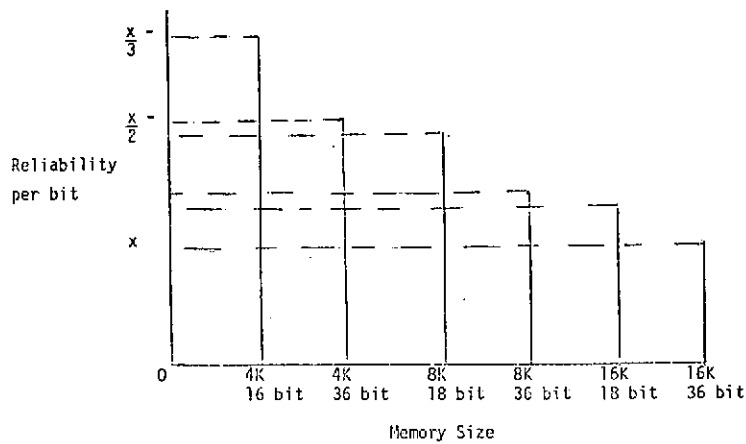
Figure 6-51. Memory Reliability As Function of Configuration
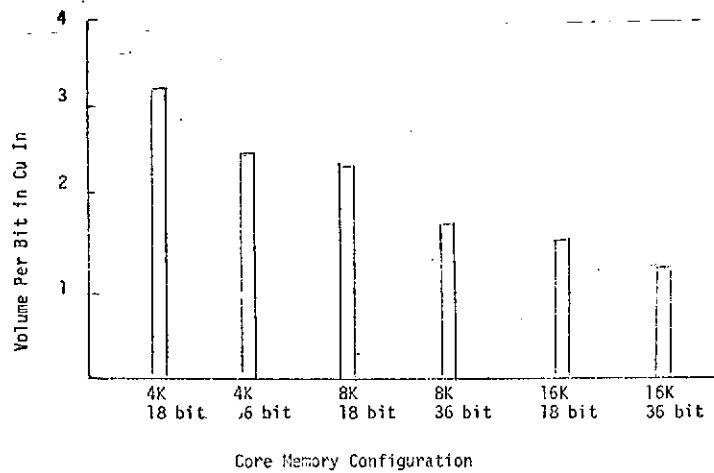
Figure 6-52. Memory Volume As Function of Configuration
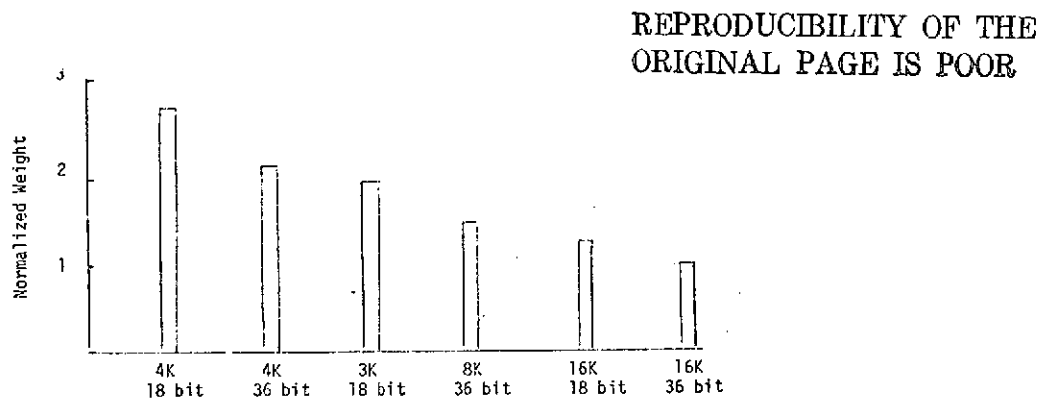
Figure 6-53. Memory Weight As Function of Configuration

The second advantage is less obvious. Read operations are quite sensitive to noise, and in read-restore operation the mistakes are perpetuated. In a memory which does not destroy the data as it reads, one can detect read errors and try again; the data is still there.

It is noted that while plated wire memories are the first choice here, they have only recently been reduced to practice. Core memory art is well established, and is therefore a logical second choice. In terms of speed and reliability, core and plated wire memories are quite similar.

A memory with a basic capability of 8,192 24-bit words of plated wire magnetic storage is considered here. The plated wire element used as the storage device provides a non-destructive readout capability assuring a more reliable restore of information as compared to destructive readout memories. The memory system is inherently non-volatile and by design could be resistant to high levels of nuclear radiation. A cycle time of 1 μsec, with a read access time of 500 nsec is expected.

The plated wire memory is basically organized in a linear select word-oriented system. A multiple word readout is utilized which accesses multiple words under a word strap. Decode at the data bit sensing selects the desired words' contents, dropping the contents of those words not desired. The NDRO characteristics of the plated wire element allow this procedure to be used thereby reducing the word driver electronics compared to linear select schemes using DRO storage elements. Stacking of eight computer words under one word strap has been used in existing designs. The system organization is shown in the memory block diagram, Figure 6-54, representing a single 8K-24 bit modular memory.

6.8.4 Memory Bus Design

The DCA internal memory bus will be used to connect four modular memory units (MMU's), two central processing units (CPU's), and provide the interface to the two input/output units of the DIA which interface with the DCA. In order to provide sufficient redundancy to approach the desired reliability, the computer modules are interconnected using a pair of DCA internal buses. Each internal bus consists of 24 data and four control lines, properly terminated to avoid reflections.

The memory cycle time is 1.50 μsec and access time is 0.5 μsec. Thus, 750 nsec is available for data transfer between memory and processors. There is time for only three data transfers in the time available, and one must be used to transmit an address in one 250 nsec period. If indexing must be accomplished without penalty, the address plus index register select bits must be sent to the processor in the first half of the data word. Thus, at a minimum, 15 bits must be transferred at a
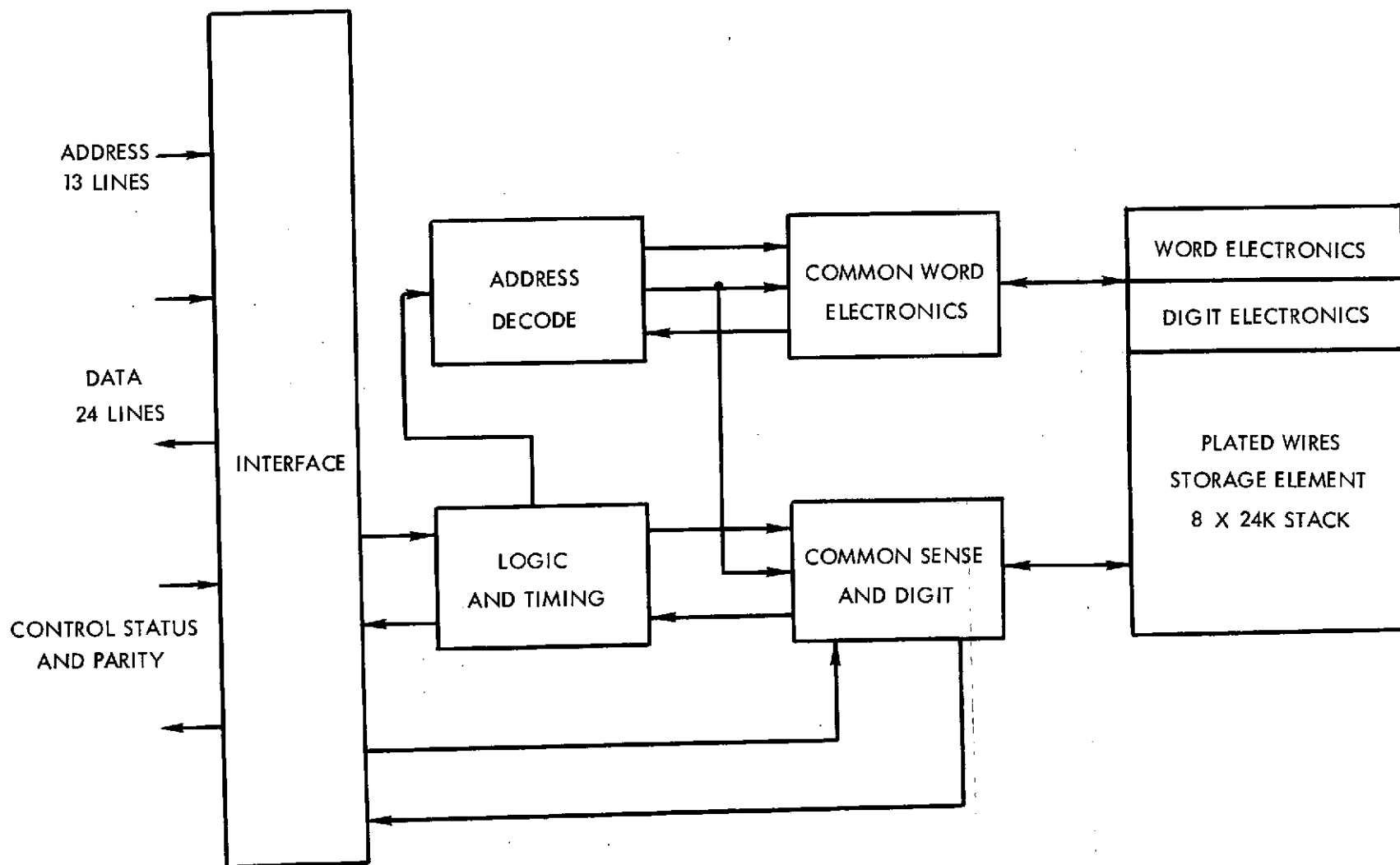
Figure 6-54. Memory System Block Diagram

time. Thus, about two thirds of a 24-bit word would have to be sent at a time, so it is most reasonable to have a 24-bit wide bus.

The memory in each case operates under control of external devices. It responds to a request for a memory cycle, by sending an acknowledge signal to the requesting external device. The external device now places an address and a read or write command on the bus for one clock period. If the command was to read from the memory, it reads the specified word, and places it on the bus two clock periods later. While the data is on the bus, the memory sends another acknowledge signal to an input/output device. The memory now begins another memory cycle.

The memory priority scheme is relatively simple. A flip-flop is set each time the memory acknowledges the computer, and reset when the I/0 processor uses the memory. The rule is, if both units request memory access, the next memory cycle will be to the opposite unit from the last.

Memory interface logic must include an address register of 13 bits, which can be loaded from the bus, and a data register, which can be loaded from either the bus or the memory. There is additional control logic for the bus.

6.9 DATA INTERFACE ASSEMBLY

The Data Interface Assembly utilizes a data bus structure to interface to the PPCS assemblies and other external interfaces. The DIA must perform the following interfacing functions:

- **DCA interface.** Required hardware for access to memory for reload and telemetry. Required control for memory stop-start locations, various interrupts

- **Telemetry interface.** Telemetry clock read, I/O clock write - buffer underflow indication

- **Command interface.** Command clock write, I/O clock read; buffer field indication - possibly discrete command registers for back-up modes

- **Data bus interface.** Data bus modems, address switching, parity generation, and checking

- **Clock function.** Provides realtime clock for data bus, I/O and possibly DCA

- **Control unit.** Necessary logic for data transfer from/to DCA, telemetry, command, data bus.

6.9.1 Data Bus Design Trades

Use of the data bus concept appears as the best choice for information transfer within PPCS. This is dictated by the large number of signals, the centralized computation, and the need for flexibility in adding or subtracting assemblies for different missions.

The data bus configuration is influenced by the carrier spacecraft layout. In a typical user spacecraft for PPCS, there may be up to six experiments, widely separated. If a single "threading" through these experiments is employed for the data bus, a line length over 200 feet could easily result. Although not precluding a data bus, this line length imposes limitations on the design arising from transmission line considerations and the difficulty in applying redundancy. One alternative is to use a configuration employing branches from a main bus. These branch points, however, are difficult to design for full-duplex operation as they must maintain impedance matching in each path. Duplex coupling techniques include hybrid transformers and resistive pods, both of which incur weight penalties and additional design limitations.

A second solution to the geometry problem is to use a central office approach. A separate line would then emerge from the central data bus controller to each remote terminal. In this concept, the maximum single line length may be minimized.

There is also an inherent reliability gain as no single failure in one line affects another. Addressing the individual data bus terminals then takes place within the computer interface unit, hence simplifying somewhat the remote terminal design.

In a sense, the experiments are PPCS "customers". As such, it is desirable that a failure in one experiment or in service to one experiment, not degrade the performance of the remainder. One way to accomplish this independence is to run dedicated data bus segments to each experiment. Not only are the experiment failures then less likely to affect the rest of PPCS, the data bus geometry is improved as described above, and the reliability of each experiment "dedicated" communication path is improved.

Other considerations, however, may be dominant for the attitude reference hardware. The hardware is all centrally located on the Reference Block Assembly, possibly somewhat remote from the DCA. Geometrically, a single data bus serving all these units is indicated. Independence is not as serious here in that loss of any one of these units is serious (or catastrophic) to the total system performance. This selected approach is shown in Figure 6-55 where each line is a half-duplex data bus.

The prime considerations of data bus design in PPCS are reliability and cost. Reliability refers to ability of the data signal to be received without error at its destination. Cost includes not only direct costs, but the effects of power, weight, and life. Table 6-10 summarizes the key parameters, basic considerations and PPCS decisions. The decisions are interrelated. Once a twisted shielded pair is chosen, transformer coupling is a natural to take advantage of the balance and high common mode noise rejection obtainable. Manchester code then avoids a DC signal component and gives a transition each cycle. This, in turn, allows for single cable distribution. The use of transfer coupling has the advantage of noise isolation but the disadvantage of high power requirement. Therefore, direct coupling may also be considered.

6.9.2 Interface Control Design

6.9.2.1 Configuration Tradeoffs

Three different conceptual designs have been studied and evaluated for the input/output control function. These are: (1) I/O controller with a fixed (hard-wired) program, (2) I/O control directed by the computer, (3) independent I/O processor with shared memory. The third approach with an independent I/O processor is selected since its complexity is similar to the computer directed I/O controlled
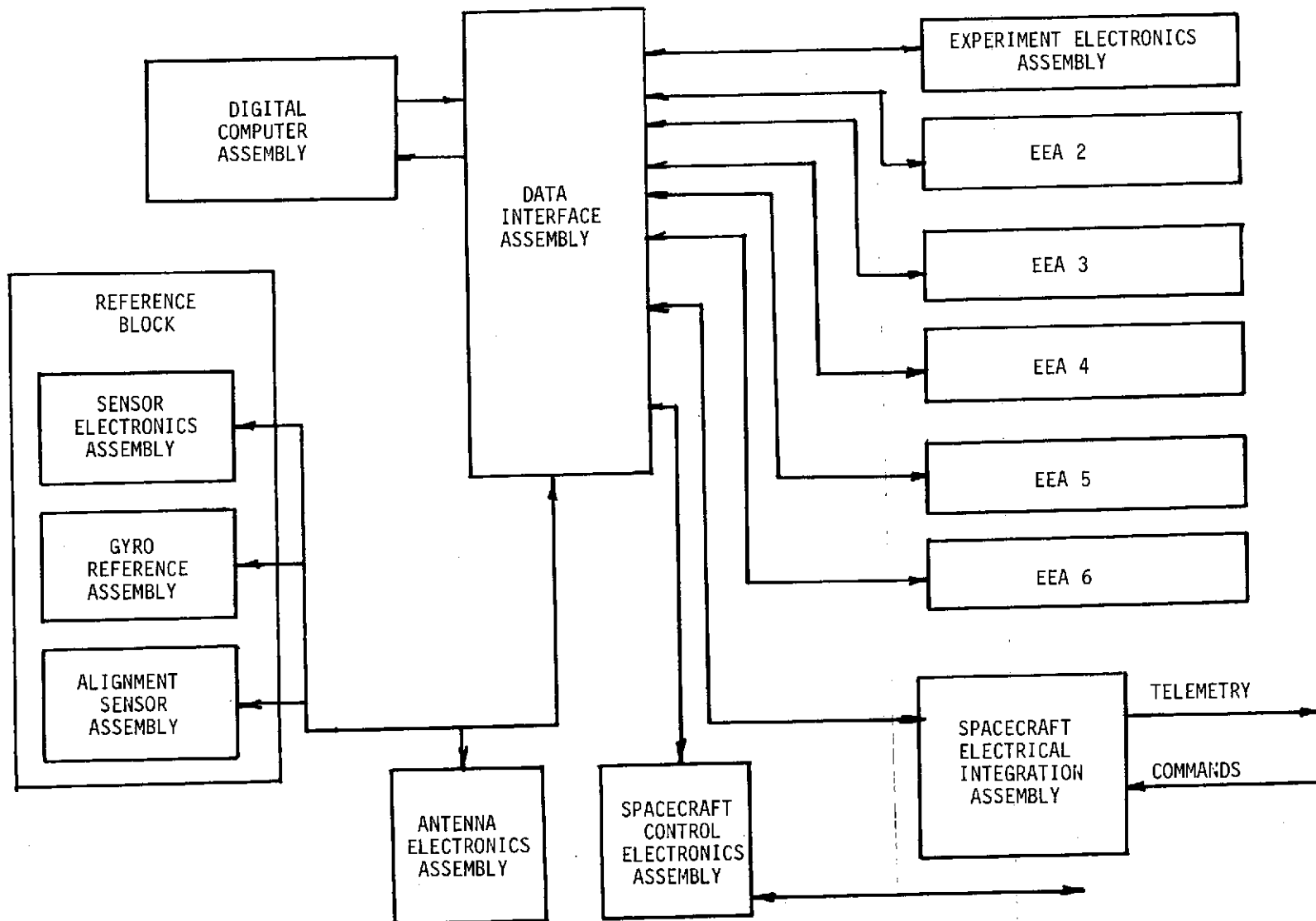
Figure 6-55. DIA Interface Configuration

Table 6-10. Data Bus Design Trades

Design Parameters	Major Candidates	Design Considerations	Selection and Rationales

Transmission Media	Twisted Shielded Pair
	Coaxial Cable
		Adequate Bandwidth
		Minimum Attenuation
		Simple Coupling
		Noise Immunity
		Physical Consideration
			Twisted Shielded Pair
			  Balanced Transmission
			  High Noise Immunity
			  Sufficient Bandwidth
			  Good Physical Characteristics
			  Simple Coupling

Multiplexing/ Modulation	Baseband
	Carrier
	TDM
	FDM
	Hybrid
		Data Rate Requirements
		Hardware Complexity
		Communication Efficiency
		Bit Error Performances
		Synchronization
			Digital Time Division Multiplexing
			  High Noise Immunity
			  Simple Synchronization
			  Digital Circuitry and LSI

Signal Design	Manchester
	NRZ/RZ DC
	Pair Selected Ternary
	Bipolar
		AC/DC Coupling
		Synchronization
		Bandwidth
		Terminal Design
			Manchester
			  No DC Component
			  Moderate Terminal Complexity
			  Good Noise Immunity
			  Clock can be Derived from Data

Data Synchronization	Separate Clock Line
	Derive from Siganl
		Terminal Complexity
		Interconnection Complexity
		Clock Skew
		Response Time
			Single Line
			  Minimum Terminal Hardware
			  No Clock Skew
			  Lower Cable Weight

Coupling	Balanced Transformer Coupled
	Single-Ended Coupled
	Probe Coupling
		Type of Transmission Media
		Noise Rejection
		Increased Propagation Delay
		DC Isolation
		Loading
			Balanced Transformer Coupling
			  Good Isolation Capability
			  Minimal Loading
			  High Common Mode Rejection

design, but it requires significantly less management by the computer. It is much more flexible than the fixed hardwired processor, which also has a minimum of computer management. Each of these conceptual designs is described briefly in the following paragraphs.

Conceptual design for a fixed (hardwired) I/O controller implies:

a) All commands to the data bus are generated by the I/O processor logic.

b) The I/O processor consists in effect of a large multiplexer, with sub-multiplexers for items that need not be sampled at high rates.

c) Storage locations for data transferred by the data bus are fixed by the logic, and may not be changed.

d) In backup mode, data will be sent over the telemetry link for ground processing.

e) In normal mode, the telemetry unit will get data from the computer, a block at a time.

f) Commands on the data bus can change the I/O processor mode of operation, and transfer of data from the bus to memory, or to telemetry, or both.

g) Commands can be used to store information in any memory location, command computers or I/O processors on or off, memories on or off, et cetera.

h) It will be possible to send single commands on the uplink to the data bus, and receive a response on the telemetry link.

Conceptual design for a computer directed I/O controller implies:

a) Commands are sent from the computer to the data bus by computer command.

b) Before sending each command to the data bus, the computer must send an input or output instruction to the I/O processor, or tell it where to put the incoming data.

c) At the end of each such data transfer, the computer receives an interrupt from the I/O processor.

d) A backup mode can be arranged which substitutes a read-only memory for the computer command. In this case, it is assumed that data will be sent via telemetry to the ground.

e) In normal mode, the telemetry unit will get data from the computer, or read it from a dedicated area in memory.

f) It shall be possible to send commands directly from the uplink to the data bus, and receive responses on the telemetry link.

The selected conceptual design for an independent I/O controller implies:

a) I/O processor takes instruction from memory. Each instruction specifies an input/output operation, or location of another instruction.

b) Each input/output instruction references a memory location which contains the command word for transmission by the data bus. The locations following this word will contain the data to be sent, or be reserved for the data being received.

c) Processor takes instructions starting at a standard location. An external timing signal is used to control the start of input/output.

d) Several backup modes are possible in this design. The first of these is to use a memory to program the I/O processor, but deliver any outputs to the telemetry link. Another possibility is to use a read-only memory as a source of input/output and other instructions.

e) In normal mode, it is assumed that the telemetry unit will get data from the dedicated area in memory, which it would read in cyclic fashion.

f) It should be possible to send commands directly from the uplink to the data bus, and receive responses on the telemetry link.

6.9.2.2   Block Diagram

The DIA block diagram is shown in Figure 6-56. The interfaces are summarized below:

- Memory bus interface - compatible with the DCA memory bus design.

- Data bus - multiples of 1 message must be sent or received, or both. One message may require processing up to 36 bytes data bus clock 500 KHz.

- Telemetry - telemetry is assumed to be supplied on a demand basis, at a rate not to exceed 10 KHz

- Commands - It is assumed that the command input rate will not exceed 2 KHz.

The DIA is designed so as to be controlled directly from a program stored in memory. A dedicated memory area is used for input/output, containing a mixture of DIA instruction words and data. The CPU loads data into appropriate locations and may modify the DIA program when necessary due to failures or system mode changes. A dedicated memory location must be continually monitored by the DIA when idle, awaiting control by the CPU.
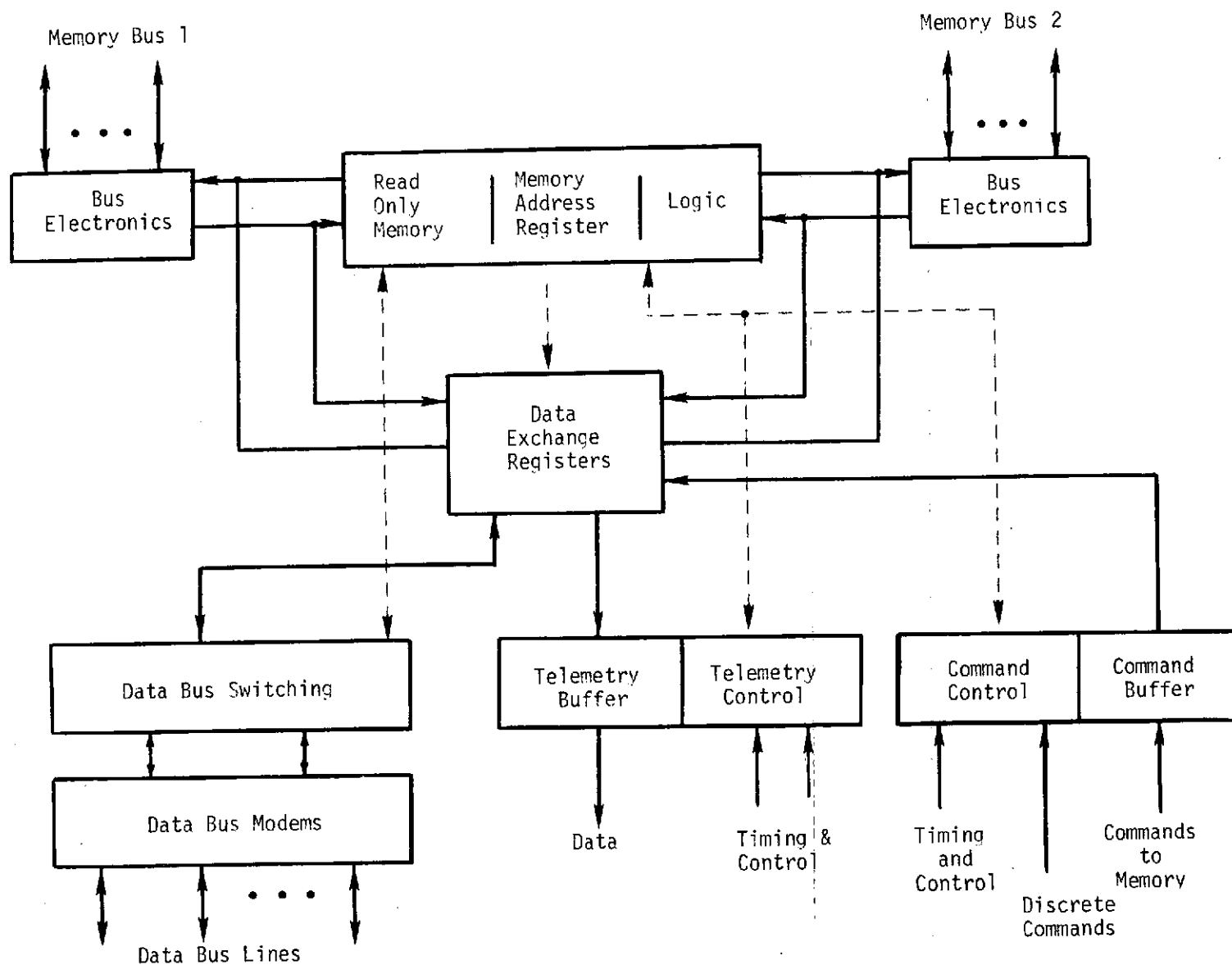
Figure 6-56. Data Interface Assembly Block Diagram

In addition, the DIA will be controllable by a Read-Only Memory (ROM) for use in failure modes. The ROM will contain a fixed instruction program to allow data bus operation, telemetry and command operation.

6.9.2.3   DIA Operation

The normal mode of operation is where all DIA processing is performed under control of the CPU via the memory. There are three basic areas of memory:

- Data bus control. This memory segment contains the "idle" location and certain other small programs needed to fetch data. One such program is the minor cycle data gathering which is a fixed cycle of data bus addresses and the associated locations for storage.

- Telemetry control. The PPCS telemetry format is stored in this area in a sequence of DIA instructions. Locations are provided for all current data. The CPU, in its normal processing, keeps these locations refreshed with the latest values.

- Command control. This sequence of memory locations contains the sequential commands as received. In some cases the CPU simply places these into the data bus area, while others may result in a number of data bus commands.

To accomplish loading of memory locations for targeting, alteration of star tables, and entering of other constants, use is made of the command channel. This data is stored in the command control area. The normal command servicing routine of the CPU recognizes this data as memory load. Checks may then be performed for data validity and the data shuffled to the commanded locations by the CPU. This approach to memory reload simplifies the DIA implementation and memory protection problem.

Certain discrete commands are distinguished by the DIA deviating it from the normal mode. One of these engages the ROM which provides a backup program. In this mode a fixed data bus format is carried out and the resulting data placed on telemetry. Commands are acted upon immediately and transmitted on the data bus. Thus, the main memory and CPU are bypassed entirely while the DIA is in this mode.

6.9.2.4   Data Bus Processing

At the end of all data bus traffic, control returns to an "idle" location in main memory. When the CPU wants to send or receive data via the data bus, it stores an appropriate instruction in this location branching the DIA to the appropriate routine.

When data is transmitted on the data bus, switching is performed dependent on the address. DIA control switches to the appropriate EEA or to the PPCS data bus and its associated modem. The modem function includes parity generation and synchronization for the data bus.

For data coming into the computer from the data bus, the switching is still set up from the immediately preceding "REQUEST" message. Parity is checked in the modem. Upon detection of a parity error, the DIA shall store its program address in a dedicated main memory location and interrupt the CPU. After a specified pause, the DIA control continues with its operation taking its next instruction from a location specified in the dedicated memory location.

The memory location for storage must be maintained in the control unit, as specified by the previous instruction.

The control unit of the DIA monitors the status of the DIA and directs data accordingly through direct control of the data exchange register. Each memory request is initiated by the control unit and the response monitored to distinguish data from instructions. The latter words are decoded and the control unit logic set up to perform this action.

Memory address registers are provided in the control unit for command, telemetry, and data bus control. Incrementing of each is handled separately.

The ROM provides the entire DIA program in the backup mode when directed by discrete commands via the command control logic.

6.9.2.5 Command and Telemetry Processing

It is assumed that commands will have the same format as data bus words, i.e., each command message will be in bytes with a parity bit on each byte and a longitudinal parity byte on the whole message. Each command will be checked for parity before execution. Most commands for PPCS will be destined for main memory where they will be acted upon by the CPU. The DIA must also accept some discrete commands which provide a PPCS command path external to the CPU. The PPCS command format will consist of an address consistent with the data bus format. This simplifies the CPU processing required and provides some failure immunity. The command portion of the DIA must contain a register large enough to hold a command plus its address. These must be buffered to resolve conflicts on the memory bus and data exchange register. The control logic will provide priority for the commands within the DIA over data bus and telemetry. A buffer fullness indicator is not required to the DIA control due to this precedence.

The command control provides logic to gate the asynchronous command bits into and out of the command buffer. There is also an interrupt from the DIA to the CPU indicating the presence of new command data. This interrupt is set upon receipt of each longitudinal parity.

The telemetry system operates asynchronously to the PPCS. Hence the telemetry unit in the DIA must request more data when its buffer is nearing empty. Data is clocked out of the buffer by telemetry clock and in by the DIA clock. The necessary synchronization is performed by the telemetry control unit. A "buffer low" signal tells the DIA control to access new data from memory. In this way, the DIA can continually service telemetry without any CPU intervention at all.

Under normal operation, the telemetry unit has immediate precedence in the DIA above data bus and below commands. In the backup mode, the telemetry input comes directly from the data bus, through the data exchange register, under control of the ROM program.

6.9.3 Data Bus/Data Interface Unit Design

Data Interface Units (terminals) will interface between the data bus and user equipment to provide data selection and formatting. The DIU's will provide D/A and A/D conversion, analog multiplexing and digital multiplexing. The relatively low data rates suggest twisted, shielded pair lines. The higher data rates achievable with coax are not needed for PPCS. Transformer coupling of data on/off the bus will solve grounding and failure isolation problems.

A separate clock line will be provided; the interface controller will clock all communication. This approach is simpler (hardware) than modulating the data line. The clock coding on the line hasn't been selected; Bi-Phase coding is most likely to keep a narrow bandwidth signal. The clock will change form to indicate the start of a message.

The low data rates suggest time division multiplexing, which is again simpler to mechanize. Again Bi-Phase coding will probably be used. All communication is initiated by the interface controller; remote units recognize the "start message" sync (clock line), check for their address on the data line, and either receive the data or provide the requested information. As a minimum, the addressed unit returns a "message received" word back. The data rates permit cycling through all assemblies and all data inputs sufficiently often that alarms, etc., will be picked up soon enough, thus no remote terminal interrupts are planned.

Selection of a standard word size is a compromise between specific user needs and the desire for commonality of equipment. PPCS typically requires long words (10-22 bits), while many other users need shorter words. A standard word of 8 bits + parity has been selected. Longer words will use multiple word slots.

The functional operation of the DIU is illustrated by reference to Figure 6-57. Various configurations of DIU's containing different numbers of digital and analog channels are being considered. Probably more than one configuration will be available to allow some flexibility for optimization.

The DIU address is 6 bits and can therefore select one of 64 DIU's. Two bits used as part of the function code and a word parity bit fill out the 9 bits in the address word. The function code consists of 5 bits (2 from the address word) coded to tell how many data words are in the message or how many data words are being requested. The 5 remaining bits contain the channel address where the first data word goes/comes from. A parity bit fills this word. The data words (0-7) have 8 bits of data and a parity bit. The last bit in the message is a vertical parity word with the first parity bit associated with bit one in each word, the second parity bit associated with each bit number two, etc.

The DIU to computer message starts by repeating the DIU address (6 bits), has two spare bits and a parity bit. Data follows in 8 bit + parity words. A vertical parity is generated as described for the computer message.

When a sync signal is detected on the clock line, each DIU compares the incoming address word to its internally stored address. If a match exists, the last two bits and the next word is shifted into the Function Code Register. The first 5 bits into the Function Code Register are loaded into the Channel Address Status Counter and the next 5 into the Channel Address Counter. The first Channel Address is decoded and the first data word (if any) is shifted serially into a register. The status counter is then decremented, the address counter incremented, and the next word shifted into another register. This proceeds until the status counter zeros. At message end, parity is verified, and, if correct, a "message received" format is returned. The stored data is then enabled to the output registers. Both parallel and serial outputs are planned. Data placed in registers designated as D/A storage is sequentially routed through the D/A converter and the resulting analog voltage stored in hold circuits.

If the incoming message had been a data request, the initial sequence would be the same. The addresses would be either the digital select matrix or the analog multiplexer. The selected data is placed on the bus behind the DIU address, and sequencing proceeds as before until the requested number of data words has been sent. Operating data rate is 250 KHz.

Figure 6-57. Data Interface Unit (Remote Terminal) Block Diagram

7.0 SOFTWARE DESIGN

The PPCS software block diagram is shown in Figure 7-1, incorporating both the on-board and ground processing (the latter shown here only for identification of interfaces). Two basic categories of on-board software are considered, namely: Application Software, i.e., that required for the specific implementation of PPCS functional/operational algorithms (Blocks 2X, 3X); and Executive software, i.e., that which is most strongly related to basic implementation of the data processing functions and maintenance of the appropriate operating configuration/environment (Block 1X). A modular approach to software organization is used in order to achieve overall cost-effectiveness with regard to software development. Individual software modules are defined to handle specific functional requirements. This approach allows the work to be conveniently segmented for detailed program design, facilitates ease of checkout, and isolates executive functions from the functional coding.

The Executive software is presented initially, and includes discussion of the program control approaches/tradeoffs, considerations related to defining program modules, definition of program flow, and a brief discussion of the Executive software modules. The Application software discussion focuses in some detail on the design of each module to the level of equation definition and flow. Preliminary generic coding of the software was conducted to determine the computational requirements, and this is summarized in the final section.

7.1 EXECUTIVE SOFTWARE

Executive software is a generic term used in the present context to include the functions of program execution, interface management, and configuration control. The principal functions of the Executive software are thus defined as:

- To schedule all of the software tasks that are pertinent to a particular mission phase.
- Assure that each task is executed in real time at an individual defined rate
- Perform or coordinate all input/output operations so that data is available to the individual software modules as it is needed.
- Respond to asynchronous demands related to ground commands and system reconfiguration within the appropriate time limitations.
- Handle computer initialization, program loading, and ground update.
- Interface with the telemetry and command.
- Provide for computer and data interface self-test.
- Provide for system monitor and test.

```
┌─────────────────────────────────┐        ┌─────────────────────────────────┐
│      ATTITUDE REFERENCE         │        │       POINTING CONTROL          │
│                                 │        │                                 │
│  ● Gyro Reference (Block 21)    │        │  ● Targeting (Block 31)         │
│                                 │        │                                 │
│  ● Star Reference (Block 22)    │        │  ● Steering (Block 32)          │
│                                 │        │                                 │
│  ● Filter Update (Block 23)     │◄──────►│                                 │
│                                 │        │                                 │
│  ● Alignment Reference          │        │                                 │
│    (Block 24)                   │        │                                 │
│                                 │        │                                 │
│  ● Heading Reference (Block 25) │        │                                 │
│                                 │        │                                 │
│                                 │        │                                 │
└─────────────────────────────────┘        └─────────────────────────────────┘
               │                                         │
               │                                         │
               ▲                                         ▼
        ┌─────────────────────────────────────┐
        │            EXECUTIVE                 │
        │                                      │
        │  ● Program Control (Block 11)        │
        │                                      │
        │  ● Bus Control (Block 12)            │
        │                                      │
        │  ● Telemetry/Command (Blk 13/14)     │
        │  ● Self Test (Block 15)              │
        │  ● System Monitor/Test (Blk 16)      │
        │                                      │
        └─────────────────────────────────────┘
                    │    ▲
─ ─ ─ ─ ─ ─ ─ ─ ─ ─ ─ ─ ─ ─ ─ ─ ─ ─ ─ ─ ─ ─ ─ ─ ─
                    ▼    │
        ┌─────────────────────────────────────┐
        │         GROUND PROCESSING            │
        │                                      │
        │  ● Orbit Determination               │
        │  ● Targeting                         │
        │  ● Calibration                       │
        │  ● Failure Detection                 │
        │    and Reconfiguration               │
        │  ● Telemetry and Command             │
        │    Processing                        │
        └─────────────────────────────────────┘
```

Figure 7-1. PPCS Software Block Diagram

7.1.1 Program Control/Execution

The program control executive routine is that portion of the operational program which controls the execution of the individual functions of the program and allocates the resources of the computer system to accommodate the performance of these tasks within the real time constraints of the system. It is the governing software which lends an organization to the execution of the overall program.

Executive software organizations can be described as being either synchronous or asynchronous. The synchronous executive concept divides time into a number of segments. These segments are assigned specific computational tasks and the list of slots is continuously recycled to create a real time system. This is a very orderly organization, with the same computations always being executed in the same time segments. Various computational rates within the total loop can be established by creating inner loops within the basic loop. An asynchronous executive is primarily based on the utilization of external interrupts. It is motivated by real time demands imposed by the external devices, and is characterized by interrupted computations and priority task tables.

The two concepts described actually constitute the terminal points of a continuous spectrum of executive organizations. The executive system defined for PPCS is between these two extremities, but leans toward the synchronous concept. The synchronous executive has as its greatest attribute its simplicity and well defined behavior. This simplifies the checkout and verification task. On the other hand, the asynchronous executive is more responsive to non-anticipated real-time demands. Since the PPCS operation is well defined and since no stringent requirement is placed on real-time responsiveness, an executive software which is basically synchronous in nature is selected.

The PPCS program control executive routine is organized using a synchronized major cycle/minor cycle concept as shown in Figure 7-2. The minor cycle contains all of the high speed computations, and is executed every 200 milliseconds. The major cycle contains those computational functions which are performed at a slower rate, segmented in such a fashion that some system flexibility is available on a program controlled priority basis. Note that there are no external interrupts required for the PPCS data processing system. Internally, however, there are several interrupts associated with program execution control. One, the real-time clock, controls initiation of the minor cycle. At least two others are associated with the data interface, including the "command data received" and the "data bus error detected" signals. Depending upon the exact memory design, memory parity errors may also cause an interrupt. Other interrupts which exist within the computer include power transient monitors, overflow indicators, etc. Among the most important of these is the "Reset" interrupt which is used to initialize and start the computer at a known memory location.

7-3
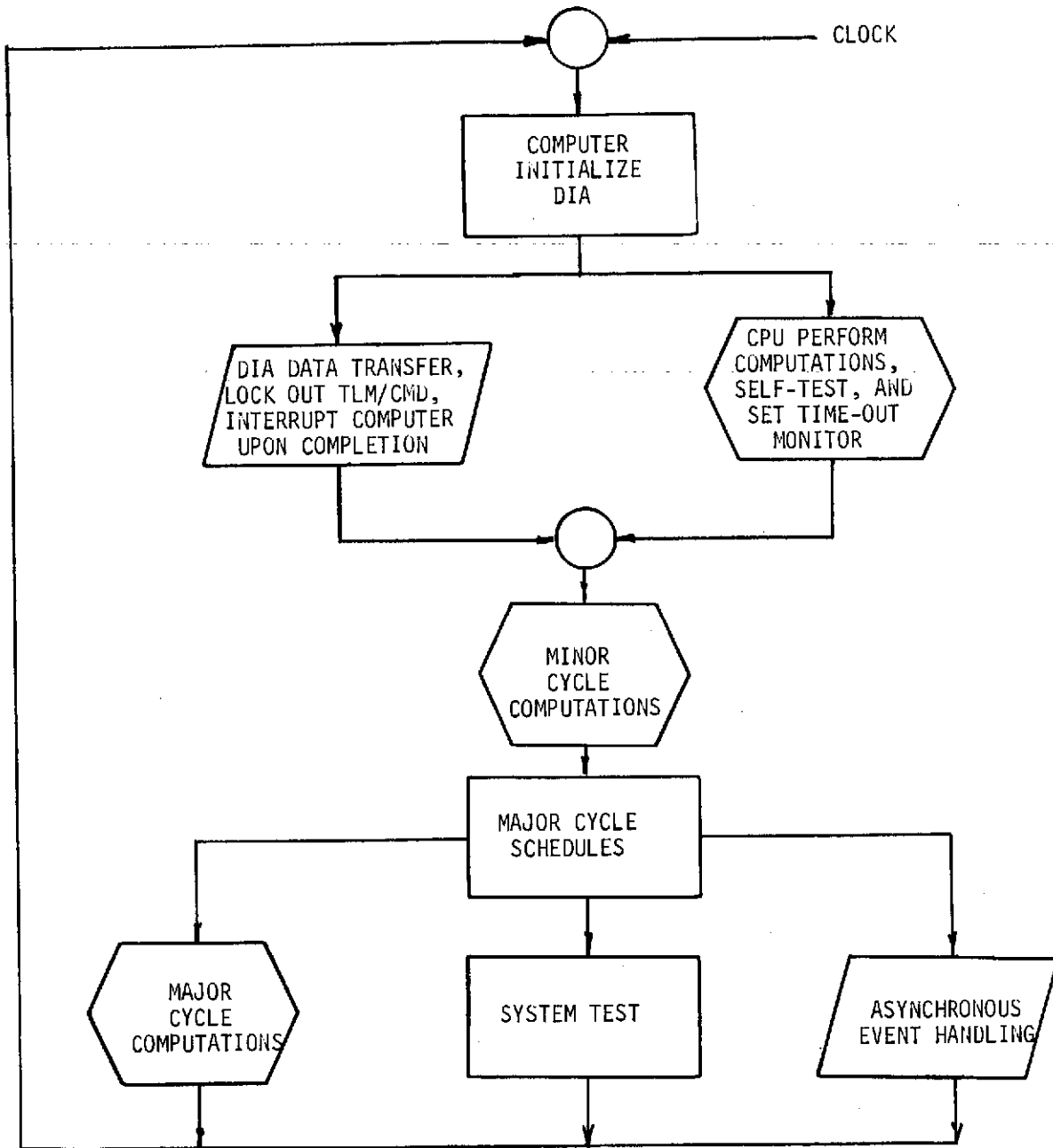
Figure 7-2. PPCS Executive Organization

The extent to which modularity is employed, coupled with the definition of module boundary conditions, have a strong influence on executive software requirements. Since the executive must provide software module interface linkage and argument transfers, the following considerations and constraints are invoked so as not to seriously complicate the executive requirements with relation to the modularity concept:

- The number of defined modules which are not placed in sequence must be consistent with the executive software ability to provide linkages. That is, the degree of modularity should be constrained so as not to severely complicate the structure of the executive software.

- Each software module must have a meaningful functional responsibility to facilitate analysis, modification, and intelligent assignment of program design responsibilities.

- Each module must be defined so that its execution time is in accordance with the time constraints established by the executive software. The module must be compatible with the time allocations for minor cycle and major cycle segments as established for a synchronous executive concept.

- Each software module should be capable of existing by itself so that boundaries can be identified. The boundaries are needed so that the module can be a physical entity.

- It is desirable that all modules be complete with regards to input/output requirements.

- It is desirable to minimize the setup and argument transfer requirements. Excessive setup penalizes modularity in terms of execution time and memory usage.

Definition of the software flow and modularity is shown in Figure 7-3.

7.1.2 Data Bus Control

The data bus control software controls the initialization of the minor cycle data transfer for application software and major cycle data transfer for system test. This software module performs the I/O initialization, data transfer execution, input/output command chaining, data buffer allocation, and data buffer monitoring. The initialization of a chain of I/O commands is done by the DCA. Once the chain of I/O commands is initialized, the DIA will take over from the DCA. The DIA will execute one I/O command at a time until the command buffer is empty. Then the DIA will interrupt the DCA. Each I/O command may execute an input data transfer or an output data transfer from or to an assembly. The buffer control is preferred by the DIA and the length of the buffer is variable and under program control.

7.1.3 Command Processing

The command processing should be initiated by an interrupt or discrete from the command decoder. This routine will interpret the message from the ground. The routine will then initiate the requested action. A large number of such actions will result in a large complex command link routine.
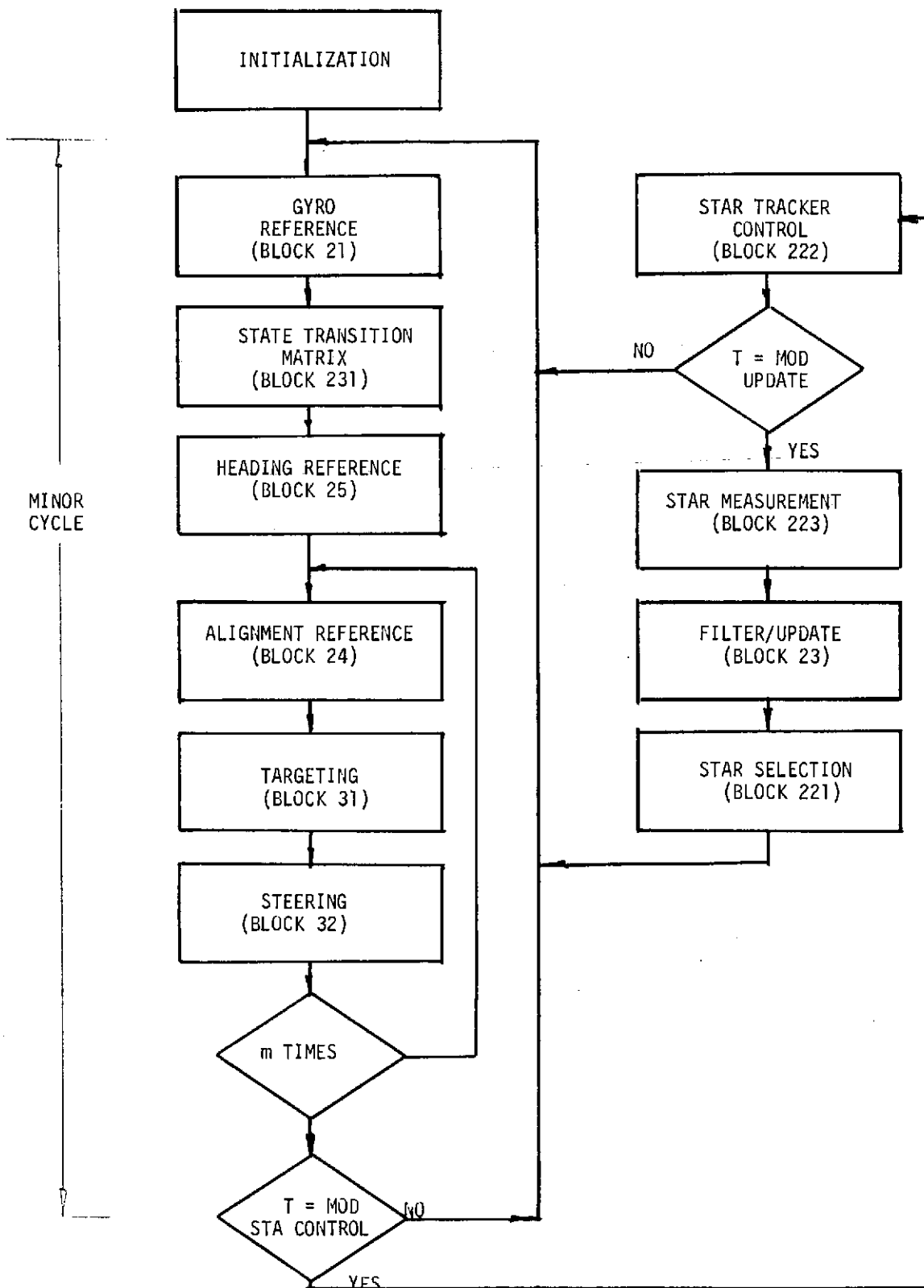
Figure 7-3. PPCS Software Modularity/Flow

7-6

7.1.4 Telemetry Processing

This software module will format and initiate the telemetry transmission on command. The telemetered data will be divided into two categories. The first category will be scientific data describing the normal operating modes. The second category will be diagnostic data requested by the ground over the command link.

7.1.5 Self-Test/System Test

This diagnostic capability will be divided into two parts: 1) a series of GO-NO-GO checks, and 2) provide diagnostic data to the ground. The GO-NO-GO checks will merely determine if a specific element is operating correctly. For elements of extreme importance, a message will be immediately transmitted to the ground. In addition, certain specified diagnostic information may be sent to the ground on command.

A number of failure detection modes for the DCA are available. These include the CPU self-test timer, memory parity, power transient monitors and data bus error detection. The basic philosophy of the fault detection scheme is to quickly bring ground attention to bear upon a fault (or possible fault) and to aid in its diagnosis. A basic tool is thus the telemetry format and the information contained therein. Some of the potential diagnostic tools used for the DCA/DIA are:

- Zero sum memory checks performed on program and other constant storage areas during self-test periods. Intermediate computations periodically transmitted via telemetry grouped so as to allow reasonableness checks.

- Self-test performed on minor cycle and major cycle basis. All instructions and registers exercised with diagnostic results stored and telemetered. Zero sum checks and other memory checks also monitor CPU.

- The data bus is checked by periodically sending data values to be D/A converted and returned to the CPU for checking. This is a partial check on DIA operation. Commands may also be sent from the ground which are turned around and telemetered for comparison.

Usual action in the case of a failure in the DCA/DIA is to switch (by ground command) the offending unit off and bring power on to a spare. The command decoding and power switching are performed in a system associated with the command unit. In some cases the action may be to change the locations of certain routines in memory (not the main program, however). In this way, particular memory faults may be avoided by never accessing particular locations.

A major failure usually requires restart. The restart sequence must be such that the PPCS system may bootstrap into proper operation from any conceivable failure mode. Provision for this is in the initialization routine which is entered via the restart interrupt. This interrupt necessarily is decoded either within the command system, or in the command control unit of the DIA.

7-7

Faults within other PPCS units are detected primarily through software monitors. These include limit checks on voltages, temperatures, etc.; reasonableness checks on certain data such as gimbal angles and angular rates; and results of computations such as gyro rates. These monitors are telemetered and ground action is implemented via the command subsystem. Diagnosis of failures are nominally performed on the ground.

7.2 APPLICATION SOFTWARE

The application software modules provide those operations to measure and establish the required attitude reference(s) (Block 2X) and to implement the pointing control operations for the experiment platform and antenna (Block 3X). These functions are briefly reviewed, with reference to the detailed application software block diagram of Figure 7-4 . The short-term inertial attitude reference is provided by processing of gyro data (Block 21). Periodic updating of attitude is provided by using star tracker data (Block 22) and employing filtering techniques to bound the gyro drift effects (Block 23). Star selection and control of the star tracker(s) is included within Block 22. Attitude reference between the primary inertial reference and remote platforms is provided by processing alignment sensor data (Block 24). In addition, attitude reference relative to the local vertical is established through knowledge of the ephemeris and appropriate transformation of the inertial reference (Block 25). Targeting (Block 31) is based upon ground generated stored data, resulting in target vectors. The steering equations yield gimbal angle and/or rate commands associated with the platform(s) or antenna to be pointed based upon the targeting inputs (Block 32).

7.2.1 Gyro Reference (Block 21)

The function of this module is to take the information from the gyros in the form of pulse counts as inputs and derive as an output the inertial attitude of the primary attitude determination reference frame with respect to ECI coordinates. The functional block diagram for this module is shown in Figure 7-5 . The functions which take place are:

- Convert pulse counts to angle change, derive rate, and transform rate from the gyro to body coordinate frame (Block 211)

- Compensate for gyro error sources (e.g., drift bias, input axis alignment, and scale factor) (Block 211)

- Maintain precise short-term reference by integrating gyro data (Block 212)

- Compute elements of direction cosine matrix relating attitude to ECI (Block 213)

The required algorithms are summarized in Figure 7-6, where the equations shown are taken from the derivation of Section 3.0.
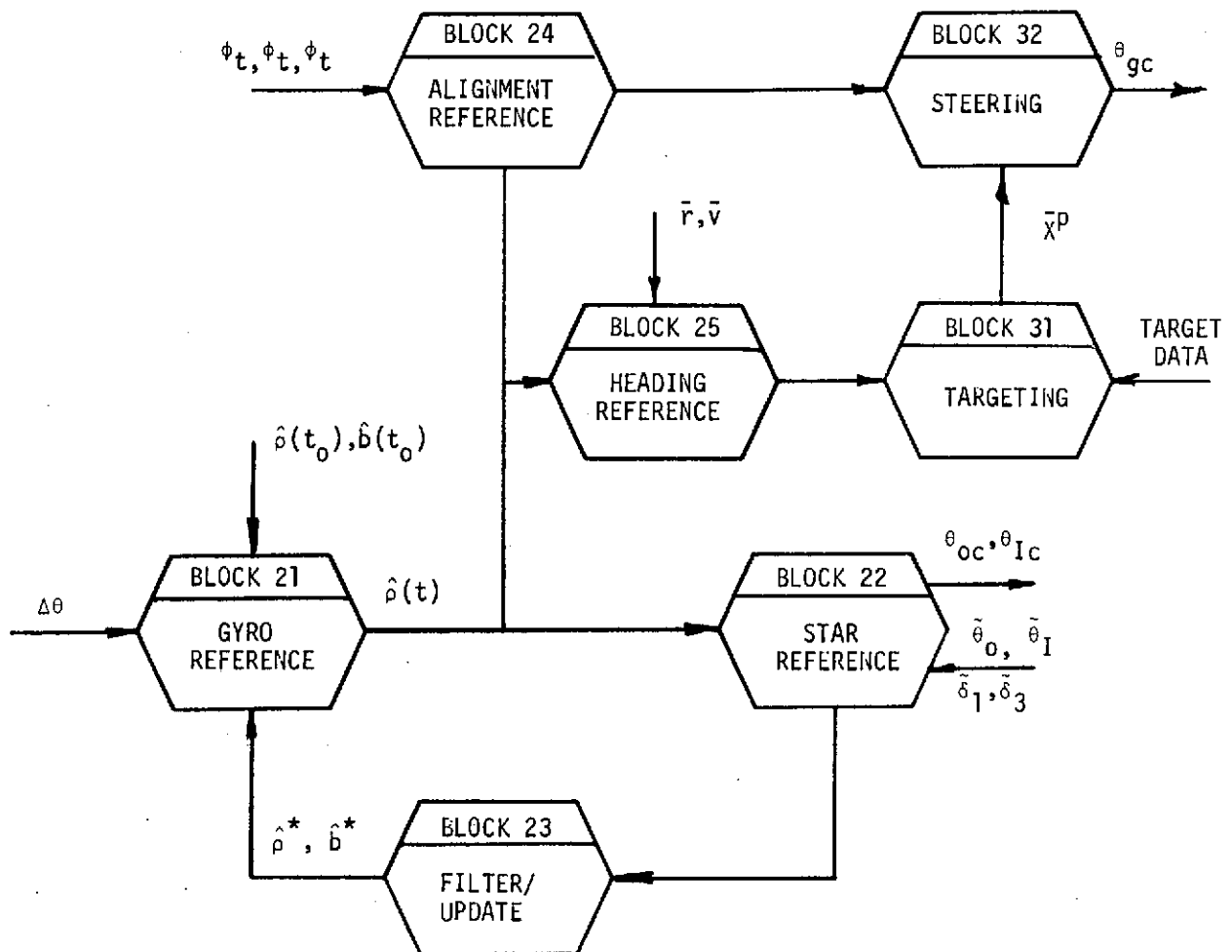
Figure 7-4. PPCS Application Software Functional Block Diagram
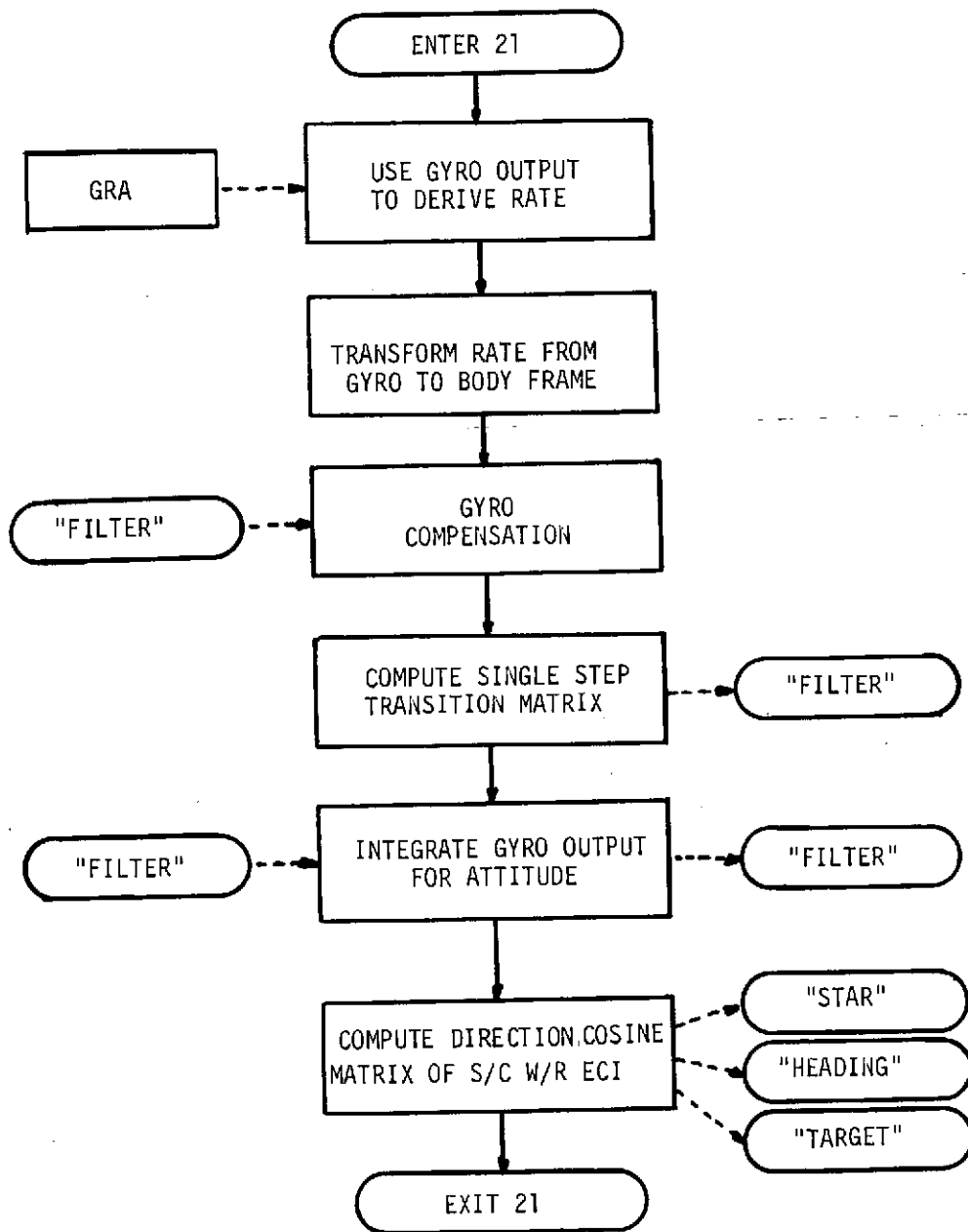
Figure 7-5. Functional Block Diagram, Block 21

For $i = 1, \cdots, N_g$

$$\omega_m^i = \hat{R}^i \, N^i / T$$

$$\omega^M = T \omega_m$$

$$\hat{\omega} = \hat{A}_g^{-1} [\omega^M - \hat{b}_g^\circ]$$

$$\Theta_o = T \sqrt{\sum_i \tfrac{1}{2} \hat{\omega}_i^2} \qquad \Theta_i = \hat{\omega}_i T, \; i=1,2,3$$

$$S_o = \frac{\sin(\Theta_o/2)}{\Theta_o} \qquad C_o = \cos(\Theta_o/2)$$

Compute Single Step Transition Matrix $R_{\hat{R}} = \exp(\tfrac{1}{2} \hat{\Omega}_{\hat{R}} T)$

$$R_{\hat{R}} = \begin{array}{|c|c|c|c|} \hline C_o & \Theta_3 S_o & -\Theta_2 S_o & \Theta_1 S_o \\ \hline -\Theta_3 S_o & C_o & \Theta_1 S_o & \Theta_2 S_o \\ \hline \Theta_2 S_o & -\Theta_1 S_o & C_o & \Theta_3 S_o \\ \hline -\Theta_1 S_o & -\Theta_2 S_o & -\Theta_3 S_o & C_o \\ \hline \end{array}$$

Propagate Attitude

$$\hat{e}(k+1) = R_{\hat{R}} \, \hat{e}(k)$$

Renormalize $\hat{e}(k+1), \; i = 1, \cdots, 4$

$$\hat{e}_i = \hat{e}_i / \| \hat{e} \|$$

$$\Gamma = \begin{array}{|c|c|c|c|} \hline x & y & -\eta & \xi \\ \hline -y & x & \xi & \eta \\ \hline \eta & -\xi & x & y \\ \hline \xi & \eta & y & -x \\ \hline \end{array} \quad t_{k+1}$$

$$A_{xz} = \{ \text{first } 3 \times 3 \text{ of } \Gamma^2 \}$$
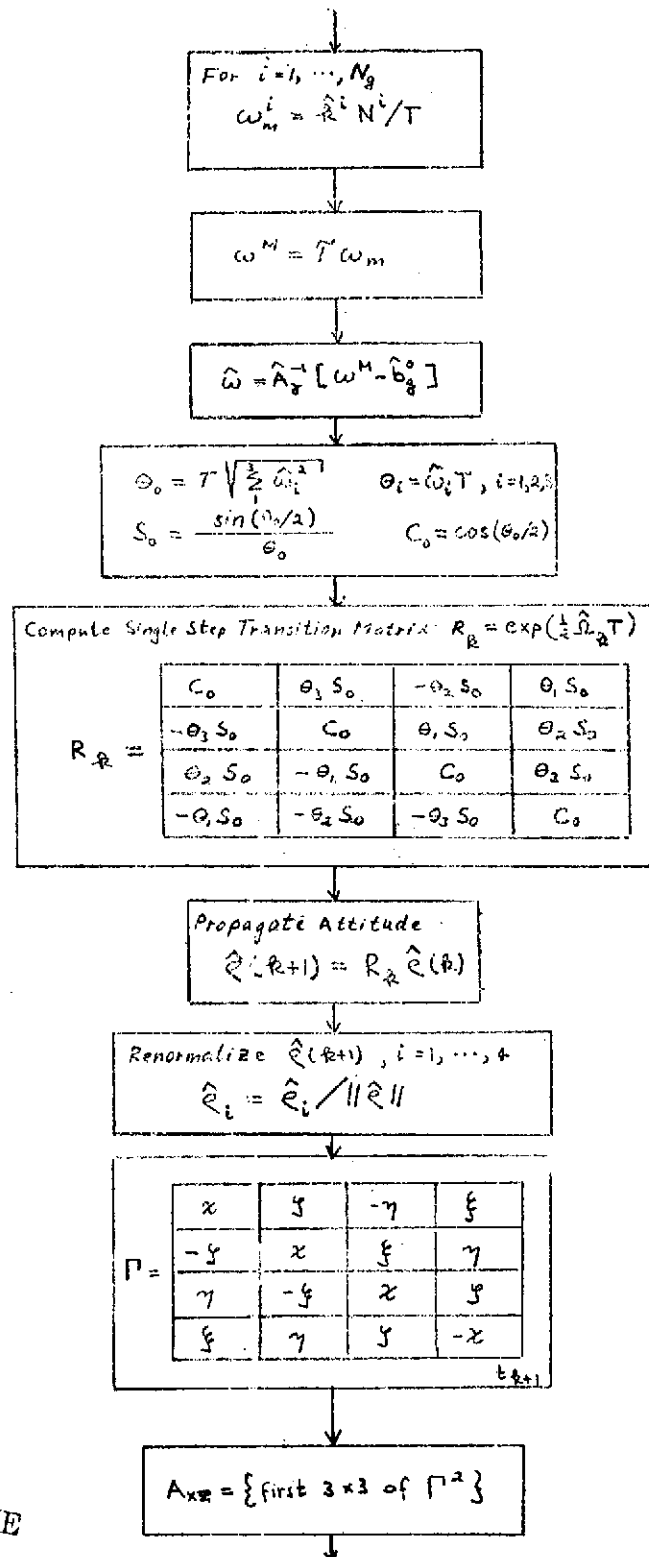
Figure 7-6.   Algorithms/Flow for Gyro Reference Module (Block 21)

7.2.2 Star Reference (Block 22)

The function of this module is to provide selection of target stars, compute tracker gimbal commands during slew and star search, compute the estimate of the STA star measurement, and compute the difference between the observed STA measurement and the estimated value. The functional block diagram for this module is shown in Figure 7-7 . The functions which take place are:

- Establish star selection/availability (Block 221)
- Compute aberration correction (Block 221)
- Compute nominal STA gimbal angles and provide STA command/control as appropriate (Block 222)
- Compute estimated STA star measurement (Block 223)
- Determine observed STA star measurement (Block 223)
- Compute difference between observed and estimated STA star measurement, i.e., measurement residual (Block 223)

The required algorithms are summarized in Figure 7-8 , where the equations shown are taken from the derivation of Section 3.0.

7.2.3 Filter/Update Reference (Block 23)

The function of this module is to maintain precise long-term attitude reference via updates of the system state using star tracker data implemented through a Kalman filter. The block diagram of this module is shown in Figure 7-9 . The following functions are included:

- Propagation of the state transition matrix is performed each minor cycle using gyro derived data (Block 231). The matrix is re-initialized following each filter update.

- The covariance matrix is propagated from the previous observation time to the current observation time using the state transition matrix (Block 232).

- The gradient matrix of sensitivities of observables relative to parameters being estimated (i.e., the measurement matrix) is computed (Block 233).

- The filter (optimum gain) weighting matrix is computed using the Kalman filter equations (Block 234).

- The covariance matrix is updated to reflect reduced uncertainty after an observation has been processed (Block 235).

- Corrections to the Euler parameter and drift bias parameters are computed using the weighting matrix and the measurement residuals, and the parameters updated (Block 236).

The required algorithms are summarized in Figure 7-10, where the equations shown are taken from the derivation of Section 3.0.

ENTER 221

STAR SORT FOR AVAILABILITY

STAR SELECTION FROM AVAILABLE STAR

COMPUTE ABERATION CORRECTION
FOR STAR COORDINATES

EXIT 221

ENTER 222

2221

"GYRO"

COMPUTE STAR COORDINATES IN
TRACKER REFERENCE FRAME

2222

STA

COMPUTE NOMINAL TRACKER GIMBAL
ANGLES, TEST STAR LOCK/LOGIC

2223

GENERATE STAR TRACKER
COMMANDS/LOGIC

STA

EXIT 222

ENTER 223

COMPUTE ESTIMATED
MEASUREMENT VECTOR

STA

COMPUTE OBSERVED MEASUREMENT VECTOR
AND MEASUREMENT RESIDUAL

"FILTER"

EXIT 223

Figure 7-7. Functional Block Diagram, Block 22

Identify Visible Stars

Star Catalog Identification Numbers Are Stored in the Array:

$$NS(ISLOT, J) \quad , \quad J = 1, NVS$$

$$J = 1. \quad ; \quad \varphi_m = 0.$$

$$K1 = NS(ISLOT, J)$$
$$\alpha = STACAT(1, K1)$$
$$\delta = STACAT(2, K1)$$

$$\begin{bmatrix} a_1 \\ a_2 \\ a_3 \end{bmatrix} = \begin{bmatrix} \cos\delta \cos\alpha \\ \cos\delta \sin\alpha \\ \sin\delta \end{bmatrix}$$

$$c = \sum_{i=1}^{3} a_i^0 \, a_i$$

$$\varphi = \tan^{-1}\left(+ \sqrt{1.-c^2} / c \right)$$

$\varphi > \varphi_m$ — No

Yes

$$KM = K1 \quad , \quad \varphi_m = \varphi$$

$J \geq NVS$ — No → $J = J+1$

Yes

$$\alpha = STACAT(1, KM)$$
$$\delta = STACAT(2, KM)$$

Next Star Selected Is

$$a^0 = \begin{bmatrix} \cos\delta \cos\alpha \\ \cos\delta \sin\alpha \\ \sin\delta \end{bmatrix}$$

Make Aberration Correction On Star Vector

$$\bar{V}^a = \bar{V} + \bar{V}^*$$

$$\beta_a = \sum_{i=1}^{3} V_i^a \, a_i^0$$

$$\begin{bmatrix} a_1 \\ a_2 \\ a_3 \end{bmatrix} = \left(1 - \frac{\beta^a}{c} \right) \begin{bmatrix} a_1^0 \\ a_2^0 \\ a_3^0 \end{bmatrix} + \frac{1}{c} \begin{bmatrix} V_1^a \\ V_2^a \\ V_3^a \end{bmatrix}$$

Figure 7-8 a. Algorithms/Flow for Star Selection Module (Block 221)

Compute Direction Cosines of Tracker No. j W/R ECI

$$A_{x^j_z} = A_{x^j_x} A_{xz}$$

$$\begin{bmatrix} u_1 \\ u_3 \\ u_3 \end{bmatrix} = A_{x^j_z} \begin{bmatrix} a_1 \\ a_2 \\ a_3 \end{bmatrix}$$

Compute Nominal Gimbal Angles

$$\theta_n^o = \tan^{-1}(u_3/u_2)$$

$$\theta_n^I = \tan^{-1}\left(\frac{-u_1}{u_2 \cos\theta_n^o + u_3 \sin\theta_n^o}\right)$$

Gimbal Stops Exceeded ? —— Yes ——▸ Set Select Flag

No

Compute Nominally Commanded Gimbal Angle Rates.
For $j = O, I$ Compute

$$\Delta\theta_n^j(k+1) = \theta_n^j(k+1) - \Delta\theta_n^j(k+1)$$

$$\dot\theta_n^j(k+1) = \frac{1}{2T}\left(3\Delta\theta_n^j(k+1) - \Delta\theta_n^j(k)\right)$$

Output Tracker Control Signal

Update and Store First Differences For Next Sampling Instant

$$\Delta\theta_n^j(k) = \Delta\theta_n^j(k+1)$$

$$\Delta\theta_n^j(k+1) = \theta_n^j(k+1)$$

Figure 7-8b. Algorithms/Flow for Tracker Control Module (Block 222)

Compute Estimates For Bearing Run-Out, Cyclic Inductosyn Errors. Constitute Estimated STA Parameter Vector $\hat{q}_m$.

$$\hat{q}_m + \tilde{q}_r = \begin{bmatrix} \alpha_{10} + \tilde{\alpha}_1 \\ \alpha_{30} + \tilde{\alpha}_3 \\ \alpha_{10}{}^I + \alpha_{11}{}^I s_n{}^I \\ \alpha_{20}{}^I + \alpha_{21}{}^I s_n{}^I \\ \alpha_{20}{}^0 + \alpha_{21}{}^0 s_n{}^0 \\ \alpha_{30}{}^0 + \alpha_{31}{}^0 s_n{}^0 \\ -\alpha_b{}^0 \\ -\alpha_b{}^I \end{bmatrix}$$

$$S_n{}^I = -u_1 \quad,$$
$$S_n{}^0 = \frac{u_3}{\sqrt{1-u_1{}^2}}$$

$$u_4 = 1 - u_1{}^2$$
$$u_5 = (u_4)^{1/2}$$

$$M(u) = \begin{bmatrix} 0 & -u_5 & 0 & 0 & u_3 & -u_2 & 0 & -u_5 \\ -\dfrac{u_2}{u_4} & 0 & -\dfrac{u_2}{u_5} & \dfrac{u_1 u_2}{u_4} & \dfrac{u_1 u_2{}^2}{u_5{}^3} & \dfrac{u_1 u_2 u_3}{u_5{}^3} & \dfrac{u_2}{u_5} & 0 \end{bmatrix}$$

$$\hat{y} \triangleq \begin{bmatrix} \hat{y}_I \\ \hat{y}_0 \end{bmatrix} = \begin{bmatrix} -u_1 \\ u_3/u_5 \end{bmatrix} + M(u) \begin{bmatrix} \hat{q}_m + \tilde{q}_r \end{bmatrix}$$

Read STA Inductosyns: $\tilde{\Theta}_I$, $\tilde{\Theta}_0$

$$\tilde{y} \triangleq \begin{bmatrix} \tilde{y}_I \\ \tilde{y}_0 \end{bmatrix} = \begin{bmatrix} \sin\tilde{\Theta}_I \\ \sin\tilde{\Theta}_0 \end{bmatrix} \; ; \quad \delta y = \tilde{y} - \hat{y}$$

Figure 7-8c. Algorithms/Flow for Star Measurement Module (Block 223)

Figure 7-9. Functional Block Diagram, Block 23
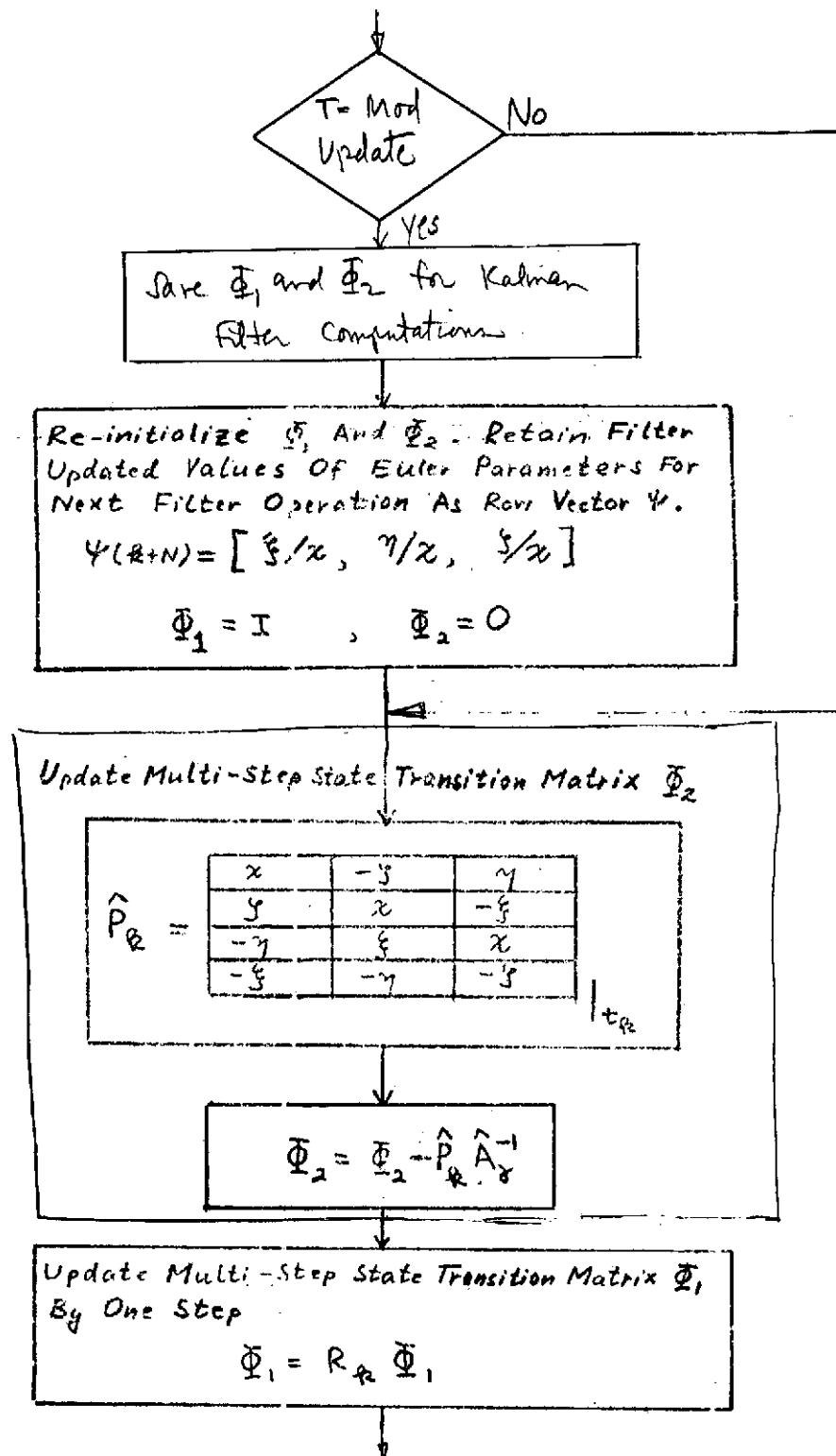
Figure 7-10a. Algorithms/Flow for State Transition Module (Block 231)

$$P_{k+N/k} = \Phi(k+N,k)\, P_{k/k}\, \Phi^T(k+N,k) + Q_k$$

Propagate Covariance Matrix P

Where
$$\Phi(k+N,k) = \left[\begin{array}{c|c} \Phi_1^0(k+N,k) & \Phi_2^0(k+N,k) \\ \hline \bigcirc & I \end{array}\right] {\scriptstyle \begin{array}{c}3\\3\end{array}}$$
$$\underbrace{\qquad}_{3}\;\underbrace{\qquad}_{3}$$

Computations Are Performed With The Submatrices Φ_1^0, Φ_2^0.

$$\Phi_1^0(k+N,k) = \Phi_{11}(k+N,k) - \Phi_{12}(k+N,k)\,\Psi(k)$$

where $\Phi_{11} = [\text{Upper left } 3\times3 \text{ of } \Phi_1]$
$\Phi_{12} = [\text{Upper right } 3\times1 \text{ of } \Phi_1]$

$$\Rightarrow \Phi_1 \triangleq \left[\begin{array}{c|c} \Phi_{11} & \Phi_{12} \\ \hline \Phi_{21} & \Phi_{22} \end{array}\right]$$

$$\Phi_2^0(k+N,k) = \left\{\text{first 3 rows of } \frac{T}{2}\Phi_2(k+N,k)\right\}$$

Let $A_{x\times x} = (a_{ik}^j)$, $i,k = 1,3$

Compute For $i = 1$ and 3:

$$\alpha_{i1} = a_{i1}^j\, x - a_{i2}^j\, \zeta + a_{i3}^j\, \eta$$
$$\alpha_{i2} = a_{i1}^j\, \zeta + a_{i2}^j\, x - a_{i3}^j\, \zeta$$
$$\alpha_{i3} = -a_{i1}^j\, \eta + a_{i2}^j\, \zeta + a_{i3}^j\, x$$
$$\alpha_{i4} = a_{i1}^j\, \zeta + a_{i2}^j\, \eta + a_{i3}^j\, \zeta$$

$$\ell_1 = \frac{u_1 u_3}{u_5^3} \qquad \ell_2 = \frac{1}{u_5}$$

$$\hat{A} = \begin{bmatrix} 0 & -a_3 & a_2 \\ a_3 & 0 & -a_1 \\ a_2 & a_1 & 0 \\ a_1 & a_2 & a_3 \end{bmatrix} - \frac{1}{x}\begin{bmatrix} a_1 \\ a_2 \\ a_3 \\ 0 \end{bmatrix}\begin{bmatrix} \zeta & \eta & \zeta \end{bmatrix}$$

$\hat{B} =$

$-\alpha_{11}$	$-\alpha_{12}$	$-\alpha_{13}$	$-\alpha_{14}$
$\ell_1\alpha_{11}+\ell_2\alpha_{31}$	$\ell_1\alpha_{12}+\ell_2\alpha_{32}$	$\ell_1\alpha_{13}+\ell_2\alpha_{33}$	$\ell_1\alpha_{14}+\ell_2\alpha_{34}$

$$H = \left[\begin{array}{cc|c} \hat{B} & \hat{A} & \bigcirc \end{array}\right]$$
$$\underbrace{\qquad}_{3}\;\underbrace{\qquad}_{3}$$

Figure 7-10b. Algorithms/Flow for Filter/Update (Blocks 232-233)

Compute Optimum Gain Matrix $K_{\hat{k}+N}$ 234

$$K_{\hat{k}+N} = P_{\hat{k}+N|\hat{k}} \, H^T_{\hat{k}+N} \left[H_{\hat{k}+N} \, P_{\hat{k}+N|\hat{k}} \, H^T_{\hat{k}+N} + R_{\hat{k}+N} \right]^{-1}$$

Update Covariance Matrix   235

$$P_{\hat{k}+N/\hat{k}+N} = \left[I - K_{\hat{k}+N} \, H_{\hat{k}+N} \right] P_{\hat{k}+N|\hat{k}}$$

                                                                          236

Compute Corrections For 3-Parameter Attitude e^o And Gyro Bias Vector b^o_g

$$\left[\frac{\delta e^o(\hat{k}+N)}{\delta b^o_g(\hat{k}+N)} \right] = K_{\hat{k}+N} \, \delta y(\hat{k}+N)$$

Update Euler Parameter Attitude Vector

$$x = x - \frac{1}{x} \left[\xi \, \delta \xi + \eta \, \delta \eta + \zeta \, \delta \zeta \right]$$

$$e^o = e^o + \delta e^o$$

$$\hat{e}(\hat{k}+N) \triangleq \begin{bmatrix} e^o \\ x \end{bmatrix}$$

Update Gyro Biases

$$\hat{b}^o_g = \hat{b}^o_g + \delta b^o_g$$
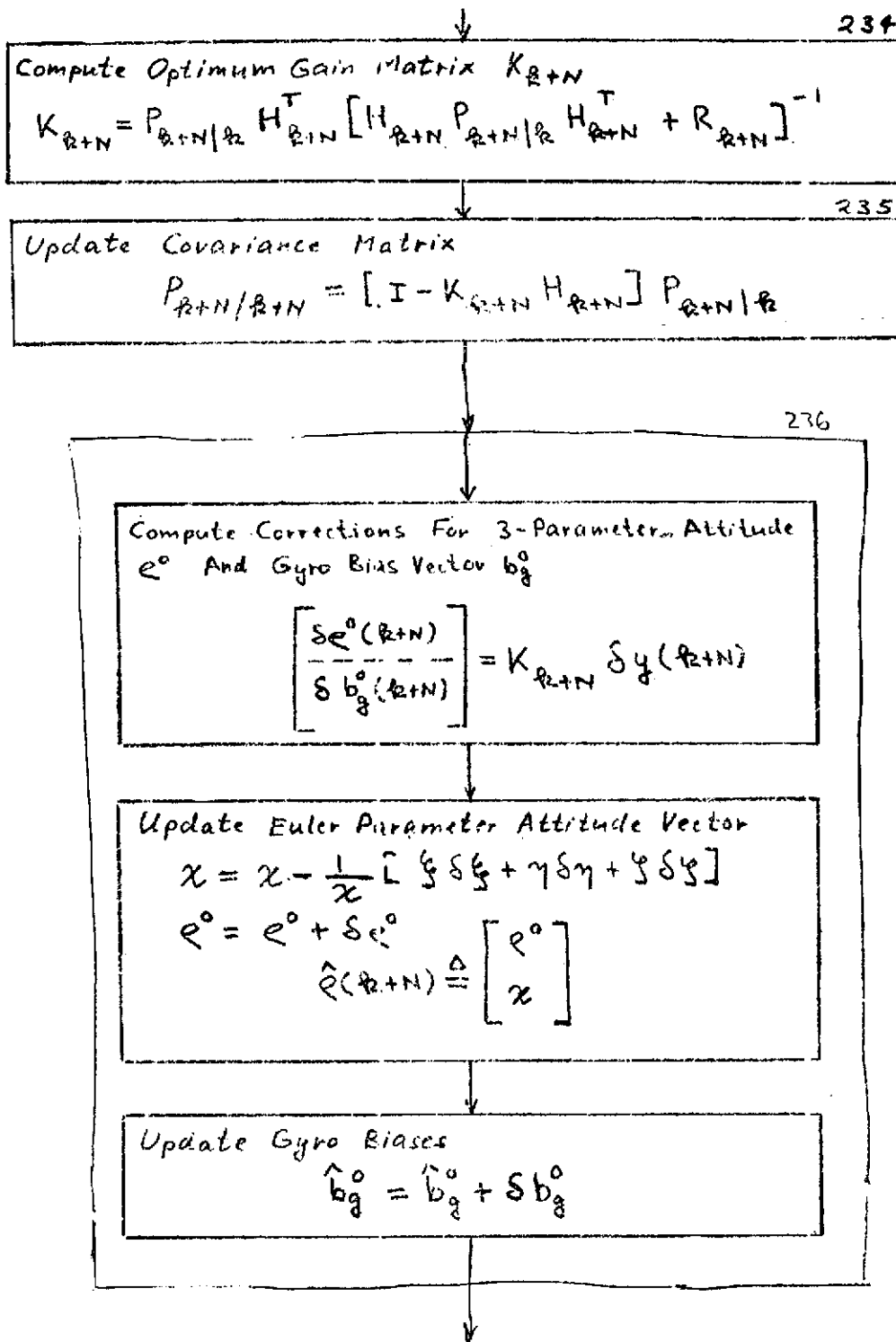
Figure 7-10c. Algorithms/Flow for Filter/Update (Blocks 234-236)

7.2.4 Alignment Reference (Block 24)

The function of this module is to establish a precision reference for up to six remote platforms using the alignment sensor measurements. The block diagram of this module is shown in Figure 7-11. The following functions are performed:

- Measure autocollimator outputs and correct for known errors (Block 241)

- Compute elements of direction cosine matrix relating orientation of remote reference to alignment instrument reference (Block 241)

- Compute elements of direction cosine matrix relating orientation of remote reference to attitude determination reference (Block 242).

The required algorithms are summarized in Figure 7-12, where the equations shown are taken from the derivation of Section 3.0.

7.2.5 Heading Reference (Block 25)

The function of this module is to establish a precision continuous local vertical/orbit plane reference. The block diagram of this module is shown in Figure 7-13. The functions performed include:

- Computation of real-time estimate of spacecraft ephemeris (i.e., position and velocity) in inertial coordinate (ECI) (Block 251). Note: The means to perform this function have been specifically excluded from PPCS design considerations. This computation is included for completeness only in the present context.

- Compute elements of the transformation matrix from inertial (ECI) coordinate to local vertical/orbit plane coordinates (Block 252).

- Compute elements of the transformation matrix from the local vertical/orbit plane frame to the attitude determination frame (Block 252).

- Compute spacecraft attitude and rate relative to the local vertical coordinate frame (Block 253).

The required algorithms are summarized in Figure 7-14, where the equations shown are taken from the derivation of Section 3.0.
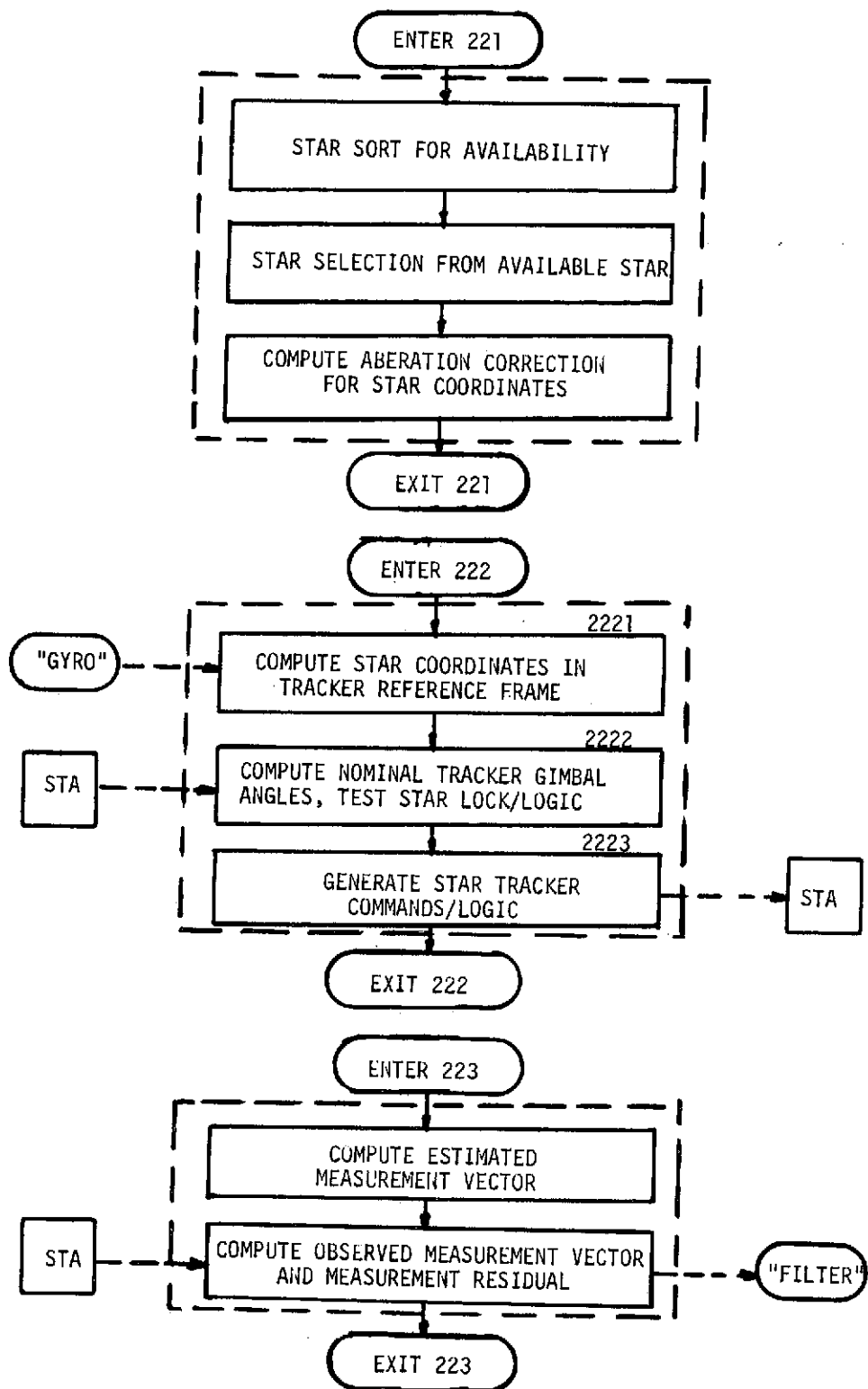
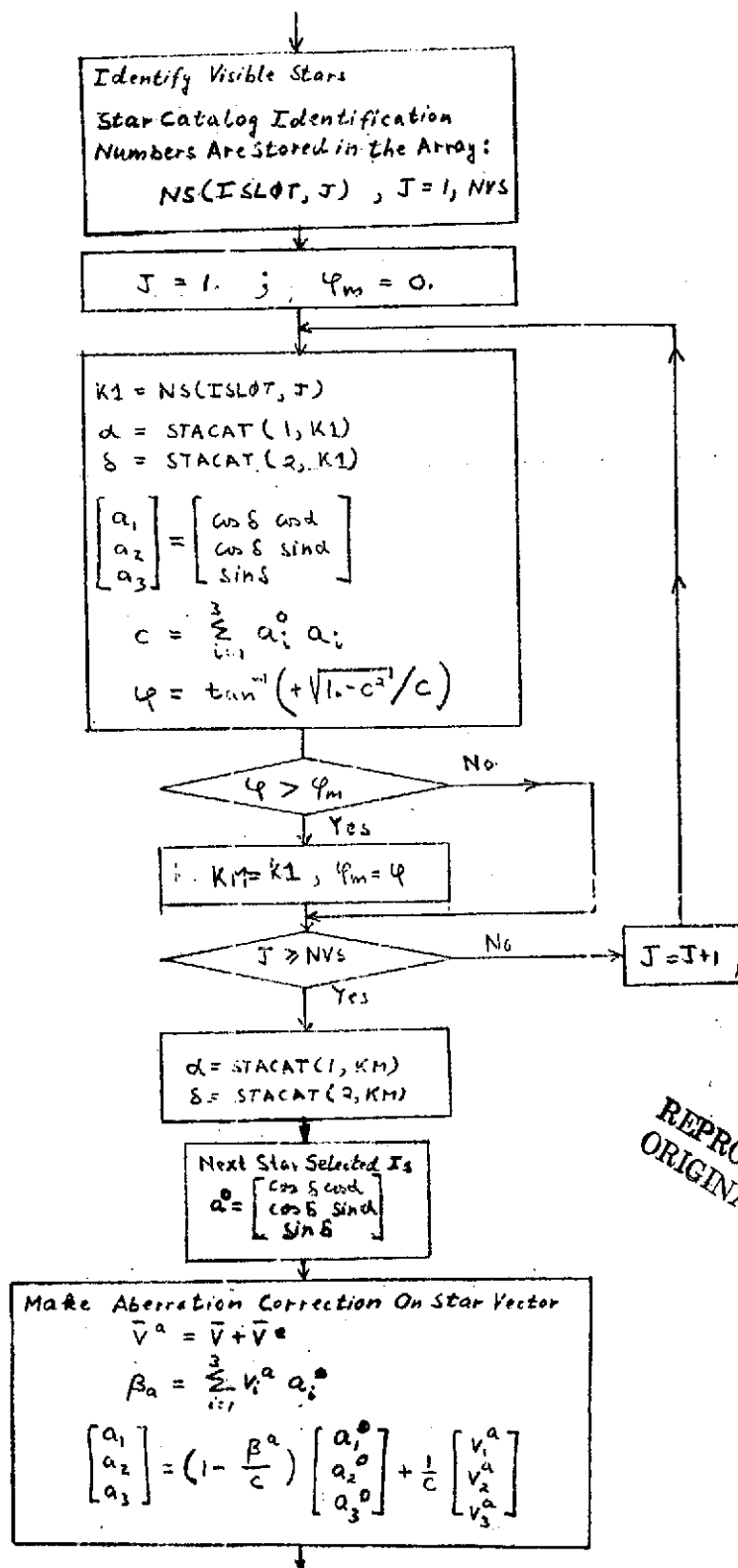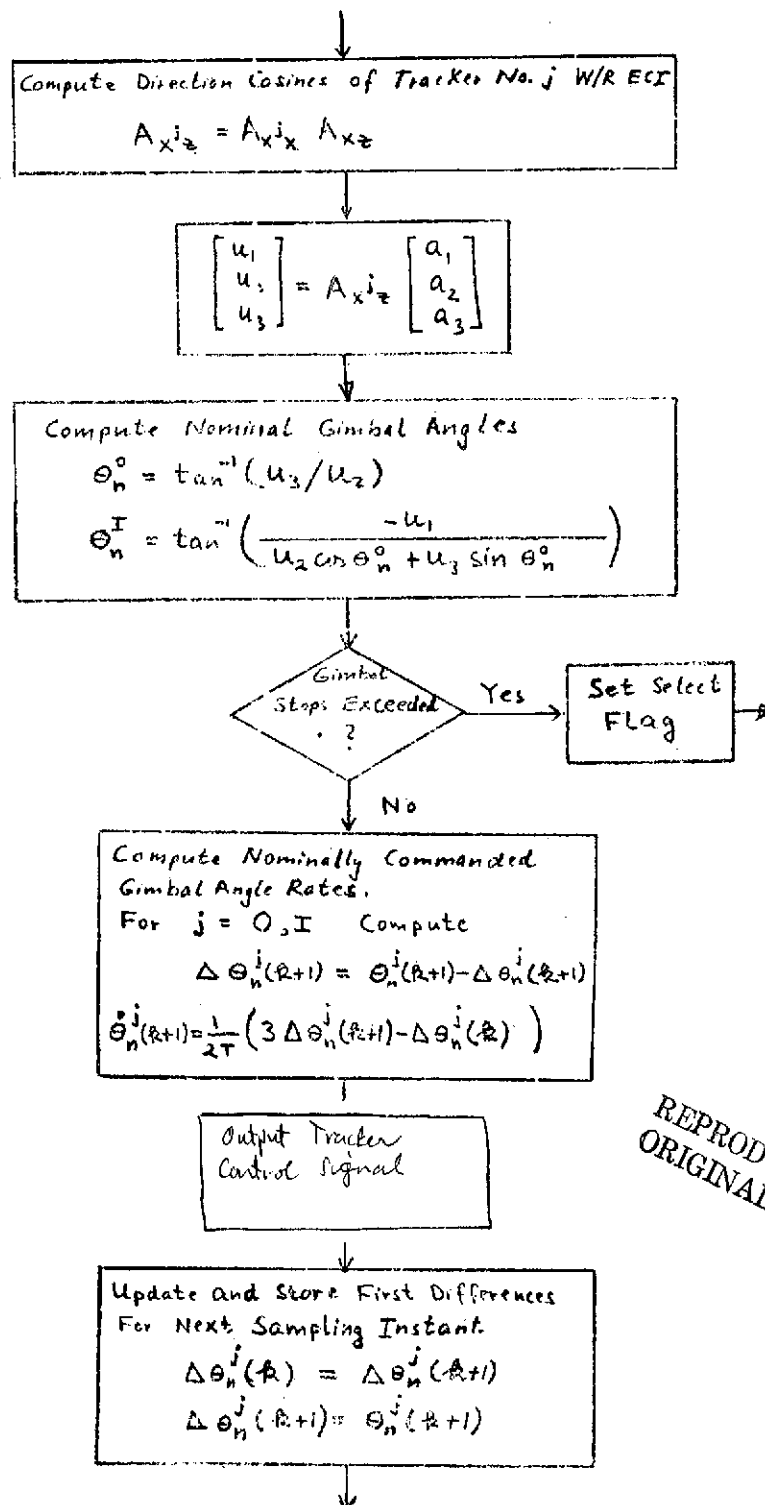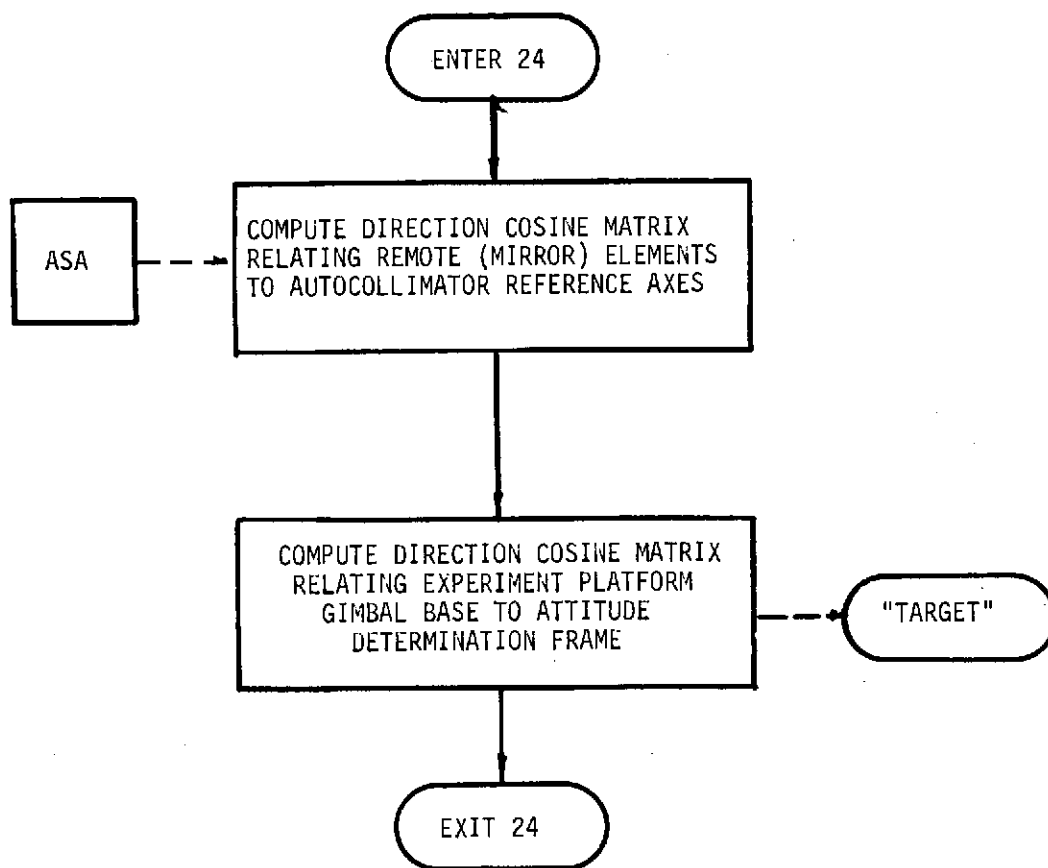Figure 7-11. Functional Block Diagram, Block 24

Read Autocollimator Angles $\tilde{\phi}_t, \tilde{\theta}_t, \tilde{\psi}_t$

Correct For Repeatable Autocollimator Bias Errors

$$\hat{\phi}_e = \tilde{\phi}_t - \hat{\epsilon}_x$$
$$\hat{\theta}_e = \tilde{\theta}_t - \hat{\epsilon}_y$$
$$\hat{\psi}_e = \tilde{\psi}_t - \hat{\epsilon}_z$$

Compute Direction Cosine Matrix of Mirror Relative to Autocollimator Reference Axes

$$\hat{A}_{tr} = \begin{bmatrix} \cos\phi_e\cos\theta_e & -\cos\phi_e\sin\theta_e\sin\psi_e - \sin\phi_e\cos\psi_e & \cos\phi_e\sin\theta_e\cos\psi_e - \sin\phi_e\sin\psi_e \\ \sin\phi_e\cos\theta_e & -\sin\phi_e\sin\theta_e\sin\psi_e + \cos\psi_e\cos\psi_e & \sin\phi_e\sin\theta_e\cos\psi_e + \cos\phi_e\sin\psi_e \\ -\sin\theta_e & -\cos\theta_e\sin\psi_e & \cos\theta_e\cos\psi_e \end{bmatrix}$$

Relate gimbal base reference to primary reference

$$A_{gx} = \hat{A}_{gt}\,\hat{A}_{tr}\,\hat{A}_{rx}$$
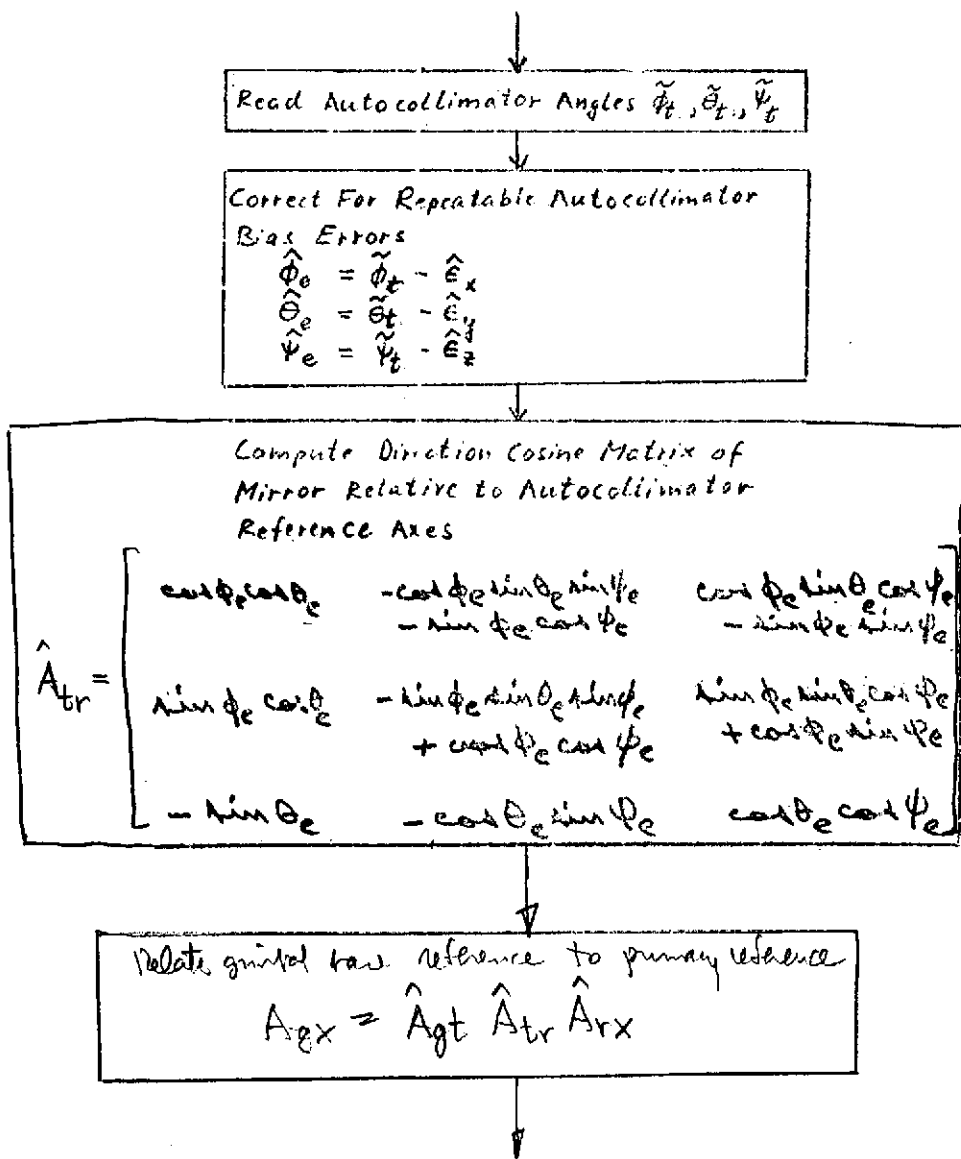
Figure 7-12. Algorithms/Flow for Alignment Reference Module (Block 24)
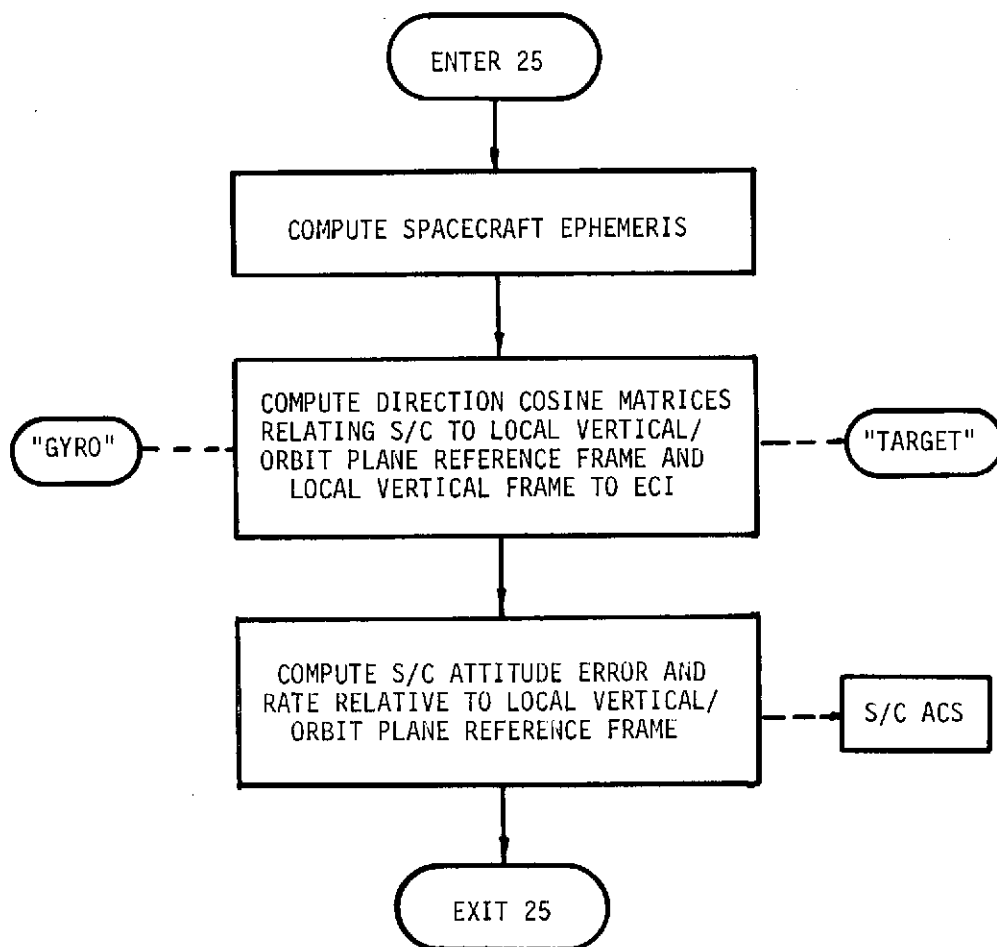
Figure 7-13. Functional Block Diagram, Block 25

From S/C Ephemeris Determination
Position (ECI): x, y, z
Velocity (ECI): $\dot{x}, \dot{y}, \dot{z}$

$$r = (x^2 + y^2 + z^2)^{1/2} \quad ; \quad v = (\dot{x}^2 + \dot{y}^2 + \dot{z}^2)^{1/2}$$

$$f = [(y\dot{z} - z\dot{y})^2 + (x\dot{z} - z\dot{x})^2 + (x\dot{y} - y\dot{x})^2]^{1/2}$$

$$A_{yz} = \begin{bmatrix} a_{11} & a_{12} & a_{13} \\ a_{21} & a_{22} & a_{23} \\ a_{31} & a_{32} & a_{33} \end{bmatrix}$$

where:

$$a_{11} = x/r \quad ; \quad a_{12} = y/r \quad ; \quad a_{13} = z/r$$

$$a_{31} = \frac{y\dot{z} - z\dot{y}}{f} \quad ; \quad a_{32} = \frac{x\dot{z} - z\dot{x}}{f} \quad ; \quad a_{33} = \frac{x\dot{y} - y\dot{x}}{f}$$

$$a_{21} = a_{32}a_{13} - a_{33}a_{12} \quad ; \quad a_{22} = a_{31}a_{13} - a_{33}a_{11} \quad ; \quad a_{23} = a_{31}a_{12} - a_{32}a_{11}$$

$$A_{xy} = A_{xz} A_{yz}^T$$

Compute "small-angle" attitude error and rate

$$\phi = a_{xy23}$$

$$\theta = a_{xy13}$$

$$\psi = a_{xy12}$$

$$\hat{\omega}_{xy} = \hat{\omega} - A_{xy} \begin{bmatrix} 0 \\ v/r \\ 0 \end{bmatrix}$$

Figure 7-14. Algorithms/Flow for Heading Reference Module (Block 25)

7.2.6 Targeting (Block 31)

The function of this module is to establish the target vectors for the experiment platforms and antenna. Target coordinates are operated upon to determine target vectors defined from the spacecraft to the target in gimbal base coordinates. The block diagram of this module is shown in Figure 7-15. The functions include:

- Experiment target selection and platform allocation (Block 311)
- Compute elements of target vectors w/r ECI frame (Blocks 312, 313)
- Compute target coordinates in nominal gimbal base axes (Block 314)
- Data relay satellite selection and computation of relay satellite ephemeris (Block 315)
- Establish data relay satellite target vector (Block 316).

The required algorithms are summarized in Figure 7-16, where the equations shown are taken from the derivation of Section 3.0.

7.2.7 Steering (Block 32)

The function of this module is to establish the steering commands for the experiment platforms and antenna. The block diagram of this module is shown in Figure 7-17. The functions to be performed include:

- Compute experiment platform gimbal angle and rate commands
- Compute antenna gimbal angle and rate commands

The required algorithms are summarized in Figure 7-18, where the equations shown are taken from the derivation of Section 3.0.

7.2.8 Data Base

The data base is comprised of initial constants and data values in natural engineering units. This data is stored prior to launch and can be updated by the ground. Included are ephemeris data, star catalog, target data, and calibration/compensation parameters.

- Ephemeris - Data from which to compute the spacecraft ephemeris must be available on-board at all times.

- Star Catalog - The star catalog stores the ECI coordinates of the stars employed for attitude determination. Since the total number of stars employed will not be excessive, the entire catalog may be committed to memory (as opposed to including only "available" stars, with occasional updating as the geometry changes).

- Target Data - Data for experiment pointing and antenna pointing requires storage. Time-tagged target coordinates (latitude, longitude, radius) will be stored for experiment pointing, and ephemeris data for three data-relay satellites will be stored for antenna pointing.

- Calibration parameters - Storage is required for parameters updated from the ground.
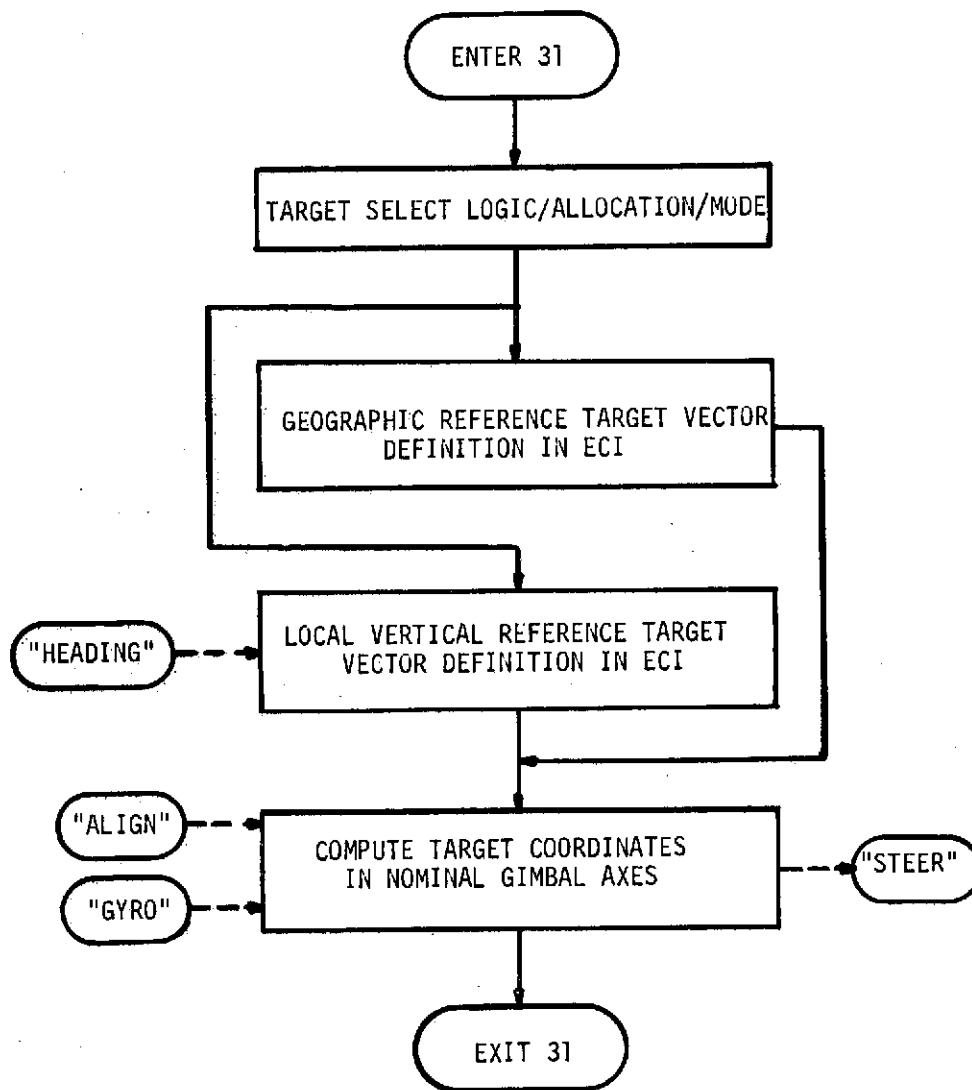
Figure 7-15. Functional Block Diagram, Block 31
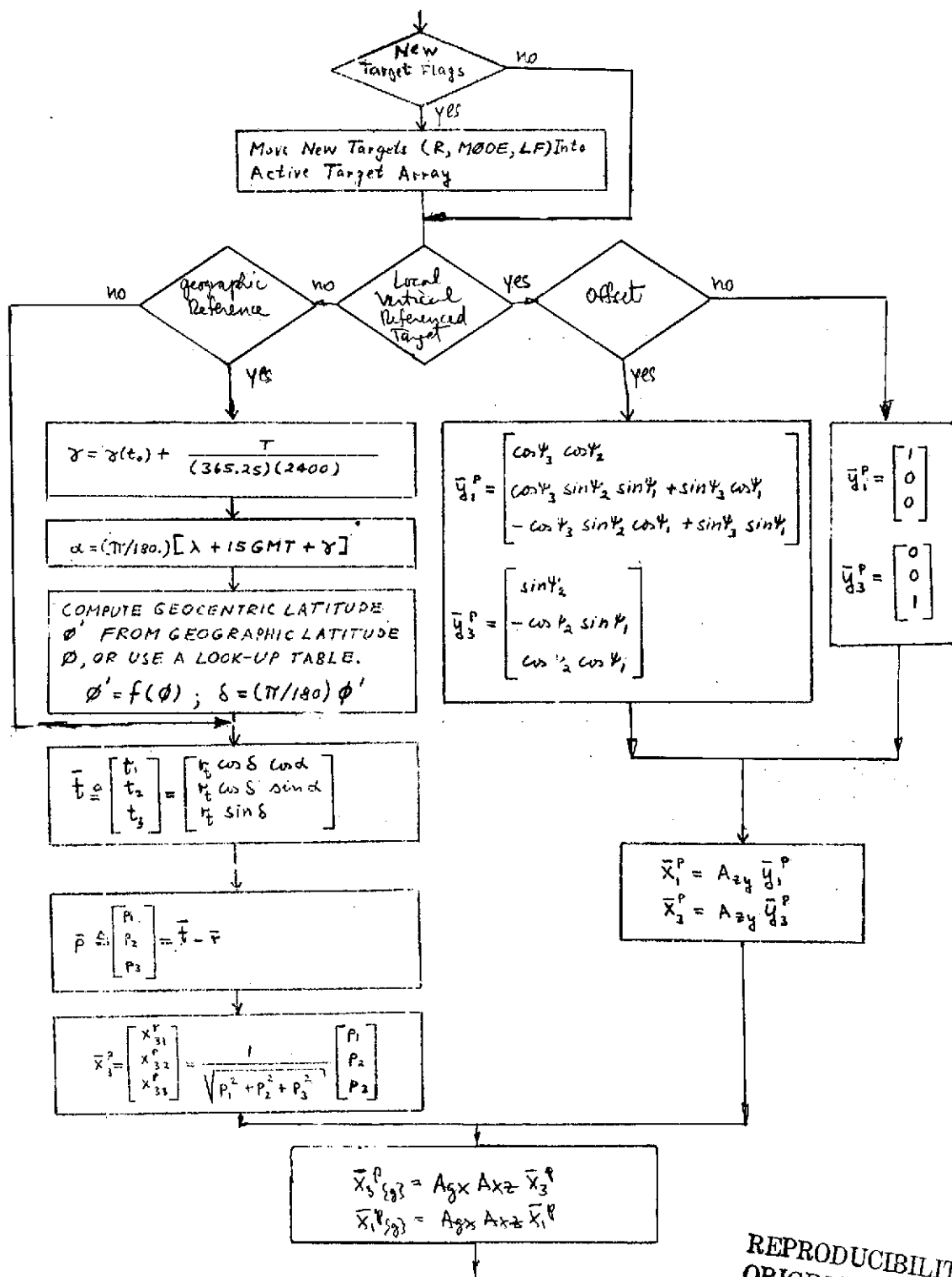
Figure 7-16. Algorithms/Flow for Targeting Module (Block 31)

```
                        ╭─────────────╮
                        │   ENTER 32   │
                        ╰──────┬──────╯
                               │
         ┌─────────────────────┤
         │      ┌──────────────▼──────────────────────┐
  ╭──────────╮  │  COMPUTE GIMBAL ANGLES FOR LOCAL     │────┐
  │ "TARGET" │--▶│ VERTICAL REFERENCED TARGETS (3 DOF) │    │
  ╰──────────╯  └────────────────────────────────────┘    │
         │                                                  │
         │      ┌─────────────────────────────────────┐    │
  ╭──────────╮  │  COMPUTE GIMBAL ANGLES FOR LINE-     │    │
  │ "TARGET" │--▶│  OF-SIGHT ONLY POINTING (2 DOF)     │    │
  ╰──────────╯  └──────────────┬──────────────────────┘    │
                               │◀──────────────────────────┘
                ┌──────────────▼──────────────────────┐   ┌──┐
                │                                      │--▶│EEA│
                │     COMPUTE GIMBAL ANGLE COMMANDS    │   └──┘
                │                                      │--▶│AEA│
                └──────────────┬──────────────────────┘   └──┘
                        ╭──────▼──────╮
                        │   EXIT 32    │
                        ╰─────────────╯
```
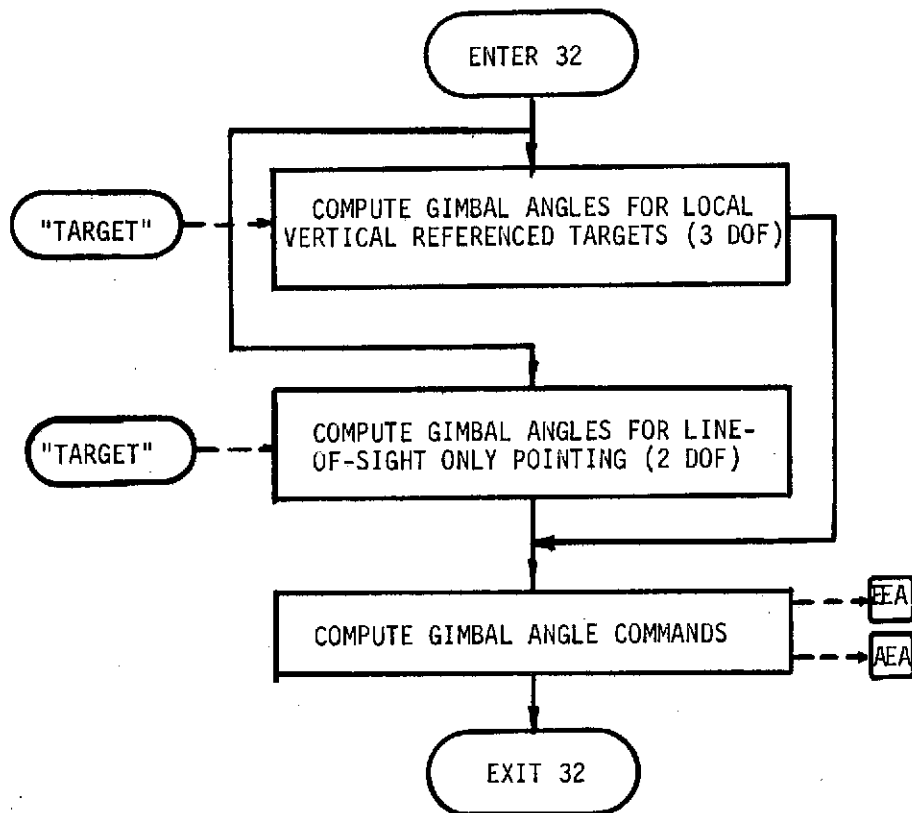
Figure 7-17. Functional Block Diagram, Block 32

INITIALIZE:
NTHETA = 0
NPHI = 0

LOS Pointing Only — no / yes

COMPUTE NOMINAL GIMBAL ANGLES

$$\psi_n = tan^{-1}\left(\frac{w_2}{w_1}\right)$$

$$\theta_n = tan^{-1}\left(\frac{-w_3}{(w_1/\cos\psi_n)}\right)$$

$$\phi_n = tan^{-1}\left(\frac{u_1\sin\psi_n - u_2\cos\psi_n}{(u_3/\cos\theta_n)}\right)$$

$|\theta_n| \leq \frac{\pi}{2}$? — Yes

No

NTHETA = 1

$|\phi_n| \leq \frac{\pi}{2}$?

NPHI = 1

Correct For Observable Experiment Misal.

$$\begin{bmatrix} a_1 \\ a_2 \\ a_3 \end{bmatrix} = \begin{bmatrix} w_1 \\ w_2 \\ w_3 \end{bmatrix} + \alpha_{e3}\begin{bmatrix} u_1 \\ u_2 \\ u_3 \end{bmatrix}$$

$$\begin{bmatrix} b_1 \\ b_2 \\ b_3 \end{bmatrix} = \begin{bmatrix} u_1 \\ u_2 \\ u_3 \end{bmatrix} - \alpha_{e3}\begin{bmatrix} w_1 \\ w_2 \\ w_3 \end{bmatrix}$$

$$\theta = \sin^{-1}(-a_3)$$

NTHETA = 1 ? — No

Yes

$$\theta = (\pi - |\theta|)\,sgn(\theta)$$

$$\psi = tan^{-1}\left(\frac{a_2 - a_1(\alpha_{m1}\tan\theta + \alpha_{\ell3}/\cos\theta)}{a_1 + a_2(\alpha_{m1}\tan\theta + \alpha_{\ell3}/\cos\theta)}\right)$$

$$\phi = \sin^{-1}(b_1\sin\psi - b_2\cos\psi - \alpha_{m1}b_3)$$

NPHI = 1 ? — No

Yes

$$\phi = (\pi - |\phi|)\,sgn(\phi)$$

$$\psi_{gc} = \psi + \epsilon_{e3}$$
$$\theta_{gc} = \theta - \alpha_{\ell2} + \epsilon_{e2}$$
$$\phi_{gc} = \phi - \alpha_{e1} + \epsilon_{e1}$$

Compute Nominal Gimbal Angles, LOS Pointing Only

$$\theta_n = tan^{-1}\left(\frac{u_1}{u_3}\right)$$

$$\phi_n = tan^{-1}\left(\frac{-u_2}{(u_3/\cos\theta_n)}\right)$$

$|\phi_n| \leq \frac{\pi}{2}$? — Yes

No

NPHI = 1

$$\begin{bmatrix} \tilde{u}_1 \\ \tilde{u}_2 \\ \tilde{u}_3 \end{bmatrix} = \begin{bmatrix} u_1 \\ u_2 + \alpha_{m1}u_3 \\ u_3 - \alpha_{m1}u_2 \end{bmatrix}$$

$$\phi = \sin^{-1}(-\tilde{u}_2)$$

NPHI = 1 ? — No

Yes

$$\phi = (\pi - |\phi|)\,sgn(\phi)$$

$$\theta = tan^{-1}\left(\frac{\tilde{u}_1 - \tilde{u}_3(\alpha_{\ell3}\tan\phi + \alpha_{e2}/\cos\phi)}{\tilde{u}_3 + \tilde{u}_1(\alpha_{\ell3}\tan\phi + \alpha_{e2}/\cos\phi)}\right)$$

$$\psi_{gc} = 0$$
$$\theta_{gc} = \theta - \alpha_{\ell2} + \epsilon_{e2}$$
$$\phi_{gc} = \phi - \alpha_{e1} + \epsilon_{e1}$$

By Definition The LOS Vector $\bar{x}_3^p$ And The Yaw Cond. Vector $\bar{x}_1^p$ Are Given In Tens Gimbal Base Coordinates As
$$\bar{x}_3^p \triangleq (u_1, u_2, u_3)^T$$
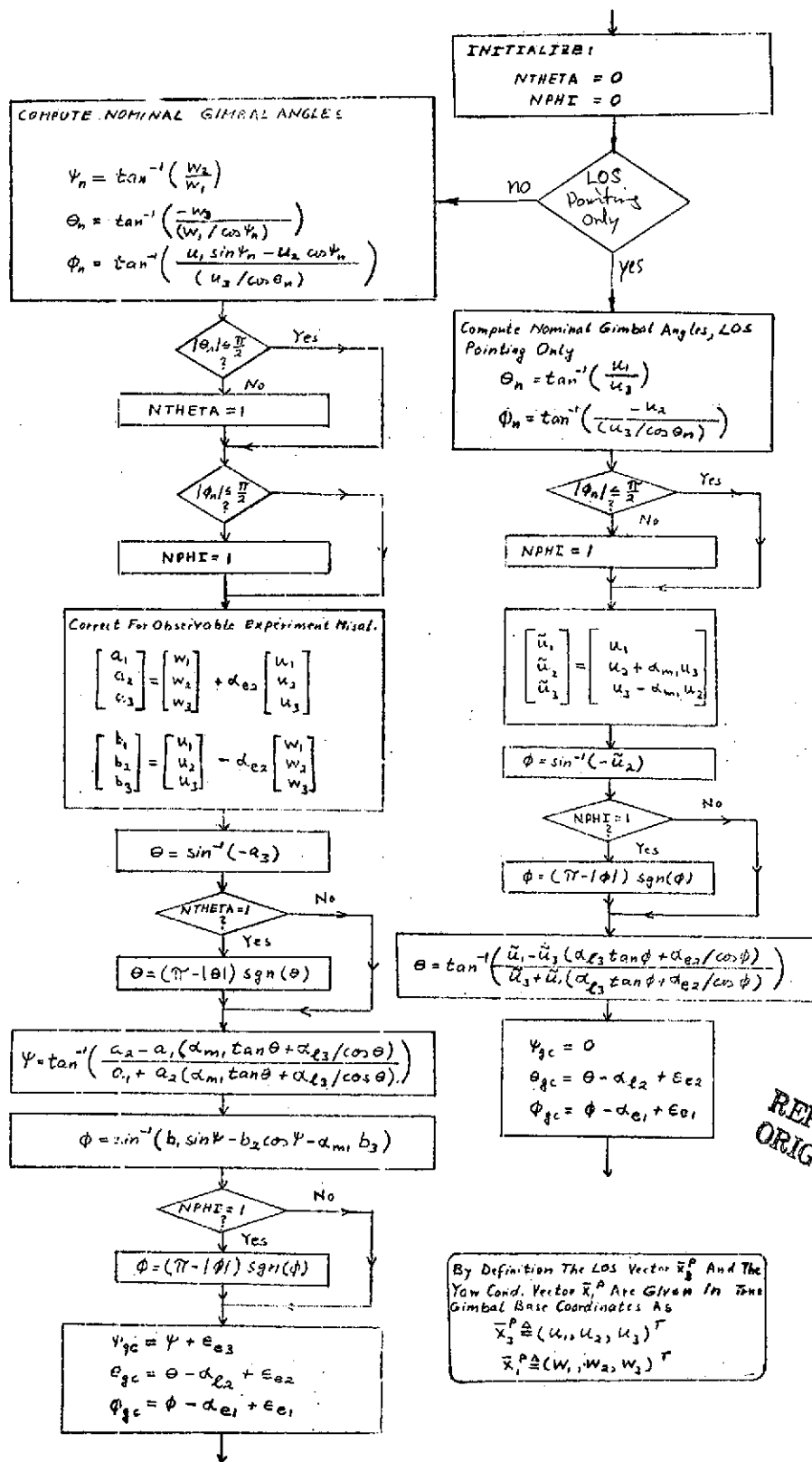$$\bar{x}_1^p \triangleq (w_1, w_2, w_3)^T$$

Figure 7-18. Algorithms/Flow for Steering Module (Block 32)

7.3 COMPUTATIONAL REQUIREMENTS

The PPCS computational requirements were developed by sizing the memory and speed for the functions and algorithms presented in the preceding section. Basic to this sizing and timing analysis are a number of assumptions, namely:

- Word length assumed adequate to perform all computations in single precision

- An instruction repertoire sufficiently flexible and sophisticated to execute given functions with a minimum of instructions.

- No penalty in timing for indexing.

- Use of the following instruction speed equivalents:

  1 multiply = 8 add times
  1 divide   = 18 add times

- All instructions other than multiply and divide are assumed to have execution times equal to an add time.

- Use of subroutines for mathematical functions, e.g., matrix operations, sine-cosine, square root, etc. Each subroutine call is assumed to take 7 instructions.

7.3.1 Memory Sizing

The memory storage requirements for instructions and data were determined. Size was computed for the application program modules through trial programming. Estimates were made for the executive program modules based upon assumed mission characteristics and past experience. Table 7-1 shows the memory requirements, which indicate a memory capacity of 8K words (PPCS DPA configuration) provides a 45% growth margin (excluding ephemeris).

7.3.2 Computational Rates

Table 7-2 summarizes the computational rates for the application program modules. For each module, the critical path was determined and used to obtain a conservative result. The number of instructions per execution is determined from the number of add, multiply, and divide operations. The frequency of execution is how many times per second the module is executed, and the (equivalent add) instructions per second is determined from multiplying the number of executed instructions by the frequency. The final total of approximately 160,000 instructions per second would require a machine with an add time of less than 4 microseconds, excluding the executive functions, to achieve a duty cycle of approximately 60% for the assumed instruction speed ratio.

Table 7-1. Memory Size Requirements

Element	Program (Words)	Data (Words)
Executive Modules		
Program Control	300	
Data Bus Control	100	
Command Processing	200	
Telemetry Processing	300	
Self-Test	300	
System Test	200	
	1400 (Estimate)	300 (Estimate)
Application Modules		
Gyro Reference	185	72
Star Reference	334	113
Filter/Update	820	110
Alignment Reference	118	42
Heading Reference	265	63
Targeting	201	42
Steering	451	81
	2374	523
Subroutines	375	
Data Base		
Star Catalog		150
Ephemeris	Not Evaluated	
Target Data		500 (Estimate, Typical)
TOTAL	4149	1473

Table 7-2. Computational Rates

Function/Module	Number of Instructions Per Execution	Frequency of Execution	Instructions Per Second
Gyro Reference	624A + 70M + 15D (= 1454A)	5/sec	7270A
Star Reference	33A + 38M + 2D (= 373A)	1/sec	373A
State Transition Matrix	457A + 64M + 3D (= 1023A)	5/sec	5115A
Filter/Update	3340A + 470M + 10D (= 7280A)	1/30 sec	243A
Alignment Reference	848A + 118M + 6D (= 1900A)	6x5/sec[1]	57000A
Heading Reference	601A + 82M + 10D (= 1437A)	5/sec	7185A
Targeting	460A + 46M + 6D (= 946A)	6x5/sec[1]	28380A
Steering	735A + 90M + 18D (= 1779A)	6x5/sec[1]	53370A

[1] Six independent experiments assumed.

8.0   NEW TECHNOLOGY

8.1   KALMAN FILTER STATE VECTOR FORMULATION

The Kalman filter devised for the PPCS attitude determination simulation employs a unique formulation of the state vector. An array of system parameters are available from which the user may construct the desired state vector at the time of data input. For example, selected gyro and/or star tracker misalignments and biases may be specified to be treated as state elements in addition to attitude. Thus, in the simplest case, the filter operates only upon the three attitude variables; in the most complex, up to 25 additional system parameters can be adjoined to the attitude in forming the filter state. Consequently, the algorithm has application in the determination of in-flight performance in which case only six states are employed; and secondly, this algorithm can be used as a ground based calibration filter employing many more states. The techniques devised to achieve such simulation flexibility are not unique to the PPCS application, but could be utilized in any application that includes constant and observable parameters as candidates for estimation.

8.2   ERROR ANALYSIS

The error analysis developed for PPCS is a unique approach for studying errors of a complex system which includes a Kalman filter. Direct addition of the error variances is not applicable since the error analysis has to handle sophisticated error models which are state dependent. A new approach which did not resort to a simulation was devised. The approach is to perform a sensitivity analysis establishing the sensitivity of the attitude determination system and the pointing angles to the system error sources. The sensitivity matrices provide then the appropriate weighting of the system error sources when the attitude determination and pointing errors are established.

Since the individual system errors are not linearly related to the attitude determination errors and the pointing errors, the derived sensitivity matrices consist of partial derivatives evaluated at the nominal, current system state.
The error model, therefore, becomes automatically a function of the state of the system (very realistic) and state dependent error models for the individual system errors can now also be easily handled. By selecting some suitable system states one can either obtain typical total system errors, or study the changes in the total system error as a function of the state.

The Kalman filter which is an important component in the attitude determination software, is handled implicitly rather than explicitly in this approach: The variances of those error quantities which are estimated by the on-board filter are attenuated by the ratio of their _a posteriori_ to _a priori_ variance as determined

by the filter in the existing (separate) dynamic simulations. Observation noise
is also attenuated.

The main advantages of this approach to the error analysis are:

(1) It is very realistic but requires no detailed dynamic
    simulation.

(2) The sensitivity matrices indicate which error sources hurt the
    system performance the most and where it is therefore most
    worthwhile to improve the system.

(3) State dependence of the total system errors can be studied and
    state dependence of individual error sources can be modeled.

(4) Because of item (3), the error analysis can be used to study
    the effects of increasing or decreasing the time between
    star tracker attitude updates. The effects of star location
    on the accuracy of the system can also be studied

9.0 REFERENCES

1. Cantor, C., _A Spacecraft Concept for the Unified Space Application Mission_, NASA Goddard Space Flight Center, Greenbelt, Maryland, NASA Report X-732-68-404, October 1968.

2. Frew, A. M., Kirby, D. K., Wheeler, P. C., _Preliminary Technical Report PPCS Functional Design, Analysis, and Error Analysis_, TRW Report 13900-6002-R0-00, 25 May 1970.

3. Farrenkopf, R. L., Frew, A. M., Haack, A. F., Iwens, R. P., Mann, R. J., _Interim Technical Report, PPCS Functional Design and Analysis_, TRW Report 13900-6007-R0-00, 25 August 1970.

4. Iwens, R. P., _Interim Technical Report, PPCS Error Analysis_, TRW Report 13900-6008-R0-00, 25 August 1970.

5. Kirby, D. K., _Preliminary Technical Report, PPCS Reliability_, TRW Report 13900-6010-R0-00, 25 September 1970.

6. Farrenkopf, R. L., _Preliminary Technical Report, Attitude Reference Simulation Development for PPCS_, TRW Report 13900-6003-R0-00, 25 June 1970.

7. Iwens, R. P., _Preliminary Technical Report, PPCS Pointing Simulation Development_, TRW Report 13900-6004-R0-00, 25 June 1970.

8. Belsky, F. J., _Preliminary Technical Report, Attitude Reference Simulation User's Manual_, TRW Report 13900-6005-R0-00, 25 June 1970.

9. Belsky, F. J., _Preliminary Technical Report, PPCS Pointing Simulation User's Manual_, TRW Report 13900-6006-R0-00, 25 June 1970.

10. Frew, A. M., Iwens, R. P., _Interim Technical Report, PPCS Simulations_, TRW Report 13900-6009-R0-00, 25 September 1970.

11. Farrenkopf, R. L., Frew, A. M., and Iwens, R. P., _Final Technical Report, PPCS Simulations_, TRW Report 13900-6013-R0-00.

12. Gates, R. F., Haack, A. F., Hughes, G. C., Mann, R. J., Tsou, H. S., Tsusaki, W., Zaremba, J. G., _Final Technical Report, PPCS Engineering Model Design_, TRW Report 13900-6011-R0-01, 7 July 1971.

13. Davis, W. R., (U) _Space Precision Attitude Reference System (SPARS)_, Phase IA Final Report, SAMSO TR-69-72, SECRET, February, 1969.

14. Davis, W. R., (U) _Precision Earth Pointing System (PEPSY), Phase IA Final Report_, SECRET, December 1970.

15. _Precision Attitude Determination System Final Report_, TRW Report 13900-6014-R0-00.

16. Collyer, P. W., et. al., _Final Report, Attitude Transfer Subsystem for the Precision Pointing Control System_, Barnes Engineering Company, December, 1970.

17. Tsou, H. S., Spencer, D. S., _Study and Preliminary Design of A Data Processing Subsystem for the Precision Pointing Control System_, TRW 7351.17-152, 11 February 1971.

18. Final Report, [Boom Design for] Unified Space Application Mission, Fairchild-Hiller Report 632-FR-090-009.

19. American Ephemeris and Nautical Almanac.

20. Zaremba, J. G., Life Test of PPCS Gimbal Suspension, PPCS Note 255, 21 December 1971.